Improved models of the human neurovascular unit

By

Benjamin D. Gastfriend

A dissertation submitted in partial fulfillment of

the requirements for the degree of

Doctor of Philosophy

(Chemical Engineering)

at the

UNIVERSITY OF WISCONSIN–MADISON

2022

Date of final oral examination: May 9, 2022

This dissertation is approved by the following members of the Final Oral Committee:

Sean P. Palecek, Professor, Chemical and Biological Engineering
Eric V. Shusta, Professor, Chemical and Biological Engineering
Regina M. Murphy, Professor, Chemical and Biological Engineering
Brian F. Pfleger, Professor, Chemical and Biological Engineering
John Svaren, Professor, Comparative Biosciences

Improved models of the human neurovascular unit

By
Benjamin D. Gastfriend

Under the supervision of Professors Sean P. Palecek and Eric V. Shusta
At the University of Wisconsin–Madison

Abstract

The neurovascular unit (NVU) is a concept that links the functions of the central nervous system (CNS) to the specialized properties of its blood vasculature. The NVU and the associated blood-brain barrier (BBB) represent an important conduit for CNS drug delivery and a potential therapeutic target in some CNS disorders. Knowledge of the molecular and cellular bases of human NVU development and function, which would facilitate such approaches, remains limited. In this work, we sought to better understand molecular mechanisms regulating the development of the NVU through the generation of new human pluripotent stem cell (hPSC)-derived models of NVU cell types, and by analysis of human NVU cells *in vivo*.

We first focused on better understanding mechanisms of BBB development (Chapter 3). CNS endothelial cells form the BBB and acquire their specialized properties through interactions with neural tissue during development; the Wnt/β-catenin signaling pathway mediates many aspects of this process of barriergenesis *in vivo*. We therefore tested the hypothesis that Wnt activation in hPSC-derived naïve endothelial progenitors would yield endothelium with BBB-like properties. Pharmacological activation of Wnt signaling led to acquisition of several canonical BBB properties, and comparison to existing *in vivo* and *in vitro* data revealed important context-dependent effects of Wnt activation in endothelial cells. This model should be useful to further interrogate endothelial barriergenesis.

We next sought to obtain a more precise molecular profile of human brain mural cells (Chapter 4). Mural cells, including pericytes and vascular smooth muscle cells, dynamically regulate vascular tone and are required for BBB development and maintenance. We integrated human brain single cell RNA-sequencing data from five independent studies to generate a consensus transcriptome profile of mural cells *in vivo*. We used the resulting dataset to reveal species differences in mural cell gene expression, profile transcriptional dysregulation underlying the *in vitro* dedifferentiation of brain pericytes, and identify genes enriched in brain mural cells compared to those of other organs. These results should therefore inform future functional studies and serve as a key resource in evaluating animal and *in vitro* models.

Finally, we investigated molecular mechanisms of brain mural cell differentiation from neural crest, the progenitor of forebrain mesenchyme (Chapter 5). Compared to the *in vivo* human mural cell transcriptome profile, we found that existing *in vitro* models of brain mural cells had markedly lower expression of *NOTCH3*, Notch target genes, and other mural cell transcription factors. Animal studies have demonstrated that Notch signaling is required for mural cell emergence; we asked whether Notch activation in hPSC-derived neural crest would be sufficient to induce mural cell differentiation. Overexpression of the Notch3 intracellular domain led to rapid upregulation of canonical mural cell transcription factors and the resulting cells had molecular and functional attributes of brain mural cells.

Acknowledgements

I am indebted foremost to my advisors, Professors Sean Palecek and Eric Shusta, who guided me in my development as an independent scientist and who allowed me considerable latitude to design and conduct research projects interesting to me. I also gratefully acknowledge the additional members of the committee, Professors Regina Murphy, Brian Pfleger, and John Svaren, who provided valuable feedback and advice.

I am also grateful to the senior members of the Palecek and Shusta research groups who trained and mentored me upon joining the lab: Drs. Matthew Stebbins, Scott Canfield, and Brandon Kim. I also wish to thank Drs. Stebbins, Canfield, and Kim, along with Drs. Angélica de Lourdes Rodríguez-López, Hannah Wilson Song, Julia Georgieva, Loukas Goulatis, and Zhou Ye, for advice on my work and for the opportunity to contribute collaboratively to their research. I am indebted to Koji Foreman and Dr. Moriah Katt, who assisted me in my research projects and made important experimental and intellectual contributions to the work presented in Chapter 3 and Chapter 4. I also am extremely grateful to Margaret Snyder, an undergraduate researcher who worked tirelessly with me on the project presented in Chapter 5. I also wish to acknowledge the many additional graduate students and postdoctoral researchers who provided me advice and assistance: Dr. Chandler Est, Elizabeth Waters, Dr. Suehelay Acevedo-Acevedo, Dr. Kaitlin Dunn, Dr. Benjamin Umlauf, Dr. Gyuhyung Jin, Aaron Simmons, Dr. Martha Floy, and Yunfeng (Bill) Ding.

I was privileged to participate in several collaborative research projects with scientists from other institutions. I gratefully acknowledge our collaborators Professor Britta Engelhardt and Dr. Hideaki Nishihara (Theodor Kocher Institute, University of Bern) and Professor Richard Daneman (University of California, San Diego).

Finally, I thank my parents, who instilled in me the importance of education; to them I dedicate this thesis. I thank my brother, grandparents, and extended family for their support and encouragement.

Table of contents

List of figures

List of tables

Chapter 1 Neurovascular unit development, function, and model systems

1.1 Summary

The neurovascular unit (NVU) comprises vascular cells (endothelial and mural) and parenchymal cells (neurons and glia) in the central nervous system (CNS) (Figure 1.1). The concept of the NVU emerged from increasing appreciation that the functions of CNS blood vessels are tightly, dynamically, and bidirectionally linked to the functions of neurons and glia (*1*). In this chapter, I will discuss our broad motivations for studying the NVU, which include its role as a contributor to neurological disorders and its potential use as a conduit for CNS drug delivery. I will review the structure, function, and development of the NVU, and highlight key topics where our knowledge is incomplete. Finally, I will summarize model systems commonly used for studies of the NVU and highlight the need for improved models of the human NVU.

1.2 Motivation

Neurological disorders are a leading cause of death and disability globally, and continue to increase in prevalence (*2*). In 2016, neurological disorders caused 276 million disability-adjusted life years (DALYs; years of life lost plus years lived with disability), the most of any disease group, and 9 million deaths, the second most of any disease group after cardiovascular diseases (*2*). These neurological disorders, in decreasing order of global DALYs, include stroke, migraine, Alzheimer's disease and other dementias, meningitis, epilepsy, spinal cord injury, traumatic brain injury, brain and other CNS cancer, tension-type headache, encephalitis, Parkinson's disease, other neurological disorders, tetanus, multiple sclerosis, and motor neuron diseases (*2*). Notably, risk factors quantified in the Global Burden of Diseases, Injuries, and Risk Factors Study fail to explain 90% of neurological disorder-associated DALYs, leading the

authors to conclude that “the scarcity of established modifiable risks for most of the neurological burden demonstrates that new knowledge is required to develop effective prevention and treatment strategies” (*2*). Further, there are very few disease-modifying treatments for neurological disorders (*3*) because of impediments to drug delivery, gaps in understanding of disease causes, and gaps in understanding of normal CNS development and function. In this context, study of the NVU is strongly motivated based on its unique position as both (i) a route for CNS drug delivery, and (ii) a cause or contributor to neurological disorders. Specifically:

(i) Blood vasculature evolved for efficient delivery of molecules to tissues. Thus, the CNS vasculature represents a promising route for drug delivery, linking the systemic circulation, which is accessible for drug administration, to the entire volume of the CNS via its high-density capillary network (*4–6*). Target cells are in close proximity to vessels: in the hippocampus, each neuron is only 8–20 μm from the nearest capillary (*7*). Other routes of drug administration partially bypass the impediments of the blood-brain barrier discussed below, but suffer from other drawbacks such as diffusion-limited transport and invasiveness (*8*). Additional knowledge of the NVU, however, is needed to overcome obstacles to transvascular transport. For example, better understanding of physiological mechanisms of molecular transport may allow these processes to be coopted as drug delivery systems (*9*, *10*).

(ii) Proper function of the NVU is compromised in several neurological disorders. For example, in multiple sclerosis, abnormally high numbers of circulating immune cells are able to enter the CNS from the blood (*11–14*). In Alzheimer’s disease, impaired brain-to-blood clearance of the neurotoxic amyloid-β peptide and decreased perfusion have been observed (*15–21*). In stroke, loss of perfusion

results in rapid neuronal death followed by a spatially and temporally complex process of blood-brain barrier breakdown (*22–25*). Concomitantly, mural cells constrict capillaries and/or die, impairing reperfusion (*26*, *27*). Indeed, strategies promoting mural cell survival in stroke have shown beneficial effects in preclinical models (*28*, *29*). Thus, in addition to serving as a potential route for drug delivery, the NVU is itself a therapeutic target. Additional mechanistic understanding of NVU dysfunction, however, is prerequisite. Further, better understanding of molecular mechanisms of normal NVU development and function is foundational for eventual molecular targeting of the NVU in disease. For example, activation of molecular pathways involved in development has been suggested as a potential strategy to restore function in disease (*30*, *31*).

1.3 Neurovascular unit function

The brain consumes energy at a rate disproportionately larger than its fraction of body mass; of the major organs, it has the third-highest specific metabolic rate (*32*, *33*). Yet the brain requires a precisely controlled extracellular environment for proper electrochemical functioning of neurons. Further, the vertebrate CNS is complex and regionalized, with energetic demands varying widely in location and time. These requirements appear difficult to reconcile: the obvious strategy for fast delivery of energy substrates and fast removal of waste products is a high-permeability vasculature. Such a system, however, would also directly transmit perturbations in blood composition, both physiological (e.g., after a meal) and pathological (e.g., toxins, pathogens), to the parenchymal compartment, and would do so uniformly, without robust spatial or temporal control. Thus, the NVU evolved to (i) efficiently deliver necessary molecules to the CNS and remove wastes, while excluding unnecessary and potentially toxic blood components, and (ii) target energy substrates to active regions. These objectives are

accomplished by the blood-brain barrier (BBB) and neurovascular coupling. Minimally, the NVU consists of endothelial cells, which form blood vessels, mural cells (pericytes and vascular smooth muscle cells, VSMCs), which line the outer surface of vessels, neurons, and astrocytes (Figure 1.1), and in some contexts, may also include oligodendrocytes, microglia, neural stem/progenitor cells, and perivascular fibroblast-like cells.

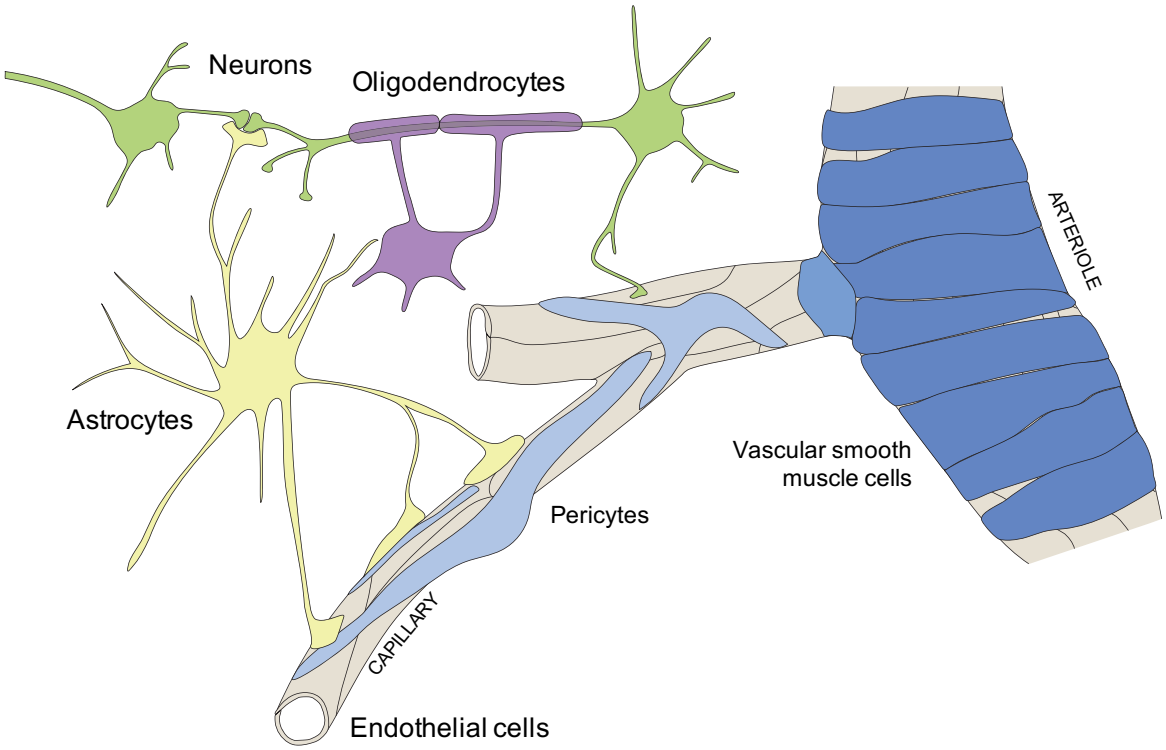

Figure 1.1. Schematic of the neurovascular unit.

1.3.1 The blood-brain barrier

Many substances injected into the blood are virtually excluded from the brain while penetrating other organs. This phenomenon was demonstrated as early as 1695, when Ridley observed a lack of brain penetration of wax and mercury injected into the vasculature of cadavers (*34*, *35*). In 1885, while investigating oxygenation of various organs in cats and rabbits using

intravenous, intraarterial, and subcutaneous injections of dyes (Alizarin blue and cerulein), Erhlich observed absence of dyes in the brain, which contrasted with varying levels of dye penetration in other organs (*36*). Goldmann found that, conversely, dye injected into the brain did not reach other organs (*37*). Lewandowsky performed functional analogues of these dye localization experiments by injecting toxins (sodium ferrocyanide and strychnine) and monitoring animals for convulsions: injections of either toxin into the subarachnoid space of the CNS produced immediate effects, while subcutaneous injections of sodium ferrocyanide were without effect, and strychnine produced more mild effects (*38*). Summarizing his conclusions, Lewandowsky wrote:

> So we must conclude that upon introduction into the bloodstream not even a hundredth of the sodium ferrocyanide penetrates the gray matter cells. […] Nevertheless, it cannot be said that the cells of the gray matter lack affinity for sodium ferrocyanide, for we saw how energetically it acts if we deliver it into the cerebrospinal fluid. This contradiction can hardly be explained in any other way than by the hypothesis that the capillary wall prevents the transfer of certain substances, such as sodium ferrocyanide, or, in other words, that the capillary cells of the central nervous system need an affinity for certain substances for them to get through and reach the nerve cells. This affinity is certainly not a purely physical one, such as that of holding back large molecules and allowing small ones to pass through, but a chemical one. Such an affinity apparently exists with regard to strychnine […]* (*38*)

Thus, Lewandowksy established the foundation for the existence of a BBB formed by the CNS vasculature. Importantly, based on the differential effects of systemic administration of two

*Translated from the original German

similarly-sized toxins*, he also noted that the BBB is *selectively* permeable and that molecular ("chemical") properties, coupled with the properties of the vasculature (the "affinity" of the capillary cells), must govern this permeability.

Later electron microscopy studies allowed more precise localization of the BBB: Using intravenous injections of horseradish peroxidase (HRP) into mice, Reese and Karnovsky demonstrated that the HRP reaction product did not penetrate beyond the tight junctions of brain endothelial cells (ECs) (*39*). They also observed an extremely low number of vesicles in brain endothelial cells (*39*) compared to the abundant vesicles present in ECs of other organs (*40*). Brightman and Reese further demonstrated that endothelial tight junctions occluded HRP from entering blood vessels when injected into the cerebrospinal fluid-containing ventricles in mice (*41*). These observations provided early evidence that the low permeability of the brain—the BBB—is a result of specialized properties of CNS ECs (Figure 1.2). These findings also showed that low vascular permeability is not attributable to the glia limitans of the astrocyte endfeet, as some had proposed (*42*), although astrocyte endfeet, vascular basement membrane, and glycocalyx likely contribute resistance to transport of some solutes (*43*, *44*). The requirement for a cellular barrier to achieve specialized control of the neural microenvironment is evolutionarily conserved, but is achieved by different cell types in other organisms: for example, in lower vertebrates, the barrier is indeed formed by perivascular glia and not endothelial cells (*45*), and in *Drosophila*, which have an open circulatory system and lack blood *per se,* subperineurial glia form a hemolymph-brain barrier (*46–48*).

Blood-brain barrier properties are also present in the spinal cord vasculature and retinal vasculature (the blood-retinal barrier) (*49*, *50*). While some differences in molecular and functional properties of ECs between these different regions of the CNS are known and more are

*ferrocyanide: 212 Da; strychnine: 334 Da

likely to be uncovered, the general properties discussed in this section are common across these regions.

1.3.1.1 Tight junctions

Tight junctions seal the paracellular space between BBB ECs. Endothelial bicellular tight junctions are formed by the transmembrane proteins occludin and claudin-5, which are linked to the cytoskeleton via the intracellular proteins zonula occludens 1 and 2 (ZO-1 and ZO-2) (*51–53*). Indeed, claudin-5 knockout mice exhibit increased BBB permeability to low molecular weight tracers (*51*), and claudin-5 appears to be the only claudin highly expressed at the BBB and necessary for tight junction function (*54–56*). While all ECs express claudin-5, CNS ECs exhibit moderately elevated expression of claudin-5, substantially elevated expression of occludin, and CNS-specific expression of tricellular tight junction components discussed below, all factors that likely contribute to the low permeability of the BBB compared to other vascular beds (*53*, *56*). Additionally, CNS EC tight junctions are highly abundant, highly complex, and intermixed with the endothelial adherens junctions formed by VE-cadherin, which span the entire length of the endothelial cleft (*57–59*) (Figure 1.2). CNS ECs also possess tricellular tight junctions, which seal the points at which three bicellular tight junctions meet; these tricellular tight junctions, formed by LSR (angulin-1), and tricellulin, are characteristic of epithelial cells and not found in non-CNS endothelium (*60–62*). Similar to claudin-5 knockout mice, LSR knockout mice exhibit increased BBB permeability to low molecular weight tracer (*62*).

1.3.1.2 Vesicle trafficking

The endothelial cells of most organs have abundant vesicles formed predominantly from caveolae (caveolin-coated invaginations of lipid-rich regions of cell membrane), and many also have fenestrae (transcellular pores of 60–80 nm diameter) (*63*). The absence of fenestrae and extremely low abundance of vesicles in CNS ECs contrasts with other endothelial cells (*39*, *40*,

64), where these organelles facilitate transcellular transport of fluid and solutes. This transcellular pathway is especially important for transport of macromolecules that are excluded

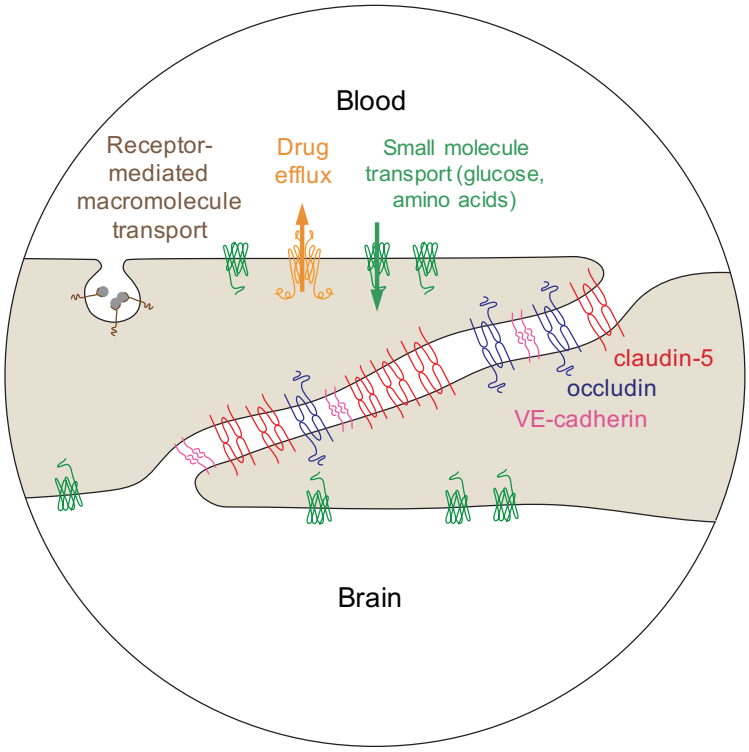

Figure 1.2. Schematic of the blood-brain barrier. Endothelial cell shown in tan.

from the paracellular pathway due to size. Expression of key molecular components of caveolae, including caveolin-1, caveolin-2, and Cavin2, is much lower in CNS versus non-CNS endothelium (*56*, *65*); plasmalemma vesicle-associated protein (PLVAP; also known as Meca32), a structural component of both caveolar and fenestral diaphragms, is undetectable in CNS ECs despite abundant expression in non-CNS ECs and its use as one of the first endothelial cell markers (*56*, *63*, *65–68*). Notably, in the ECs of most circumventricular organs (CVOs), the choroid plexuses, choriocapillaris, and ciliary body, which are regions of the CNS with high

permeability vasculatures that facilitate the secretory and sensory (sampling of blood composition) functions of these regions (*69*, *70*), PLVAP is highly expressed (*71*).

1.3.1.3 Efflux transport

Efflux transporters are an additional mechanism that serves to limit transcellular transport of molecules across the BBB. These ATP binding cassette (ABC) transporters are transmembrane proteins preferentially localized to the apical EC surface; they use ATP to pump small, usually blood-derived, membrane-soluble molecules against their concentration gradients (i.e., back into the blood) (*72*, *73*), although there are emerging examples of efflux transporter-mediated clearance of CNS-derived solutes (*74*). In addition to lipids, steroids, nucleosides, cholesterol, peptides, and toxins, many drugs are substrates for efflux transporters, leading to the original identification of efflux transporters, including P-glycoprotein (P-gp, also known as Mdr1a and ABCB1), Multidrug Resistance Proteins (MRPs, also known as ABCC family members), and Breast Cancer Resistance Protein (BCRP, also known as ABCG2), as the mechanism of the multidrug resistance (MDR) phenotype frequently observed in cancers (*75–78*). Indeed, multiple ABC transporters are expressed by CNS ECs: P-gp is highly expressed and enriched compared to other ECs (*56*, *79*, *80*), and P-gp (Mdr1a) knockout mice exhibit marked increases in BBB permeability to multiple drugs (*81*). BCRP is broadly expressed by ECs in multiple organs, but enriched at the BBB (*65*, *82*, *83*). In the MRP family, MRP-4 (ABCC4) is highly expressed and enriched in CNS ECs (*83*, *84*). The failure of numerous small molecule drugs to achieve clinically-relevant brain penetrance can be partially attributed to efflux transporters (*85–87*), and species differences in efflux transporter expression also confound efforts to translate results from animal experiments to clinical studies (*88–90*).

1.3.1.4 Immune surveillance

The CNS also has "immune privilege," a phenomenon defined by lack of immune rejection of tissue grafts (*91*). Early evidence of this phenomenon was provided by Shirai, who observed rapid growth of rat sarcoma transplanted into the brain of mouse and rabbit, but complete absence of growth after subcutaneous transplantation (*92*). In addition to grafts, lipopolysaccharide, bacteria, and viruses introduced into the CNS do not provoke the robust immune responses observed in other tissues (*93–96*). This immune privilege is afforded by a low (but nonzero) level of CNS surveillance by peripheral immune cells. The low level of transvascular immune cell infiltration in health is conferred partially by BBB properties, which extend to postcapillary venules, the segment of the vascular tree mediating the majority of transvascular immune cell infiltration during inflammation (*95*, *96*). These properties include low expression of immune cell adhesion molecules, including ICAM-1 and VCAM-1, compared to the vasculature of other organs (*97*).

1.3.1.5 Solute carriers

BBB tight junctions, low rates of vesicle trafficking, efflux transporters, and low expression of immune cell adhesion molecules are properties that evolved to exclude unnecessary blood-derived molecules and cells from the CNS. Small lipid-soluble molecules that are not substrates for efflux transporters can diffuse across EC membranes; oxygen and carbon dioxide transport are also accomplished via this route (*98*). The BBB also has mechanisms to facilitate uptake of required substances. First, CNS ECs express numerous solute carriers (SLC transporters), most of which facilitate the uptake of specific ions and molecules from blood. Unlike ABC transporters, SLCs are not ATP-dependent; transport is driven either by the substrate concentration gradient, or by coupling substrate transport to sodium ion cotransport (*99*). The prototypical example is the glucose transporter GLUT-1, which is highly expressed at

the BBB, enriched on the apical membrane, and among the genes most highly enriched in CNS versus non-CNS endothelium (*65*, *83*, *100–102*). Notably, GLUT-1 is absent in the leaky vasculature of CVOs, with an expression pattern opposing that of PLVAP, and with a remarkably abrupt transition from GLUT-1^{+}PLVAP^{-} to GLUT-1^{-}PLVAP^{+} ECs within the same vessel extending between brain and CVO (*71*) (Figure 1.3). Other SLC transporters are expressed at the BBB and are responsible for the uptake of amino acids, lactate, nucleosides, hormones, and ions (*98*, *103–105*). Non-SLC family transport proteins are also expressed in CNS ECs. For example, the receptor Stra6 is expressed at the BBB and likely transports retinol into the CNS (*106*, *107*).

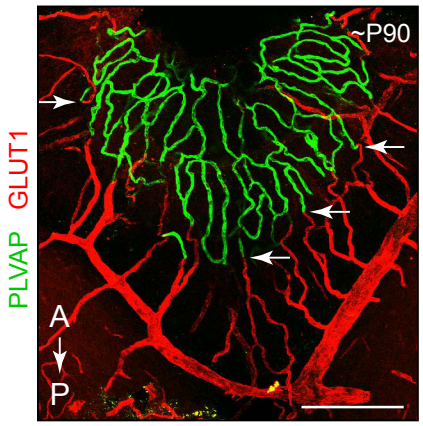

Figure 1.3. Abrupt transition between CVO and BBB vasculature. Non-BBB-forming vessels of the area postrema (GLUT-1^{-} PLVAP^{+}) and BBB-forming vessels of the surrounding hindbrain (GLUT-1^{+}PLVAP^{-}) are shown. Image from Wang *et al.*, 2019 (*71*). Used under a Creative Commons Attribution License (https://creativecommons.org/licenses/by/4.0/).

1.3.1.6 Receptor-mediated transcytosis

While the total rate of vesicle trafficking is much lower in CNS ECs compared to non-CNS ECs, this predominantly reflects a lower rate of caveolin-based, non-specific fluid-phase uptake (also referred to as pinocytosis or fluid-phase endocytosis) (*108*, *109*). CNS ECs express an array of receptors that mediate vesicular uptake and transcellular transport of specific macromolecules, in a process termed receptor-mediated transcytosis (RMT). A well-

characterized example is the transferrin receptor (TfR), with early evidence suggesting enrichment of this receptor in brain ECs compared to ECs in other tissues (*110*). Indeed, the TfR is responsible BBB uptake of iron-bound holo-transferrin (*111*, *112*), a process that occurs via clathrin-mediated endocytosis (*113*). Similarly, insulin uptake is mediated by the insulin receptor (*114*, *115*). Other receptors facilitate endocytosis of immunoglobulin (*116*), low density lipoproteins (*117*, *118*), leptin (*119*), and other substrates (reviewed in (*120*)). The BBB additionally carries out adsorptive-mediated transcytosis of some cationic molecules (*109*, *121*).

1.3.1.7 Dynamic regulation of BBB properties

Finally, while BBB function is compromised in neurological disorders, as discussed briefly in Section 1.2 above and reviewed in refs. (*16*, *122*), emerging data demonstrate that BBB function is also dynamically tuned by physiological processes. For example, circadian rhythms regulate BBB efflux transporter activity in *Drosophila* subperineurial glia, in mouse brain ECs, and in cultured human brain ECs (*48*, *123*, *124*). The circadian clock also regulates claudin-5 expression at the mouse blood-retinal barrier (*125*). In mice, increased neuronal activity leads to changes in EC gene expression and decreased efflux transport, potentially as a strategy to temporarily divert energy substrates to neurons and away from ATP-intensive BBB efflux transporters (*124*). Notably, this activity-dependent decrease in efflux occurs via a mechanism linked to components of the EC circadian clock (*124*). The links between circadian rhythms, efflux transport, and transcytosis have been suggested as mechanisms contributing to the proposed waste-clearance function of sleep, and also may be important considerations for timing of drug administration (*126*, *127*). Furthermore, BBB function changes with age: Yang *et al.* demonstrated that numerous plasma proteins undergo transcytosis at the BBB in young mice, but the rate of such uptake diminishes with age (*128*).

1.3.2 Control of blood flow

The NVU mediates neurovascular coupling, the mechanism that achieves functional hyperemia, a transient increase in blood flow to brain regions with elevated neuronal activity (*129*, *130*). Early observations of this phenomenon were made in cats by Schmidt and Hendrix, who demonstrated increased temperature in visual cortex after light stimulation (Figure 1.4) (*131*), and by Freygang and Sokoloff, who used a radioactive tracer to quantify blood flow after visual stimulation (*132*). In many cases, these localized increases in blood flow deliver oxygen in excess of neuronal and glial demand, and thus lead to net increases in blood oxygen concentration (*133*, *134*). Though the physiological rationale for this oxygen excess is not well understood, it lends clinical utility to neurovascular coupling as the basis of blood oxygen level-dependent (BOLD) functional magnetic resonance imaging (fMRI), where active brain regions are identified based changes to the relative concentration of oxyhemoglobin and deoxyhemoglobin (*135–137*).

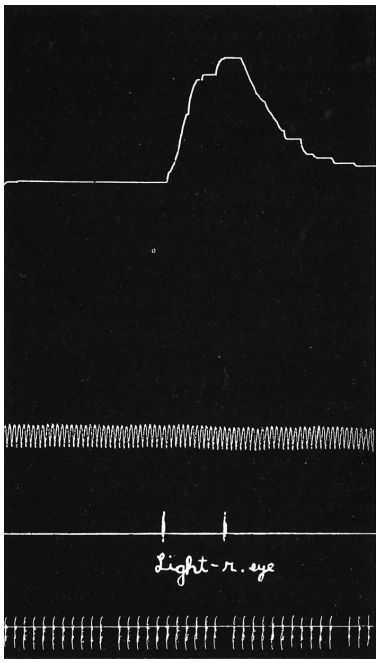

Figure 1.4. Early evidence of neurovascular coupling. Temperature profile (top) of cat "occipital cortex […] on mesial surface of right side, just below calcarine fissure" (i.e., visual cortex). Dashes indicate beginning and end of light stimulation of the right eye. The corresponding text notes that temperature changes were not detected elsewhere upon light stimulation, and that electrical stimulation of cervical sympathetic nerves did not produce a temperature change in this region. Recording from Schmidt and Hendrix, 1938 (*131*).

The molecular and cellular bases of neurovascular coupling are complex and remain incompletely understood. An early hypothesis was that functional hyperemia is achieved by vessel dilation in response to a local metabolic signal, for example decreased oxygen, decreased glucose, or increased carbon dioxide (the "negative-feedback" hypothesis). However, studies that experimentally altered these variables generally ruled out this explanation (reviewed in (*129*)). For example, neurovascular coupling still occurs in rats maintained under conditions of hyperoxygenation (*138*). Instead, a "feed-forward" mechanism, where molecular signals produced by activated neurons are relayed to the vasculature, likely predominates, although some evidence for feedback-based fine-tuning exists (reviewed in (*1*)).

Neuronal nitric oxide (NO) is a critical mediator of neurovascular coupling: the Ca^{2+} influx effected by glutamate binding to *N*-methyl-D-aspartate (NMDA) receptors leads to production of NO via the neuronal NO synthase (nNOS), and NO evokes dilation of vascular

smooth muscle (*129*). For example, increased cerebellar blood flow observed after electrical stimulation of the lip is strongly attenuated in nNOS (*Nos1*) knockout mice (*139*). Whether neuronal NO is sufficient to achieve vessel dilation, or simply one necessary component of the mechanism, seems to differ between brain regions (reviewed in (*129*)). Astrocytes may also participate in propagating neuronal activity signals to vessels. Glutamate binding to astrocytic metabotropic glutamate receptors (mGluRs) leads to increased intracellular Ca^{2+}, which activates phospholipase A_2 (PLA_2), an enzyme that releases arachidonic acid (AA) from phospholipids (*129*, *140–143*). Derivatives of AA, including epoxyeicosatrienoic acids and prostaglandins, the enzymes for synthesis of which are expressed by astrocytes, are capable of dilating vascular smooth muscle via prostaglandin receptors (*129*, *140*, *144–146*). Neurons may also directly contribute to synthesis of AA and derivatives in some brain regions (*147*). In contrast to vasodilatory AA derivatives, AA itself can cause vasoconstriction via conversion to 20-hydroxyeicosatetraenoic acid (20-HETE) within vascular smooth muscle cells (*148*, *149*). The directionality of the vascular response to neural signals is partially regulated by local oxygen concentration, the oxygen-dependence and affinities of relevant AA-metabolizing enzymes, and lactate production: high oxygen concentration promotes vascular smooth muscle cell-mediated AA conversion to 20-HETE resulting in constriction, and low oxygen promotes neuron/astrocyte-mediated conversion of AA to epoxyeicosatrienoic acids and prostaglandins resulting in vasodilation (*129*, *150*). NO also serves to modulate production of AA metabolites (*129*, *149*). Together, these multiple, partially competing mechanisms and messengers likely serve to achieve temporal and spatial fine-tuning of the vascular response to neuronal activity.

1.3.2.1 Pericytes in neurovascular coupling

The mechanisms described above consider neurons as the initiators of the neurovascular coupling signal and VSMCs (at the level of arterioles) as the effectors of neurovascular coupling,

with a critical role for astrocytes in relaying the signal. The importance of astrocytes, however, has been questioned (*151*) and two additional observations suggest a role for other cell types in shaping the blood flow response to neuronal activity. First, the capillary bed originating from a single arteriole is vast, and neurovascular coupling should permit a higher degree of spatial control than is achievable by arteriolar VSMC dilation alone. Second, the average distance from (activated) neuron to arteriolar VSMC is much larger than the average distance from neuron to capillary. These observations lead to the questions: Do capillary mural cells (pericytes) regulate vessel diameter in response to neuronal activity, and how is the neuron-derived signal propagated upstream to a distant arteriole?

I first consider the question of direct control of capillary diameter by pericytes. While observations of pericytes were recorded by Eberth in 1871 (*152*), Rouget is widely considered as having discovered pericytes (or "Rouget cells," as they were once known (*153*, *154*)). In 1874, based on observations of frog (*Hyla viridis*) larvae, he lucidly described these cells and distinguished them from VSMCs based both on nuclear density and cytoplasmic morphology:

> On vessels thus contracted and alive, one can observe annular bands, refractive, projecting on the edges of the vessel, to which they give a crenellated appearance. Their surface, of natural section, reproduces in part the image of that of the fiber-cells [VSMCs] of the arteries, and presents here and there nuclei very far apart from each other. The same appearances are found, with a gradual decrease in the diameter of the bands and an increasingly marked rarity of the nuclei, on the ramifications more and more distant from the arterioles, and even on the capillary arches closest to the free edge of the tail and on the capillaries of the intermediate network. The refractive annular bands and the nuclei belong to cells with branched protoplasmatic extensions, absolutely identical to those which I

> previously observed on the vessels of the hyaloid membrane of the adult frog.* (*155*)

In the same work, Rouget reported that pericytes were contractile:

> New research on vessel development, continued since the beginning of spring, on amphibian larvae, allowed me to put beyond doubt the contractility of cells with branched protoplasmatic extensions, which I observed last year in the vessels of the hyaloid membrane of the adult frog […] Cells which are entirely similar in fact constitute in the larvae a so-called adventitious tunica on the arterial capillaries, on the venous capillaries, and on the true capillaries. This tunica being only the continuity of the muscular tunicae of the arteries and the veins, it follows that the whole blood vascular system, from the heart to the capillaries inclusive, is enveloped in a contractile tunica.* (*155*)

Peppiat, Attwell, and colleagues therefore asked whether brain pericytes could regulate capillary diameter using *ex vivo* preparations of rat retina and cerebellum (*156*). Pericyte constriction was observed upon electrical stimulation and upon superfusion of ATP, noradrenaline, or a purinergic receptor inhibitor; glutamate superfusion subsequent to noradrenaline caused dilation (*156*). Hall *et al.* similarly showed that electrical stimulation of neurons in cerebellar slices led to capillary dilation subsequent to noradrenaline-mediated constriction, an effect blocked by inhibiting action potentials with tetrodotoxin or by inhibiting the pericyte-expressed prostaglandin receptor EP_4 (*27*).

Ex vivo cultures, however, have drawbacks, including the lack of blood pressure/flow, constant (and sometimes supraphysiological) oxygen concentration, and the requirement to pre-constrict vessels to observe glutamate-mediated dilation (*157*). Thus, multiple groups undertook

---

*Translated from the original French

corroboration of these results *in vivo*, using two-photon imaging of mouse cerebral cortex to assess vascular diameter after pharmacological or physiological (e.g., whisker pad stimulation) stimulus (*27*, *158*, *159*). In one study, the authors observed whisker pad stimulation-induced capillary dilation that slightly preceded arteriolar dilation, suggesting that initial capillary dilation is not a consequence of increased flow from upstream arteriole dilation, and rather that pericytes actively dilate in response to neuronal signals (*27*). Another study found that pericytes *in vivo* constricted in response to a prostaglandin receptor agonist, but did not dilate in response to bicuculline-induced neuronal activity (*158*). Still another study reported that arterioles, but not capillaries, dilated upon whisker stimulation; further, direct optogenetic activation of smooth muscle cells, but not pericytes, caused vessel constriction (*159*).

1.3.2.2 Mural cell diversity and nomenclature

Among the many potential contributors to the apparent discrepancy is a lack of widespread agreement on how to classify mural cells as pericytes versus VSMCs (*160*) (also see Section 4.5), with some investigators relying on (i) morphological characteristics, (ii) position on the vascular tree, and (iii) expression of markers, especially α-smooth muscle actin (α-SMA). Detailed imaging studies have shown that brain mural cells are more heterogeneous with respect to these parameters than can be adequately conveyed by a binary distinction between pericyte and VSMC (Figure 1.5), and that while these parameters are correlated, they are not uniquely predictive (i.e., one parameter does not uniquely determine another) (*161*). The issue of nomenclature is most relevant with respect to the mural cells of the proximal branches of penetrating arterioles, which have been called “first-order capillaries” (*27*), “precapillary arterioles” (*161*), or the “arteriole-capillary transition” (*162*). The cell bodies of these mural cells have ovoid, “bump on a log” morphology, which would fit the traditional definition of pericyte. These cells, however, have circumferential processes and α-SMA expression similar to arteriolar

VSMCs, leading some authors to refer to these cells as precapillary SMCs to contrast them with capillary pericytes (*159*). In a murine brain single cell RNA-seq (scRNA-seq) study, the mural cell cluster lacking *ACTA2* was termed "pericyte"; the three mural cell clusters with *ACTA2* expression were termed arterial, arteriolar, and venular smooth muscle cells (*56*). Thus, the lack of standard nomenclature makes cross-study comparisons difficult. The work of Grant *et al.* provides a logical framework for unambiguous classification of vessels and mural cells that should aid future studies and discussion of mural cell function (Figure 1.5) (*161*).

Where studies provide adequate data to identify the vessel branches or mural cells under investigation independent of the authors' terminology, they generally support the conclusion that ensheathing pericytes of precapillary arterioles (using the nomenclature of Grant *et al*.) are contractile and participate in neurovascular coupling (*27*, *159*). For example, in a detailed study, the earliest dilation after odor stimulation occurred at the level of precapillary arterioles, followed shortly by the upstream penetrating (parenchymal) arteriole, and then by downstream capillaries (*163*). Therefore, nomenclature controversy aside, the question remains whether capillary pericytes (using the nomenclature of Grant *et al.*) contribute actively to neurovascular coupling, or whether capillary dilation is a passive response to increased flow as a result of upstream dilation. Using *in vivo* imaging, Hartmann, Shih, and colleagues demonstrated that capillaries (5^{th} to 9^{th} order) constricted upon optogenetic activation of capillary pericytes, but with slower kinetics and smaller relative diameter changes than observed for ensheathing pericytes or arteriolar VSMCs (*164*). The authors suggest that such slight changes to capillary diameter may serve an important physiological role in homogenizing blood flow across capillaries during functional hyperemia (*164*), although the dynamics of dilation after a physiological stimulus were not studied. In the aforementioned study, inhibition of Rho-associated protein kinase, a positive regulator of actin polymerization and actomyosin-based

contraction, attenuated capillary constriction (*164*). Thus, despite the lack of detectable α-SMA, these results suggest that capillary pericytes are capable of constricting via mechanisms similar to those employed by VSMCs. The authors suggest that capillary pericytes could have very low levels of α-SMA, a possibility supported by the finding that immunohistochemical detection of α-SMA is sensitive to technical factors (*165*), or that capillary pericyte-expressed myosins couple to other cytoskeletal actins (*162*, *164*).

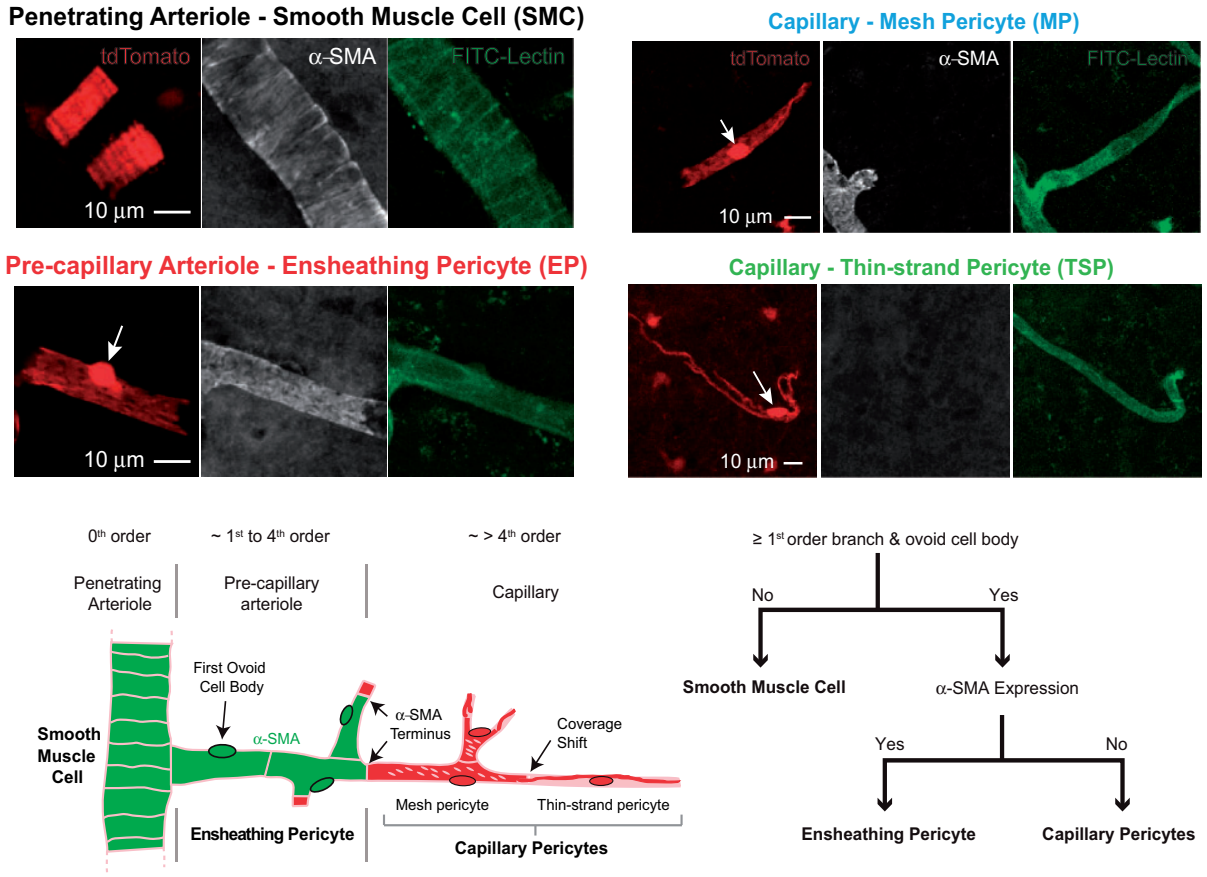

Figure 1.5. Brain mural cell diversity. tdTomato-labeled mural cells (NG2-CreER™; R26-LSL-tdTomato) in mouse cortex, with α-SMA immunohistochemistry and lectin labeling. At bottom, authors' suggested scheme for classification of brain mural cells. From Grant *et al.* 2019 (*161*). Used under a Creative Commons Attribution-NonCommercial License (https://creativecommons.org/licenses/by-nc/4.0/).

1.3.2.3 Other mechanisms in control of CNS blood flow

Pericytes also regulate resting vessel tone and blood flow. While several studies have reported disrupted brain perfusion with global pericyte deficiency (*166–168*), the mechanistic link is inconclusive given the possible genetic targeting of other mural cells and/or extensive pathology in such animals. More convincing evidence has recently been provided by acute, local pericyte ablation: capillaries from which pericytes are ablated dilate and exhibit increased blood flow (*164*, *169*). Further, global knockout of *Kcnj8* (encoding $K_{ir}6.1$, a component of the K_{ATP} channel), which is pericyte-specific in the brain, causes reduced resting cerebral blood flow, but peripheral contributions to this phenotype were not ruled out (*170*). Considered together, results

from single capillary pericyte ablation (*164*, *169*), single capillary pericyte optogenetic stimulation (*164*, *171*), and the observation of altered calcium signaling in capillary pericytes after stimulation (*163*, *172*), support a potential role for capillary pericytes in direct regulation of capillary diameter during functional hyperemia; however, conclusive evidence for such a phenomenon from studies employing physiological stimuli does not yet exist, due in part to the difficulty isolating the direct effect of capillary pericytes when the entire vascular tree is engaged.

Finally, both endothelial cells and mural cells participate in propagation of the neuron-derived neurovascular coupling signal. Endothelial cells mediate retrograde signal propagation from capillaries to arterioles, potentially via interendothelial gap junctions (*173*, *174*). For example, Longden *et al.* demonstrated that *in vivo* administration of potassium in the vicinity of a "second-order capillary" (a third-order vessel, a precapillary arteriole, in the nomenclature of Grant *et al.*, Figure 1.5) caused upstream arteriole dilation and hyperemia, and this effect was attenuated in EC-specific *Kcnj2* ($K_{ir}2.1$)-knockout mice (*174*). These results suggest that the neuronal activity-associated elevation in extracellular potassium increases conductance of Kir2.1 channels on capillary ECs, leading to a wave of EC hyperpolarization that is propagated upstream, eventually leading to arteriolar VSMC hyperpolarization and dilation. Similar experiments also revealed a role for capillary EC TRPA1 channels in this process (*151*). While arteriolar ECs and VSMCs may be directly connected by gap junctions (myoendothelial junctions), caveolae in arteriolar ECs are also required for neurovascular coupling and may play a role in EC-to-VSMC signaling (*175*). Given that pericytes extensively cover capillaries, are located between the parenchyma and endothelium, and express a diverse repertoire of receptors and ion channels (*176*), they may have a role in such retrograde signal propagation. For example, activation of pericyte K_{ATP} channels via local administration of pinacidil led to vessel dilation,

and blocking K_{ATP} channels with PNU37883 attenuated dilation in response to whisker pad stimulation (*177*). These results suggest that activation of pericyte K_{ATP} channels during neurovascular coupling, via a yet-unidentified mechanism, may cause pericyte hyperpolarization that can be propagated upstream. Finally, evidence that pericytes might facilitate an additional mode of signal propagation came from the identification of thin processes connecting pericytes on different capillary branches (*178*). These processes, termed interpericyte tunneling nanotubes, electrically and functionally couple distant pericytes; interestingly, retinal capillaries bridged by a pair of coupled pericytes consistently undergo opposite responses to light stimulation (one dilating, one constricting), with nanotube ablation eliminating this coordinated response (*178*).

1.3.3 Other aspects of molecular and fluid transport in the CNS and PNS

Other cell types of the NVU have critical roles in inducing and regulating the BBB phenotype of CNS ECs (discussed in Section 1.4 below), but some non-EC NVU cells also participate directly the delivery of key molecules to target cells. Reversing the ion fluxes associated with action potentials and postsynaptic currents are extremely energy-intensive processes; thus, neurons, which constitute roughly half of all cells in the CNS, consume the vast majority of the CNS energy supply (*179–181*). Astrocytes serve as the principal conduit between the vasculature and neurons for delivery of glucose and other nutrients (*142*, *182*); astrocytes also synthesize glycogen, which has been proposed to serve as a short-term energy store, and metabolize glucose and glycogen to lactate and transfer this lactate to neurons, although the contribution of astrocyte-derived lactate to neuron metabolism is debated (*182–185*). Furthermore, astrocytes synthesize lipids and deliver these lipids to neurons, where they are required for presynapse function (*186*). In addition to astrocytes, pericytes may contribute to NVU molecular transport: one single cell RNA-sequencing study found that brain pericytes have enriched expression of transporter-encoding genes compared to lung pericytes (*56*), and another

identified a putative brain pericyte subpopulation with an enriched transport-related gene signature (*187*). Pericytes are positioned between ECs and astrocyte endfeet, extensively cover the surface of microvessels, and participate in clearance of wastes (*188*); thus, pericytes are good candidates as contributors to blood-brain molecular transport, but functional evidence of such a process is still lacking.

In addition to the NVU and associated BBB, multiple additional spatially- and functionally-distinct systems work in concert to control the ionic, molecular, and cellular composition of the CNS. While not the focus of this work, these systems merit brief discussion to form a more complete picture of the multiple mechanisms that control the CNS microenvironment, and to better understand shared and distinct features of relevant cell types. The CNS is bathed in cerebrospinal fluid (CSF), a low-protein solution contained in the ventricles and subarachnoid spaces that supports and cushions the brain, and regulates parenchymal ionic/molecular composition and waste clearance via exchange with interstitial fluid (ISF, discussed below). The majority of CSF is produced by the epithelial cells of the choroid plexuses, using water and solutes derived from blood; as such, the choroid plexuses are densely vascularized and, as discussed in Section 1.3.1, have fenestrated blood vessels that do not form a BBB. Instead, the choroid plexus epithelial cells form tight junctions and express efflux transporters to isolate the CSF from blood, forming the blood-cerebrospinal fluid barrier (BCSFB) (*14*, *96*). The outer surface of the CNS is covered by the meninges, a three-layer structure comprising the outermost dura mater, arachnoid mater, and innermost pia mater (*96*, *189*). The CSF-containing subarachnoid space is isolated from non-CNS, non-BBB-forming vasculature in the dura mater by the arachnoid mater (also referred to as the arachnoid membrane or arachnoid barrier) (*14*, *96*, *189*).

Several routes likely contribute to CSF drainage from the brain, including via absorption into dural venous sinuses (*190*, *191*), via lymphatic vessels in the dura mater adjacent to dural sinuses (*192*, *193*), along nerves that pass through the cribriform plate at the roof of the nasal cavity, and along cranial nerves that pass through foramina in the base of the skull (*194*). The CNS parenchyma, however, lacks a traditional lymphatic system, and the exchange of ISF with CSF may be accomplished by fluid and solute transport along perivascular spaces (*195*, *196*). The outer border of the perivascular space is formed by astrocyte endfeet and the inner border by the endothelial basement membrane (*197*). While the existence of perivascular spaces around large vessels is well-established (*197*, *198*), classic and more recent work has demonstrated that such spaces may exist around capillaries and that tracers introduced into CSF rapidly undergo perivascular distribution along the entire vascular tree under some conditions (*190*, *196–199*). Further, astrocyte endfoot localization at the outer border of perivascular spaces and the recent discovery that knockout of endfoot aquaporin-4 disrupts CSF-ISF exchange led to the concept that this route of fluid and solute transport constitutes a "glymphatic" (glia-lymphatic) system (*196*). Although many aspects of this hypothesis remain controversial (*197*, *200–203*), CSF-ISF exchange and perivascular spaces play an important role in CNS physiology and should be considered as a potential component of the NVU.

Finally, the peripheral nervous system (PNS) possesses barrier systems similar to those present in the CNS. The endothelial blood-nerve barrier (BNB) is directly analogous to the blood-brain and blood-retinal barriers of the CNS. The BNB regulates molecular and cellular transport between blood and peripheral nerves, and is formed by microvessels in the endoneurium, the innermost layer of peripheral nerves that contains neuronal axons and glia (*204*, *205*). Early observations with small and large molecule tracers in rats and frogs revealed that endoneurial microvessels were impermeable compared to vessels in the epineurium (the

outer layer of nerves) and in other vascular beds (*206–209*), reminiscent of similar observations in the CNS. The barrier properties of BNB-forming endoneurial endothelial cells include lack of fenestrae, enriched expression of tight junction proteins, expression of nutrient and efflux transporters, and low rates of nonspecific transcytosis (*210–213*). Tight-junction forming perineurial fibroblasts form another barrier, restricting transport between endoneurium and epineurium (*214*). Despite recent advances in molecular characterization of the rodent and human BNB (*215*, *216*), knowledge of the cellular and molecular mechanisms regulating BNB development remain limited.

1.4 Neurovascular unit development

1.4.1 CNS angiogenesis and BBB formation

During embryogenesis, the CNS forms from the ectoderm-derived neural tube and therefore lacks mesoderm-derived endothelial progenitors (angioblasts). Thus, vascularization of the CNS occurs exclusively by angiogenesis, the formation of new blood vessels from existing blood vessels in the perineural vascular plexus (PNVP) that surrounds the neural tube (*217*). Stewart and Wiley first showed that developing neural tissue stimulates both invasion of endothelial cells and acquisition of BBB properties (*218*). They transplanted fragments of embryonic quail brain into the coelomic cavities of chick embryos, and subsequently observed invasion of blood vessels comprising chick (host) endothelium into the quail (graft)-derived neural tissue, with cells of the two species being distinguished by their distinctive nuclear characteristics. Host-derived blood vessels had BBB characteristics, including tight junctions, low vesicle number, and low permeability to trypan blue (*218*). These findings support a model in which neural tissue-derived factors signal to naïve endothelial cells to stimulate invasion and acquisition of BBB properties.

1.4.1.1 Wnt-mediated angiogenesis and barriergenesis

Later work uncovered these molecular factors: CNS angiogenesis is dependent on neural tube-derived vascular endothelial growth factor (VEGF) (*219*), but is atypical for its additional requirement of Wnt/β-catenin signaling (also referred to as canonical Wnt signaling). Canonical Wnt signaling is activated by extracellular Wnt ligands binding to transmembrane Frizzled (Fz) receptors and low-density lipoprotein receptor-related proteins 5 and 6 (Lrp5/6). In the absence of Wnt ligands, cytoplasmic β-catenin is sequestered by a destruction complex comprising Axin, glycogen synthase kinase 3 (GSK-3), casein kinase 1α (CK1α), adenomatosis polyposis coli (APC), and protein phosphatase 2A (PP2A); within the destruction complex, β-catenin is continually phosphorylated by GSK-3 and CK1α, targeting it for ubiquitination and proteolysis (*220*, *221*). The Wnt ligand-induced formation of the Fz-Lrp5/6 complex causes a conformational change in Lrp5/6 leading to phosphorylation of the Lrp5/6 cytoplasmic tail. The destruction complex is recruited to the membrane via binding of Axin to the tail of Lrp5/6, and the phosphorylated regions of the Lrp5/6 tail bind and inhibit activity of GSK-3 (*220–223*). In the absence of GSK-3 kinase activity, β-catenin accumulates in the cytoplasm and nucleus; in the nucleus it forms a complex with T cell factor (TCF)/lymphoid enhancer-binding factor (LEF) transcription factors, which regulate transcription of target genes (*220*, *221*, *224*). Canonical target genes include both positive (*TCF7, LEF1*) and negative (*AXIN2*) regulators of Wnt/β-catenin signaling, although the broader transcriptional response is context-dependent.

Wnt target genes are highly enriched in CNS ECs compared to ECs of other organs both during embryogenesis (*225*), the postnatal period (*65*), and in adulthood (*56*, *226*). Furthermore, Wnt reporters show active signaling in ECs in the PNVP and neural tube during embryogenesis (*225*, *227*, *228*). In mice with EC-specific deletion of β-catenin (*Ctnnb1*), angiogenesis is disrupted in the CNS (*225*, *227*), but not in the heart, lung, or limbs (*225*). Wnt7a and Wnt7b are

broadly expressed in the developing forebrain and ventral spinal cord, and *Wnt7a/Wnt7b* knockout mice display deficits in CNS angiogenesis similar to those observed with EC β-catenin-knockout (*225*, *227*). There also appears to be a requirement for temporal control of the level of Wnt signaling: after initial vessel ingrowth in the cerebral cortex, ablation of radial glia elevated Wnt signaling in ECs and led to vessel regression, suggesting that radial glia attenuate Wnt signaling to promote vessel stability at later developmental stages (*229*).

Though the requirement of Wnt signaling for angiogenesis is observed throughout the CNS, there are regional differences in ligands. Even before the finding that Wnt7s direct angiogenesis in the ventral neural tube and forebrain, Xu, Wang, Nathans, and colleagues demonstrated that Norrin activates Wnt signaling to direct angiogenesis in the retina (*230*). Norrin (also called Norrie disease protein), a secreted protein with no homology to Wnt ligands, is the product of the Norrie disease gene *NDP*; Norrie disease is characterized by blindness, retinal vascular deficits, and hearing loss (*231*, *232*). *Ndp* knockout mice exhibit incomplete vascularization of the retina and loss of cochlear vessels (*232*, *233*). *Fz4* knockout mice phenocopy *Ndp* knockouts, and Norrin binds Fz4 and Lrp5 and activates canonical Wnt signaling (*230*, *234*). Additional work identified Müller glia as the source of Norrin in the retina (*235*), and found that *Fz4* and *Ndp* knockout mice also exhibit vascular malformations in the cerebellum, but not in other brain regions (*230*, *236*). These data support a model in which neural tissue-derived Wnt7a/Wnt7b and Norrin activate Wnt/β-catenin signaling in ECs to regulate angiogenesis in distinct regions of the CNS. While these insights have been gained through mouse models, zebrafish, another common *in vivo* model system for investigating NVU development (Section 1.5.1), also require Wnt signaling for CNS angiogenesis (*237*).

Concurrently with angiogenesis, CNS ECs begin to acquire their unique BBB properties (Section 1.3.1) in a process termed barriergenesis. Molecular markers of this process include

acquisition of GLUT-1 expression and downregulation of PLVAP expression. Notably, Wnt/β-catenin signaling also controls barriergenesis, with EC-specific β-catenin knockout mice exhibiting a lack of endothelial GLUT-1 expression (*225*), a deficit also observed in *Wnt7a/Wnt7b* knockouts (*227*). These mice also have a severe CNS hemorrhage phenotype and are embryonic lethal (*225*, *227*). Conversely, in mice with ectopic expression of Wnt7a outside the neural tube, ECs in these non-CNS regions acquire GLUT-1 expression (*227*). The necessity of Wnt/β-catenin signaling persists into postnatal development; inducible deletion of β-catenin in ECs in postnatal day 11-14 mice leads to loss of brain EC tight junctions, marked upregulation of PLVAP, and increased BBB permeability to the albumin-binding dye Evans blue (*228*). Similarly, *Fz4* knockout mice exhibit BBB leakage in multiple brain regions, which correlates with upregulation of PLVAP; *Ndp* knockout mice also exhibit leakage, with the most severe deficits in the retina and cerebellum (*238*, *239*). Thus, Wnt/β-catenin signaling is the key regulator of the tightly coupled processes of CNS angiogenesis and barriergenesis.

In humans and mice, there are at least 19 different Wnt ligands and Norrin, which bind promiscuously to Lrp5/6 and the 10 Fz receptors, and are involved in numerous developmental processes (*240*). Thus, a key question is: how do ECs discriminate between these ligands to activate the barriergenesis gene program in response to specific ligands (i.e., Wnt7a, Wnt7b, Norrin)? Clues emerged with the identification of two genes for which knockouts generated CNS vascular defects in mice reminiscent of the previously discussed β-catenin and *Wnt7a/Wnt7b* mutants. The first gene identified was an orphan G protein-coupled receptor, *Gpr124* (also known as *Adgra2*), knockout of which disrupts CNS angiogenesis and leads to CNS hemorrhage (*241–243*). Subsequently, Zhou and Nathans showed that Gpr124 knockout mouse phenotypes could be partially rescued by artificial stabilization of β-catenin in ECs, and that Gpr124 promotes Wnt signaling in response to Wnt7a and Wnt7b preferentially over other ligands (*244*).

Another study demonstrated a direct biochemical interaction between Wnt7a/Wnt7b and Gpr124 (*245*). The second gene, *Reck*, was initially identified as an inhibitor of matrix metalloproteinases that is required for vascular development (*246*). Subsequent work demonstrated that RECK and Gpr124 serve as EC Wnt/Fz coreceptors that confer Wnt7a/Wnt7b specificity in both Zebrafish and mouse (*237*, *247–249*). Analogously, tetraspanin-12 (Tspan12) was identified as a Norrin-specific coreceptor in retinal ECs (*250*).

1.4.1.2 Pericytes in BBB development and maintenance

While Wnt/β-catenin signaling controls CNS angiogenesis and the initial steps of barriergenesis, several additional cellular and molecular factors are required for development and maintenance of the BBB. Early work suggested that the BBB forms postnatally in response to cues from astrocytes, a late-born cell type (*251*), but the evidence discussed above from Wnt/β-catenin mutant embryos challenges this view. While there are temporal differences in the emergence of different BBB characteristics—for example, GLUT-1 is induced during embryogenesis, but P-gp appears postnatally (*30*)—multiple studies have demonstrated the functionality of the embryonic BBB based on its ability to exclude injected tracers (*30*, *252*).

Pericytes are mural cells that line the outer surface of microvessels and are embedded in the vascular basement membrane, and developing CNS pericytes migrate into the neural tube from the PNVP alongside ECs (*253*). Thus, Daneman, Barres, and colleagues asked whether pericytes, which extensively cover CNS microvessels, play a role in inducing the BBB EC phenotype, using mice with mutations in the platelet-derived growth factor receptor β (PDGFRβ) (*30*). Platelet-derived growth factor B (PDGF-B) is secreted by ECs and activates PDGFRβ, a receptor tyrosine kinase, on pericytes, mediating their proliferation, recruitment, and attachment to vessels (*253*, *254*). The authors used mice in which seven tyrosine residues on the intracellular domain of PDGFRβ were mutated to phenylalanine. Normally, these residues, when

autophosphorylated, serve as binding sites for downstream signal transduction molecules, and therefore the hypomorphic *Pdgfrb*^{F7} allele leads to attenuated PDGFRβ signaling activity and reductions in pericyte coverage of vessels (*255*), but avoids the embryonic lethality of *Pdgfrb* knockout (*30*, *253*). Compared to control mice, *Pdgfrb*$^{F7/F7}$ and *Pdgfrb*$^{F7/-}$ neonates have progressive reductions in brain pericyte coverage that correlate with progressive increases in BBB permeability to Evans blue (*30*). Brain ECs in *Pdgfrb* knockout embryos also have (i) abnormal tight junction morphology, (ii) increased vesicle number, which correlates with increased *Plvap* expression, and (iii) increased expression of the leukocyte adhesion molecules ICAM-1, ALCAM, and galectin-3, which correspond to an increased number of leukocytes in the brain of *Pdgfrb*$^{F7/F7}$ mice (*30*).

Using pericyte-deficient mice derived via alternative genetic strategies (hypomorphic *Pdgfb* alleles preventing EC-derived PDGF-B ligand from being retained in the vascular extracellular matrix), Armulik, Betsholtz, and colleagues showed similar BBB deficits in adult mice, which were primarily driven by increased transcytosis, and also revealed a lack of astrocyte endfoot polarization (*256*). Independent studies with *Pdgfrb*^{F7} and *Pdgfrb*$^{+/-}$ mice confirmed BBB leakage to injected tracers and endogenous serum proteins, and additionally found deficits in vascular extracellular matrix composition, blood flow, and neuron structure and function (*257*). While specific molecular factors produced by pericytes that mediate regulation of the BBB remain largely unknown, pericyte-derived pleiotrophin (PTN) was identified as a factor mediating the brain pericyte neuroprotective effect (*167*). Additional work further characterized the increased leukocyte infiltration observed in pericyte-deficient mice (*258*) and profiled changes to the EC transcriptome in these mice (*259*). In summary, pericytes regulate several aspects of BBB function, including suppression of transcytosis and immune cell infiltration, and also regulate other NVU functions.

1.4.1.3 Other mechanisms in BBB development

Endothelial cell-autonomous mechanisms controlling BBB development have also been investigated. One common approach to identify potential regulators of BBB phenotype is to identify genes highly enriched in CNS ECs compared to non-CNS ECs using microarrays or RNA-sequencing. The gene *Mfsd2a* was identified using this strategy, and is highly expressed in cortical ECs but not expressed in lung ECs (*252*). *Mfsd2a* encodes a lipid transporter responsible for brain uptake of docosahexaenoic acid (*260*). *Mfsd2a* knockout mice exhibit BBB leakage without defects in angiogenesis or vessel morphology. On the ultrastructural level, knockout mice have normal brain EC tight junctions, but striking increases in brain EC vesicle number, demonstrating that *Mfsd2a* is required to limit transcytosis (*252*). Additional examination of blood-retinal barrier formation revealed additional temporal details: while functional tight junctions form upon vessel entry into developing retinal tissue (at ~postnatal day 1), ECs have abundant vesicles at this timepoint. Suppression of transcytosis, as evidenced by a sharp decrease in the number of vesicles, occurs between postnatal day 8 and 10, and is *Mfsd2a*-dependent (*261*). A similar *Mfsd2a*-dependent process of transcytosis suppression subsequent to angiogenesis occurs in zebrafish (*262*). *Mfsd2a* overexpression is sufficient to suppress vesicle formation *in vitro*, and a single amino acid mutation in MFSD2A that eliminates lipid transport function also eliminates its ability to suppress EC vesicle formation *in vivo* (*263*). Profiling of the CNS EC lipidome and additional electron microscopy-based quantification of caveolae revealed that MFSD2A likely serves to modify the lipid composition of CNS EC plasma membranes, making them less amenable to formation of caveolae (*263*). Thus, MFSD2A-mediated regulation of membrane composition together with Wnt-mediated suppression of PLVAP achieves the low rate of non-specific transcytosis observed at the BBB. What extrinsic factor induces MFSD2A expression in CNS ECs? Some evidence suggests a role for pericytes (*252*) and Wnt (*264*), but

given the temporal difference between Wnt-mediated barriergenesis/pericyte recruitment and transcytosis suppression, other yet-unidentified factors likely contribute.

Retinoic acid (RA), a derivative of retinol (vitamin A), serves as a signaling molecule and regulates anteroposterior patterning of the neural tube, among other developmental processes (*265*). RA derived from radial glia and the meninges additionally regulates striatal and neocortical neurogenesis (*266*, *267*). RA is synthesized by retinaldehyde dehydrogenases (RALDHs), and is typically secreted to act on other cells; in target cells, RA binds RA receptors (RARs) which heterodimerize with retinoid X receptors (RXRs) and regulate transcription of genes with retinoic acid response elements (RAREs). RARβ is expressed by ECs in the developing cortex, and experiments with cultured ECs suggested that RA/RARβ signaling regulates expression of BBB-associated proteins including VE-cadherin, occludin, ZO-1, P-gp, and GLUT-1 (*268*). *In vivo*, mice with impaired RA synthesis (*Rdh10* knockout mice) have vascular defects in neocortex due to increased abundance of neural progenitor-derived Wnt-inhibitory factors (*269*). In other brain regions of *Rdh10* knockout mice, however, ECs exhibited elevated levels of Wnt signaling; examination of mice with EC-specific expression of a dominant negative RAR revealed that RA signaling is required for EC-autonomous attenuation of Wnt signaling in these regions (*270*). These mice also exhibit slight increases in pericyte number, likely a result of increased expression of the Wnt target Sox17 leading to increased expression of PDGF-B (*271*). In brain regions where vascular development proceeds normally in *Rdh10* knockout mice (i.e., regions other than neocortex), vessels do not exhibit defects in BBB properties, suggesting that the BBB-inductive effects in cultured ECs may be due to the use of supraphysiological concentrations of RA (*270*). In sum, physiological RA appears to regulate brain vascular development by tuning Wnt signaling: RA promotes Wnt-mediated angiogenesis in the neocortex by a non-EC-autonomous mechanism, and attenuates Wnt signaling in other

regions by an EC-autonomous mechanism to achieve precise control over pericyte number and potentially other phenotypes.

Building on a considerable body of work demonstrating BBB-inductive effects of astrocytes and astrocyte-conditioned medium *ex vivo* and *in vitro* (*251*, *272–275*), several specific molecular mechanisms by which astrocytes control BBB development have also been identified. For example, astrocyte-derived Sonic hedgehog (Shh) suppresses brain EC expression of immune cell adhesion molecules, production of chemokines, and extravasation of T cells *in vitro*, and mice with EC-specific knockout of the Shh receptor Smoothened exhibit increased BBB permeability and decreased tight junction protein expression (*276*). Desert hedgehog (Dhh) may play an analogous role in regulating endoneurial EC permeability and immune surveillance at the blood-nerve barrier (*277*). Astrocytes are also the major source of Wnt ligands (Wnt7a and Wnt7b) in the adult brain (*56*), reflecting the continuing requirement of Wnt signaling for BBB maintenance even after completion of developmental neurogenesis and the loss of neural progenitors. Mice with astrocyte-specific knockout of Wntless (also known as Evi), a protein required for secretion of Wnt ligands (*278*), undergo normal CNS vascular development, but adults exhibit BBB leakage, increased EC vesicle number, and astrocyte endfoot abnormalities (*279*). In addition to these roles in BBB development, astrocytes also serve as templates for postnatal vessel development in the retina (*280*), and regulate the stability of vessel networks in the postnatal cortex (*281*). As is the case with pericytes, additional work is necessary to more completely characterize the astrocyte-derived molecules that mediate their regulation of ECs.

1.4.2 Mural cell development

Like ECs, mural cells originate outside the neural tube, and invade alongside ECs during CNS angiogenesis (*30*), potentially guided along interendothelial junctions (*282*). Mural cells throughout the body differentiate from mesenchymal progenitor populations, the embryonic

origins of which differ along the anteroposterior axis, with cranial (cephalic) neural crest supplying the most anterior region and mesoderm supplying posterior regions of the embryo (*283*). Consequently, in the avian face and forebrain, the neural crest gives rise to many cell types derived from mesoderm elsewhere in the body, including mural cells, bone, cartilage, and connective tissue, including the meninges (derivatives collectively termed "mesectoderm") (*284*, *285*). Some authors, however, have suggested that in mammals, the neural crest supplies mural cells to the entire CNS (*286*, *287*). This view is supported indirectly by the presence of the neural crest linage transcription factor *ZIC1* in human brain and spinal cord mural cells (Figure 1.6 and Chapter 4), and its striking absence in mural cells of other organs, including heart, liver, lung, and skeletal muscle (Chapter 4). *Zic1* is also expressed by murine spinal cord mural cells (*288*). Definitive lineage tracing studies, however, have not been performed. Additionally, it is intriguing to speculate that the neural crest origin might confer specializations to brain mural cells that contribute to their ability to induce BBB properties; however, transplantation studies testing this hypothesis have not been performed. Thus, I focus below on the development of the neural crest and neural crest-derived mural cells.

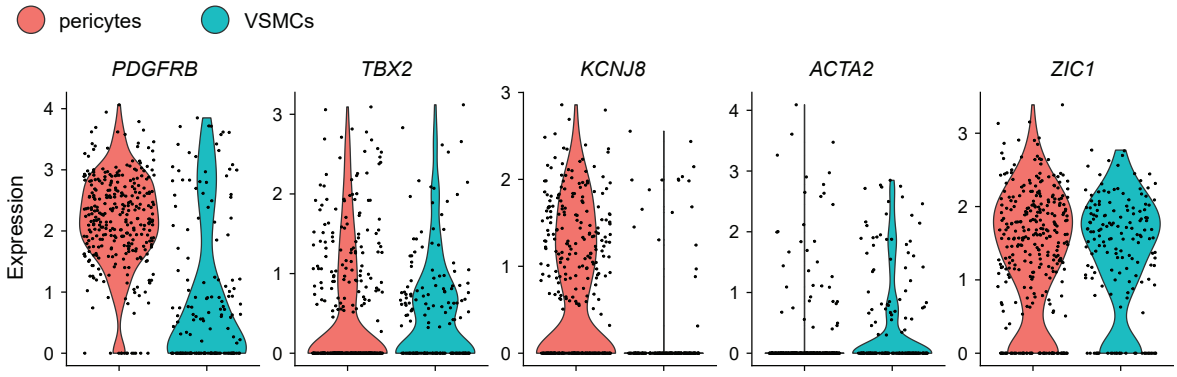

Figure 1.6. Molecular profile of human spinal cord mural cells. Expression of pan-mural cell genes *PDGFRB* and *TBX2*, pericyte-enriched *KCNJ8*, VSMC-enriched *ACTA2*, and the neural crest lineage transcription factor *ZIC1* in pericytes and VSMCs in developing human spinal cord (gestational weeks 4–7). Data from Rayon *et al.* 2021 (*289*).

The neural crest is an embryonic population of cells that originates at the border between the neural plate and nonneural ectoderm (presumptive epidermis) (*290*, *291*). Shortly after neural tube closure, premigratory neural crest cells in the dorsal-most region of the neural tube undergo an epithelial-to-mesenchymal transition and emigrate from the neural tube (*292*, *293*). The resulting migratory neural crest cells travel along pathways in the dorsoventral and mediolateral directions, but are mostly confined to narrow regions along the anteroposterior axis close to the site of emigration, and are guided by tissue-derived signals (*294–296*). Neural crest cells differentiate to an extraordinarily diverse set of cell types. These encompass components of the peripheral nervous system, including sensory neurons (dorsal root ganglia), autonomic neurons, and gila (Schwann and Satellite cells) (*297–300*), melanocytes (*301*), corneal endothelial cells (*302*), the cardiac outflow tract (*303*), and mesenchymal derivatives in the head, thyroid, and thymus (*284*, *304*). The ability to generate mesenchymal derivatives (the "mesectoderm" or "ectomesenchyme") is a property of cranial, but not trunk, neural crest (*284*, *305*). While molecular signals and gene regulatory networks controlling the different potency of neural crest along the anteroposterior axis have been identified (*305–307*), premigratory and even migratory neural crest cells at a given axial level appear multipotent (*308–312*), suggesting that their fate is determined by target tissue-derived signals. Evidence for early fate-restriction also exists, however (*313–318*), and most of the experiments assessing neural crest multipotency have been carried out on trunk, and not cranial, cells. For some derivatives, such as neurons and glia, signaling molecules and downstream gene regulatory networks controlling differentiation have been characterized (reviewed in (*293*, *319*)), but much less is known about molecular mechanisms underlying differentiation of cranial neural crest-derived mural cells, and mesenchymal derivatives in general.

1.4.2.1 PDGF and TGF-β signaling in mural cell development

Endothelium-derived PDGF-B is required for recruitment of mural cells to developing blood vessels in most tissues throughout the embryo; *Pdgfb* and *Pdgfrb* knockout mice exhibit widespread defects in mural cell coverage, leading to malformed, tortuous capillaries and microaneurysms (*253*, *254*). Further, mural cell-specific knockout of CD146 (also known as melanoma cell adhesion molecule [MCAM]), a putative PDGF-B coreceptor, leads to reduced pericyte coverage; CD146 may also have an endothelial cell-autonomous role in BBB development (*320*). Although PDGF-B is widely supplemented in media for culture and/or differentiation of pericytes/VSMCs *in vitro* (*321–324*), it remains unclear whether PDGF-B/PDGFRβ signaling plays a role in specification or differentiation of mural cells from mesenchymal progenitors *in vivo*, or whether its role is restricted to influencing mural cell proliferation, migration, recruitment, and/or attachment to endothelial cells. These phenomena are difficult to uncouple *in vivo*, as defects in either class of processes (specification/differentiation or proliferation/migration/recruitment/attachment) could conceivably lead to the same phenotype: a lack or reduction of mural cell vessel coverage. For example, in PDGF-B-deficient mice, mural cells are not observed within the brain, but PDGFRβ-expressing cells are observed in the PNVP (*253*). The authors infer that these PDGFRβ$^+$ cells are pericytes, and interpret this as evidence that a signal other than PDGF-B must mediate pericyte specification (*253*, *254*), but the identity of these PDGFRβ$^+$ cells was not rigorously established. Because PDGFRβ is expressed by multiple cell types in the perineural niche, including neural crest, naïve mesenchyme, and meningeal fibroblasts (*56*, *325–328*), it remains possible that PDGF-B/PDGFRβ plays a role in specification/differentiation. On the other hand, this broad PDGFRβ expression profile can also be interpreted as evidence that other signaling pathways must control specification of these diverse cell types.

In addition to PDGF-B/PDGFRβ signaling, several additional signaling pathways have been implicated in brain mural cell development. Transforming growth factor (TGF)-β signaling is one such pathway: Hirschi *et al.* demonstrated that the multipotent mesenchymal cell line 10T1/2 gained expression of smooth muscle cell markers and morphology upon treatment with TGF-β or coculture with aortic ECs, and that EC coculture effects could be abolished with a TGF-β neutralizing antibody (*322*). Later work in zebrafish using pharmacological inhibition of TGF-β receptor I (ALK5) and morpholino-based knockdown of *alk1*, however, suggested that while TGF-β signaling may play a role in recruitment or migration of mural cells, it is dispensable for initial specification (*326*). Similarly, endothelial-specific knockout of *Smad4* led to a slight reduction in pericyte coverage of CNS vessels without affecting the number of $NG2^+$ pericytes; the authors of this study further demonstrated that endothelial N-cadherin positively regulates pericyte coverage, with TGF-β/Smad4 and Notch signaling pathways in ECs inducing N-cadherin expression (*329*, *330*).

1.4.2.2 Notch signaling in mural cell development

Multiple lines of evidence suggest a critical role for Notch signaling in mural cell development. Notch proteins are transmembrane receptors, of which there are four in mammals (Notch1, 2, 3, and 4). In the canonical model of Notch signaling, "signal-sending" cells express transmembrane Notch ligands (in mammals: Delta-like [Dll] 1, 3, and 4; Jagged [Jag] 1 and 2), which bind in *trans* to Notch receptors on "signal-receiving" cells; initiation of ligand endocytosis (transendocytosis) creates a pulling force on the receptor sufficient to induce a conformational change and expose protease cleavage sites on Notch. Extracellular cleavage by an ADAM (a disintegrin and metalloproteinase) followed by intracellular cleavage by the γ-secretase complex releases the Notch intracellular domain (NICD) in the signal-receiving cell (*331–333*). The NICD undergoes rapid nuclear translocation and forms a transcriptional

transactivation complex with Mastermind-like (MAML) and the transcription factor RBPJ (Recombination Signal Binding Protein for Immunoglobulin Kappa J Region; also known as CSL), displacing co-repressors from RBPJ and activating Notch target genes, including *HES1, HEY1, HEY2,* and *HEYL* (*332–334*). Emerging evidence suggests considerable complexity in regulation of Notch signaling, for example, through binding of Notch receptors and ligands expressed on the same cell (the *cis* interaction), receptor endocytosis (*331*), and differential effects of different ligands on clustering of the same receptor resulting in different signaling dynamics and downstream transcriptional programs (*335*).

Notch3 is highly expressed by both brain and non-brain mural cells in humans and animal models (*56*, *90*, *336*) (also see Chapter 4). Furthermore, the canonical Notch target genes *Heyl* and *Hey2* are highly enriched in mural cells compared to both neural crest and other neural crest-derived mesenchymal cells (i.e., fibroblasts), suggesting Notch signaling as a key pathway controlling specification of mural cells (*56*, *325*, *336*). Early evidence for a role of Notch3 in neurovascular unit function came from the identification of mutations in the *NOTCH3* gene as the cause of cerebral autosomal dominant arteriopathy with subcortical infarcts and leukoencephalopathy (CADASIL) (*337*, *338*). These mutations occur in the region of the *NOTCH3* gene encoding the extracellular domain of the receptor, which likely cause impaired clearance of the extracellular domain after cleavage (the ectodomain) (*339*). VSMCs and pericytes likely both contribute to CADASIL pathogenesis (*339*, *340*). Although the presence of mural cells in CADASIL brains could be interpreted as evidence that Notch3 is dispensable for mural cell development, CADASIL mutations likely do not cause complete loss of Notch3 function.

To address the necessity of Notch3 for brain mural cell development and function, Wang and colleagues analyzed *notch3*-deficient zebrafish (*341*). These animals had BBB defects and a

dramatic reduction in brain pericyte abundance compared to controls, which could be partially rescued by overexpression of the Notch3 intracellular domain. The authors used heat shock-inducible ubiquitous expression of Notch3 extracellular domain (N3ECD), which interferes with ligand binding to endogenous Notch receptors, to attenuate Notch3 signaling after initial establishment of pericytes on brain vasculature. This strategy led to moderate reductions in pericyte number and a decreased percentage of EdU-incorporating pericytes, suggesting that Notch3 controls pericyte proliferation (*341*). This study, however, did not directly address whether Notch3 also controls initial specification/differentiation. A landmark study by Ando *et al.* used zebrafish with fluorescent reporters for mural cells (*pdgfrb*-mCherry and *abcc9*-GFP) to clarify the role of Notch signaling in mural cell development (*326*). This work convincingly demonstrated that (i) naïve mesenchyme initially expresses low levels of *pdgfrb*, (ii) *pdgfrb*^{high} mural cells emerge from naïve mesenchyme in the vicinity of arteries between 36 and 48 hours post-fertilization (the "specification period"), (iii) concomitant with the increase in *pdgfrb* expression, these cells acquire expression of the pericyte marker *abcc9* (*342*), (iv) subsequently, mural cells of large vessels acquire VSMC characteristics, including *tagln* and *acta2* expression, (v) pharmacological inhibition of Notch signaling with the γ-secretase inhibitor DAPT during the specification period leads to virtually complete loss of mural cells, (vi) morpholino-based knockdown of *notch2* leads to a ~50% loss of arterial intrasegmental (trunk) vessel mural cell coverage and knockdown of *notch2* and *notch3* leads to complete loss (Figure 1.7), (vii) compared to wildtype zebrafish, combinations of *notch2*-null or heterozygous and *notch3*-null or heterozygous animals exhibit partial to complete mural cell loss in both neural crest-origin and mesoderm-origin regions, and (viii) the relative contribution of Notch2 versus Notch3 exhibits modest regional variation, with Notch3 more important in brain (*326*). Thus, we can conclude that Notch signaling is required for mural cell specification, Notch2 and Notch3 function

partially redundantly in this process, and the "default" mural cell fate has characteristics of pericytes, with yet-unidentified signals controlling the transition to VSMCs. Arterial ECs are likely the source of Notch ligands given their proximity to emerging *pdgfrb*^{high} cells (*326*) and expression profiling suggesting high levels of *Dll4* and *Jag2* expression (*56*).

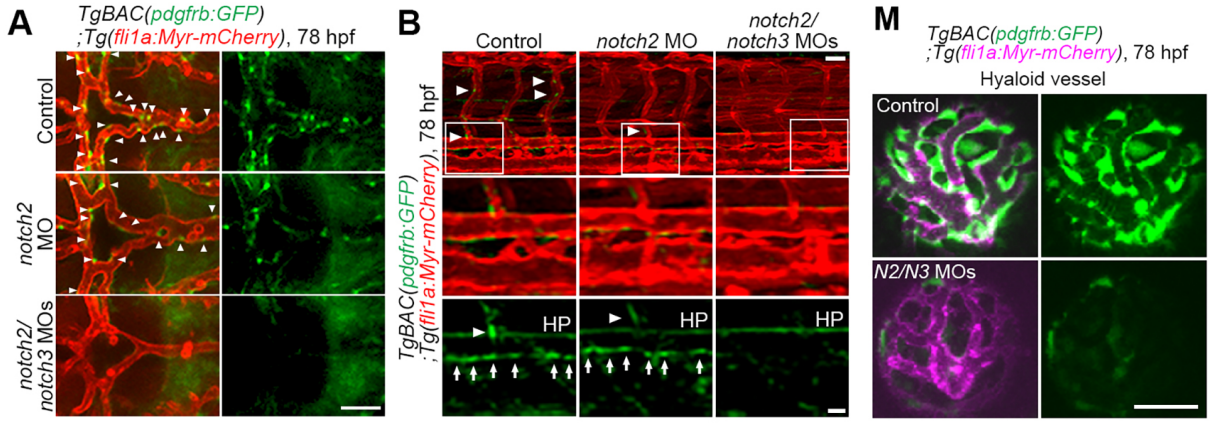

Figure 1.7. Notch signaling in zebrafish mural cell development. Emergence of *pdgfrb*$^{+}$ mural cells around developing blood vessels of the cerebral base (A), trunk (B), and hyaloid (M), in control, *notch2* morpholino (MO)-treated, and/or *notch2/notch3* MO-treated embryos. Mural cells of the cerebral base and trunk are mesoderm-derived, while those of the hyaloid are neural crest-derived. MO-mediated inhibition of Notch signaling results in deficits in mural cell development. Republished with permission of the Company of Biologists Ltd., from Ando *et al.,* "Peri-arterial specification of vascular mural cells from naïve mesenchyme requires Notch signaling." *Development* **146** (2):dev165589, 2019 (*326*); permission conveyed through Copyright Clearance Center, Inc.

1.4.2.3 Other mechanisms in mural cell development

Some studies have addressed cell-autonomous mechanisms of mural cell development. For example, the forkhead box transcription factors *Foxc1* and *Foxf2* are expressed by brain mural cells (among other cell types, including brain ECs), and deletion of either gene results in abnormally high mural cell proliferation (*343*, *344*). Conditional knockout of *Foxc1* in *Pdgfrb*$^{+}$ cells led to increased mural cell proliferation and microhemorrhages, suggesting a mural cell-autonomous effect (*343*). *Foxf2* knockouts had similar hemorrhages, increased endothelial caveolae, and thinned vascular basement membrane, which correlated with decreased TGF-β signaling, although the authors did not rule out a role for endothelial Foxf2 in these phenotypes

(*344*). Notably, *Foxf2* knockout did not affect expression of *Foxc1*, suggesting these transcription factors function independently despite similar downstream roles in regulating mural cell proliferation and potential crosstalk with endothelium (*344*). Signaling inputs to these and other transcription factors identified by expression profiling as brain mural cell-enriched (e.g., *Foxs1*, *Foxd1*, *Ebf1*, *Hic1*, *Tbx2, Tbx15, Tbx18*) (*56*, *83*, *90*, *102*, *336*, *345*), however, remain unknown. Finally, while molecular mechanisms controlling mural cell specification require additional clarification, mechanisms controlling diversification of mural cell subtypes (VSMCs, ensheathing, mesh, and thin strand pericytes; see Section 1.3.2.2), are virtually altogether unknown. One hypothesis that merits investigation is that differences in endothelial cell phenotype along the vascular tree impart signals to mural cells causing them to adopt these different fates.

1.4.3 Vascular regulation of neuronal and glial development

While the majority of studies discussed previously have investigated regulation of the vasculature by neural tissue, the CNS vasculature also regulates neuronal and glial development. For example, Palmer *et al.* observed that in the adult rat subgranular zone, a region of the hippocampus in which neurogenesis continues throughout life, proliferating cells are found in clusters, and these clusters contain both endothelial and neural cells (*346*). Subsequent coculture experiments demonstrated that in the presence of endothelial cells, neural stem cells have an increased rate of symmetric division (proliferation), and retain their ability to differentiate to neurons, astrocytes, and oligodendrocytes upon withdrawal of ECs (*347*). Angiogenesis and neurogenesis are also coupled in the adult *Serinus canarius* (canary) forebrain: testosterone stimulates VEGF production by neural tissue, which induces EC proliferation and EC production of brain-derived neurotrophic factor (BDNF), which promotes recruitment of neurons (*348*).

Similarly, neuroblasts originating in the subventricular zone of adult mice migrate along the rostral migratory stream to the olfactory bulb, guided by blood vessel-derived BDNF (*349*).

There are numerous additional examples of the importance of the "vascular niche" for adult neurogenesis (reviewed in (*350*)), and although adult neurogenesis in humans is the subject of debate (reviewed in (*351*)), there are similar examples of the vasculature regulating neural cell generation and migration during embryonic development. Oligodendrocyte progenitor cells (OPCs) are generated in spatially restricted domains and must migrate throughout the CNS. An overwhelming majority of these OPCs closely associate with and migrate along blood vessels shortly after their generation; OPC migration is disrupted in *Gpr124* knockout mice, with OPCs spatially restricted to the incompletely-formed vascular plexus (*352*). The interaction between OPCs and the vasculature is likely mediated by vascular SDF1 (Cxcl12) and OPC Cxcr4 (*352*). Bidirectional signaling between the vasculature and neural progenitors is also required for OPC specification: in the motor neuron progenitor domain of the developing spinal cord, neural progenitor-derived angiopoietin-1 signaling to its EC receptor Tie2 induces TGF-β1 production by ECs, which drives OPC generation (*353*).

The vasculature also plays a role in neuron development. Reelin is a protein secreted by Cajal-Retzius cells that controls neuron migration in the developing brain, with Reelin mutant mice (*reeler* mice) exhibiting a loss of the layered neuronal cytoarchitecture in cerebellum, neocortex, and hippocampus (*354–356*). In the canonical model of Reelin signaling, ligand binding to the receptors ApoER2 (LRP8) and VLDLR induces Dab1 phosphorylation by Src and Fyn; phosphorylated Dab1 activates downstream signaling cascades, such as PI3K (*357*). Notably, though Reelin was initially thought to act directly on neurons, ECs express ApoER2 and Dab1, and EC-specific knockout of *Dab1* in mouse embryos causes slight defects in neocortical and retinal vascular density and marked disruption of neuronal layering in the

neocortex (*358*). Endothelial *Dab1* mutants also have (i) decreased radial glia density at the pial basement membrane, (ii) reduced coverage of the vasculature by astrocyte endfeet, and (iii) increased BBB permeability, which correlates with EC tight junction abnormalities and increased vesicle density, among other defects (*358*). Taken together, these examples demonstrate that complex, bidirectional interactions between the vasculature and parenchymal cells are required for normal CNS development.

1.5 Model systems for studying the neurovascular unit

In the previous section, I reviewed current knowledge of neurovascular unit development and function and highlighted key areas where improved understanding is necessary, with only brief mention of the model systems used in the investigations. Given that all model systems have limitations and underlying assumptions that can profoundly affect interpretation of results, a more complete discussion of model systems themselves is warranted. Generally, model systems commonly employed for studying neurovascular unit development and function can be categorized as animal models, *in vitro* (cell culture) models, and human tissue models, along with a relatively small number clinical studies in the context of disease (*359*, *360*) and computational studies (*361–363*). Prior to examining benefits and drawbacks of each, it is important to consider general principles related to the use of model systems in biological research: (i) our goal is to better understand human biology, and we use model systems as a proxy for human biology; (ii) virtually all model systems are imperfect mimics of human biology; and (iii) the extent to which a model system can adequately mimic human biology differs depending on the specific scientific question under investigation. Therefore, the strengths and weaknesses of different model systems must be considered in the context of a particular question or application, and these considerations should inform choice of model, or lead to the conclusion that no currently available model is suitable and that further model development is

necessary. Further, different model systems are often complementary, such that the most complete understanding of a phenomenon can be achieved through the use of multiple model systems.

1.5.1 Animal models

Principles of biological function are highly conserved across species at multiple levels: basic cellular functions are conserved from single cell organisms to humans, and perhaps more surprisingly, mechanisms of cell fate determination and differentiation are conserved from the simplest animals to humans. In *Molecular Biology of the Cell*, *4th Ed.* (2002), the authors write:

> One would no more expect the worm, the flea, the eagle and the giant squid all to be generated by the same developmental mechanisms, than one would suppose that the same methods were used to make a shoe and an airplane […] One of the most astonishing revelations of the past ten or twenty years has been that our initial suspicions are wrong. In fact, much of the basic machinery of development is essentially the same, not just in all vertebrates but in all the major phyla of invertebrates too. (*364*)

Signaling pathways, transcription factor-gene regulatory networks, and specific anatomical features (e.g., of particular interest here, the mechanisms for regulating the neural microenvironment, as discussed in Section 1.3.1), become increasingly similar with decreasing evolutionary distance, such that vertebrates, tetrapods, and mammals are increasingly good models of the human (Table 1.1). Species-specific differences, however, do exist and are important in some contexts (discussed further below). Given the high level of conservation, we can learn a considerable amount about human neurovascular unit development and function using animal models, and such models are currently indispensable for a complete understanding of physiology. The complexity of an animal, including simultaneous development of dozens (or

hundreds) of cell types, cell-cell interactions, spatially organized tissues, multiple interacting organ systems, environmental influences, and changes to cell/tissue/organ function occurring on multiple timescales, is simply impossible to replicate *in vitro*. Take, for example, neurovascular coupling as discussed above in Section 1.3.2: this process involves stimulus-evoked activation of neurons in a specific brain region, transduction of a signal from neurons to VSMCs and ensheathing pericytes (via astrocytes, capillary pericytes, capillary endothelial cells, arterial endothelial cells, and/or potentially other yet-unidentified cell types), VSMC and ensheathing pericyte (and potentially capillary pericyte) dilation/constriction of vessels existing under blood pressure, and an eventual return to baseline vascular tone. While certain aspects of this process can be studied using isolated cells (e.g., function of K_{ATP} channels in pericytes), the entire process is simply too complex to replicate *in vitro* using currently available technologies.

Table 1.1. Animal models.

Species	Relevant considerations
Rodent (mouse/rat) vertebrate, tetrapod, mammal	• High level of human conservation • Large number of genetic models available • Large number of analysis reagents (antibodies) available
Avian vertebrate, tetrapod	• Fast-developing • Established methods for tissue grafting and chimera generation
Zebrafish vertebrate	• Fast-developing • Optically clear • Moderate number of genetic models available

With this complexity, however, comes difficulty in studying functions of specific cell types and investigating molecular mechanisms. For example, simple gene knockouts (e.g., *Pdgfrb* knockout discussed above) often lead to widespread dysfunction or lethality, and even cell type-specific "marker" genes are likely expressed in multiple organs, making it difficult to pinpoint the specific function of a gene in a certain cell population. An ever-growing set of genetic tools, however, permits manipulation of specific populations of cells in a temporally-

controlled manner. In rodents, the Cre-Lox system has been widely adopted for this purpose, in which animals are genetically engineered to express Cre recombinase, which acts on LoxP sites that have been introduced into the genome (*365*). Numerous strains have been developed in which Cre expression is controlled by promoters of cell type-specific genes, and in which Cre is fused to the estrogen receptor (Cre-ER), permitting inducible activity upon administration of tamoxifen or similar molecules. For example, in the context of neurovascular unit studies, commonly used drivers are *Cdh5*-Cre (*352*), *Cdh5*-CreER^{T2} (*124*, *248*, *366*, *367*), *Tie2* (*Tek*)-Cre (*65*, *71*, *123*, *247*), *Pdgfb*-CreER (*71*, *226*, *238*, *241*), and *Slco1c1*-CreER^{T2} (*20*, *368*) for endothelial cells and NG2 (*Cspg4*)-CreER^{T2} (*163*), NG2 (*Cspg4*)-CreER^{TM} (*159*, *369*), *Pdgfrb*-Cre (*164*, *343*, *370*, *371*), and α-SMA (*Acta2*)-CreER^{T2} (*369*) for mural cells. Imperfect cell type-specificity is an important caveat of such drivers: *Cdh5* is expressed in all ECs, not just CNS ECs. Similarly, *Cspg4* and *Pdgfrb* are not CNS-specific and are also expressed in some non-mural cells (*372*). Thus, improved specificity remains a goal, and recent advances include *Atp13a5*-CreER^{T2} as a highly specific driver for murine CNS pericytes (*373*) and the combination of *Cspg4* and *Pdgfrb* as a more specific driver for pericytes (*167*).

Cre acts on LoxP sites, and numerous strains have been developed containing LoxP sites in endogenous genes, which permits gene knockout or generation of truncated/modified proteins. Other strains have been engineered with LoxP sites flanking a stop codon upstream of a transgene, usually inserted into a constitutively expressed locus, which enables Cre-mediated transgene expression. These transgenes include: (i) additional alleles of endogenous genes (e.g., for overexpression); (ii) genes encoding "reporters" such as fluorescent proteins or β-galactosidase (e.g., for labeling specific cell populations *in vivo*, for subsequent sorting or identification of cells in tissue sections, or for linage tracing), or calcium-sensitive fluorescent proteins; (iii) genes that permit manipulation of cells (e.g., optogenetic stimulation using

channelrhodopsins (*159*, *164*), ablation using the diphtheria toxin receptor (*167*), or activation using designer receptors exclusively activated by designer drugs (*124*)). The ability to mate Cre-expressing strains with LoxP site-containing (or "floxed") strains generates substantial combinatorial flexibility. Mouse models with fluorescent reporters directly under the control of cell type-specific promoters, including *Tie2* (*Tek*)-GFP (*71*, *102*, *159*, *196*, *226*), *Pdgfrb*-GFP (*83*, *374*), *NG2*-DsRed (*27*, *83*, *196*, *374*), α-SMA (*Acta2*)-mCherry (*159*), and *Col1a1*-GFP (*369*), have also been widely adopted for imaging and sorting.

Such fluorescent reporters have also facilitated adoption of zebrafish as a model system for studying the neurovascular unit (*249*, *262*, *375*). Zebrafish, although more evolutionarily distant from humans than rodents, have several advantages, including faster development, and smaller size and translucence, which enables imaging the entire brain of live animals (Table 1.1). Injection or electroporation of morpholinos, antisense oligonucleotide analogs, permits spatially and temporally controlled knockdown of gene expression (*237*, *249*, *341*, *360*, *376*). CRISPR/Cas* systems, which permit both targeted and screening-based genetic modification, have also facilitated studies of neurovascular unit development and function in zebrafish (*249*, *262*) and other animal models (*247*). The avian model system has been widely used for chimera or grafting studies, in which portions of quail embryos are grafted into chick embryos, or vice-versa, and the resulting cell types, phenotypes, and graft versus host origin analyzed. Homotopic grafts are useful for lineage tracing, for example, in cataloging the derivatives of the neural crest (*377*, *378*), and heterotopic grafts are useful for studying roles of microenvironmental factors, for example, in revealing that neural tissue induces BBB properties in ECs (*218*).

*clustered regularly interspersed short palindromic repeats/CRISPR-associated protein (nuclease); a prokaryotic adaptive immune system that has been engineered for sequence-specific genome editing (*669*)

Even with these tools, some mechanistic conclusions remain elusive. For example, as discussed above, it is difficult to ascertain whether capillary pericytes actively dilate in response to physiological stimuli. Further, establishing the sufficiency of a molecule to elicit a specific cellular phenotype is difficult given the complex molecular environment *in vivo*. For example, while β-catenin stabilization is sufficient to induce GLUT-1 and/or suppress PLVAP in ECs of some CVOs (*71*, *379*), such an effect is not observed in liver or lung ECs (*367*), suggesting that unknown molecular signals in CVOs make ECs responsive to β-catenin or, conversely, unknown molecular signals in liver/lung make ECs nonresponsive to β-catenin. In other words, findings of sufficiency are context-dependent and difficult to generalize. Despite these drawbacks, animal models are the only available experimental tool that captures the full complexity of physiology and are vital to advance our understanding of the NVU. Specific examples of such advances have been extensively illustrated in the previous sections on NVU function and development.

Animals have also been used to model disorders with NVU involvement and evaluate trans-BBB transport of candidate drugs or drug delivery strategies for CNS disorders. These topics have been extensively reviewed (*16*, *122*, *380*) and are not a direct focus of this work, so I will limit discussion to a few examples that highlight the benefits and drawbacks of animal models for these applications. In the context of disease, NVU pathology typically involves multiple cell types and often involves alterations to blood flow or blood composition; thus, animal models are well-suited to modeling these complex, interacting phenomena. For example, mouse models have been used to understand the potential role for pericytes in capillary constriction after ischemia (*26*, *27*), the temporal evolution of BBB integrity after stroke (*23*), the multicellular mechanism by which the Alzheimer's disease (AD) risk variant apolipoprotein E4 causes a cascade of vascular and neuronal dysfunction (*381*), and the sites and mechanisms of immune cell entry into the CNS during neuroinflammation (*382*, *383*), among numerous other

examples. Similarly, animal models have been used to test strategies for trans-BBB drug delivery and are necessary for pharmacokinetic and pharmacodynamic studies, and for evaluating the degree to which "platform" BBB delivery vehicles (*384*) target sites other than the CNS. In this context, a paradigm of initial *in vitro* screens followed by *in vivo* validation has been used to identify antibody candidates that cross the BBB and have varying levels of CNS-specificity versus other organs (*385*). *In vivo* screening approaches have also been used to directly identify antibodies that target the rodent brain endothelium (*386*). Animal studies can also contribute key insight into spatiotemporal aspects of BBB drug delivery: a recent *in vivo* imaging study demonstrated that postcapillary venules serve as the predominant site of TfR-targeted nanoparticle transcytosis (*387*), an experimental finding inaccessible to *in vitro* models, which lack endothelial arteriovenous zonation observed *in vivo*.

1.5.1.1 Species differences

Species differences are an important consideration in using animals to model human disease or to identify drug delivery strategies. Notably, many human diseases with NVU involvement do not develop naturally in animals, and therefore must be artificially induced. For example, common animal models of Alzheimer's disease (AD) are mice that overexpress or express mutant forms of amyloid precursor protein (APP) and/or presenilin 1 (PSEN1) (*18*, *388*); although some cases of early-onset AD are caused by mutations in *APP*, *PSEN1*, and *PSEN2*, these constitute only 0.1–1% of all AD cases, the vast majority of which are of the late-onset, sporadic form (*389*). Similarly, EAE, a widely employed model of multiple sclerosis, involves immunization of rodents with myelin antigens and adjuvant (*390*). Thus, such strategies may not completely replicate pathogenic mechanisms. Furthermore, specific differences in gene/protein expression profiles complicate the investigation of specific disease mechanisms in animal models. For example, EC-expressed low density lipoprotein receptor-related protein 1 (LRP1) is

required for BBB clearance of amyloid-β in mice (*20*, *21*), yet, multiple sources agree that human CNS endothelial cells express little to no LRP1 (*187*, *391*, *392*).

Species differences in expression profiles, especially those of CNS endothelial transporters and other transmembrane proteins, are also important considerations in the use of animal models to identify drugs or drug delivery technologies that can cross the BBB. There are well-known differences in receptor, solute carrier, and efflux transporter expression and activity between humans and mice (*90*, *393*, *394*). Functionally, brain uptake of P-gp substrates differs between rodents, nonhuman primates, and humans (*88*). Further, recombinant adeno-associated viruses (AAVs) are under investigation as delivery vehicles for gene therapies, and several natural and engineered AAV capsid variants have been identified that cross the BBB and transduce neural cells (*395–397*). AAV-PHP.B is a promising candidate that was identified by screening in C56BL/6J mice (*396*), but was later found to be ineffective in several alternative mouse strains due to differences in expression and/or sequence of the AAV-PHP.B receptor Ly6a (lymphocyte antigen 6 family member A) (*398–400*); this AAV is also ineffective in non-human primates (*401*), as no Ly6a homolog exists in nonhuman primates or humans. This example illustrates the importance of identifying the molecular target of a BBB transport technology (virus or antibody), consulting human data, and using complementary human *in vitro* models early in the process of developing such a technology.

In summary, animal models are essential for advancing our understanding of NVU development and function, and for evaluating therapeutics, but have inherent limitations in species differences and complexity. These limitations can be mitigated by parallel use of complementary model systems, namely, targeted application of *in vitro* models and analysis of human tissue data, which are discussed below.

1.5.2 In vitro models

In vitro[*] models are constructed using cells isolated from an organism and maintained in culture. Common cell sources are summarized in Table 1.2. Such models are complementary to animal models for understanding NVU function and offer several advantages: First, *in vitro* models can be constructed using human cells, including primary cultures (e.g., those derived from blood, biopsy, or postmortem tissue) and cell lines. Human cells permit an assessment of whether an experimental finding in an animal model may be conserved in humans. Such comparisons, however, are often imperfect due to confounding effects discussed below. Second, both human cell- and animal cell-based *in vitro* models permit simplification of a biological system, and controlled manipulation and/or analysis of specific cells of interest. This facilitates efforts to understand the functions of a single cell type, the impacts of environmental factors (e.g., growth factors, drugs), and the mechanisms by which two cell types interact, in the absence of the *in vivo* milieu of cell types that would also respond to experimental treatments and indirectly influence the cells of interest. *In vitro* models also represent an attractive system for studying the impact of genetic manipulations (gene overexpression, knockdown, knockout, and/or mutation, achieved via transgene or siRNA transfection/transduction, CRISPR/Cas, and/or CRISPRi/a[†] systems) on specific cell types, without the need for Cre-Lox or similar strategies to achieve cell type-specificity. Third, *in vitro* models can be employed for large-scale exploratory or screening-based experiments without the ethical concerns of using animals for such studies.

The removal of cells from the complex *in vivo* environment is both an advantage of *in vitro* models, as discussed above, and a limitation. The lack of *in vivo* environmental cues often causes changes to cell phenotype. This phenomenon of "phenotype drift" or "dedifferentiation"

[*]meaning "in glass"
[†]CRISPR inhibition/activation (*670*)

occurs rapidly in culture for many cell types, including those of the NVU: isolated brain microvessels and monolayers of brain ECs from rodent, bovine, porcine, and human sources are well-established as *in vitro* models of the BBB (*402–407*); while acutely isolated (passage 1) ECs achieve transendothelial electrical resistance (TEER) of approximately 200 $\Omega \cdot cm^2$, passage 2 cells measure ~25 $\Omega \cdot cm^2$, indicative of a rapid decline in tight junction function (*408*). Immortalized brain EC lines such as hCMEC/D3 (human) (*409*), RBE4 (rat) (*410*), and bEnd.3 (mouse), which are widely used for *in vitro* experiments, also exhibit very low TEER of ~30–50 $\Omega \cdot cm^2$ (*409*, *411*, *412*). In contrast, *in vivo* TEER has been estimated at 1,400–8,000 $\Omega \cdot cm^2$ (*413–415*). Other BBB properties, such as efflux transporter activity, solute carrier and receptor expression, and low rates of vesicle trafficking (as discussed in Section 1.3.1) are also dysregulated to varying degrees in many *in vitro* models. The comprehensive review by Helms and colleagues provides additional detail on the properties of numerous *in vitro* models of the BBB (*412*). To profile CNS endothelial cell dedifferentiation on the transcriptome-scale, Calabria and Shusta used suppression subtractive hybridization to compare acutely isolated rat brain ECs to those cultured for 4 days (*416*). Culture-downregulated genes included those involved in canonical BBB functions (e.g., *Slc2a1*, *Mdr1a* (*Abcb1a*), *Tfrc*), and novel genes such as *Reck* that would later be implicated in Wnt signal transduction in CNS ECs. A recent study profiled transcriptomic and epigenomic differences between acutely purified mouse brain ECs and those cultured for 8 days (*226*). RNA-seq revealed maintenance of generic EC identity (similar expression of *Cdh5*, *Pecam1*, *Erg*), but loss of BBB-specific identity (downregulation of *Abcb1a*, *Mfsd2a*, *Slc22a8* and other solute carrier-encoding genes*, Lef1* and other Wnt-related genes, and upregulation of *Cav1*); ATAC-seq* revealed a marked loss of TCF/LEF peaks in cultured ECs, but, paradoxically, stabilization of β-catenin using the *Ctnnb1*^{flex3} allele (discussed

*assay for transposase-accessible chromatin with high-throughput sequencing (*671*)

in Chapter 3) was not sufficient to prevent or attenuate EC dedifferentiation (*226*). Finally, brain pericytes also undergo dedifferentiation in culture. A well-established hallmark of this process is upregulation of α-SMA (*417*), and additional molecular insight into this phenomenon is provided in Chapter 4.

Table 1.2. *In vitro* models.

Model	Relevant considerations
Primary cells	• Closely resemble cells *in vivo* if used immediately after isolation • Limited availability
Cell lines	• Scalable • Phenotype drift/dedifferentiation (loss of *in vivo* characteristics)
Cells derived from stem cells	• Scalable • Allow investigation of developmental processes • Can model some genetic diseases • Prone to discrepancies in cell identity, phenotype, maturity

1.5.2.1 Stem cells as a source of NVU in vitro models

Stem cells are an emerging alternative to primary cells and cell lines for the construction of *in vitro* models of the NVU. A stem cell is a cell type that possesses two attributes not shared by most adult somatic cells: (i) the capability to replicate and form more stem cells ("self-renewal") and (ii) the capability to differentiate into multiple distinct cell types (*364*). Stem cells can be further categorized by the number of cell types into which they are capable of differentiating ("potency"): multipotent stem cells are capable of differentiating into multiple cell types of a particular lineage (neural crest cells, for example, are multipotent; see Section 1.4.2), pluripotent stem cells are capable of differentiating into all cell types of the adult animal, and totipotent stem cells are additionally capable of forming extraembryonic tissues (*418*). Stem cells exist both during development and adulthood, with a prototypical example of adult stem cells being the multipotent hematopoietic stem cells of the bone marrow (*364*). Pluripotent stem cells *in vivo* form the inner cell mass of the blastocyst, and thus exist only transiently (*418*); Kaufman

and Evans (*419*) and Martin (*420*) first isolated these cells from mice and identified conditions that permitted *in vitro* culture of these embryonic stem cells (ESCs). Thomson and colleagues subsequently established nonhuman primate and human ESC lines, which retain self-renewal ability and potency to form cells of the three germ layers (*421*, *422*). Overexpression of the transcription factors Oct3/4, Klf4, Sox2, and c-Myc (*423*, *424*) or Oct4, Sox2, Nanog, and Lin28 (*425*) can "reprogram" terminally differentiated cells into pluripotent stem cells. The resulting induced pluripotent stem cells (iPSCs) can therefore be generated from skin biopsies or blood, and offer opportunities in patient-specific modeling of disease and regenerative medicine (reviewed in (*426*)). Finally, human pluripotent stem cells (hPSCs, a collective term for human ESCs and iPSCs) offer an unprecedented window into human developmental biology: while properties of terminally differentiated cells can be examined in tissue sections or in culture, molecular mechanisms of human cellular development and differentiation have been largely impossible to investigate except by analogy to findings in animal models. Human pluripotent stem cell differentiation offers an *in vitro* system to profile and manipulate transient developmental processes.

Both hPSCs and hematopoietic stem cells have been used to generate models of the BBB. Cecchelli *et al.* demonstrated that cord-blood derived $CD34^+$ hematopoietic stem cells could be differentiated into ECs, and that primary bovine pericyte coculture led to acquisition of BBB-like properties, including reduced permeability to Lucifer yellow and TEER of ~175 $\Omega \cdot cm^2$; the resulting cells also exhibited efflux transporter activity and drug permeabilities that correlated with *in vivo* data (*427*). Peripheral blood-derived $CD34^+$ cells have also been used to generate a similar BBB model (*428*). Lippmann, Azarin, and colleagues developed a method to differentiate hPSCs into cells having many attributes of BMECs: robust tight junctions, very high TEER, GLUT-1 expression, efflux transporter activity, and small molecule permeability that correlates

well with *in vivo* data (*429–431*). Several modifications and derivatives of this method have also been reported (*432–436*), and the resulting BMEC-like cells have been incorporated into three-dimensional and microfluidic systems (*436–439*) (also see Chapter 2), and used extensively for diverse applications including assessing candidate drug permeability (*385*, *440*, *441*), modeling genetic disease (*442–444*), and investigating impacts of environmental factors on BBB function or dysfunction (*445–450*). More recent evidence, however, suggests that the hPSC-derived BMEC-like cells resulting from the above differentiation protocols have epithelial rather than EC identity (*451–456*). Thus, while these cells remain well-suited for some applications, including drug permeability experiments that require the very high TEER not achievable in other human *in vitro* systems, new hPSC-derived models with definitive endothelial identity are needed for studies addressing molecular mechanisms of CNS EC development, function, and dysfunction.

To this end, there exist several well-established methods to differentiate hPSCs into ECs. Common protocols use growth factors (e.g., BMP4, Activin A, FGF2, VEGF) and/or small molecules (e.g., CHIR 99021) to direct hPSC differentiation to mesoderm, endothelial progenitors, and then ECs, followed by purification of ECs (*323*, *457–459*). Overexpression of the EC lineage transcription factor ETV2 in hPSCs can also be used to generate ECs, but the extent to which this strategy mimics natural EC development is unknown (*460–463*). In all cases, the resulting ECs lack tissue-specific specializations, such as those underlying BBB function, and are thus termed "generic" or "naïve." There have been several recent advances in modifying such generic ECs to serve as BBB models. Treatment of hPSC-derived endothelial progenitors with Wnt3a, RA, and VEGF yielded ECs with reduced Lucifer yellow permeability and increased TEER (~60 $\Omega \cdot cm^2$) compared to controls (*464*). Coculturing the resulting cells with pericytes induced P-gp activity. In another study, the authors overexpressed BBB-related transcription factors in hPSC-derived ECs and identified single factors and combinations of

factors that led to modest increases in TEER and BBB-like shifts in gene expression (*465*). Similarly, screening a compound library for increased claudin-5 expression in generic hPSC-derived ECs identified the TGF-β inhibitor RepSox as capable of modestly increasing TEER (~30 $\Omega \cdot cm^2$), reducing macromolecule permeability, and producing gene expression changes indicative of barriergenesis (downregulation of *PLVAP* and *ICAM1*, upregulation of *SLC2A1* and *ABCC4*) (*466*).

In collaborative work*, we recently adapted similar hPSC-derived generic ECs into a BBB model suitable for studying interactions with immune cells. Such interactions are important in diseases such as multiple sclerosis, where an abnormally high number of T cells interact with and cross the BBB, subsequently causing demyelination (*14*). T cells cross the BBB in a complex, multi-step process requiring endothelial expression of several adhesion molecules (reviewed in (*467*)), which are lacking in existing models of the BBB (*468*). We found that hPSC-derived generic ECs at Passage 1 (~6 days after isolation of endothelial progenitors), and at Passage 2 in some differentiations, exhibited constitutive and/or inflammatory cytokine-inducible expression of immune cell adhesion molecules such as ICAM-1, ICAM-2, VCAM-1, P-selectin, and E-selectin (*468*), but cultures contained contaminating smooth muscle-like cells and lacked paracellular barrier characteristics (Figure 1.8A and ref. (*468*)). Selective dissociation and extended culture of these ECs under serum-free, low growth factor conditions was sufficient to markedly decrease sodium fluorescein permeability and increase TEER to a level similar to that observed in existing *in vitro* BBB models constructed from primary BMECs or hematopoietic stem cells (Figure 1.8B-C and ref. (*468*)). Decreased permeability correlated with

*The collaboration was led by Dr. Hideaki Nishihara and Prof. Britta Engelhardt at the Theodor Kocher Institute, University of Bern and the study published as Nishihara H, Gastfriend BD, Soldati S, Perriot S, Mathias A, Sano Y, Shimizu F, Gosselet F, Kanda T, Palecek SP, Du Pasquier R, Shusta EV, Engelhardt B (2020). Advancing human induced pluripotent stem cell-derived blood-brain barrier models for studying immune cell interactions. *FASEB J* **34**:16693–715.

increased claudin-5 abundance, and the resulting cells had junctional occludin expression, a characteristic of CNS ECs (Figure 1.8D-F and ref. (*468*)). Unfortunately, inflammatory cytokine-inducible VCAM-1 expression was lost at this timepoint (Passage 3) (*468*). We noticed that treatment of ECs with $CoCl_2$ reduced SMLC contamination and also abolished VCAM-1 inducibility (Figure 1.9A), and therefore hypothesized that SMLC-derived signals were important for endothelial VCAM-1. Indeed, treatment of Passage 3 ECs with conditioned medium from SMLCs rescued VCAM-1 inducibility without compromising paracellular barrier properties (Figure 1.9B and ref. (*468*)); the resulting "extended EC culture method" (EECM)-BMEC-like cells were capable of functional interactions with T cells (*468*). EECM-BMEC-like cells were subsequently differentiated from control and multiple sclerosis patient iPSC lines, and differences in molecular properties and T cell interactions were suggestive of a potential EC-autonomous defect in multiple sclerosis (*469*). Chapter 3 describes the use of Wnt activation to achieve additional CNS-like properties in these ECs.

Other NVU cells have also been generated from hPSCs. Methods to differentiate neurons and astrocytes, including directed differentiation and transcription factor-based approaches, are well-established. These cells have been widely used to study cellular and molecular mechanisms of disease, identify drug targets and candidate drugs, and as potential cell therapy (e.g., for Parkinson's disease) (reviewed in (*470–472*)). The resulting cells have also been incorporated into multicellular models of the NVU, as described in Chapter 2. The pericyte is another neurovascular cell type that merits inclusion in hPSC-derived *in vitro* models. As discussed above (Section 1.4.2), pericytes of most organs are derived from mesoderm, and a number of well-established protocols exist to generate pericytes and/or VSMCs from hPSC-derived mesodermal progenitors that also have endothelial potential (so-called "early vascular cells" or "mesenchymoangioblasts") (*321*, *323*, *457*, *458*, *473*). While these cells share many attributes of

brain mural cells and have been incorporated in NVU models (*449*, *474*), deriving cells via a neural crest intermediate would better mimic the developmental trajectory of forebrain mural cells *in vivo*, and might yield cells with molecular or functional distinctions from those derived from mesoderm.

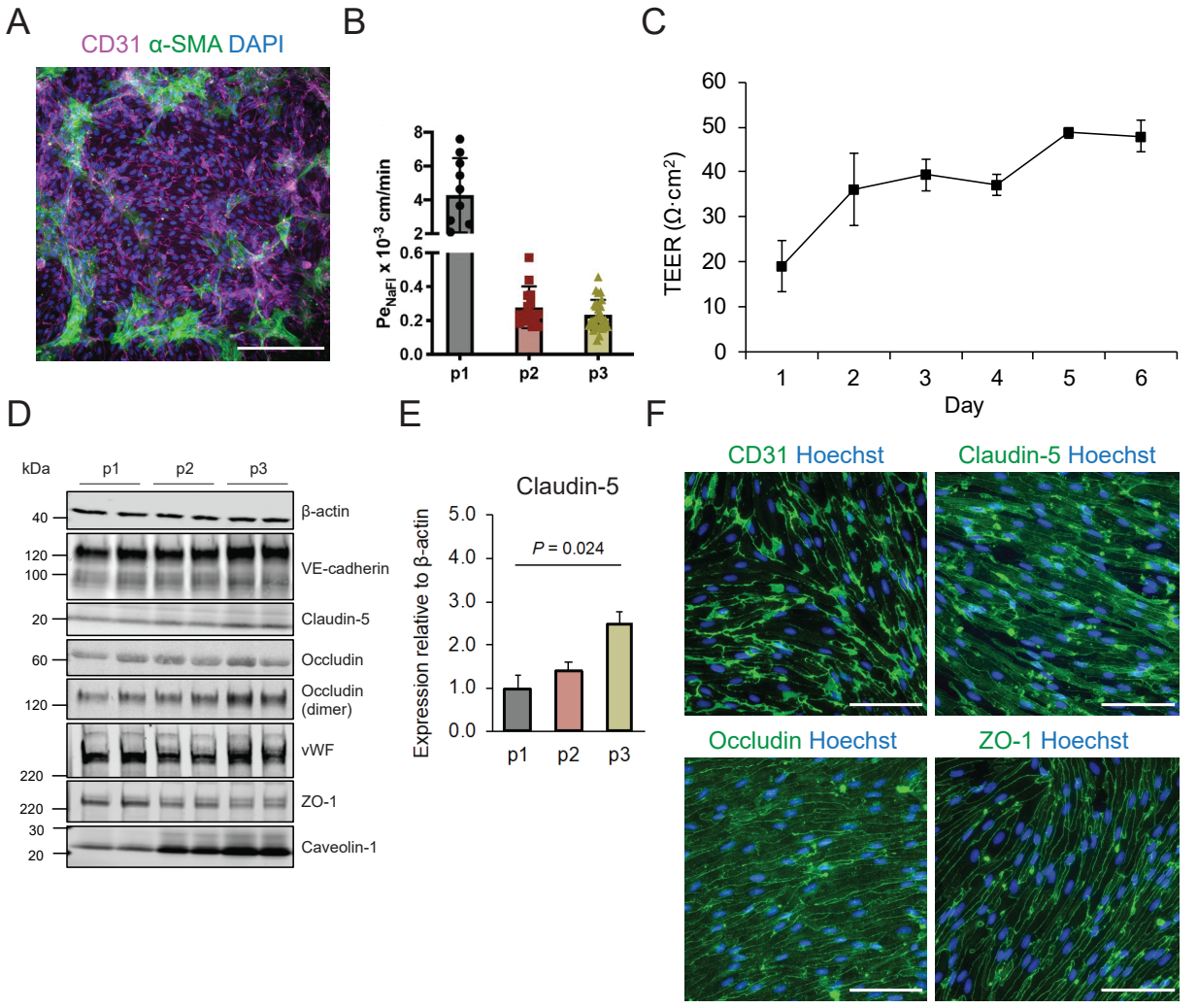

Figure 1.8. Extended culture of generic ECs yields cells with improved paracellular barrier properties. (A) Immunocytochemistry analysis of Passage 1 generic ECs derived from the IMR90-4 iPSC line. α-SMA$^+$ smooth muscle-like cells are present among the CD31$^+$ ECs. DAPI nuclear counterstain overlaid. Scale bar: 200 µm. (B) Sodium fluorescein (NaFl) permeability across Passage 1 ECs (p1) and Passage 2 and 3 EECM-BMEC-like cells (p2 and p3, respectively) derived from donor 2 iPSCs. Permeability was measured 6 days after seeding cells on 0.4 µm pore size Transwell filters. Points represent triplicate Transwells from at least three independent differentiations per condition; bars show means ± SD. Data courtesy of Dr. Hideaki Nishihara. (C) TEER profile of Passage 3 EECM-BMEC-like cells derived from the IMR90-4 iPSC line. Cells were seeded onto 0.4 µm pore size Transwell filters and TEER measured daily for 6 days. Plotted data are means ± SD of triplicate Transwells. (D) Western blots of Passage 1 ECs (p1) and Passage 2 and 3 EECM-BMEC-like cells (p2 and p3, respectively) derived from the IMR90-4 iPSC line. (E) Quantification of Western blot band intensity of claudin-5 normalized to β-actin. Plotted data are means ± SD of duplicate wells shown in (D). P-value: one-way ANOVA followed by Tukey's HSD test. (F) Immunocytochemistry analysis of Passage 3 EECM-BMEC-like cells from the IMR90-4 iPSC line. Cells were stained for CD31, claudin-5, occludin, and ZO-1. Hoechst nuclear counterstain overlaid. Scale bars: 100 µm. All figure panels from Nishihara *et al.*, 2020 (*468*). Used under a Creative Commons Attribution-NonCommercial-NoDerivatives License (https://creativecommons.org/licenses/by-nc-nd/4.0/).

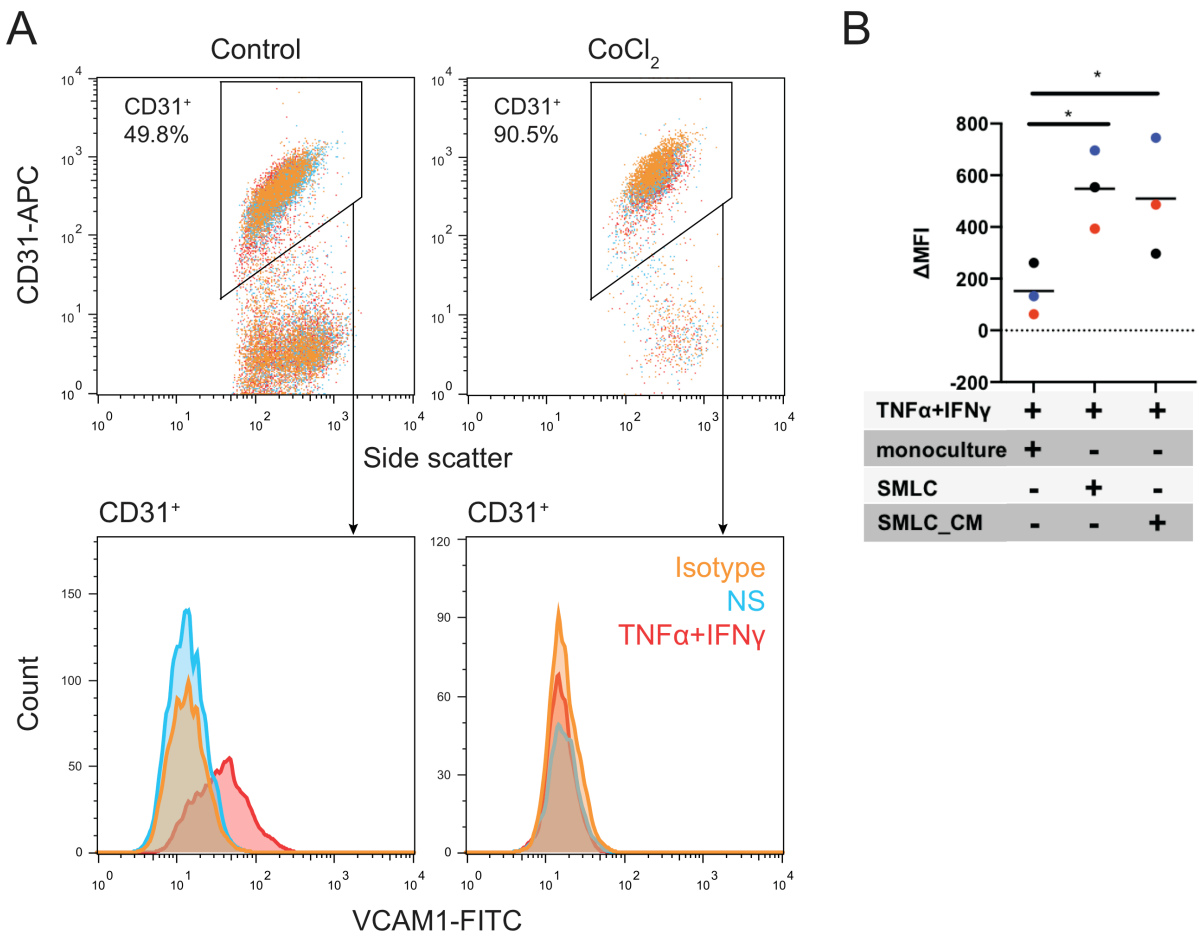

Figure 1.9. VCAM-1 expression in generic ECs and EECM-BMEC-like cells. (A) Flow cytometry analysis of CD31 and VCAM-1 expression in Passage 2 ECs from the IMR90-4 iPSC line. Cells were isolated via MACS at D5 and cultured in hECSR medium supplemented with 10 ng/mL VEGF. Cells shown right plots were cultured in medium additionally supplemented with 100 µM $CoCl_2$. 16 h prior to flow cytometry analysis, some wells were stimulated with 10 ng/mL TNF-α and 200 IU/mL IFN-γ (TNFα+IFNγ, red). Non-stimulated (NS, blue) cells and cells stained with mouse IgG_1 isotype control antibody (orange) are also shown. (B) Flow cytometry analysis of VCAM-1 expression in EECM-BMEC-like cells. The change in geometric mean VCAM-1 expression (VCAM-1 – isotype control) from cells in monoculture, cells cocultured with smooth muscle-like cells (SMLC), or cells cultured with conditioned medium from smooth muscle-like cells (SMLC_CM) are shown. Cells were stimulated with 1 ng/mL TNF-α + 20 IU/mL IFN-γ. Points represent the mean of at least three independent differentiations of donor 1 (black), donor 2 (red), and donor 3 (blue) iPSC lines. *$P < 0.05$, one-way ANOVA followed by Tukey's HSD test. Panel (B) from Nishihara *et al.*, 2020 (*468*). Used under a Creative Commons Attribution-NonCommercial-NoDerivatives License (https://creativecommons.org/licenses/by-nc-nd/4.0/).

Early reports by Cheung and colleagues demonstrated smooth muscle cell differentiation from hPSC-derived neuroectoderm and neural crest via treatment with PDGF-BB and TGF-β1, but the extent to which these cells had physiological properties similar to NVU mural cells was not addressed in detail (*475–477*). More recently, several groups have developed strategies to differentiate "brain-like" or "cranial" pericytes and VSMCs from hPSC-derived neural crest: In collaborative work*, we demonstrated that treatment of neural crest with minimal E6 medium (*478*) supplemented with 10% fetal bovine serum (FBS) was sufficient to yield cells with brain pericyte-like attributes, including expression of PDGFRB, NG2, and other markers, low expression of α-SMA, the ability to self-assemble with and stabilize EC cords, and the ability to improve barrier properties of hPSC-derived BMEC-like cells (*447*, *479*). On the transcriptome level, these cells compared favorably to primary human pericytes. Several additional groups have also reported pericyte-like cell differentiation from hPSC-derived neural crest using other basal media supplemented with FBS and, in some cases, PDGF-BB and/or FGF2 (*28*, *324*, *480*). The transcriptomic profiles of hPSC-derived brain pericyte-like cells derived via these protocols are remarkably similar to that of cultured primary human brain pericytes. Consequently, however, deficiencies in gene expression observed in cultured primary brain pericytes compared to pericytes *in vivo* (Chapter 4) are also observed in existing hPSC-derived brain pericyte-like cells. Thus, Chapter 5 describes a novel approach based on activation of Notch3 signaling to differentiate hPSC-derived neural crest into brain mural cells with an improved transcriptional profile.

---

*The collaboration was led by Dr. Matthew J. Stebbins and the study published as Stebbins MJ, Gastfriend BD, Canfield SG, Lee M-S, Richards D, Faubion MG, Li W-J, Daneman R, Palecek SP, Shusta EV (2019). Human pluripotent stem cell-derived brain pericyte-like cells induce blood-brain barrier properties. *Sci Adv* **5**:eeau7375.

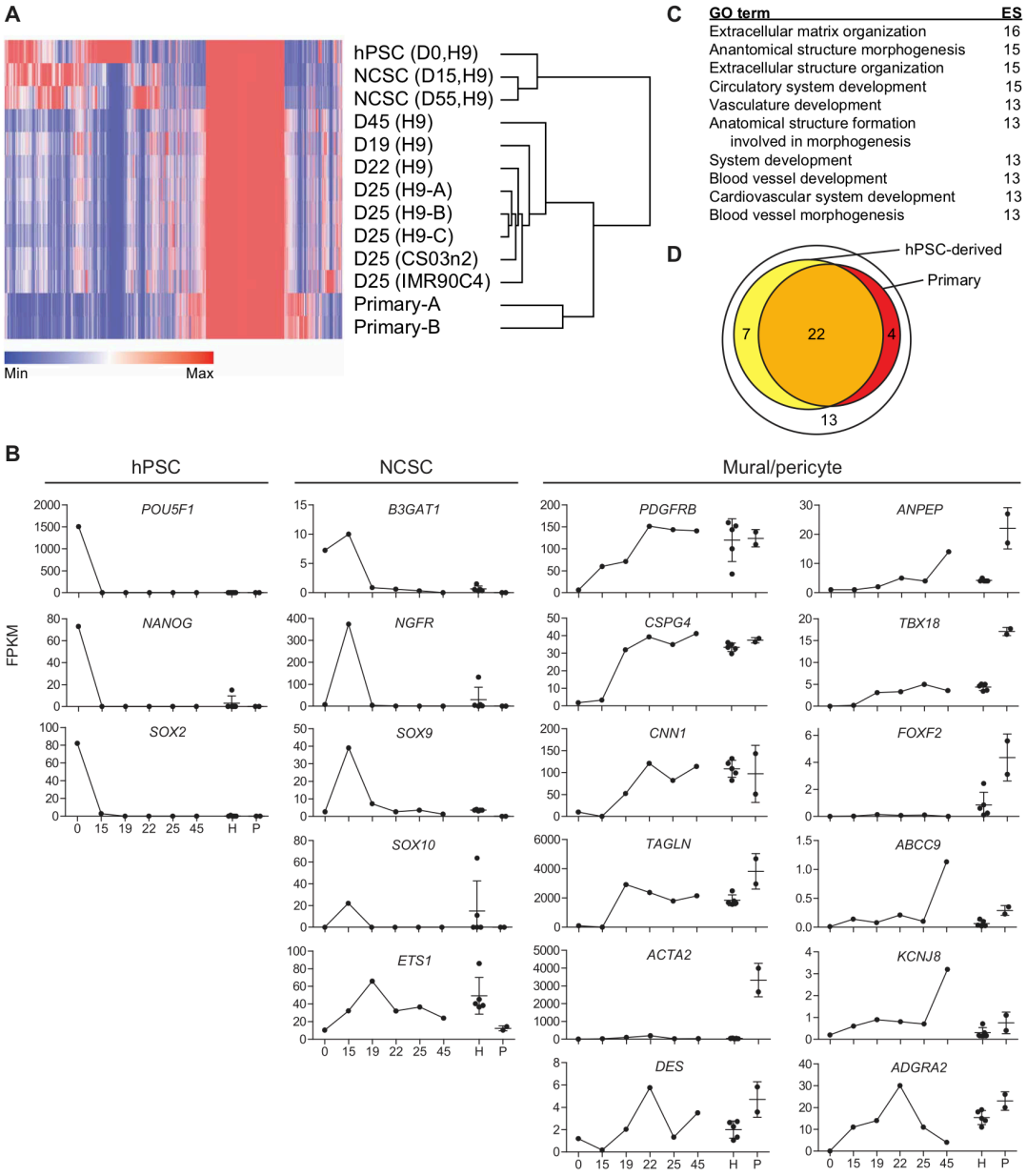

Figure 1.10. RNA-seq of pericyte-like cells and related cell types. (A) Hierarchical clustering based on all transcripts of undifferentiated H9 hESCs; H9-derived neural crest stem cells (NCSCs) at D15 and after an additional 40 days in E6-CSFD (D55); H9-derived pericyte-like cells at D19, D22, and D25 (three independent differentiations at the D25 time point, indicated as "H9-A," "H9-B," and "H9-C"); H9-derived pericyte-like cells maintained for an additional 20 days in E6 + 10% FBS (D45); CS03n2- and IMR90C4 derived pericyte-like cells at D25; and primary brain pericytes (from two distinct cultures of the same cell source, indicated as "Primary-A" and "Primary-B"). **(B)** Expression (FPKM) of selected transcripts in H9 hPSCs (day "0"), NCSCs ("15"), and during the differentiation of pericyte-like cells ("19," "22," "25," and "45"). The mean transcript expression in all D25 hPSC derived pericyte-like cells (H9-A to H9-C, CS03n2, and IMR90C4; "H") and in primary brain pericytes ("P") is also shown. Error bars represent SEM of five independent differentiations ("H") or of two primary pericyte samples ("P"). **(C)** Top 10 Gene Ontology terms sorted by enrichment score [ES = $-\log_{10}$(FDR)] for hPSC-derived pericyte-like cells. Genes included in the dataset were enriched in pericyte-like cells (average of all D25 samples) compared to NCSCs (average of D15 and D55 samples) ($FPKM_{\text{pericyte-like cells}}/FPKM_{NCSC} \geq 10$) and were expressed at ≥1 FPKM in pericyte-like cells. **(D)** Expression (≥1 FPKM) of murine pericyte-enriched transcripts [46 transcripts from ref. (*56*)] in hPSC-derived pericyte-like cells (29 transcripts) and primary brain pericytes (26 transcripts). A detailed listing of genes and FPKM values can be found in Table S2 of ref. (*447*). Figure from Stebbins *et al.*, 2020 (*447*). Used under a Creative Commons Attribution-NonCommercial License (https://creativecommons.org/licenses/by-nc/4.0/).

1.5.2.2 Multicellular models

Coculture experiments are a key application of *in vitro* models derived from primary cells, cell lines, and stem cells. Coculture experiments can be used to understand bidirectional signaling between two, or potentially more than two, cell types. For example, as discussed in Section 1.4.3, Shen *et al.* used Transwell cocultures to demonstrate that endothelium-derived factors stimulate neural progenitor cell expansion and neuron differentiation; notably, the authors of this work used two independent endothelial cell sources, and included control cell types (primary neural cells and NIH/3T3 fibroblasts) to rule out the possibility that generic effects such as nutrient consumption could explain the effects observed in endothelial cell cocultures (*347*). Additional examples of coculture-based *in vitro* studies are provided in Chapter 2, along with a more comprehensive discussion of coculture modalities common in NVU modeling, including Transwell, microfluidic, and aggregate-based approaches. Although cocultures have the potential to yield important insights, pervasive in the literature is the practice of combining more than two cell types without adequate effort to gain a mechanistic understanding of how each cell type contributes to the phenotype of each other cell type (*481–483*). The purported rationale for such studies is typically to better mimic the *in vivo* situation, but it is unlikely that any *in vitro* model constructed via the combination of three, four, five, or even a dozen independently cultured cell types better mimics *in vivo* phenotype given the phenomenon of culture-induced dedifferentiation and the abundance of other factors differing between *in vivo* and *in vitro* systems. Thus, at present, scientific questions requiring a mimic of the *in vivo* NVU are best addressed in animal models, and complementary questions addressing specific cellular functions or the interaction of two cell types are appropriately addressed by *in vitro* models. These limitations also highlight the need for improved *in vitro* models.

1.5.2.3 Organoid models

Organoids are an emerging *in vitro* system that may partially replicate the complexity of tissues *in vivo*, and offer an experimental bridge between animal models and *in vitro* cultures of single or multiple cell types. Organoids are three-dimensional cell aggregates that (i) contain multiple cell types, which have developed simultaneously from a common progenitor such as hPSCs or adult stem cells and (ii) have cytoarchitecture ("self-organization") resembling that of the relevant organ (*484–487*). Of interest here are brain organoids (or cerebral organoids), which develop from hPSCs into aggregates containing diverse populations of neural progenitors, neurons, and glia, arranged into layers similar to those in developing brain; depending on specific protocol, these organoids can spontaneously develop domains with cell compositions resembling specific brain regions, or be directed to adopt specific regional identity (*488–492*). Choroid plexus organoids, which replicate the barrier attributes and CSF-secretion of the choroid plexus epithelium, have also been generated by rational modifications of a cerebral organoid differentiation protocol (*493*). Recent evidence indicates that some brain organoids contain nonneural cells, including microglia (*494*), leaving open the possibility that small populations of vascular cells may also spontaneously arise in these models.

Directed approaches for incorporating vasculature into brain organoids have also been pursued, and such organoids may offer a promising new *in vitro* model of the NVU. For example, one approach has been to incorporate independently-differentiated hPSC-derived endothelial cells in the exogenous extracellular matrix (typically Matrigel) used to embed hPSC-derived brain organoids (*495*). Similar studies have incorporated hPSC-derived mesodermal progenitors (*496*) or primary human endothelial cells (human umbilical vein endothelial cells, HUVECs) (*497*) with hPSCs during organoid formation. Another approach used *ETV2* overexpression in a small fraction of hPSCs to generate brain organoids containing endothelial

cells (*498*). In general, these approaches yield organoids with endothelial cells organized into primitive vascular networks, but in most cases these structures are located superficially and not well-integrated into the core neural tissue. In a landmark study, Mansour and colleagues demonstrated an alternative approach for incorporating vessels: grafting of hPSC-derived brain organoids into mouse brain. The authors observed vascularization of the organoids by host-derived, perfused blood vessels, along with functional integration of organoid- and host-derived neurons (*499*). These observations were largely replicated in an independent study (*500*). While this approach is the only currently available strategy for generating brain organoids with *perfusable* vasculature, the resulting organoids no longer constitute a true *in vitro* model, and organoid-perfusing vessels are mouse-derived. In summary, organoids represent a promising *in vitro* model system for studies of NVU development, function, and disease, but additional work is needed to achieve the close interactions between endothelial and neural cells observed *in vivo*, and to develop genetic tools for cell type-specific manipulation.

1.5.3 Human tissue

Analysis of human tissue has the potential to complement studies in animal or *in vitro* models by providing insight into the potential relevance of findings to the *in vivo* human NVU. Tissue samples are distinct from *in vitro* (cell culture) models because the former are analyzed immediately upon collection or preserved by freezing or fixation, which permits analysis of molecular properties of cells that have not undergone culture-induced dedifferentiation, in addition to preserving cellular diversity and cytoarchitecture. Unlike cultured cells, however, tissues cannot be expanded, and human tissue is extremely limited in availability, with the only sources of brain tissue being postmortem samples and rare samples from neurosurgical resection. Further, the ability to experimentally manipulate tissue samples and measure physiological phenomena such as metabolism, molecular transport, and vessel dilation/contraction are

inherently very limited. For many questions related to the biology of the healthy human neurovascular unit, however, high-throughput, open-access databases can be an extremely powerful resource. Databases include transcriptomic (both bulk and single-cell) (*90*, *187*, *506*, *336*, *391*, *392*, *501–505*), proteomic (*507*), and epigenomic (*508*) data.

In collaborative work*, we contributed one such database by using bulk RNA-seq to profile the transcriptome of human brain microvessels isolated via laser-capture microdissection (LCM) from flash-frozen neurosurgical samples. Genes enriched in microvessels compared to matched whole brain samples included known markers of both the EC and pericyte constituents of microvessels (*90*). While LCM does not achieve cell type specificity afforded by other approaches, such as fluorescence activated cell sorting or scRNA-seq, it does not require tissue dissociation, a process known to cause transcriptional artifacts (*509*). Using mouse brain samples that were dissected and sequenced in parallel, we identified mouse-human species differences in brain microvessel transcriptomes (*90*). Finally, we performed a subtractive comparison between our human microvessel data and brain endothelial data from the literature (*501*) to generate a putative transcriptome profile of human brain pericytes; this analysis yielded known markers, such as *NOTCH3*, *PDGFRB*, *ZIC1*, and *ABCC9*, and also novel markers such as *SLC12A7* and *SLC6A12*, which are not expressed by mouse brain pericytes (Figure 1.11) (*90*). Chapter 4 presents a further refinement in the transcriptomic profile of human brain pericytes and VSMCs derived from multiple independent scRNA-seq studies.

Dr. Hannah Wilson Song designed the experiments and performed laser-capture microdissection; Koji L. Foreman and Benjamin D. Gastfriend analyzed and interpreted the data. This study was published as Song HW, Foreman KL*, Gastfriend BD*, Kuo JS, Palecek SP, Shusta EV (2020). Transcriptomic comparison of human and mouse brain microvessels. *Sci Rep* **10**:12358. (*contributed equally)

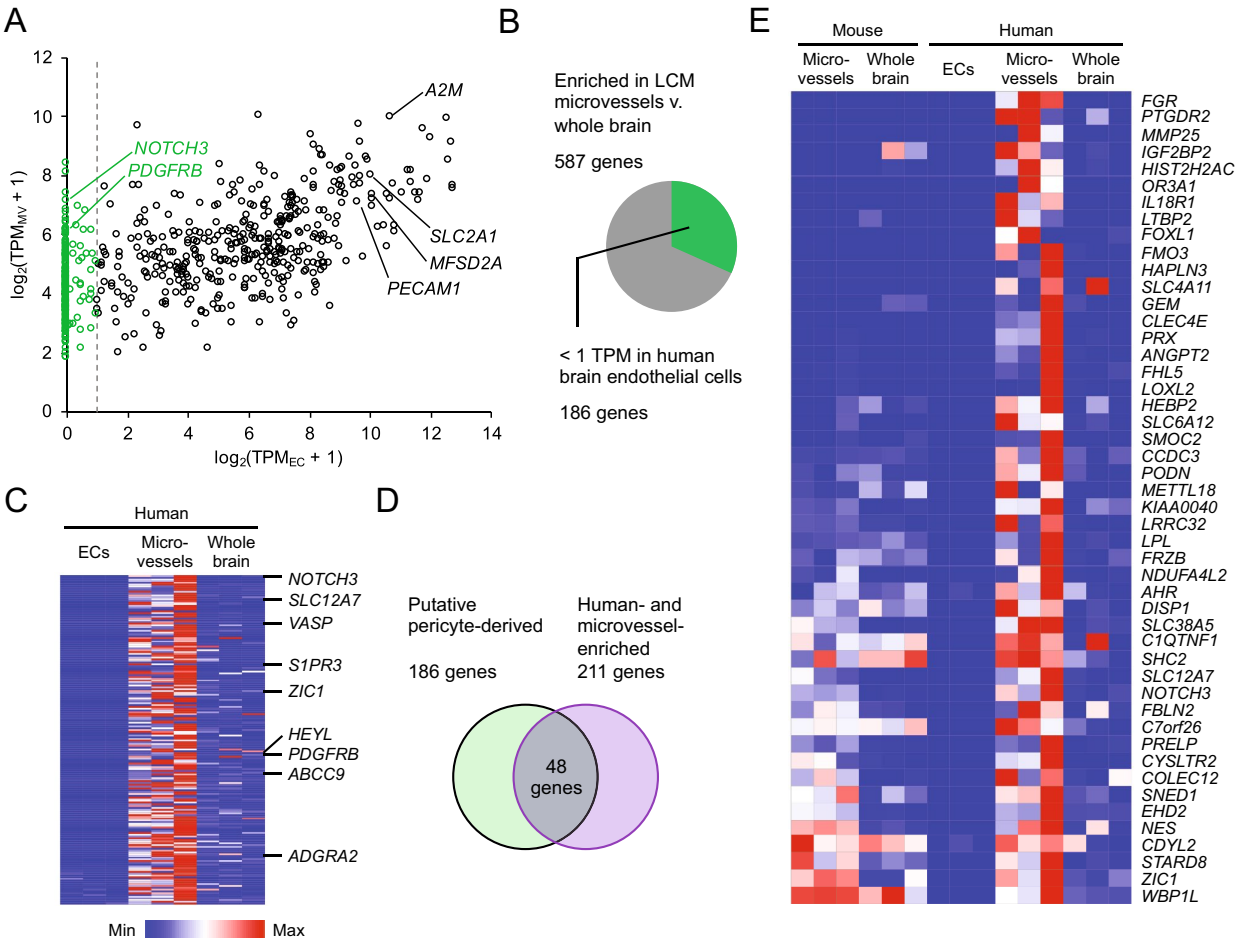

Figure 1.11. A putative gene expression profile of human brain pericytes derived via comparison of human LCM microvessel and brain endothelial cell transcriptomes. (A) Average transcript abundance of 587 human microvessel-enriched genes (as determined in ref. (*90*)) in human LCM microvessels (TPM_{MV}) versus reference human adult brain endothelial cells analyzed by single cell RNA-seq (TPM_{EC}) (*501*). Vertical line at $\log_2(TPM_{EC} + 1) = 1$ indicates the 1 TPM threshold employed to identify putative pericyte-derived transcripts in the microvessel samples. Endothelial genes (e.g. *PECAM1*, *MFSD2A*, *SLC2A1*, *A2M*) fall to the right of this line and are excluded, while known pericyte genes (e.g. *NOTCH3*, *PDGFRB*) fall to the left. Full results of this analysis are in Supplementary Table S6 of ref. (*90*). **(B)** Summary of results of thresholding analysis described in (A). **(C)** Heat map illustrating transcript abundance in biological triplicates of human brain endothelial cells and LCM microvessels and whole brain for the 186 putative pericyte genes identified in (A). Known and putative novel pericyte genes are annotated. Color indicates expression that has been normalized within each gene (row). **(D)** Summary of filtering strategy used to identify putative human-specific pericyte genes. Of the 186 putative pericyte genes identified in (A), 48 are also human-enriched (as determined in ref. (*90*)). **(E)** Heat map illustrating transcript abundance in biological triplicates of mouse LCM microvessels and whole brain, human brain endothelial cells, and human LCM microvessels and whole brain for the 48 putative human-enriched pericyte genes identified in (D). Genes are ranked by fold change in human versus mouse microvessels. Color indicates expression that has been normalized within each gene (row). Figure from Song *et al.*, 2020 (*90*).

One important application of human tissue is in benchmarking animal and *in vitro* models. Namely, transcriptomic and proteomic databases can be consulted to evaluate expression of genes/proteins of interest in relevant cell types. For example, two recent mouse studies have reported roles for brain pericyte-derived vitronectin in regulating neurogenesis (*510*) and BBB function (*511*). While *Vtn* is among the most highly enriched markers of brain pericytes in multiple mouse RNA-seq and scRNA-seq datasets (*56*, *83*), neither of the studies that evaluated functional roles for vitronectin addressed its expression in human brain pericytes, and lack of *VTN* transcript is apparent in multiple independent human RNA-seq and scRNA-seq datasets (*90*, *187*, *336*, *391*, *392*, *502–504*). Thus, it is unclear whether in humans, (i) pericytes do not carry out these functions, (ii) pericytes carry out these functions via alternative ligand(s), (iii) other cell types produce vitronectin, or (iv) lack of pericyte *VTN* expression is erroneous. Consulting expression data is similarly important in validating hPSC-based models of NVU cell types. In Chapter 3 we compare RNA-seq data from hPSC-derived ECs treated with a Wnt activator to publicly available scRNA-seq data from human brain ECs. In Chapter 5 we compare RNA-seq data from putative mural cells differentiated from hPSC-derived neural crest via Notch3 overexpression to publicly available scRNA-seq data from human brain mural cells.

Finally, human tissue is useful in performing early-stage validation of BBB drug delivery systems. For example, Georgieva *et al.* set out to identify single-chain variable fragments (scFvs) that undergo RMT across the BBB and could potentially be used to deliver drugs to the CNS. Initial rounds of scFv library screening were performed *in vitro*, using binding to primary human heart and lung ECs for negative selection, and binding to and internalization into hPSC-derived BMEC-like cells for positive selection. Lead candidate scFvs were evaluated for binding to microvessels in mouse and human brain tissue sections prior to mouse *in vivo* experiments assessing trans-BBB transport and biodistribution (*385*). Human and mouse brain tissue sections

were similarly used in parallel to identify variable lymphocyte receptors (VLRs, molecules from jawless vertebrates analogous to immunoglobulins) capable of binding to extracellular matrix prior to *in vivo* biodistribution and efficacy studies in mice (*512*). Such strategies that employ human tissue to complement *in vitro* and animal models may improve the likelihood that candidate drug delivery molecules will have translational relevance.

1.6 Conclusions

The NVU supports CNS homeostasis, is impaired in CNS disorders, and represents both an opportunity and challenge for CNS drug delivery. Understanding of NVU function has advanced dramatically from the early observations of dye exclusion to the present era of high-resolution ‘omics profiling and powerful tools for genetic manipulation. Nonetheless, we still understand only a small fraction of the cellular and molecular mechanisms regulating development and function of the NVU. Improving foundational knowledge in these areas may inform future strategies to treat human CNS disease. Some important questions, described in detail above, include:

- What signals control the acquisition of BBB properties in CNS ECs?
- From which cell types do these signals derive?
- How do CNS ECs signal reciprocally to mural cells, astrocytes, neurons, and other cells and what properties are regulated in this manner?
- What are the mechanisms controlling development of CNS mural cells?
- What are the molecular mechanisms underlying diversification of mural and endothelial subtypes?
- How do CNS mural cells differ functionally from those of other organs?

Answering these questions requires rational application of model systems, including animal models, *in vitro* models, and human tissue. In many cases, new or improved models are required to fully address these questions.

To this end, we focus in this work on advancing hPSC-based models of CNS endothelial and mural cells, using data from human tissue to understand the extent to which these models mimic cells *in vivo*. Because hPSCs are uniquely suited for examination of developmental processes, we use these models to address questions related to molecular mechanisms of mural cell differentiation and acquisition of BBB properties in ECs.

Chapter 2 *In vitro* models of the blood-brain barrier and neurovascular unit*

2.1 Summary

The blood-brain barrier (BBB) regulates the transport of ions, nutrients, and metabolites to help maintain proper brain function. This restrictive interface formed by brain microvascular endothelial cells excludes the majority of small and large molecule drugs from entering the brain, and blood-brain barrier dysfunction is a signature of many neurological diseases. Thus, *in vitro* models of the BBB based on brain endothelial cells have been developed to facilitate screening drugs for BBB permeability. However, while brain endothelial cells form the main interface, they work in concert with other brain-resident cells such as neural progenitor cells, pericytes, astrocytes, and neurons to form the neurovascular unit (NVU). Importantly, non-endothelial cells of the NVU play key roles in eliciting BBB phenotypes and in regulating the dynamic responses of the BBB to brain activity and disease. As a result, emerging *in vitro* BBB models have incorporated these NVU cell types in addition to endothelial cells. These multicellular BBB or NVU models have found increasing application not only in drug screening, but also in studying complex cellular and molecular mechanisms underlying BBB biology and disease.

2.2 Introduction

The blood-brain barrier (BBB) comprises highly specialized brain microvascular endothelial cells (BMECs) that maintain the delicate balance of ions, nutrients, and other molecules essential for proper brain function, while also excluding toxins from the central nervous system (CNS). Among the specialized properties of BMECs are (i) lack of fenestrae, (ii)

---

*This chapter published as Gastfriend BD, Palecek SP, Shusta EV (2018). Modeling the blood-brain barrier: beyond the endothelial cells. *Curr Opin Biomed Eng* **5:**6–12.

tight junctions between adjacent endothelial cells, (iii) presence of solute carriers that regulate ion and small molecule transport, (iv) expression of efflux transporters including P-glycoprotein (P-gp), Breast Cancer Resistance Protein (BCRP), and Multidrug Resistance Proteins (MRPs), (v) low levels of pinocytosis, and (vi) receptor-mediated processes for specific uptake of macromolecules (reviewed in (*16*, *98*, *513*)).

Although the microvascular endothelium constitutes this restrictive interface, other cell types present in the neurovascular microenvironment during development and adulthood including neural progenitor cells, pericytes, astrocytes, and neurons contribute significantly to the BBB phenotype. Increasing appreciation of the importance of multiple cell types in regulating dynamic BBB responses to physiological and disease stimuli has led to the concept of an integrated neurovascular unit (NVU), which minimally consists of BMECs, pericytes, astrocytes, and neurons (Figure 2.1A), and for some studies can extend to include neural stem cells or microglia.

The development of *in vitro* BBB models has been driven by the desire to understand BBB function in development, health, and disease. Moreover, because the BBB excludes the vast majority of small molecule, protein, and gene therapeutics (*85*), *in vitro* BBB models also offer a platform for screening drug candidates for BBB permeability. To date, considerable effort has led to the generation of many BMEC-based models of the BBB (reviewed in (*394*, *412*, *514*)). Importantly, *in vitro* models that incorporate multiple NVU cell types can have advantages over BMEC-only models. First, the presence other NVU cell types can induce or improve barrier properties, such as the formation of continuous tight junctions to reduce paracellular diffusion or "leakiness". When used for drug permeability screening, such models may therefore yield results that are more predictive of *in vivo* permeability. Second, multicellular models can provide a tool to interrogate paracrine and juxtacrine signaling that may underlie elements of BBB development

and maintenance. Finally, given emerging knowledge about the roles of neurovascular dysfunction in many diseases of the CNS (reviewed in (*16*, *515*)), *in vitro* models of the NVU, including those derived from patient-specific induced pluripotent stem cells (iPSCs), may provide opportunities to better understand molecular and cellular mechanisms of CNS diseases.

We will first briefly discuss the roles of neural progenitor cells, pericytes, astrocytes, and neurons in regulating the development and maintenance of the BBB. We will then review recent advances in BBB modeling resulting from incorporation of NVU cells to form multicellular BBB models, and highlight several examples of the utility of such models in understanding BBB biology and disease.

2.3 Roles of non-endothelial NVU cells in BBB formation and function

Stewart and Wiley (*218*) used quail-chick transplantation studies to show that developing neural tissue was necessary for endothelial BBB development. Subsequent work established the ability of both astrocytes (*251*, *516*) and neurons (*516*, *517*) to induce BBB phenotypes in endothelial cells. In addition, during early embryogenesis the BBB initially forms in the presence of neural progenitor cells when astrocytes are not yet present. Studies have demonstrated the ability of embryonic neural progenitor cells (NPCs) to induce BBB properties such as decreased endothelial permeability and improved tight junction formation *in vitro* (*518*), and it was later determined that Wnt/β-catenin signaling driven by NPCs is required for CNS angiogenesis and contributes to barriergenesis during development (*225*). In addition, signaling through retinoic acid secreted by radial glial cells (*268*), Hedgehog secreted by astrocytes (*276*), and GPR124 (*241*, *242*) have also been implicated in aspects of BBB development. Key roles for pericytes in barriergenesis have also been described, as pericytes regulate BBB endothelial tight junction morphology, transcytosis, and expression of leukocyte adhesion molecules (*30*). Pericytes are also required for the maintenance of the BBB in adulthood, as demonstrated by pericyte-

dependent endothelial gene expression, reduction in endothelial transcytosis, and astrocyte end-foot polarization (*256*). Furthermore, given the ability of astrocytes to induce and maintain endothelial BBB properties *in vitro*, the close association of astrocytes with endothelial cells *in vivo*, and correlations between astrocyte pathologies and BBB breakdown (reviewed in (*517*)), it is likely that continued astrocyte-endothelial signaling is necessary for BBB maintenance. Neurons similarly have the ability to induce and maintain BBB properties *in vitro* (*445*, *516*, *517*), but currently a detailed picture of neuron-endothelial crosstalk is lacking. Taken together, there is a clear impact of non-BMEC cell types on BBB formation and function motivating the development and use of multicellular NVU-type models to continue to advance our understanding of these complex phenomena in neural health, disease, and therapy.

2.4 Advances in multicellular BBB models

Recently developed multicellular BBB models have incorporated neural progenitor cells, pericytes, astrocytes, and neurons. These models have employed both primary and immortalized cells from human, rodent, bovine, and porcine sources. NVU cells derived from pluripotent stem cell or neural stem cell sources have also been used (Table 2.1). Most models have been constructed using either Transwell culture inserts or microfluidic devices, and models based on cell aggregates are an emerging alternative (Table 2.1). Below we will summarize each of these configurations as they pertain to the contribution of NVU cells to the BBB model.

Table 2.1. Summary of cell types and cell sources used in multicellular BBB models.

Neurovascular unit cell type	Species and cell source	References
BMECs	Human primary	(*519–524*)
	Human immortalized	(*521*, *525–528*)
	Human pluripotent stem cell-derived	(*429*, *430*, *435*, *442*, *445*, *450*, *529–532*)
	Porcine primary	(*407*, *533*)
	Rat primary	(*445*, *518*, *528*, *534*)
	Rat immortalized	(*517*)
	Mouse primary	(*530*)
	Mouse immortalized	(*530*, *531*, *535*, *536*)
Neural progenitor/stem cells	Human primary	(*430*, *529*, *534*)
	Human pluripotent stem cell-derived	(*529*)
	Rat primary	(*518*, *534*)
Pericytes	Human primary	(*430*, *435*, *519–521*, *523*, *524*, *529*)
	Human pluripotent stem cell-derived	(*532*)
	Porcine primary	(*407*, *533*)
	Rat primary	(*528*)
	Mouse immortalized	(*536*)
Astrocytes	Human primary	(*519*, *521–524*, *529*)
	Human pluripotent stem cell-derived	(*435*, *442*, *445*, *520*, *529*, *530*, *532*)
	Human neural progenitor cell-derived	(*430*)
	Porcine primary	(*407*, *533*)
	Rat primary	(*429*, *518*, *525*, *528*, *531*, *534*)
	Mouse primary	(*530*)
	Mouse immortalized	(*520*, *535*, *536*)
Neurons	Human pluripotent stem cell-derived	(*442*, *445*, *519*, *520*, *532*)
	Human neural progenitor cell-derived	(*430*)
	Rat primary	(*517*, *525*)

2.4.1 Transwell models

Transwell-based BBB models typically consist of endothelial cells cultured on an extracellular matrix-coated permeable membrane of a cell culture insert, which is then suspended within a well of a 12- or 24-well plate (Figure 2.1B). Benefits of the Transwell platform include ease of use, moderate scalability, and the ability to rapidly and nondestructively quantify barrier integrity via measurement of transendothelial electrical resistance (TEER). Additionally, for permeability screening, molecules or cells can be added to the culture medium in the top (apical or "blood-side") chamber and their accumulation in the bottom (basolateral or "brain-side") chamber evaluated over time, or vice versa. Drawbacks of the Transwell system include the inability to apply flow and the relatively large media volume, which may attenuate the effect of

cell-cell signaling through soluble factors. Additionally, the permeable membrane prevents contact between BMECs and other NVU cell types.

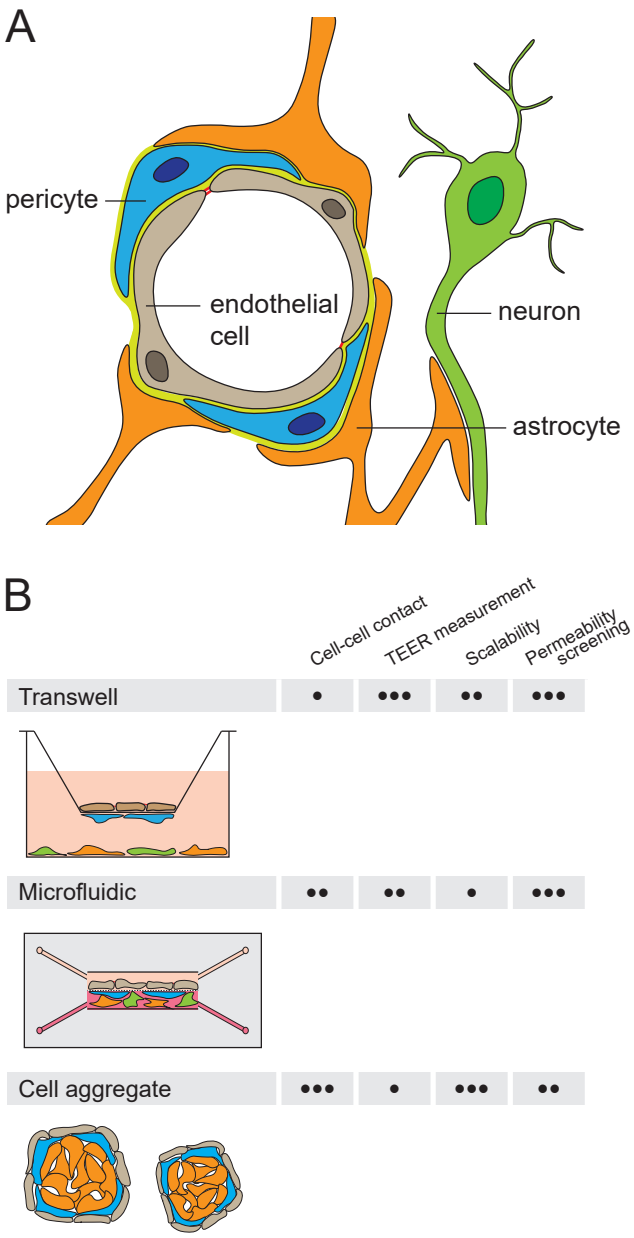

Figure 2.1. The NVU and multicellular BBB models. (A) Cross-section of a brain capillary, showing the organization of BMECs, pericytes, astrocytes, and neurons. (B) Transwell, microfluidic, and cell aggregate-based in vitro model systems incorporating BMEC monolayers along with other NVU cell types. General attributes of in vitro model systems, including: (i) the ability to achieve cell-cell contact, (ii) the ability to quantify barrier formation by transendothelial electrical resistance (TEER) measurement, (iii) the ease of scale up for high-throughput experiments and (iv) the ease of permeability screening, are characterized as • poor, •• moderate, or ••• excellent.

The Transwell system can be readily adapted to multicellular BBB models, and offers flexibility in the arrangement of different cell types depending on the intended application of the model. NVU cell types can be cultured on the bottom of the well, allowing the exchange of soluble factors with BMECs cultured on the insert. For example, human pluripotent stem cell (hPSC)-derived BMECs have been co-cultured sequentially with primary human pericytes and human neural progenitor cell-derived neurons and astrocytes in this manner, demonstrating robust increases in TEER up to 5,000 $\Omega \times cm^2$ (*430*). In addition to allowing sequential co-culture with different cell types, the Transwell platform also allows simultaneous co-culture of three distinct cell types while maintaining spatial separation of each cell type for subsequent molecular analysis. BMECs are typically cultured on the top surface of the membrane, a second cell type is cultured on the bottom surface of the membrane (sometimes referred to as "contact" co-culture, though the membrane prevents *in vivo*-like cell-cell contact), and the third cell type is cultured on the bottom of the well (Figure 2.1B). For example, Thomsen *et al.* developed a Transwell BBB model incorporating primary porcine brain endothelial cells, pericytes, and astrocytes (*407*). Both pericytes and astrocytes increased TEER and decreased mannitol permeability compared to BMEC monoculture. "Contact" co-culture of pericytes and BMECs or astrocytes and BMECs increased expression of the gene encoding the tight junction protein claudin-5, an effect not observed in analogous "non-contact" co-cultures. Transwells are also amenable to alternative arrangements of cells. As a recent example, Hawkins *et al.* demonstrated that endothelial cells could be cultured on the bottom of the insert to facilitate a comparison of monolayer (two-dimensional, 2D) and collagen hydrogel (three-dimensional, 3D) astrocyte culture in the top chamber (*535*). Addition of TGF-β1 to 3D astrocyte-endothelial co-cultures led to a larger decrease in TEER than in 2D, and this effect was not observed in the absence of astrocytes.

Several recently reported Transwell-based models incorporate one or more cell types derived from hPSCs. hPSCs are an attractive cell source for *in vitro* modeling since they are renewable and scalable, there are established protocols for their differentiation to many relevant NVU cell types including BMEC-like cells (*429*, *430*, *435*), and the resulting cells may have more relevance to human biology than immortalized cell lines or cells isolated from nonhuman animals, particularly for modeling human disease. For example, a quadruple-culture model encompassing hPSC-derived brain endothelial cells, hPSC-derived and primary astrocytes and neural stem cells, and primary pericytes exhibited increased TEER, decreased permeability to 40 kDa dextran, and increased expression of the glucose transporter Glut-1 (*SLC2A1*) compared to endothelial monoculture (*529*). Another potentially powerful application of stem cell technology is the use of patient-derived iPSCs to create patient-specific multicellular BBB models wherein all cell types are derived from the same donor iPSC line. Recently, Canfield *et al.* demonstrated the differentiation of BMECs, neurons, and astrocytes from the same iPSC line (*445*). Subsequent triple-culture of BMECs with a mixture of neurons and astrocytes in a physiologically-relevant 1:3 ratio increased TEER and improved tight junction continuity compared to BMECs cultured alone. As another example, co-differentiation of endothelial cells and pericytes from iPSCs by sequential treatment with several growth factors, and co-culture with iPSC-derived neurons and astrocytes induced BBB properties in the endothelial cells, including expression of nutrient and efflux transporters and development of tight junctions (*532*). Subsequently, the resultant BMEC-like cells were purified via FACS and incorporated in a Transwell model in co-culture with astrocytes. Examples of the utility of such NVU models derived from patient-specific iPSCs in disease modeling are discussed below.

2.4.2 Microfluidic models

Microfluidic devices offer several benefits in multicellular BBB modeling. Compared to Transwells, the smaller relative medium volume in microfluidic systems minimizes dilution of secreted factors that may be important in modulating BBB properties. These systems also facilitate the application of shear stress by medium flow, mimicking the effect of blood flow *in vivo*, and therefore serve as a platform to investigate influences of shear stress on BBB properties (*450*, *522*). Microfluidic models also permit a more physiologically-relevant arrangement of the different NVU cell types, including the possibility of legitimate cell-cell contacts (Figure 2.1B). Drawbacks of microfluidic BBB models include limited scalability and the requirement of specialized equipment and expertise for their construction.

As a recent example of a microfluidic device facilitating physiologically-relevant arrangement of cell types, Adriani *et al.* developed a BBB model employing primary rat NVU cells in four parallel channels (*525*). The first channel contained a neural cell culture medium, the second and third contained hydrogels with neurons and astrocytes, respectively, and the fourth contained a tubular BMEC monolayer and endothelial cell culture medium. The authors demonstrated close association of astrocyte processes with endothelial cells, confirmed the formation of a barrier by evaluating dextran permeability from the lumen, and assayed the barrier's restrictiveness to glutamate via neuronal calcium imaging.

Other microfluidic devices employ permeable membranes as a BMEC substrate. For example, primary rat BMECs and pericytes were cultured on opposite sides of a membrane and astrocytes were cultured on the bottom surface of the device, reminiscent of the common Transwell arrangement (*528*). The device also incorporates transparent electrodes for TEER measurement and imaging during operation. Wang *et al.* similarly constructed a microfluidic device for the triple-culture of immortalized mouse BMECs, pericytes, and astrocytes, and

showed a significant increase in P-gp activity in a model incorporating all three cell types compared to an endothelial-pericyte co-culture (*536*). Furthermore, increasing the medium volume decreased TEER, likely as a result of the dilution of astrocyte- or pericyte-secreted factors.

Finally, microfluidic systems incorporating iPSC-derived BMECs are also emerging. Wang *et al.* co-cultured iPSC-derived BMECs with primary rat astrocytes in a microfluidic device where flow is driven by gravity and scaled to achieve a medium residence time similar to that observed in the brain microcirculation (*531*). The multicellular BBB system maintained TEER above 3000 $\Omega \times cm^2$ up to day 10 of operation, and permeabilities for six evaluated small and large molecules correlated well to *in vivo* transport across the BBB. In the future, microfluidic models incorporating multiple iPSC-derived NVU cell types, rather than from primary or immortalized sources, may offer improvements in fidelity and scalability.

2.4.3 Cell aggregate-based models

Self-assembled cell aggregates comprising BMECs, astrocytes, and pericytes are emerging as a possible alternative to Transwell and microfluidic models for certain applications. These "spheroid" models permit direct contact between different NVU cell types and develop an endothelial monolayer for permeability studies (Figure 2.1B). Furthermore, such models are highly scalable and simpler to fabricate and operate than microfluidic devices. Drawbacks of these models include the inability to measure TEER, and their present lack of neurons.

Urich *et al.* first demonstrated that under low-attachment culture conditions, primary human brain endothelial cells, astrocytes, and pericytes self-assembled into organized spheroidal structures with an astrocyte core covered with pericytes surrounded by an outer monolayer of endothelial cells (*524*). BMECs in the assembled spheroids possess tight junctions and P-gp activity, and proof-of-concept screening of a panel of fluorescently-labeled cell-penetrating

peptides identified four peptides that appeared to enter the brain after intravenous injection (*521*). Incorporating iPSC-derived cell types will be an important next step toward realizing the full utility of this emerging aggregate-based BBB model system.

2.5 Applications of NVU models

The significant technical advances in multicellular BBB models described above have facilitated recent applications in understanding neurovascular biology and disease. One exciting set of applications has leveraged patient-specific iPSCs for neurovascular disease modeling. For example, astrocytes were differentiated both from normal iPSCs and those carrying mutations in Amyotrophic Lateral Sclerosis linked genes *SOD1* or *FUS* (*530*). The authors showed that endothelial cells co-cultured with *SOD1*-mutant astrocytes had increased P-gp expression and activity compared to endothelial cells co-cultured with normal astrocytes, and that this effect was dependent on nuclear translocation of NF-κB and correlated with increased reactive oxygen species (ROS) in endothelial cells. They also demonstrated that *FUS*-mutant astrocytes induced similar effects on P-gp and NF-κB activity, but these effects correlated with TNF-α production rather than ROS (*530*). As another example, BMECs, astrocytes, and neurons were differentiated from iPSCs carrying mutations in the thyroid hormone transporter monocarboxylate transporter 8 (MCT8), which has been linked to Allan-Herndon-Dudley syndrome (AHDS), a severe form of mental retardation (*442*). Using the iPSC-derived cells to individually model the effects of MCT8-deficiency indicated that neural cell development proceeded normally in a T_3 thyroid hormone-dependent fashion. However, MCT8-deficiency substantially reduced T_3 thyroid hormone transport across BMECs in a Transwell model to suggest that AHDS may be a result of a BBB transport deficiency. Notably, through the use of genome editing tools, the phenotype could be rescued by correcting the MCT8 mutation in patient-derived iPSCs.

Other applications have sought to use multicellular BBB models to understand the response of the NVU to inflammatory stimuli. Brown *et al.* constructed a NVU model from primary human BMECs and pericytes, mouse astrocytes, and human iPSC-derived neurons in a two-chamber microfluidic device (*520*). After exposure of the vascular (apical) chamber to lipopolysaccharide (LPS) or a cocktail of inflammatory cytokines, the authors harvested media from the vascular and brain chambers and used LC-MS-based metabolomics to identify metabolic pathways influenced by inflammatory stimuli, including several that were differentially-affected between the two chambers, indicating the impact of the multicellular configuration. Similarly, a microfluidic NVU model comprising a tubular monolayer of primary human BMECs surrounded by pericytes or astrocytes was employed to evaluate cytokine release upon TNF-α stimulation (*523*). The authors demonstrated that astrocyte and pericyte co-cultures showed increased basal levels of the pro-survival cytokine granulocyte colony stimulating factor (G-CSF) compared to BMEC monoculture, and co-cultures also displayed increased induction of G-CSF upon TNF-α stimulation. They further showed that these effects were not detectable in an analogous Transwell model. Taken together, these examples demonstrate the unique ability of multicellular *in vitro* models of the NVU to provide novel biological insights that would be difficult or impossible to discern with BMEC-only models.

2.6 Conclusions

The shift from BMEC-centric *in vitro* BBB models to multicellular BBB models with one or more additional NVU cell types has greatly expanded their potential beyond drug permeability screening to the interrogation of molecular and cellular mechanisms underlying BBB physiology and disease. We therefore anticipate increasing application of multicellular BBB models incorporating iPSC-derived BMECs and other NVU cell types to the study of neurovascular contributions to diseases. As new models of the NVU are developed, additional elements that

merit consideration include the composition of extracellular matrix (*533*) and inclusion of additional cell types such as microglia, especially in the context of inflammation (*537*). Finally, we suggest that incorporating additional cell types present in vascular microenvironments may improve the utility of other *in vitro* models such as those related to the blood-nerve barrier or other organ-specific endothelia.

Chapter 3 Wnt signaling mediates acquisition of blood-brain barrier properties in naïve endothelium derived from human pluripotent stem cells*

3.1 Summary

Endothelial cells (ECs) in the central nervous system (CNS) acquire their specialized blood-brain barrier (BBB) properties in response to extrinsic signals, with Wnt/β-catenin signaling coordinating multiple aspects of this process. Our knowledge of CNS EC development has been advanced largely by animal models, and human pluripotent stem cells (hPSCs) offer the opportunity to examine BBB development in an *in vitro* human system. Here we show that activation of Wnt signaling in hPSC-derived naïve endothelial progenitors, but not in matured ECs, leads to robust acquisition of canonical BBB phenotypes including expression of GLUT-1, increased claudin-5, decreased PLVAP and decreased permeability. RNA-seq revealed a transcriptome profile resembling ECs with CNS-like characteristics, including Wnt-upregulated expression of *LEF1*, *APCDD1*, and *ZIC3*. Together, our work defines effects of Wnt activation in naïve ECs and establishes an improved hPSC-based model for interrogation of CNS barriergenesis.

3.2 Introduction

In the central nervous system (CNS), vascular endothelial cells (ECs) are highly specialized, with complex tight junctions, expression of a spectrum of nutrient and efflux transporters, low rates of vesicle trafficking, no fenestrae, and low expression of immune cell

---

*This chapter published as Gastfriend BD, Nishihara H, Canfield SG, Foreman KL, Engelhardt B, Palecek SP, Shusta EV (2021). Wnt signaling mediates acquisition of blood-brain barrier properties in naïve endothelium derived from human pluripotent stem cells. *eLife* **10**:e70992.
Supplementary files referenced in this chapter are available in the online version of this publication at http://doi.org/10.7554/eLife.70992

adhesion molecules (*39*, *538*). ECs bearing these attributes, often referred to as the blood-brain barrier (BBB), work in concert with the other brain barriers to facilitate the tight regulation of the CNS microenvironment required for proper neuronal function (*122*, *539*). During development, the Wnt/β-catenin signaling pathway drives both CNS angiogenesis, during which vascular sprouts originating from the perineural vascular plexus invade the developing neural tube, and the coupled process of barriergenesis by which resulting ECs begin to acquire BBB properties (*225*, *227*, *228*, *375*, *540*). Specifically, neural progenitor-derived Wnt7a and Wnt7b ligands signal through Frizzled receptors and the obligate co-receptors RECK and GPR124 (ADGRA2) on endothelial cells (*237*, *241*, *242*, *247–249*). Other ligands function analogously in other regions of the CNS, including Norrin in the retina and cerebellum (*235*, *238*) and potentially Wnt3a in the dorsal neural tube (*225*). Furthermore, Wnt/β-catenin signaling is required for maintenance of CNS EC barrier properties in adulthood (*541*), with astrocytes as a major source of Wnt7 ligands (*56*, *279*, *542*).

Molecular hallmarks of Wnt-mediated CNS EC barriergenesis are (i) acquisition of glucose transporter GLUT-1 expression, (ii) loss of plasmalemma vesicle-associated protein (PLVAP), and (iii) upregulation of claudin-5 (*71*, *225*, *241*, *247*, *375*). Notably, the Wnt-mediated switch between the "leaky" EC phenotype (GLUT-1^{-} PLVAP^{+} claudin-5^{low}) and the barrier EC phenotype (GLUT-1^{+} PLVAP^{-} claudin-5^{high}) correlates with reduced permeability to molecular tracers (*238*, *247*) and is conserved in multiple contexts. For instance, medulloblastomas that produce Wnt-inhibitory factors have leaky vessels (*543*). Moreover, vasculature perfusing circumventricular organs is leaky due to low levels of Wnt signaling (*71*, *379*). Notably, ectopic activation of Wnt in ECs of circumventricular organs induces GLUT-1 and suppresses PLVAP (*71*, *379*). However, similar ectopic activation of Wnt in liver and lung ECs produces only very minor barriergenic effects (*367*), and Wnt activation in cultured primary

mouse brain ECs does not prevent culture-induced loss of barrier-associated gene expression (*226*). The reasons for the apparent context-dependent impacts of Wnt activation in ECs remain unclear and motivate systematic examination of this process in a simplified model system. Further, given species differences in brain EC transporter expression (*544*), drug permeability (*88*), and gene expression (*90*), this process warrants investigation in human cells to complement mouse *in vivo* studies.

Prior studies have evaluated the impact of Wnt activation in immortalized human brain ECs and observed only modest effects on barrier phenotype (*545*, *546*). Combined with the aforementioned deficits observed in primary adult mouse brain endothelial cells that are not rescued by ectopic Wnt activation (*226*), one possibility is that mature, adult endothelium is largely refractory to Wnt activation, and that Wnt responsiveness is a property of immature endothelial cells analogous to those in the perineural vascular plexus. Human pluripotent stem cells (hPSCs) offer an *in vitro* human model system for systematic investigation of molecular mechanisms of BBB phenotype acquisition, especially given their ability to model early stages of endothelial specification and differentiation. However, currently available hPSC-based models of CNS endothelial-like cells are not well suited for modeling the BBB developmental progression as they do not follow a developmentally-relevant differentiation trajectory, lack definitive endothelial identity, or have been incompletely characterized with respect to the role of developmental signaling pathways (*452*, *453*, *456*). As a potential alternative, hPSCs can also be used to generate immature, naïve endothelial progenitors (*458*) that could be used to better explore the induction of BBB phenotypes. For example, we recently reported that extended culture of such hPSC-derived endothelial progenitors in a minimal medium yielded ECs with improved BBB tight junction protein expression and localization which led to improved paracellular barrier properties (*468*). However, as shown below, these cells exhibit high

expression of PLVAP and little expression of GLUT-1, indicating the need for additional cues to drive CNS EC specification.

In this work, we aimed to define the effects of activating Wnt/β-catenin signaling in hPSC-derived, naïve endothelial progenitors and assess the extent to which this strategy would drive development of a CNS EC-like phenotype. We found that many aspects of the CNS EC phenotype, including the canonical GLUT-1, claudin-5, and PLVAP expression effects, were regulated by CHIR 99021, a small molecule agonist of Wnt/β-catenin signaling. CHIR treatment in matured ECs produced a more limited response. Whole-transcriptome analysis revealed definitive endothelial identity of the resulting cells and CHIR-upregulated expression of known CNS EC transcripts, including *LEF1*, *APCDD1*, *AXIN2*, *SLC2A1*, *CLDN5*, *LSR*, *ABCG2*, *SOX7*, and *ZIC3*. We also observed an unexpected CHIR-mediated upregulation of caveolin-1, which did not, however, correlate with increased uptake of a dextran tracer. Thus, we provide evidence that Wnt activation in hPSC-derived naïve endothelial progenitors is sufficient to induce many aspects of the CNS barrier EC phenotype, and we establish a model system for further systematic investigation of putative barriergenic cues.

3.3 Methods

Table 3.1. Key resources table.

Reagent type	Designation	Source or reference	Identifier	Additional information
Cell line (human)	iPSC: IMR90-4	Available from WiCell; Ref. (*425*)	RRID: CVCL_C437	
Cell line (human)	iPSC: WTC11	Available from Gladstone Institutes; Ref. (*547*)	RRID: CVCL_Y803	
Cell line (human)	iPSC: 19-9-11-7TGP-ishcat3	Laboratory stock		
Cell line (human)	hESC: H9-7TGP-ishcat2	Laboratory stock Ref. (*548*)		
Cell line (human)	hESC: H9-CDH5-eGFP	Laboratory stock Ref. (*549*)		
Antibody	Anti-CD31-FITC (mouse monoclonal IgG1, clone AC128)	Miltenyi Biotec	Cat# 130-117-390 RRID:AB_2733637	
Antibody	Anti-CD31-APC (mouse monoclonal IgG1, clone AC128)	Miltenyi Biotec	Cat# 130-119-891 RRID:AB_2784124	
Antibody	Anti-CD34-FITC (mouse monoclonal IgG2a, clone AC136)	Miltenyi Biotec	Cat# 130-113-178 RRID:AB_2726005	
Antibody	Anti-β-catenin-Alexa Fluor 488 (mouse monoclonal IgG1, clone 14)	BD Biosciences	Cat# 562505 RRID:AB_11154224	(1:100, ICC)
Antibody	Anti-GLUT-1 (mouse monoclonal IgG2a, clone SPM498)	Invitrogen	Cat# MA5-11315 RRID:AB_10979643	(1:100, ICC) (1:500, WB)
Antibody	Anti-calponin (mouse monoclonal IgG1, clone hCP)	Sigma-Aldrich	Cat# C2687 RRID:AB_476840	(1:15000, ICC)
Antibody	Anti-SM22α (rabbit polyclonal)	Abcam	Cat# ab14106 RRID:AB_443021	(1:1000, ICC)
Antibody	Anti-claudin-5 (mouse monoclonal IgG1, clone 4C3C2)	Invitrogen	Cat# 35-2500 RRID:AB_2533200	(1:100, ICC) (1:500, WB)
Antibody	Anti-caveolin-1 (rabbit polyclonal)	Cell Signaling Technology	Cat# 3238 RRID:AB_2072166	(1:500, ICC)
Antibody	Anti-CD31 (rabbit polyclonal)	Lab Vision	Cat# RB-10333-P RRID:AB_720502	(1:100, ICC)
Antibody	Anti-Ki67 (mouse monoclonal IgG1, clone B56)	BD Biosciences	Cat# 550609 RRID:AB_393778	(1:100, ICC)
Antibody	Anti-VE-cadherin (mouse monoclonal IgG2a, clone BV9)	Santa Cruz Biotechnology	Cat# sc-52751 RRID:AB_628919	(1:100, ICC) (1:250, WB)
Antibody	Anti-β-actin (rabbit monoclonal IgG, clone 13E5)	Cell Signaling Technology	Cat# 4970 RRID:AB_2223172	(1:1000, WB)
Antibody	Anti-PLVAP (rabbit polyclonal)	Prestige Antibodies	Cat# HPA002279 RRID:AB_1079636	(1:200, ICC) (1:250, WB)
Antibody	Anti-LSR (rabbit polyclonal)	Prestige Antibodies	Cat# HPA007270 RRID:AB_1079253	(1:250, WB)
Antibody	Alexa Fluor 488 goat anti-mouse IgG (goat polyclonal)	Invitrogen	Cat# A-11001 RRID:AB_2534069	(1:200, ICC)
Antibody	Alexa Fluor 647 goat anti-rabbit IgG (goat polyclonal)	Invitrogen	Cat# A-21245 RRID:AB_2535813	(1:200, ICC)
Antibody	Alexa Fluor 488 goat anti-mouse IgG1 (goat polyclonal)	Invitrogen	Cat# A-21121 RRID:AB_2535764	(1:200, ICC)

Antibody	Alexa Fluor 647 goat anti-mouse IgG2a (goat polyclonal)	Invitrogen	Cat# A-21241 RRID:AB_2535810	(1:200, ICC)
Antibody	Alexa Fluor 555 goat anti-rabbit IgG (goat polyclonal)	Invitrogen	Cat# A-21428 RRID:AB_2535849	(1:200, ICC)
Antibody	IRDye 800CW goat anti-mouse IgG (goat polyclonal)	LI-COR Biosciences	Cat# 926-32210 RRID:AB_621842	(1:5000, WB)
Antibody	IRDye 800CW goat anti-rabbit IgG (goat polyclonal)	LI-COR Biosciences	Cat# 926-32211 RRID:AB_621843	(1:5000, WB)
Antibody	IRDye 680RD goat anti-rabbit IgG (goat polyclonal)	LI-COR Biosciences	Cat# 926-68071 RRID:AB_10956166	(1:5000, WB)
Commercial assay or kit	RNeasy Plus Micro Kit	Qiagen	Cat# 74034	
Chemical compound or drug	CHIR 99021	Tocris	Cat# 4423	
Chemical compound or drug	Vybrant DyeCycle Green Stain	Invitrogen	Cat# V35004	
Chemical compound or drug	Dextran, Alexa Fluor 488; 10,000 MW, Anionic, Fixable	Invitrogen	Cat# D22910	
Software or algorithm	RSEM	Ref. (*550*)	RRID:SCR_013027	v1.3.3
Software or algorithm	Bowtie2	Ref. (*551*)	RRID:SCR_016368	v2.4.2
Software or algorithm	R	R Foundation	RRID:SCR_001905	v3.6.3
Software or algorithm	DESeq2	Ref. (*552*)	RRID:SCR_015687	v1.26.0
Software or algorithm	biomaRt	Ref. (*553*)	RRID:SCR_019214	v2.42.1
Software or algorithm	WGCNA	Ref. (*554*)	RRID:SCR_003302	v1.70-3
Software or algorithm	Cytoscape	Ref. (*555*)	RRID:SCR_003032	v3.8.2
Software or algorithm	FIJI/ImageJ	Ref. (*556*)	RRID:SCR_002285	v2.0.0-rc-68
Software or algorithm	Image Studio	LI-COR Biosciences	RRID:SCR_015795	v5.2
Software or algorithm	FlowJo	BD Biosciences	RRID:SCR_008520	v10.7.1
Software or algorithm	JMP Pro	SAS Institute	RRID:SCR_014242	v15.0.0
Software or algorithm	Prism	GraphPad Software	RRID:SCR_002798	v5.0.1

3.3.1 hPSC maintenance

Tissue culture plates were coated with Matrigel, Growth Factor Reduced (Corning, Glendale, AZ). A 2.5 mg aliquot of Matrigel was thawed and resuspended in 30 mL DMEM/F-12 (Life Technologies, Carlsbad, CA), and the resulting solution used to coat plates at 8.7 μg/cm^2 (1 mL per well for 6-well plates; 0.5 mL per well for 12-well plates). Plates were incubated at 37°C for at least 1 h prior to use. hPSCs were maintained on Matrigel-coated plates in E8 medium (STEMCELL Technologies, Vancouver, Canada) at 37°C, 5% CO_2. hPSC lines used were: IMR90-4 iPSC, WTC11 iPSC, H9-CDH5-eGFP hESC, H9-7TGP-ishcat2 hESC, and 19-9-11-7TGP-ishcat3 iPSC. Medium was changed daily. When hPSC colonies began to touch, typically at approximately 70–80% confluence, cells were passaged using Versene (Life Technologies). Briefly, cells were washed once with Versene, then incubated with Versene for 7 min at 37°C. Versene was removed and cells were dissociated into colonies by gentle spraying with E8 medium. Cells were transferred at a split ratio of 1:12 to a new Matrigel-coated plate containing E8 medium. hPSC cultures were routinely tested for mycoplasma contamination using a PCR-based assay performed by the WiCell Research Institute (Madison, WI).

3.3.2 Endothelial progenitor cell differentiation

EPCs were differentiated according previously published protocols (*458*, *459*, *468*) with slight modifications. On day -3 (D-3), hPSCs were treated with Accutase (Innovative Cell Technologies, San Diego, CA) for 7 min at 37°C. The resulting single cell suspension was transferred to 4× volume of DMEM/F-12 (Life Technologies) and centrifuged for 5 min, 200×g. Cell number was quantified using a hemocytometer. Cells were resuspended in E8 medium supplemented with 10 μM ROCK inhibitor Y-27632 dihydrochloride (Tocris, Bristol, United Kingdom) and seeded on Matrigel-coated 12-well plates at a density of (1.5–2.5)×10^4 cells/cm^2, 1 mL per well. Cells were maintained at 37°C, 5% CO_2. On the following two days (D-2 and D-

1), the medium was replaced with E8 medium. The following day (D0), differentiation was initiated by changing the medium to LaSR medium (Advanced DMEM/F-12 [Life Technologies], 2.5 mM GlutaMAX [Life Technologies], and 60 µg/mL L-ascorbic acid 2-phosphate magnesium [Sigma-Aldrich, St. Louis, MO]) supplemented with 7–8 µM CHIR 99021 (Tocris), 2 mL per well. The following day (D1), medium was replaced with LaSR medium supplemented with 7–8 µM CHIR 99021, 2 mL per well. On the following three days (D2, D3, and D4), the medium was replaced with pre-warmed LaSR medium (without CHIR), 2 mL per well.

On D5, EPCs were isolated using CD31 magnetic activated cell sorting (MACS). Cells were treated with Accutase for 15–20 min at 37°C. The resulting cell suspension was passed through a 40 µm cell strainer into an equal volume of DMEM (Life Technologies) supplemented with 10% FBS (Peak Serum, Wellington, CO) and centrifuged for 5 min, 200×g. Cell number was quantified using a hemocytometer. Cells were resuspended in MACS buffer (Dulbecco's phosphate buffered saline without Ca and Mg [DPBS; Life Technologies] supplemented with 0.5% bovine serum albumin [Sigma-Aldrich] and 2 mM EDTA [Sigma-Aldrich]) at a concentration of 10^7 cells per 100 µL. The CD31-FITC antibody (Miltenyi Biotec, Auburn, CA) was added to the cell suspension at a dilution of 1:50. The cell suspension was incubated for 30 min at room temperature, protected from light. The cell suspension was brought to a volume of 15 mL with MACS buffer and centrifuged for 5 min, 200×g. The supernatant was aspirated and the pellet resuspended in MACS buffer at a concentration of 10^7 cells per 100 µL. The FITC Selection Cocktail from the EasySep Human FITC Positive Selection Kit (STEMCELL Technologies) was added at a dilution of 1:10 and the cell suspension was incubated for 20 min at room temperature, protected from light. The Dextran RapidSpheres (magnetic particles)

solution from the Selection Kit was added at a dilution of 1:20 and the cell suspension was incubated for an additional 15 min at room temperature.

The cell suspension was brought to a total volume of 2.5 mL with MACS buffer (for total cell number less than 2×10^8, the approximate maximum yield from two 12-well plates; for a larger number of plates/cells, a total volume of 5 mL was used). 2.5 mL of cell suspension was transferred to a sterile 5 mL round-bottom flow cytometry tube and placed in the EasySep magnet (STEMCELL Technologies) for 5 min. The magnet was inverted to pour off the supernatant, the flow tube removed, the retained cells resuspended in 2.5 mL of MACS buffer, and the flow tube placed back in the magnet for 5 min. This step was repeated 3 times, and the resulting cell suspension transferred to a centrifuge tube, and centrifuged for 5 min, 200×g. Cell number was quantified using a hemocytometer. Resulting EPCs were used directly for experiments as described below or cryopreserved in hECSR medium supplemented with 30% FBS and 10% DMSO for later use. hESCR medium is Human endothelial serum-free medium (Life Technologies) supplemented with 1× B-27 supplement (Life Technologies) and 20 ng/ml FGF2 (Waisman Biomanufacturing, Madison, WI).

3.3.3 Endothelial cell culture and treatment

Collagen IV (Sigma-Aldrich) was dissolved in 0.5 mg/mL acetic acid to a final concentration of 1 mg/mL. Collagen IV-coated plates were prepared by diluting a volume of this stock solution 1:100 in water, adding the resulting solution to tissue culture plates, or #1.5 glass bottom plates (Cellvis, Sunnyvale, CA) for cells intended for confocal imaging (1 mL per well for 6-well plates, 0.5 mL per well for 12-well plates, 0.25 mL per well for 24-well plates), and incubating the plates for 1 h at RT. Collagen IV coating solution was removed and EPCs obtained as described above were suspended in hECSR medium and plated at approximately 3×10^4 cells/cm^2. In some experiments, ligands and small molecules were added to hECSR

medium: CHIR 99021 (Tocris) was used at 4 μM except where indicated; DMSO (Sigma-Aldrich) was used as a vehicle control for CHIR; Wnt3a (R&D Systems) was used at 20 ng/mL; doxycycline was used at 1, 2, or 4 μg/mL. The hECSR medium, including any ligands or small molecules, was replaced every other day until confluent (typically 6 days). We denote this time point "Passage 1."

For extended culture, ECs were selectively dissociated and replated as previously described (*468*). Cells were incubated with Accutase until endothelial cells appeared round, typically 2–3 min at 37°C. The plate was tapped to release the ECs while SMLCs remained attached, and the EC-enriched cell suspension transferred to 4× volume of DMEM/F-12 and centrifuged for 5 min, 200×g. Cells were resuspended in hECSR medium and seeded on a new collagen IV-coated plate at approximately 3×10^4 cells/cm^2. hECSR medium was replaced every other day until confluent (typically 6 days). The selective dissociation and seeding described above was repeated, and hECSR medium was again replaced every other day until confluent (typically 6 days). We denote this time point "Passage 3." In one experiment, these steps were repeated for another two passages. Except where indicated, CHIR 99021 or vehicle (DMSO) was included in the hECSR medium for the entire duration of culture.

3.3.4 RNA-seq

RNA-seq was performed on ECs and SMLCs from the IMR90-4 hPSC line. Four independent differentiations were performed, with DMSO- and CHIR-treated ECs at Passage 1 analyzed from all four differentiations. DMSO- and CHIR-treated ECs at Passage 3 were analyzed from three of the four differentiations. DMSO-treated SMLCs at Passage 1 were analyzed from two of the four differentiations. Fluorescence-activated cell sorting (FACS) was used to isolate CD31$^+$ ECs and CD31$^-$ SMLCs from mixed Passage 1 cultures. Cells were incubated with Accutase for 10 min at 37°C, passed through 40 μm cell strainers into 4× volume

of DMEM/F-12, and centrifuged for 5 min, 200×g. Cells were resuspended in MACS buffer and incubated with CD31-APC antibody (Miltenyi Biotec) for 30 min at 4°C, protected from light. The cell suspension was brought to a volume of 15 mL with MACS buffer and centrifuged at 4°C for 5 min, 200×g. Cells were resuspended in MACS buffer containing 2 μg/mL 4',6-diamidino-2-phenylindole (DAPI; Life Technologies). A BD FACSAria III Cell Sorter (BD Biosciences, San Jose, CA) was used to isolate $DAPI^{-}CD31^{+}$ cells (live ECs) and $DAPI^{-}CD31^{-}$ cells (live SMLCs). The resulting cell suspensions were centrifuged at 4°C for 5 min, 200×g, and cell pellets immediately processed for RNA extraction as described below.

RNA was isolated using the RNeasy Plus Micro Kit (Qiagen, Germantown, MD). Buffer RLT Plus supplemented with 1% β-mercaptoethanol was used to lyse cells (pellets from FACS of Passage 1 cells, or directly on plates for Passage 3 ECs). Lysates were passed through gDNA Eliminator spin columns, loaded onto RNeasy MinElute spin columns, washed with provided buffers according to manufacturer instructions, and eluted with RNase-free water. Sample concentrations were determined using a NanoDrop spectrophotometer (Thermo Scientific, Waltham, MA) and RNA quality assayed using an Agilent 2100 Bioanalyzer with Agilent RNA 6000 Pico Kit (Agilent, Santa Clara, CA). First-strand cDNA synthesis was performed using the SMART-Seq v4 Ultra Low Input RNA kit (Takara Bio, Mountain View, CA) with 5 ng input RNA followed by 9 cycles of PCR amplification and library preparation using the Nextera XT DNA Library Prep Kit (Illumina, San Diego, CA). Sequencing was performed on a NovaSeq 6000 (Illumina), with approximately 40–60 million 150 bp paired-end reads obtained for each sample.

FASTQ files were aligned to the human genome (hg38) and transcript abundances quantified using RSEM (v1.3.3) (*550*) calling bowtie2 (v2.4.2) (*551*). Estimated counts from RSEM were input to DESeq2 (v1.26.0) (*552*) implemented in R (v3.6.3) for differential

expression analysis. Elsewhere, transcript abundances are presented as transcripts per million (TPM). Differentiation pairing as described above was included in the DESeq2 designs. The Wald test with Benjamini-Hochberg correction was used to generate adjusted P-values. Principal component analysis was performed on counts after the DESeq2 variance stabilizing transformation. Transcription factor annotations were based on the list available at http://humantfs.ccbr.utoronto.ca/ (*557*); secreted and transmembrane annotations were based on the UniProt database (*558*). Weighted Gene Correlation Network Analysis (WGCNA) (v1.70-3) (*554*, *559*) was performed on the 14 EC datasets. Genes with an average of fewer than 50 estimated counts across these datasets were excluded, and the DESeq2 variance stabilizing transformation was used to generate the expression matrix for input to WGCNA. The topological overlap matrix (TOM) was constructed using the signed network type and a power of 20. Hierarchical clustering was performed on dissimilarity (1 – TOM) with average linkage. Gene modules were detected by a constant height (0.99) cut of the hierarchical clustering dendrogram with a minimum module size of 30 genes. Module eigengenes (the first principal component of the expression matrix for genes in each module) were computed as described, and the Pearson correlation between module eigengenes and experimental variables (CHIR v. DMSO: CHIR = 1, DMSO = 0; Passage 3 v. Passage 1: Passage 3 = 1, Passage 1 = 0) was used to identify modules of interest. Cytoscape (v3.8.3) (*555*) was used to visualize the 30 genes in the green module (strong positive correlation with CHIR treatment) with the highest intramodular connectivity. The list of genes, corresponding modules, and correlations to experimental variables and module eigengenes is provided in Supplementary file 3.

Bulk RNA-seq data from the literature (FASTQ files; see Table 3.2) were obtained from the Gene Expression Omnibus (GEO). These FASTQ files were aligned to the mouse genome (mm10) and transcript abundances quantified as described above. DESeq2 was used for

differential expression analysis as described above. For direct comparison of human and mouse data, the biomaRt package (v2.42.1) (*553*) and Ensembl database (*560*) was used to map human gene names to mouse homologs. Venn diagrams were generated using the tool available at http://bioinformatics.psb.ugent.be/webtools/Venn/. To identify solute carrier and efflux transporter genes highly expressed at the human BBB *in vivo*, we used five human brain scRNA-seq datasets (see Table 3.2) integrated in a previous meta-analysis (*336*). *SLC* and *ABC* genes with average expression greater than 100 TPM in endothelial cells across the five independent datasets were selected. For pathway enrichment analysis, lists of upregulated genes (log_2(fold change) > 0, adjusted P-value < 0.05, DESeq2 Wald test with Benjamini-Hochberg correction) were tested against the Hallmark gene sets collection (*561*) using the tool available at http://www.gsea-msigdb.org/gsea/msigdb/annotate.jsp.

Table 3.2. Previously published datasets used.

Citation	Description	Identifiers	Source
Ref. (*65*)	Adult mouse postnatal day 7 brain, liver, lung, and kidney ECs	GSM3040844 GSM3040845 GSM3040852 GSM3040853 GSM3040858 GSM3040859 GSM3040864 GSM3040865	https://www.ncbi.nlm.nih.gov/geo/query/acc.cgi?acc=GSE111839
Ref. (*367*)	Adult mouse liver ECs (controls and β-catenin gain-of-function)	GSM2498580 GSM2498581 GSM2498582 GSM2498583 GSM2498584 GSM2498585 GSM2498586 GSM2498587	https://www.ncbi.nlm.nih.gov/geo/query/acc.cgi?acc=GSE95201
Ref. (*71*)	Adult mouse anterior and posterior pituitary ECs (controls and β-catenin gain-of-function)	GSM3455653 GSM3455654 GSM3455657 GSM3455658 GSM3455661 GSM3455662 GSM3455665 GSM3455666	https://www.ncbi.nlm.nih.gov/geo/query/acc.cgi?acc=GSE122117
Ref. (*226*)	Adult mouse brain ECs cultured *in vitro* (controls and β-catenin gain-of-function)	GSM4160534 GSM4160535 GSM4160536 GSM4160537 GSM4160538 GSM4160539 GSM4160540 GSM4160541 GSM4160542 GSM4160543	https://www.ncbi.nlm.nih.gov/geo/query/acc.cgi?acc=GSE118731
Ref. (*336*) (Chapter 4)	Meta-analysis of human brain single cells across multiple developmental stages and brain regions (enumerated below)		
Ref. (*502*)	Adult neocortex		https://portal.brain-map.org/atlases-and-data/rnaseq/human-multiple-cortical-areas-smart-seq
Ref. (*392*)	GW17-18 neocortex		http://solo.bmap.ucla.edu/shiny/webapp/
Ref. (*503*)	Adult temporal lobe and cerebellum	GSM3980129 GSM4008656 GSM4008657 GSM4008658	https://www.ncbi.nlm.nih.gov/geo/query/acc.cgi?acc=GSE134355
Ref. (*391*)	GW6-11 ventral midbrain		https://www.ncbi.nlm.nih.gov/geo/query/acc.cgi?acc=GSE76381
Ref. (*504*)	GW16-27 hippocampus		https://www.ncbi.nlm.nih.gov/geo/query/acc.cgi?acc=GSE119212

3.3.5 Immunocytochemistry

Immunocytochemistry was performed in 24-well plates. Cells were washed once with 500 µL DPBS and fixed with 500 µL cold (–20°C) methanol for 5 min, except cells intended for calponin/SM22a and CD31/Ki67 detection, which were fixed with 500 µL of 4% paraformaldehyde for 15 min. Cells were washed three times with 500 µL DPBS and blocked in 150 µL DPBS supplemented with 10% goat serum (Life Technologies) for 1 h at room temperature, except cells intended for calponin/SM22α detection, which were blocked and permeabilized in DPBS supplemented with 3% BSA and 0.1% Triton X-100, or cells intended for CD31/Ki67 detection, which were blocked and permeabilized in DPBS supplemented with 5% non-fat dry milk and 0.4% Triton X-100. Primary antibodies diluted in 150 µL of the above blocking solutions (see Table 3.1 for antibody information) were added to cells and incubated overnight at 4°C on a rocking platform. Cells were washed three times with 500 µL DPBS. Secondary antibodies diluted in 150 µL of the above blocking solutions (see Table 3.1 for antibody information) were added to cells and incubated for 1 h at room temperature on a rocking platform, protected from light. Cells were washed three times with 500 µL DPBS, followed by 5 min incubation with 500 µL DPBS plus 4 µM Hoechst 33342 (Life Technologies). Images were acquired using an Eclipse Ti2-E epifluorescence microscope (Nikon, Tokyo, Japan) with a 20× or 30× objective or an A1R-Si+ confocal microscope (Nikon) with a 100× oil objective. Confocal images were acquired with 1 µm slice spacing.

Images were analyzed using FIJI (ImageJ) software. For epifluorescence images, 5 fields (20× or 30×) were analyzed per well, with 3–4 wells per treatment condition. For quantification of cell number, EC colonies were manually outlined, and the Analyze Particles function was used to estimate the number of nuclei within the EC colonies. Nuclei outside the EC colonies were manually counted. EC purity (% EC) was calculated as the number of nuclei within EC

colonies relative to total nuclei. To estimate % GLUT-1$^+$ ECs, cells within the EC colonies with membrane-localized GLUT-1 immunoreactivity were manually counted. To estimate % Ki67$^+$ ECs, cells within the EC colonies with at least one nuclear-localized Ki67 punctum were manually counted. For quantification of fluorescence intensity in epifluorescence images, EC colonies were manually outlined, and the Measure function was used to obtain the mean fluorescence intensity for each image channel (fluorophore). A cell-free area of the plate was similarly quantified for background subtraction. Following background subtraction, the mean fluorescence intensity of each protein of interest was normalized to the mean fluorescence intensity of Hoechst to correct for effects of cell density. For confocal images, 3–4 fields (100×) containing only VE-cadherin$^+$ ECs were analyzed per well, with 4 wells per treatment condition. The first slice with visible nuclei (closest to glass) was defined as $Z = 0$, and the Measure function was used to obtain the mean fluorescence intensity for each image channel (fluorophore) in each slice from $Z = 0$ to $Z = 7$ μm. A cell-free area of the plate was similarly quantified for background subtraction. After background subtraction, to approximate total abundance (area under the fluorescence versus Z curve, AUC) for each channel, mean fluorescence intensities were summed across all slices. AUC for the proteins of interest were normalized to Hoechst AUC.

3.3.6 Cell cycle analysis

Passage 1 cultures were dissociated by treatment with Accutase for 10 min at 37°C. Cell suspensions were passed through 40 μm cell strainers into 4× volume of DMEM/F-12 and centrifuged for 5 min, 200×g. Approximately 5×10^5 cells per replicate were resuspended in MACS buffer and incubated with the CD31-APC antibody (Miltenyi Biotec) for 30 min at 4°C, protected from light. Cell suspensions were brought to a volume of 5 mL with MACS buffer and centrifuged at 4°C for 5 min, 200×g. Cells were resuspended in 500 μL MACS buffer containing

2 µg/mL DAPI and 0.5 µL Vybrant DyeCycle Green Stain (Invitrogen) and incubated at room temperature for 1 h, protected from light. Cells were analyzed on an Attune NxT flow cytometer (Invitrogen). FlowJo software (BD Biosciences) was used to gate $CD31^+$ cells and quantify the percentage of S/G2/M phase cells.

3.3.7 Western blotting

To enrich samples from Passage 1 cultures for ECs, the Accutase-based selective dissociation method described above was employed. Dissociated cells were centrifuged for 5 min, 200×g, and resulting cell pellets were lysed in RIPA buffer (Rockland Immunochemicals, Pottstown, PA) supplemented with 1× Halt Protease Inhibitor Cocktail (Thermo Scientific). Passage 3 cells were lysed with the above buffer directly on plates. Lysates were centrifuged at 4°C for 5 min, 14,000×g, and protein concentration in supernatants quantified using the Pierce BCA Protein Assay Kit (Thermo Scientific). Equal amounts of protein were diluted to equal volume with water, mixed with sample buffer, and heated at 95°C for 5 min, except lysates intended for GLUT-1 Western blotting, which were not heated. Samples were resolved on 4–12% Tris-Glycine gels and transferred to nitrocellulose membranes. Membranes were blocked for 1 h in tris-buffered saline plus 0.1% Tween-20 (TBST) supplemented with 5% non-fat dry milk. Primary antibodies (see Table 3.1 for antibody information) diluted in TBST plus 5% non-fat dry milk were added to membranes and incubated overnight at 4°C on a rocking platform. Membranes were washed five times with TBST. Secondary antibodies (see Table 3.1 for antibody information) diluted in TBST were added to membranes and incubated for 1 h at room temperature on a rocking platform, protected from light. Membranes were washed five times with TBST and imaged using an Odyssey 9120 (LI-COR, Lincoln, NE). Band intensities were quantified using Image Studio software (LI-COR).

3.3.8 Dextran accumulation assay

A fixable, Alexa Fluor 488-conjugated dextran with an average molecular weight of 10 kDa (Invitrogen) was used as a tracer to estimate total fluid-phase endocytosis. Dextran was added at 10 μM to the medium of Passage 1 cultures. Plates were incubated on rotating platforms at 37°C or 4°C for 2 h. For inhibitor experiments, 20 μM chlorpromazine (Sigma), 100 U/mL nystatin (Sigma), or 2 μM rottlerin (Tocris) were added to the medium 30 min prior to addition of dextran. Medium was removed and cells were washed once with DPBS, and then incubated with Accutase for 10 min at 37°C. Cell suspensions were passed through 40 μm cell strainers into 4× volume of DMEM/F-12 and centrifuged for 5 min, 200×g. Cells were resuspended in MACS buffer and incubated with the CD31-APC antibody (Miltenyi Biotec) for 30 min at 4°C, protected from light. Cell suspensions were brought to a volume of 5 mL with MACS buffer and centrifuged at 4°C for 5 min, 200×g. Pellets were resuspended in DPBS supplemented with 4% paraformaldehyde and incubated for 15 min at room temperature, protected from light. Cells were centrifuged for 5 min, 200×g. Pellets were resuspended in MACS buffer and analyzed on a BD FACSCalibur flow cytometer (BD Biosciences). FlowJo software was used to gate $CD31^+$ cells and quantify geometric mean fluorescence intensity and coefficient of variation (CV) of dextran. For imaging, the dextran accumulation assay was performed on cells cultured on #1.5 glass bottom plates. After 2 h of dextran treatment, medium was removed and cells washed with DPBS. Cells were fixed with 4% paraformaldehyde for 15 min. Cells were washed three times with 500 μL DPBS and blocked and permeabilized with DPBS supplemented with 10% goat serum and 0.1% Triton X-100 for 1 h at room temperature. Cells were stained with the caveolin-1 primary antibody and imaged on a confocal microscope as described above.

3.3.9 Transendothelial electrical resistance and sodium fluorescein permeability

Transwell inserts (6.5 mm diameter with 0.4 μm pore polyester filters) (Corning) were coated with 50 μl of a solution of collagen IV (400 μg/mL) and fibronectin (100 μg/mL) in water for 4 h at 37°C. Passage 3 DMSO- and CHIR-treated ECs were seeded on Transwell inserts at 10^5 cells/cm^2 in hECSR medium supplemented with DMSO or CHIR. Medium volumes were 200 μL for the apical chamber and 800 μL for the basolateral chamber. Beginning the day after seeding, TEER was measured daily for 6 days using an EVOM2 epithelial voltohmmeter with STX2 chopstick electrodes (World Precision Instruments, Sarasota, FL). Medium was replaced every other day. TEER values were corrected by subtracting the resistance of a collagen IV/fibronectin-coated Transwell insert without cells and multiplying by the filter surface area of 0.33 cm^2. Permeability of endothelial monolayers to sodium fluorescein was assessed 6 days after seeding cells on Transwell inserts. Medium in both apical and basolateral chambers was replaced and cells returned to the incubator for 1 h. Medium in apical chambers, including the apical chamber of a collagen IV/fibronectin-coated Transwell insert without cells, was then replaced with medium supplemented with 10 μM sodium fluorescein (Sigma Aldrich), and plates placed on an orbital platform in an incubator. At 15, 30, 45, and 60 min, an 80 μL sample of the basolateral chamber medium was withdrawn from each Transwell, transferred to a 96-well plate, and 80 μL fresh medium replaced in the basolateral chamber of each Transwell. At 60 min, an 80 μL sample of apical chamber medium was also withdrawn from each Transwell and transferred to the 96-well plate. 80 μL of medium lacking sodium fluorescein was also transferred to the 96-well plate for background subtraction. Fluorescence intensity of all samples was measured using an Infinite M1000 PRO plate reader (Tecan, Männedorf, Switzerland) with 485 nm excitation and 530 nm emission wavelengths. Background-subtracted fluorescence intensity values at the 30, 45, and 60 min timepoints were corrected for sampling-induced dilution as previously

described (*431*). The endothelial permeability coefficient (P_e), which is a concentration-independent parameter corrected for the permeability of a cell-free Transwell insert, was calculated as previously described (*431*).

3.3.10 Statistics

Individual wells of cultured cells that underwent identical experimental treatments are defined as replicates, and all key experiments were repeated using multiple independent hPSC differentiations. Detailed information about replication strategy is provided in figure legends. Student's *t* test was used for comparison of means from two experimental groups. One-way analysis of variance (ANOVA) was used for comparison of means from three or more experimental groups, followed by Dunnett's post-hoc test for comparison of multiple treatments to a single control, or Tukey's honest significant difference (HSD) post-hoc test for multiple pairwise comparisons. When data from multiple differentiations were combined, two-way ANOVA (one factor being the experimental treatment and one factor being the differentiation) was used for comparison of means to achieve blocking of differentiation-based variability, followed by post-hoc tests as described above if more than two experimental treatments were compared. For fluorescence intensities (a.u.), two-way ANOVA was performed prior to normalization of these values to the control group within each differentiation (for visualization in plots). Statistical tests were performed in JMP Pro (v15.0.0). For RNA-seq differential expression analysis, the DESeq2 Wald test with Benjamini-Hochberg correction was used to calculate P-values. Descriptions of the statistical tests used are provided in figure legends.

3.4 Results

3.4.1 Wnt activation in hPSC-derived endothelial progenitors

We adapted an existing protocol to produce endothelial progenitor cells (EPCs) from hPSCs (*458*, *459*) (Figure 3.1A). To achieve mesoderm specification, this method employs an

initial activation of Wnt/β-catenin signaling with CHIR 99021 (CHIR), a small molecule inhibitor of glycogen synthase kinase-3 (GSK-3), which results in inhibition of GSK-3β-mediated β-catenin degradation. After 5 days of expansion, the resulting cultures contained a mixed population of $CD34^{+}CD31^{+}$ EPCs and $CD34^{-}CD31^{-}$ non-EPCs (Figure 3.1B-C). We used magnetic-activated cell sorting (MACS) to isolate $CD31^{+}$ cells from this mixed culture and plated these cells on collagen IV-coated plates in a minimal endothelial cell medium termed hECSR (*468*). We first asked whether Wnt3a, a ligand widely used to activate canonical Wnt/β-catenin signaling (*228*, *427*, *464*, *562*, *563*), could induce GLUT-1 expression in the resulting ECs. After 6 days of treatment, we observed a significant increase in the fraction of GLUT-1^{+} ECs in Wnt3a-treated cultures compared to controls (Figure 3.1D-E). Consistent with previous observations (*468*), we also detected a population of calponin^{+} smooth muscle protein 22-α^{+} putative smooth muscle-like cells (SMLCs) outside the endothelial colonies (Figure 3.2) and these SMLCs expressed GLUT-1 in both control and Wnt3a-treated conditions (Figure 3.1D).

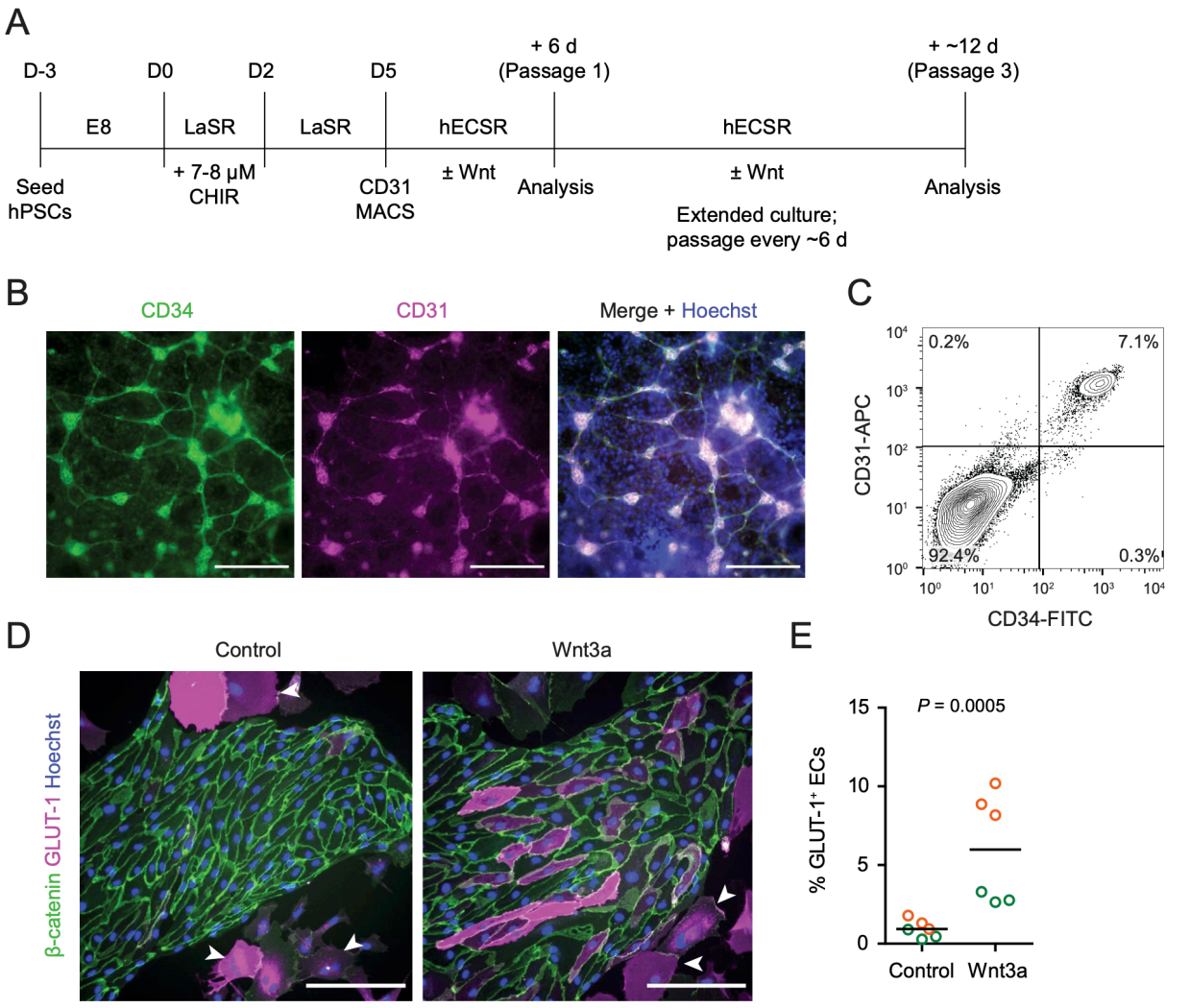

Figure 3.1. hPSC-derived endothelial progenitors as a model for studying Wnt-mediated barriergenesis. (A) Overview of the endothelial differentiation and Wnt treatment protocol. (B) Immunocytochemistry analysis of CD34 and CD31 expression in D5 EPCs prior to MACS. Hoechst nuclear counterstain is overlaid in the merged image. Scale bars: 200 μm. (C) Flow cytometry analysis of CD34 and CD31 expression in D5 EPCs prior to MACS. (D) Immunocytochemistry analysis of β-catenin and GLUT-1 expression in Passage 1 ECs treated with Wnt3a or control. Hoechst nuclear counterstain is overlaid. Arrowheads indicate smooth muscle-like cells (SMLCs). Scale bars: 200 μm. (E) Quantification of the percentage of GLUT-1$^+$ ECs in control- and Wnt3a-treated conditions. Points represent replicate wells from 2 independent differentiations of the IMR90-4 line, each differentiation indicated with a different color. Bars indicate mean values. P-value: Two-way ANOVA.

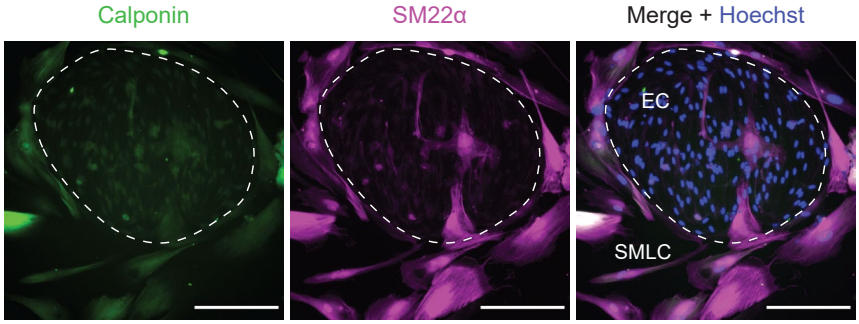

Figure 3.2. Smooth muscle-like cells (SMLCs). Immunocytochemistry analysis of calponin and smooth muscle protein 22-α (SM22α) in Passage 1 cultures containing ECs and SMLCs. Hoechst nuclear counterstain is overlaid in the merged image. Dashed area indicates an EC colony. Scale bars: 200 μm.

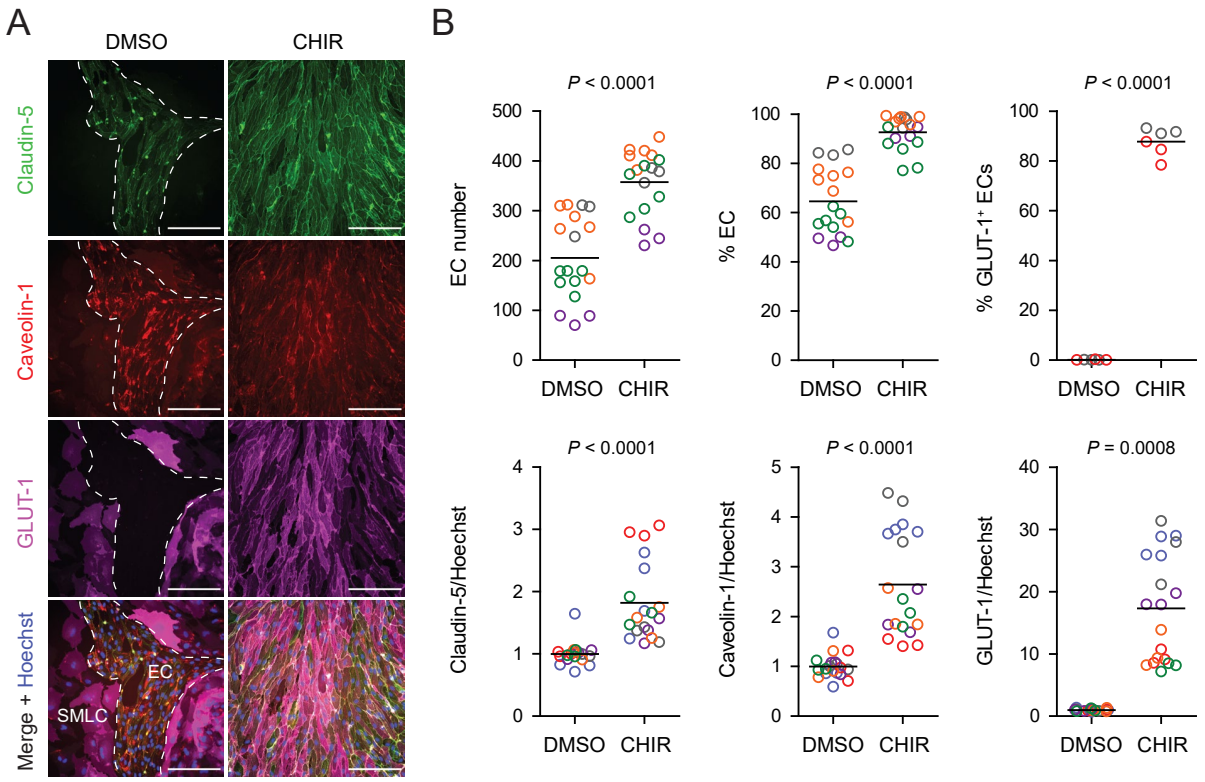

Figure 3.3. Effect of CHIR on endothelial properties. (A) Immunocytochemistry analysis of claudin-5, caveolin-1, and GLUT-1 expression in Passage 1 ECs treated with DMSO or 4 μM CHIR. Hoechst nuclear counterstain is overlaid in the merged images. Dashed lines indicate the border between an EC colony and SMLCs in the DMSO condition. Scale bars: 200 μm. (B) Quantification of images from the conditions described in (A) for number of ECs per 20× field, percentage of ECs (claudin-5$^+$ cells relative to total nuclei), percentage of GLUT-1$^+$ ECs (relative to total claudin-5$^+$ ECs), and mean fluorescence intensity of claudin-5, caveolin-1, and GLUT-1 normalized to Hoechst mean fluorescence intensity within the area of claudin-5$^+$ ECs only. Points represent replicate wells from 2–6 independent differentiations of the IMR90-4 line, each differentiation indicated with a different color. Bars indicate mean values. For the fluorescence intensity plots, values were normalized within each differentiation such that the mean of the DMSO condition equals 1. P-values: Two-way ANOVA on unnormalized data.

Based on these promising results with Wnt3a, we next tested a low concentration (4 μM) of the GSK-3 inhibitor CHIR because of its ability to activate Wnt signaling in a receptor/co-receptor-independent manner. In addition to GLUT-1, we evaluated expression of two other key proteins: claudin-5, which is known to be upregulated in CNS ECs in response to Wnt (*379*), and caveolin-1, given the low rate of caveolin-mediated transcytosis in CNS compared to non-CNS ECs (*39*, *263*) (Figure 3.3A). 4 μM CHIR robustly induced GLUT-1 expression in approximately 90% of ECs while increasing EC number and increasing EC purity to nearly 100% (Figure 3.3B). Furthermore, CHIR led to an approximately 1.5-fold increase in average claudin-5 abundance and a 10- to 30-fold increase in GLUT-1 abundance, but also a 2- to 4-fold increase in caveolin-1 (Figure 3.3B). We therefore titrated CHIR to determine an optimal concentration for EC expansion, purity, GLUT-1 induction, and claudin-5 upregulation while limiting the undesirable non-CNS-like increase in caveolin-1 abundance. Although 2 μM CHIR did not lead to increased caveolin-1 expression compared to vehicle control (DMSO), it also did not elevate claudin-5 or GLUT-1 expression compared to control and was less effective in increasing EC number and EC purity than 4 μM CHIR (Figure 3.4). On the other hand, 6 μM CHIR further increased GLUT-1 abundance but also further increased caveolin-1 abundance and did not improve EC number, EC purity, or claudin-5 expression (Figure 3.4). Therefore, we conducted further experiments using 4 μM CHIR. We confirmed that the CHIR-mediated increases in EC purity, EC number, and caveolin-1 and GLUT-1 expression were conserved in an additional hPSC line, although claudin-5 upregulation was not apparent (Figure 3.5). We also used two hPSC lines with doxycycline-inducible expression of short hairpin RNAs targeting *CTNNB1* (β-catenin) to confirm that CHIR-mediated upregulation of GLUT-1 in ECs was β-catenin-dependent. Indeed, doxycycline treatment in combination with CHIR significantly reduced GLUT-1 abundance in ECs derived from these hPSC lines (Figure 3.6). Finally, we confirmed

that increased EC number was the result of increased EC proliferation in CHIR-treated cultures (Figure 3.7). Together, these results suggest that activation of the Wnt/β-catenin pathway is capable of inducing CNS-like phenotypes in hPSC-derived endothelial progenitors.

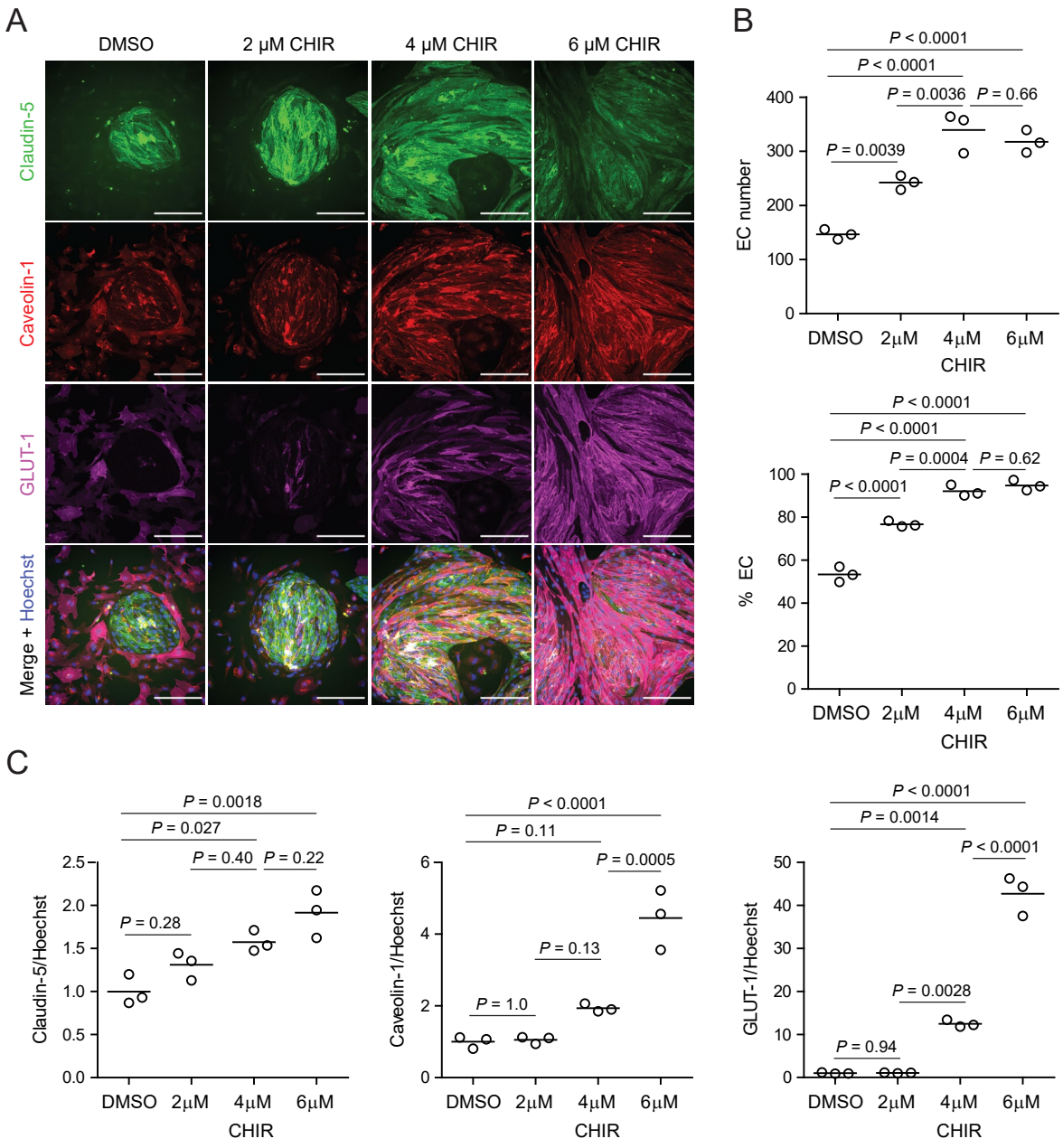

Figure 3.4. Dose-dependent effects of CHIR on endothelial properties. (A) Immunocytochemistry analysis of claudin-5, caveolin-1, and GLUT-1 expression in Passage 1 ECs treated with 2 μM, 4 μM, or 6 μM CHIR, or DMSO vehicle control. Hoechst nuclear counterstain is overlaid in the merged images. Scale bars: 200 μm. (B) Quantification of images from the conditions described in (A) for number of ECs per 20× field and percentage of ECs (claudin-5$^+$ cells relative to total nuclei). Points represent replicate wells from one differentiation of the IMR90-4 line and bars indicate mean values. P-values: ANOVA followed by Tukey's HSD test. (C) Quantification of claudin-5, caveolin-1, and GLUT-1 mean fluorescence intensity normalized to Hoechst mean fluorescence intensity within the area of claudin-5$^+$ ECs only. Points represent replicate wells from one differentiation of the IMR90-4 line. Bars indicate mean values, with values normalized such that the mean of the DMSO condition equals 1. P-values: ANOVA followed by Tukey's HSD test.

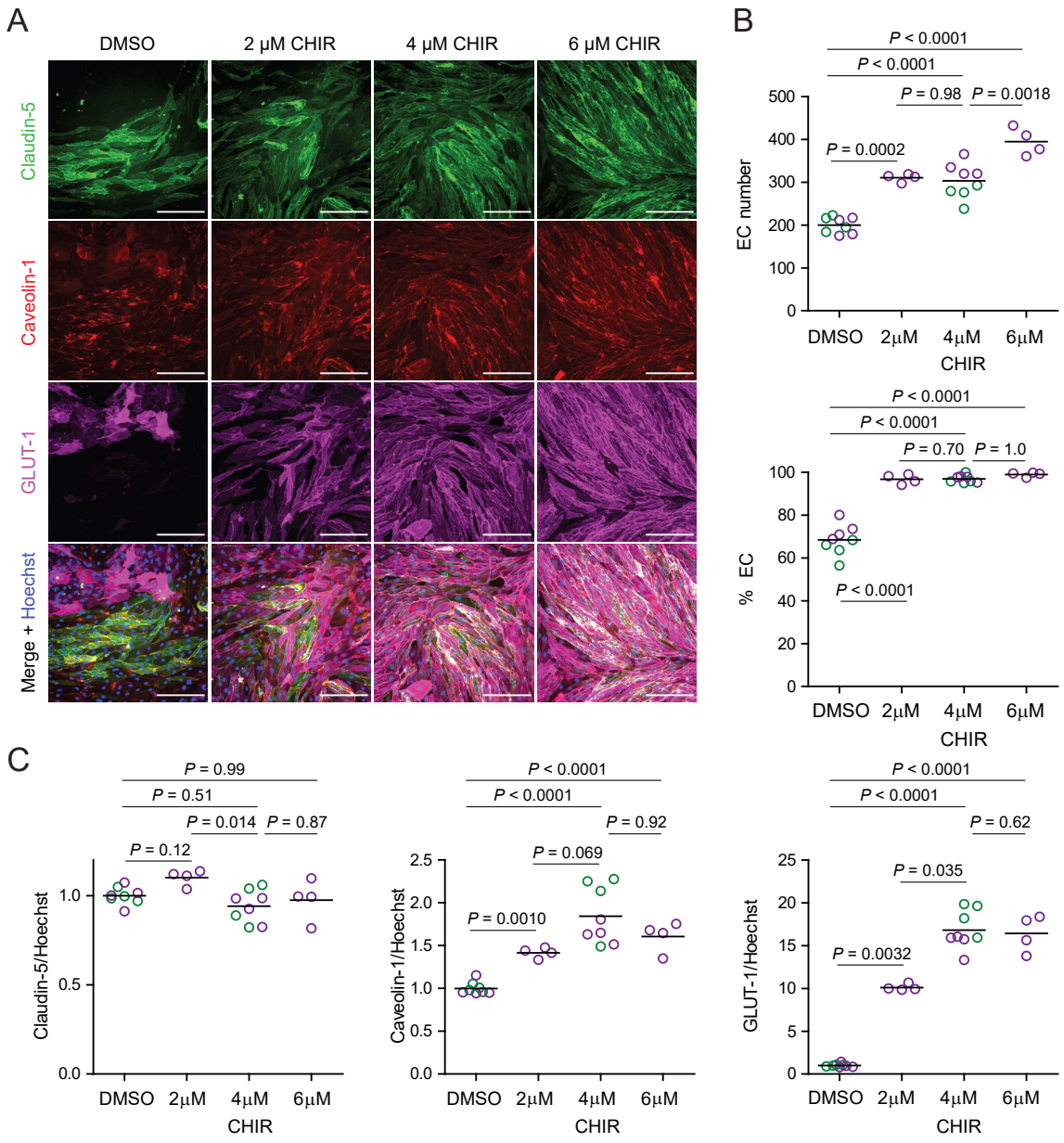

Figure 3.5. CHIR-mediated effects in an additional hPSC line. (A) Immunocytochemistry analysis of claudin-5, caveolin-1, and GLUT-1 expression in Passage 1 ECs differentiated from the WTC11 iPSC line treated with 2 μM, 4 μM, or 6 μM CHIR, or DMSO vehicle control. Hoechst nuclear counterstain is overlaid in the merged images. Scale bars: 200 μm. (B) Quantification of images from the conditions described in (A) for number of ECs per 20× field and percentage of ECs (claudin-5$^+$ cells relative to total nuclei). Points represent replicate wells from 1–2 differentiations of the WTC11 line, each differentiation indicated with a different color. Bars indicate mean values. P-values: Two-way ANOVA followed by Tukey's HSD test. (C) Quantification of claudin-5, caveolin-1, and GLUT-1 mean fluorescence intensity normalized to Hoechst mean fluorescence intensity within the area of claudin-5$^+$ ECs only. Points represent replicate wells from 1–2 differentiations of the WTC11 line, each differentiation indicated with a different color. Bars indicate mean values, with values normalized within each differentiation such that the mean of the DMSO condition equals 1. P-values: Two-way ANOVA followed by Tukey's HSD test on unnormalized data.

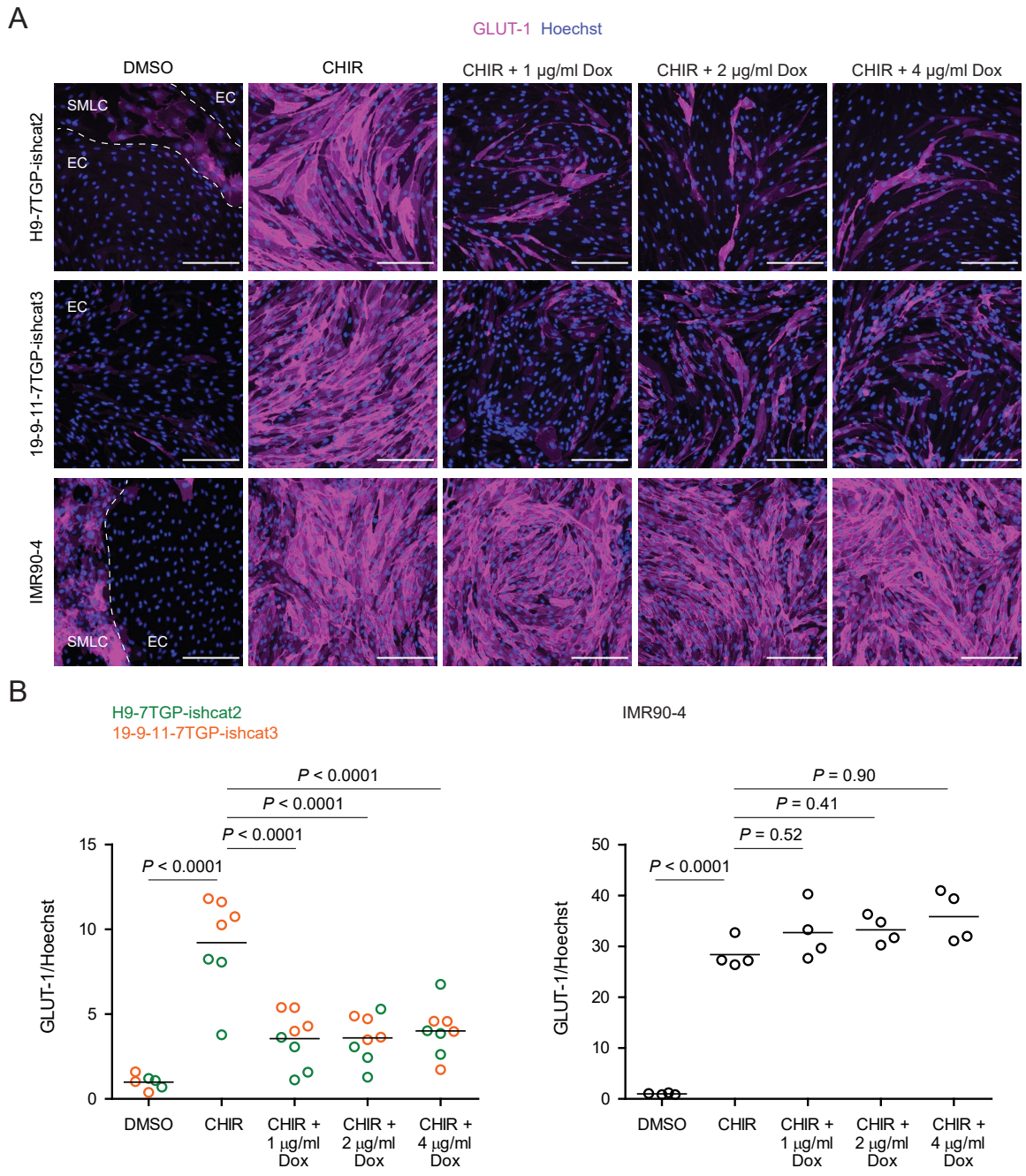

Figure 3.6. β-catenin-dependence of CHIR-mediated GLUT-1 induction. (A) Immunocytochemistry analysis of GLUT-1 expression in Passage 1 ECs treated with DMSO, CHIR, or CHIR + doxycycline (Dox) at 1, 2, or 4 µg/mL. Images from the H9-7TGP-ishcat2, 19-9-11-7TGP-ishcat3, and IMR90-4 lines are shown. Hoechst nuclear counterstain is overlaid. Dashed lines indicate borders between EC colonies and SMLCs in the DMSO condition. Scale bars: 200 µm. (B) Quantification of images from the conditions described in (A) for GLUT-1 mean fluorescence intensity normalized to Hoechst mean fluorescence intensity within the area of ECs only. At left, points represent replicate wells from one differentiation of the H9-7TGP-ishcat line (green) and one differentiation of the 19-9-11-7TGP-ishcat3 line (orange). Bars indicate mean values, with values normalized within each differentiation such that the mean of the DMSO condition equals 1. P-values: Two-way ANOVA followed by Tukey's HSD test on unnormalized data. At right, points represent replicate wells from one differentiation of the IMR90-4 line. Bars indicate mean values, with values normalized such that the mean of the DMSO condition equals 1. P-values: ANOVA followed by Tukey's HSD test.

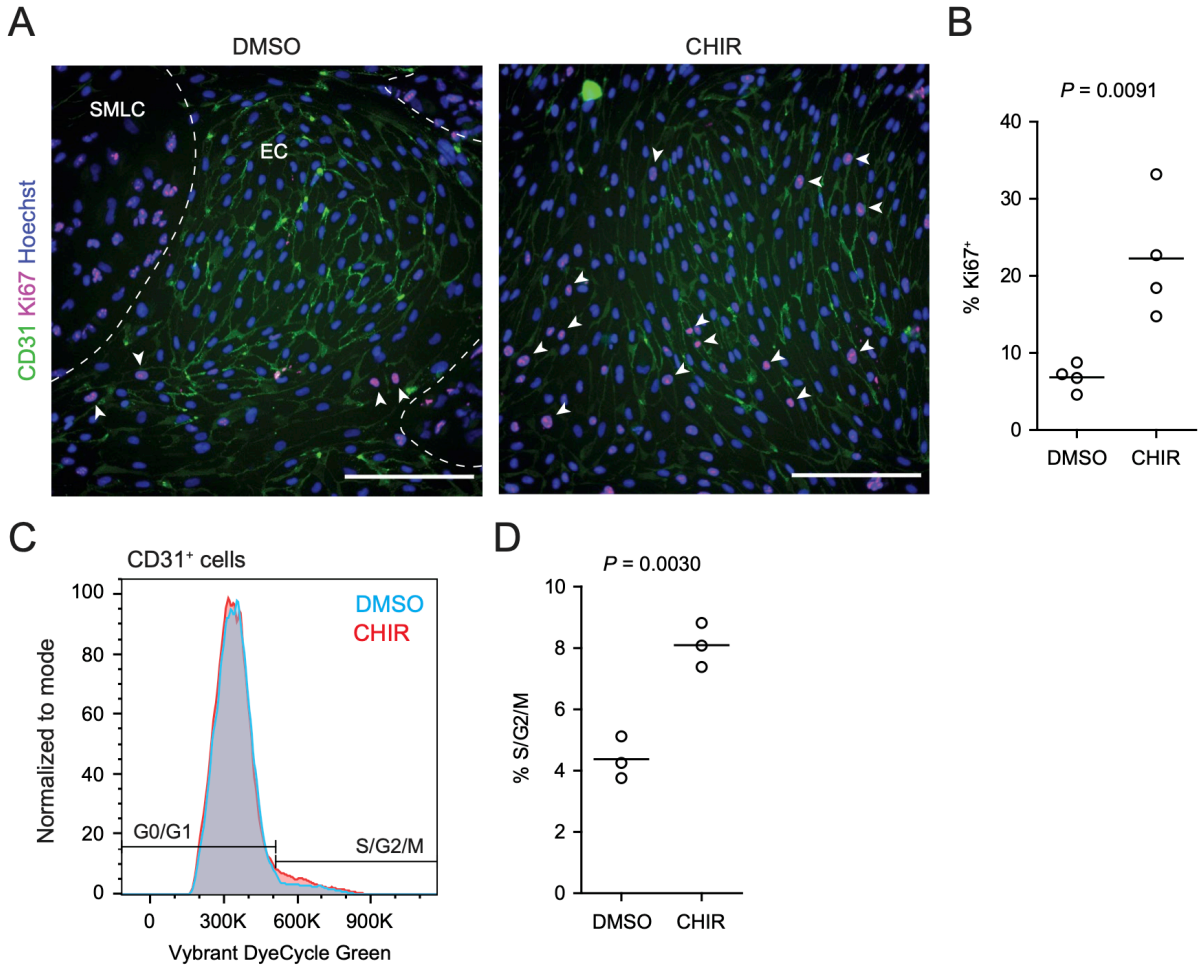

Figure 3.7. Effect of CHIR on endothelial cell proliferation. (A) Immunocytochemistry analysis of CD31 and Ki67 expression in Passage 1 ECs treated with DMSO or CHIR. Hoechst nuclear counterstain is overlaid. Dashed lines indicate borders between the EC colony and SMLCs in the DMSO condition. Arrowheads indicate examples of Ki67$^+$ ECs. Scale bars: 200 µm. (B) Quantification of the percentage of Ki67$^+$ ECs in DMSO- and CHIR-treated conditions. Points represent replicate wells from one differentiation of the WTC11 line, and bars indicate mean values. P-value: Student's *t* test. (C) Flow cytometry-based cell cycle analysis. Representative plots of Vybrant DyeCycle Green Stain abundance in CD31$^+$ cells from Passage 1 cultures treated with DMSO or CHIR. (D) Quantification of the percentage of S/G2/M phase ECs. Points represent replicate wells from one differentiation of the WTC11 line, and bars indicate mean values. P-value: Student's *t* test.

3.4.2 Effects of CHIR-mediated Wnt activation in endothelial progenitors

Since CHIR elicited a robust Wnt-mediated response, we next asked whether other aspects of the CNS EC barrier phenotype were CHIR-regulated. PLVAP, a protein that forms bridges across both caveolae and fenestrae (*66*), is one such canonically Wnt-downregulated protein. We therefore first evaluated PLVAP expression in Passage 1 control (DMSO) or CHIR-

treated ECs using confocal microscopy (Figure 3.8A). We observed numerous PLVAP$^+$ punctate vesicle-like structures in both conditions, with CHIR treatment reducing PLVAP abundance by approximately 20% (Figure 3.8A-B). This effect was not apparent in Western blots of Passage 1 ECs, likely due to the relatively modest effect (Figure 3.9A-B). However, after two more passages (Figure 3.1A), Passage 3 ECs demonstrated a robust downregulation of PLVAP in CHIR-treated cells compared to controls (Figure 3.9C-D). We also used Western blotting to confirm CHIR-mediated upregulation of GLUT-1 and claudin-5 both at Passage 1 and Passage 3 (Figure 3.9A-D). We next evaluated expression of the tricellular tight junction protein LSR (angulin-1) because of its enrichment in CNS versus non-CNS ECs, and the temporal similarity between LSR induction and the early stage of Wnt-mediated CNS barriergenesis (*62*). We found that CHIR treatment led to a strong increase in LSR expression in both Passage 1 and Passage 3 ECs (Figure 3.9A-D), suggesting that Wnt signaling upregulates multiple necessary components of the CNS EC bicellular and tricellular junctions.

CHIR treatment produced two apparently competing changes in ECs related to vesicular transport: an expected downregulation of PLVAP and an unexpected upregulation of caveolin-1. We therefore asked whether the rate of total fluid-phase endocytosis differed between CHIR-treated and control ECs, using a fluorescently-labeled 10 kDa dextran as a tracer. After incubating Passage 1 cultures with dextran for 2 h at 37°C, we used flow cytometry to gate CD31$^+$ ECs and assess total dextran accumulation (Figure 3.10A-B). In ECs incubated at 37°C, CHIR treatment did not change the geometric mean dextran signal compared to DMSO (Figure 3.10B,C), but did cause a broadening of the distribution of dextran intensities as quantified by the coefficient of variation (CV), indicative of sub-populations of cells with decreased and increased dextran uptake (Figure 3.10B,D). We confirmed that the dextran signal measured by this assay was endocytosis-dependent by carrying out the assay at 4°C and with inhibitors of

specific endocytic pathways (Figure 3.11A-C). Compared to vehicle control, chlorpromazine (inhibitor of clathrin-mediated endocytosis) and rottlerin (inhibitor of macropinocytosis) both decreased dextran uptake, while nystatin (inhibitor of caveolin-mediated endocytosis) did not significantly affect uptake (Figure 3.11B,C), consistent with the very small number of dextran^{+} caveolin-1^{+} puncta observed by confocal imaging (Figure 3.11D). Thus, despite the generally uniform elevation of caveolin-1 and decrease of PLVAP observed by immunocytochemistry in CHIR-treated ECs, our functional assay suggests neither an overall increase nor decrease in total fluid-phase endocytosis. Instead, it indicates that CHIR increases the heterogeneity of the EC population with respect to the rate of endocytosis.

We also compared the paracellular barrier properties of DMSO- and CHIR-treated ECs. Because Passage 1 cultures contain SMLCs that preclude formation of a confluent endothelial monolayer, we evaluated paracellular barrier properties of Passage 3 ECs that had undergone selective dissociation and replating (see Section 3.3), a strategy that effectively purifies the cultures (*468*). CHIR-treated Passage 3 ECs had elevated transendothelial electrical resistance (TEER) (Figure 3.10E) and decreased permeability to the small molecule tracer sodium fluorescein (Figure 3.10F). Together, these results are consistent with CHIR-mediated increases to tight junction protein expression (e.g., claudin-5 and LSR) and suggest Wnt activation leads to functional improvements to paracellular barrier in this system.

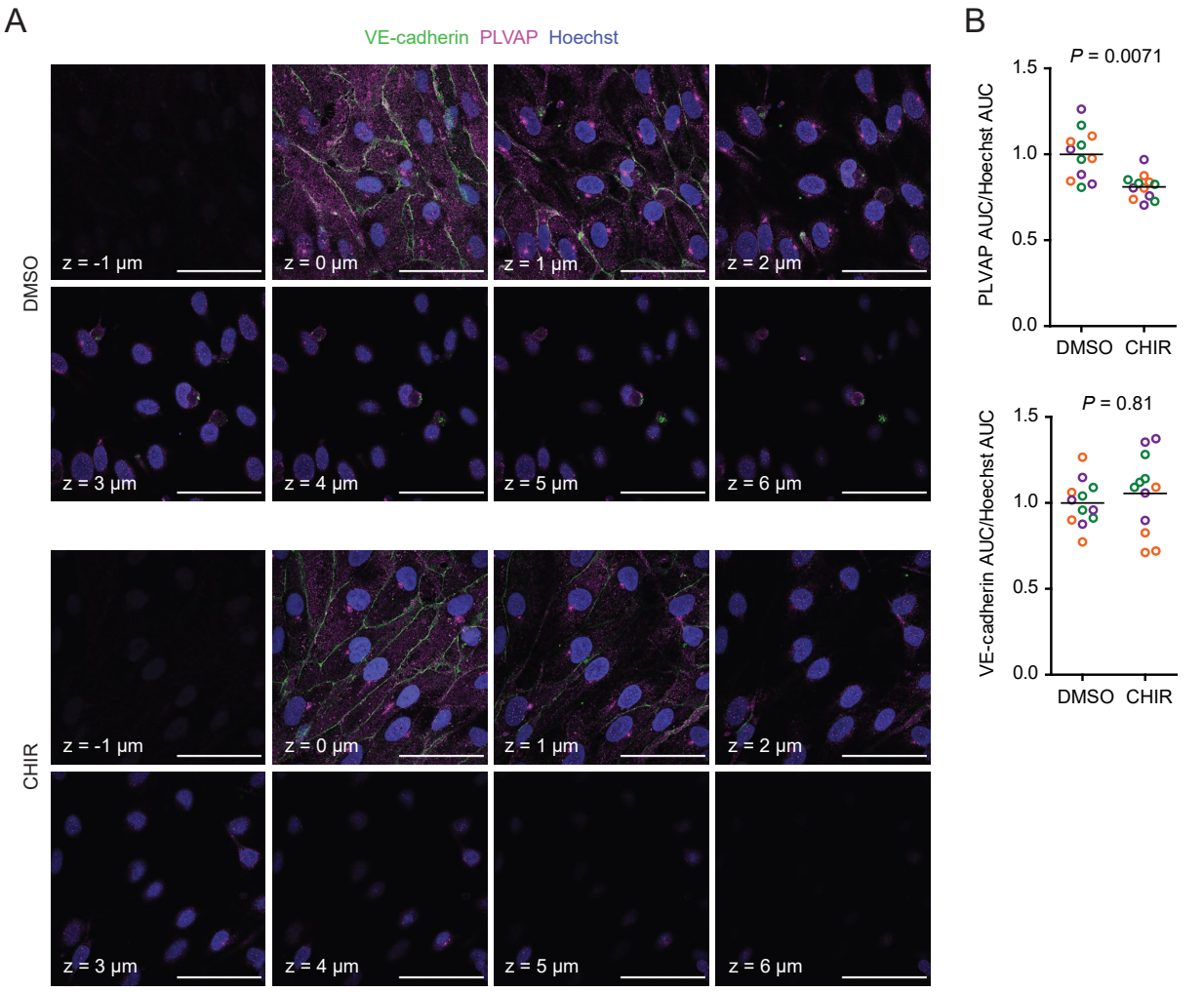

Figure 3.8. Effect of CHIR on endothelial PLVAP expression. (A) Confocal immunocytochemistry analysis of VE-cadherin and PLVAP expression in Passage 1 ECs treated with DMSO or CHIR. Hoechst nuclear counterstain is overlaid. Eight serial confocal Z-slices with 1 µm spacing are shown. Scale bars: 50 µm. (B) Quantification of PLVAP and VE-cadherin area under the curve (AUC) of mean fluorescence intensity versus Z-position normalized to Hoechst AUC. Points represent replicate wells from 3 independent differentiations of the IMR90-4 line, each differentiation indicated with a different color. Bars indicate mean values, with values normalized within each differentiation such that the mean of the DMSO condition equals 1. P-values: Two-way ANOVA on unnormalized data.

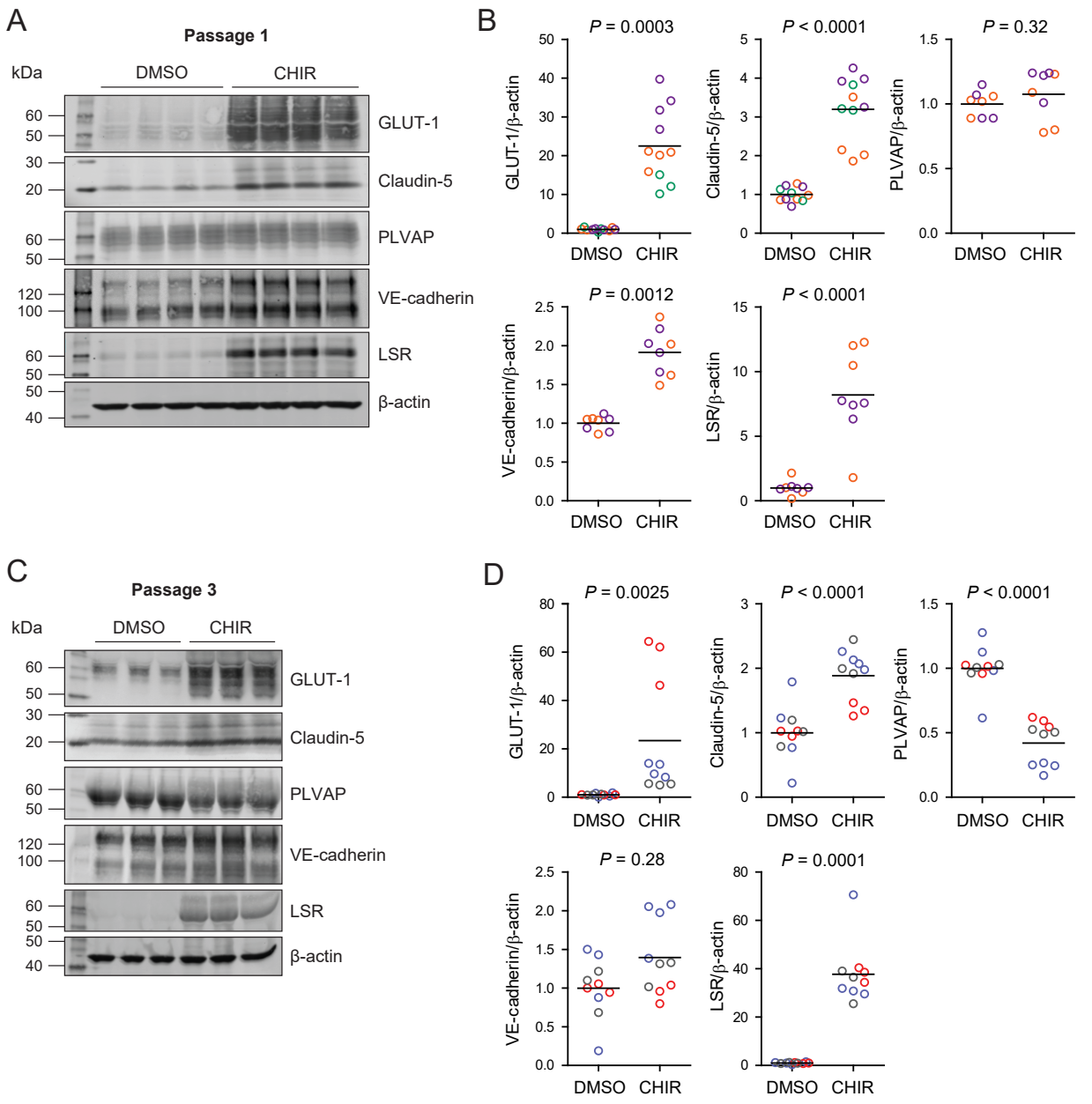

Figure 3.9. Effect of CHIR on protein expression in Passage 1 and Passage 3 ECs. (A) Western blots of Passage 1 ECs treated with DMSO or CHIR probed for GLUT-1, claudin-5, PLVAP, VE-cadherin, LSR, and β-actin. (B) Quantification of Western blots of Passage 1 ECs. GLUT-1, claudin-5, PLVAP, VE-cadherin, and LSR band intensities were normalized to β-actin band intensity. Points represent replicate wells from 2–3 independent differentiations of the IMR90-4 line, each differentiation indicated with a different color. Bars indicate mean values, with values normalized within each differentiation such that the mean of the DMSO condition equals 1. P-values: Two-way ANOVA on unnormalized data. (C) Western blots of Passage 3 ECs treated with DMSO or CHIR probed for GLUT-1, claudin-5, PLVAP, VE-cadherin, LSR, and β-actin. (D) Quantification of Western blots of Passage 3 ECs. GLUT-1, claudin-5, PLVAP, VE-cadherin, and LSR band intensities were normalized to β-actin band intensity. Points represent replicate wells from 3 independent differentiations of the IMR90-4 line, each differentiation indicated with a different color. Bars indicate mean values, with values normalized within each differentiation such that the mean of the DMSO condition equals 1. P-values: Two-way ANOVA on unnormalized data.

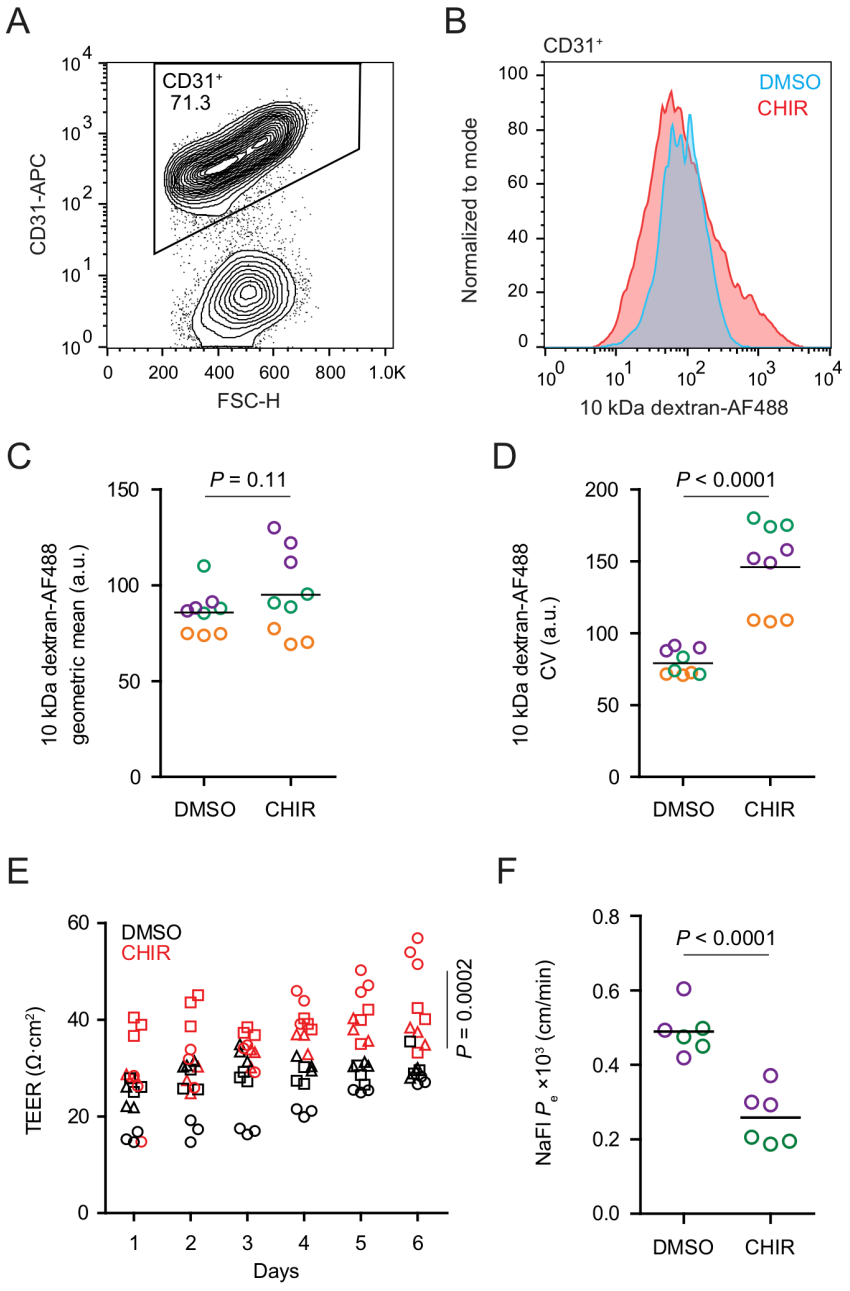

Figure 3.10. Functional properties of CHIR- and DMSO-treated ECs. (A) Flow cytometry analysis of CD31 expression in Passage 1 ECs following the dextran internalization assay. CD31⁺ cells were gated for further analysis. (B) Flow cytometry analysis of 10 kDa dextran-Alexa Fluor 488 (AF488) abundance in CD31⁺ cells. Cells were treated with DMSO or CHIR for 6 d prior to the assay. Representative plots from cells incubated with dextran for 2 h at 37°C are shown. (C) Quantification of 10 kDa dextran-AF488 geometric mean fluorescence intensity in CD31⁺ cells. Treatment and assay conditions were as described in (B). Points represent replicate wells from 3 independent differentiations of the IMR90-4 line, each differentiation indicated with a different color. Bars indicate mean values. P-value: Two-way ANOVA. (D) Quantification of the coefficient of variation (CV) of 10 kDa dextran-AF488 fluorescence intensity in CD31⁺ cells. Points represent replicate wells from 3 independent differentiations of the IMR90-4 line, each differentiation indicated with a different color. Bars indicate mean values. P-value: Two-way ANOVA. (E) Transendothelial electrical resistance (TEER) of Passage 3 ECs. The x-axis indicates the number of days after seeding cells on Transwell inserts. Points represent replicate wells from three independent differentiations of the IMR90-4 line, each differentiation indicated with a different shape. P-value: Two-way ANOVA. (F) Permeability of Passage 3 ECs to sodium fluorescein. Points represent replicate wells from two independent differentiations of the IMR90-4 line, each differentiation indicated with a different color. Bars indicate mean values. P-value: Two-way ANOVA.

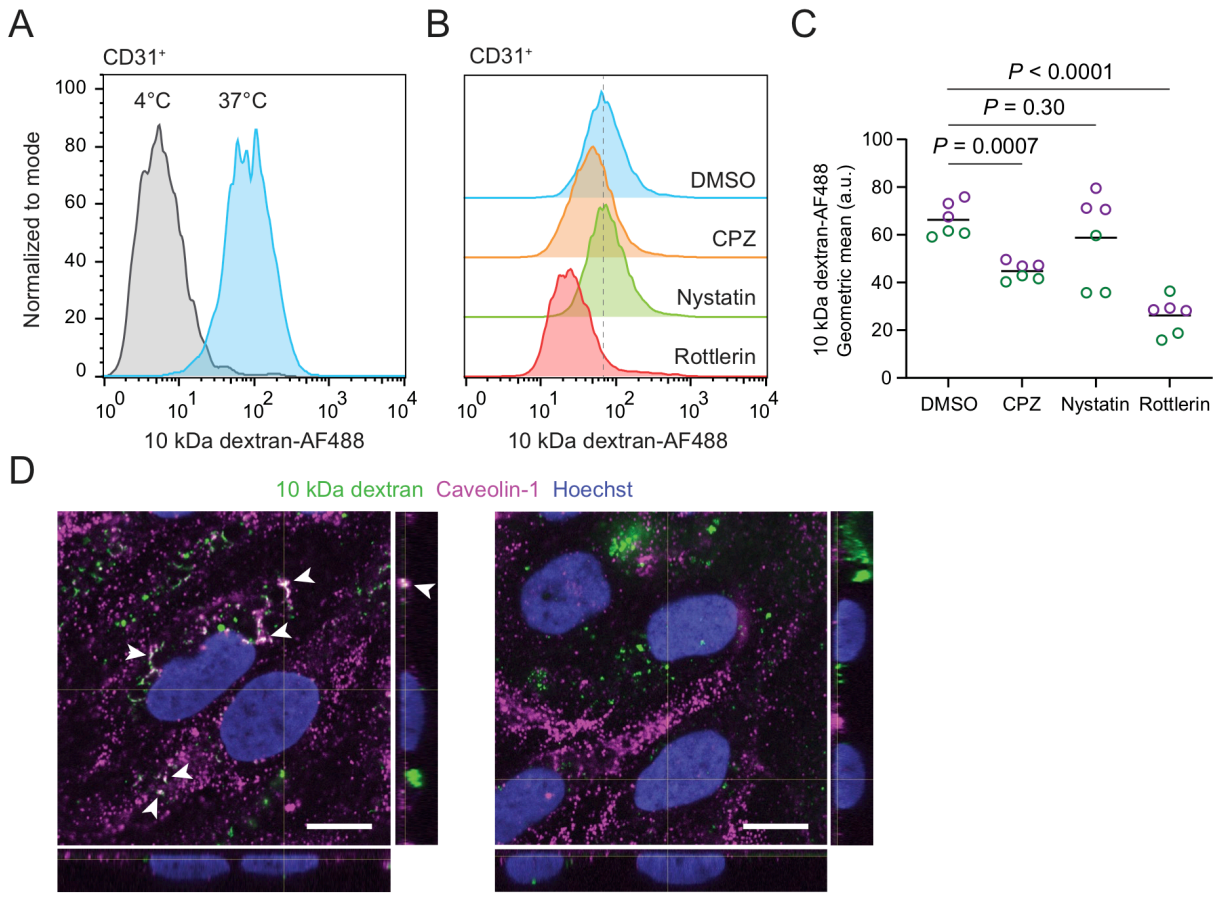

Figure 3.11. Endocytosis-dependence of dextran uptake. (A-B) Flow cytometry analysis of 10 kDa dextran-Alexa Fluor 488 (AF488) abundance in DMSO-treated CD31$^+$ cells. Representative plots from cells incubated with dextran for 2 h at 37°C (same plot shown in Figure 5B) or 4°C (A) or cells incubated with dextran and indicated inhibitors (B) are shown. (C) Quantification of 10 kDa dextran-AF488 geometric mean fluorescence intensity in CD31$^+$ cells. Treatment and assay conditions were as described in (B). Points represent replicate wells from 2 independent differentiations of the IMR90-4 line, each differentiation indicated with a different color. Bars indicate mean values. P-values: Two-way ANOVA followed by Dunnett's test. CPZ: chlorpromazine. (D) Confocal immunocytochemistry analysis of caveolin-1 expression and 10 kDa dextran internalization in Passage 1 DMSO-treated ECs. Hoechst nuclear counterstain is overlaid. Single confocal Z-slices from two representative fields are shown. XZ and YZ projections derived from serial Z-slices with 0.25 µm spacing are shown at right and below. Arrowheads indicate dextran$^+$ caveolin-1$^+$ puncta. Scale bars: 10 µm.

Given the relatively weak responses to Wnt activation in adult mouse liver ECs *in vivo* (*367*) and adult mouse brain ECs cultured *in vitro* (*226*), we sought to determine whether the immature, potentially more plastic state of hPSC-derived endothelial progenitors contributed to the relatively robust CHIR-mediated response we observed. To test this hypothesis, we matured hPSC-derived ECs *in vitro* for 4 passages (until approximately day 30) prior to initiating CHIR treatment for 6 days, and compared the resulting cells to differentiation-matched samples treated with CHIR immediately after MACS (Figure 3.12A). Both Passage 1 DMSO-treated ECs and Passage 5 DMSO-treated ECs, which are analogous to EECM-BMEC-like cells we previously reported (*468*), did not have detectable GLUT-1 expression (Figure 3.12B). Compared to DMSO controls, the CHIR-treated Passage 5 ECs exhibited no increase in GLUT-1 abundance (Figure 3.12B-D), which contrasts with the marked increase observed when CHIR treatment was initiated immediately after MACS (Figure 3.12B-D). Furthermore, CHIR treatment in matured ECs did not increase claudin-5 expression and did not increase EC number (Figure 3.12B-D), in contrast to the increases observed in both properties when treatment was initiated immediately after MACS (Figure 3.12B-D). We observed a similar lack of robust GLUT-1 induction in an additional differentiation and an additional hPSC line in which CHIR treatment was carried out at Passage 4 (Figure 3.13). Together, these data suggest that early, naïve endothelial progenitors are more responsive to Wnt activation than more mature ECs derived by the same differentiation protocol.

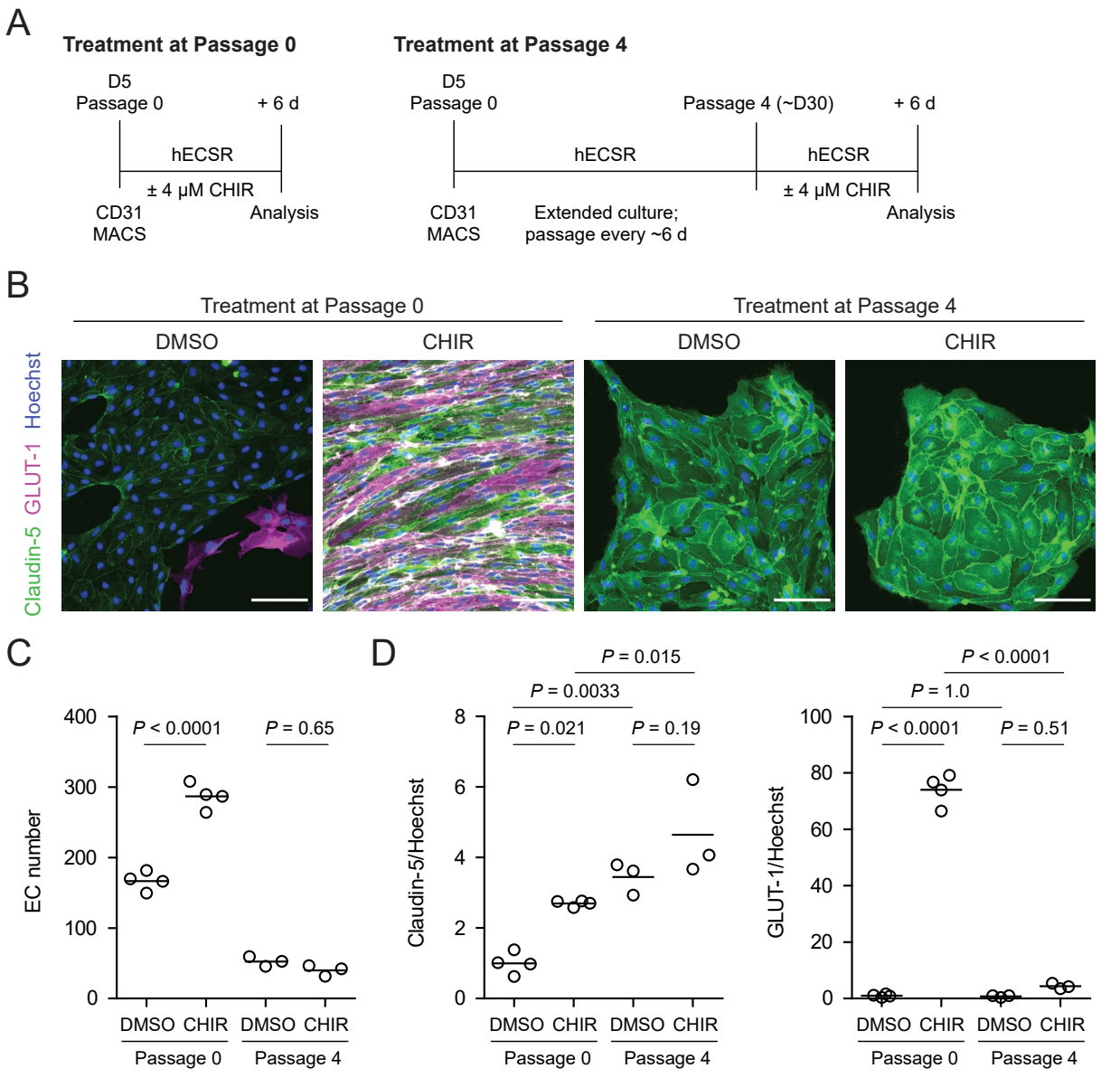

Figure 3.12. Effect of CHIR treatment in EPCs and matured endothelium. (A) Overview of the endothelial differentiation, extended culture, and CHIR treatment protocols. (B) Immunocytochemistry analysis of claudin-5 and GLUT-1 expression in ECs treated with DMSO or CHIR as outlined in (A). Images from the IMR90-4 line are shown. Hoechst nuclear counterstain is overlaid. Scale bars: 100 μm. (C) Quantification of images from the conditions described in (B) for number of ECs per 30× field. Points represent replicate wells from one differentiation of the IMR90-4 line. Bars indicate mean values. P-values: ANOVA followed by Tukey's HSD test. (D) Quantification of images from the conditions described in (B) for GLUT-1 and claudin-5 mean fluorescence intensity normalized to Hoechst mean fluorescence intensity within the area of claudin-5^{+} ECs only. Points represent replicate wells from one differentiation of the IMR90-4 line. Bars indicate mean values, with values normalized such that the mean of the DMSO condition equals 1. P-values: ANOVA followed by Tukey's HSD test.

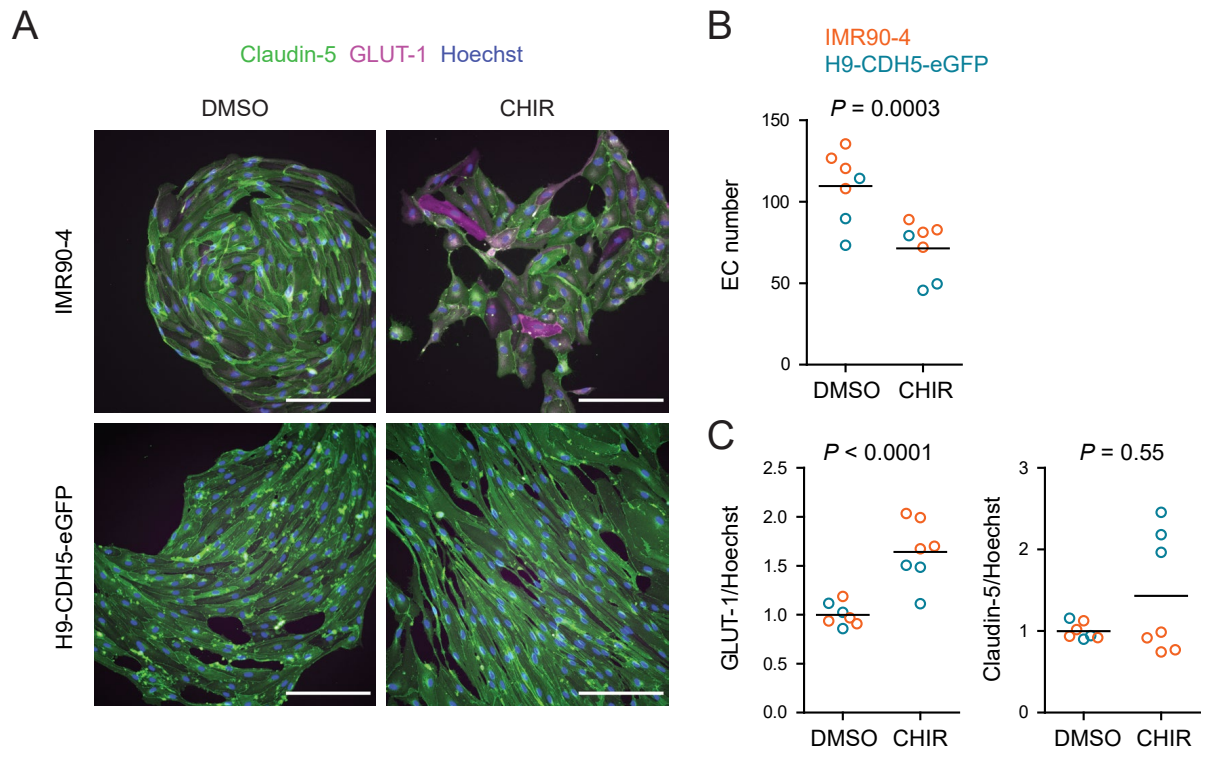

Figure 3.13. Effect of CHIR treatment in matured endothelium. (A) Immunocytochemistry analysis of claudin-5 and GLUT-1 expression in ECs treated with DMSO or CHIR at Passage 4 (as outlined in Figure 3.12). Images from the IMR90-4 and H9-CDH5-eGFP lines are shown. Hoechst nuclear counterstain is overlaid. Scale bars: 100 μm. (B) Quantification of images from the conditions described in (A) for number of ECs per 20× field. Points represent replicate wells from one differentiation of the IMR90-4 line (orange) and one differentiation of the H9-CDH5-eGFP line (blue). Bars indicate mean values. P-value: Two-way ANOVA. (C) Quantification of images from the conditions described in (A) for GLUT-1 and claudin-5 mean fluorescence intensity normalized to Hoechst mean fluorescence intensity within the area of claudin-5$^+$ ECs only. Points represent replicate wells from one differentiation of the IMR90-4 line (orange) and one differentiation of the H9-CDH5-eGFP line (blue). Bars indicate mean values, with values normalized within each differentiation such that the mean of the DMSO condition equals 1. P-values: Two-way ANOVA on unnormalized data.

3.4.3 Comprehensive profiling of the Wnt-regulated endothelial transcriptome

We turned next to RNA-sequencing as an unbiased method to assess the impacts of Wnt activation on the EC transcriptome. We performed four independent differentiations and analyzed Passage 1 ECs treated with DMSO or CHIR, using fluorescence-activated cell sorting (FACS) to isolate CD31$^+$ ECs from the mixed EC/SMLC cultures. We also sequenced the SMLCs from DMSO-treated cultures at Passage 1 from two of these differentiations. DMSO- and CHIR-treated ECs at Passage 3 from three of these differentiations were also sequenced. Principal component analysis of the resulting whole-transcriptome profiles revealed that the two

cell types (ECs and SMLCs) segregated along principal component (PC) 1, which explained 57% of the variance. In ECs, the effects of passage number and treatment were reflected in PC 2, which explained 21% of the variance (Figure 3.14A). We next validated the endothelial identity of our cells; we observed that canonical endothelial marker genes (including *CDH5, CD34, PECAM1, CLDN5, ERG,* and *FLI1*) were enriched in ECs compared to SMLCs and had high absolute abundance, on the order of 100–1,000 transcripts per million (TPM) (Figure 3.14B; Supplementary file 1). SMLCs expressed mesenchymal (mural/fibroblast)-related transcripts (including *PDGFRB, CSPG4, PDGFRA, TBX2, CNN1,* and *COL1A1*), which ECs generally lacked, although we did observe slight enrichment of some of these genes in Passage 1 DMSO-treated ECs, likely reflective of a small amount of SMLC contamination despite CD31 FACS (Figure 3.14B). SMLCs also expressed *SLC2A1* (Supplementary file 1) consistent with protein-level observations (Figure 3.14D). We also observed little to no expression of the epithelial genes *CDH1*, *EPCAM*, *CLDN1*, *CLDN3* (*54*), *CLDN4*, and *CLDN6*, reflecting the definitive endothelial nature of the cells (Figure 3.14B; Supplementary file 1).

First comparing CHIR- and DMSO-treated ECs at Passage 1, we identified 1,369 significantly upregulated genes and 2,037 significantly downregulated genes (Figure 3.14C; Supplementary file 2). CHIR-upregulated genes included *SLC2A1*, *CLDN5*, *LSR*, and *CAV1*, consistent with protein-level assays. *PLVAP* was downregulated, as were a number of mesenchymal genes (*TAGLN*, *COL1A1*), again reflective of slight contamination of SMLC transcripts in the DMSO-treated EC samples (Figure 3.14C-D). Additionally, important downstream effectors of Wnt signaling were upregulated, including the transcription factors *LEF1* and *TCF7*, the negative regulator *AXIN2*, and the negative regulator *APCDD1*, which is known to modulate Wnt-regulated barriergenesis in retinal endothelium (*564*) (Figure 3.14C-D). We also identified upregulated transcription factors: *ZIC3,* which is highly enriched in brain and

retinal ECs *in vivo* and downstream of Frizzled4 signaling (*65*, *238*), and *SOX7*, which acts cooperatively with *SOX17* and *SOX18* in retinal angiogenesis (*565*), were upregulated by CHIR in our system (Figure 3.14D). *MSX1* and *EBF1*, which are expressed by murine brain ECs *in vivo* (*56*) were also CHIR-upregulated (Figure 3.14D). Additional CHIR-upregulated genes included *ABCG2* (encoding the efflux transporter Breast Cancer Resistance Protein, BCRP), *APLN*, a tip cell marker enriched in postnatal day 7 murine brain ECs compared to those of other organs, and subsequently downregulated in adulthood (*65*, *226*), and *FLVCR2*, a disease-associated gene with a recently-identified role in brain angiogenesis (*566*) (Figure 3.14C-D). Finally, we detected CHIR-mediated downregulation of the fatty acid-binding protein-encoding *FABP4*, which is depleted in brain ECs compared to those of peripheral organs (*65*). We also observed similar downregulation of *SMAD6*, which is depleted in brain ECs compared to lung ECs and is a putative negative regulator of BMP-mediated angiogenesis (*56*, *567*) (Figure 3.14D).

In Passage 3 ECs, many of the CHIR-mediated gene expression changes observed at Passage 1 persisted, including *SLC2A1*, *LSR*, *LEF1*, *AXIN2*, *APCDD1*, *ZIC3*, *EBF1*, *FLVCR2* and *ABCG2* upregulation and *PLVAP* downregulation (Figure 3.14E; Figure 3.15). Additional concordantly CHIR-upregulated genes encoding secreted factors, transcription factors, and transmembrane proteins are shown in Figure 3.16, and include *REEP1*, a gene enriched in brain versus non-brain ECs (*56*, *65*) that encodes a regulator of endoplasmic reticulum function, and the Notch ligand-encoding gene *JAG2*. On the other hand, at Passage 3, *CLDN5* was not upregulated in CHIR-treated cells compared to DMSO-treated cells, but was highly expressed (~2,500 TPM). Similarly, *CAV1* abundance remained high, but was not CHIR-upregulated in Passage 3 cells (Figure 3.15). Conversely, *JAM2*, which encodes junctional adhesion molecule 2, a component of EC tight junctions (*568*, *569*), was upregulated by CHIR at Passage 3, but not at Passage 1, as was the retinol-binding protein-encoding gene *RBP1* (Figure 3.15).

We used Weighted Gene Correlation Network Analysis (WGCNA) (*554*, *559*) to identify modules containing genes with highly correlated expression across the 14 EC samples (Figure 3.17A; Supplementary file 3). One such module (the green module, containing 441 genes) had a representative gene expression profile (module eigengene) with a strong, positive correlation with CHIR treatment (Figure 3.17B). Importantly, genes central to this module included canonical transcriptional targets of Wnt/β-catenin signaling, including *AXIN2* and *APCDD1*, further supporting the key role of β-catenin signaling in transcriptional changes observed in CHIR-treated ECs. Additional central (highly correlated) genes within the green module included *SLC2A1*, *ZIC3*, and *FLVCR2*, consistent with pairwise differential expression analysis, transcription factors (*CASZ1*, *PRRX1*), and genes with putative roles in vesicle trafficking (*SNX4*, *ARL8B*, *AP1AR*, *VTI1A*, *VPS41*) and lipid metabolism (*AGPAT5*, *ASAH1*) (Figure 3.17C).

To determine the effects of extended culture, we next compared control (DMSO-treated) ECs at Passage 3 versus Passage 1 (Figure 3.18; Supplementary file 2). Extended culture to Passage 3 in the absence of exogeneous Wnt activation led to 1,521 upregulated genes, including *CLDN5* and *CAV1*, consistent with previously-reported protein-level observations in EECM-BMEC-like cells (*468*), which are analogous to Passage 3 DMSO-treated cells. We also observed 1,625 downregulated genes, including marked downregulation of *PLVAP* (Figure 3.18). *SLC2A1,* however, was not upregulated at Passage 3 (Figure 3.18), concordant with absence of GLUT-1 protein expression in the control ECs (Figure 3.12B), nor was *LSR*. Further, despite some similarly-regulated genes between the passage number and CHIR treatment comparisons (e.g., *CLDN5, CAV1*, *PLVAP*), the transcriptional responses to these two experimental variables were globally distinct as assessed by gene correlation network analysis (Figure 3.17B). We also evaluated transcript-level expression of components of the Wnt signaling pathway in Passage 3

control (DMSO-treated) ECs as a first step towards understanding the relative lack of responsiveness observed when CHIR treatment was initiated in matured (Passage 4) ECs (Figure 3.18). While *CTNNB1*, *GSK3B*, and genes encoding components of the destruction complex were not significantly different between Passage 3 and Passage 1, *LEF1* and *TCF7* were strongly downregulated in Passage 3 cells (Figure 3.18).

Finally, to further understand the strengths and limitations of this model system both as a readout of early developmental changes in CNS ECs (Passage 1 cells) or as a source of CNS-like ECs for use in downstream modeling applications, we evaluated absolute transcript abundance and effects of treatment or passage number on 53 characteristic CNS EC genes encompassing tight junction components, vesicle trafficking machinery, solute carriers, and ATP-binding cassette (ABC) efflux transporters selected based on high expression in human brain endothelial cells from a meta-analysis of single cell RNA-seq data (*336*) (Figure 3.19). While ECs expressed *CLDN5*, *TJP1*, *TJP2*, *OLCN*, and *LSR*, they lacked *MARVELD2* (encoding tricellulin) under all conditions. ECs under all conditions also lacked *MFSD2A* and, despite CHIR-mediated downregulation of *PLVAP*, retained high absolute expression of this and other caveolae-associated genes. Finally, while many solute carriers and ABC transporters were expressed (*SLC2A1*, *SLC3A2*, *SLC16A1*, *SLC38A2*, *ABCG2*), others expressed at the *in vivo* human BBB were not (*SLC5A3*, *SLC7A11*, *SLC38A3*, *SLCO1A2*, *ABCB1*) (Figure 3.19). Thus, while CHIR treatment yields ECs with certain elements of CNS-like character, additional molecular signals are likely necessary to impart other aspects of the *in vivo* CNS EC phenotype.

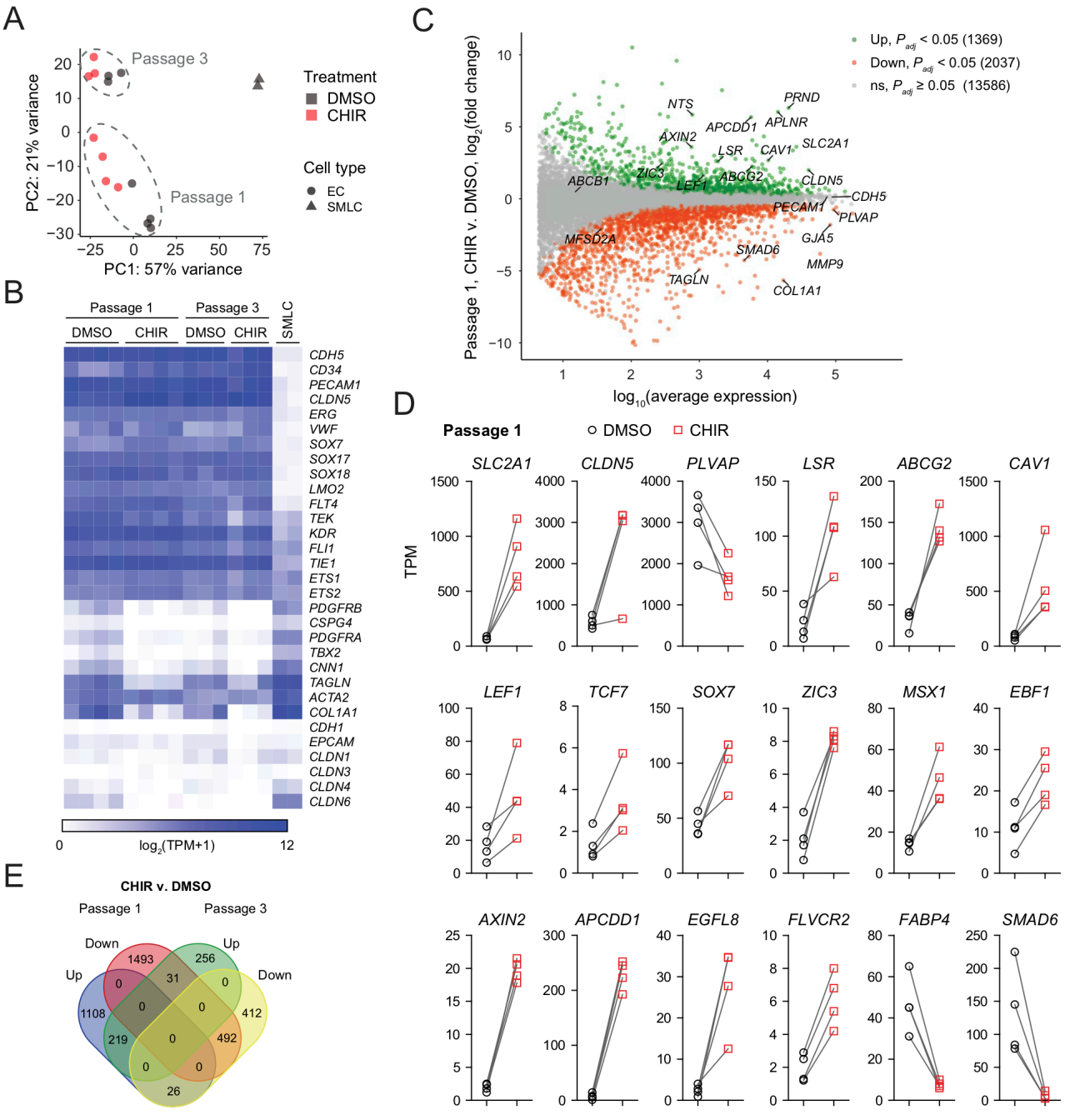
A
Passage 3
Passage 1
PC2: 21% variance
PC1: 57% variance
Treatment
DMSO
CHIR
Cell type
EC
SMLC
B
Passage 1
Passage 3
DMSO
CHIR
DMSO
CHIR
SMLC
CDH5
CD34
PECAM1
CLDN5
ERG
VWF
SOX7
SOX17
SOX18
LMO2
FLT4
TEK
KDR
FLI1
TIE1
ETS1
ETS2
PDGFRB
CSPG4
PDGFRA
TBX2
CNN1
TAGLN
ACTA2
COL1A1
CDH1
EPCAM
CLDN1
CLDN3
CLDN4
CLDN6
log2(TPM+1)
C
Up, Padj < 0.05 (1369)
Down, Padj < 0.05 (2037)
ns, Padj ≥ 0.05 (13586)
Passage 1, CHIR v. DMSO, log2(fold change)
log10(average expression)
NTS
PRND
APLNR
APCDD1
AXIN2
LSR
CAV1
SLC2A1
ABCB1
ZIC3
LEF1
ABCG2
CLDN5
CDH5
PECAM1
PLVAP
MFSD2A
GJA5
SMAD6
MMP9
TAGLN
COL1A1
D
Passage 1
DMSO
CHIR
TPM
SLC2A1
CLDN5
PLVAP
LSR
ABCG2
CAV1
LEF1
TCF7
SOX7
ZIC3
MSX1
EBF1
AXIN2
APCDD1
EGFL8
FLVCR2
FABP4
SMAD6
E
CHIR v. DMSO
Passage 1
Passage 3
Down
Up
Up
Down
1493
256
31
0
0
1108
0
0
412
219
0
492
0
0
26

Figure 3.14. RNA-seq of DMSO- and CHIR-treated ECs. (A) Principal component analysis of EC and SMLC whole-transcriptome data subject to variance stabilizing transformation by DESeq2. Points from Passage 1 ECs represent cells from 4 independent differentiations of the IMR90-4 line, points from Passage 3 ECs represent cells from 3 independent differentiations of the IMR90-4 line, and points from SMLCs represent 2 independent differentiations of the IMR90-4 line. Points are colored based on treatment: DMSO (black), CHIR (red). Data are plotted in the space of the first two principal components, with the percentage of variance explained by principal component 1 (PC1) and principal component 2 (PC2) shown in axis labels. Dashed lines indicate points from Passage 1 and Passage 3 ECs, and are not confidence ellipses. (B) Heat map of transcript abundance [$\log_2$(TPM+1)] for endothelial, mesenchymal, and epithelial genes across all samples. Abundance data for all transcripts are provided in Supplementary file 1. (C) Differential expression analysis of Passage 1 CHIR-treated ECs compared to Passage 1 DMSO-treated ECs. Differentially expressed genes (adjusted P-values < 0.05, DESeq2 Wald test with Benjamini-Hochberg correction) are highlighted in green (upregulated) and red (downregulated). The number of upregulated, downregulated, and non-significant (ns) genes are shown in the legend. Complete results of differential expression analysis are provided in Supplementary file 2. (D) Transcript abundance (TPM) of Wnt-regulated, barrier-related genes in Passage 1 DMSO- and CHIR-treated ECs. Points represent cells from 4 independent differentiations of the IMR90-4 line and lines connect points from matched differentiations. All genes shown were differentially expressed (adjusted P-values < 0.05, DESeq2 Wald test with Benjamini-Hochberg correction). P-values are provided in Supplementary file 2. (E) Venn diagram illustrating the number of genes identified as upregulated or downregulated (adjusted P-values < 0.05, DESeq2 Wald test with Benjamini-Hochberg correction) in ECs treated with CHIR versus DMSO at Passage 1 compared to Passage 3. Gene lists are provided in Supplementary file 2 and selected genes are shown in Figure 3.15 and Figure 3.16.

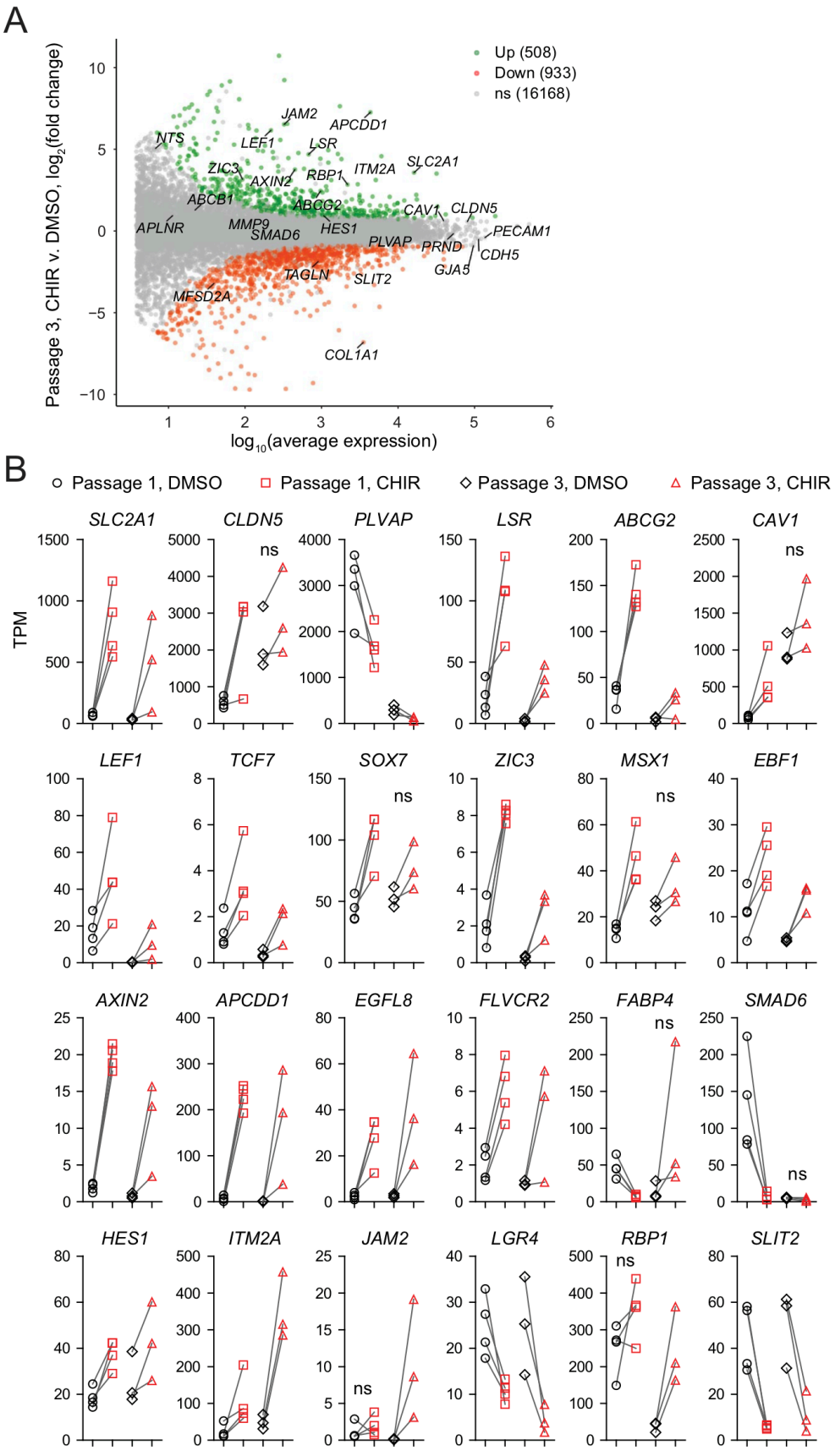
A
Up (508)
Down (933)
ns (16168)
Passage 3, CHIR v. DMSO, log2(fold change)
log10(average expression)
JAM2
APCDD1
NTS
LEF1
LSR
ZIC3
AXIN2
RBP1
ITM2A
SLC2A1
ABCB1
ABCG2
CAV1
CLDN5
APLNR
MMP9
SMAD6
HES1
PECAM1
PLVAP
PRND
CDH5
GJA5
TAGLN
SLIT2
MFSD2A
COL1A1
B
Passage 1, DMSO
Passage 1, CHIR
Passage 3, DMSO
Passage 3, CHIR
TPM
SLC2A1
CLDN5
PLVAP
LSR
ABCG2
CAV1
LEF1
TCF7
SOX7
ZIC3
MSX1
EBF1
AXIN2
APCDD1
EGFL8
FLVCR2
FABP4
SMAD6
HES1
ITM2A
JAM2
LGR4
RBP1
SLIT2
ns

Figure 3.15. Differential expression analysis of Passage 3 ECs treated with CHIR versus DMSO.(A) Differential expression analysis of Passage 3 CHIR-treated ECs compared to Passage 3 DMSO-treated ECs. Differentially expressed genes (adjusted P-values < 0.05, DESeq2 Wald test with Benjamini-Hochberg correction) are highlighted in green (upregulated) and red (downregulated). The number of upregulated, downregulated, and non-significant (ns) genes are shown in the legend. Complete results of differential expression analyses are provided in Supplementary file 2. (B) Transcript abundance (TPM) of selected genes in Passage 1 and Passage 3 DMSO- and CHIR-treated ECs. Points represent cells from 3–4 independent differentiations of the IMR90-4 line. Lines connect points from matched differentiations between the DMSO and CHIR conditions; for clarity, lines connecting points between Passage 1 and Passage 3 are omitted. Genes shown were differentially expressed (CHIR v. DMSO, adjusted P-values < 0.05, DESeq2 Wald test with Benjamini-Hochberg correction), except where indicated as ns. P-values are provided in Supplementary file 2.

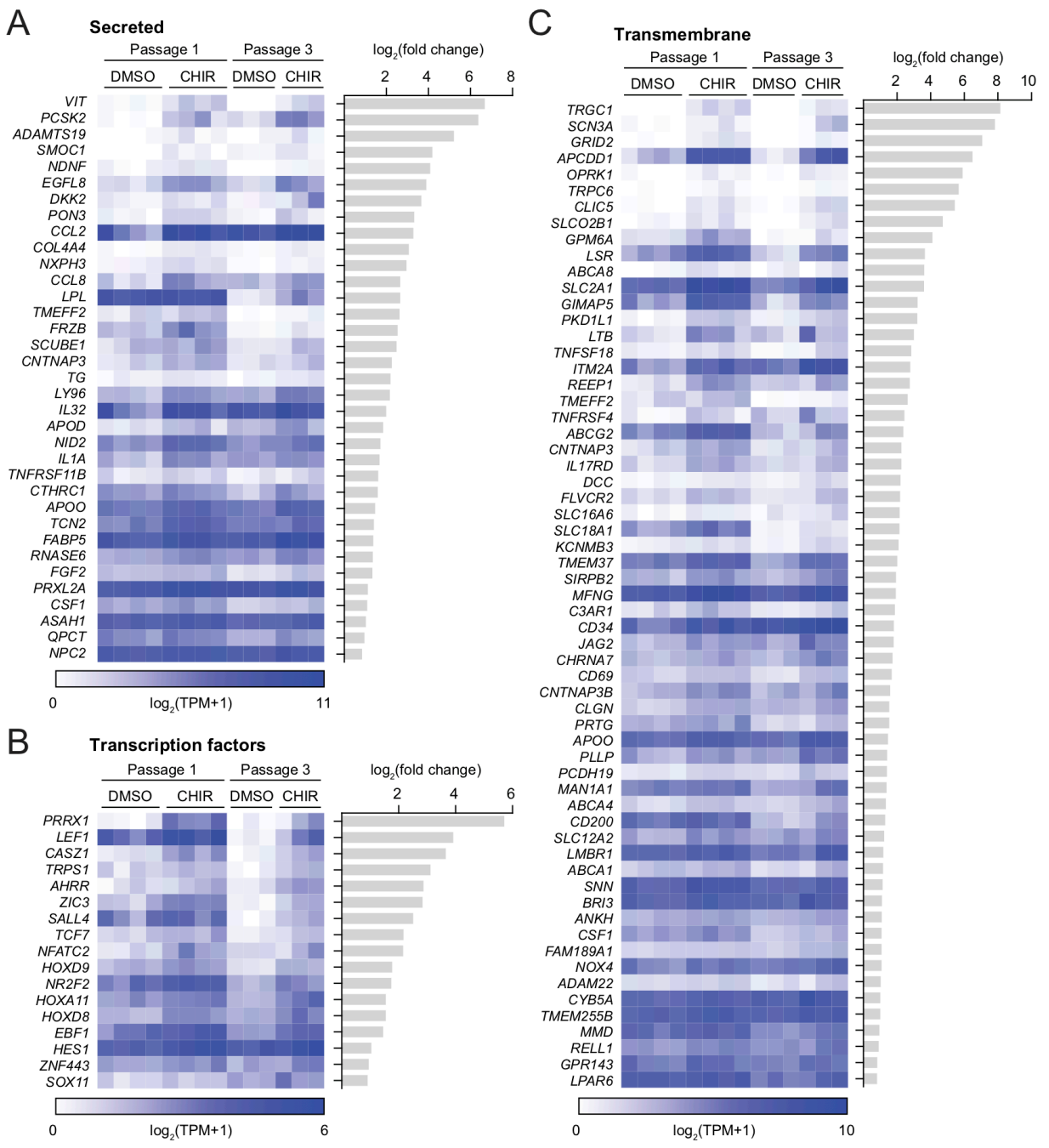

Figure 3.16. Genes upregulated by CHIR at both Passage 1 and Passage 3. (A-C) Heat maps of transcript abundance [$\log_2$(TPM+1)] for genes encoding secreted factors (A), transcription factors (B), and transmembrane proteins (C) that are CHIR-upregulated (adjusted P-values < 0.05, DESeq2 Wald test with Benjamini-Hochberg correction) in both Passage 1 and Passage 3 ECs. P-values are provided in Supplementary file 2. The $\log_2$(fold change) (CHIR v. DMSO, average of Passage 1 and Passage 3 values) for each gene is shown at left.

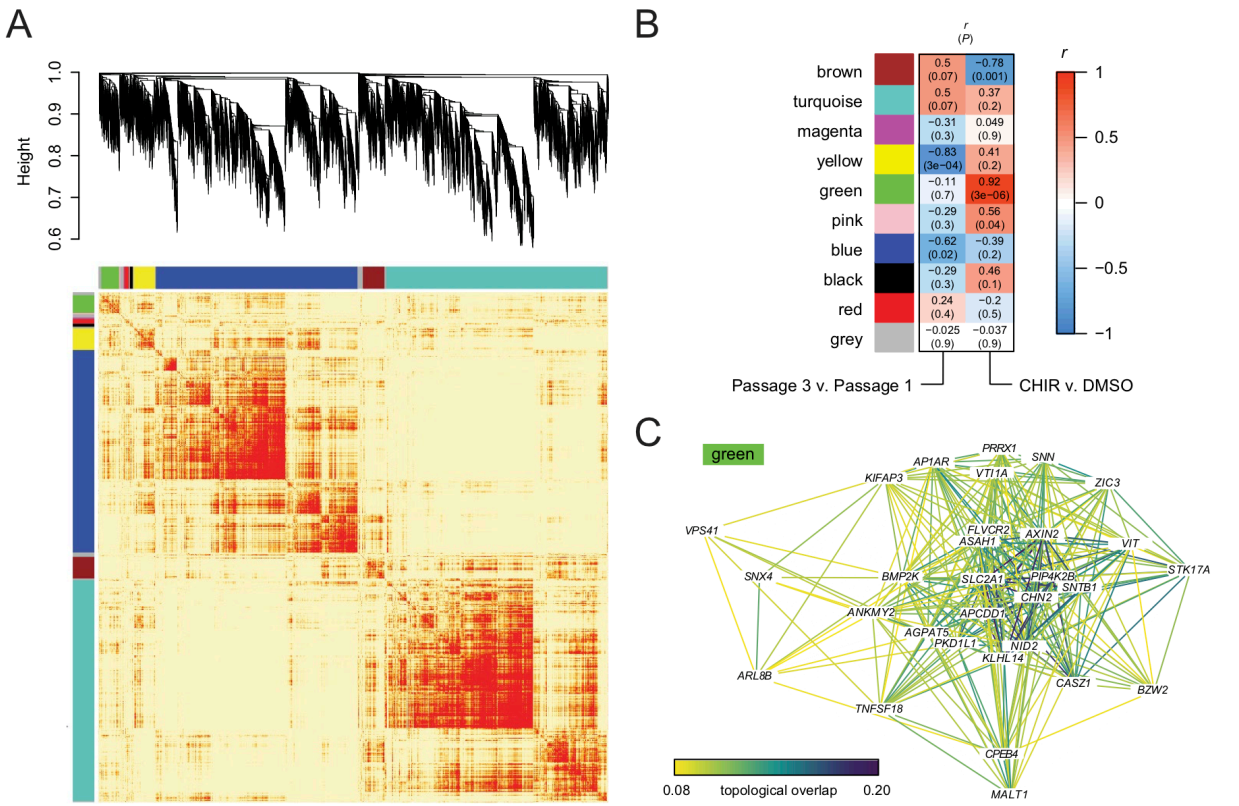

Figure 3.17. Gene correlation network analysis. (A) Heatmap representation of the WGCNA topological overlap matrix (TOM). Red indicates high topological overlap. Dendrogram from hierarchical clustering of genes based on dissimilarity (1 – TOM) is shown above. Module assignments (colors) are shown above and at left. (B) Correlation between module eigengenes and experimental variables (Passage number and CHIR treatment). Each box shows the Pearson correlation coefficient *r* and the P-value (*P*). (C) Network representation of the 30 genes in the green module with the highest intramodular connectivity. Edge color represents topological overlap. Edges with topological overlap less than 0.08 are not shown. For reference, maximum topological overlap (excluding the diagonal) within the entire network is 0.38, and topological overlap between *AXIN2* (green module) and *ACTB* (turquoise module) is 3.8×10^{-4}.

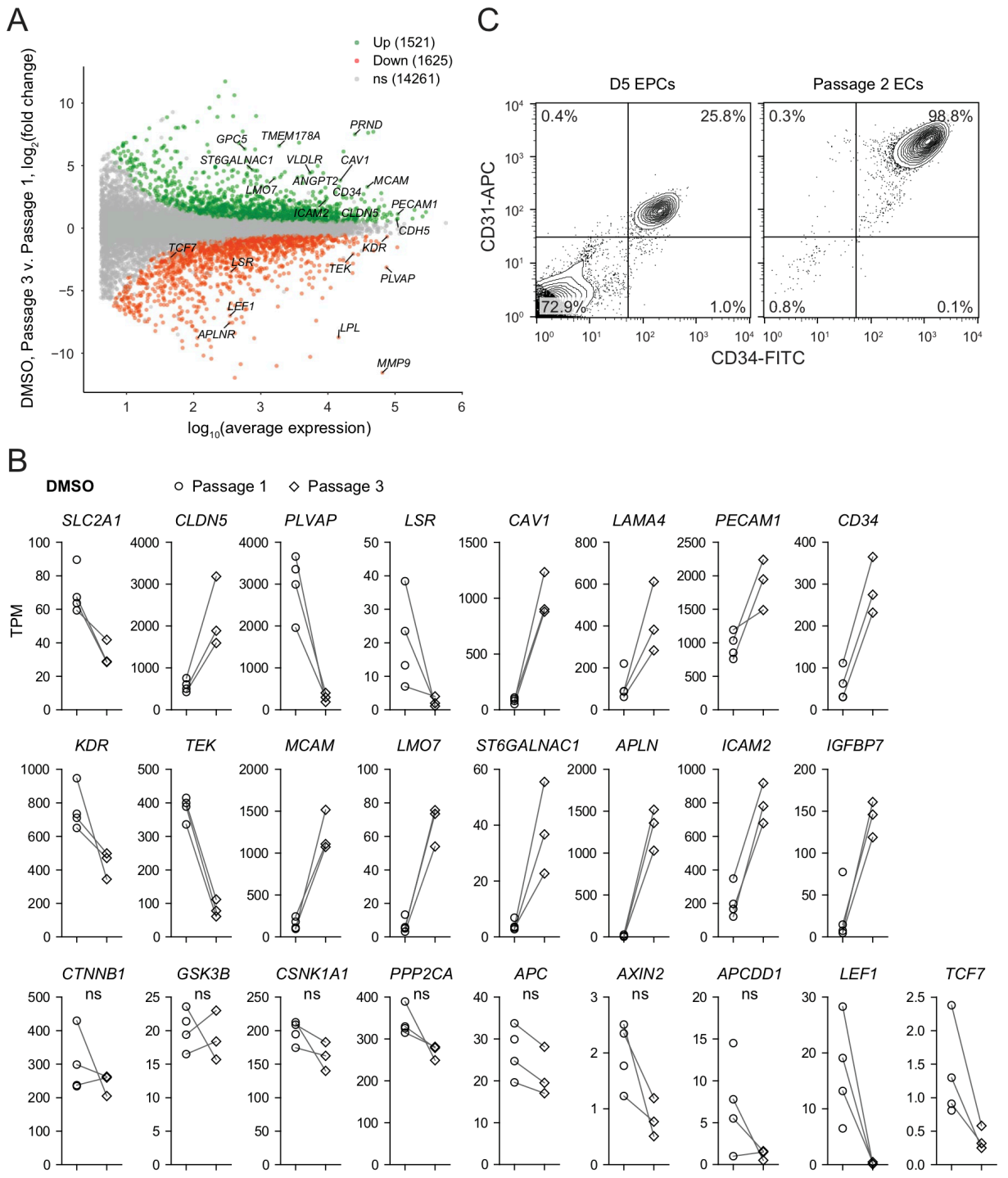

Figure 3.18. Differential expression analysis of Passage 1 versus Passage 3 ECs (A) Differential expression analysis of Passage 3 DMSO-treated ECs compared to Passage 1 DMSO-treated ECs. Differentially expressed genes (adjusted P-values < 0.05, DESeq2 Wald test with Benjamini-Hochberg correction) are highlighted in green (upregulated) and red (downregulated). The number of upregulated, downregulated, and non-significant (ns) genes are shown in the legend. Complete results of differential expression analyses are provided in Supplementary file 2. (B) Transcript abundance (TPM) of selected genes. Genes shown were differentially expressed (adjusted P-values < 0.05, DESeq2 Wald test with Benjamini-Hochberg correction) except those indicated as ns. P-values are provided in Supplementary file 2. (C) Flow cytometry analysis of CD34 and CD31 expression in D5 EPCs (prior to MACS) and in Passage 2 ECs.

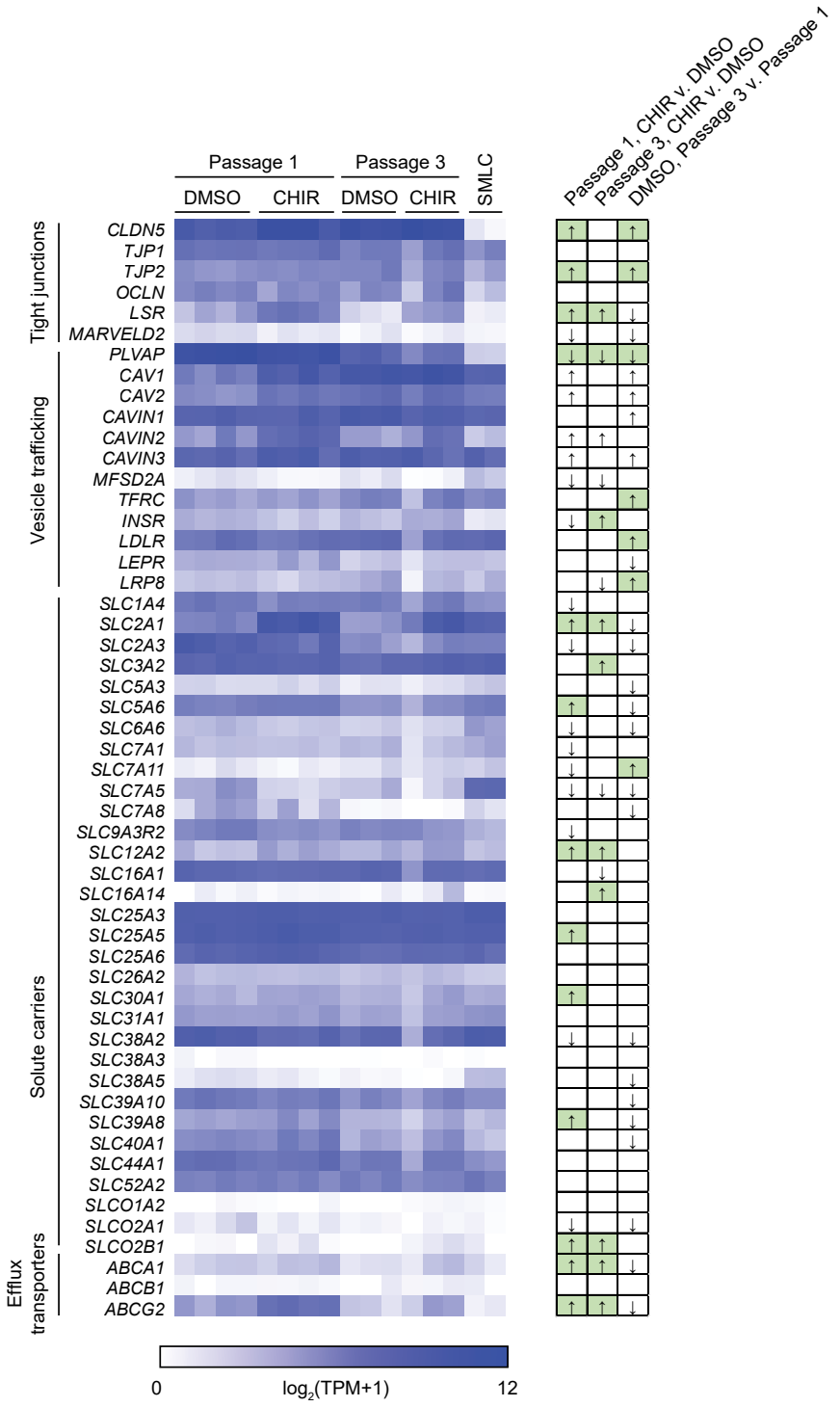

Figure 3.19. Blood-brain barrier transcriptional profile. Heat map of transcript abundance [$\log_2$(TPM+1)] for BBB genes encompassing tight junctions, vesicle trafficking components, solute carriers, and efflux transporters. Solute carrier and efflux transporter genes that were expressed in human brain ECs at an average of >100 TPM in a meta-analysis of scRNA-seq datasets (*336*) are included. Abundance data for all transcripts is provided in Supplementary file 1. At right, arrows indicate directionality of change for differentially expressed genes (adjusted P-values < 0.05, DESeq2 Wald test with Benjamini-Hochberg correction) for the three comparisons shown above. Changes with expected directionality for gain of CNS EC character have arrows highlighted in green.

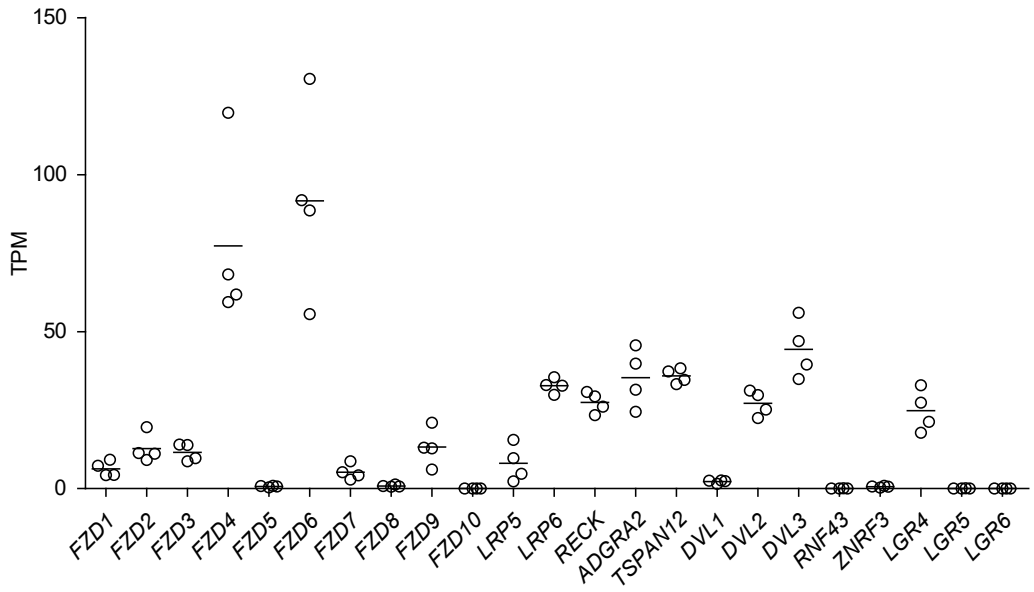

Figure 3.20. Expression of Wnt pathway components in naïve ECs. Abundance of transcripts (in transcripts per million, TPM) encoding Wnt receptors, co-receptors, and other pathway components in Passage 1 DMSO-treated ECs. Points represent cells from 4 independent differentiations of the IMR90-4 line. Bars indicate mean values. *ADGRA2* is also known as *GPR124*.

3.4.4 The Wnt-regulated endothelial transcriptome in multiple contexts

To globally assess whether CHIR-mediated gene expression changes in our system are characteristic of the responses observed in ECs *in vivo* and similar to those observed in other *in vitro* contexts, we compared our RNA-seq dataset to those of studies that employed a genetic strategy for β-catenin stabilization (the *Ctnnb1*^{flex3} allele) in adult mouse ECs in several contexts: (i) pituitary ECs, which acquire some BBB-like properties upon β-catenin stabilization (*71*); (ii) liver ECs, which exhibit little to no barriergenic response to β-catenin stabilization (*367*); (iii) brain ECs briefly cultured *in vitro*, which rapidly lose their BBB-specific gene expression profile even with β-catenin stabilization (*226*), and offer the most direct comparison to our *in vitro* model system. Upon recombination, the *Ctnnb1*^{flex3} allele produces a dominant mutant β-catenin lacking residues that are phosphorylated by GSK-3β to target β-catenin for degradation (*570*); as such, this strategy for ligand- and receptor-independent Wnt activation by β-catenin stabilization

is similar to CHIR treatment, although GSK-3 phosphorylates targets other than β-catenin (discussed below).

We first used literature RNA-seq data from postnatal day 7 murine brain, liver, lung, and kidney ECs (*65*) to define core sets of genes in brain ECs that are differentially expressed compared to all three of the other organs (Figure 3.21A-B). Using the resulting sets of 1094 brain-enriched and 506 brain-depleted genes, we asked how many genes in our Passage 1 ECs were concordantly-regulated by CHIR: 130 of the brain-enriched genes were CHIR-upregulated and 116 of the brain-depleted genes were CHIR-downregulated (Figure 3.21C). At Passage 3, 61 genes were concordantly upregulated and 46 downregulated (Figure 3.22). In pituitary ECs with β-catenin stabilization, 102 of the brain-enriched genes were upregulated and 48 of the brain-depleted genes were downregulated (Figure 3.21D). Compared with the pituitary ECs, there were far fewer concordantly-regulated genes in liver ECs with β-catenin stabilization, with 25 upregulated and 1 downregulated (Figure 3.21E). Finally, cultured primary mouse brain ECs with β-catenin stabilization exhibited 72 concordantly upregulated and 16 downregulated genes (Figure 3.21F). The only gene concordantly-regulated in all four comparisons was the canonical Wnt target *AXIN2*. Several additional genes were concordantly upregulated in three of four, including *TCF7*, *FAM107A*, *NKD1*, *TNFRSF19*, *GLUL*, *SLC30A1*, and *ABCB1*, which was the only gene concordantly regulated in all comparisons except the hPSC-derived ECs (Figure 3.21G). Several canonical target genes were shared by the hPSC-derived EC and pituitary EC systems, including *APCDD1*, *LEF1*, *CLDN5*, and *SLC2A1*; also in this category were *LSR*, the zinc/manganese transporter *SLC39A8*, and 12 additional genes (Figure 3.21G). Notably, the caveolae inhibitor *MFSD2A* was robustly upregulated by β-catenin in pituitary ECs, but not in any other context (Figure 3.21C-F), suggesting other brain-derived factors may cooperate with Wnt to regulate expression of this important inhibitor of caveolin-mediated transcytosis.

Complete gene lists from this comparative analysis are provided in Supplementary file 4. In sum, the data suggest that the hPSC-derived ECs responded to Wnt activation in a fashion that led to modest induction of CNS transcriptional programs and that the response was most similar to the pituitary β-catenin stabilization model. Importantly, this analysis also supports the hypothesis that immature endothelium is highly responsive to Wnt activation where mature (adult) endothelium is largely refractory except in regions proximal to barrier-forming regions.

Last, because GSK-3 is a component of numerous signaling pathways in addition to Wnt/β-catenin (*571–573*), we used RNA-seq data to infer pathways that might be differentially regulated by the two strategies for activating Wnt/β-catenin signaling employed in the experiments above: CHIR treatment, which increases β-catenin stability by inhibiting GSK-3, or direct stabilization of β-catenin. We tested lists of upregulated genes in (i) our Passage 1 ECs treated with CHIR versus DMSO, (ii) Passage 3 ECs treated with CHIR versus DMSO, and (iii) pituitary ECs with β-catenin stabilization versus controls (*71*), against the Hallmark gene set collection (*561*) (Figure 3.23; Supplementary file 5). In all three comparisons, the *Wnt/β-catenin signaling* gene set was significantly enriched (Figure 8–figure supplement 2A). Similarly, the *Notch signaling*, *TNFα signaling via NF-κB*, *KRAS signaling up*, and several additional gene sets were consistently enriched in all three comparisons (Figure 3.23A-B; Supplementary file 5), suggesting similar regulation by GSK-3 inhibition and direct β-catenin stabilization. In contrast, the *PI3K AKT mTOR signaling* gene set was enriched in Passage 1 ECs, but not in Passage 3 ECs or pituitary ECs. Similarly, the gene set *mTORC1 signaling* was enriched in Passage 1 ECs and pituitary ECs, but genes driving this enrichment were distinct (Figure 3.23C), and this gene set was not enriched in Passage 3 ECs. Thus, given the known, bidirectional interactions of GSK-3 and AKT/mTOR pathway components (*572*), these results suggest that CHIR-mediated inhibition of GSK-3 may transiently activate this pathway in Passage 1 ECs. Conversely, the

gene set *TGF-β signaling* was enriched only in pituitary ECs with β-catenin stabilization (Figure 3.23; Supplementary file 5). Taken together, these results, coupled with those of our *CTNNB1* knockdown experiments and gene correlation network analysis, suggest a central role for β-catenin as a key effector of CHIR-mediated signaling, but also highlight some potential differences in the pathways activated in response to CHIR treatment versus β-catenin stabilization. Differences in other aspects of these two experimental paradigms (*in vitro* versus *in vivo*, naïve versus CNS-proximal, human versus mouse), however, caution against over-interpretation of these results.

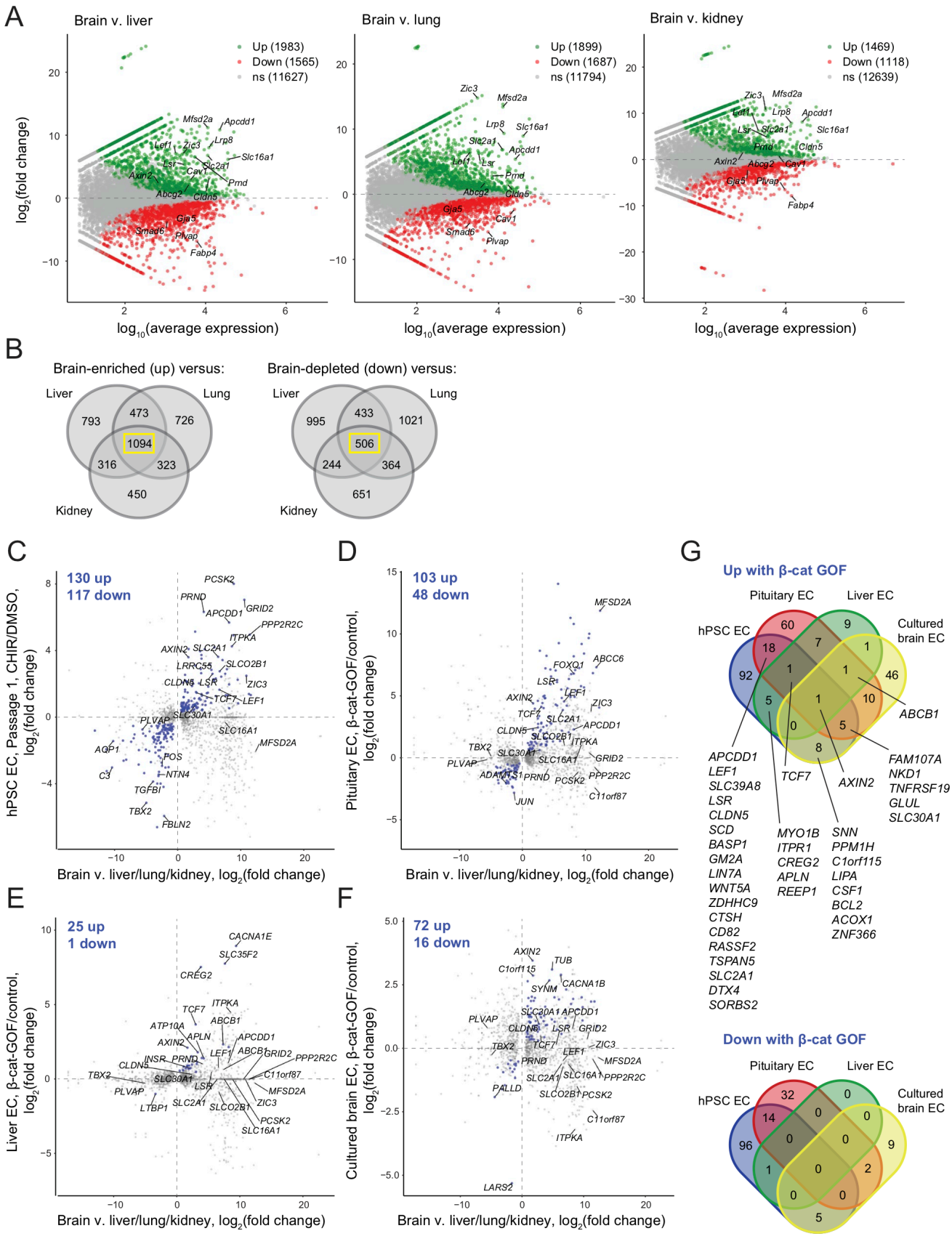
A
Brain v. liver
Up (1983)
Down (1565)
ns (11627)
Brain v. lung
Up (1899)
Down (1687)
ns (11794)
Brain v. kidney
Up (1469)
Down (1118)
ns (12639)
log2(fold change)
log10(average expression)
B
Brain-enriched (up) versus:
Liver
Lung
Kidney
793
473
726
1094
316
323
450
Brain-depleted (down) versus:
995
433
1021
506
244
364
651
C
130 up
117 down
hPSC EC, Passage 1, CHIR/DMSO, log2(fold change)
Brain v. liver/lung/kidney, log2(fold change)
D
103 up
48 down
Pituitary EC, β-cat-GOF/control, log2(fold change)
E
25 up
1 down
Liver EC, β-cat-GOF/control, log2(fold change)
F
72 up
16 down
Cultured brain EC, β-cat-GOF/control, log2(fold change)
G
Up with β-cat GOF
Pituitary EC
Liver EC
hPSC EC
Cultured brain EC
APCDD1
LEF1
SLC39A8
LSR
CLDN5
SCD
BASP1
GM2A
LIN7A
WNT5A
ZDHHC9
CTSH
CD82
RASSF2
TSPAN5
SLC2A1
DTX4
SORBS2
MYO1B
ITPR1
CREG2
APLN
REEP1
SNN
PPM1H
C1orf115
LIPA
CSF1
BCL2
ACOX1
ZNF366
TCF7
AXIN2
ABCB1
FAM107A
NKD1
TNFRSF19
GLUL
SLC30A1
Down with β-cat GOF

Figure 3.21. Identification of concordantly Wnt-regulated CNS EC-associated genes in RNA-seq data.(A) Differential expression analysis of P7 murine brain ECs compared to liver, lung, or kidney ECs (*65*). Differentially expressed genes (adjusted P-values < 0.05, DESeq2 Wald test with Benjamini-Hochberg correction) are highlighted in green (up, brain-enriched) and red (down, brain-depleted). The number of up, down, and non-significant (ns) genes are shown in the legends. (B) Venn diagrams illustrating the number of genes identified as brain EC-enriched (left) or brain EC-depleted (right) versus liver, lung, or kidney ECs (adjusted P-values < 0.05, DESeq2 Wald test with Benjamini-Hochberg correction). The 1094 genes enriched in brain ECs compared to each other organ, and the 506 genes depleted in brain ECs compared to each other organ, were used for subsequent analysis of the effects of Wnt activation in the various experimental contexts. (C-F) In each plot, the x-axis indicates average $\log_2$(fold change) of gene expression in brain ECs compared to liver, lung, and kidney ECs for the 1094 brain EC-enriched genes and 506 brain EC-depleted genes described in (B) with known mouse-human homology. Homologous human gene names are shown. The y-axes indicate differential expression [$\log_2$(fold change)] in Passage 1 CHIR-treated ECs compared to Passage 1 DMSO-treated ECs (C), in adult mouse pituitary ECs with stabilized β-catenin (gain-of-function, GOF) compared to controls (*71*) (D), in adult mouse liver ECs with stabilized β-catenin compared to controls (*367*) (E), or in cultured adult mouse brain ECs with stabilized β-catenin compared to controls (*226*) (F). Points are highlighted in blue if concordantly-regulated (upregulated in both comparisons or downregulated in both comparisons). The number of concordantly upregulated and concordantly downregulated genes is shown. Genes were identified as upregulated or downregulated based on adjusted P-values < 0.05, DESeq2 Wald test with Benjamini-Hochberg correction. (G) Venn diagrams illustrating the number of brain EC-enriched genes concordantly upregulated with β-catenin GOF (top) and the number of brain EC-depleted genes concordantly downregulated with β-catenin GOF (bottom) for the four comparisons shown in (C-F). Complete results of this analysis are provided in Supplementary file 4.

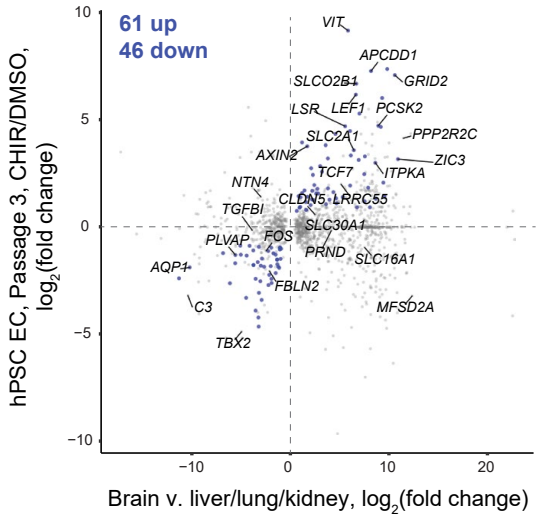

Figure 3.22. Concordantly Wnt-regulated CNS EC-associated genes in RNA-seq data of Passage 3 ECs. The x-axis indicates average $\log_2$(fold change) of gene expression in brain ECs compared to liver, lung, and kidney ECs for the 1094 brain EC-enriched genes and 506 brain EC-depleted genes described in Figure 8B with known mouse-human homology. Homologous human gene names are shown. The y-axis indicates differential expression [$\log_2$(fold change)] in Passage 3 CHIR-treated ECs compared to Passage 3 DMSO-treated ECs. Points are highlighted in blue if concordantly-regulated (upregulated in both comparisons or downregulated in both comparisons). The number of concordantly upregulated and concordantly downregulated genes is shown. Genes were identified as upregulated or downregulated based on adjusted P-values < 0.05, DESeq2 Wald test with Benjamini-Hochberg correction.

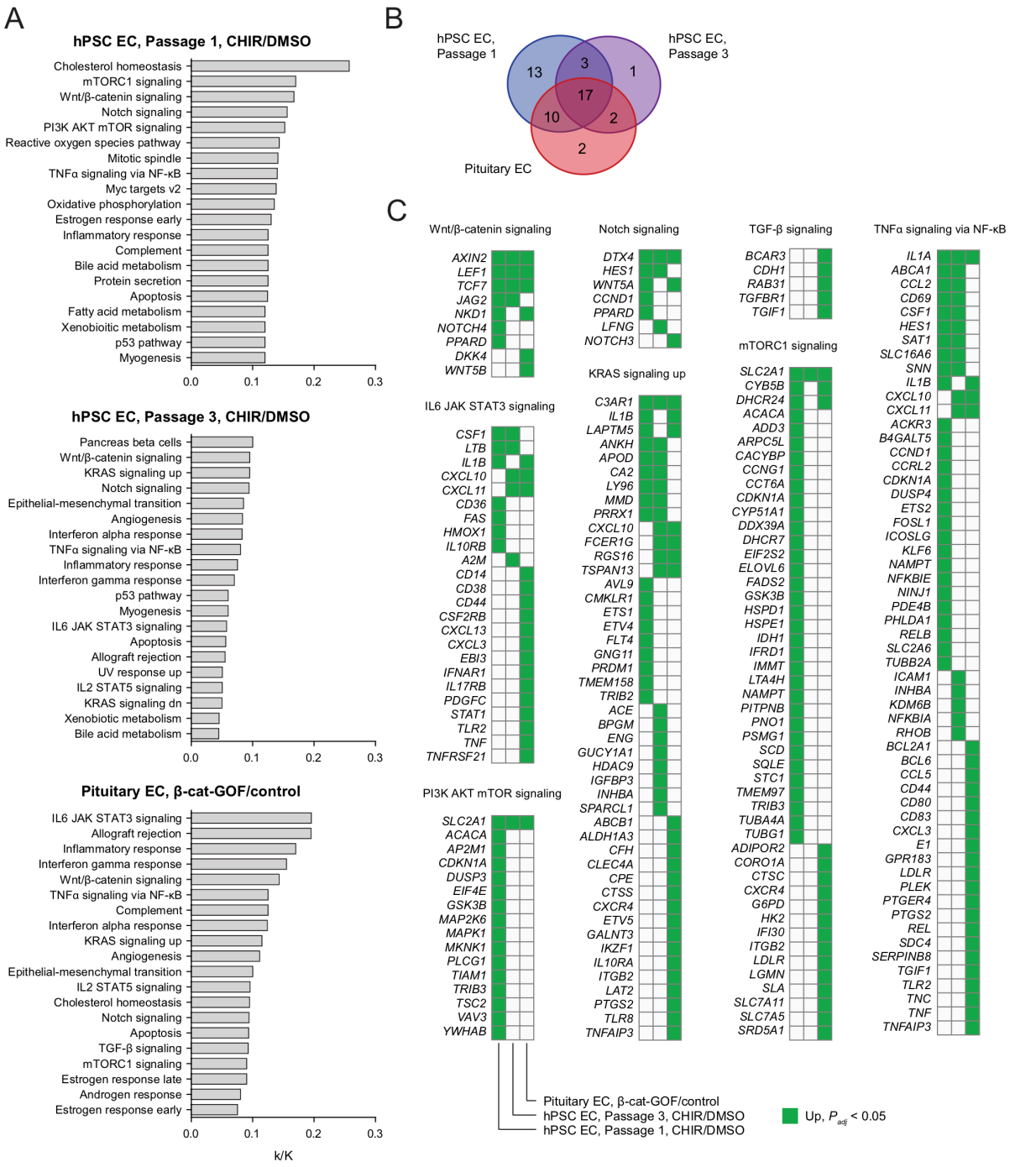

Figure 3.23. Pathway analysis of ECs with Wnt activation. (A) Enriched gene sets (false discovery rate < 0.05) in Passage 1 CHIR-treated ECs compared to Passage 1 DMSO-treated ECs (top), Passage 3 CHIR-treated ECs compared to Passage 3 DMSO-treated ECs (middle), or adult mouse pituitary ECs with stabilized β-catenin (gain-of-function, GOF) compared to controls (*71*) (bottom). For each gene set, the ratio of the number of genes in the gene set that are upregulated ($\log_2$(fold change) > 0, adjusted P-value < 0.05, DESeq2 Wald test with Benjamini-Hochberg correction) in the relevant comparison (k) to the total number of genes in the gene set (K) is shown. For each comparison, the 20 gene sets with the highest k/K ratio are shown. Supplementary file 5 lists all enriched gene sets, and values of k, K, and false discovery rate. (B) Venn diagram illustrating the number of enriched gene sets for the three comparisons in (A). (C) Genes driving gene set enrichment. Selected gene sets enriched in at least one comparison shown in (A) are shown, with squares highlighted in green indicating upregulation ($\log_2$(fold change) > 0, adjusted P-value < 0.05, DESeq2 Wald test with Benjamini-Hochberg correction). Only genes upregulated in at least one of the three comparisons are shown.

3.5 Discussion

The Wnt/β-catenin signaling pathway plays a central role in CNS angiogenesis and in establishing the unique properties of CNS ECs (*225*, *227*, *228*, *237*, *241*, *242*, *247*). In this work, we investigated the role of Wnt/β-catenin signaling in induction of BBB properties in a human EC model, using naïve endothelial progenitors derived from hPSCs. We reasoned that these immature EPCs (*458*) would be similar to the immature endothelium in the perineural vascular plexus and thus competent to acquire CNS EC phenotypes in response to Wnt activation. To activate Wnt signaling, we evaluated the widely used ligand Wnt3a (*228*) and the GSK-3 inhibitor CHIR.

We found that CHIR treatment robustly induced several canonical CNS EC molecular phenotypes, including a marked induction of GLUT-1, upregulation of claudin-5, and downregulation of PLVAP, which correlated with differential gene expression in RNA-seq data. We also observed a functional decrease in paracellular permeability. Further, using RNA-seq and Western blotting, we identified LSR (angulin-1) as CHIR-induced in this system, supporting the notion that this highly CNS EC-enriched tricellular tight junction protein (*62*, *102*) is Wnt-regulated. In RNA-seq data, we observed differential expression of known CNS EC-enriched/depleted and Wnt-regulated genes including upregulated *LEF1*, *AXIN2*, *APCDD1*, *ABCG2*, *SOX7*, *ZIC3*, *FLVCR2*, *JAM2*, and *RBP1*, and downregulated *PLVAP*, *FABP4*, *SMAD6*, and *SLIT2*. These RNA-seq data should therefore be useful in generating hypotheses of BBB-associated genes regulated by Wnt activation in ECs for future functional studies. Our work also defines an important set of phenotypes for which Wnt activation in ECs is not sufficient in our system: in the context of vesicle trafficking, we observed caveolin-1 (*CAV1*) upregulation, no change in mean functional endocytosis, virtually no expression of *MFSD2A*, and high absolute *PLVAP* abundance in RNA-seq data despite CHIR-mediated downregulation. Given roles of

brain pericytes in regulating PLVAP, MFSD2A, and functional transcytosis (*30*, *256*, *447*, *574*), and the observation that MFSD2A is Wnt-regulated in pituitary ECs *in vivo* (*71*), where pericytes are present, it is plausible that pericyte-derived cues are necessary in addition to Wnts to achieve the characteristically low rate of CNS EC pinocytosis. Next, while *ABCG2* (BCRP) was Wnt-induced in our system, other hallmark efflux transporters were not Wnt-regulated and either expressed at low levels (e.g., *ABCC4*, encoding MRP-4) or not expressed (e.g. *ABCB1*, encoding P-glycoprotein). Notably however, *Abcb1a* was Wnt-regulated in the three other β-catenin stabilization experiments from the literature that we evaluated (*71*, *226*, *367*). Thus, pericyte-derived cues, astrocyte-derived cues, and/or activation of the pregnane X or other nuclear receptors may be important for complete acquisition of the complement of CNS EC efflux transporters (*464*, *575*, *576*).

CHIR is widely used to activate Wnt/β-catenin signaling in cell culture (*323*, *458*, *493*, *577–580*). It remains unknown, however, to what extent CHIR-mediated inhibition of GSK-3 in ECs mimics the effects of Wnt ligand-induced inhibition of GSK-3 or direct stabilization of β-catenin. In our system, although the GLUT-1-inductive effect of CHIR was partially inhibited by β-catenin knockdown and our RNA-seq data revealed a transcriptional response characteristic of canonical Wnt signaling, it is possible that CHIR affects other signaling pathways, as suggested by pathway enrichment analysis. Thus, employing ligand-based strategies to activate Wnt signaling will be an important next step. Our RNA-seq data suggests that the receptors and coreceptors necessary to transduce Wnt7 and Norrin signaling (e.g., *FZD4*, *LRP6*, *RECK*, *ADGRA2* [*GPR124*], *TSPAN12*, *DVL2*) are expressed by hPSC-derived ECs (Figure 3.20). Given evidence that Wnt ligands have poor solubility (*581*) and our preliminary data suggesting that supplementation of culture medium with Wnt7a and Wnt7b is largely ineffective in activating Wnt/β-catenin signaling in this system, special emphasis should be placed on strategies that

present Wnt7a, Wnt7b, and/or Norrin in a manner that concentrates ligands at the cell surface, for example, by using direct cocultures of endogenously Wnt-producing cells (neural progenitors or astrocytes) or Wnt-overexpressing cells. Importantly, neural progenitor cells and astrocytes likely would also contribute other yet-unidentified ligands important for acquisition of CNS EC phenotype. Finally, it would also be informative to directly compare CHIR and/or Wnt ligand treatment to direct stabilization of β-catenin in this system, for example, by generating a hPSC line with inducible expression of a dominant active β-catenin.

We also directly addressed the hypothesis that immature ECs are more plastic, that is, more competent to acquire BBB properties upon Wnt activation, than mature ECs. This hypothesis is supported by existing observations that ectopic expression of Wnt7a is sufficient to induce GLUT-1 expression in non-CNS regions of the mouse embryo (*227*), but β-catenin stabilization in adult mouse liver and lung ECs produces only a slight effect (*367*). We repeated our CHIR treatment paradigm in hPSC-derived ECs after an extended period of *in vitro* culture (Passage 4 ECs), and observed much weaker induction of GLUT-1 and no pro-proliferative effect. Thus, our results support this hypothesis and suggest that the loss of BBB developmental plasticity in ECs is an intrinsic, temporally-controlled process rather than a result of the peripheral organ environment. The molecular mechanisms underlying this loss of plasticity remain poorly understood. While previous studies have demonstrated that the level of Wnt/β-catenin signaling in CNS ECs peaks early in development and subsequently declines (*582*, *583*), this finding does not address mechanisms underlying the competence of ECs (CNS and non-CNS) to respond to Wnt signals. In RNA-seq data of Passage 3 control (DMSO-treated) ECs, *LEF1* and *TCF7* were strongly downregulated compared to Passage 1 cells. This result suggests that low baseline expression of these transcription factors, which form a complex with nuclear β-catenin to regulate Wnt target genes, may partially explain the poor efficacy of CHIR in matured

ECs, although additional work is necessary to assess the functional relevance of these differences. Interestingly, ECs in non-BBB-forming regions of the CNS (i.e., CVOs), and in the anterior pituitary, which is directly proximal to the CNS, retain some of their plasticity in adulthood (*71*), possibly as the result of a delicate balance between Wnt ligands and Wnt-inhibitory factors in these regions. Our model should facilitate additional systematic examination of factors that may enhance or attenuate EC Wnt responsiveness.

Finally, our work establishes an improved hPSC-based model for investigating mechanisms of BBB development in naïve ECs. hPSCs are an attractive model system to complement *in vivo* animal studies because they (i) are human, (ii) permit investigation of developmental processes in contrast to primary or immortalized cells, (iii) are highly scalable, (iv) can be derived from patients to facilitate disease modeling and autologous coculture systems, and (v) are genetically tractable. While widely used hPSC-based BBB models are useful for measuring molecular permeabilities and have been employed to understand genetic contributions to barrier dysfunction (*442*, *443*, *455*), they have not been shown to proceed through a definitive endothelial progenitor intermediate (*429*, *452*) and express epithelial-associated genes (*451*, *452*, *455*, *584*). Thus, new models with developmentally relevant differentiation trajectories and definitive endothelial phenotype are needed for improved understanding of developmental mechanisms. Motivated in part by prior use of endothelial cells derived from hematopoietic progenitors in human cord blood to generate BBB models (*427*, *428*), we and others recently showed that hPSC-derived naïve endothelial progenitors or ECs are good candidates for such a system (*464–466*, *468*). For example, Praça *et al.* showed that a combination of VEGF, Wnt3a, and retinoic acid directed EPCs to brain capillary-like ECs with moderate transendothelial electrical resistance (TEER) similar in order of magnitude to that reported here. We previously showed that BBB-like paracellular barrier characteristics are induced in hPSC-EPC-derived ECs

after extended culture in a minimal medium. These so-called EECM-BMEC-like cells had TEER and small molecule permeability similar to primary human brain ECs, well-developed tight junctions, and an immune cell adhesion molecule profile similar to brain ECs *in vivo* (*468*). In this study, we showed it was possible to use the small molecule Wnt agonist CHIR to induce additional hallmarks of CNS EC phenotype in hPSC-EPC-derived ECs, including canonical GLUT-1, claudin-5, and PLVAP effects (both Passage 1 and 3 CHIR-treated ECs). However, it is important to note that despite the improvements in CNS EC character with CHIR treatment, further improvements to functional endocytosis, and efflux transporter and solute carrier phenotype should be targets of future study and may be facilitated by cocultures and/or additional molecular factors. Along these lines, the Passage 1 CHIR-treated CNS-like ECs would be at a differentiation stage well suited to investigate cues subsequent to Wnt signaling that may be key for the induction of additional CNS EC properties. Alternatively, the Passage 3 CHIR-treated CNS-like ECs may be suitable for other BBB modeling applications. In summary, our work has defined the EC response to Wnt activation in a simplified, human system and established a new hPSC-derived *in vitro* model that will facilitate improved understanding of endothelial barriergenesis.

Chapter 4 Integrative analysis of the human brain mural cell transcriptome*

4.1 Summary

Brain mural cells, including pericytes and vascular smooth muscle cells, are important for vascular development, blood-brain barrier function, and neurovascular coupling, but the molecular characteristics of human brain mural cells are incompletely characterized. Single cell RNA-sequencing (scRNA-seq) is increasingly being applied to assess cellular diversity in the human brain, but the scarcity of mural cells in whole brain samples has limited their molecular profiling. Here, we leverage the combined power of multiple independent human brain scRNA-seq datasets to build a transcriptomic database of human brain mural cells. We use this combined dataset to determine human-mouse species differences in mural cell transcriptomes, culture-induced dedifferentiation of human brain pericytes, and human mural cell organotypicity, with several key findings validated by RNA fluorescence *in situ* hybridization. Together, this work improves knowledge regarding the molecular constituents of human brain mural cells, serves as a resource for hypothesis generation in understanding brain mural cell function, and will facilitate comparative evaluation of animal and *in vitro* models.

4.2 Introduction

Vascular smooth muscle cells (VSMCs) and pericytes, collectively termed mural cells, line the abluminal surface of blood vessels and regulate vascular development and function. VSMCs surround large vessels while pericytes line microvessels. In the brain, mural cells fulfill

---

*This chapter published as Gastfriend BD, Foreman KL, Katt ME, Palecek SP, Shusta EV (2021). Integrative analysis of the human brain mural cell transcriptome. *J Cereb Blood Flow Metab* **41**:3052–68.
Supplementary tables referenced in this chapter are available in the online version of this publication at http://doi.org/10.1177/0271678X211013700

additional specialized roles as constituents of the neurovascular unit. VSMCs mediate neurovascular coupling (*159*, *163*), while pericytes regulate blood-brain barrier (BBB) development and maintenance (*30*, *256*, *257*), immune cell infiltration (*258*), and potentially contribute to neurovascular coupling (*27*, *156*, *166*). Further, pericytes provide trophic support to neurons via pleiotrophin (*PTN*) secretion (*167*), and may regulate astrocyte end-foot polarization and the function of perivascular spaces (*256*, *585*). Brain mural cell dysfunction or degeneration contributes to neurological diseases (reviewed in (*586*)), such as Alzheimer's disease (*17*, *381*, *587*, *588*), cerebral small vessel and associated white matter diseases (*589*), and CADASIL (cerebral autosomal dominant arteriopathy with subcortical infarcts and leukoencephalopathy), a disease caused by mutations in the mural cell-expressed *NOTCH3* gene (*339–341*). Despite the functional importance of mural cells, our knowledge of molecules that mediate key brain mural cell functions remains limited, with molecular and functional properties largely characterized in rodent models (*27*, *30*, *156*, *159*, *163*, *166*, *167*, *256–258*). Therefore, improved knowledge of *human* brain mural cell gene expression profiles will expand understanding of the molecular mechanisms by which these cells contribute to physiological and pathological phenomena and facilitate molecular-level evaluation of animal and *in vitro* models.

Microarrays and bulk RNA-sequencing (RNA-seq) have been used to profile both mouse and human brain vascular cells. Most studies have focused on endothelial cells, although some studies characterized mural cells by marker-based isolation or subtractive comparison of microvessel and endothelial gene expression (*65*, *90*, *102*, *342*, *345*, *367*, *590*). Single-cell RNA-seq (scRNA-seq) can provide comprehensive information about cellular diversity and cell type-specific gene expression, and lacks bias associated with isolation of cells based on expression of canonical markers (*591*, *592*). The technique has been widely employed to profile cellular diversity in the mouse nervous system, including in recent studies that have provided detailed

transcriptome profiles of mouse brain mural cells and related perivascular cell populations, such as fibroblast-like cells (*56*, *372*, *542*). These studies have greatly advanced our knowledge of mouse brain mural cell biology and provided unambiguous molecular definitions of distinct mural cell populations (i.e., pericytes and multiple VSMC subtypes) that share expression of canonical marker genes and have historically been defined based predominantly on anatomical or morphological characteristics. An increasing number of studies have applied scRNA-seq to human brain samples (*391*, *392*, *503*, *504*, *593*), but the scarcity of mural cells in whole brain samples is a major limitation in using these datasets to investigate human brain mural cell biology.

We reasoned that integrating the limited mural cell data from multiple human brain scRNA-seq datasets could reveal a more precise transcriptomic profile of human brain mural cells than is currently available. To this end, we made use of five human brain scRNA-seq datasets from the published literature (*391*, *392*, *503*, *504*, *593*) and employed computational tools that can identify common populations of cells across multiple independent scRNA-seq datasets (*594–596*). Our results reveal high quality markers for human brain mural cells that are conserved across multiple brain regions and developmental stages. We also identify mural cell genes with human- or mouse-enriched expression, describe differences in gene expression profiles between *in vivo* and cultured human brain pericytes, and discover genes with enriched expression in brain mural cells compared to mural cells in other organs. Together, this work establishes high quality, consensus datasets for exploration of the human brain mural cell transcriptome.

4.3 Methods

4.3.1 RNA-seq datasets and analysis

We obtained scRNA-seq gene expression matrices and bulk RNA-seq FASTQ files from sources provided in Table 4.1. We used R (version 3.6.2), the package Seurat (version 3.1.5) (*594*, *595*), and the package sctransform (version 0.2.1) (*596*) for all analyses except where indicated. Statistical analyses of differential expression used the Wilcoxon rank sum test (a non-parametric test that does not assume normally-distributed data) with Bonferroni correction. Fold-change results are presented using the natural logarithm except where indicated. We also compared the expression of protein-coding genes in scRNA-seq data from *in vivo* pericytes and bulk RNA-seq data from cultured pericytes.

Table 4.1. Dataset sources and accession numbers.

Dataset	Source/accession number	Dataset identifier(s), if applicable
Allen Institute (*502*)	http://portal.brain-map.org/atlases-and-data/rnaseq/human-multiple-cortical-areas-smart-seq	transcript.tome
Polioudakis *et al.* (*392*)	http://solo.bmap.ucla.edu/shiny/webapp/	
Han *et al.* (*503*)	GEO accession GSE134355	GSM3980129, GSM4008656, GSM4008657, GSM4008658
La Manno *et al.* (*391*)	GEO accession GSE76381	GSE76381_EmbryoMoleculeCounts.cef.txt.gz
Zhong *et al.* (*504*)	GEO accession GSE119212	
Karrow *et al.* (*597*)	GEO accession GSE113036	
Cui *et al.* (*598*)	GEO accession GSE106118	
Aizarani *et al.* (*599*)	GEO accession GSE124395	
Travaglini *et al.* (*600*)	Synapse accession syn21041850	
Rubenstein *et al.* (*601*)	GEO accession GSE130646	
Vanlandewijck, He *et al.* (*56*, *542*)	GEO accession GSE98816; cell type annotations from http://doi.org/10.6084/m9.figshare.6170075.v1	
Zeisel *et al.* (*372*)	http://mousebrain.org/downloads.html	L5_All.loom
Kumar *et al.* (*321*)	GEO accession GSE75990	GSM2358894
Griffin *et al.* (*324*)	GEO accession GSE104141	GSM2790560, GSM2790561
Stebbins *et al.* (*447*)	GEO accession GSE124579	GSM3537071, GSM3537072

4.3.2 scRNA-seq data analysis

Expression matrices provided in comma-separated or tab-separated formats were imported into R using read.table; matrices provided in .mtx format were imported using the

ReadMM function from the Matrix package. The package scrattch.io was used to import the Allen Institute .tome file (*502*) and the package loomR was used to import the .loom file provided by Zeisel *et al.* (*372*) After importing scRNA-seq gene expression (count) matrices, we used the package sctransform (*596*) (version 0.2.1) to normalize data and identify 3000 highly variable features (genes) for each dataset independently. We performed principal component analysis and used the first 30–50 principal components to perform UMAP embedding and graph-based clustering using the FindNeighbors function, followed by cluster identification using the FindClusters function with resolutions of 0.5–1.5, except for the heart dataset where a resolution of 5 was necessary to resolve visually apparent clusters Table 4.2.

Table 4.2. Clustering parameters.

Dataset	PCs[a]	Resolution[b]
Allen Institute (*502*)	1:40	1.5
Polioudakis *et al.* (*392*)	1:40	0.8
Han *et al.* (*503*)	1:40	1.0
La Manno *et al.* (*391*)	1:40	0.8
Zhong *et al.* (*504*)	1:40	0.8
Karow *et al.* (*597*)	1:50	0.5
Cui *et al.* (*598*)	1:50	5.0
Aizarani *et al.* (*599*)	1:50	0.5
Travaglini *et al.* (*600*)	1:50	1.0
Rubenstein *et al.* (*601*)	1:30	1.0
Vanlandewijck, He *et al.* (*56*, *542*)	1:40	N/A[c]
Zeisel *et al.* (*372*)	1:50	N/A

[a] Principal components used for UMAP embedding and FindNeighbors
[b] Resolution used for FindClusters
[c] N/A: not applicable; authors' cluster annotations were used.

For marker identification, we used the FindAllMarkers function (with parameters min.pct = 0.25, logfc.threshold = 0.25, only.pos = TRUE), and selected genes with adjusted *P*-values < 0.05 based on the default Wilcoxon rank sum test (a non-parametric test that does not assume normally-distributed data) with Bonferroni correction. We used the Seurat functions DimPlot, FeaturePlot, VlnPlot, DoHeatmap, and DotPlot for visualization. For Venn diagram construction, we used the tool available at http://bioinformatics.psb.ugent.be/webtools/Venn/.

To integrate the five human brain scRNA-seq datasets, we used the Seurat workflow that harmonizes Pearson residuals output by sctransform, using the SelectIntegrationFeatures,

PrepSCTIntegration, FindIntegrationAnchors, and IntegrateData functions. We performed principal component analysis on the resulting integrated dataset, followed by UMAP embedding and FindNeighbors using the first 50 principal components, and FindClusters using a resolution of 1. After integration and clustering, we performed marker identification using raw log-normalized counts, with the FindAllMarkers parameters described above. To generate differential expression results for input to Gene Set Enrichment Analysis (GSEA), we used the Seurat function FindMarkers (with parameter logfc.threshold = 0.25), comparing the cluster of interest (mural: cluster 30; endothelial: cluster 32; fibroblast-like: cluster 40) to all other cells in the integrated dataset. For each gene, we calculated a ranking metric $-\log_{10}(P)\times\log(\text{fold change})$. We input the ranked gene lists into GSEA (version 4.0.2) (*602*, *603*) and tested them against the KEGG canonical pathways gene set. For sub-clustering of mural cells, we isolated cluster 30 from the integrated dataset and preserved the original UMAP coordinates, but re-ran PCA, FindNeighbors using the first 10 principal components, and FindClusters with a resolution of 1. We collapsed the resulting 12 clusters into a single pericyte-enriched and a single VSMC-enriched cluster based on expression of *ACTA2* (Figure 4.4e,f) and removed multiplet or contaminant cells with nonzero counts for *CLDN5* (endothelial cells), *TUBB3* (neurons), *AQP4* (astrocytes), *OLIG1/2* (oligodendrocytes and oligodendrocyte precursor cells), *AIF1* (microglia/macrophages), and *GYPA* (erythrocytes) as shown in Figure 4.4G. These filtered mural cell sub-clusters are shown in Fig. 2F and were used for subsequent analyses except where indicated. Differential expression analysis comparing the pericyte-enriched and VSMC-enriched clusters was performed using the FindMarkers function (with parameter min.pct = 0.25).

For comparison of human and mouse scRNA-seq datasets, we used mouse-human gene homology data from the Ensembl database (release 100; http://ensembl.org/biomart/martview/) (*560*) to assign homologous human gene names to the mouse brain vascular scRNA-seq data. We

manually curated the resulting gene expression matrix using mouse gene name synonym data from the Mouse Genome Database (http://www.informatics.jax.org/batch) (*604*). We used Seurat to perform UMAP embedding of the mouse data as described above, and selected the cells annotated as pericytes by Vanlandewijck, He *et al.* (*56*, *542*) for differential expression analysis. To compare mouse pericytes and human pericytes (cluster 0'), we used the FindMarkers function with the following parameters: min.pct = 0.5, logfc.threshold = 0.25. We chose a higher value of min.pct to increase the relative number of human-enriched genes that are expressed in pericytes from multiple human source datasets. We excluded mitochondrial and ribosomal genes, and used a volcano plot to visualize the differential expression results (adjusted *P*-values from the Wilcoxon rank sum test with Bonferroni correction versus average log(fold change)).

4.3.3 Bulk RNA-seq data analysis

We compared the expression of protein-coding genes (based on the list available from the HUGO at https://www.genenames.org/download/statistics-and-files/) in scRNA-seq data from *in vivo* pericytes and bulk RNA-seq data from cultured pericytes. We used RSEM (version 1.3.1) (*550*) to align FASTQ files from bulk RNA-seq of cultured human brain pericytes to the human genome (hg38) and quantify transcript abundances in transcripts per million (TPM). For each human brain scRNA-seq source dataset, we constructed a mock bulk RNA-seq dataset using average gene counts across all cells in the pericyte cluster (cluster 0'). We generated mock TPM values by normalizing each mock bulk RNA-seq dataset to 10^6. We averaged TPM values for each gene across the five cultured pericyte bulk RNA-seq datasets, and averaged TPM values for each gene across the five mock bulk RNA-seq datasets from *in vivo* pericytes. We calculated the Pearson correlation coefficient on the log-transformed average transcript abundances [$\log_2$(TPM + 1)]. For each gene, we calculated the log(fold change) between cultured and *in vivo* pericytes

and input the gene list ranked based on log(fold change) to GSEA and tested it against the KEGG canonical pathways gene set.

4.3.4 Validation via immunohistochemistry and RNA in situ hybridization (FISH)

We validated a subset of brain mural cell-enriched genes using immunohistochemistry data from the Human Protein Atlas (*507*) Table 4.3. We performed immunohistochemistry on de-identified, normal human brain tissue and mouse brain tissue. For human tissue, research was conducted in accordance with the ethical guidelines of the University of Wisconsin–Madison Institutional Review Board and with patient consent that tissue removed during surgery could be used for research purposes. For mouse tissue, research was conducted in accordance with the ethical guidelines of the University of Wisconsin–Madison Institutional Animal Care and Use Committee following National Institutes of Health (NIH) guidelines for care and use of laboratory animals. Results and methods are reported in compliance with the ARRIVE guidelines; inclusion/exclusion criteria, randomization, and blinding are not applicable to the study design. We also performed RNA FISH on human brain tissue obtained as described above. Statistical analysis of quantified RNA FISH data was performed using the Kruskal-Wallis test followed by Steel-Dwass test (non-parametric tests as data were not normally distributed as assessed by the Shapiro-Wilk test).

Table 4.3. Human Protein Atlas image URLs.

Protein	Antibody	Brain region	Image URL
PDGFRB	CAB018144	Cortex	images.proteinatlas.org/18144/43120_B_7_5.jpg
		Hippocampus	images.proteinatlas.org/18144/43120_B_8_6.jpg
		Caudate nucleus	images.proteinatlas.org/18144/43120_B_7_7.jpg
		Cerebellum	images.proteinatlas.org/18144/43120_B_7_8.jpg
ACTA2	CAB000002	Cortex	images.proteinatlas.org/2/310_B_8_5.jpg
		Hippocampus	images.proteinatlas.org/2/310_B_7_6.jpg
		Caudate nucleus	images.proteinatlas.org/2/310_B_8_7.jpg
		Cerebellum	images.proteinatlas.org/2/310_B_7_8.jpg
S100A6	HPA007575	Cortex	images.proteinatlas.org/7575/21633_B_8_5.jpg
		Hippocampus	images.proteinatlas.org/7575/21633_B_7_6.jpg
		Caudate nucleus	images.proteinatlas.org/7575/21633_B_7_7.jpg
		Cerebellum	images.proteinatlas.org/7575/21633_B_9_8.jp
SLC6A1	CAB022293	Cortex	images.proteinatlas.org/22293/56980_B_7_5.jpg
		Hippocampus	images.proteinatlas.org/22293/56980_B_9_6.jpg
		Caudate nucleus	images.proteinatlas.org/22293/56980_B_8_7.jpg
		Cerebellum	images.proteinatlas.org/22293/56980_B_7_8.jpg
SLC6A12	HPA034973	Cortex	images.proteinatlas.org/34973/70402_B_8_5.jpg
		Hippocampus	images.proteinatlas.org/34973/70402_B_9_6.jpg
		Caudate nucleus	images.proteinatlas.org/34973/70402_B_7_7.jpg
		Cerebellum	images.proteinatlas.org/34973/70402_B_7_8.jpg
ADIRF	HPA026810	Cortex	images.proteinatlas.org/26810/57107_B_7_5.jpg
		Hippocampus	images.proteinatlas.org/26810/57107_B_7_6.jpg
		Caudate nucleus	images.proteinatlas.org/26810/57107_B_7_7.jpg
		Cerebellum	images.proteinatlas.org/26810/57107_B_8_8.jpg
GPER1	HPA027052	Cortex	images.proteinatlas.org/27052/56949_B_7_5.jpg
		Hippocampus	images.proteinatlas.org/27052/56949_B_7_6.jpg
		Caudate nucleus	images.proteinatlas.org/27052/56949_B_8_7.jpg
		Cerebellum	images.proteinatlas.org/27052/56949_B_7_8.jpg

4.3.5 Immunohistochemistry

Normal human brain tissue specimens were obtained during neurosurgeries, immediately flash-frozen in liquid nitrogen, and stored at –80°C. Mouse brain tissue was obtained from a 7 week-old male C57/BL6N mouse used for an unrelated experiment (injection with a rabbit-Fc brain vasculature-targeting antibody) 48 h before the mouse was sacrificed by cardiac perfusion with 4% paraformaldehyde containing 0.5 mg/mL heparin, 1 mg/mL BSA, and *Lycopersicon esculentum* (tomato) lectin-DyLight 488 (Invitrogen, L32470). Mouse brain was flash-frozen in liquid nitrogen and stored at –80°C. The anti-FRZB (FRP-3) antibody (Santa Cruz, B-5, mouse IgG1) and mouse IgG1 isotype control antibody (BD Biosciences, MOPC-21) were concentrated to 1 mg/mL in Amicon Ultra 100 kDa nominal molecular weight limit centrifugal filter units and preconjugated using the Alexa Fluor 647 Antibody Labeling Kit (Invitrogen, A20186) according to the manufacturer's protocol. 8 μm cryosections of the human brain tissue and mouse brain

(sagittal) were cut and fixed with 1% paraformaldehyde for 10 min at room temperature. Sections were washed once with PBS, blocked with PBS supplemented with 15% goat serum, 1% bovine serum albumin, 0.15% saponin, and 0.1% Triton X-100 for 30 min, and incubated with primary antibodies in blocking solution lacking Triton X-100 overnight at 4°C. Human brain sections were labeled with anti-PDGFRβ (Cell Signaling Technology, 28E1, rabbit monoclonal, 1:100) and anti-FRZB-AF647 (1:100) or mouse IgG1 isotype control-AF647 (1:100). Mouse brain sections were labeled with anti-FRZB-AF647 (1:100). Sections were washed 5 times with PBS for 5 min each. Human brain sections were incubated with secondary antibody (goat anti-rabbit IgG-Alexa Fluor 488, Invitrogen A11008, 1:200) in blocking solution lacking Triton X-100 for 30 min at room temperature, followed 5 washes with PBS for 5 min each. Coverslips were mounted with ProLong Gold Antifade Mountant with DAPI (Invitrogen, P36935) and sections were imaged on a Nikon Eclipse Ti2-E microscope with a 40× objective.

4.3.6 RNA in situ hybridization

RNAscope* was performed on de-identified, normal human brain tissue obtained as described above. Specimens were fixed in 10% neutral-buffered formalin for 36 h at room temperature and transferred to 70% ethanol, followed by paraffin embedding and sectioning. RNAscope was performed according to manufacturer protocols using the RNAscope Multiplex Fluorescent Reagent Kit v2 with 4-plex Ancillary Kit (Advanced Cell Diagnostics). RNAscope probes, channels, and Opal fluorophores (Akoya Biosciences) were: Assay 1: *FRZB*-C1-Opal520), *ATP1A2*-C2-Opal570, *CLDN5*-C3-Opal620, *PDGFRB*-C4-Opal690; Assay 2: *SLC6A12*-C1-Opal 520, *SLC6A1*-C2-Opal570, *CLDN5*-C3-Opal620, *PDGFRB*-C4-Opal690. Imaging was performed using a Nuance Multispectral Imaging System (PerkinElmer) with a 40×

*I thank Rebecca Baus and Karla Esbona of the University of Wisconsin Translational Research in Pathology (TRIP) laboratory for performing RNAscope.

objective. Signals were unmixed using the Nuance Multispectral Imaging System and inForm software. ImageJ (FIJI) software was used to manually select endothelial cell nuclei (*CLDN5*$^{+}$), mural cell nuclei (*PDGFRB*$^{+}$), and non-endothelial/non-mural cell nuclei (*CLDN5*$^{-}$*PDGFRB*$^{-}$) from one tissue specimen and quantify mean fluorescence intensity of each channel. The non-parametric Kruskal-Wallis test followed by the Steel-Dwass test was used to compare fluorescence intensity in endothelial cell and mural cell nuclei to non-endothelial/non-mural cell nuclei.

4.4 Results

4.4.1 Identification of mural cell populations in human brain scRNA-seq datasets

We began by identifying and evaluating five human brain scRNA-seq datasets from the published literature (*391*, *392*, *503*, *504*, *593*). These five datasets were generated using samples from several different developmental stages, brain regions, and scRNA-seq library preparation methodologies (Figure 4.1A). Thus, our analysis of these datasets permits us to define a mural cell gene expression profile that is conserved across developmental stage and brain region. The five datasets also vary considerably in the total number of cells analyzed and in average sequencing depth (i.e., the average number of different genes detected) per cell (Figure 4.1A). Therefore, simultaneous analysis of multiple datasets may be beneficial, as datasets with high sequencing depth in few cells can complement datasets with large numbers of cells but low depth.

We first performed normalization, variable feature identification, and dimensionality reduction on each dataset independently, using the Seurat and sctransform packages (*594*, *596*) (see Methods). We visualized the heterogeneity in cell transcriptomes in two dimensions using UMAP embedding (*605*) and performed unbiased clustering of single cells (Figure 4.1B). We identified putative mural cell clusters based on the expression of pan-mural cell canonical

markers *PDGFRB* and *RGS5* or the VSMC-enriched gene *ACTA2* (*606*), and observed at least one cluster enriched for the combination of *PDGFRB* and *RGS5* and/or *ACTA2*, in each dataset (Figure 4.1A; Figure 4.2). We next identified markers of these clusters, defined as genes enriched in the putative mural cell cluster(s) relative to all other cells in the same source dataset ($P < 0.05$, log(fold-change) > 0.25) and expressed by at least 25% of cells in the putative mural cell cluster(s) (Supplementary Table S1). Comparing the results of this analysis for the five datasets revealed that 26 genes were identified as mural cell markers in all five datasets (Figure 4.1C,D). Several additional genes were identified as mural cell markers in four out of five datasets, and many others appeared in three or fewer datasets (Figure 4.1C,D). Importantly, in addition to the canonical markers used to identify the putative mural cell clusters, the list of mural cell markers identified in all five datasets included several known pericyte and VSMC genes, including *PTN*, *MYL9*, and *NOTCH3* (Figure 4.1E). In the list of genes identified as mural cell markers in four out of five datasets, additional known markers of brain mural cells appeared, including *ABCC9*, *COL1A2*, *FOXC1*, *MCAM* (CD146) and *ZIC1* (*83*, *320*, *342*, *343*, *345*), and shared mural/endothelial markers *B2M* and *COL4A1* (*56*, *345*) (Figure 4.1F). The lack of enrichment of these genes in all five data sets is likely attributable to the low sequencing depth of the dataset from Han *et al.* (*503*), which lacks enrichment of these markers (Supplementary Table S1), rather than biological differences. Therefore, genes enriched in 4 or more datasets are likely high quality markers of human brain mural cells. Together, these results support the identification of mural cell clusters in the selected datasets, suggest striking similarities in marker gene expression in human brain mural cells across the evaluated developmental stages and brain regions, and provide genes that should robustly identify mural cells in human brain samples.

A

	Allen Institute Neocortex	Polioudakis *et al.* Neocortex	Han *et al.* Temporal lobe, cerebellum	La Manno *et al.* Ventral midbrain	Zhong *et al.* Hippocampus
Stage	Adult	GW17-18	Adult	GW6-11	GW16-27
Cells	49,494	33,986	40,000	1,977	33,113
Platform	SMART-Seq v4	Drop-seq	Microwell-seq	Fluidigm C1	10x GemCode
Depth	4,600 ± 1,600	1,000 ± 600	400 ± 200	2,300 ± 900	1,600 ± 700

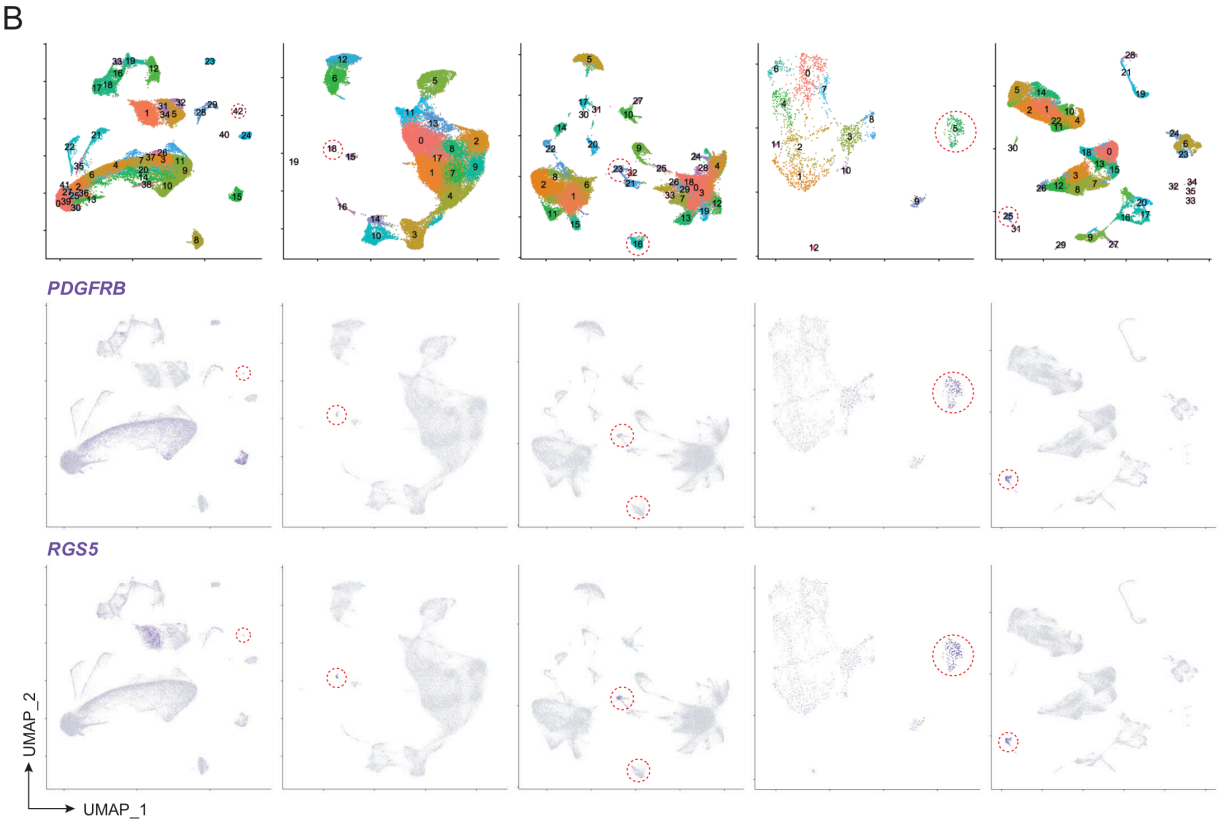

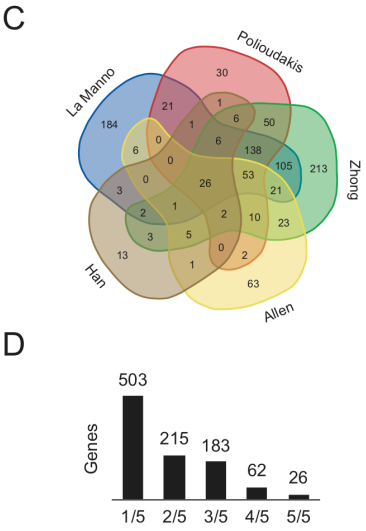

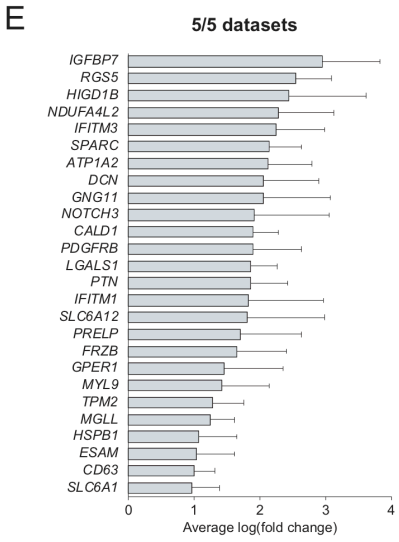

F

4/5 datasets

ABCC9	*FN1*	*PMP22*
ANXA2	*FOXC1*	*PPP1R14A*
ANXA5	*GJC1*	*PRKCDBP*
APOLD1	*HES1*	*RBMS3*
ARHGAP29	*ID3*	*RCSD1*
ARHGDIB	*ISYNA1*	*RHOJ*
B2M	*ITIH5*	*RPLP1*
BGN	*LAMA2*	*SERPING1*
CD9	*LHFP*	*SERPINH1*
CFH	*MCAM*	*SLC12A7*
COBLL1	*MSN*	*SLC20A2*
COL1A2	*MT2A*	*SPARCL1*
COL4A1	*MYL12A*	*TFPI*
COX7A1	*MYL6*	*TIMP1*
CYBA	*MYO1B*	*TJP1*
EBF1	*MYOF*	*TXNIP*
EDNRA	*NR2F2*	*UACA*
EPAS1	*OLFML3*	*VIM*
EPS8	*PFN1*	*ZFP36L1*
FCGRT	*PLCE1*	*ZIC1*
FERMT2	*PLXDC1*	

Figure 4.1. Identification of mural cell populations in human brain scRNA-seq datasets. (A) Overview of the five scRNA-seq datasets. For each dataset, the sampled brain region(s), developmental stage, total number of cells analyzed, scRNA-seq platform, and sequencing depth (mean ± SD of genes detected per cell), are indicated. GW: gestational week. (B) UMAP plots of all single cells arranged in columns below the corresponding source dataset overview in (A). Plotted points (cells) are colored by cluster identity (top row) or by expression of *PDGFRB* or *RGS5* (bottom). Dashed circles mark putative mural cell clusters. Cluster numbers shown correspond to those in Figure 4.2 and Supplementary Table S1. (C) Venn diagram depicting the number of genes identified as markers of mural cells ($P < 0.05$, average log(fold change) > 0.25, expressed by at least 25% of cells in the putative mural cell cluster(s)) in the five scRNA-seq datasets. Complete lists of marker genes are provided in Supplementary Table S1. (D) Number of genes identified as markers of mural cells in a single dataset (1/5) or multiple datasets. 26 genes were identified as markers of mural cells in all datasets (5/5). (E) Average log(fold change) of gene expression in mural cell clusters compared to all other cells in the corresponding dataset for the 26 genes identified as markers of mural cells in all five datasets. Points represent average log(fold change) from each dataset and bars indicate the mean. (F) Genes identified as markers of mural cells in 4/5 datasets.

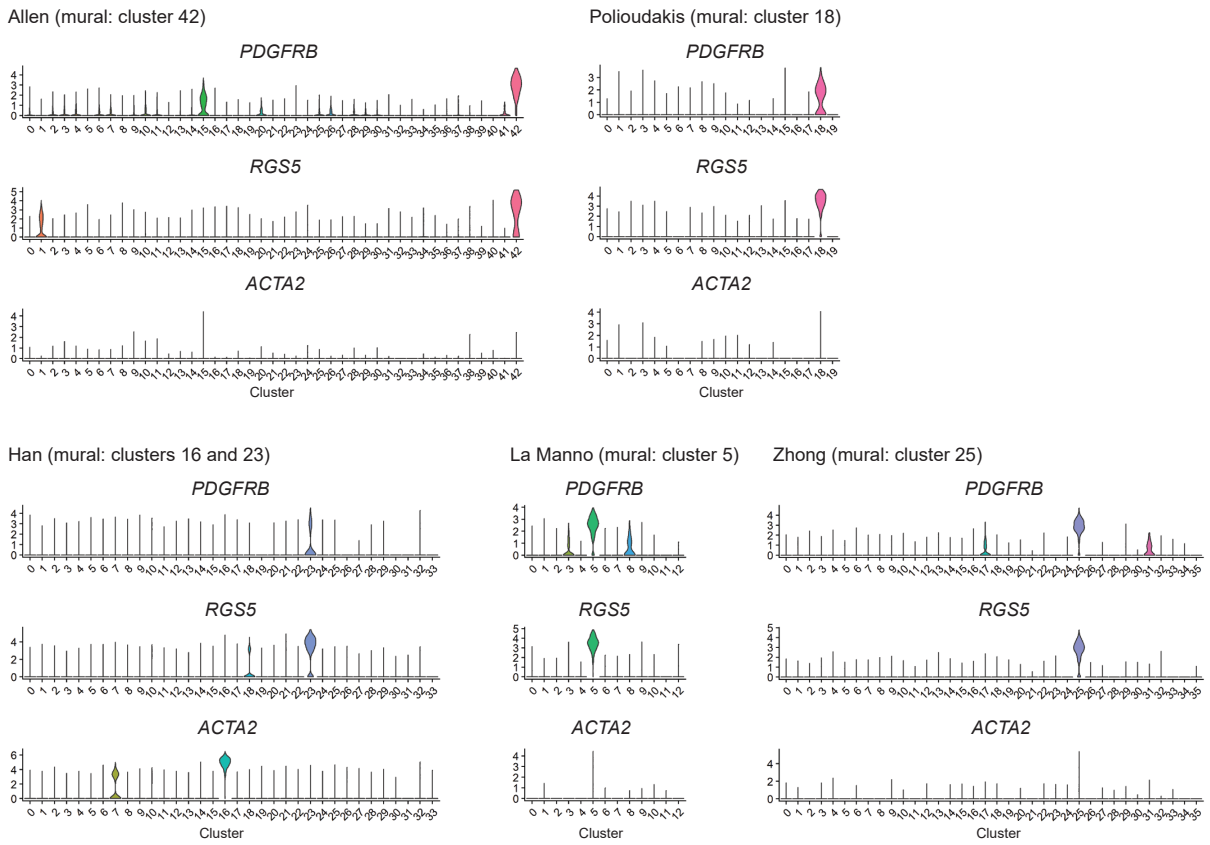

Figure 4.2. Mural cell clusters in human brain scRNA-seq datasets. Expression of mural cell markers (*PDGFRB*, *RGS5*, and *ACTA2*) in clusters identified in each scRNA-seq dataset. The putative mural cell cluster(s) is shown above each set of plots. Cluster numbers correspond to those in Figure 4.1A and Supplementary Table S1.

4.4.2 Integrated analysis of human brain mural cell transcriptome profiles

To take advantage of the combined power of the five scRNA-seq datasets and build a consensus molecular profile of human brain mural cells, we used the "anchoring" methodology in Seurat to integrate the five source datasets (*595*) (see Methods). This combined dataset comprises more than 150,000 human brain cells. Visualization in low-dimensional space revealed both cell clusters that are unique to a single source dataset and cell clusters comprising cells from multiple or all source datasets (Figure 4.3A). We performed unbiased clustering on this combined dataset (Figure 4.3B) and used canonical markers of mural cells to identify cluster 30 as the putative mural cell cluster, which contained a total of 1,489 cells, representing 0.9% of

total cells (Figure 4.3B,C). Importantly, cluster 30 contained cells derived from all five source datasets (Figure 4.3A,B; Figure 4.4A), suggesting gross similarity in the transcriptional profiles of mural cells from multiple brain regions and developmental stages. This finding is further supported by the lack of substantial spatial segregation of cerebellum- and temporal lobe-derived mural cells from the source dataset of Han *et al.* (*503*) (Figure 4.4B). The majority (77%) of cells from the mural cell clusters identified by analysis of independent datasets (Fig. 1) were included in the integrated cluster 30 (Figure 4.4A). Cells in cluster 30 expressed *KCNJ8*, a pericyte marker (*342*), and *ACTA2*, a VSMC-enriched gene, suggesting that both of these mural cell subtypes are present in this cluster (Figure 4.3C). Of note, the mural cell cluster did not contain a large number of *COL1A1*$^{+}$ cells, and we identified a separate, very small cluster (cluster 40) with enrichment of *COL1A1* that may comprise brain perivascular fibroblast-like cells (*56*, *372*) (Figure 4.3C). We identified markers (as defined previously) of mural cells in cluster 30 and fibroblast-like cells in cluster 40 (Figure 4.3D; Supplementary Table S2). Among the mural cell-enriched genes were all 26 markers previously identified in all five individual dataset analyses, a majority of markers identified in four out of five datasets, and importantly, additional genes not identified in any individual analysis, including *HCFC1R1* and *CYB5R3* (Figure 4.4C); Supplementary Table S2). We performed Gene Set Enrichment Analysis (GSEA) using the results of this differential expression

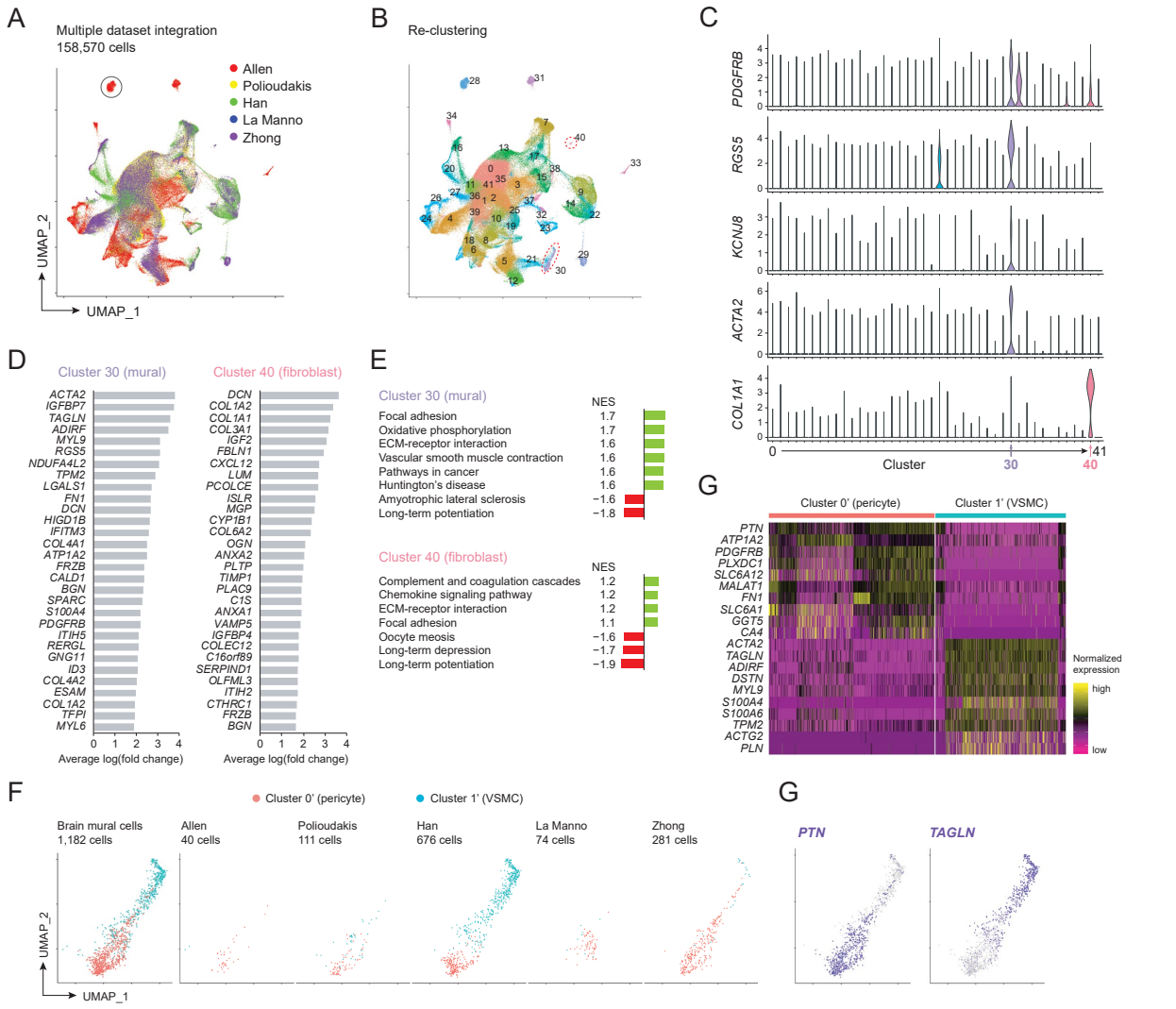

Figure 4.3. Dataset integration and analysis of mural and fibroblast transcriptional profiles. (A) UMAP plot of all single cells after integration of the five scRNA-seq datasets described in Figure 4.1. Plotted points (cells) are colored by source dataset. An example of a cluster comprising cells from a single source dataset is circled; most clusters comprise cells from multiple source datasets. (B) UMAP plot of all single cells colored by cluster identity after re-clustering. Dashed circles mark the putative mural cell cluster (30) and fibroblast cluster (40). (C) Expression of known markers of mural cells (*PDGFRB*, *RGS5*), pericytes (*KCNJ8*), VSMCs (*ACTA2*), and fibroblasts (*COL1A1*) in the 42 clusters identified in (B). The position of the putative mural cell cluster (30) is indicated by an arrow below the x axis. (D) Genes identified as markers ($P < 0.05$, average log(fold change) > 0.25, expressed by at least 25% of cells in the putative mural cell cluster(s)) of mural cells (left) and fibroblasts (right). The average log(fold change) of gene expression in the mural or fibroblast cell cluster compared to all other cells is plotted for the 30 genes with largest average log(fold change). Complete lists of marker genes are provided in Supplementary Table S2. (E) Gene sets enriched and depleted ($P < 0.05$) in mural (top) and fibroblast (bottom) clusters compared to all other brain single cells as identified by GSEA. NES: normalized enrichment score. The GSEA input was a list of genes ranked from the highest-confidence mural- or fibroblast-enriched to the highest-confidence mural- or fibroblast-depleted gene, using the ranking metric $-\log_{10}(P)\times\log(\text{fold change})$. Complete results of GSEA are provided in Supplementary Table S2. (F) UMAP plot of all mural cells (cluster 30 in b) after sub-clustering and cluster collapsing to two clusters, pericytes (cluster 0') and VSMCs (cluster 1') (Figure 4.4). UMAP plots split by source dataset are shown at right. Plotted points (cells) are colored by cluster identity. The number of cells in the integrated mural cell dataset derived from each source dataset is shown above each plot. (G) Differential expression analysis comparing pericytes (cluster 0') and VSMCs (cluster 1'). The heatmap shows expression of the 10 genes with the largest average log(fold change) for each cell type. Complete results of differential expression analysis are provided in Supplementary Table S3. (H) UMAP plots of all mural cells. Plotted points (cells) are colored by expression of *PTN* or *TAGLN*. *PTN*-expressing cells concentrate in the lower region identified as cluster 0' (pericyte), while *TAGLN*-expressing cells concentrate in the upper region identified as cluster 1' (VSMC).

analysis, and identified the KEGG gene sets *focal adhesion* and *ECM-receptor interaction* as enriched in both mural and fibroblast-like cell clusters, while *oxidative phosphorylation* and *vascular smooth muscle contraction* were enriched only in the mural cell cluster (Figure 4.3E; Supplementary Table S2). We also identified an endothelial cell cluster comprising 768 cells (cluster 32; 0.5% of total cells) with enrichment for known endothelial and BBB genes including *CLDN5, SLC2A1*, *VWF*, *FLT1*, *MFSD2A*, *ABCG2*, and *PODXL* (Figure 4.5A-E; Supplementary Table S2). Finally, we identified transcription factors enriched in these three vascular cell clusters; we observed mural cell-specific enrichment of *FOXS1*, *EBF1*, *ZEB1*, *TBX2*, and *HEYL*, several shared mural- and fibroblast-enriched transcription factors (including *ZIC1*, *HES4*, and *FOXF2*), and pan-vascular enrichment of intermediate early genes (including *JUNB*, *NR4A1*, *FOS*, and *JUN*), potentially suggestive of dissociation-induced transcriptional changes (Figure 4.5F).

We next asked whether sub-clustering the mural cell cluster could resolve distinct populations of pericytes and VSMCs. Initial sub-clustering yielded 12 clusters, some of which were largely driven by source dataset (Figure 4.4D). We therefore collapsed the five *ACTA2*^{high} clusters into one putative VSMC-enriched sub-cluster (cluster 1') and the remaining seven *ACTA2*^{low} clusters into a single putative pericyte-enriched subcluster (cluster 0') (Figure 4.4E,F). We also eliminated a small number of potential endothelial, neuronal, glial, microglial, and blood cell contaminants or multiplets based on expression of canonical markers (Figure 4.4G), for a filtered mural cell cluster containing 1,182 cells (Figure 4.3F). When visualized in the original UMAP embedding, cells in the pericyte sub-cluster and cells in the VSMC sub-cluster appeared spatially segregated (Figure 4.3F). We performed differential expression analysis to identify genes that distinguish the two mural sub-clusters, and found that putative pericytes were enriched for genes including *PTN*, *ATP1A2*, *PDGFRB*, *PLXDC1*, *SLC6A12*, *SLC6A1*, *MALAT1*,

and *FN1*, while putative VSMCs were enriched for genes including *ACTA2*, *TAGLN*, *ADIRF*, *S100A6*, and *DSTN*, many of which have been previously identified to discriminate between mouse brain mural cell sub-types (Figure 4.3G,H; Figure 4.6; Supplementary Table S3). We also evaluated a subset of these markers on the protein level using immunohistochemistry data from the Human Protein Atlas (*507*), which confirmed robust expression of SLC6A12 and weak expression of SLC6A1 in smaller vessels, and enrichment of S100A6 and ADIRF in larger vessels across multiple brain regions (Figure 4.7). While all source datasets contained cells classified as both pericytes and VSMCs, the vast majority of mural cells were classified as pericytes in all datasets except that from Han *et al.* (*503*) (Figure 4.3F), potentially a result of the brain regions sampled, technical differences in tissue isolation, or increased pial vessel contamination. Taken as a whole, however, these combined human pericyte and VSMC datasets are derived from multiple independent studies and exhibit good representation of known pericyte and VSMC markers. We therefore propose that these datasets will be useful in identifying novel mural cell genes and in validating appropriate expression of these genes in model systems of these cell types.

A

	Allen	Polioudakis	Han	La Manno	Zhong	Overall
Mural cell cluster(s) (Fig. 4.1)	42	18	16 23	5	25	
Number of cells in mural cell cluster(s) in:						
Individual analyses only (Fig. 4.1)	0	5	246 89	7	13	432
Individual + integrated analyses	39	112	536 301	112	3	1445
Integrated analysis only (Fig. 4.3)	14	0	28	0	2	44

B

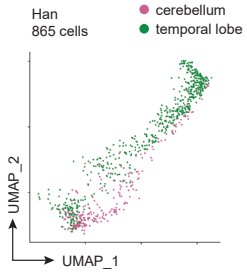

C

Mural cell markers identified in Fig. 4.1 as appearing in:	5/5	4/5	3/5	2/5	1/5 datasets
Number of genes	26	62	183	215	503
Number of genes also identified as markers in integrated analysis (Fig. 4.3)	26	53	121	67	72

63 markers identified in integrated analysis (Fig. 4.3) but in no individual analysis (Fig. 4.1)
339 markers identified in integrated analysis (Fig. 4.3) and at least one individual analysis (Fig. 4.1)

D

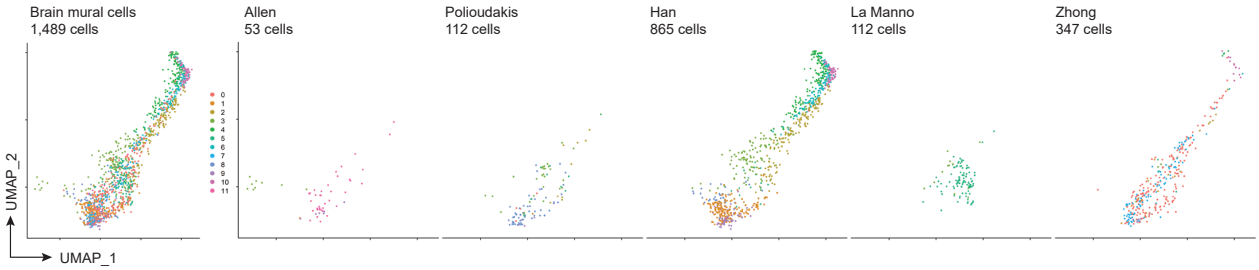

E

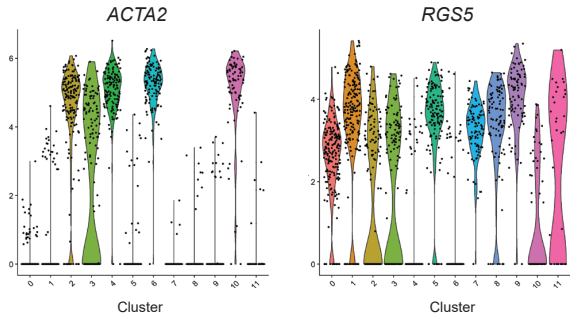

F

G

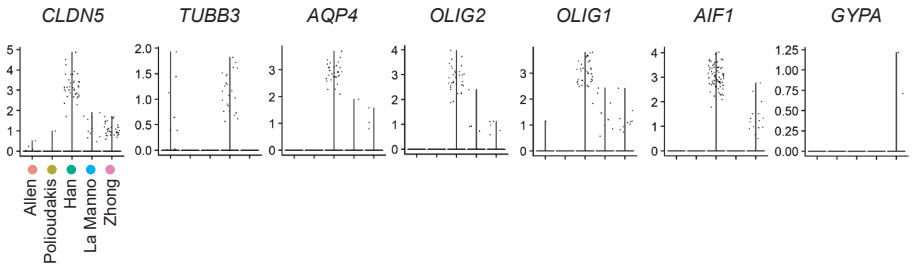

Figure 4.4. Sub-clustering of the integrated brain mural cell dataset. (A) Comparison of cells classified as mural cells in analyses of individual datasets (Figure 4.1) and those classified as mural cells in the integrated analysis (Figure 4.3). The majority of cells from the Han *et al.* (*503*) dataset that were classified as mural cells in the individual analysis only (246 + 89 cells) map to integrated cluster 21, which contains *RGS5*$^{+}$*PDGFRB*^{low} cells, and not integrated cluster 30, which contains *RGS5*$^{+}$*PDGFRB*$^{+}$ putative mural cells (Figure 4.3C). (B) UMAP plot of mural cells (cluster 30 in Figure 4.3B) from Han *et al.* (*503*) colored by brain region. (C) Comparison of mural cell markers identified in analyses of individual datasets (Fig. 1) and those identified in the integrated analysis (Figure 4.3). (D) UMAP plot of all mural cells (cluster 30 in Figure 4.3B) after sub-clustering, but prior to cluster collapsing and filtering. UMAP plots split by source dataset are shown at right. Plotted points (cells) are colored by cluster identity. The number of cells in the integrated mural cell dataset derived from each source dataset is shown above each plot. (E) Expression of *ACTA2* and *RGS5* in the 12 clusters in the integrated mural cell dataset. (F) Cluster collapsing scheme. *ACTA2*^{high} clusters (2, 3, 4, 6, and 10) were combined to form cluster 1' while the remaining clusters were combined to form cluster 0'. (G) Expression of canonical brain cell type marker genes in the integrated mural cell dataset grouped by source dataset. Cells with nonzero counts for *CLDN5* (endothelial cells), *TUBB3* (neurons), *AQP4* (astrocytes), *OLIG1/2* (oligodendrocytes and oligodendrocyte precursor cells), *AIF1* (microglia/macrophages), and *GYPA* (erythrocytes) were excluded from the integrated brain mural cell dataset.

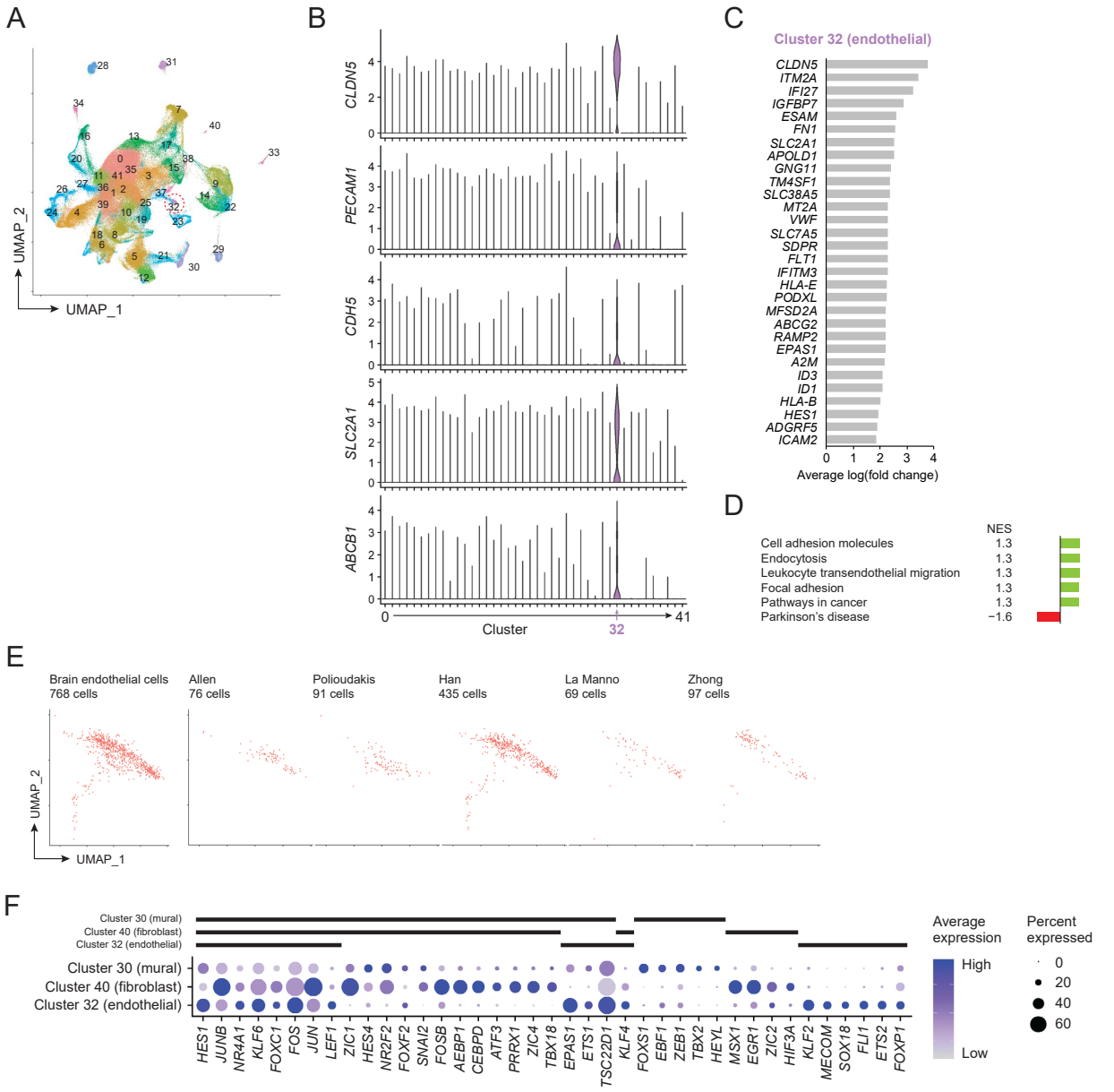

Figure 4.5. Endothelial transcriptional profile and vascular-enriched transcription factors in the integrated dataset. (A) UMAP plot of all single cells colored by cluster identity after re-clustering. The dashed circle marks the putative endothelial cell cluster (32). (B) Expression of known markers of brain endothelial cells (*CLDN5, PECAM1*, *CDH5*, *SLC2A1*, *ABCB1*) in the 42 clusters identified in (A). The position of the putative endothelial cell cluster (32) is indicated by an arrow below the x axis. (C) Genes identified as markers ($P < 0.05$, average log(fold change) > 0.25) of endothelial cells. The average log(fold change) of gene expression in the endothelial cell cluster compared to all other cells is plotted for the 30 genes with largest average log(fold change). Complete lists of marker genes are provided in Supplementary Table S2. (D) Gene sets enriched and depleted ($P < 0.05$) in endothelial cell clusters compared to all other brain single cells as identified by GSEA. NES: normalized enrichment score. The GSEA input was a list of genes ranked from the highest-confidence endothelial cell-enriched to the highest-confidence endothelial cell-depleted gene, using the ranking metric $-\log_{10}(P)\times\log(\text{fold change})$. Complete results of GSEA are provided in Supplementary Table S3. (E) UMAP plot of all endothelial cells (cluster 32 in a). UMAP plots split by source dataset are shown at right. The number of cells in the integrated mural cell dataset derived from each source dataset is shown above each plot. (F) Dot plot of transcription factor gene expression in clusters containing mural cells (cluster 30), fibroblast-like cells (cluster 40), and endothelial cells (cluster 32). Transcription factors identified as markers in at least one of the three clusters are shown. Color indicates expression level and dot size indicates the fraction of cells that express a given gene. Bars above dot plot indicate statistically significant enrichment ($P < 0.05$).

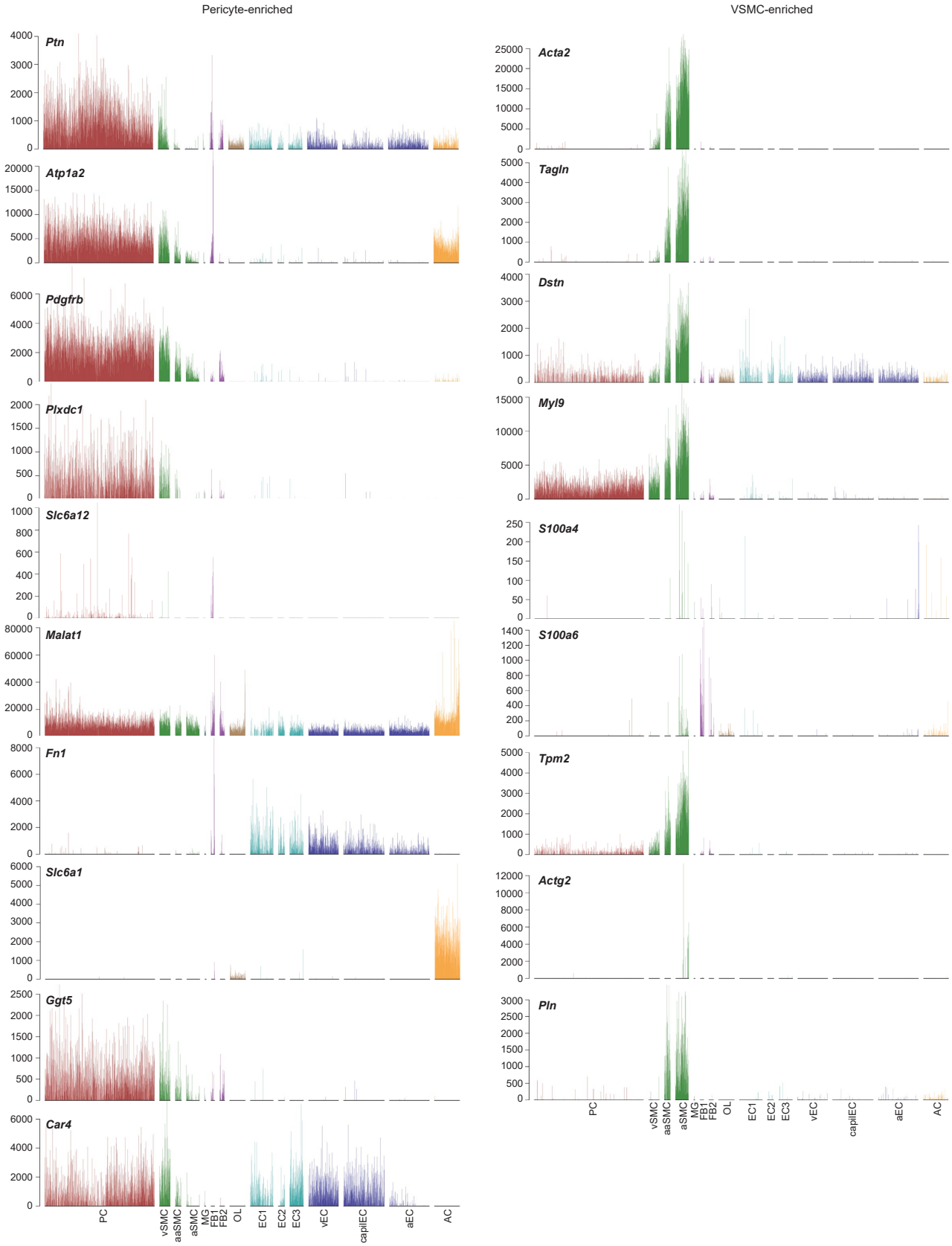
Pericyte-enriched
VSMC-enriched
Ptn
Atp1a2
Pdgfrb
Plxdc1
Slc6a12
Malat1
Fn1
Slc6a1
Ggt5
Car4
Acta2
Tagln
Dstn
Myl9
S100a4
S100a6
Tpm2
Actg2
Pln
PC
vSMC
aaSMC
aSMC
MG
FB1
FB2
OL
EC1
EC2
EC3
vEC
capilEC
aEC
AC

Figure 4.6. Pericyte- and VSMC-enriched genes in a mouse brain vascular scRNA-seq dataset. Figures adapted from http://betsholtzlab.org/VascularSingleCells/database.html (*56*, *542*). Cell clusters are as defined by the authors: PC: pericytes; vSMC: venous VSMCs; aSMC: arterial VSMCs; aaSMC: arteriolar VSMCs; MG: microglia; FB1, FB2: fibroblast-like cells; OL: oligodendrocytes; EC1, EC2, EC3: endothelial cells; vEC: venous endothelial cells; capilEC: capillary endothelial cells; aEC: arterial endothelial cells; AC: astrocytes.

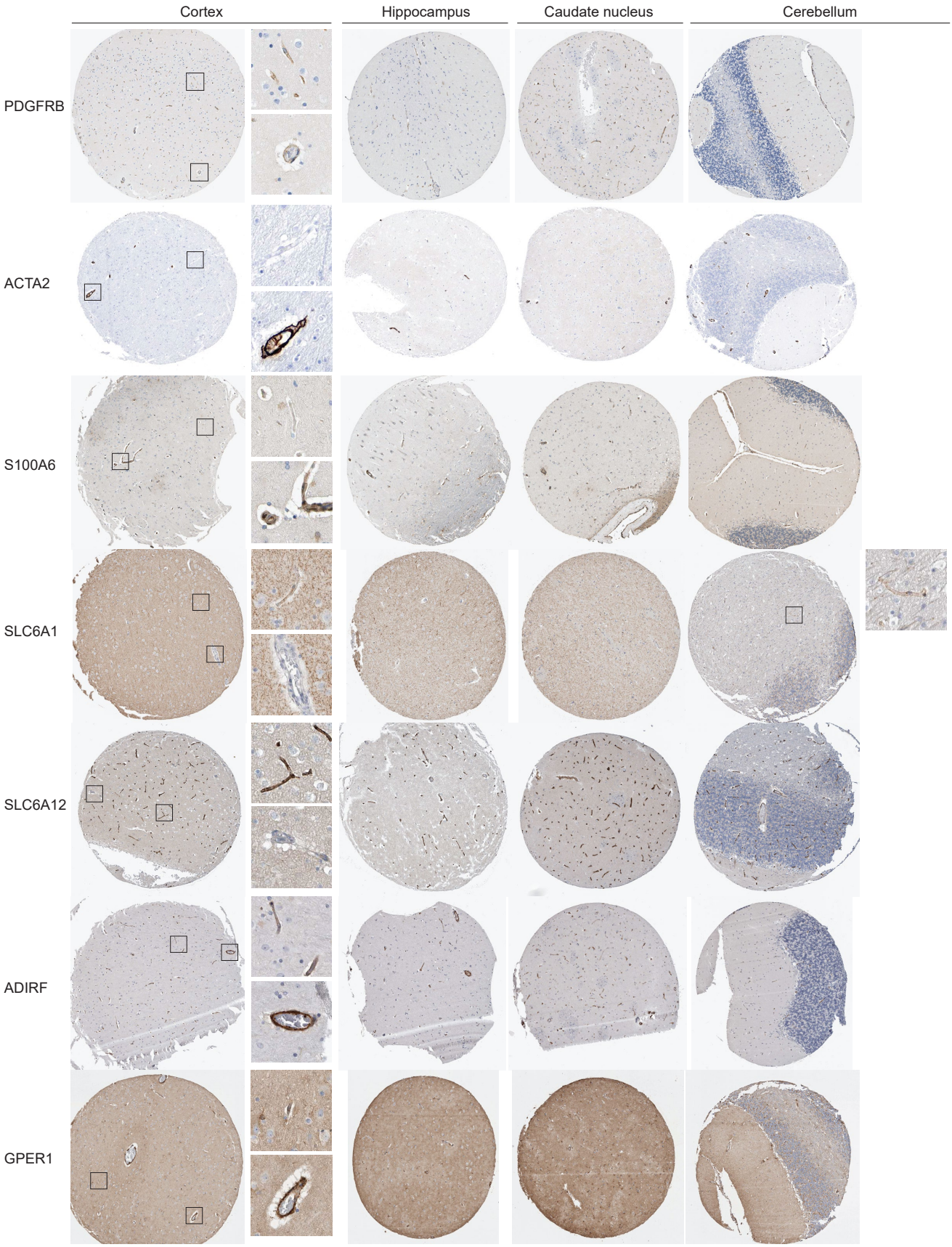
Cortex
Hippocampus
Caudate nucleus
Cerebellum
PDGFRB
ACTA2
S100A6
SLC6A1
SLC6A12
ADIRF
GPER1

Figure 4.7. Mural cell-enriched protein expression in multiple brain regions. Human Protein Atlas (*507*) (v19.proteinatlas.org) immunohistochemistry data for PDGFRB, ACTA2, S100A6, SLC6A1, SLC6A12, ADIRF, and GPER1 expression in human cortex, hippocampus, caudate nucleus, and cerebellum. Enlarged images of microvessels and large vessels are shown for each cortex image and an enlarged image of a $SLC6A1^{+}$ microvessel is shown for the cerebellum image. URLs for each image are provided in Table 4.3.

4.4.3 Mouse-human species differences in brain pericyte gene expression

We next applied our combined human brain pericyte single cell transcriptomic dataset to evaluate potential mouse-human species differences in brain pericyte gene expression. We used a mouse brain vascular scRNA-seq dataset (*56*, *542*) for initial comparison (Figure 4.8A). We chose to focus on pericytes given that all five human source datasets contributed substantially to the pericyte sub-cluster, and the average sequencing depth of human and mouse pericytes was more closely matched than that of human and mouse VSMCs (Figure 4.9A). We visualized the mouse dataset by UMAP embedding and overlaid the authors' cell type annotations (Figure 4.8B) and expression of the mural cell marker genes *Pdgfrb*, *Rgs5*, and *Acta2* (Figure 4.8C). Mural cells, including pericytes (PC) and arterial, arteriolar, and venous VSMCs (aSMC, aaSMC, and vSMC, respectively), formed a cluster distinct from endothelial cells, fibroblast-like cells, and small populations of other cell types (Figure 4.8B). The VSMC cluster was spatially distinct from the pericyte cluster and was *Acta2*$^{+}$ (Figure 4.8B,C), consistent with the authors' report (*56*).

We used differential expression analysis to compare homologous gene expression in human brain pericytes (cluster 0' in Figure 4.3F) versus mouse brain pericytes (cluster PC in Figure 4.8B). We identified 541 mouse-enriched genes, including *Atp13a5*, *Slc6a20a*, and *Sod3*, and 168 human-enriched genes including *DCN*, *PPIA*, *FRZB*, *SLC6A1*, *FN1*, and *MGLL* ($P < 0.05$, log(fold change) > 0.25, expressed by at least 50% of cells in either the human or mouse pericyte cluster), excluding mitochondrial and ribosomal genes (Figure 4.8D; Supplementary Table S4). A majority of human and mouse pericytes expressed *PDGFRB*, *RGS5*, and *PTN*, a majority of human and mouse VSMCs expressed *ACTA2*, and a similar proportion of human and mouse VSMCs expressed *CNN1* (i.e., putative arterial VSMCs) (Figure 4.8E). *RGS4*, *SNX33*, *VTN*, *PLXDC2*, and *SLC22A8* were strongly enriched in mouse pericytes compared to human

pericytes, and all except *SLC22A8* were also expressed by some mouse and nearly no human VSMCs (Figure 4.8E). *Vtn* is robustly and selectively expressed in mouse brain pericytes, and absence of *VTN* transcript in human brain pericytes is consistent with our previous observations (*90*). *DCN* (encoding decorin), *FN1* (fibronectin), *PPIA* (proinflammatory cytokine cyclophilin A), *FRZB* (Wnt-binding frizzled-related protein), and *SLC6A1* (GABA transporter) were strongly enriched in human pericytes compared to mouse pericytes, and similar to the mouse-enriched case, many were also enriched in human VSMCs compared to mouse VSMCs (Figure 4.8E). In adult mouse brain, *Dcn* and *Fn1* are enriched in fibroblast-like cells and endothelial cells, respectively (*56*). While *DCN* is also expressed by human fibroblast-like cells (Figure 4.3D) and *FN1* by human brain endothelial cells (Figure 4.5C), human-enrichment of these genes in pericytes suggests that the pericyte contribution to the vascular basement membrane may differ between human and mouse.

We validated a subset of human- and mouse-enriched genes using an additional mouse scRNA-seq dataset (*372*), identifying the authors' cluster PER3 as containing a relatively pure population of brain pericytes (*Pdgfrb*$^{+}$*Rgs5*$^{+}$*Cldn5*$^{-}$*Acta2*$^{-}$*Col1a1*$^{-}$) (Figure 4.9C). Consistent with the mouse dataset used for differential expression analysis, cells in the PER3 cluster had little to no expression of *Slc6a1*, *Slc6a12*, *Frzb*, *Dcn*, and *Fn1* and did express *Slc6a20a* and *Vtn* (Figure 4.9C). Some pericytes in the PER3 cluster (~43%) expressed *Ppia*, however, suggesting that populations of both human and mouse pericytes express this gene, consistent with previous protein-level and functional observations (*381*). Together, these data validate several human brain pericyte markers previously identified in mouse, but also highlight key transcriptional differences between brain pericytes in these two species. These species-specific pericyte genes motivate future examination of functional differences between human and mouse brain pericytes, for example, in regulation of Wnt signaling (*FRZB*), GABA uptake/transport *(SLC6A1*), and

vascular extracellular matrix composition. Finally, this human brain mural cell dataset can aid in the design and interpretation of experiments in murine models.

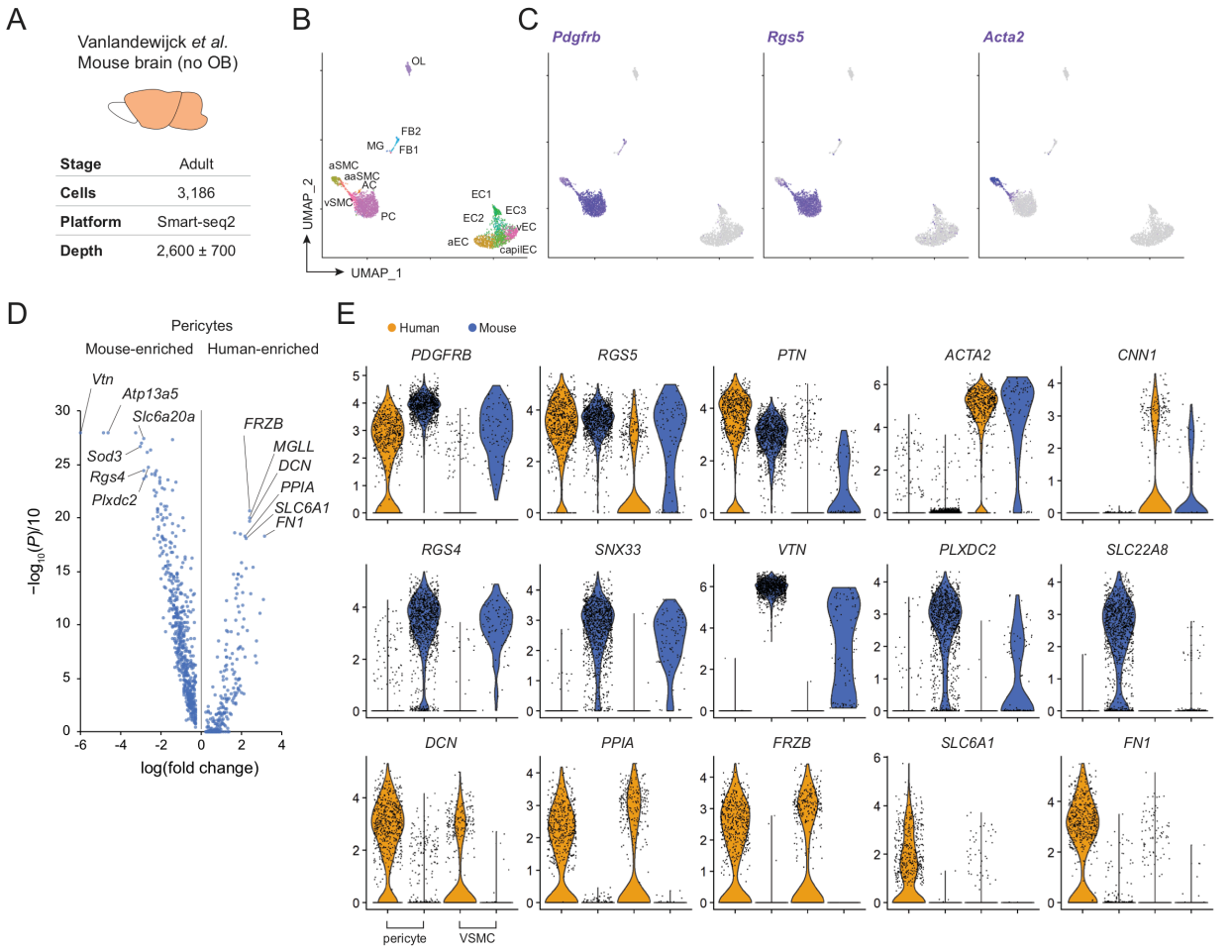

Figure 4.8. Human-mouse species differences in brain pericyte gene expression. (A) Overview of the mouse brain vascular scRNA-seq dataset. The sampled brain region, developmental stage, total number of cells analyzed, scRNA-seq platform, and sequencing depth (mean ± SD of genes detected per cell), are indicated. OB: olfactory bulb. (B) UMAP plot of mouse brain vascular single cells. Plotted points (cells) are colored by cluster identity. Cluster identities are as assigned by Vanlandewijck, He *et al.* (*56*, *542*). OL: oligodendrocytes; FB1, FB2: fibroblast-like cells; aEC: arterial ECs; vEC: venous ECs; capilEC: ECs; EC1, EC2, EC3: other EC subtypes; MG: microglia; PC: pericytes; AC: astrocytes; aSMC: arterial VSMCs; aaSMC: arteriolar VSMCs; vSMC: venous VSMCs. (C) UMAP plots of mouse brain vascular single cells. Plotted points (cells) are colored by expression of *Pdgfrb*, *Rgs5*, or *Acta2*. (D) Volcano plot illustrating differential expression analysis of human brain pericytes (Figure 4.3F, cluster 0') and mouse brain pericytes. Mitochondrial genes, ribosomal genes, genes with log(fold change) < 0.25, and genes expressed by fewer than 50% of human or mouse pericytes were excluded. Complete results of differential expression analysis are provided in Supplementary Table S4. (E) Expression of selected genes in human and mouse brain pericytes and VSMCs. Genes with expression consistent across species (top row), mouse-enriched expression ($P < 0.05$; middle row), and human-enriched expression ($P < 0.05$; bottom row) are shown.

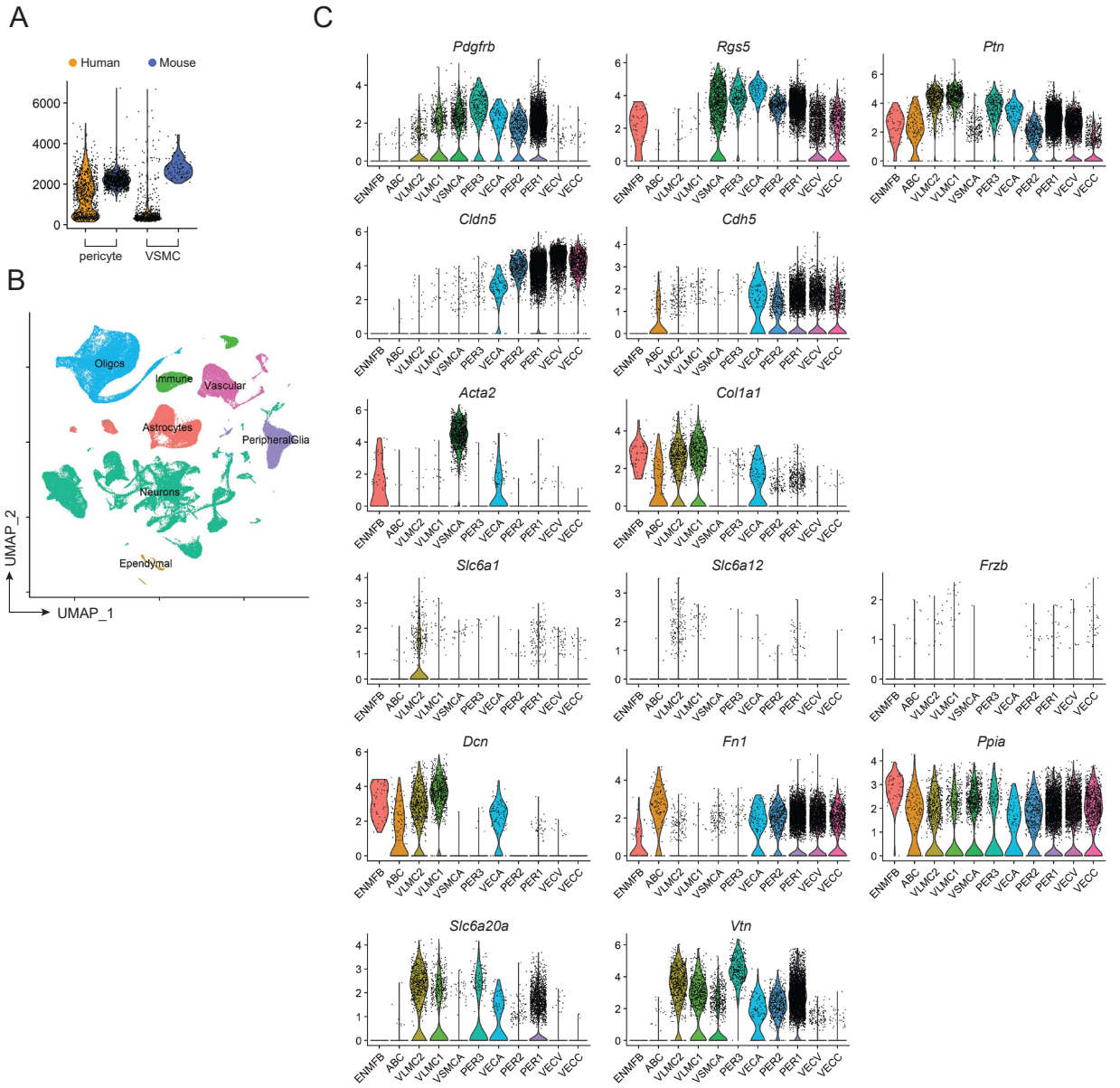

Figure 4.9. Human-enriched brain pericyte gene expression. (A) Comparison of sequencing depth (number of distinct features detected per cell) in the combined human brain pericyte and VSMC datasets (clusters 0' and 1' in Figure 4.3F) and mouse brain pericyte and VSMC (vSMC, aSMC, and aaSMC) datasets as identified by Vanlandewijck, He *et al.* (*56*, *542*). (B) UMAP plot of mouse nervous system single cells. Plotted points (cells) are colored by cell class as annotated by Zeisel *et al.* (*372*). (C) Expression of selected genes in mouse nervous system vascular single cell clusters. Markers shared between human and mouse pericytes (*Pdgfrb, Rgs5, Ptn*; top row), endothelial cells (*Cldn5, Cdh5*; second row), VSMCs and fibroblast-like cells (*Acta2* and *Col1a1*, respectively; third row), are shown. Human-enriched pericyte genes (*Slc6a1*, *Slc6a12*, *Frzb*; fourth row) and mouse-enriched pericyte genes (*Slc6a20a*, *Vtn*; fifth row) are also shown. Cluster identities are as assigned by Zeisel *et al.* (*372*). ENMFB: enteric mesothelial fibroblasts ABC: arachnoid barrier cells; VLMC1, VLMC2: vascular leptomeningeal cells; PER1, PER2, PER3: pericytes; VSMCA: vascular smooth muscle cells, arterial; VECA: vascular endothelial cells, arterial; VECV: vascular endothelial cells, venous; VECC: vascular endothelial cells, capillary.

4.4.4 Transcriptional alterations in brain pericytes cultured in vitro

Primary cell culture is widely employed to study human brain pericytes, and we therefore asked whether our integrated human brain pericyte scRNA-seq dataset could be used to reveal potentially important molecular differences between *in vivo* and cultured pericytes. Cultured primary human brain pericytes from commercial sources (see Methods) are widely used and have been analyzed by bulk RNA-seq in several independent studies (*321*, *324*, *447*). To compare these data to the gene expression profile of brain pericytes *in vivo*, we constructed mock bulk RNA-seq datasets from the single cells identified as pericytes (cluster 0' in Figure 4.3F) from each source dataset (see Methods). The Pearson correlation between average log-transformed transcript abundances from cultured and *in vivo* pericytes was moderately high (r = 0.81), although numerous dysregulated genes were apparent (Figure 4.10A; Supplementary Table S5). For example, while *PDGFRB* was moderately downregulated *in vitro*, the well-established pericyte marker *KCNJ8* was highly and consistently downregulated in cultured pericytes from all three studies (Figure 4.10A,B). *P2RY14*, *COL9A1*, *SLC6A12*, *and HIGD1B* were similarly downregulated in cultured pericytes (Figure 4.10A,B). Among genes consistently upregulated in cultured pericytes were *COL1A1*, which is a marker of fibroblasts *in vivo* (Figure 4.10C), several additional collagens (*COL8A1*, *COL11A2*), and the protease inhibitor *SERPINE1* (Figure 4.10A,B). GSEA revealed that the KEGG gene set *ECM-receptor interaction* contained genes that were both highly upregulated and downregulated in cultured pericytes, effects driven by collagens, integrins, perlecan, and laminins, among others (Figure 4.10C; Supplementary Table S6). The KEGG gene set *neuroactive ligand-receptor interaction* was strongly enriched in the *in vivo* pericyte dataset, an effect driven by metabotropic glutamate receptor genes (*GRM3*, *GRM8*), the purinurgic receptor *P2RY14* identified above, the endothelin receptor *EDNRB*, and the sphingosine-1-phosphate receptor *S1PR3*, among others (Figure 4.10C). Collectively, these

data suggest that while cultured human brain pericytes retain expression of some key markers and have moderately well-correlated global gene expression profile, they downregulate receptors for neuroactive ligands when compared to pericytes *in vivo* and have markedly dysregulated extracellular matrix (ECM)-associated gene expression.

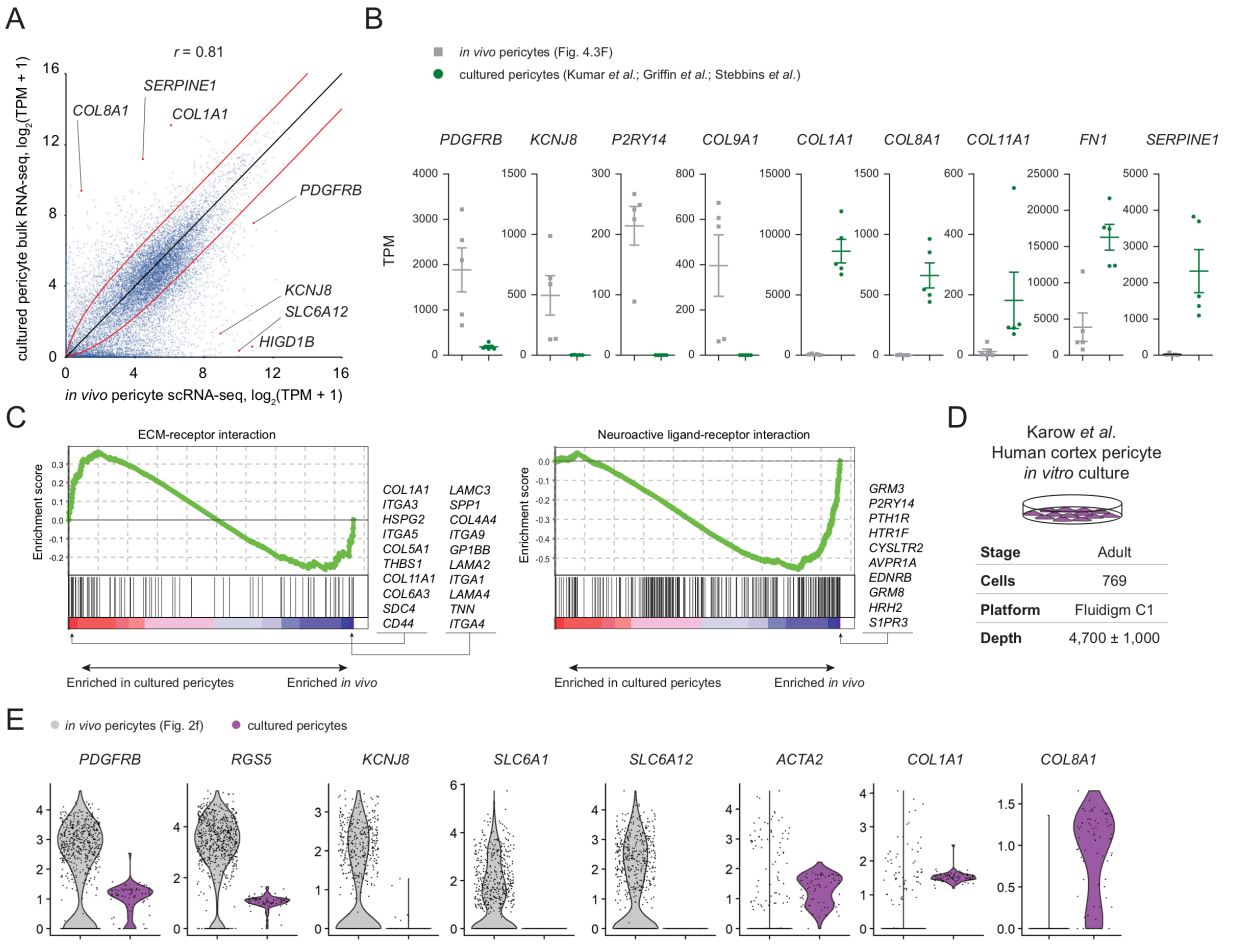

Figure 4.10. Transcriptional alterations in brain pericytes cultured *in vitro*. (A) Comparison of gene expression in cultured human pericytes as quantified by bulk RNA-seq and *in vivo* human pericytes as quantified by constructing a mock bulk RNA-seq dataset from *in vivo* pericyte scRNA-seq data (Figure 4.3F, cluster 0'). The Pearson correlation coefficient (r) is shown. Red lines indicate $\log_2$(fold change) = ±2. Complete expression data are provided in Supplementary Table S5. (B) Comparison of expression of selected genes in mock bulk RNA-seq data from *in vivo* pericytes (Figure 4.3F, cluster 0') and bulk RNA-seq data from cultured pericytes. Average expression for each of the five *in vivo* pericyte datasets is indicated with a gray point. Expression in five bulk RNA-seq datasets from cultured pericytes are indicated with green points. Bars indicate the mean. (C) GSEA enrichment plots for the *ECM-receptor interaction* and *neuroactive ligand-receptor interaction* gene sets. The GSEA input was a list of genes ranked from cultured pericyte-enriched to *in vivo* pericyte-enriched gene based on log(fold change). The 10 genes in each gene set with highest and/or lowest rank are indicated at right. Complete results of GSEA are provided in Supplementary Table S6. (D) Overview of the cultured human brain pericyte scRNA-seq dataset. The sampled brain region, developmental stage, total number of cells analyzed, scRNA-seq platform, and sequencing depth (mean ± SD of genes detected per cell) are indicated. (E) Expression of selected genes in *in vivo* pericytes (Figure 4.3F, cluster 0') and cultured pericytes as described in (D) and Figure 4.11. Genes with culture-induced downregulation (left) and genes with culture-induced upregulation (right) are shown.

To address the possibility that upregulation of *COL1A1* and other ECM-related genes actually reflects proliferation of contaminating fibroblast-like cells in pericyte cultures, rather than culture-induced dedifferentiation of pericytes, we analyzed scRNA-seq data from cultured human brain pericytes (*597*) (Figure 4.10D). We selected control (non-transfected) pericytes that were acutely isolated and cultured for two days *in vitro* for further analysis (Figure 4.11A). The control cells formed two spatially distinct clusters when visualized by UMAP embedding, but both clusters expressed *PDGFRB* and *RGS5* (Figure 4.11B,C). We compared expression of key genes in human brain pericytes *in vivo* (cluster 0' in Figure 4.3F) and these cultured human brain pericytes. While *PDGFRB* and *RGS5* were downregulated in cultured pericytes, nearly all cells still expressed these genes; conversely, the pericyte marker *KCNJ8* was downregulated in cultured pericytes to the point where most cells did not have detectable expression of this gene (Figure 4.10E). Similarly, most cultured pericytes did not express detectable levels of *SLC6A1* and *SLC6A12* (Figure 4.10E). Consistent with previous observations that pericytes rapidly upregulate α-smooth muscle actin (α-SMA) *in vitro* (*417*), the cultured pericytes had elevated levels of *ACTA2* transcript (Figure 4.10E). Finally, all cultured pericytes expressed *COL1A1* and many expressed *COL8A1* and other collagens that were not expressed by pericytes *in vivo* (Figure 4.10E). The presence of $RGS5^{+}COL1A1^{+}$ cells suggests that the dysregulated ECM gene signature identified in bulk RNA-seq of cultured brain pericytes is not the result of a population of contaminating $COL1A1^{+}$ fibroblast-like cells. Together, these data support the notion that culture induces dedifferentiation/activation of brain pericytes marked by downregulation of neuroactive receptors and upregulation of fibroblast and VSMC gene signatures, among other transcriptional changes. Thus, these datasets should be useful for detailed evaluation of *in vitro* models based on presence or absence of relevant genes.

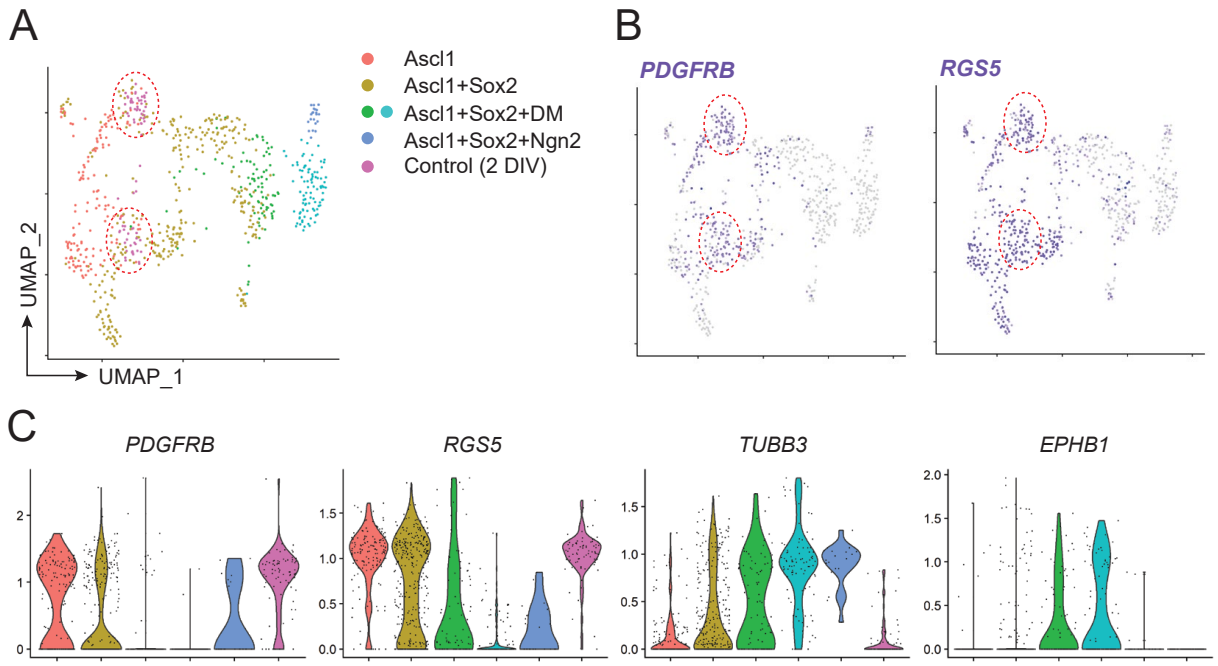

Figure 4.11. scRNA-seq analysis of human brain pericytes cultured *in vitro*. (A) UMAP plot of cultured human brain pericyte single cells. Plotted points (cells) are colored by experimental treatment as reported by Karow *et al.* (*597*). Dashed circles mark the control (non-transfected) cell clusters selected for further analysis. (B) UMAP plots of cultured human brain pericyte single cells. Plotted points (cells) are colored by expression of *PDGFRB* or *RGS5*. Dashed circles mark the clusters as described in (A). (C) Expression of mural (*PDGFRB, RGS5*) and neuronal (*TUBB3, EPHB1*) marker genes in human brain pericytes cultured *in vitro*. Cells are grouped and colored by experimental treatment as reported by Karow *et al.* (*597*) and correspond to the UMAP plot in (A).

4.4.5 Human mural cell organotypicity

The specialized functions of brain mural cells in regulating the neurovascular unit are likely established by brain-selective gene expression. We therefore attempted to use the integrated human brain mural cell scRNA-seq dataset (Figure 4.3F) to identify shared and distinct gene expression profiles by comparison to mural cells in human liver, lung, heart, and skeletal muscle scRNA-seq datasets (*598–601*). Characteristics of these datasets are shown in Figure 4.12A. As before, we performed dimensionality reduction and unbiased clustering of the cells in each dataset, and identified putative mural cell clusters by visualizing expression of the canonical markers *PDGFRB*, *RGS5*, and *ACTA2* (Figure 4.12B). Because some datasets had too few cells or inadequate sequencing depth to fully resolve distinct mural cell subtypes (i.e.,

pericytes and VSMCs), we instead elected to make comparisons between the combined mural cell clusters from different organs. We identified markers of the mural cell clusters from each organ, defined as genes enriched in the putative mural cell cluster(s) relative to all other cells in the same organ ($P < 0.05$, log(fold change) > 0.25, expressed by at least 25% of cells in the putative mural cell cluster(s)) (Supplementary Table S7). 17 genes were identified as markers of mural cells in all five organs (Figure 4.13A,B): in addition to *PDGFRB* and *RGS5*, additional highly-enriched genes included *IGFBP7*, *TPM2*, *CALD1*, *BGN*, and *SPARC* (Figure 4.13C). An additional 37 genes were identified as markers of mural cells in four out of five organs, including known markers such as *ACTA2*, *COL4A1*, *MYL9*, *NOTCH3*, and *TAGLN* (Figure 4.13D). Further, *KCNJ8* was identified as a mural cell marker in four out of five organs, extending the potential utility of this gene that was previously identified as a pericyte marker in the brain (*342*) (Figure 4.13D).

We next compared gene expression in the mural cell clusters between the five organs to identify potential organ-specific differences. We focused on identifying genes with brain-enriched expression, as the mural cell clusters from some peripheral organ scRNA-seq datasets appeared to contain multiplets or non-resolvable populations of non-mural cells, exemplified by expression of the hepatocyte marker *ALB* in the liver mural cell cluster (Figure 4.12C). We found several genes with enriched expression in brain mural cells ($P < 0.05$, log(fold change) > 0.25, excluding mitochondrial and ribosomal genes) including *ATP1A2* (encoding a Na^+/K^+ ATPase subunit), *SLC6A1* and *SLC6A12* (GABA/betaine transporters), *GPER1* (G protein-coupled estrogen receptor), *ZIC1* (neural crest lineage transcription factor), and *NTM* (neurotrimin, a GPI-anchored cell adhesion molecule) (Figure 4.13E; Supplementary Table S7). Importantly, the brain-enriched mural cell genes *ATP1A2*, *SLC6A1*, *SLC6A12*, and *GPER1* were consistently expressed in pericytes from all five human brain scRNA-seq source datasets (Figure 4.13F),

suggesting that these genes are expressed across multiple brain regions and developmental stages. Further, we observed vascular localization of SLC6A1, SLC6A12, and GPER1 immunoreactivity in Human Protein Atlas data from multiple brain regions (Figure 4.7). We also found that a majority of brain-enriched mural cell genes were downregulated in cultured pericytes (Figure 4.12D; Supplementary Table S7), supporting the possibility that environmental cues are required to maintain organ-specific gene expression. Together, this analysis permits identification of brain mural cell-enriched genes, which may yield hypotheses for mechanisms underlying the unique functions of brain mural cells. Our combined brain scRNA-seq dataset should facilitate further identification of mural cell gene expression organotypicity as additional high-resolution scRNA-seq datasets from human peripheral organs become available.

4.4.6 Validation of human brain mural cell genes

We selected *FRZB*, *ATP1A2*, *SLC6A1*, and *SLC6A12*, genes identified in the bioinformatic analyses described above, for further validation. We assessed *FRZB* expression because it was identified as a brain mural cell marker, enriched in human mural cells versus mouse, and also expressed by human mural cells of other organs (Supplementary Table S7). This Wnt-binding protein might help modulate Wnt-mediated CNS angiogenesis and barriergenesis. We assessed *ATP1A2* expression because it was identified as a brain mural cell marker, enriched in pericytes versus VSMCs, and was the gene with the highest enrichment in human brain mural cells compared to mural cells of other organs. Furthermore, mutations in *ATP1A2* are associated with familial hemiplegic migraine and potentially other neurological disorders (reviewed in (*607*)). Thus, while *ATP1A2* is also expressed by neurons and glia (*607*), confirming pericyte expression of this gene may advance understanding of cell type-specific contributions to these disorders. Finally, we assessed *SLC6A12* and *SLC6A1* expression given that both genes were identified as brain mural cell markers, highly enriched in pericytes compared to VSMCs,

enriched in human mural cells versus mouse, absent in cultured pericytes, and absent in mural cells of other organs. These solute carriers might fulfill functional roles in GABA or betaine uptake by human pericytes. Importantly, all four of these putative mural cell markers were not identified as shared markers of endothelial cells (Supplementary Table S2).

A

	Cui *et al.* Heart	Aizarani *et al.* Liver	Travaglini *et al.* Lung	Rubenstein *et al.* Skeletal muscle
Stage	GW5-25	Adult	Adult	Adult
Cells	4,948	12,622	65,662	2,876
Platform	STRT-seq	mCEL-Seq2	10x Chromium	10x Chromium
Depth	3,800 ± 1,800	1,400 ± 960	1,900 ± 1,200	640 ± 310

B

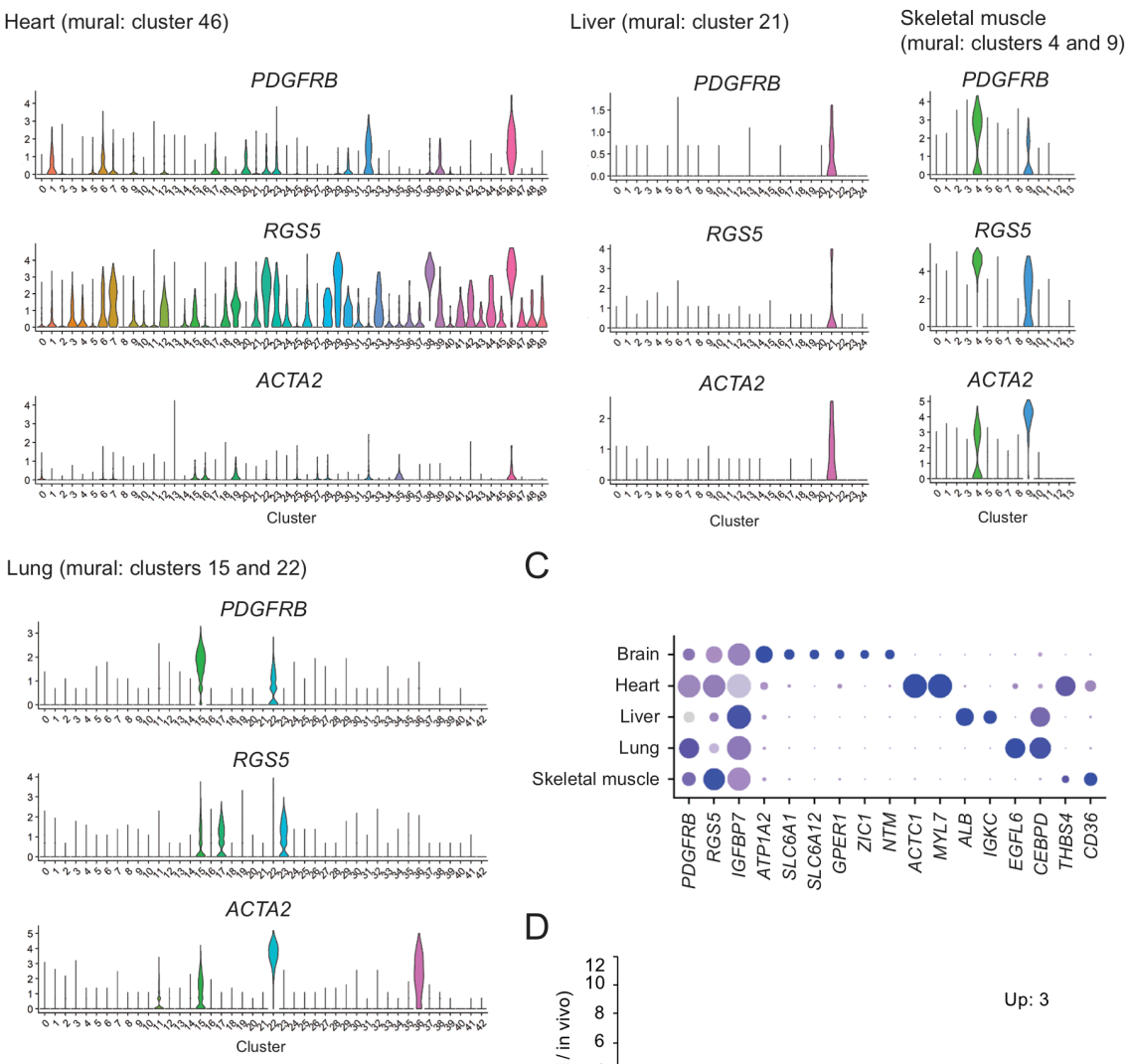

C

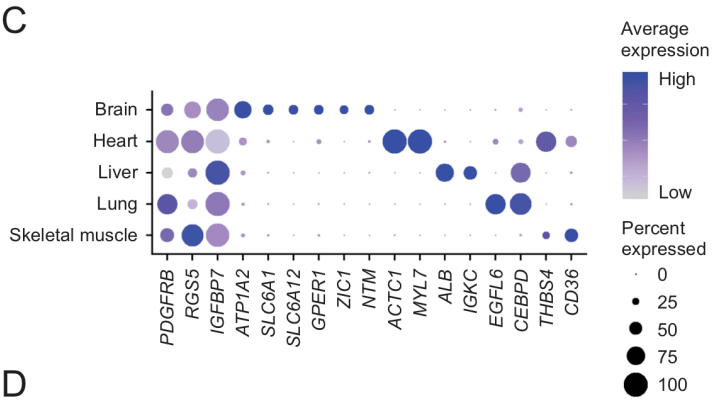

D

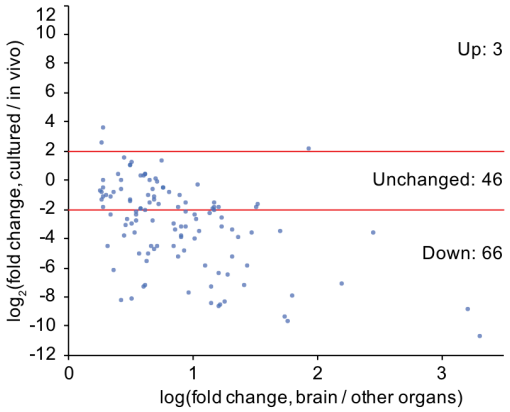

Figure 4.12. Mural cell populations in other organs. (A) Overview of the human heart, liver, lung, and skeletal muscle scRNA-seq datasets. For each dataset, the developmental stage, total number of cells analyzed, scRNA-seq platform, and sequencing depth (mean ± SD of genes detected per cell), are indicated. GW: gestational week. (B) Expression of mural cell markers (*PDGFRB*, *RGS5*, and *ACTA2*) in clusters identified in each scRNA-seq dataset. The putative mural cell cluster(s) for each organ is shown above each set of plots. (C) Dot plot of gene expression in the mural cell cluster(s) from multiple organs. Genes with shared expression across mural cells of the five organs and genes with organ-specific expression are shown. Color indicates expression level and dot size indicates the fraction of cells that express a given gene. (D) Comparison of gene enrichment in cultured human pericytes versus *in vivo* human pericytes for those genes identified as enriched in brain mural cells versus mural cells of organs ($P < 0.05$, log(fold change) > 0.25, expressed in at least 25% of brain mural cells). Red lines indicate $\log_2$(fold change) = ±2. Of the 115 protein-coding genes enriched in brain mural cells versus mural cells of organs, the number upregulated ($\log_2$(fold change) > 2), downregulated ($\log_2$(fold change) < –2), or approximately unchanged in culture are shown. Gene lists and numerical data are provided in Supplementary Table S7.

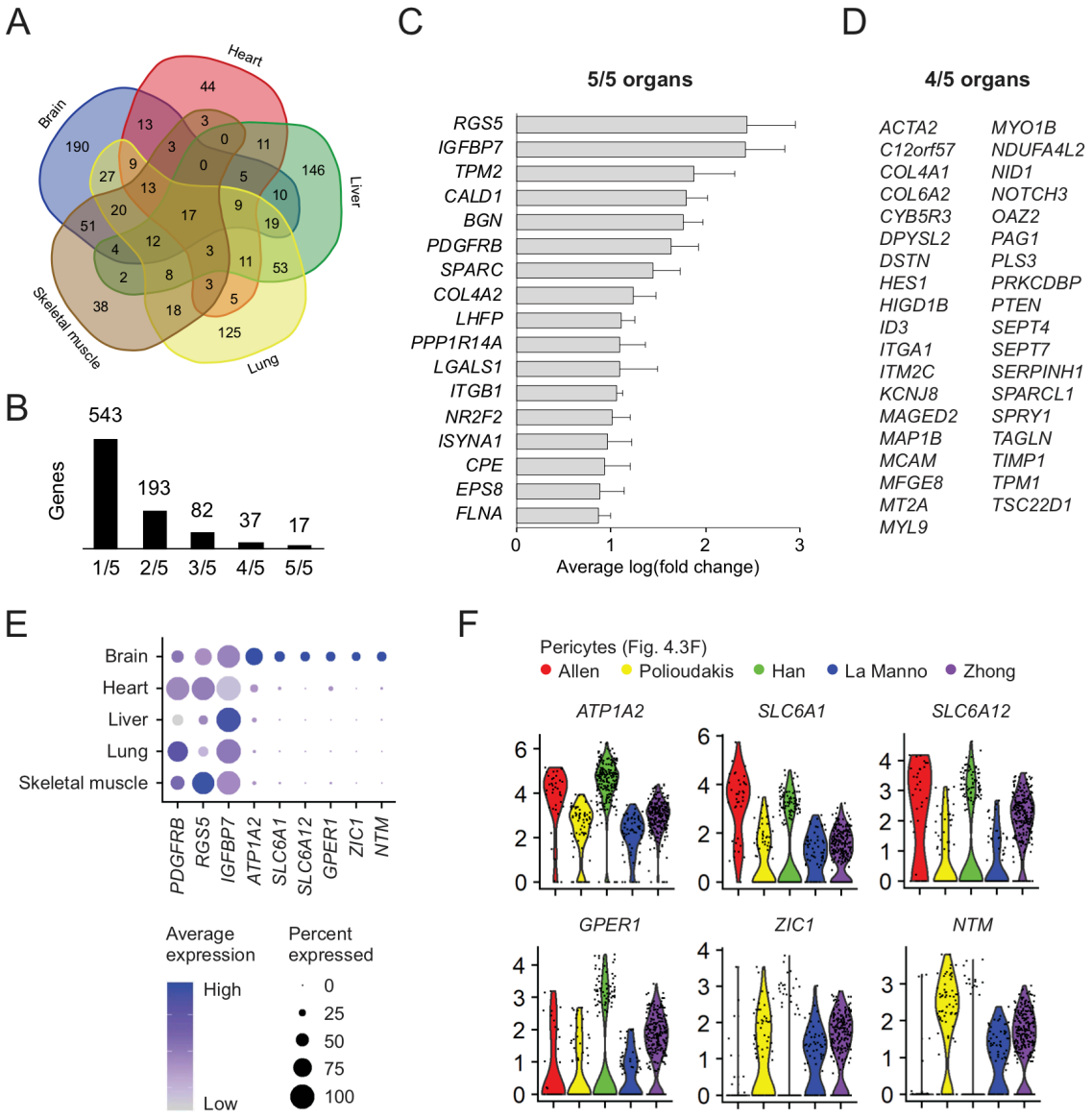

Figure 4.13. Shared and distinct gene expression profiles of mural cells of multiple organs. (A) Venn diagram depicting the number of genes identified as markers of mural cells ($P < 0.05$, average log(fold change) > 0.25, expressed by at least 25% of cells in the putative mural cell cluster(s)) in the scRNA-seq datasets from five organs. The brain mural cells analyzed were from the integrated dataset (Figure 4.3B, cluster 30). Overviews and cluster identification for the heart, liver, lung, and skeletal muscle scRNA-seq datasets are shown in Figure 4.12. Complete lists of marker genes are provided in Supplementary Table S7. (B) Number of genes identified as markers of mural cells in a single organ (1/5) or multiple organs. 17 genes were identified as markers of mural cells in all organs (5/5). (C) Average log(fold change) of gene expression in mural cell clusters compared to all other cells in the corresponding organ for the 17 genes identified as markers of mural cells in all five organs. Points represent average log(fold change) from each organ and bars indicate the mean. (D) Genes identified as markers of mural cells in 4/5 organs. (E) Dot plot of gene expression in mural cells clusters from multiple organs. Genes with shared expression across mural cells of the five organs and genes with brain-enriched expression are shown. Color indicates expression level and dot size indicates the fraction of cells that express a given gene. (F) Expression of selected brain mural cell-enriched genes in pericytes from the five human brain scRNA-seq datasets.

We used RNA fluorescence *in situ* hybridization (RNAscope) to evaluate transcript expression in flash-frozen human brain neurosurgical samples. To identify mural cells and closely-associated endothelial cells, we employed the canonical markers *PDGFRB* and *CLDN5*, respectively. In resulting images, we observed sparsely distributed *PDGFRB*$^+$ and *CLDN5*$^+$ nuclei, which in some cases were closely associated (Figure 4.14A,E). We observed colocalization of *FRZB* and *ATP1A2* with *PDGFRB*$^+$, but not *CLDN5*$^+$, nuclei (Figure 4.14A-C; Figure 4.15), with significant enrichment of *FRZB* and *ATP1A2* mean fluorescence intensity in *PDGFRB*$^+$ nuclei compared to parenchymal (*CLDN5*$^-$*PDGFRB*$^-$) nuclei (Figure 4.14D). While robust *ATP1A2* signals were associated with most *PDGFRB*$^+$ nuclei, we observed a comparative lack of *ATP1A2* signal in *PDGFRB*$^+$ nuclei in a large diameter vessel (Figure 4.15), consistent with enriched expression in pericytes compared to VSMCs. We also observed colocalization of *SLC6A12* and *SLC6A1* with *PDGFRB*$^+$ mural cell nuclei (Figure 4.14E-G; Figure 4.16), with significant enrichment of *SLC6A1* mean fluorescence intensity in *PDGFRB*$^+$ nuclei compared to parenchymal (*CLDN5*$^-$*PDGFRB*$^-$) nuclei (Figure 4.14H). These *in situ* data therefore support the scRNA-seq-based identification of *FRZB*, *ATP1A2*, *SLC6A1*, and *SLC6A12* as novel human brain mural cell-expressed genes. Finally, to validate one such differentially expressed gene on the protein level, we stained human and mouse brain tissue sections for FRZB. Consistent with scRNA-seq data, we detected FRZB colocalization with PDGFRβ$^+$ mural cells in human brain, but did not detect vascular FRZB immunoreactivity in mouse brain, although mouse olfactory ensheathing cells, which express *Frzb* transcript (*608*, *609*), did have FRZB immunoreactivity (Figure 4.17).

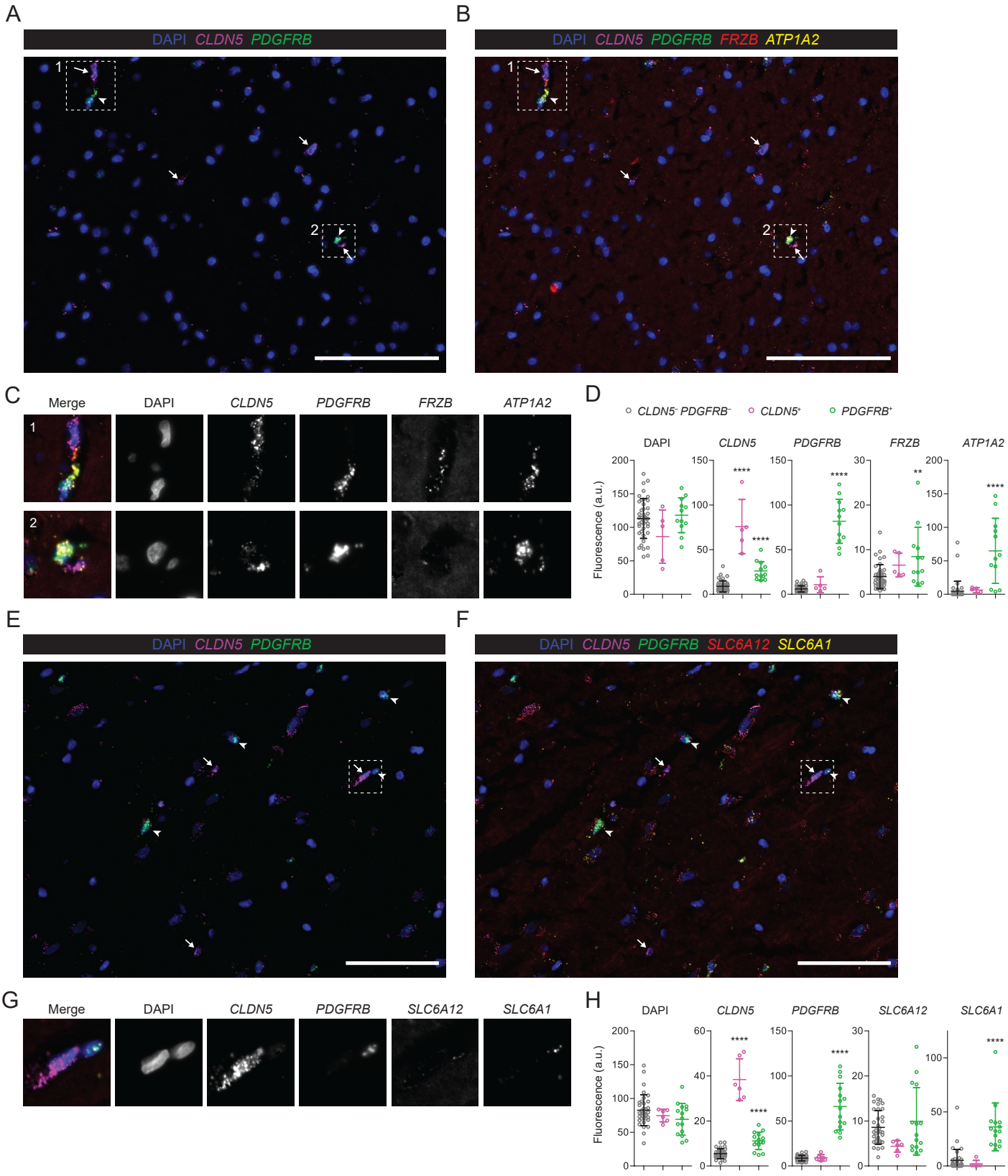
A
DAPI CLDN5 PDGFRB
B
DAPI CLDN5 PDGFRB FRZB ATP1A2
C
Merge
DAPI
CLDN5
PDGFRB
FRZB
ATP1A2
D
CLDN5⁻ PDGFRB⁻
CLDN5⁺
PDGFRB⁺
Fluorescence (a.u.)
E
DAPI CLDN5 PDGFRB
F
DAPI CLDN5 PDGFRB SLC6A12 SLC6A1
G
Merge
DAPI
CLDN5
PDGFRB
SLC6A12
SLC6A1
H
Fluorescence (a.u.)

Figure 4.14. RNA fluorescence *in situ* hybridization validates novel human mural cell genes. (A) Expression of *CLDN5* and *PDGFRB* mRNA in a human brain tissue section. *CLDN5*$^{+}$ endothelial cells are indicated with arrows; *PDGFRB*$^{+}$ mural cells are indicated with arrowheads. DAPI nuclear counterstain is also shown. Scale bar: 100 μm. (B) Same image field as in (A) with expression of *FRZB* and *ATP1A2* overlaid. Dashed boxes indicate regions displayed in (C). Scale bar: 100 μm. (C) Enlarged regions 1 and 2 of image as indicated in (B). Merged image displays all five channels with colors as defined in (B). Data from an additional human brain sample are shown in Figure 4.15. (D) Quantification of DAPI, *CLDN5*, *PDGFRB*, *FRZB*, and *ATP1A2* mean fluorescence intensity in endothelial cell nuclei (*CLDN5*$^{+}$, $n = 5$), mural cell nuclei (*PDGFRB*$^{+}$, $n = 12$), and non-endothelial/non-mural cell nuclei (*CLDN5*$^{-}$*PDGFRB*$^{-}$, $n = 42$). Mean ± SD is shown. * $P < 0.05$, ** $P < 0.01$, *** $P < 0.001$, **** $P < 0.0001$ versus *CLDN5*$^{-}$*PDGFRB*$^{-}$, Kruskal-Wallis test followed by Steel-Dwass test. (E) Expression of *CLDN5* and *PDGFRB* mRNA in a human brain tissue section. *CLDN5*$^{+}$ endothelial cells are indicated with arrows; *PDGFRB*$^{+}$ mural cells are indicated with arrowheads. DAPI nuclear counterstain is also shown. Scale bar: 100 μm. (F) Same image field as in (E) with expression of *SLC6A12* and *SLC6A1* overlaid. Dashed box indicates region displayed in (G). Scale bar: 100 μm. (G) Enlarged region of image as indicated in (F). Merged image displays all five channels with colors as defined in (F). Data from an additional human brain sample are shown in Figure 4.16. (h) Quantification of DAPI, *CLDN5*, *PDGFRB*, *SLC6A12*, and *SLC6A1* mean fluorescence intensity in endothelial cell nuclei (*CLDN5*$^{+}$, $n = 6$), mural cell nuclei (*PDGFRB*$^{+}$, $n = 15$), and non-endothelial/non-mural cell nuclei (*CLDN5*$^{-}$*PDGFRB*$^{-}$, $n = 35$). Mean ± SD is shown. * $P < 0.05$, ** $P < 0.01$, *** $P < 0.001$, **** $P < 0.0001$ versus *CLDN5*$^{-}$*PDGFRB*$^{-}$, Kruskal-Wallis test followed by Steel-Dwass test.

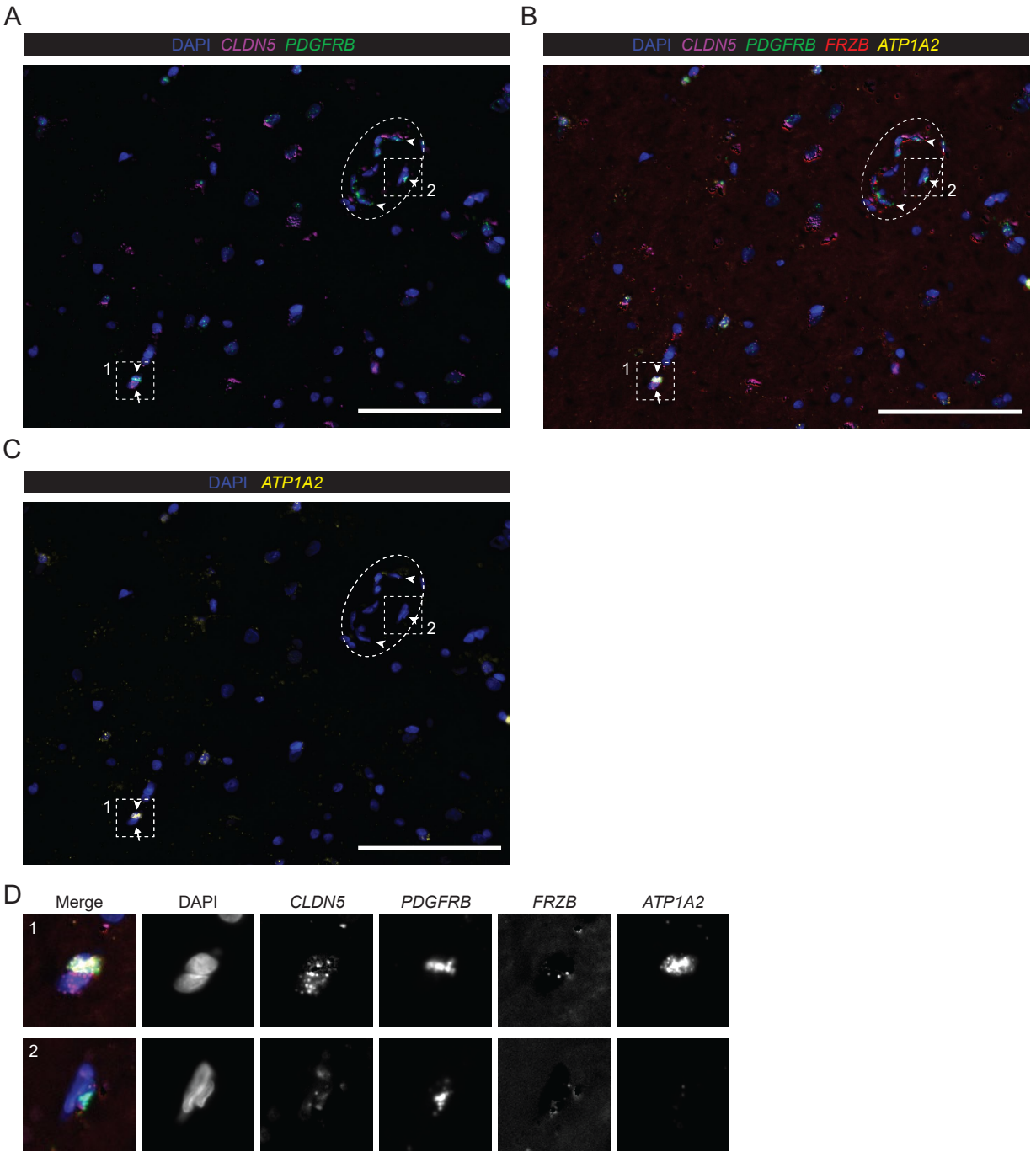

Figure 4.15. RNA *in situ* hybridization data from an additional human brain sample (*FRZB*/*ATP1A2*). (A) Expression of *CLDN5* and *PDGFRB* mRNA in a human brain tissue section. *CLDN5*$^{+}$ endothelial cells are indicated with arrows; *PDGFRB*$^{+}$ mural cells are indicated with arrowheads. Dashed ellipse indicates a large diameter vessel. DAPI nuclear counterstain is also shown. Scale bar: 100 µm. (B) Same image field as in (A) with expression of *FRZB* and *ATP1A2* overlaid. Dashed box indicates region displayed in (D). Scale bar: 100 µm. (C) Same image field as in (A) with *ATP1A2* and DAPI only shown. Scale bar: 100 µm. (D) Enlarged region of image as indicated in (B). Merged image displays all five channels with colors as defined in (B).

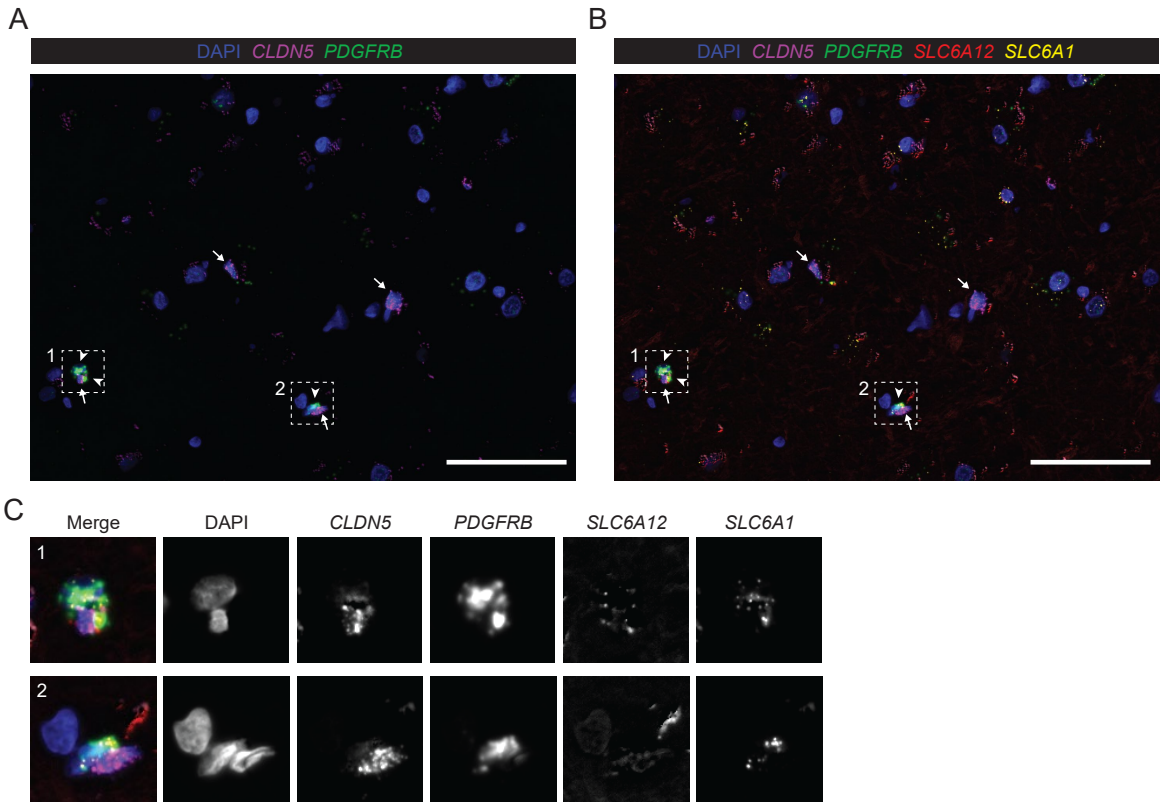

Figure 4.16. RNA *in situ* hybridization data from an additional human brain sample (*SLC6A12*/*SLC6A1*). (A) Expression of *CLDN5* and *PDGFRB* mRNA in a human brain tissue section. *CLDN5*$^{+}$ endothelial cells are indicated with arrows; *PDGFRB*$^{+}$ mural cells are indicated with arrowheads. DAPI nuclear counterstain is also shown. Scale bar: 100 µm. (B) Same image field as in (A) with expression of *SLC6A12* and *SLC6A1* overlaid. Dashed boxes indicate regions displayed in (C). Scale bar: 100 µm. (C) Enlarged regions 1 and 2 of image as indicated in (B). Merged image displays all five channels with colors as defined in (B).

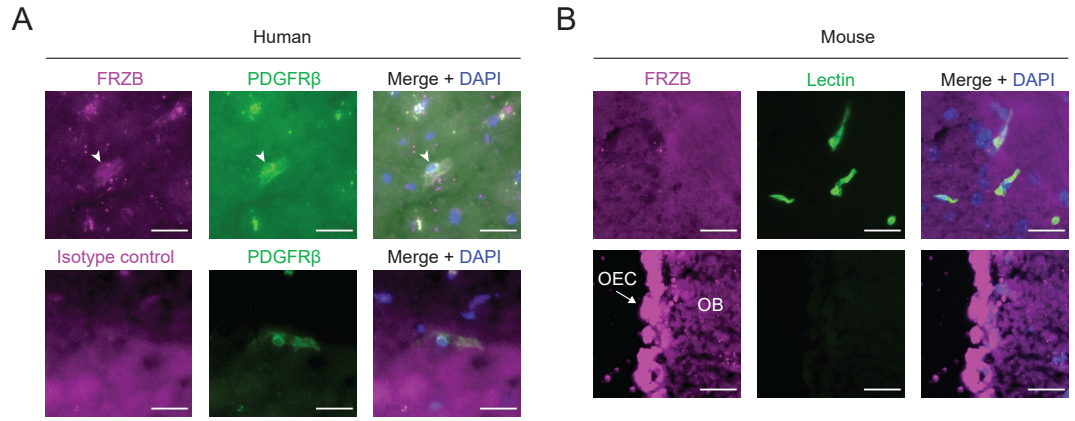

Figure 4.17. Immunohistochemistry analysis of FRZB expression in human and mouse brain. (A) Immunohistochemistry analysis of FRZB expression in human brain. Human brain sections were immunolabeled for FRZB and PDGFRβ (top), or mouse IgG1 isotype control and PDGFRβ (bottom). DAPI nuclear counterstain is also shown. Arrowhead indicates a pericyte with FRZB immunoreactivity. The two images were subject to the same linear brightness and contrast adjustment. Scale bars: 25 µm. (B) Immunohistochemistry analysis of FRZB expression in mouse brain. Mouse vessels were labeled with perfused lectin and sections were immunolabeled for FRZB using the same antibody as in (A). DAPI nuclear counterstain is also shown. The two images were subject to the same linear brightness and contrast adjustment, but this adjustment differed from that in (A) due to differences in tissue autofluorescence. OEC: olfactory ensheathing cells. Scale bars: 25 µm.

4.5 Discussion

Brain mural cells play important roles in neurovascular function, but remain incompletely characterized, especially in humans. scRNA-seq has the potential to reveal detailed, cell type-specific gene expression profiles that will aid in classifying distinct cell populations and identifying mechanisms of cellular function, but existing human brain scRNA-seq datasets contain exceedingly few mural cells. Further, mural cell scRNA-seq profiles are frequently underanalyzed in studies focusing on neuronal or glial diversity, yet recent studies have begun to employ scRNA-seq to better understand roles of brain mural cells in off-target effects of CAR-T therapy (*610*) and viral tropism (*611*). Here, we integrated multiple scRNA-seq datasets to increase sample size and mitigate the potential impact of technical artifacts in single datasets, exemplified by the exclusion of *PDGFRB*^{low} cells previously assigned to a mural cluster in the individual analysis of a low sequencing depth dataset (Figure 4.4A). We analyzed the gene expression profiles of human brain mural cells in five scRNA-seq datasets that differ in brain region (neocortex, hippocampus, midbrain, cerebellum) and developmental stage (GW6 through adult) (*391*, *392*, *503*, *504*, *593*). Our analysis suggests broad similarity in mural cell marker gene expression across the analyzed developmental stages and brain regions. This observation is consistent with previous scRNA-seq analysis demonstrating that mouse brain vascular and oligodendrocyte gene expression profiles were largely brain region-independent, in contrast to neurons and astrocytes (*372*), and that clustering of mural cells is driven predominantly by zonation along the vascular tree (*56*). While there may be brain region-dependent differences in mural cell gene expression not identified in our analysis, additional datasets, or scRNA-seq studies that directly compare brain regions, will be required to identify such differences. Similarly, additional studies will be required to understand changes in mural cell gene expression

during development, ageing, and disease, factors which have begun to be examined in brain endothelium (*128*, *367*) and are key to potential therapeutic targeting of mural cells.

In the combined mural cell dataset, we observed separation between *ACTA2*-enriched and *PTN*-enriched cells, which we classified into VSMC and pericyte clusters, respectively, based on previous classifications in mouse scRNA-seq studies (*56*, *372*). In addition to capillary pericytes, our pericyte cluster also contains a small number of $PTN^{+}ACTA2^{+}$ cells, which are likely the mural cells of postcapillary venules, which have been termed both pericytes (*160*) and venular VSMCs (*56*, *159*). In mouse scRNA-seq data, these cells also express *Ptn* and are transcriptionally more similar to the cells identified as pericytes than those identified as arterial and arteriolar VSMCs (*56*). Though we observed clear pericyte-VSMC separation, we were not able to further resolve distinct VSMC subtypes (e.g. venous, arterial, arteriolar) that have been previously observed in mouse (*56*), likely because the combined dataset contains only a small number of VSMCs, with most derived from a low sequencing depth dataset (*503*). Though the expression of α-SMA (encoded by *ACTA2*) in brain capillary pericytes is a subject of debate in the field (*165*), as is the definition of a brain pericyte (*159*, *160*, *286*), our data support the presence of a relatively large population of $ACTA2^{-}$ cells. Deeper sequencing better able to detect transcripts with very low abundance and single cell proteomics approaches (*612*) may aid in reconciling these observations. However, the ability of scRNA-seq to clarify questions surrounding mural cell identities is inherently limited by its lack of spatial information. Improved characterization of different mural cell populations demands additional spatial data to facilitate linking of mural cell functional properties (e.g., contractility) and protein expression, which vary along the vascular tree, to scRNA-seq-derived transcriptome profiles. Emerging spatial transcriptomics approaches (*613–615*) may facilitate such mapping. Once additional spatial, protein-level, and functional data exist for murine brain mural cells to facilitate correlations with

existing mouse scRNA-seq data, our combined human scRNA-seq dataset will be useful in comparing and interpreting such results. Finally, we also identified a distinct population of *COL1A1*$^{+}$ cells, which likely represent perivascular fibroblast-like (vascular leptomeningeal) cells or meningeal fibroblasts, which are extremely similar on the transcriptome level (*56*, *327*). Although perivascular fibroblast-like cells are not mural cells, these cells share a proposed neural crest-meningeal developmental origin (*285*, *327*, *377*, *616*) and further molecular characterization of these cells is warranted given their role in scar formation after injury and disease (*369*, *617*) and poorly understood physiological function.

We applied the integrated dataset to assess differences between human brain mural cells *in vivo* and (i) mouse brain mural cells, (ii) human brain mural cells cultured *in vitro*, and (iii) human mural cells from other organs. We first identified species differences in gene expression, including in solute carrier-encoding genes, of which *SLC6A1* and *SLC6A12* were human-enriched and *Slc6a20a* was mouse-enriched, extracellular matrix-associated genes, of which *DCN* and *FN1* were human-enriched and *Vtn* was mouse-enriched, and signaling-associated genes, of which *FRZB* was human-enriched and *Rgs4* and *Plxdc2* were mouse-enriched. These results corroborate and extend previous observations of species differences in brain microvessel gene expression(*90*). We also compared *in vivo* human brain pericytes to cultured primary human brain pericytes, which are widely employed as an *in vitro* model (*321*, *324*, *447*). Notably, while cultured pericytes retained *PDGFRB* and *RGS5* expression, they lacked expression of the pericyte marker *KCNJ8*, receptors for neuroactive ligands such as *P2RY14*, and the human-enriched genes *SLC6A1* and *SLC6A12*. In addition to elevated expression of *ACTA2*, which has been previously observed (*417*), cultured pericytes also had dysregulated expression of extracellular matrix-associated genes, with aberrantly high expression of fibroblast-associated genes such as *COL1A1* and *COL8A1*. These results were consistent in scRNA-seq data from

primary human brain pericytes that were acutely isolated and briefly cultured (*597*), suggesting that pericytes undergo fairly rapid dedifferentiation to a mixed mural/fibroblast-like phenotype. These findings of brain mural cell dedifferentiation in culture complement existing knowledge of brain endothelial cell dedifferentiation (*226*, *618*). Last, we characterized human mural cell organotypicity using our integrated brain scRNA-seq dataset and scRNA-seq datasets from human heart, liver, lung, and skeletal muscle. Despite differences in developmental origin, this analysis identified mural cell marker genes conserved across all five organs. We also identified mural cell genes with brain-enriched expression, including *ZIC1*, a neural crest lineage transcription factor previously reported to be brain-enriched with expression in mural and fibroblast-like cells (*56*, *619*), and *SLC6A1*, *SLC6A12*, *ATP1A2*, *GPER1*, and *NTM*.

Finally, we used RNA *in situ* hybridization (RNAscope) to validate brain mural cell expression of *SLC6A1*, *SLC6A12*, *FRZB*, and *ATP1A2* in flash-frozen human brain neurosurgical samples. We observed colocalization of all four of these transcripts with *PDGFRB*$^{+}$ mural cell nuclei. Furthermore, we observed vascular localization of FRZB protein in human brain, but not in mouse brain. Together, these data improve confidence in the many additional putative mural cell genes identified by the same integrative analysis of scRNA-seq data, and highlight protein-level validation as a necessary prerequisite to further studies. Additional work will be required to investigate potential functional roles for mural cell genes, but our results highlight the power of scRNA-seq to generate hypotheses of genes that may control cellular function. For example, mural cell-derived FRZB may modulate parenchyma-derived Wnt signaling to endothelial cells, and SLC6A1 or SLC6A12 may mediate GABA uptake by mural cells. Furthermore, given the known influence of pericytes on blood-brain barrier development and brain endothelial function *in vivo* (*30*, *256*, *257*, *620*, *621*) and *in vitro* (*447*, *622*), scRNA-seq data may aid in identifying other putative pericyte-derived factors that might mediate interactions with endothelial cells or

other neurovascular cells such as astrocytes and microglia (*585*, *623*, *624*). Mural cells are also required for maintenance of normal cerebral blood flow (CBF) and mediate neurovascular coupling (*27*, *156*, *159*, *163*, *164*, *166–168*, *625*, *626*). Notably, the potassium channel $K_{ir}6.1$, encoded by the pericyte marker gene *KCNJ8*, plays a role in resting CBF (*170*). Thus, human scRNA-seq data may help generate hypotheses of additional mural cell receptors and channels with roles in these processes, and facilitate comparisons to recently published analysis of these genes in mouse (*176*).

In summary, we present a comprehensive analysis of the human brain mural cell transcriptome based on scRNA-seq data from five independent scRNA-seq datasets. These data should be useful to evaluate animal and *in vitro* models, and advance understanding of human brain mural cell function.

Chapter 5 Notch3 directs differentiation of brain mural cells from human pluripotent stem cell-derived neural crest*

5.1 Summary

Brain pericytes and vascular smooth muscle cells, collectively termed mural cells, regulate development and function of the blood-brain barrier (BBB) and control brain blood flow. Unlike the mesoderm-derived mural cells of other organs, forebrain mural cells are derived from the neural crest, but molecular signals controlling this differentiation process are poorly understood. Furthermore, existing *in vitro* models of human brain mural cells derived both from primary cultures and human pluripotent stem cells (hPSCs) have markedly reduced expression of key mural cell genes, including *NOTCH3*, compared to *in vivo* samples. Thus, we asked whether activation of Notch3 signaling in hPSC-derived neural crest could direct the differentiation of brain mural cells with an improved transcriptional profile. Lentiviral overexpression of the Notch3 intracellular domain (N3ICD-GFP) in neural crest cells led to rapid differentiation of cells with molecular and functional properties of mural cells. Resulting cells exhibited upregulated expression of mural markers including PDGFRβ, TBX2, endogenous Notch3, *FOXS1*, and the pericyte-enriched genes *KCNJ8* and *SLC6A12*. These cells produced extracellular matrix that supported endothelial cord formation, self-assembled with endothelial cells, and contracted in response to potassium. Together, our work demonstrates that activation of Notch3 signaling is sufficient to direct the differentiation of neural crest to mural cells and establishes a developmentally relevant protocol for generation of hPSC-derived brain mural cells.

---

*A version of this chapter will be submitted for publication as Gastfriend BD, Snyder ME, Daneman R, Palecek SP, Shusta EV. Notch3 directs differentiation of brain mural cells from human pluripotent stem cell-derived neural crest.

5.2 Introduction

Vascular mural cells, which encompass microvessel-associated pericytes and large vessel-associated vascular smooth muscle cells (VSMCs), regulate blood vessel development, stability, and vascular tone (reviewed in (*286*, *627*)). In the brain, mural cells regulate resting cerebral blood flow, neurovascular coupling, blood-brain barrier development and maintenance, and neuron survival (*27*, *30*, *257*, *625*, *626*, *156*, *159*, *163*, *164*, *166*, *167*, *170*, *256*). Brain mural cells are also implicated in the pathogenesis of neurological disorders including Alzheimer's disease (*17*, *381*, *587*) and cerebral autosomal dominant arteriopathy with subcortical infarcts and leukoencephalopathy (CADASIL) (*339*, *340*).

In contrast to the mesodermal origin of most mural cells, those in the face and forebrain are derived from the neural crest (*284*, *377*, *616*, *628*). During embryogenesis, cranial neural crest-derived mesenchyme surrounds the anterior neural tube, and mural cells are specified and invade the developing prosencephalon alongside mesoderm-derived endothelial cells from the perineural vascular plexus (*30*, *629*). This neural crest-derived mesenchyme also forms portions of the meninges, facial cartilage and connective tissue, and skull (*284*, *285*). Molecular signals controlling specification of neural crest-derived mesenchyme to these diverse fates are poorly understood; however, endothelium-derived signals likely direct mural cell differentiation. *In vivo* loss of function experiments have suggested roles for TGF-β, PDGF, and Notch signaling in this process (*253*, *254*, *326*, *341*, *630*). Notably, *NOTCH3* mutations form the genetic basis of CADASIL (*339*, *340*), and studies in Zebrafish have implicated Notch signaling in brain pericyte proliferation (*341*) and specification of pericytes from naïve mesenchyme (*326*). It is difficult, however, to discriminate between deficits in specification/differentiation and recruitment of mural cells to nascent vessels in most *in vivo* studies. Thus, *in vitro* studies may provide

complementary mechanistic insight into the effects of molecular factors on neural crest differentiation (*631*).

Human pluripotent stem cells (hPSCs) are an *in vitro* model system well suited for such developmental studies, as they can generate multipotent neural crest cells (*632*, *633*) and potentially account for species differences in mural cell phenotype (*90*, *336*). The resulting cells could be further used in diverse *in vitro* modeling applications (*634*). We recently demonstrated that brain pericyte-like cells could be differentiated from hPSC-derived neural crest via treatment with serum-supplemented E6 medium (*447*, *479*). Other protocols for generating hPSC-derived brain pericyte-like cells via a neural crest intermediate use PDGF-BB and/or FGF2, but add these factors to serum-containing media (*28*, *324*). The sufficiency of serum to cause differentiation of neural crest cells makes interrogation of specific molecular factors difficult, motivating development of a serum-free differentiation scheme. Furthermore, while existing hPSC-derived pericyte-like cells have many molecular and functional attributes of pericytes *in vivo*, they lack expression of several key brain mural cell genes and have aberrant expression of some fibroblast-associated genes, features also observed in cultured primary brain pericytes (*336*). This further motivates development of a new method for differentiation of hPSCs to brain mural cells with an improved molecular phenotype.

In this work, we found that expression levels of *NOTCH3* and canonical transcriptional targets of Notch signaling were very low in existing hPSC-derived brain pericyte-like cells compared to human brain pericytes *in vivo*. We therefore tested the hypothesis that activation of Notch3 signaling would direct the differentiation of hPSC-derived neural crest to brain mural cells. Because ligand-induced activation of Notch signaling requires complex cell-cell interactions and ligand endocytosis (*331*), we instead activated Notch signaling by lentiviral overexpression of the human Notch3 intracellular domain in neural crest cells maintained in

serum-free medium. The resulting cells were PDGFRβ$^+$ and displayed robust upregulation of mural cell markers, including Tbx2, *HEYL*, *RGS5*, *TBX2*, *FOXS1*, and endogenous Notch3. Genes enriched in pericytes compared to VSMCs, including *KCNJ8*, *ABCC9*, and *HIGD1B*, were also upregulated, while VSMC-enriched genes (*ACTA2*, *CNN1*, *TAGLN*) were unchanged, supporting the notion that pericytes represent the "default" mural cell fate. The resulting cells produced extracellular matrix (ECM) that supported endothelial cord formation, self-assembled into compact aggregates with endothelial cells, and contracted in response to KCl-induced depolarization. Thus, our work suggests that Notch3 signaling is sufficient to direct differentiation of neural crest to brain mural cells, and establishes a new, serum-free protocol for generation of brain mural cells from hPSCs.

5.3 Methods

5.3.1 hPSC maintenance

Matrigel-coated plates were prepared by resuspending a frozen 2.5 mg aliquot of Matrigel, Growth Factor Reduced (Corning, Glendale, AZ) in 1 mL of DMEM/F12 (Life Technologies, Carlsbad, CA) and diluting the resulting solution in 29 mL of DMEM/F12. 1 mL of this solution was used to coat each well of five 6-well plates. Plates were stored at 37°C for at least 1 h prior to use, and up to 1 week. The following hPSC lines were used: H9 hESCs (*422*) (WiCell, Madison, WI); IMR90-4 iPSCs (*425*) (WiCell); DF19-9-11T iPSCs (*635*) (WiCell); WTC11 iPSCs (*547*) (Gladstone Institutes, San Francisco, CA). hPSCs were maintained at 37°C, 5% CO_2 on Matrigel-coated plates in E8 medium (STEMCELL Technologies, Vancouver, Canada) with daily medium changes. When hPSCs colonies began to touch, cells were dissociated as colonies using ~7 min of Versene (Life Technologies) treatment and transferred to a new Matrigel-coated plate at a split ratio of 1:12.

5.3.2 Neural crest differentiation

Neural crest was differentiated according to a previously established protocol (*447*, *479*). When hPSC colonies began to touch, 3–4 wells of cells were dissociated using ~7 min of Accutase (Innovative Cell Technologies, San Diego, CA) treatment, 1 mL per well. The Accutase/single cell suspension was transferred to 4× volume of DMEM/F12 medium and cells were counted using a hemocytometer. Cells were centrifuged for 5 min at 200×g. The cell pellet was resuspended in 1 mL of E8 medium and a volume of the resulting suspension containing 2.84×10^6 cells transferred to a tube containing 6.5 mL E8 medium supplemented with 10 μM ROCK inhibitor Y-27632 (Tocris, Bristol, United Kingdom). The resulting cell suspension was distributed to 3 wells of a Matrigel-coated 6-well plate, 2 mL per well. Cells were incubated at 37°C, 5% CO_2. The following day, differentiation was initiated by changing medium to E6-CSFD medium. E6-CSFD medium is E6 medium prepared according to ref. (*636*) supplemented with 1 μM CHIR 99021 (Tocris), 10 μM SB431542 (Tocris), 10 ng/mL FGF2 (Waisman Biomanufacturing, Madison, WI), 1 μM dorsomorphin dihydrochloride (Tocris), and 22.5 μg/mL heparin sodium salt from porcine intestinal mucosa (Sigma-Aldrich, St. Louis, MO). E6-CSFD medium was replaced daily for 15 days. Cells were passaged when confluent: one well of cells was dissociated with 1 mL of Accutase for ~5 min. The Accutase/single cell suspension was transferred to 4× volume of DMEM/F12 medium and centrifuged for 5 min at 200×g. The cell pellet was resuspended in 600 μL of E6-CSFD medium and 100 μL of the resulting suspension transferred to each of 3–6 wells of a 6-well plate each containing 2 mL E6-CSFD medium (for a split ratio of 1:6).

5.3.3 Magnetic-activated cell sorting of neural crest

On day 15, 3–6 wells of neural crest cells were dissociated using ~5 min of Accutase treatment, 1 mL per well. The Accutase/single cell suspension was transferred to 4× volume of

DMEM/F12 medium and cells were counted using a hemocytometer. Cells were centrifuged for 5 min at 180×g, 4°C. MACS buffer was prepared by supplementing Dulbecco's phosphate-buffered saline, no calcium, no magnesium (Life Technologies) with 0.5% bovine serum albumin (Sigma-Aldrich) and 2 mM ethylenediaminetetraacetic acid (Sigma-Aldrich). The cell pellet was resuspended in 60 µL MACS buffer per 10^7 cells. FcR Blocking Reagent, human (Miltenyi Biotec, Auburn, CA) and Neural Crest Stem Cell Microbeads, human (Miltenyi Biotec) were added to the cell suspension at 20 µL each per 10^7 cells. Cells were incubated for 15 min at 4°C. Cells were sorted through an LS Column in a MidiMACS Separator (Miltenyi Biotec) according to manufacturer protocols. Briefly, the column was primed with 3 mL MACS buffer, cells were loaded onto the column, the column was washed 3 times with 3 mL MACS buffer, the column was removed from the MidiMACS Separator, and the cells were eluted with 5 mL MACS buffer. The eluate was centrifuged for 5 min at 180×g, 4°C and sorted through another LS Column. Cells in the eluate were counted using a hemocytometer. The eluate was centrifuged for 5 min at 180×g, 4°C. The resulting cell pellet was resuspended in a volume of E6-CSFD medium required to achieve a concentration of 10^5 cells/mL. The resulting cell suspension was distributed to Matrigel-coated 6-well plates, 2 mL per well. For some experiments, Matrigel-coated 12-well plates (1 mL cell suspension per well), 24-well plates (500 µL cell suspension per well), or 48-well plates (250 µL cell suspension per well) were used. Cells were incubated at 37°C, 5% CO_2.

5.3.4 Flow cytometry

On D15 of the neural crest differentiation, two aliquots of 10^6 cells were transferred to conical tubes prior to MACS and kept on ice until MACS was complete. 10^6 cells from the final MACS eluate were also transferred to a conical tube. These three cell suspensions were centrifuged for 5 min at 180×g, 4°C. One pre-MACS cell pellet and the post-MACS cell pellet

were each resuspended in 100 µL DPBS containing 0.2 µL p75 antibody and 0.2 µL HNK-1 antibody (Table 5.1). The other pre-MACS cell pellet was resuspended in 100 µL DPBS containing the mouse IgG1 isotype control antibody and the mouse IgM isotype control antibody (Table 5.1) at concentrations matched to the corresponding p75 and HNK-1 antibodies. Samples were incubated for 30 min on ice, washed by adding 2 mL DPBS, and centrifuged for 5 min at 180×g, 4°C. Each cell pellet was resuspended in 100 µL DPBS containing 1:500 goat anti-mouse IgG1 Alexa Fluor 647 antibody and 1:500 goat anti-mouse IgM Alexa Fluor 488 antibody. Samples were incubated for 30 min on ice protected from light, washed by adding 2 mL DPBS, and centrifuged for 5 min at 180×g, 4°C. Cell pellets were fixed in 500 µL 4% paraformaldehyde (Electron Microscopy Sciences, Hatfield, PA) for 15 min at room temperature protected from light. Samples were centrifuged for 5 min at 180×g, resuspended in 300 µL DPBS, transferred to 5 mL flow cytometry tubes, and analyzed on a FACSCalibur flow cytometer (BD Biosciences, San Jose, CA) with excitation at 488 nm and 635 nm, Alexa Fluor 488 emission detected with a 530/30 filter and Alexa Fluor 647 emission detected with a 661/16 filter. FlowJo software (BD Biosciences) was used for analysis.

Table 5.1. Antibodies.

Target	Species/ isotype	Manufacturer, clone (product number), RRID	Fluorophore	App.[a]	Dilution
p75-NGFR	Mouse IgG1	Advanced Targeting Systems, ME20.4 (AB-N07) RRID:AB_171797	Unconjugated	FC	0.2 µL / 10^6 cells
HNK-1	Mouse IgM	Sigma-Aldrich, VC1.1 (C6680) RRID:AB_1078474	Unconjugated	FC	0.2 µL / 10^6 cells
PDGFRβ	Rabbit IgG	Cell Signaling Technology, 28E1 (3169) RRID:AB_2162497	Unconjugated	ICC	1:100
				WB	1:500
Notch3	Rabbit IgG	Cell Signaling Technology, D11B8 (5276) RRID:AB_10560515	Unconjugated	ICC	1:100
				WB	1:1000
				IP	1:200
Isotype control	Rabbit IgG	Cell Signaling Technology, DA1E (3900) RRID:AB_1550038	Unconjugated	IP	1:688
Notch1	Rabbit IgG	Cell Signaling Technology, D1E11 (3608) RRID:AB_2153354	Unconjugated	WB	1:1000
VE-cadherin	Mouse IgG2a	Santa Cruz, BV9 (sc-52751) RRID:AB_628919	Unconjugated	ICC	1:100
Tbx2	Rabbit polyclonal	Prestige Antibodies, (HPA008586) RRID:AB_1080222	Unconjugated	ICC	1:100
				WB	1:500
Fibronectin	Mouse IgG1	Santa Cruz, EP5 (sc-8422) RRID:AB_627598	Unconjugated	ICC	1:50
				WB	1:250
Calponin	Mouse IgG1	Sigma-Aldrich, hCP (C2687) RRID:AB_476840	Unconjugated	ICC	1:15,000
SM22α	Rabbit polyclonal	Abcam, (ab14106) RRID:AB_443021	Unconjugated	ICC	1:1000
α-SMA	Mouse IgG2a	Lab Vision, 1A4 (MS-113-P) RRID:AB_64000	Unconjugated	ICC	1:100
GFP	Mouse IgG2a	Santa Cruz, B-2 (sc-9996) RRID:AB_627695	Unconjugated	ICC	1:50
				WB	1:250
RBPJ	Rabbit IgG	Cell Signaling Technology, D10A4 (5313) RRID:AB_2665555	Unconjugated	WB	1:1000
β-actin	Rabbit IgG	Cell Signaling Technology, 13E5 (4970) RRID:AB_2223172	Unconjugated	WB	1:1000
Rabbit IgG (conformation-specific)	Mouse IgG	Cell Signaling Technology, L27A9 (3678) RRID: RRID:AB_1549606	Unconjugated	WB	1:2000
Rabbit IgG	Goat polyclonal	LI-COR, (925-68071) RRID:AB_10956166	IRDye 680RD	WB	1:5000

Mouse IgG	Goat polyclonal	LI-COR, (926-68070) RRID:AB_10956588	IRDye 680RD	WB	1:5000
Rabbit IgG	Goat polyclonal	LI-COR, (926-32211) RRID:AB_621843	IRDye 800CW	WB	1:5000
Mouse IgG	Goat polyclonal	LI-COR, (926-32210) RRID:AB_621842	IRDye 800CW	WB	1:5000
Mouse IgG1	Goat polyclonal	Invitrogen, (A-21240) RRID:AB_2535809	Alexa Fluor 647	FC	1:500
Mouse IgM	Goat polyclonal	Invitrogen, (A-21042) RRID:AB_2535711	Alexa Fluor 488	FC	1:500
Rabbit IgG	Goat polyclonal	Invitrogen, (A-21245) RRID:AB_2535813	Alexa Fluor 647	ICC	1:200
Mouse IgG	Goat polyclonal	Invitrogen, (A-21235) RRID:AB_2535804	Alexa Fluor 647	ICC	1:200
Mouse IgG	Goat polyclonal	Invitrogen, (A-11001) RRID:AB_2534069	Alexa Fluor 488	ICC	1:200
Mouse IgG	Goat polyclonal	Invitrogen, (A-21424) RRID:AB_141780	Alexa Fluor 555	ICC	1:200

[a]Application: FC, Flow cytometry; ICC, immunocytochemistry; WB, Western blotting; IP, immunoprecipitation

5.3.5 Lentivirus production

The lentiviral plasmids pWPI (Addgene plasmid #12254), psPAX2 (Addgene plasmid #12260), and pMD2.G (Addgene plasmid #12259) were obtained from Addgene (Watertown, MA) as gifts from Didier Trono. To generate pWPI-N3ICD, we amplified a cDNA fragment encoding the intracellular domain of Notch3 from a cDNA library generated from hPSC-derived neural crest. This fragment spans nucleotides 5,074–7056 of NCBI Reference Sequence NM_000435.3, corresponding to amino acids 1,662–2,321 of NP_00426.2. To generate pWPI-N1ICD, we amplified a cDNA fragment encoding the intracellular domain of Notch1 from the neural crest cDNA library. This fragment spans nucleotides 5,522–7,930 of NM_017617.5, corresponding to amino acids 1,754–2,556 of NP060087.3. For N3ICD and N1ICD, the forward primers (Table 5.2) contained a Kozak consensus sequence and start codon; forward and reverse primers (Table 5.2) included PacI restriction enzyme sites. To generate pWPI-TBX2, we amplified the TBX2 coding sequence from pcDNA3.1-TBX2 (NCBI Reference Sequence NM_005994.4) (GenScript, Piscataway, NJ). The forward primer (Table 5.2) contained a Kozak consensus sequence; forward and reverse primers (Table 5.2) included PacI restriction enzyme sites. pWPI and the resulting PCR fragments were digested with PacI. Ligation was performed with Instant Sticky-end Ligase Master Mix (New England Biolabs, Ipswich, MA), and resulting products transformed into NEB Stable Competent *E. coli* (New England Biolabs). Single ampicillin-resistant colonies were picked and PCR screened for presence of insert using primers annealing to the EF-1α promoter and IRES (Table 5.2). Sanger sequencing was used to identify clones with forward-oriented inserts. pWPI, pWPI-N3ICD, pWPI-N1ICD, and pWPI-TBX2 plasmids were expanded and purified using the EndoFree Plasmid Maxi Kit (Qiagen, Germantown, MD).

Table 5.2. Primer sequences.

Gene	Forward primer sequence
Primers for cloning	
NOTCH3 forward	TAA GCA TTA ATT AAG CCA CCA TGG TCA TGG TGG CCC GG
NOTCH3 reverse	TGC TTA TTA ATT AAT CAG GCC AAC ACT TGC C
NOTCH1 forward	TAA GCA TTA ATT AAG CCA CCA TGG TGC TGC TGT CCC GCA AGC G
NOTCH1 reverse	TGC TTA TTA ATT AAT TAC TTG AAG GCC TCC GGA A
TBX2 forward	TAA GCA TTA ATT AAG CCA CCA TGA GAG AGC CGG CGC
TBX2 reverse	TGC TTA TTA ATT AAT CAC TTG GGC GAC TCC C
EF-1α promoter forward	TCA AGC CTC AGA CAG TGG TTC
IRES reverse	CCT CAC ATT GCC AAA AGA CG
Primers for RT-qPCR	
eGFP forward	GAA CCG CAT CGA GCT GAA
eGFP reverse	TGC TTG TCG GCC ATG ATA TAG
NGFR forward	GTG GGA CAG AGT CTG GGT GT
NGFR reverse	AAG GAG GGG AGG TGA TAG GA
PDGFRB forward	GCT CAC CAT CAT CTC CCT TAT C
PDGFRB reverse	CTC ACA GAC TCA ATC ACC TTC C
RGS5 forward	GGA GGC TCC TAA AGA GGT GAA TA
RGS5 reverse	CCA TCA GGG CAT GGA TTC TTT
KCNJ8 forward	AAC CTG GCG CAT AAG AAC ATC
KCNJ8 reverse	CCA CAT GAT AGC GAA GAG CAG
NOTCH3 forward[a]	GAG ACG CTC GTC AGT TCT TAG
NOTCH3 reverse[a]	GGT GGA AAG AGA AGA GGA TGA A
TBX2 forward	ACA TCC TGA AGC TGC CTT AC
TBX2 reverse	AGC TGT GTG ATC TTG TCA TTC T
HEYL forward	CAG ATG CAA GCC AGG AAG AA
HEYL reverse	GGA AGA GCC CTG TTT CTC AAA
FOXS1 forward	CCA AGG ACA ACC ACA CAG AA
FOXS1 reverse	GCC ACA GAG TAA ATC CCA AGA G
TBX18 forward	CCC AGG ACT CCC TCC TAT GT
TBX18 reverse	TAG GAA CCC TGA TGG GTC TG
FOXF2 forward[b]	ACC AGA GCG TCT GTC AGG ATA TT
FOXF2 reverse[b]	GTG ACT TGA ATC CGT CCC AGT TTC
MYL9 forward	GTC CCA GAT CCA GGA GTT TAA G
MYL9 reverse	CAT CAT GCC CTC CAG GTA TT
NDUFA4L2 forward	AGA GGA CCA GAC TGG GAA A
NDUFA4L2 reverse	CAG GCA GAT TAA GCC GAT CA
HIGD1B forward	CGA AGA CTG TGT GTC TGA GAA G
HIGD1B reverse	CTC AGC CGG TAA ATC CTG TAT G
ACTA2 forward	TGT TCC AGC CAT CCT TCA TC
ACTA2 reverse	GCA ATG CCA GGG TAC ATA GT

[a]Primers target 3'UTR and thus do not amplify transgene-derived transcripts
[b]From ref. (*637*)

293TN cells (System Biosciences, Palo Alto, CA) were maintained on uncoated 6-well plates in DMEM (Life Technologies) supplemented with 10% fetal bovine serum (Peak Serum, Wellington, CO), 1 mM sodium pyruvate (Life Technologies), and 0.5× GlutaMAX Supplement (Life Technologies). When 293TN cells reached 90% confluence, psPAX2 (1 μg/well), pMD2.G (0.5 μg/well), and pWPI or pWPI-N3ICD or pWPI-N1ICD or pWPI-TBX2 (1.5 μg/well) were cotransfected using FuGENE HD Transfection Reagent (9 μL/well) (Promega, Madison, WI). Medium was replaced 16 hours after transfection, and virus-containing supernatants collected 24, 48, and 72 hours later. Supernatants were filtered through a 0.45 μm filter and concentrated 100× using Lenti-X Concentrator (Takara Bio, Mountain View, CA).

5.3.6 Lentiviral transduction

When neural crest cells reached ~40–50 % confluence (~2–3 days post-MACS), lentiviral transduction was performed by replacing medium in each well with E6-CSFD medium containing 30–50 μL N3ICD-GFP, N1ICD-GFP, or TBX2-GFP lentivirus per mL, or 5–8 μL GFP (control) lentivirus per mL, which achieved transduction efficiencies of 50–80%. E6-CSFD medium was replaced every other day for 6 days. In some experiments, culture medium was supplemented with 10 μM CB-103 (MedChemExpress, Monmouth Junction, NJ). The resulting cultures were either used directly for analysis or sorted to isolate GFP^+ and GFP^- cells as described below.

5.3.7 Reverse-transcription-quantitative polymerase chain reaction (RT-qPCR)

RNA extraction was performed using the RNeasy Plus Micro Kit (Qiagen). Cells were lysed with 350 μL Buffer RLT supplemented with 1% β-mercaptoethanol (Sigma) and transferred to gDNA Eliminator spin columns. 350 μL 70% ethanol was added to each lysate, and lysates were loaded onto RNeasy MinElute spin columns. Columns were washed with Buffer RW1, Buffer RPE, and 80% ethanol according to manufacturer protocols. RNA was eluted with

RNase-free water and concentration quantified using a NanoDrop 2000 spectrophotometer (Thermo Scientific, Waltham, MA). 250–1000 ng of RNA was reverse-transcribed for 1 h at 37°C using the OmniScript RT Kit (Qiagen) and 1 µM Oligo(dT)$_{12–18}$ primers (Life Technologies). 1 U/µL RNaseOUT (Life Technologies) was included in the reverse-transcription reactions. Reaction products were diluted to 10 ng/µL. 20 µL qPCR reactions were carried out with 10 ng cDNA and 500 nM each forward and reverse primers (Table 5.2) using PowerUp SYBR Green Master Mix (Life Technologies) and an AriaMx Real-Time PCR System (Agilent Technologies, Santa Clara, CA). An annealing temperature of 60°C was used for all reactions.

5.3.8 Immunoprecipitation

Cells were washed once with DPBS and lysed with Cell Lysis Buffer (Cell Signaling Technology, Danvers, MA) supplemented with 1× Halt Protease Inhibitor Cocktail (Thermo Scientific). Lysates were sonicated with three 5 s pulses at 40% power with a 1/8-inch probe and centrifuged at 4°C for 5 min, 14,000×g. Supernatants were transferred to new tubes and protein concentrations quantified using the Pierce BCA Protein Assay Kit (Thermo Scientific). Lysates were diluted with lysis buffer to 1 mg/mL. 420 µl of each lysate was precleared by adding 40 µl of prewashed Protein A Magnetic Beads (Cell Signaling Technology) and incubating with rotation for 20 min at room temperature. Beads were removed using a magnetic separation rack. To reduce nonspecific adsorption of DNA to magnetic beads, DNA was fragmented by adding 2 µl (2000 U) micrococcal nuclease to each lysate, and incubating for 30 min at 37°C. Digestion was stopped by adding 10 µl of 0.5 M EDTA to each lysate. A 20 µl aliquot of each lysate was removed and stored at –80°C to serve as a 10% input control. The remaining 400 µl of each lysate was split between two new tubes, and Notch3 or isotype control antibody (at matched concentration, Table 5.1) added. Lysates were incubated with rotation overnight at 4°C. 20 µl of prewashed Protein A Magnetic Beads were added to each lysate and incubated with rotation for

20 min at room temperature. Beads were pelleted using a magnetic separation rack, supernatant removed, and beads washed with 500 µl of lysis buffer. This step was repeated for a total of 5 washes. After the final wash, beads were pelleted, supernatant removed, and beads resuspended in 20 µl of Western blot sample buffer. 20 µl Western blot sample buffer was also added to each 10% input sample. All samples were heated at 95°C for 5 min. Beads were pelleted via centrifugation and resulting supernatants and 10% input samples processed for anti-RBPJ Western blotting as described below, except a mouse anti-rabbit IgG conformation-specific secondary antibody (Table 5.1) was used for detection.

5.3.9 Western blotting

Cells were lysed with radioimmunoprecipitation assay (RIPA) buffer (Rockland Immunochemicals, Pottstown, PA) supplemented with 1× Halt Protease Inhibitor Cocktail and centrifuged at 4°C for 5 min, 14,000×g. Supernatants were collected, transferred to new tubes, and protein concentrations quantified using the Pierce BCA Protein Assay Kit. For each sample, ~20 µg of protein was diluted to equal volume with water, mixed with sample buffer, and heated at 95°C for 5 min. Samples were resolved on 4–12% Tris-Glycine gels and transferred to nitrocellulose membranes. Membranes were blocked for 1 h in tris-buffered saline plus 0.1% Tween-20 (TBST) supplemented with 5% non-fat dry milk. Primary antibodies (Table 5.1) were diluted in TBST supplemented with 5% non-fat dry milk and were added to membranes and incubated overnight at 4°C on a rocking platform. Membranes were washed five times with TBST. Secondary antibodies (Table 5.1) were diluted in TBST supplemented with 5% non-fat dry milk and were added to membranes and incubated for 1 h at room temperature on a rocking platform, protected from light. Membranes were washed five times with TBST and imaged using an Odyssey 9120 (LI-COR, Lincoln, NE). Band intensities were quantified using Image Studio software (LI-COR).

5.3.10 Fluorescence-activated cell sorting (FACS) and post-FACS culture

6 days after lentiviral transduction, cells were dissociated using ~30 min of Accutase treatment, 1 mL per well. The Accutase/single cell suspension was transferred to 4× volume of DMEM/F12 medium and centrifuged for 5 min at 200×g. The cell pellet was resuspended in MACS buffer supplemented with 2 µg/mL 4',6-diamidino-2-phenylindole (DAPI; Life Technologies). A FACSAria III Cell Sorter (BD Biosciences) was used to isolate $DAPI^{-}GFP^{+}$ cells (live, N3ICD-overexpressing cells) and $DAPI^{-}GFP^{-}$ cells (live, non-overexpressing cells). Excitation was at 405 nm and 488 nm, with DAPI emission detected with a 450/50 filter and GFP emission detected with a 502LP dichroic and 530/30 filter. Cells from a non-transduced well were used as a gating control. The resulting cell suspensions were centrifuged for 5 min at 200×g, 4°C. Cell pellets were resuspended in E6 medium and seeded on Matrigel-coated plates at 2×10^4 cells/cm^2. Medium was replaced daily.

5.3.11 Immunocytochemistry

Cells were washed once with DPBS and fixed with 4% paraformaldehyde for 15 min. Cells were washed three times with DPBS and blocked/permeabilized with DPBS supplemented with 10% goat serum (Life Technologies) and 0.1% Triton-X100 (Sigma-Aldrich) for 1 h at room temperature. Primary antibodies (Table 5.1) diluted in DPBS supplemented with 10% goat serum were added to cells and incubated overnight at 4°C on a rocking platform. Cells were washed three times with DPBS. Secondary antibodies (Table 5.1) diluted in DPBS supplemented with 10% goat serum were added to cells and incubated for 1 h at room temperature on a rocking platform, protected from light. Cells were washed three times with DPBS. Cells were incubated for 5 min in DPBS supplemented with 4 µM Hoechst 33342 (Life Technologies). Images were acquired using an Eclipse Ti2-E epifluorescence microscope (Nikon, Tokyo, Japan) with a 20× objective.

5.3.12 RNA-seq

RNA-seq was performed on cells from the H9, IMR90-4, DF19-9-11T, and WTC11 hPSC lines. For each line, differentiation-matched samples of neural crest cells, and GFP^- and GFP^+ cells isolated via FACS 6 days after transduction of neural crest with N3ICD-GFP lentivirus, were analyzed. Neural crest cells were dissociated with Accutase for ~5 min. The Accutase/single cell suspension was transferred to 4× volume of DMEM/F12 medium and centrifuged for 5 min at 200×g, 4°C. FACS was performed as described above; resulting GFP^- and GFP^+ populations were centrifuged for 5 min at 200×g, 4°C. Supernatants were aspirated and the resulting cell pellets immediately lysed with Buffer RLT Plus (Qiagen) supplemented with 1% β-mercaptoethanol and frozen at –80°C. RNA extraction was performed using the RNeasy Plus Micro Kit (Qiagen). Lysates were thawed on ice, processed through gDNA Eliminator spin columns, processed through RNeasy MinElute spin columns per manufacturer instructions, and eluted into RNase-free water.

RNA quality control, library preparation, and sequencing were performed by Novogene (Sacramento, CA). RNA quantity was assessed using a NanoDrop spectrophotometer; RNA quality was assessed using an Agilent 2100 Bioanalyzer. Poly(A) mRNA enrichment was performed using poly(T) oligo-conjugated magnetic beads, first-strand cDNA synthesis performed using random hexamer primers, second-strand cDNA synthesis performed, and libraries prepared using the NEBNext Ultra II RNA Library Prep Kit for Illumina (New England Biolabs). Libraries were sequenced on a NovaSeq 6000 (Illumina, San Diego, CA) with approximately 20 million 150 bp paired-end reads obtained for each sample.

5.3.13 RNA-seq data analysis

A DNA sequence from lentiviral transfer plasmid pWPI extending from the PacI site to the 3’ end of the WPRE (containing the IRES and eGFP CDS) was added to the reference

genome (hg38) to permit quantification of transgene-derived transcripts. RNA-seq FASTQ files from the experiment described above and from the literature (obtained from the Gene Expression Omnibus, Table 5.3) were aligned to the resulting reference genome using STAR (version 2.5.3a) (*638*). Gene-level counts were generated using the featureCounts function from Subread (version 2.0.3) (*639*). Transcripts per million (TPM) were calculated using gene lengths derived from featureCounts as previously described (*90*).

Transcriptome comparison between hPSC-derived brain pericyte-like cells, GFP^+ cells from this work, and *in vivo* human brain pericytes was performed for protein-coding genes (based on the list at genenames.org/download/statistics-and-files). Data for *in vivo* brain pericytes were obtained from a previous meta-analysis of single cell RNA-seq studies (*336*). In this meta-analysis, a mock bulk RNA-seq dataset was constructed from each source dataset (*391*, *392*, *502–504*) by (i) averaging gene counts across the pericyte cluster, (ii) obtaining the subset of protein-coding genes, and (iii) generating mock TPM values by normalizing total counts to 10^6. Bulk RNA-seq TPM values from hPSC-derived brain pericyte-like cells (from the literature) and GFP^+ cells (this work) were similarly re-normalized to 10^6 after obtaining the subset of protein-coding genes. To generate the scatterplots in Figure 5.1A and Figure 5.10G, resulting TPM values for each gene across the 11 hPSC-derived brain pericyte-like cell datasets or 4 GFP^+ cell datasets were averaged, and TPM values for each gene across the 5 *in vivo* human brain pericyte datasets were averaged, followed by log-transformation as $\log_2(TPM+1)$. The Pearson correlation coefficients were calculated based on the log-transformed average TPM values.

Raw counts from featureCounts were input to DESeq2 (version 1.32.0) (*552*) for differential expression and principal component analyses. The DESeq2 variance stabilizing transformation was used to generate counts data for input to principal component analysis and hierarchical clustering. Hierarchical clustering on genes and samples (one minus Pearson

correlation with average linkage) was performed using Morpheus (software.broadinstitute.org/morpheus/). Differential expression analysis was performed using the DESeq2 Wald test with Benjamini-Hochberg correction. The DESeq2 design included differentiation (hPSC line) matching as described above. Genes with adjusted P-values < 0.05 were considered differentially-expressed. Gene Set Enrichment Analysis (version 4.2.3) (*603*) was performed using DESeq2-normalized counts for neural crest and GFP^+ cell samples. GSEA was performed with gene set permutation and otherwise default settings. Genes enriched in GFP^+ cells compared to neural crest were tested against the KEGG (*640*) and gene ontology-biological processes (GO-BP, (*641*)) databases (version 7.5.1). Gene sets with false discovery rates (FDR) < 0.05 were considered enriched. Visualization of reads aligned to the human genome was performed using Integrative Genomics Viewer (version 2.5.0).

Analysis of single cell RNA-seq data from developing mouse brain (*325*) was performed in Scanpy (*642*) (version 1.9.1). The loom file containing expression data and metadata was obtained from the authors' website (Table 5.3). Clusters annotated as neural crest and mesenchymal cell types by the authors were selected for analysis. A complete list of the authors' ClusterName identifiers is shown in Figure 5.2A, along with the authors' Subclass, Age, and PseudoAge annotations. For visualization, we selected of highly variable genes, regressed out total counts and percent of counts derived from mitochondrial genes, and performed principal component analysis, neighbor finding, and UMAP embedding (40 principal components) using Scanpy default parameters. A dot plot was used to visualize expression of neural crest, pan-mesenchymal, fibroblast, pan-mural, pericyte, and VSMC markers.

Table 5.3. Published RNA-seq datasets used.

Reference	Description	Source	Accession Numbers/Identifiers
Ref. (*447*)	hPSC-derived brain pericyte-like cells	https://www.ncbi.nlm.nih.gov/geo/query/acc.cgi?acc=GSE124579	GSM3537065 (SRR8385490, SRR8385491) GSM3537067 (SRR8385494, SRR8385495) GSM3537068 (SRR8385496, SRR8385497) GSM3537069 (SRR8385498, SRR8385499) GSM3537070 (SRR8385500, SRR8385501)
Ref. (*324*)	hPSC-derived brain pericyte-like cells	https://www.ncbi.nlm.nih.gov/geo/query/acc.cgi?acc=GSE104141	GSM2790557 (SRR6059668) GSM2790558 (SRR6059669) GSM2790559 (SRR6059670)
Ref. (*28*)	hPSC-derived brain pericyte-like cells	https://www.ncbi.nlm.nih.gov/geo/query/acc.cgi?acc=GSE132857	GSM3895132 (SRR9312712) GSM3895133 (SRR9312713) GSM3895134 (SRR9312714) GSM3895135 (SRR9312715)
Ref. (*325*)	Mouse developing brain scRNA-seq	http://mousebrain.org/development/downloads.html	dev_all.loom
Ref. (*336*) (Chapter 4)	Meta-analysis of human brain scRNA-seq datasets (enumerated below)		
Ref. (*502*)	Adult human neocortex scRNA-seq	https://portal.brain-map.org/atlases-and-data/rnaseq/human-multiple-cortical-areas-smart-seq	
Ref. (*392*)	GW17-18 human neocortex scRNA-seq	http://solo.bmap.ucla.edu/shiny/webapp/	
Ref. (*503*)	Adult human temporal lobe and cerebellum scRNA-seq	https://www.ncbi.nlm.nih.gov/geo/query/acc.cgi?acc=GSE134355	GSM3980129, GSM4008656, GSM4008657, GSM4008658
Ref. (*391*)	GW6-11 human ventral midbrain scRNA-seq	https://www.ncbi.nlm.nih.gov/geo/query/acc.cgi?acc=GSE76381	
Ref. (*504*)	GW16-27 human hippocampus scRNA-seq	https://www.ncbi.nlm.nih.gov/geo/query/acc.cgi?acc=GSE119212	

5.3.14 Decellularization and quantification of extracellular matrix

Decellularization was performed 6 days after transduction of neural crest cultures in 12-well plates with GFP or N3ICD-GFP lentiviruses as described above. The decellularization protocol was adapted from ref. (*643*). The following buffers were pre-warmed to 37°C: DPBS, Wash Buffer 1 (100 mM disodium phosphate, 2 mM magnesium chloride, 2 mM EDTA, pH

9.6), Lysis Buffer (8 mM disodium phosphate, 1% Triton X-100, pH 9.6), Wash Buffer 2 (10 mM disodium phosphate, 300 mM potassium iodide, pH 7.5). Cells were washed twice with 1 mL DPBS and three times with 1 mL Wash Buffer 1. Cells were incubated with 1 mL Lysis Buffer for 15 min at 37°C. Lysis Buffer was replaced with 1 mL fresh Lysis Buffer; cells were incubated for 1 h at 37°C. Lysis Buffer was replaced with 1 mL fresh Lysis Buffer; cells were incubated for an additional 1 h at 37°C. Lysis Buffer was removed and the resulting extracellular matrix washed 3 times with 1 mL Wash Buffer 2 and 4 times with 1 mL water. Water was removed and 250 μL RIPA buffer added. Extracellular matrix was scraped from the bottom of the well. The resulting solution was transferred to a microcentrifuge tube and sonicated with two 10 s pulses at 40% power with a 1/8-inch probe. Protein concentration in the resulting solution was quantified using the BCA assay. For normalization of total protein to cell number, cells from a parallel well of the 12-well plate were dissociated using Accutase and counted using a hemocytometer.

5.3.15 Cord formation assays

The coculture cord formation assay was performed 5 days after isolation of GFP^+ and GFP^- cells via FACS from a N3ICD-GFP-transduced culture as described above. 8-well chamber slides were coated with Matrigel, growth factor reduced, at 250 μL per well. Matrigel was allowed to gel at 37°C for 1 h. HUVECs (American Type Culture Collection, Manassas, VA) maintained in EGM-2 medium (Lonza, Walkersville, MD), were dissociated using a ~15 min treatment with 0.25% trypsin-EDTA (Gibco). The resulting cell suspension was transferred to a 4× volume of DMEM supplemented with 10% FBS. Neural crest cells, GFP^+ cells, and GFP^- cells were dissociated using 5-15 min of Accutase treatment and the resulting cell suspensions were transferred to 4× volumes of DMEM/F12 medium. Cells were counted using a hemocytometer and centrifuged for 5 min at 200×g. Supernatants were removed and cell pellets

resuspended in 1 mL EGM-2 medium. For the HUVEC-only control, HUVEC cell suspension and EGM-2 medium were combined to yield a suspension containing 2.2×10^4 HUVECs per 500 µL. For the coculture conditions, HUVEC cell suspension, coculture cell suspension (neural crest, GFP^+, or GFP^- cell suspension), and EGM-2 medium were combined to yield suspensions containing 2.2×10^4 HUVECs and 6.6×10^4 coculture cells per 500 µL. 500 µL of the resulting cell suspensions were added to the prepared wells of the 8-well chamber slides. Phase contrast and GFP images were acquired after 24 h and 72 h using an Eclipse Ti2-E microscope with a 4× objective.

To assess the ability of extracellular matrix from GFP- and N3ICD-GFP-transduced cells to support endothelial cord formation, neural crest cultures in 48-well plates 6 days post-transduction with GFP or N3ICD-GFP lentiviruses were decellularized. The decellularization protocol was as described above, except all wash and incubation steps performed using 200 µL of solution, and the protocol terminated after the final wash with water. This procedure was also performed on parallel cell-free wells to serve as a no-extracellular matrix control. Additional parallel wells were coated with 200 µL Matrigel, Growth Factor Reduced, which was allowed to gel at 37°C for 1 h. 2.75×10^4 HUVECs in 250 µL EGM-2 medium were added to each well. Phase contrast images were acquired 16 h after addition of HUVECs using an Eclipse Ti2-E microscope with a 4× objective. Cells were subsequently fixed and processed for VE-cadherin immunocytochemistry as described above. To quantify the extent of cord formation, blinded phase contrast images were scored on the following 4-point scale. 0: No cords apparent. 1: Few cords apparent, most cells not associated with cords. 2: Many cords apparent, most cells associated with cords. 3: Virtually all cells associated with cords.

5.3.16 Calcium imaging and contraction assay

Calcium imaging was performed 6 days after transduction of a neural crest cultures with N3ICD-GFP lentivirus as described above. FLIPR Calcium 6 dye (Molecular Devices, San Jose, CA) was prepared according to manufacturer instructions. 500 µL of prepared dye was added to the existing 500 µL of culture medium and cells incubated at 37°C, 5% CO_2 for 2 h. The plate was transferred to a microscope environmental chamber at 37°C, 5% CO_2 and equilibrated for 30 min. Images were acquired every 5 s for 300 s using an Eclipse Ti2-E microscope with a 4× objective. At t = 50 s, a 1:114 dilution of saturated potassium chloride solution (4.56 M, for a final concentration of 40 mM) was added to the well. ImageJ was used to quantify mean fluorescence intensity F_t at each time point and data are displayed as $\Delta F/F = (F_t - F_0)/F_0$.

The contraction assay was performed 2 days after isolation of GFP^+ cells via FACS from a N3ICD-GFP-transduced culture as described above. The plate was transferred to a microscope environmental chamber at 37°C, 5% CO_2 and equilibrated for 30 min. At t = 0 min, a 1:114 dilution of saturated potassium chloride solution, or an equivalent volume of water, was added to the culture medium and the plate briefly rocked to mix. Phase contrast images were acquired immediately upon addition of potassium chloride or water and 15 min thereafter using an Eclipse Ti2-E microscope with a 20× objective. The Freehand Selection Tool in ImageJ was used to trace the outlines of 16 cells per 20× field at times 0 and 15 min, and the Measure function used to obtain A_0 and A_{15}, the cell areas at times 0 and 15 min, respectively. For each cell, the percent change in area was computed as $(A_{15} - A_0)/A_0 \times 100\%$. These values were averaged across the 16 cells in each field to generate the values shown in Fig. 4.

5.3.17 Statistics

Individual wells of cultured cells that underwent identical experimental treatments are defined as replicates. Details of replication strategy are provided in figure legends. Student's

unpaired or paired *t* tests were used for comparison of means from two experimental groups. One-way analysis of variance (ANOVA) was used for comparison of means from three or more experimental groups. Two-way ANOVA was used for comparison of means and blocking of differentiation-based variability if data from multiple differentiations were combined (one factor being the experimental treatment and one factor being the differentiation). Following ANOVA, Dunnett's post-hoc test was used for comparison of multiple treatments to a single control, or Tukey's honest significant difference (HSD) test was used for multiple pairwise comparisons. For cord formation score data, the nonparametric Kruskal-Wallis test was used followed by the Steel-Dwass test for multiple pairwise comparisons.

5.4 Results

5.4.1 Transcriptome analysis of hPSC-derived brain pericyte-like cells

We analyzed RNA-sequencing (RNA-seq) gene expression profiles of brain pericyte-like cells differentiated from hPSCs from three independent studies (*28*, *324*, *447*). While methodologies differ slightly, all three protocols proceed through a neural crest intermediate and yield cells with molecular and functional characteristics similar to mural cells. We compared these cells to human brain pericytes *in vivo*, using single cell RNA-seq data from a previous meta-analysis (*336*). There was moderate correlation between the transcriptome of hPSC-derived pericyte-like cells and *in vivo* pericytes, and similar expression of some canonical markers such as *PDGFRB*, *ANPEP*, *CSPG4*, *COL4A1*, *IGFBP7*, and *MYL9* (Figure 5.1A; Supplementary File). Compared to *in vivo* pericytes, however, hPSC-derived pericyte-like cells had markedly lower expression of several key mural cell signaling mediators and transcription factors, including *RGS5*, *NOTCH3*, *HEYL*, *HEY2*, *HES4*, *TBX2*, *FOXS1*, and *FOXF2* (Figure 5.1A-B; Supplementary File). We previously demonstrated downregulation of many of these same genes in cultured primary human brain pericytes (*336*), and a murine developmental single cell RNA-

seq study (*325*) supports selective expression of many of these genes in mural cells compared to both neural crest and other mesenchymal derivatives (Figure 5.2). These results therefore suggest that key molecular factors for induction and maintenance of the brain mural cell phenotype are absent under traditional culture conditions, and that augmentation of these factors during hPSC differentiation might yield mural cells with improved phenotype.

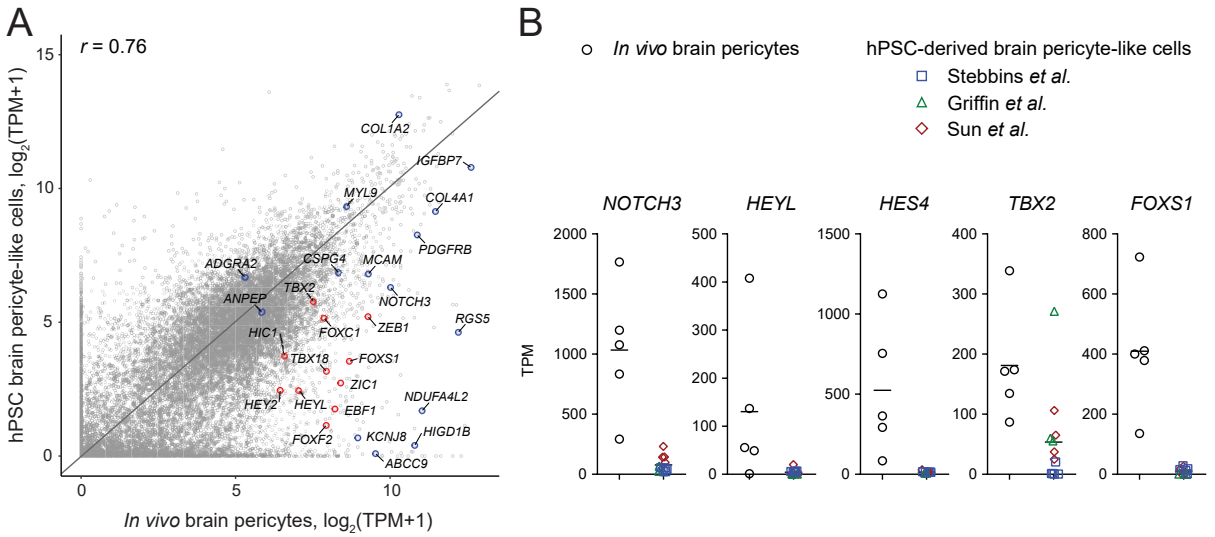

Figure 5.1. Comparison of human brain pericytes *in vivo* and hPSC-derived brain pericyte-like cells. (A) Comparison of protein-coding transcript abundances in hPSC-derived brain pericyte-like cells versus *in vivo* human brain pericytes. Data for hPSC-derived brain pericyte like cells were generated by averaging transcripts per million (TPM) across 11 bulk RNA-seq datasets: 5 datasets from (*447*), 3 datasets from (*324*), and 4 datasets from (*28*) (Table 5.3). Data for *in vivo* human brain pericytes were obtained from a previous meta-analysis of 5 single cell RNA-seq datasets (*336*). The Pearson correlation coefficient *r* is shown. Genes of interest are annotated in red (transcription factors) or blue (others). (B) Transcript abundance of selected genes. Abundances for each of the five *in vivo* human brain pericyte datasets are indicated with black circles. Abundances for each of the hPSC-derived brain pericyte-like cell datasets are indicated with blue squares (*447*), green triangles (*324*), and red diamonds (*28*). Bars indicate mean values. TPM: transcripts per million.

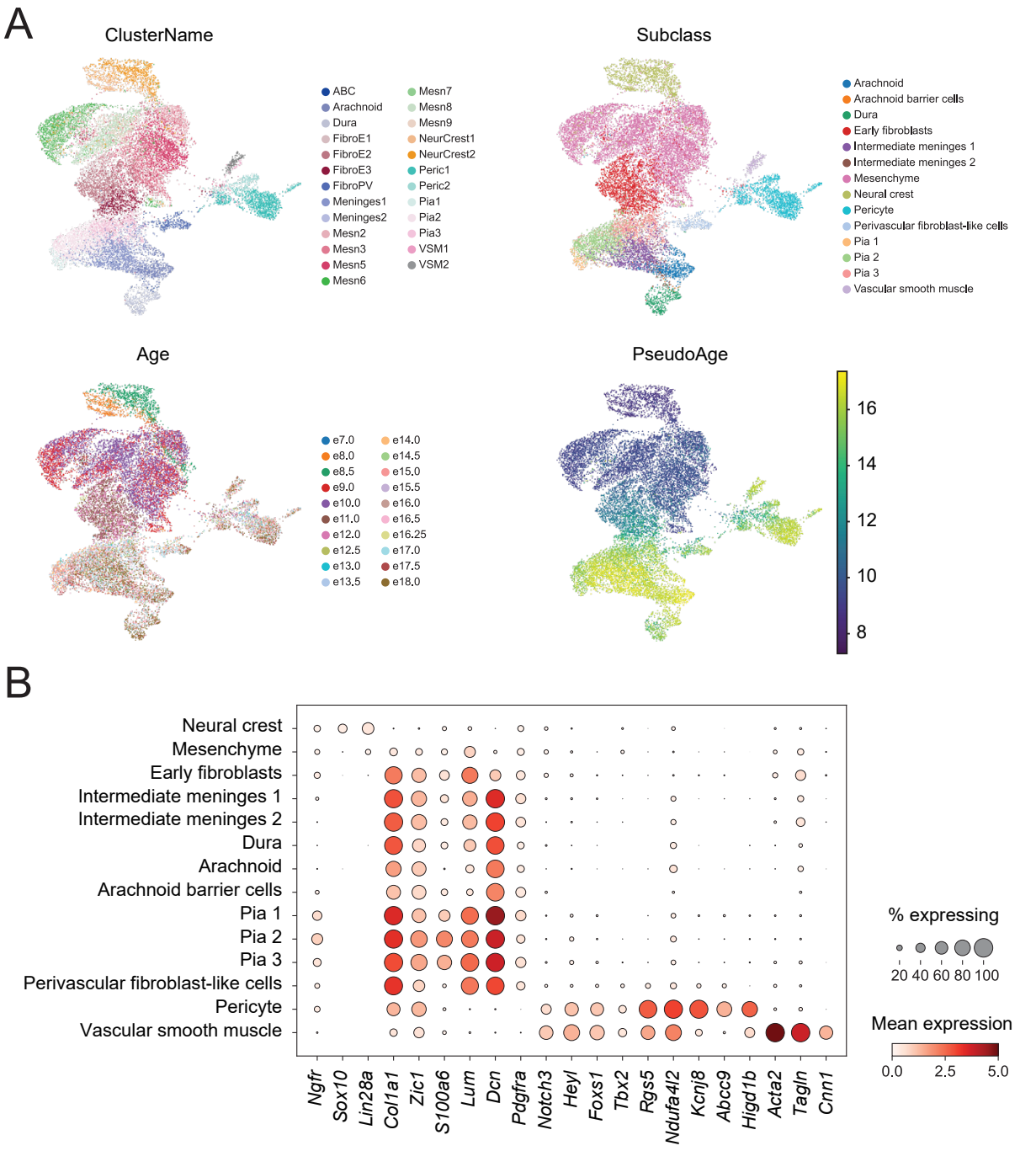

Figure 5.2. Markers of murine neural crest, mural cells, and other mesenchymal derivatives. (A) UMAP plots of all single cells colored by authors' ClusterName, Subclass, Age, and PseudoAge annotations. (B) Dot plot of gene expression in cell Subclasses. Neural crest, pan-mesenchymal, fibroblast, pan-mural, pericyte, and VSMC marker genes are shown. Color indicates expression level and dot size indicates the percent of cells in the indicated Subclass that express a given gene. Data from ref. (*325*).

5.4.2 Overexpression of N3ICD as a strategy to derive mural cells

Given low expression of *NOTCH3* and Notch target genes (e.g., *HEYL*, *HEY2*, *HES4*) in existing hPSC-derived pericyte-like cells and the known roles of Notch signaling in mural cell development (*326*), we asked whether overexpression of the human Notch3 intracellular domain (N3ICD) in neural crest cells could direct mural cell differentiation. We also evaluated overexpression of Tbx2, a mural cell-enriched transcription factor with similarly low expression in existing hPSC models. We cloned the portion of the *NOTCH3* coding sequence (CDS) corresponding to the intracellular domain, and the *TBX2* CDS, into bicistronic lentiviral vectors for GFP coexpression (see Section 5.3.5) (Figure 5.3A-B). As a starting cell type, we used neural crest cells differentiated from hPSCs according to a previously-established protocol (*447*). After 15 days of differentiation in E6-CSFD medium, we selected $p75^+$ cells via magnetic-activated cell sorting (MACS), resulting in a homogenous population of $p75^+$ HNK-1^+ neural crest cells that were briefly expanded prior to transduction (Figure 5.3A,C). We transduced neural crest cells with GFP-only, N3ICD-GFP, or TBX2-GFP lentiviruses, and after 6 days, either analyzed the resulting populations or performed fluorescence-activated cell sorting (FACS) to isolate GFP^+ cells.

6 days after lentiviral transduction, N3ICD-GFP-transduced cells had significantly elevated expression of *HEYL* and endogenous *NOTCH3* (using primers targeting the 3' untranslated region, which is not present in transgene-derived transcripts) compared to GFP controls (Figure 5.3D). Notably, these cells also had increased expression of other mural cell transcription factors (*TBX2*, *FOXS1*) and canonical markers (*PDGFRB*, *RGS5*, *KCNJ8*), suggesting that Notch3 signaling may be sufficient activate a genetic program for mural cell differentiation (Figure 5.3D). In contrast, while TBX2-GFP-transduced cells had elevated expression of *TBX2*, suggesting successful overexpression, and a slight increase in *PDGFRB*

expression, all other mural cell genes evaluated were unchanged versus GFP controls (Figure 5.3D). We confirmed that N3ICD-GFP-mediated transcriptional changes occurred via a canonical Notch transactivation mechanism using Notch3-RBPJ coimmunoprecipitation and a loss-of-function experiment with CB-103, a small molecule inhibitor of Notch intracellular domain-RBPJ assembly (*644*) (Figure 5.4). We also asked whether overexpression of an alternative Notch would achieve a similar effect; indeed, N1ICD-GFP-transduced neural crest cells underwent similar transcriptional changes to N3ICD-GFP-transduced cells (Figure 5.5). We elected, however, to conduct further experiments using cells derived via N3ICD overexpression, given enrichment of Notch3 compared to other Notch receptors in brain mural cells, and existing loss-of-function studies establishing the necessity of Notch3 for mural cell development (*326*, *341*).

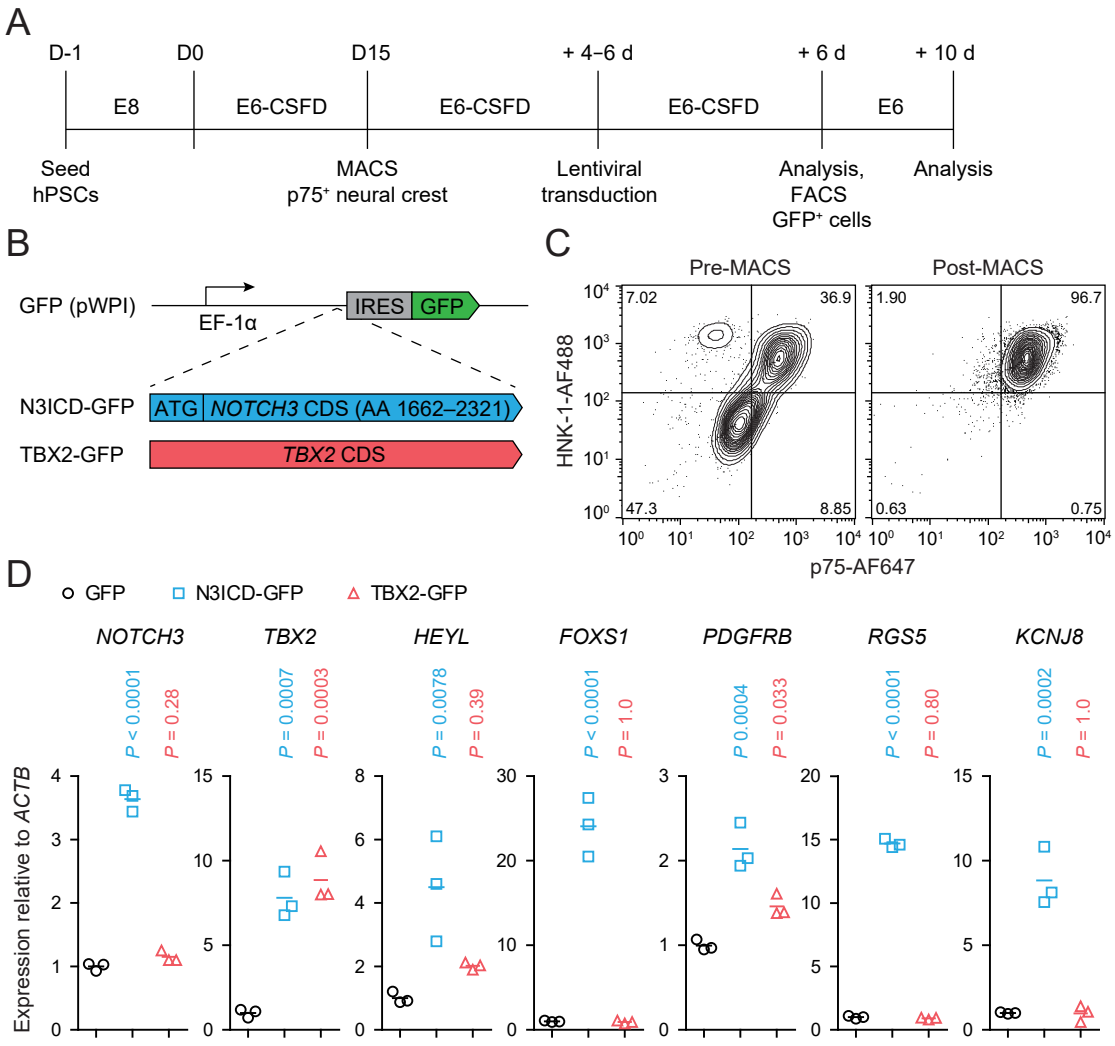

Figure 5.3. Overview of differentiation strategy. (A) Timeline of the differentiation protocol. (B) Schematic of lentiviral overexpression constructs. A fragment of the human *NOTCH3* coding sequence (CDS) encoding the intracellular domain of Notch3, and the human *TBX2* CDS, were cloned into the bicistronic lentiviral vector pWPI. The parental pWPI vector was used as a GFP-only control. IRES: internal ribosome entry site; AA: amino acids. (C) Flow cytometry analysis of p75 and HNK-1 expression in D15 neural crest cells before and after p75 MACS. (D) RT-qPCR analysis of mural cell gene expression 6 days after transduction with GFP, N3ICD-GFP, or TBX2-GFP lentiviruses. Expression of each gene is shown relative to *ACTB* expression and normalized to expression in GFP-transduced cells. Points represent replicate wells from a differentiation of the H9 hPSC line and bars indicate mean values. P-values: ANOVA followed by Dunnett's test versus GFP-transduced cells.

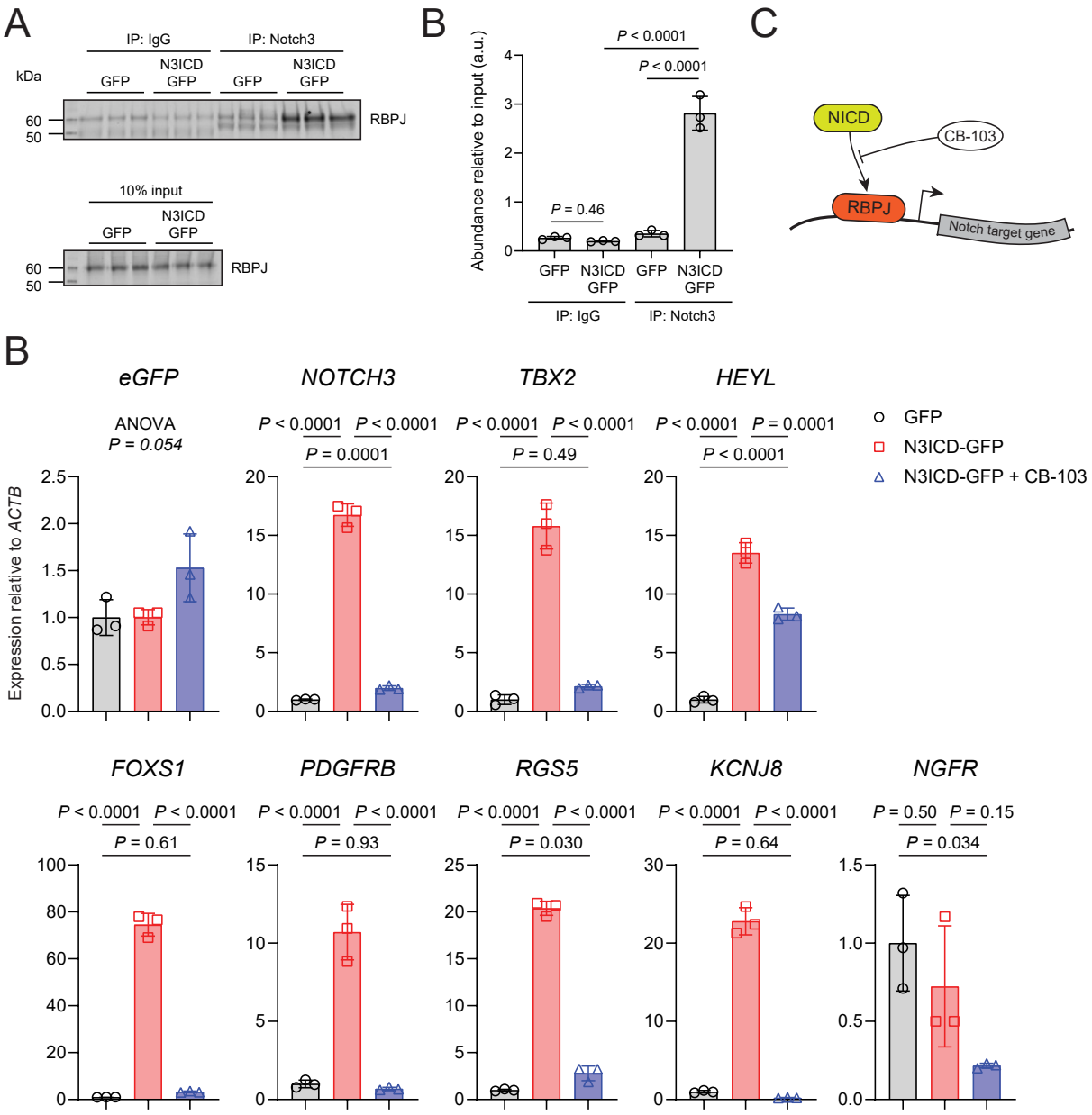

Figure 5.4. Notch-dependence of observed transcriptional changes. (A) Western blots of isotype control IgG and Notch3 immunoprecipitates (top) and input controls (bottom) from cells 6 days after transduction with GFP or N3ICD-GFP lentiviruses. Membranes were probed with the RBPJ antibody. (B) Quantification of RBPJ Western blot. Band intensities from immunoprecipitates were normalized to respective input control band intensities. Points represent replicate wells from a differentiation of the H9 hPSC line. Bars indicate mean values ± SD. P-values: ANOVA followed by Tukey's HSD test. (C) Schematic of the mechanism of action of CB-103, a small molecule inhibitor of the Notch transcriptional activation complex. NICD: Notch intracellular domain. (B) RT-qPCR analysis of mural cell gene expression 6 days after transduction of neural crest cells with GFP or N3ICD-GFP lentiviruses. Expression of each gene is shown relative to *ACTB* expression and normalized to expression in GFP-transduced cells. Points represent replicate wells from a differentiation of the H9 hPSC line and bars indicate mean ± SD. P-values: ANOVA followed by Tukey's HSD test.

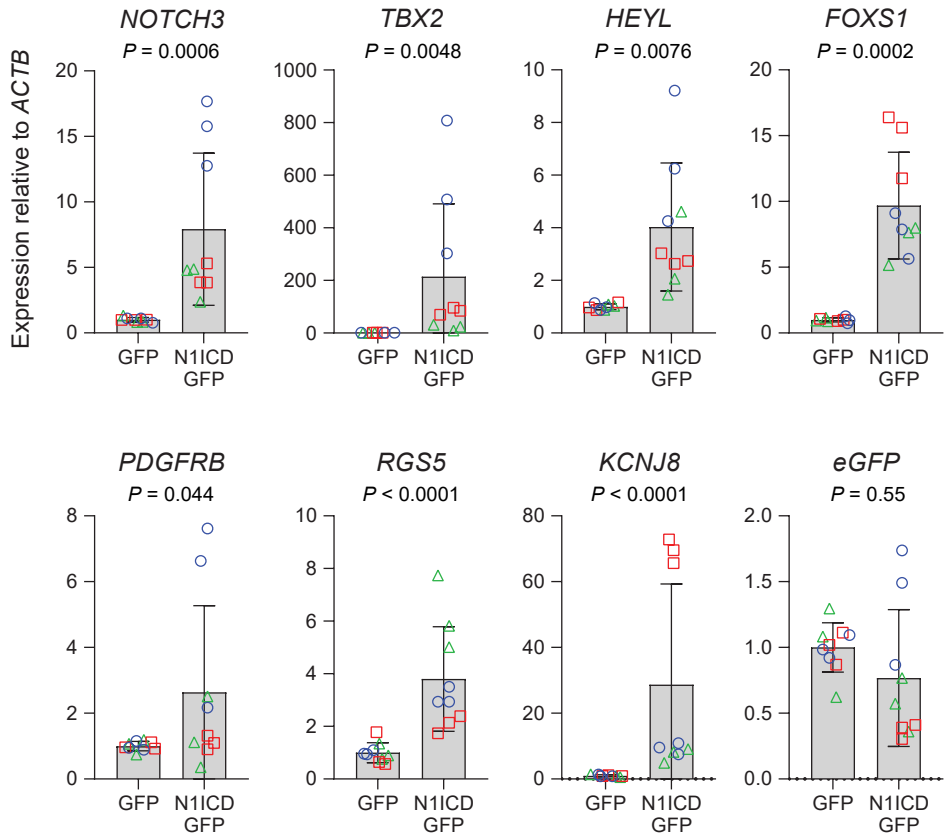

Figure 5.5. Transcriptional effects of N1ICD overexpression. RT-qPCR analysis of mural cell gene expression 6 days after transduction of neural crest cells with GFP or N1ICD-GFP lentiviruses. Expression of each gene is shown relative to *ACTB* expression. Points represent replicate wells from three independent differentiations, two in the H9 hPSC line (blue circles, green triangles) and one in the IMR90-4 hPSC line (red squares). Bars indicate mean values ± SD, with values normalized within each differentiation such that the mean of the GFP condition equals 1. P-values: two-way ANOVA on unnormalized data.

We validated protein-level overexpression of N3ICD via Western blotting with a Notch3 antibody detecting a C-terminal (intracellular domain) epitope. As expected, we observed a significant increase in the intensity of a low molecular weight band corresponding to the Notch transmembrane fragment and intracellular domain in N3ICD-GFP-transduced cultures compared to GFP-transduced cultures (Figure 5.6A-B). A high molecular weight band corresponding to full-length Notch3 also had increased abundance in N3ICD-GFP-transduced cultures, suggestive of positive feedback and consistent with enrichment of Notch3 in brain mural cells compared to neural crest *in vivo* (*56*, *325*, *645*) (Figure 5.2). The canonical mural cell marker PDGFRβ and transcription factor Tbx2 were also upregulated in N3ICD-GFP-transduced cultures, despite lower GFP abundance, reflective of slightly lower transduction efficiency by N3ICD-GFP lentivirus compared to GFP lentivirus (Figure 5.6A-B). We also observed a marked increase in fibronectin abundance in N3ICD-GFP-transduced cultures (Figure 5.6A-B), consistent with human brain mural cell expression of *FN1 in vivo* (*336*). Immunocytochemistry corroborated these findings and revealed clear nuclear localization of Notch3 and Tbx2 in N3ICD-GFP-transduced cells (Figure 5.6C). Consistent with transcript-level observations, N1ICD overexpression also achieved similar effects to N3ICD on the protein level (Figure 5.7). Together, these results suggest that activation of Notch signaling in neural crest cells is sufficient to drive mural cell differentiation.

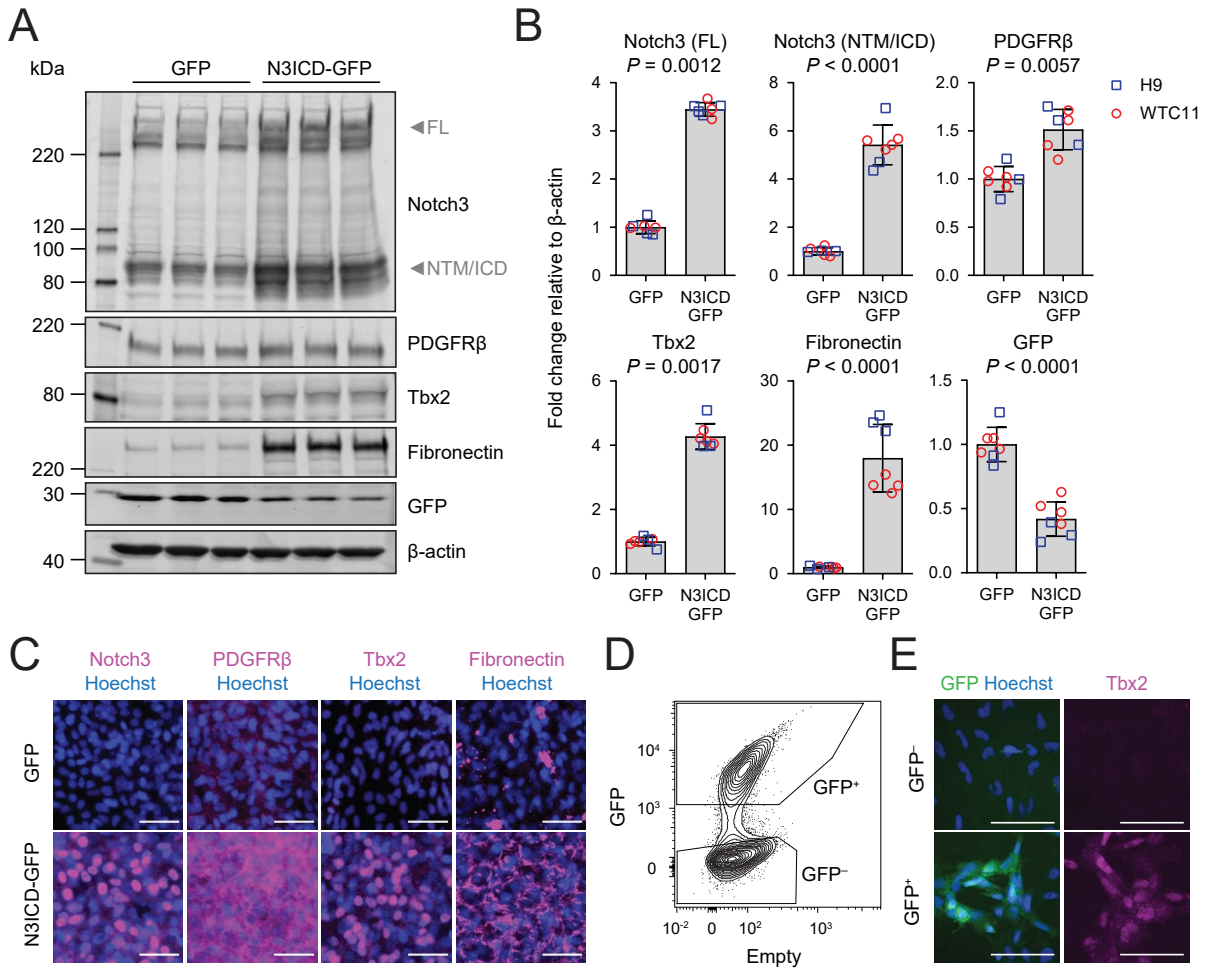

Figure 5.6. Results of Notch3 intracellular domain overexpression in neural crest cells. (A) Western blots of cells 6 days after transduction with GFP or N3ICD-GFP lentiviruses. Membranes were probed with Notch3, PDGFRβ, Tbx2, fibronectin, GFP, and β-actin antibodies. On the Notch3 Western blot, arrows indicate the full-length (FL) and Notch transmembrane/intracellular domain (NTM/ICD) bands. (B) Quantification of Western blots. Band intensities were normalized to β-actin band intensities. Points represent replicate wells from two independent differentiations, one in the H9 hPSC line (blue squares) and one in the WTC11 hPSC line (red circles). Bars indicate mean values ± SD, with values normalized within each differentiation such that the mean of the GFP condition equals 1. P-values: two-way ANOVA on unnormalized data. (C) Immunocytochemistry analysis of Notch3, PDGFRβ, Tbx2, and fibronectin expression in cells 6 days after transduction with GFP or N3ICD-GFP lentiviruses. Hoechst nuclear counterstain overlaid in all images. Scale bars: 50 μm. (D) Flow cytometry analysis of GFP expression 6 days after transduction of neural crest cells with N3ICD-GFP lentivirus. GFP^+ and GFP^- gates are representative of those used to isolate populations via FACS. (E) Immunocytochemistry analysis of GFP and Tbx2 expression in cells expanded in E6 medium for 4 days after FACS. Hoechst nuclear counterstain is overlaid in the GFP images. Scale bars: 100 μm.

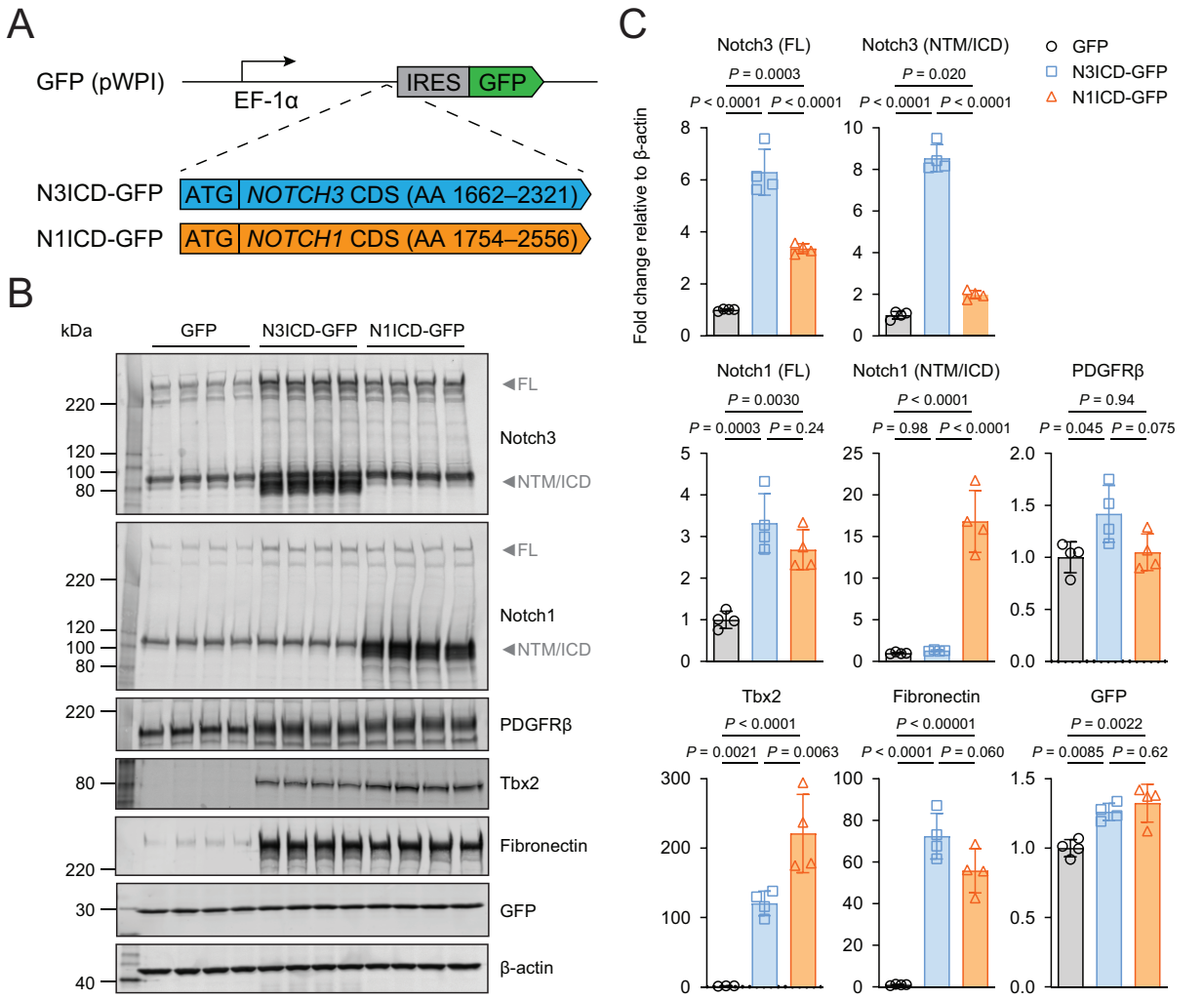

Figure 5.7. Comparison of N1ICD and N3ICD overexpression. (A) Schematic of lentiviral overexpression constructs. The parental pWPI vector and N3ICD-GFP are as described in Figure 1. To generate N1ICD-GFP, a fragment of the human *NOTCH1* coding sequence (CDS) encoding the intracellular domain of Notch1 was cloned into pWPI. IRES: internal ribosome entry site; AA: amino acids. (B) Western blots of cells 6 days after transduction with GFP, N3ICD-GFP, or N1ICD-GFP lentiviruses. Membranes were probed with Notch3, Notch1, PDGFRβ, Tbx2, fibronectin, GFP, and β-actin antibodies. On the Notch3 and Notch1 Western blots, arrows indicate the full-length (FL) and Notch transmembrane/intracellular domain (NTM/ICD) bands. (C) Quantification of Western blots. Band intensities were normalized to β-actin band intensities. Points represent replicate wells from a differentiation of the H9 hPSC line. Bars indicate mean values ± SD, with values normalized such that the mean of the DMSO condition equals 1. P-values: ANOVA followed by Tukey's HSD test.

5.4.3 Molecular properties of cells derived via N3ICD overexpression

We used FACS to isolate GFP^+ and GFP^- cells from cultures 6 days after N3ICD-GFP lentiviral transduction (Figure 5.6D). We compared acutely isolated GFP^+ and GFP^- cells by RT-qPCR; GFP^+ cells had significantly reduced expression of *NGFR*, consistent with loss of neural crest identity, and significantly higher expression of markers of mesenchyme (e.g., *TBX18*), mural cells (e.g., *NOTCH3*, *TBX2*, *HEYL*, *FOXS1*), and pericytes (e.g., *KCNJ8*), while the VSMC-enriched gene *ACTA2* was not differentially expressed (Figure 5.8A). Immunostaining conducted 4 days after FACS confirmed that Tbx2 was selectively expressed in GFP^+ cells (Figure 5.6D). Importantly, these results suggest that N3ICD-GFP functions cell-autonomously to direct neural crest-to-mural cell differentiation, and that the resulting cells have molecular hallmarks of pericytes. After briefly expanding the resulting cells in minimal E6 medium, however, we observed marked downregulation of *KCNJ8* and upregulation of *ACTA2* despite maintained expression of the N3ICD-GFP transgene; at 4 days post-FACS, cells expressed the VSMC-enriched proteins α-SMA, calponin, and SM22α (Figure 5.8B-C). Loss of *KCNJ8* and induction of these contractile proteins is a phenomenon also observed upon *in vitro* culture of primary brain pericytes (*336*, *417*), and suggests that while Notch3 is sufficient to direct initial specification and differentiation of mural cells with pericyte-like marker expression, additional yet-unidentified factors are required for maintenance of pericyte phenotype. Therefore, to further characterize the initial Notch-mediated specification and differentiation process, we focused on acutely isolated GFP^+ cells.

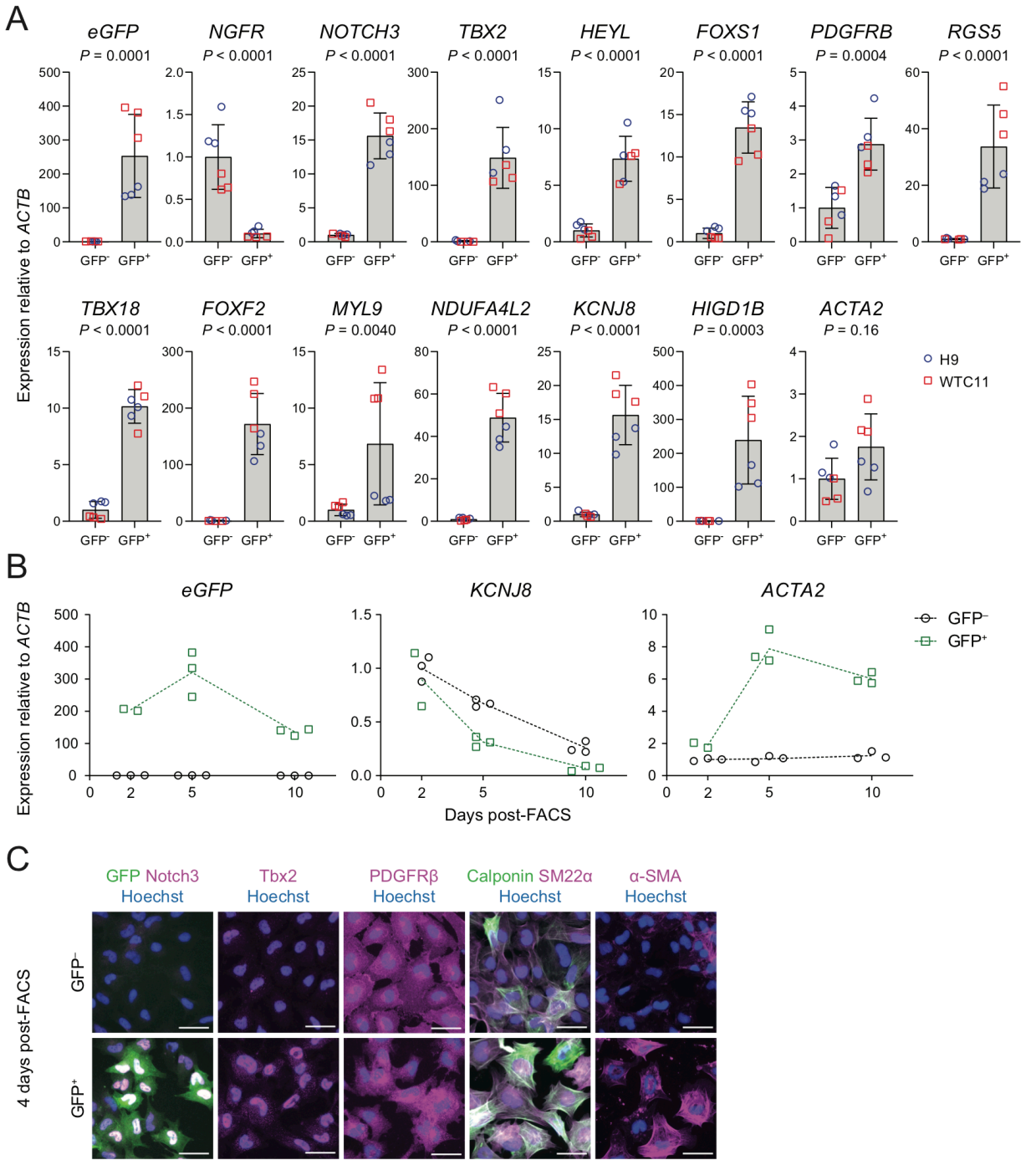

Figure 5.8. Cell-autonomous and time-dependent effects of N3ICD overexpression. (A) RT-qPCR analysis of GFP⁻ and GFP⁺ cells isolated via FACS 6 days after transduction of neural crest cultures with N3ICD-GFP lentivirus. Expression of each gene is shown relative to *ACTB* expression and normalized to expression in GFP⁻ cells. *NOTCH3* primers target the 3'UTR and thus amplify only endogenous *NOTCH3* transcripts. Points represent replicate wells from two independent differentiations, one in the H9 hPSC line (blue circles) and one in the WTC11 hPSC line (red squares). Bars indicate mean values ± SD. P-values: Two-way ANOVA. (B) RT-qPCR analysis of GFP⁺ and GFP⁻ cells 2, 5, and 10 days after isolation via FACS as described above. Points represent replicate wells from a differentiation of the H9 hPSC line. (C) Immunocytochemistry analysis of GFP, Notch3, Tbx2, PDGFRβ, calponin, SM22α, and α-SMA expression in GFP⁻ and GFP⁺ cells 4 days after isolation via FACS as described above. Hoechst nuclear counterstain overlaid in all images. Scale bars: 50 μm.

We used RNA-seq to obtain transcriptomic profiles of neural crest cells and FACS-isolated GFP$^-$ and GFP$^+$ cells from N3ICD-GFP-transduced cultures from four hPSC lines (Figure 5.9; Supplementary File). In principal component analysis, the three cell types segregated along principal component 1, which explained 66% of the variance (Figure 5.10A). Visualization of RNA-seq reads confirmed that in addition to transgene-derived *NOTCH3* transcripts, endogenous *NOTCH3* was also upregulated in GFP$^+$ cells (Figure 5.10B). We identified differentially-expressed genes in GFP$^+$ cells compared to neural crest (Figure 5.10C; Figure 5.11A; Supplementary File) and in GFP$^+$ cells compared to GFP$^-$ cells (Figure 5.10D; Figure 5.11B; Supplementary File). In both comparisons, GFP$^+$ cells were enriched for mural cell and pericyte marker genes, including the key transcription factors *HEYL*, *HES4*, *TBX2*, *FOXS1*, *FOXF2*, and *FOXC1*, some of which have established functional roles in brain pericyte development and function (*343*, *344*) (Figure 5.10C-E; Figure 5.11). *PDGFRB*, *RGS5*, *NDUFA4L2*, *KCNJ8*, *ABCC9*, *HIGD1B*, *IGFBP7*, *PLXDC1*, *CSPG4*, and *ADAMTS1* were similarly enriched in GFP$^+$ cells (Figure 5.10C-E; Figure 5.11). Consistent with results of RT-qPCR, *ACTA2* was expressed at moderate levels (~40–60 TPM) in all cell types and was not differentially expressed (Figure 5.10C-E).

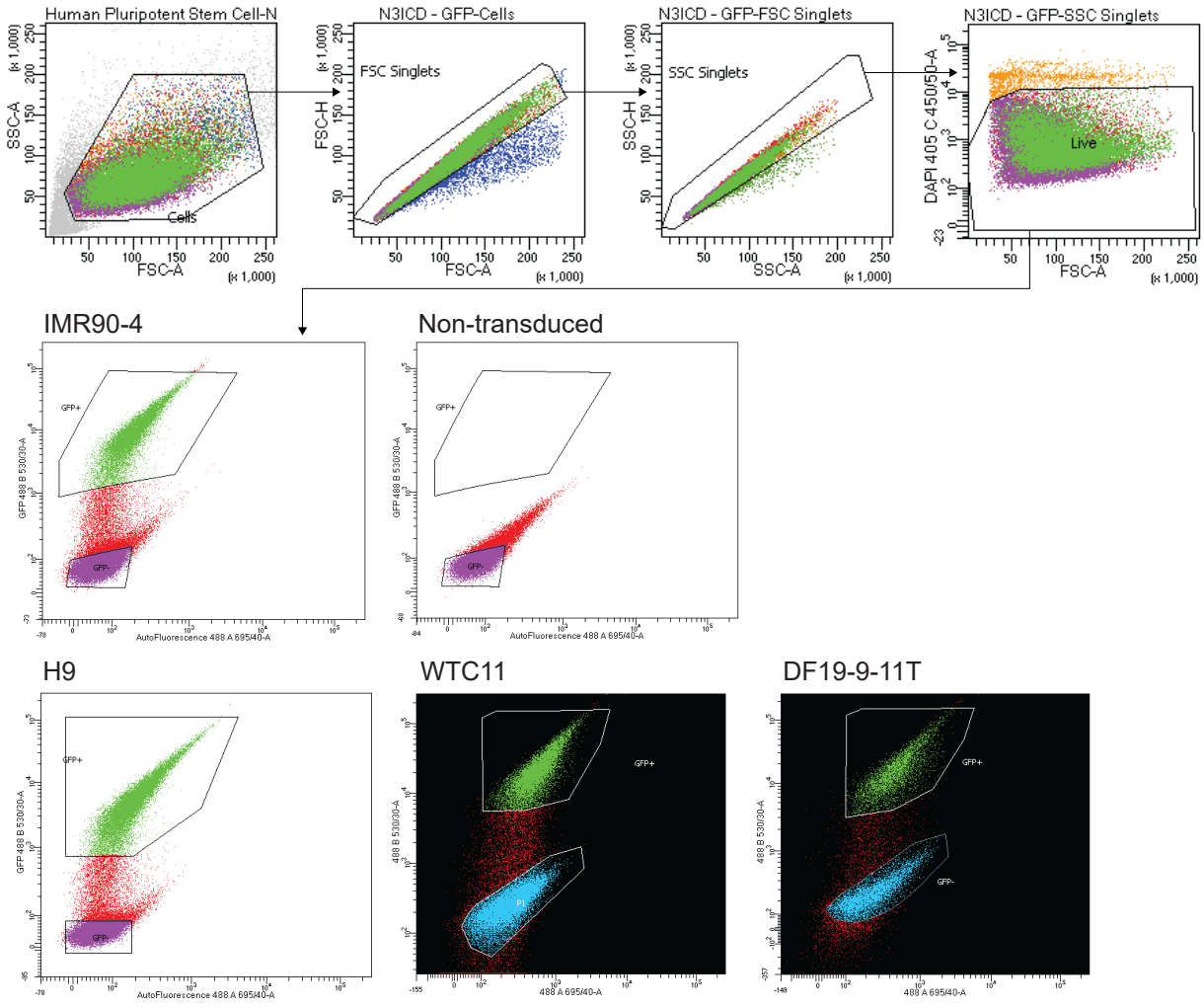

Figure 5.9. FACS gating strategy for RNA-seq samples. Examples of initial gating strategies for single cells based on forward and side scatter, followed by gating strategy for live (DAPI$^-$) cells, are shown at top. Gates for GFP$^+$ and GFP$^-$ cells are shown below for each of the four hPSC lines evaluated (IMR90-4, H9, WTC11, and DF19-9-11T). An example of a non-transduced culture from the IMR90-4 hPSC line is also shown.

The canonical neural crest marker *NGFR* was downregulated in GFP$^+$ cells compared to both neural crest and GFP$^-$ cells, as was *LIN28A*, which plays a role in neural crest multipotency (*646*). *PDGFRA*, which is enriched in fibroblasts compared to mural cells *in vivo* (*56*, *187*), was nearly absent in GFP$^+$ cells, but expressed by GFP$^-$ cells (Figure 5.10E). Although GFP$^-$ cells also expressed *PDGFRB*, they lacked several other mural cell markers and retained some expression of neural crest genes (Figure 5.10E), suggesting that interactions with N3ICD-overexpressing GFP$^+$ cells cause partial differentiation of these cells to a non-mural fate.

Hierarchical clustering revealed a gene module with highly enriched expression in GFP^+ cells compared to both $GFP^–$ cells and neural crest; this module contained known mural/pericyte transcripts, including *FOXD1*, *GJA4*, *PTGIR*, and *MCAM* (*CD146*) in addition to many of those mentioned above (Figure 5.11C-D), further supporting the mural/pericyte identity of cells derived via Notch3 activation. Genes with known enrichment in brain mural cells compared to those of other organs, including *PTN*, *GPER1*, and *SLC6A17* (*56*, *336*), were also enriched in GFP^+ cells (Figure 5.11C-D; Supplementary File), supporting the notion that brain-enriched expression is at least partially attributable to the neural crest origin Furthermore, the GABA transporter gene *SLC6A12*, which we and others recently identified as enriched in human compared to mouse brain pericytes (*90*, *187*, *336*), was robustly upregulated in GFP^+ cells compared to neural crest and $GFP^–$ cells (Figure 5.10C-E). *SLC6A1*, another human-enriched pericyte gene (*187*, *336*), however, was not expressed (Figure 5.11D), highlighting that while Notch signaling activates a mural cell transcriptional program, other factors are likely required for complete acquisition of mural cell phenotype. We also observed minimal expression of *VTN* in all cells (approximately 1 TPM), consistent with observations that human brain pericytes lack *VTN* despite robust expression in mouse brain pericytes (*90*, *336*, *505*), while other ECM-related genes (*FN1*, *COL4A1*, *COL4A2*, *COL1A1*, and *LAMA4*) were indeed upregulated in GFP^+ cells (Figure 5.10C-E). Together, these results suggest that cells derived from hPSCs via this strategy (i) are mural cells, (ii) have molecular hallmarks that distinguish brain and non-brain mural cells, and (iii) can at least partially capture species-specific differences in mural cell gene expression observed *in vivo*.

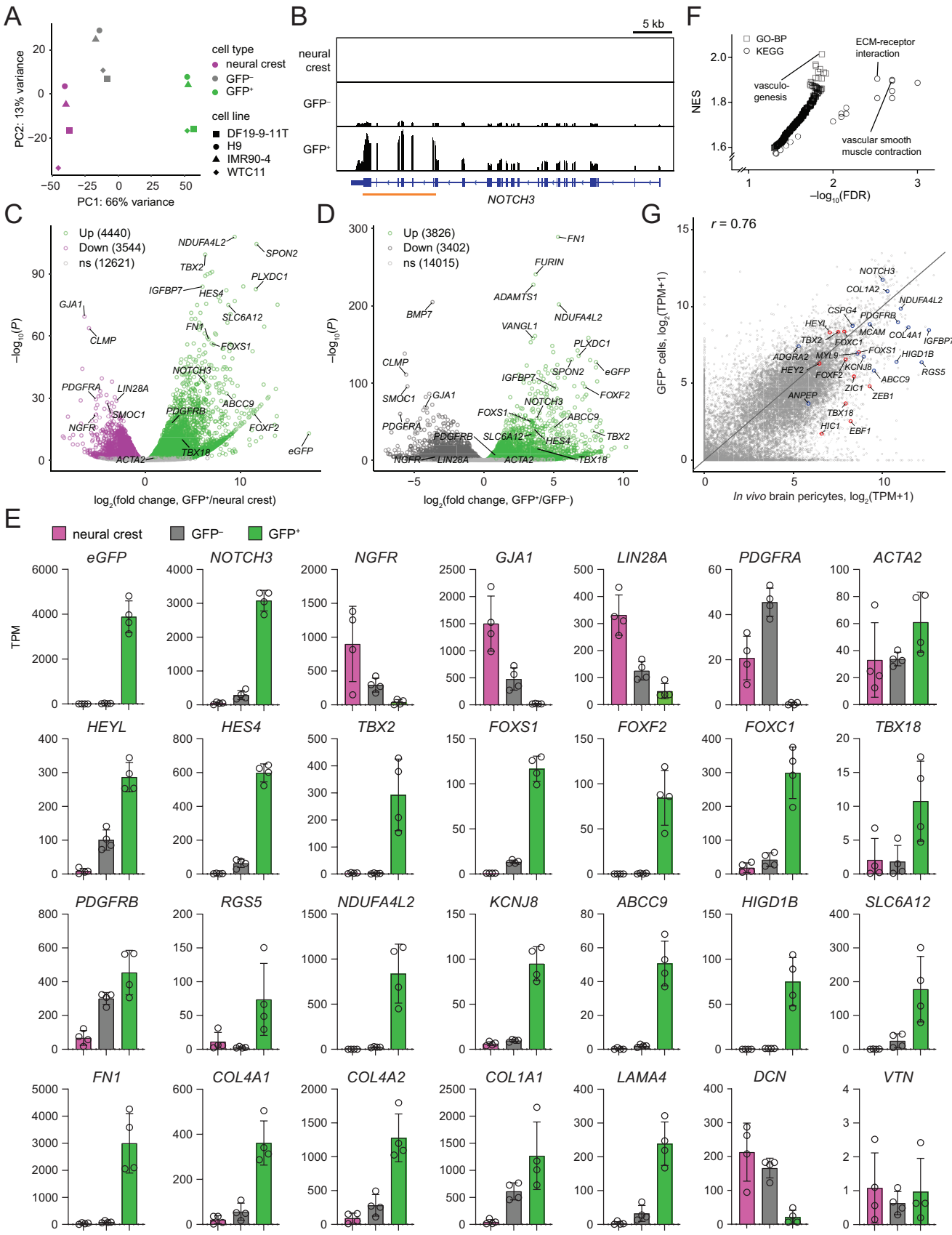
A
PC2: 13% variance
PC1: 66% variance
cell type
neural crest
GFP⁻
GFP⁺
cell line
DF19-9-11T
H9
IMR90-4
WTC11
B
5 kb
neural crest
GFP⁻
GFP⁺
NOTCH3
C
Up (4440)
Down (3544)
ns (12621)
log2(fold change, GFP⁺/neural crest)
D
Up (3826)
Down (3402)
ns (14015)
log2(fold change, GFP⁺/GFP⁻)
E
neural crest
GFP⁻
GFP⁺
TPM
eGFP
NOTCH3
NGFR
GJA1
LIN28A
PDGFRA
ACTA2
HEYL
HES4
TBX2
FOXS1
FOXF2
FOXC1
TBX18
PDGFRB
RGS5
NDUFA4L2
KCNJ8
ABCC9
HIGD1B
SLC6A12
FN1
COL4A1
COL4A2
COL1A1
LAMA4
DCN
VTN
F
GO-BP
KEGG
vasculo-genesis
ECM-receptor interaction
vascular smooth muscle contraction
NES
–log10(FDR)
G
r = 0.76
GFP⁺ cells, log2(TPM+1)
In vivo brain pericytes, log2(TPM+1)

Figure 5.10. RNA-seq of neural crest, GFP$^-$, and GFP$^+$ cells. (A) Principal component analysis of whole-transcriptome data after the DESeq2 variance stabilizing transformation. Points are colored by cell type: neural crest (magenta), GFP$^-$ cells (gray), GFP$^+$ cells (green). Data are from four independent differentiations, one each from the DF19-9-11T (squares), H9 (circles), IMR90-4 (triangles), and WTC11 (diamonds) hPSC lines. (B) Representative genome browser plots (from DF19-9-11T-derived neural crest, GFP$^-$, and GFP$^+$ cells) of RNA-seq read alignment to the *NOTCH3* gene. The orange line at bottom indicates the region of *NOTCH3* encoding the intracellular domain. (C, D) Differential expression analysis of GFP$^+$ cells compared to neural crest (C) and GFP$^+$ cells compared to GFP$^-$ cells (D). Data are displayed in volcano plots; MA plots are shown in Figure 5.11A-B. Differentially expressed genes (adjusted P-values < 0.05, DESeq2 Wald test with Benjamini-Hochberg correction) are highlighted, and the numbers of upregulated and downregulated genes are shown in the legends. Complete results of differential expression analysis are provided in Supplementary File. (E) Transcript abundance (TPM) of selected transcripts. The top row displays expression of transgene (*eGFP*), total *NOTCH3* (encompassing endogenous and transgene-derived transcripts), neural crest markers, the non-mural transcript *PDGFRA*, and the VSMC-enriched transcript *ACTA2*). The second row displays mesenchymal and mural cell transcription factors; the third row displays mural and pericyte markers; the fourth row displays genes encoding components of extracellular matrix. Additional genes are shown in Figure 5.11D, and abundance data for all genes are provided in Supplementary File. (F) Results of Gene Set Enrichment Analysis (GSEA). Gene sets from the KEGG and GO-BP databases enriched in GFP$^+$ cells compared to neural crest (*FDR* < 0.05) are shown. NES: normalized enrichment score. Additional results of GSEA are shown in Figure 5.12 and complete results are provided in Supplementary File. (G) Comparison of protein-coding transcript abundances in GFP$^+$ cells versus *in vivo* human brain pericytes. Data for hPSC-derived brain pericyte like cells were generated by averaging transcripts per million (TPM) across 11 bulk RNA-seq datasets: 5 datasets from (*447*), 3 datasets from (*324*), and 4 datasets from (*28*) (Table 5.3). Data for *in vivo* human brain pericytes were obtained from a previous meta-analysis of 5 single cell RNA-seq datasets (*336*). The Pearson correlation coefficient *r* is shown. Genes of interest are annotated in red (transcription factors) or blue (others).

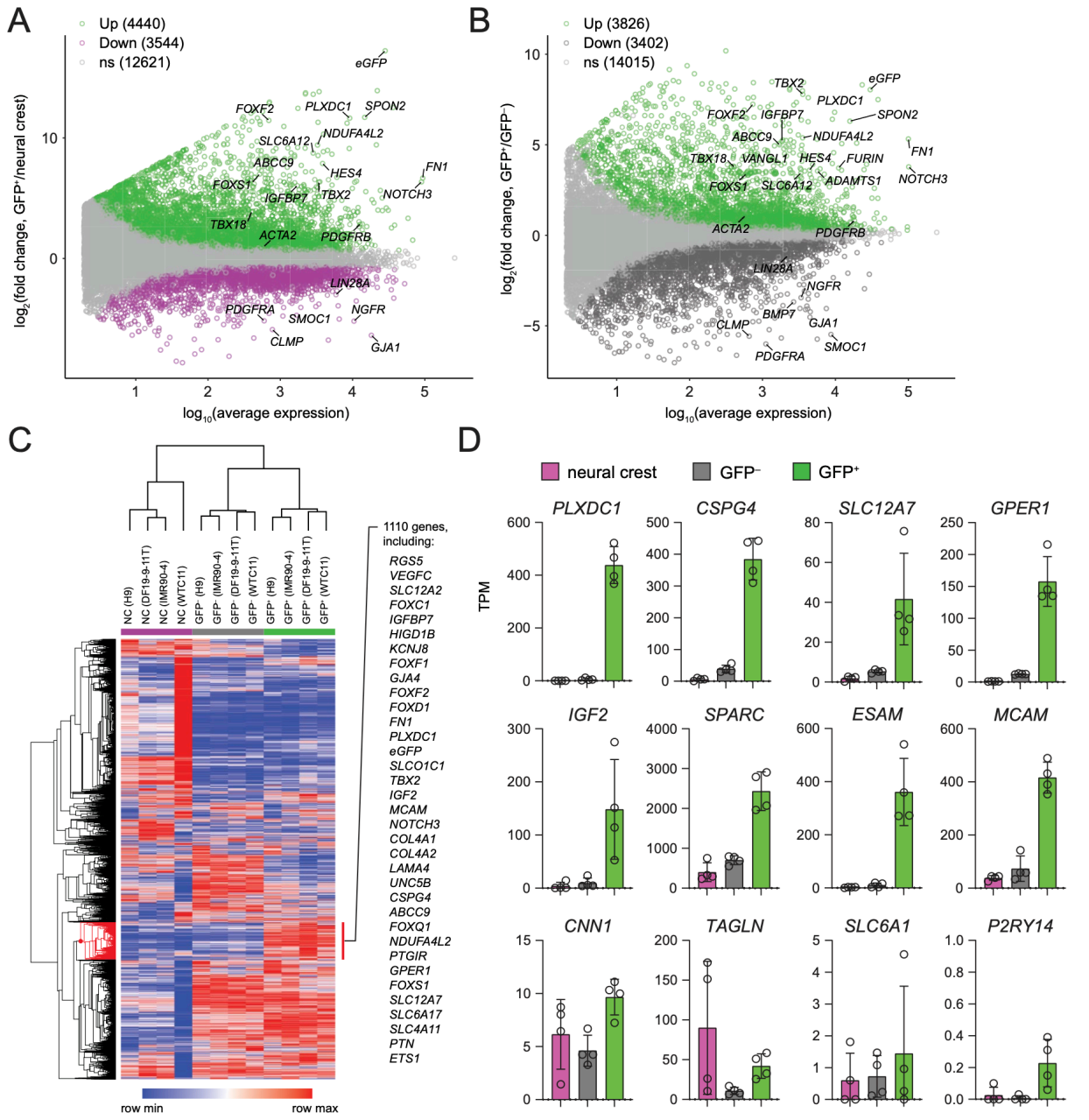

Figure 5.11. RNA-seq differential expression analysis and clustering. (A,B) Differential expression analysis of GFP$^+$ cells compared to neural crest (A) and GFP$^+$ cells compared to GFP$^-$ cells (B). Data are displayed in MA plots; volcano plots are shown in Figure 5.10C-D. Differentially expressed genes (adjusted P-values < 0.05, DESeq2 Wald test with Benjamini-Hochberg correction) are highlighted, and the numbers of upregulated and downregulated genes are shown in the legends. Complete results of differential expression analysis are provided in Supplementary File. (C) Hierarchical clustering of samples and genes. The red-colored portion of the dendrogram at left indicates a 1110-gene module exhibiting selective expression in GFP$^+$ cells compared to both GFP$^-$ cells and neural crest. Selected genes from this module are displayed at right and the complete list is provided in Supplementary File. (D) Transcript abundance (TPM) of selected mural cell-enriched transcripts. Abundance data for all genes are provided in Supplementary File.

We next identified gene sets enriched in GFP$^+$ cells compared to neural crest, using the KEGG and gene ontology-biological process (GO-BP) databases (Figure 5.10F; Figure 5.12; Supplementary File). As expected, the *Notch Signaling Pathway* gene sets from both KEGG and GO-BP databases were enriched (Figure 5.12; Supplementary File). Additional enriched gene sets included GO-BP *Vasculogenesis*, GO-BP *Nitric Oxide-Mediated Signal Transduction*, and KEGG *Vascular Smooth Muscle Contraction*, which was driven by enrichment of genes encoding guanylate and adenylate cyclases (e.g., *GUCY1B1*, *GUCY1A2*, *ADCY5*) and regulators of actomyosin contraction and cytoskeleton (e.g., *PPP1R14A*, *MYLK*, *ROCK1*), consistent with vascular mural cell identity (Figure 5.10F; Figure 5.12). Other vasculature-related GO-BP gene sets were similarly enriched (Supplementary File). Consistent with previously noted upregulation of ECM-related genes, the KEGG gene set *ECM-Receptor Interaction* was enriched (Figure 5.10F; Figure 5.12). Notably, we observed enrichment of the KEGG gene set *Neuroactive Ligand-Receptor Interaction*, which we previously reported as depleted in cultured primary brain pericytes compared to *in vivo* pericytes (*336*) (Figure 5.10F). Highly enriched genes in this set included *PTGIR*, *PTH1R*, *EDNRA*, and *GIPR* (Figure 5.12), but some genes encoding key mural cell receptors such as *P2RY14*, were not expressed (Figure 5.11D; Supplementary File), suggesting that other factors would be required to obtain cells with the complete mural cell receptor repertoire. Finally, we directly compared the average transcriptome profile of GFP$^+$ cells to that of *in vivo* human brain pericytes (Figure 5.10G). While the overall correlation was similar to that of existing hPSC-derived brain pericyte-like cells (Figure 5.1A), GFP$^+$ cells exhibited a notable improvement in the expression of key mural cell transcription factors and other markers (Figure 5.10G).

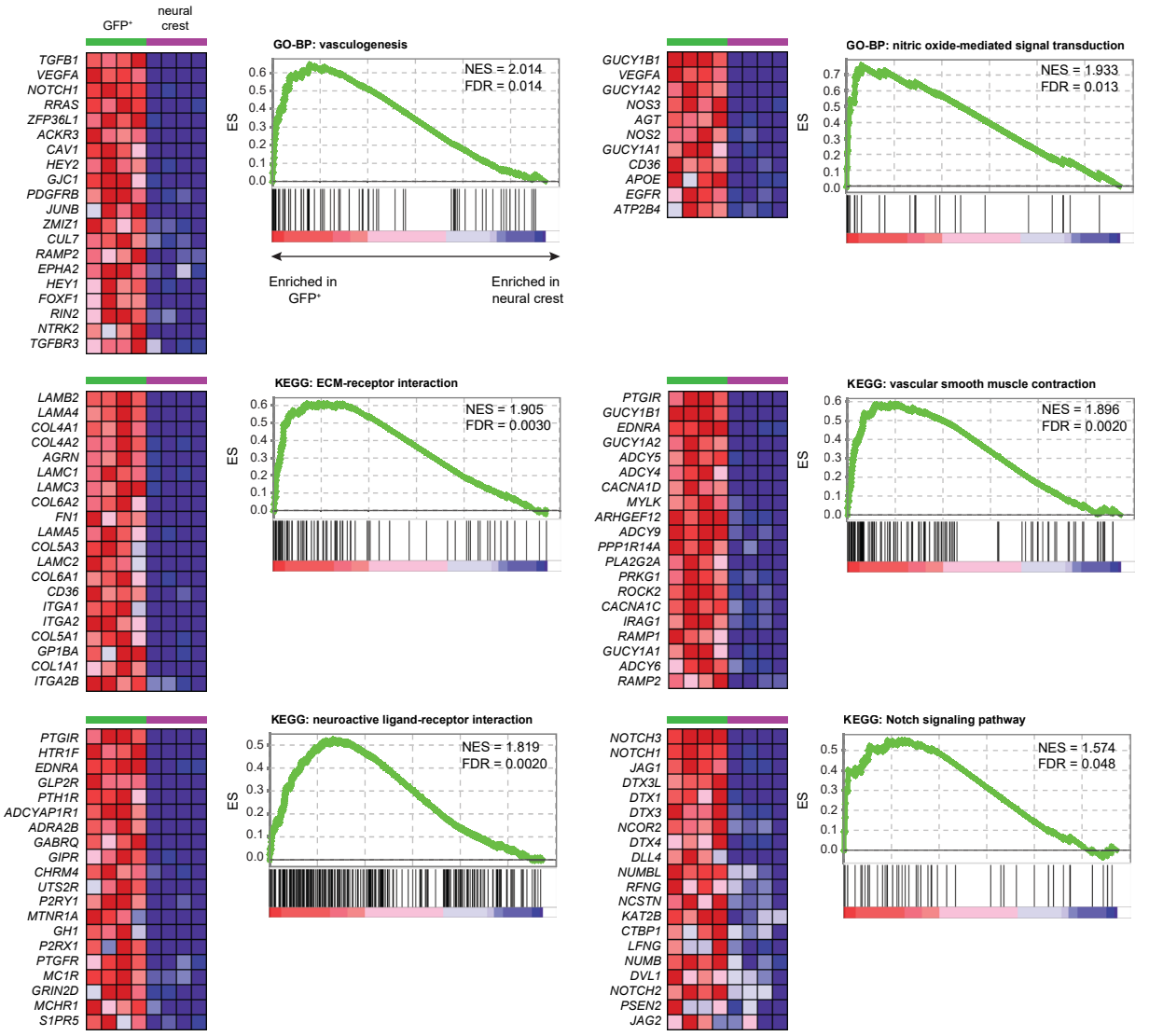

Figure 5.12. Gene sets enriched in GFP⁺ cells compared to neural crest. GSEA enrichment plots for 6 gene sets of interest are shown. For each gene set, plots at left display normalized expression of up to 20 genes listed as core enrichments for each gene set, in order of GSEA rank. NES: normalized enrichment score. Complete GSEA results are provided in Supplementary File.

5.4.4 Functional attributes of resulting mural cells

Production of vascular basement membrane is a key function of mural cells. We visually observed an apparent enrichment in the amount of ECM produced by cultures transduced with N3ICD-GFP compared to GFP, which we confirmed by decellularization followed by quantification of remaining total protein (see Section 5.3.14). Compared to GFP-transduced

cultures, N3ICD-overexpressing cultures generated approximately 20 times more extracellular matrix per cell despite a slight reduction in total cell number (Figure 5.13A-B), consistent with the marked upregulation of ECM-encoding genes in RNA-seq data and protein-level enrichment of fibronectin. We next evaluated the ability of these decellularized matrices to support formation of endothelial cords, a widely used *in vitro* proxy for angiogenic potential (*28*, *321*, *447*, *647*). While human umbilical vein endothelial cells (HUVECs) cultured on ECM from GFP-transduced cultures adopted the same cobblestone morphology as HUVECs cultured on no ECM, HUVECs cultured on ECM from N3ICD-GFP-transduced cultures formed cords, albeit more variably than on the positive control Matrigel substrate (Figure 5.13C-D). We also directly cocultured neural crest cells, and GFP^+ and GFP^- cells 5 days after FACS with HUVECs on the Matrigel substrate. 24 h after cell seeding, cords formed from HUVECs alone and those formed in neural crest cocultures were similar, while cords in GFP^- cell cocultures were longer, consistent with the ability of many mesenchymal cell types to associate with endothelial cords and modulate cord formation (*321*, *648*). In GFP^+ cell cocultures, however, we observed highly reproducible formation of mural-endothelial aggregates, a phenomenon previously observed in primary pericyte cocultures at later timepoints (*28*) and in cocultures with immature smooth muscle cells derived from hPSCs (*321*) (Figure 5.13E). Thus, while GFP^+ cells undergo molecular changes after FACS and replating (Figure 5.8), these results support a persistent, striking difference in functional phenotype between GFP^+ and GFP^- cells.

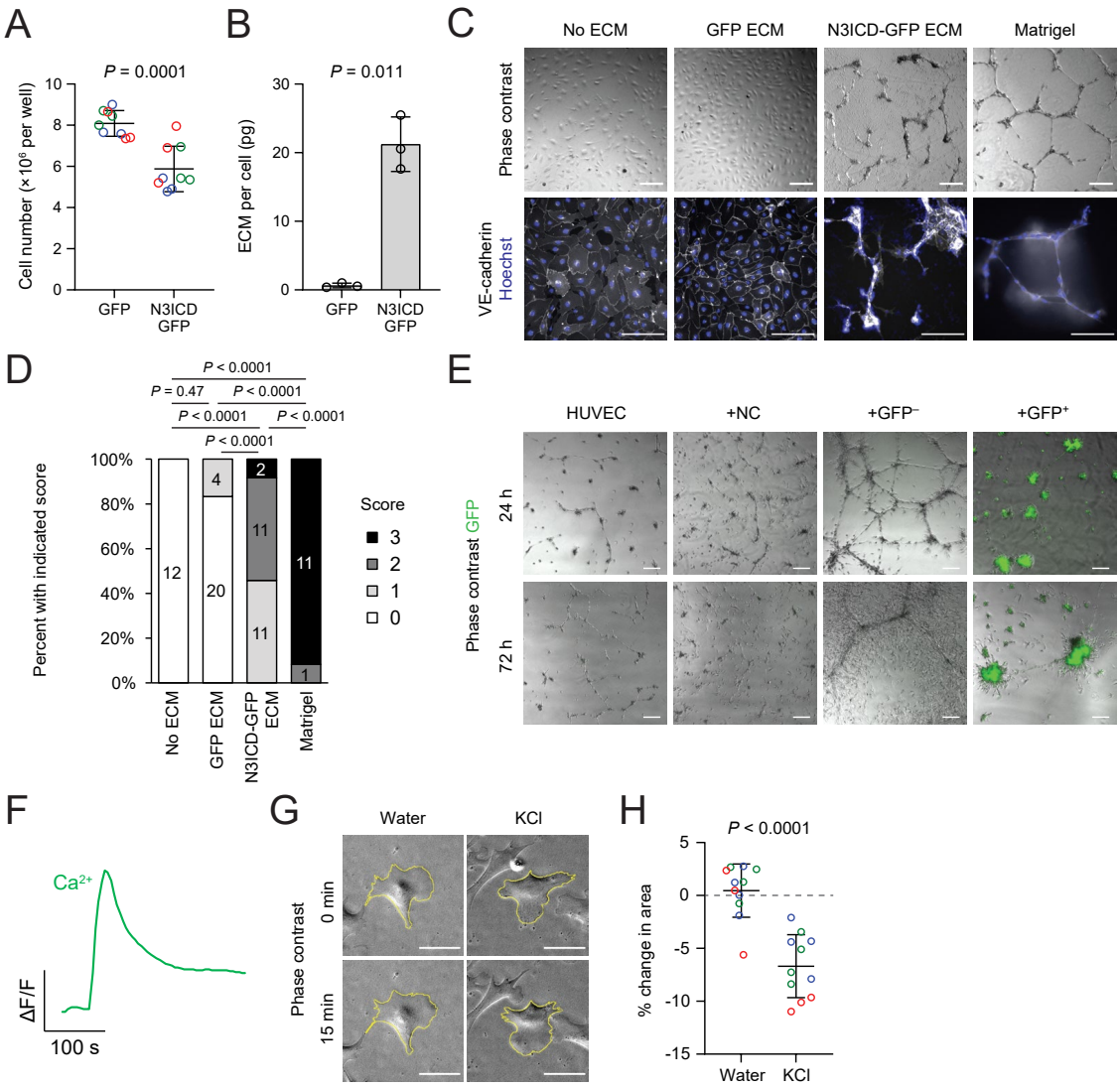

Figure 5.13. Functional properties of mural cells. (A) Number of resulting cells 6 days after transduction of neural crest with GFP or N3ICD-GFP lentiviruses. Points represent replicate wells from three differentiations of the H9 hPSC line, each differentiation indicated with a different color. Bars indicate mean values ± SD. P-value: two-way ANOVA. (B) Total extracellular matrix production 6 days after transduction of neural crest with GFP or N3ICD-GFP lentiviruses. Each point represents the average ECM quantity from three wells of a differentiation of the H9 hPSC line, normalized to average cell number from three parallel wells within the differentiation. P-value: paired Student's *t* test. (C) HUVEC cord formation assay on decellularized ECM from GFP- or N3ICD-GFP-transduced cultures, and from no ECM and Matrigel controls. Phase contrast and VE-cadherin immunocytochemistry images are shown. Hoechst nuclear counterstain overlaid in immunocytochemistry images. Scale bars: 200 µm. (D) Quantification of HUVEC cord formation for the conditions described in (C). Blinded images were scored from 0 (no cords) to 3 (virtually all cells associated with cords); see section 5.3.15. Data from the GFP ECM and N3ICD-GFP ECM conditions are derived from three independent differentiations, two in the H9 hPSC line and one in the IMR90-4 hPSC line; data from no ECM and Matrigel controls are derived from two independent experiments. P-values: Kruskal-Wallis test followed by Steel-Dwass test. (E) Coculture cord formation assay with HUVECs, HUVECs and neural crest cells (+NC), HUVECs and GFP⁻ cells from a N3ICD-GFP-transduced culture (5 days post-FACS; +GFP⁻), and HUVECs and GFP⁺ cells from a N3ICD-GFP-transduced culture (+GFP⁺). Images (overlays of phase contrast and GFP fluorescence) are shown from 24 h and 72 h after initiating assay. Scale bars: 200 µm. (F) Calcium response of cells in a N3ICD-GFP-transduced culture to KCl application. 40 mM KCl was added at $t = 50$ s. (G) Phase contrast images of GFP⁺ cells from a N3ICD-GFP-transduced culture (2 days post-FACS) at $t = 0$ min and $t = 15$ min after treatment with water (vehicle) or 40 mM KCl. Scale bars: 50 µm. (H) Change in area of GFP⁺ cells (2 days post-FACS) 15 min after treatment with water (vehicle) or 40 mM KCl. Points represent replicate wells from three differentiations of the H9 hPSC line, each differentiation indicated with a different color. Bars indicate mean values ± SD. P-value: two-way ANOVA.

Mural cells regulate vascular tone, and while the relative contributions of different mural cell subtypes to neurovascular coupling remain the subject of debate, virtually all mural cells appear capable of contraction, at least under artificial stimuli (*162*). Potassium (at concentrations causing depolarization) is widely used to assess contractility of pericytes and smooth muscle cells *in vitro* and *in vivo* (*324*, *649*). We first used calcium imaging of a N3ICD-GFP-transduced culture to confirm that application of 40 mM KCl led to depolarization and calcium influx (Figure 5.13F). Because the cell density at this time point precludes assessment of cell size, we asked whether KCl application would cause contraction of GFP^+ cells isolated via FACS and replated at low cell density (Figure 5.13G). Two days after FACS, cells underwent an average reduction in area of approximately 7% 15 min after KCl addition, compared to an average 0% change after addition of water, with cells in both conditions extending and withdrawing cellular processes (Figure 5.13G,H). Together, these results support the contractile ability of mural cells derived from neural crest via N3ICD overexpression.

5.5 Discussion

In vivo loss of function experiments have demonstrated that Notch signaling is required for mural cell development from both mesoderm- and neural crest-derived progenitors (*326*, *341*). Here, using hPSC-derived neural crest, we show that Notch signaling is sufficient to direct specification and differentiation of mural cells *in vitro*. Overexpression of the Notch3 intracellular domain in neural crest cells caused cell-autonomous differentiation to cells with molecular and functional properties of mural cells. Compared to controls, N3ICD-overexpressing cells exhibited increased expression of PDGFRβ, increased expression of full-length Notch3, and induction of mural cell transcription factors such as *HEYL*, *HES4*, *TBX2*, *FOXS1*, *FOXF2*, and *FOXC1*, some of which have previously reported roles in mural cell development (*343*, *344*). Cells derived via N3ICD overexpression produced abundant extracellular matrix, which

supported endothelial cell cord formation; these cells also self-assembled with endothelial cells and contracted in response to KCl-induced depolarization. Overexpression of the Notch1 intracellular domain had similar effects, consistent with promiscuous binding of intracellular domains from all Notch family members to RBPJ and MAML (*333*, *644*). Other signaling pathways implicated in mural cell development such as PDGF-B and TGF-β (*253*, *322*, *650*), were not required for mural cell differentiation in our model system, suggesting that these pathways may regulate other aspects of mural cell development such as recruitment to vessels and/or maturation. PDGF-BB and TGF-β, however, merit future examination for their potential ability to (i) achieve aspects of mural cell phenotype not observed using Notch3, (ii) mature the resulting cells, or (iii) maintain cell phenotype during extended culture.

Using RNA-seq, we observed Notch-induced upregulation of genes previously identified as enriched in brain mural cells compared to mural cells of other organs, such as *PTN*, *GPER1*, *SLC6A12*, *SLC6A17*, *SLC38A11*, and *ZIC1* (*56*, *336*). Observation of this brain-enriched mural cell gene signature in our *in vitro* culture system, which lacks CNS tissue-derived factors, strongly suggests that the neural crest origin at least partially defines the brain-specific molecular profile. Future work evaluating the results of N3ICD overexpression in mesodermal progenitors derived from hPSCs could further inform these findings and permit functional comparisons of mural cells derived from these two distinct lineages. Similarly, we observed upregulation of genes previously identified as enriched in human compared to mouse mural cells, including *FN1*, *SLC6A12* (*90*, *187*, *336*, *505*). Additionally, *VTN*, which is highly expressed by mouse brain mural cells, but not expressed by human brain mural cells *in vivo* (*56*, *83*, *90*, *187*, *336*, *505*), was negligibly expressed in our hPSC-derived cells. These results suggest that species differences in brain mural cell gene expression are at least partially attributable to cell-intrinsic genetic programs.

A common approach for differentiating mural cells from hPSCs, via both mesodermal and neural crest intermediates, has been to employ media supplemented with fetal bovine serum (FBS) and growth factors such as PDGF-BB, TGF-β1, Activin A, and/or FGF2 (*28*, *321*, *323*, *324*, *475*, *476*, *480*), but the necessity and/or sufficiency of each factor to drive mural cell differentiation has not been rigorously established. Several studies have used commercially available "pericyte medium," which includes FBS and a proprietary cocktail of growth factors (*28*, *324*, *480*), precluding systematic examination of molecular mechanisms. Our work establishes a serum-free method for mural cell differentiation that relies on a single, defined molecular factor, which should enable future mechanistic studies. Furthermore, while the molecular profile of existing hPSC-derived brain pericyte-like cells is remarkably similar across studies and to cultured primary brain pericytes (*28*, *324*, *447*), this molecular profile has notable departures from the *in vivo* phenotype. For example, cultured cells coexpress mural and fibroblast-associated markers and lack robust expression of canonical mural and pericyte genes such as *HEYL*, *FOXS1*, and *KCNJ8*. Our approach achieves rapid and robust induction of these mural cell transcripts without concomitant upregulation of fibroblast-associated *PDGFRA*.

Among the genes upregulated by N3ICD overexpression were markers that distinguish pericytes from VSMCs *in vivo* (e.g., *KCNJ8*, *ABCC9*, and *HIGD1B* (*56*, *336*)). These results are consistent with rapid expression of *abcc9* upon zebrafish mural cell emergence (*326*), and suggest that pericytes may be the "default" mural cell fate and that additional molecular signals may be required for VSMC specification. Our GFP^+ cells did, however, express low to moderate levels of VSMC-enriched genes (e.g., *ACTA2*, *TAGLN*, and *CNN1*), although these transcripts were also present in neural crest cells and were not upregulated upon N3ICD overexpression. Nonetheless, an alternative hypothesis is that emerging mural cells adopt an intermediate pericyte-VSMC phenotype, and that additional factors would be required to fully achieve either

fate. Our hPSC-based mural cell model is well suited to identify molecular drivers of such a pericyte/VSMC switch using either candidate factor or genetic/pharmacologic screening approaches.

Finally, we found that mural cells derived via N3ICD overexpression produce extracellular matrix capable of supporting endothelial cord formation, consistent with expression data suggesting that brain mural cells produce components of the vascular basement membrane (*56*, *336*), and with a previous study employing placental pericyte-derived ECM (*651*). We also observed that the resulting GFP^+ cells self-assemble with endothelial cells into compact aggregates, a phenomenon distinct from that observed in this work with neural crest and GFP^- cells from a N3ICD-transduced culture, and from that previously observed with hPSC-derived pericyte-like cells and primary brain pericytes (*447*). These aggregates permit direct cell-cell contact and 3-dimensional cytoarchitecture, features that are not readily achievable in monolayer cultures, and therefore represent a potential system for interrogating mural-endothelial interactions. Such interactions are important in physiological processes such as BBB development and maintenance, and in disease (*17*, *30*, *167*, *256*, *257*, *381*, *589*). hPSC-based models have been used to advance understanding of neurovascular unit physiology and pathology (*469*, *474*, *634*, *652*), motivating similar use of mural cells derived from hPSCs via N3ICD overexpression and their incorporation into multicellular models. In summary, we show that activation of Notch signaling in hPSC-derived neural crest is sufficient to direct the differentiation of brain mural cells, and establish an improved *in vitro* model that should facilitate improved understanding of brain mural cell development and function.

Chapter 6 Conclusions and future directions

6.1 Summary

In this work, we developed and applied improved models of the human NVU, using hPSCs to model cellular development *in vitro* and human tissue data to characterize the molecular properties of cells *in vivo*. Specifically, we demonstrated that activation of Wnt/β-catenin signaling in hPSC-derived endothelial progenitors is sufficient to induce several canonical BBB phenotypes in the resulting endothelial cells, and that the endothelial response to Wnt/β-catenin signaling is context-dependent (Chapter 3). We established an improved transcriptional profile of human brain mural cells *in vivo*, which enabled us to identify potentially important organ-specific and species-specific features, and broadly characterize the culture-induced dedifferentiation of brain pericytes (Chapter 4). Finally, we used these molecular data to identify a strategy to generate an improved hPSC-based model of brain mural cells: activation of Notch signaling was sufficient to direct specification and differentiation of mural cells from hPSC-derived neural crest. Broadly, this work demonstrates the utility of hPSCs and human tissue data in complementing animal studies to advance our understanding of NVU development and function.

6.2 Future directions

6.2.1 Wnt/β-catenin signaling in hPSC-based models of CNS endothelium

Wnt signaling plays a central role in CNS angiogenesis and barriergenesis. In Chapter 3, we demonstrated that activation of Wnt/β-catenin signaling in hPSC-derived naïve endothelial progenitors was sufficient to yield ECs with BBB characteristics, including robust GLUT-1 expression, partial loss of PLVAP, and increased expression of the tight junction proteins claudin-5 and LSR. To achieve Wnt activation, we employed the small molecule GSK-3

inhibitor CHIR 99021. We optimized CHIR concentration to achieve a balance between the desirable induction of GLUT-1 and the undesirable upregulation of caveolin-1; additional optimization of concentration and treatment duration, for example, to mimic the gradual attenuation of Wnt signaling observed as development progresses (*582*) (also see Section 3.5), may have beneficial effects on EC phenotype. Additionally, while CHIR is widely used to activate Wnt/β-catenin signaling, and in our system achieves a transcriptional response characteristic of Wnt/β-catenin activation (e.g., *LEF1* and *AXIN2* upregulation) and its effect was partially inhibitable by *CTNNB1* knockdown, this strategy has notable drawbacks: First, GSK-3 is involved in several signaling pathways in addition to Wnt, and CHIR-mediated GSK-3 inhibition modulates these diverse pathways; such "off-target" (β-catenin-independent) effects are likely different than those resulting from Wnt-Frizzled-Lrp5/6-mediated GSK-3 inhibition. Second, CHIR bypasses the cell surface receptors and much of the intracellular signal transduction cascade that normally transduce the signal from Wnt ligand binding, and which are under tight feedback control. Notably, the commonly used *in vivo* approach for Wnt activation, dominant active β-catenin produced by the *Ctnnb1*^{flex3} allele, does not suffer from the first drawback, but also bypasses receptor and intracellular transduction machinery. Thus, it would be informative to investigate how Wnt activation in hPSC-derived endothelial progenitors achieved via (i) overexpression of dominant active β-catenin, and (ii) natural ligands (e.g., Wnt7a, Wnt7b, and/or norrin), might result in ECs with phenotypes different from those achieved via CHIR treatment.

Preliminary data, however, suggest that recombinant Wnt7 ligands are not effective: Using the same experimental paradigm as in Chapter 3, we tested the effects of recombinant Wnt7a and Wnt7b proteins alone and in combination with R-spondin 1 (Rspo1), a potentiator of Wnt signaling that inhibits the RNF43/ZNRF3-mediated negative feedback mechanism by which

Frizzled receptors are endocytosed (*221*, *562*, *563*, *653*). Wnt7a and the combination of Wnt7a and Wnt7b, but not Wnt7b alone, slightly increased the fraction of GLUT-1$^+$ ECs, while Rspo1 did not affect EC purity or expression of GLUT-1, claudin-5 or caveolin-1. Wnt7a also increased the proportion of ECs compared to SMLCs. GLUT-1 expression, however, was markedly weaker than that achieved using 4 μM CHIR (Figure 6.1). Further supporting the ineffectiveness of recombinant Wnt7 ligands in this system is the lack of *LEF1* and *AXIN2* upregulation in RNA-seq data (Figure 6.2).

Wnt ligands are poorly soluble in aqueous solutions, exist naturally as lipidated species, and are often released from cells bound to cofactors or exosomes (*654*). Thus, conditioned medium produced by Wnt ligand-secreting mammalian cells may outperform purified recombinant ligands. Using the same paradigm as in Chapter 3, we performed preliminary evaluation of hPSC-derived neural rosette- and astrocyte-conditioned media, which are putative sources of Wnt7 ligands. Both conditioned media decreased the number of contaminating non-ECs and neural rosette-conditioned medium led to a slight increase in endothelial GLUT-1 expression, but did not approach the level of induction observed with CHIR (Figure 6.3). As an alternative, primary neural progenitors, astrocytes, or Wnt ligand-overexpressing cells could be used to produce conditioned media potentially containing higher Wnt ligand concentrations. Furthermore, Wnt ligands *in vivo* often diffuse along extracellular heparin sulfate proteoglycans or are transported along thin cellular processes (cytonemes), both mechanisms that may serve to increase the local concentration of ligand in proximity to target cells (*654*). These observations motivate the use of *contact* cocultures of naïve ECs and Wnt ligand-producing cells, for example, HEK or COS cells engineered to overexpress Wnt7a, Wnt7b, and/or norrin, as a potential strategy to increase the intensity of ligand-induced Wnt signaling in ECs. Alternatively, “next-generation surrogate” Wnts, which are water-soluble, engineered bispecific proteins

containing a Frizzled-binding domain and a Lrp5/6-binding domain (*655*), could be employed. Such engineered ligands outperform Wnt3a-conditioned medium in several *in vitro* contexts and can be designed to achieve Frizzled subtype-specificity (*655*). Finally, similar ligand-based strategies or CHIR treatment could be evaluated for their ability to prevent or slow the *in vitro* dedifferentiation of acutely-isolated primary brain ECs, given the ineffectiveness of β-catenin stabilization in this context (*226*).

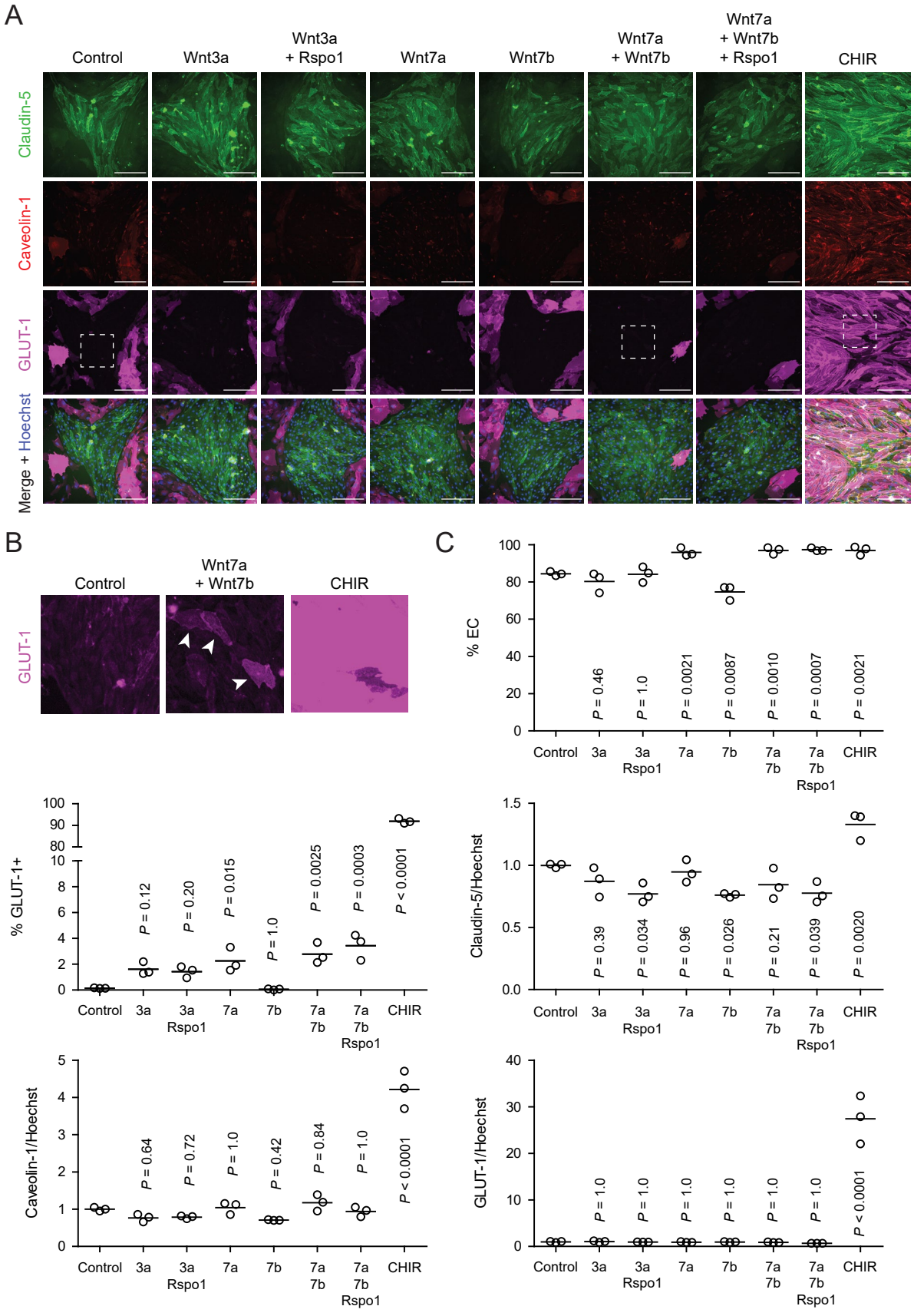
A
Control
Wnt3a
Wnt3a + Rspo1
Wnt7a
Wnt7b
Wnt7a + Wnt7b
Wnt7a + Wnt7b + Rspo1
CHIR
Claudin-5
Caveolin-1
GLUT-1
Merge + Hoechst
B
Control
Wnt7a + Wnt7b
CHIR
GLUT-1
% GLUT-1+
P = 0.12
P = 0.20
P = 0.015
P = 1.0
P = 0.0025
P = 0.0003
P < 0.0001
Caveolin-1/Hoechst
P = 0.64
P = 0.72
P = 1.0
P = 0.42
P = 0.84
P = 1.0
P < 0.0001
C
% EC
P = 0.46
P = 1.0
P = 0.0021
P = 0.0087
P = 0.0010
P = 0.0007
P = 0.0021
Claudin-5/Hoechst
P = 0.39
P = 0.034
P = 0.96
P = 0.026
P = 0.21
P = 0.039
P = 0.0020
GLUT-1/Hoechst
P = 1.0
P = 1.0
P = 1.0
P = 1.0
P = 1.0
P = 1.0
P < 0.0001
Control
3a
3a Rspo1
7a
7b
7a 7b
7a 7b Rspo1
CHIR

Figure 6.1. Effect of Wnt ligands and pathway modulators on endothelial properties. (A) Immunocytochemistry analysis of claudin-5, caveolin-1, and GLUT-1 expression in Passage 1 ECs treated with Wnt3a (20 ng/mL), Wnt3a + R-spondin 1 (Rspo1, 50 ng/mL), Wnt7a (50 ng/mL), Wnt7b (50 ng/ml), Wnt7a + Wnt7b, Wnt7a + Wnt7b + Rspo1, CHIR (4 μM), or control. All conditions include DMSO (vehicle for CHIR). Hoechst nuclear counterstain is overlaid in the merged images. Dashed boxes indicate fields displayed in (B). Scale bars: 200 μm. (B) Immunocytochemistry analysis of GLUT-1 expression in the fields indicated with dashed boxes in (A) from the control and Wnt7a + Wnt7b conditions. To visualize weak GLUT-1 immunoreactivity in Wnt7a + Wnt7b-treated ECs, a linear brightness/contrast adjustment was applied identically to the three fields but differs from that of the images shown in (A). Arrowheads indicate GLUT-1$^+$ ECs. (C) Quantification of images from the conditions described in (A) for percentage of ECs (claudin-5$^+$ cells relative to total nuclei), GLUT-1$^+$ ECs (relative to total claudin-5$^+$ ECs), and mean fluorescence intensity of claudin-5, caveolin-1, and GLUT-1 normalized to Hoechst mean fluorescence intensity within the area of claudin-5$^+$ ECs only. Points represent replicate wells from one differentiation of the IMR90-4 line and bars indicate mean values. For the fluorescence intensity plots, values were normalized such that the mean of the control condition equals 1. P-values: ANOVA followed by Dunnett's test versus control. Data from control (DMSO) and CHIR conditions are also shown in Figure 3.3.

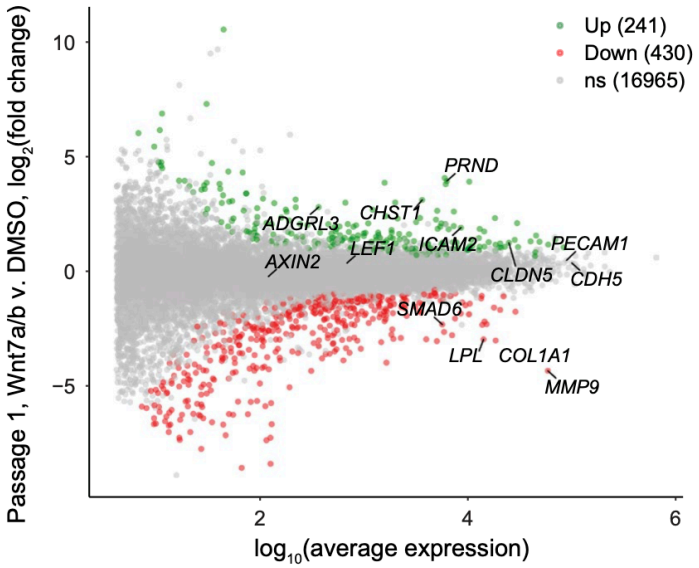

Figure 6.2. RNA-seq of Wnt7a/b-treated endothelial cells. Differential expression analysis of Passage 1 ECs treated with Wnt7a (50 ng/mL) + Wnt7b (50 ng/mL) + DMSO compared to Passage 1 DMSO-treated ECs. After 6 days of treatment, CD31+ ECs were isolated using FACS as described in Section 3.3.4. Differentially expressed genes (adjusted P-values < 0.05, DESeq2 Wald test with Benjamini-Hochberg correction) are highlighted in green (upregulated) and red (downregulated). The number of upregulated, downregulated, and non-significant (ns) genes are shown in the legends.

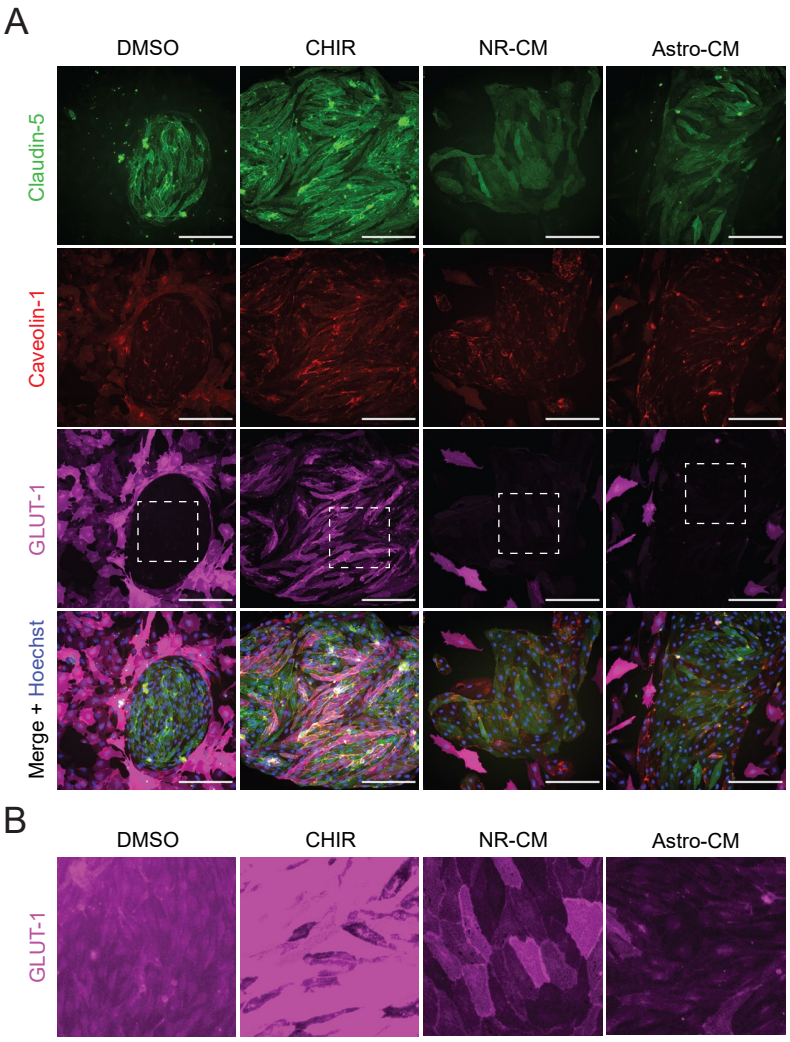

Figure 6.3. Effect of neural rosette- and astrocyte-conditioned media on endothelial properties. (A) Immunocytochemistry analysis of claudin-5, caveolin-1, and GLUT-1 expression in Passage 1 ECs treated with DMSO, CHIR, neural rosette-conditioned medium (NR-CM), or astrocyte-conditioned medium (Astro-CM). Hoechst nuclear counterstain is overlaid in the merged images. Dashed boxes indicate fields displayed in (B). Scale bars: 200 μm. (B) Immunocytochemistry analysis of GLUT-1 expression in the fields indicated with dashed boxes in (A). A linear brightness/contrast adjustment was applied identically to the four fields but differs from that of the images shown in (A).

6.2.2 Other desired properties in hPSC-derived ECs

Activation of Wnt/β-catenin signaling in hPSC-derived endothelial progenitors only partially achieves the CNS EC phenotype. Three notable attributes of CNS ECs lacking in the cells described in Chapter 3 are: (i) complete suppression of PLVAP, expression of *MFSD2A*, and functional reduction in nonspecific caveolin-mediated endocytosis, (ii) expression and function of efflux transporters such as P-gp and BCRP, and (iii) extremely low paracellular

permeability and high TEER. Identifying strategies to achieve these additional phenotypes would both generate an improved *in vitro* model of CNS endothelium for downstream applications and yield important knowledge about the cellular and molecular signals underlying acquisition of these phenotypes. Three broad classes of strategies could be employed toward this end: First, candidate molecular factors could be directly added to culture medium or produced via overexpression in cocultured cells. Candidate factors include those with known or putative roles in CNS EC development, such as retinoic acid, hedgehog, and reelin (see Section 1.4), or those identified from molecular databases as expressed by relevant CNS cell types. Second, cocultures with other NVU cells such as neural progenitors, astrocytes, and/or pericytes could be performed, with an emphasis on contact cocultures for the reasons discussed above. Acutely isolated primary cells would be ideal for such an application given that they most closely resemble cells *in vivo*. Cell lines and hPSC-derived cells, which are commonly used in such coculture models, suffer from phenotype drift and/or immaturity, and thus make negative results poorly interpretable. Third, pharmacological or genetic screens could be carried out to identify pathways or genes that control the phenotypes of interest. For example, CRISPRi/a screening could be used to identify genes that modulate endocytosis or induce efflux transporter activity. Both phenotypes are assayable on the single-cell level, and fluorescence-activated cell sorting can be used to isolate populations of ECs exhibiting reduced endocytic uptake of nonspecific fluorescent tracers, increased efflux transporter surface expression, or decreased uptake of fluorescent efflux transporter substrates. This strategy benefits from built-in positive controls (e.g., gRNAs targeting the P-gp gene itself should appear in a CRISPRa screen for P-gp inducers). Such an approach, however, is EC-autonomous, and thus may only partially reveal mechanisms by which BBB phenotypes are acquired: for example, a transcription factor may be identified as positively-regulating P-gp, but the upstream signaling pathway controlling the

transcription factor, and cell-extrinsic signals controlling the signaling pathway, may remain unclear.

Finally, in addition to Wnt activation and other molecular factors, additional time in culture may be required to achieve some BBB phenotypes. Such a strategy may be especially important to achieve phenotypes appearing in late stages of *in vivo* development, such as P-gp, which appears postnatally in rodents (*30*). Although *in vitro* "maturation" of hPSC-derived ECs has not been rigorously studied, we observed improved tight junctions and reduced proliferation rate after several passages (*468*, *656*) (see Section 1.5.2). Furthermore, other hPSC-derived cell types are immature upon initial differentiation and undergo maturation upon extended culture: for example, hPSC-derived cardiac myocytes (CMs) can be derived within 7–15 days (*577*, *657*), but have fetal-like structural, metabolic, and electrophysiological properties. Substantial additional time in culture (e.g., 100 days) can partially achieve CM maturation, among other strategies (*658*, *659*). Similarly, some hPSC-derived neuron subtypes differentiate only after prolonged *in vitro* culture (e.g., 20–30 weeks for somatostatin interneurons); such neurons emerge on a similar timeline even when progenitors are transplanted into the permissive environment of mouse brain (*660*). These analogies underscore the likelihood that intrinsic temporal programs regulate maturation of hPSC-derived cells, motivating additional investigation of hPSC-derived CNS-like ECs maturation over time.

6.2.3 Advancing hPSC-derived models of brain mural cells.

In Chapter 5, we demonstrated that activation of Notch3 signaling is sufficient to direct initial specification and differentiation of hPSC-derived neural crest cells to mural cells. 6 days after activation of Notch signaling, the resulting cells exhibited upregulated and high absolute expression of characteristic pericyte genes (e.g., *KCNJ8*, *ABCC9*, *PTN*, and *SLC6A12*), while VSMC genes (e.g., *ACTA2*, *CNN1*, *TAGLN*) had low to moderate absolute abundance and were

not differentially expressed. Some pericyte-characteristic genes such as *SLC6A1* and *P2RY14*, however, were not expressed, suggesting that additional factors are required for complete acquisition of brain pericyte phenotype. Furthermore, after isolation of GFP^+ (N3ICD-overexpressing) cells via FACS, cells replated in minimal E6 medium rapidly lost pericyte phenotype: *KCNJ8* was downregulated and *ACTA2* upregulated. One possibility is that the E6-CSFD medium (containing FGF2 and small molecule inhibitors of Wnt, BMP, and TGF-β signaling), which is used for the first 6 days after N3ICD transduction, contains factors that cooperate with Notch3 to induce and maintain pericyte phenotype. We therefore directly compared gene expression in N3ICD-overexpressing cells cultured in E6 medium versus E6-CSFD medium for 10 days after FACS and replating, and found that E6-CSFD did not rescue *KCNJ8* expression, and led to undesirable maintenance of neural crest identity (evidenced by increased *NGFR* expression), and undesirable downregulation of mural cell genes (*NOTCH3*, *TBX2*, and *FOXS1* (Figure 6.4A). An alternative hypothesis is that additional molecular factors are required for maintenance of pericyte phenotype. We evaluated effects of PDGF-BB supplementation given the important roles of PDGF signaling in mural cell development (*253*) (see Section 1.4.2). Five days after FACS and replating, N3ICD-overexpressing cells cultured in E6 medium supplemented with PDGF-BB exhibited a moderate increase in *KCNJ8* expression and a moderate reduction in *ACTA2* expression, although an undesirable reduction in *RGS5* was also observed (Figure 6.4B). Nonetheless, this result motivates further optimization of PDGF-BB concentration and timing. Similarly, other factors should be evaluated for their ability to enhance induction and maintenance of brain pericyte phenotype. As described above, genetic or pharmacological screening approaches could be employed, or candidate molecules identified from expression databases. For example, a recent scRNA-seq study of murine CNS development includes time-resolved samples of neural crest (enriched between embryonic days 8 and 10),

neural crest-derived mesenchymal cells, including fibroblasts and mural cells (first emerging at embryonic day 11), and endothelial cells across these time points (*325*); pathway and receptor/ligand interaction inference approaches (*603*, *661–664*) could be used to identify endothelium-derived signals that might regulate mural cell development.

A plausible interpretation of increased pericyte marker gene expression in N3ICD-overexpressing cells is that pericytes are the "default" mural cell fate, a hypothesis supported by early induction of the pericyte marker *abcc9* during zebrafish mural cell emergence (*326*). Thus, a key question is: what are the molecular mechanisms underlying VSMC specification and differentiation? Although FACS-isolated and replated N3ICD-overexpressing cells acquired expression of VSMC contractile proteins (α-SMA, calponin, SM22α), it remains unclear whether the mechanisms underlying this transition are developmentally relevant or artifactual. A similar gain of VSMC contractile proteins is observed during *in vitro* culture of primary brain pericytes, but in this context, cells also gain expression of fibroblast-related genes, indicative of a culture-induced dedifferentiation process likely not representative of VSMC development (see Section 4.4.4). Additional molecular characterization of the isolated and replated N3ICD-overexpressing cells is warranted to identify whether these cells lack this fibroblast-like phenotype and resemble true VSMCs. If so, experiments described above for identifying pericyte "maintenance" factors may provide insight into the pathways controlling this pericyte-VSMC transition.

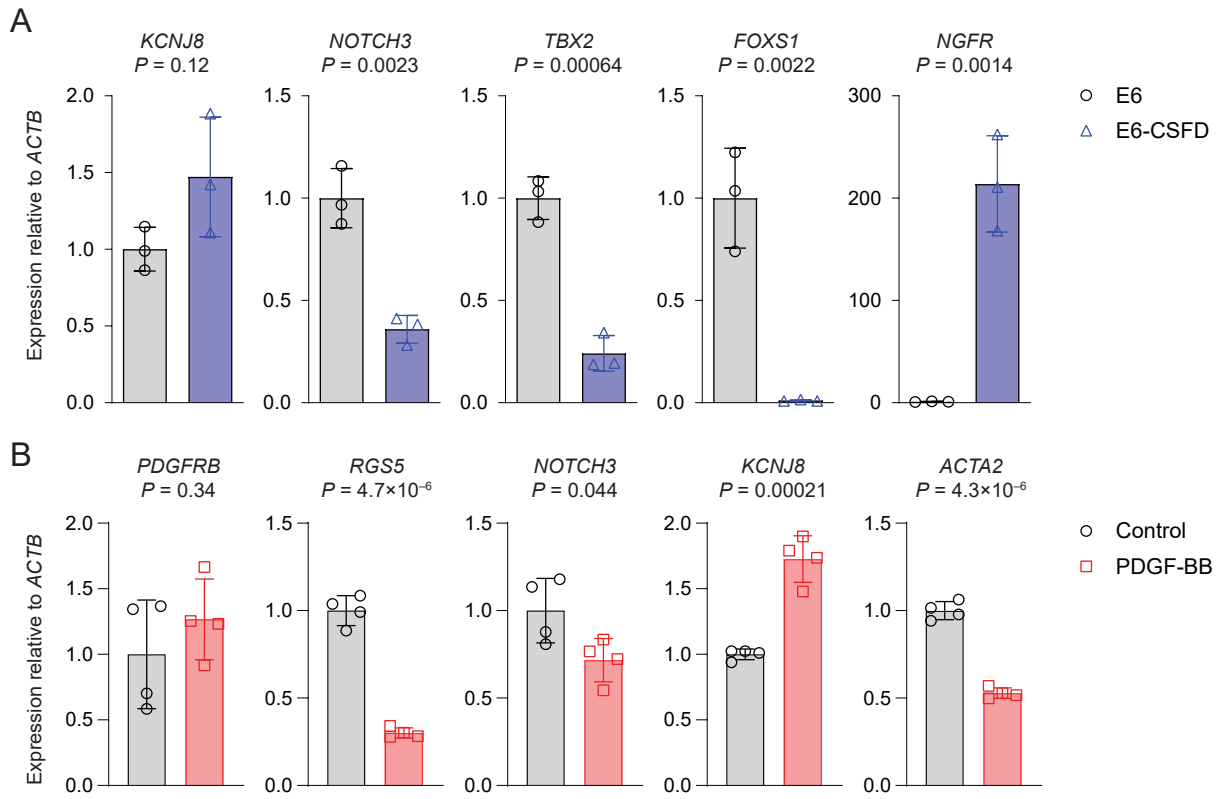

Figure 6.4. Effect of medium composition on mural cell gene expression after replating. (A) RT-qPCR analysis of mural cell and neural crest cell markers 10 days after replating FACS-isolated GFP$^+$ (N3ICD-overexpressing) cells in E6 medium or E6-CSFD medium. Points represent replicate wells from a differentiation of the H9 hPSC line. Bars represent mean ± SD. P-values: Student's *t* test. (B) RT-qPCR analysis of mural cell markers 5 days after replating cells as described in (A) in E6 medium (control) or E6 medium supplemented with 20 ng/mL PDGF-BB. Points represent replicate wells from a differentiation of the H9 hPSC line. Bars represent mean ± SD. P-values: Student's *t* test.

Finally, the lentiviral construct we employed for N3ICD overexpression does not transduce 100% of cells, necessitating either FACS or analysis of mixed cultures of transduced and non-transduced cells. Alternative overexpression strategies could be pursued to simplify the differentiation protocol. Such strategies include addition of a drug resistance gene to the lentiviral vector or generation of a hPSC line with an inducible N3ICD transgene. The latter approach would additionally permit control of N3ICD dose and timing, optimization of which might yield mural cells with improved phenotype.

6.2.4 Future applications of hPSC-derived NVU models

Much of the effort described in this work involved (i) defining expected molecular features of human NVU cells *in vivo* and (ii) developing hPSC-derived *in vitro* models that optimally mimic these characteristics. While additional work is required to further improve these models (as described above), we must not focus only on "model development" and also direct some attention toward using these models to address important scientific questions for which the models are appropriately suited. As described in Section 1.5.2, hPSCs are well suited for studies of molecular mechanisms of human cellular development. For example, one application of our Notch-mediated mural cell differentiation scheme could be to further define the transcription factor-gene regulatory network underlying this differentiation process. In the canonical model of Notch signaling, Notch intracellular domains regulate transcription of a small number of transcription factors (i.e., *HES* and *HEY* family members); however, there are tens of thousands of putative RBPJ binding sites, and Notch intracellular domains regulate a more diverse array of genes in a cell type/tissue-specific context (*333*). Thus, as a first step towards defining the gene regulatory network (GRN) underlying neural crest-to-mural cell differentiation, Notch3 chromatin immunoprecipitation and sequencing (ChIP-seq) could be used to identify genomic loci directly bound by N3ICD in a N3ICD-GFP-transduced culture. These data would illuminate Notch3 target genes, which could be evaluated for functional importance in mural cell differentiation (e.g., by knockout/knockdown). Notch3-regulated transcription factors could be similarly analyzed by ChIP-seq to further define the GRN, an approach that has been extensively applied to other neural crest derivatives (*293*). Notch3 ChIP-seq may also identify putative enhancers, which could be evaluated for functional importance (e.g., by CRISPRi-mediated disruption (*665*)); such enhancer profiling is motivated by findings that genetic variants within enhancers underlie some diseases (*666*).

Furthermore, hPSC-derived organoids are a promising model for studying human brain development and function *in vitro*, given their advantages in cell diversity, tissue architecture, and cell-cell interactions (see section 1.5.2). As models of the NVU, organoids would enable the close interactions between ECs, mural cells, and parenchymal cells that are likely required for many aspects of NVU development and function. Organoids remain underutilized for such studies, however, partially because ECs and mural cells have not been widely incorporated. Further, in several models of "vascularized" organoids, ECs are typically poorly integrated with neural tissue (Section 1.5.2). Consistent with these observations, we found that a small population of ECs spontaneously developed within cerebral organoids differentiated according to a widely-used protocol (*489*) without exogenous VEGF supplementation or other interventions, but that these ECs were located in regions without the characteristic architecture of neural tissue (Figure 6.5). Thus, additional technical advances are needed to achieve better endothelial integration, and to incorporate mural cells, such as those generated in this work via N3ICD overexpression. Such advances would enable organoids to be used to (i) define the extent to which ECs in brain organoids acquire BBB properties, potentially including those not currently achievable in hPSC-derived ECs, (ii) temporally profile this process, and (iii) identify novel cell-cell interactions important for EC and/or mural cell phenotype, using cell type-specific loss-of-function screening (e.g., CRISPRi) or split proximity labeling (*667*, *668*).

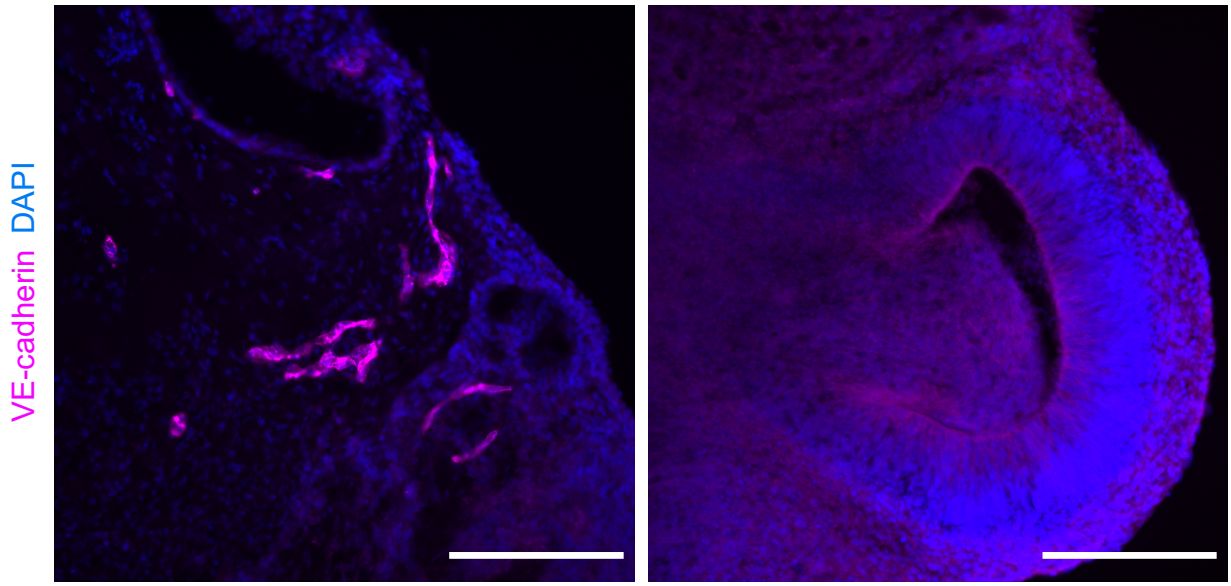

Figure 6.5. Spontaneous development of endothelial cells in cerebral organoids. Immunohistochemistry analysis of a day 60 cerebral organoid differentiated from the IMR90-4 hPSC line according to the protocol of Lancaster *et al.* (*489*). Two fields from the same organoid are shown. At left, a region containing VE-cadherin^{+} endothelial cells but lacking the layered cytoarchitecture characteristic of neural tissue is shown; at right, a region of such neural tissue. Images from 40 µm cryosections. Scale bars: 200 µm.

References

1. C. Iadecola, The Neurovascular Unit Coming of Age: A Journey through Neurovascular Coupling in Health and Disease. *Neuron*. **96**, 17–42 (2017).

2. GBD 2016 Neurology Collaborators, Global, regional, and national burden of neurological disorders, 1990-2016: a systematic analysis for the Global Burden of Disease Study 2016. *Lancet. Neurol.* **18**, 459–480 (2019).

3. M. Rezak, M. De Carvalho, Disease modification in neurodegenerative diseases: Not quite there yet. *Neurology*. **94**, 12–13 (2020).

4. W. M. Pardridge, Drug transport across the blood-brain barrier. *J. Cereb. Blood Flow Metab.* **32**, 1959–1972 (2012).

5. H. M. Duvernoy, S. Delon, J. L. Vannson, Cortical blood vessels of the human brain. *Brain Res. Bull.* **7**, 519–79 (1981).

6. H. Duvernoy, S. Delon, J. L. Vannson, The vascularization of the human cerebellar cortex. *Brain Res. Bull.* **11**, 419–80 (1983).

7. T. A. Lovick, L. A. Brown, B. J. Key, Neurovascular relationships in hippocampal slices: Physiological and anatomical studies of mechanisms underlying flow-metabolism coupling in intraparenchymal microvessels. *Neuroscience*. **92**, 47–60 (1999).

8. N. N. Kumar, M. E. Pizzo, G. Nehra, B. Wilken-Resman, S. Boroumand, R. G. Thorne, Passive Immunotherapies for Central Nervous System Disorders: Current Delivery Challenges and New Approaches. *Bioconjug. Chem.* **29**, 3937–3966 (2018).

9. J. M. Lajoie, E. V. Shusta, Targeting receptor-mediated transport for delivery of biologics across the blood-brain barrier. *Annu. Rev. Pharmacol. Toxicol.* **55**, 613–31 (2015).

10. A. R. Jones, E. V. Shusta, Blood-brain barrier transport of therapeutics via receptor-mediation. *Pharm. Res.* **24**, 1759–1771 (2007).

11. S. Hochmeister, R. Grundtner, J. Bauer, B. Engelhardt, R. Lyck, G. Gordon, T. Korosec, A. Kutzelnigg, J. J. Berger, M. Bradl, R. E. Bittner, H. Lassmann, Dysferlin is a new marker for leaky brain blood vessels in multiple sclerosis. *J. Neuropathol. Exp. Neurol.* **65**, 855–865 (2006).

12. H. Lassmann, Pathogenic mechanisms associated with different clinical courses of multiple sclerosis. *Front. Immunol.* **10**, 1–14 (2019).

13. R. I. Grossman, F. Gonzalez-Scarano, S. W. Atlas, S. Galetta, D. H. Silberberg, Multiple sclerosis: gadolinium enhancement in MR imaging. *Radiology*. **161**, 721–5 (1986).

14. H. Nishihara, B. Engelhardt, Brain Barriers and Multiple Sclerosis: Novel Treatment Approaches from a Brain Barriers Perspective. *Handb. Exp. Pharmacol.* (2020),

doi:10.1007/164_2020_407.

15. Z. Zhao, A. P. Sagare, Q. Ma, M. R. Halliday, P. Kong, K. Kisler, E. A. Winkler, A. Ramanathan, T. Kanekiyo, G. Bu, N. C. Owens, S. V. Rege, G. Si, A. Ahuja, D. Zhu, C. A. Miller, J. A. Schneider, M. Maeda, T. Maeda, T. Sugawara, J. K. Ichida, B. V. Zlokovic, Central role for PICALM in amyloid-β blood-brain barrier transcytosis and clearance. *Nat. Neurosci.* **18**, 978–987 (2015).

16. B. V Zlokovic, The Blood-Brain Barrier in Health and Chronic Neurodegenerative Disorders. *Neuron*. **57**, 178–201 (2008).

17. M. R. Halliday, S. V Rege, Q. Ma, Z. Zhao, C. A. Miller, E. a Winkler, B. V Zlokovic, Accelerated pericyte degeneration and blood-brain barrier breakdown in apolipoprotein E4 carriers with Alzheimer's disease. *J. Cereb. Blood Flow Metab.* **36**, 1–9 (2015).

18. J. R. Cirrito, R. Deane, A. M. Fagan, M. L. Spinner, M. Parsadanian, M. B. Finn, H. Jiang, J. L. Prior, A. Sagare, K. R. Bales, S. M. Paul, B. V Zlokovic, D. Piwnica-Worms, D. M. Holtzman, P-glycoprotein deficiency at the blood-brain barrier increases amyloid-beta deposition in an Alzheimer disease mouse model. *J. Clin. Invest.* **115**, 3285–90 (2005).

19. M. Shibata, S. Yamada, S. R. Kumar, M. Calero, J. Bading, B. Frangione, D. M. Holtzman, C. a Miller, D. K. Strickland, J. Ghiso, B. V Zlokovic, Clearance of Alzheimer's amyloid-β1-40 peptide from brain by LDL receptor–related protein-1 at the blood-brain barrier. *J. Clin. Invest.* **106**, 1489–1499 (2000).

20. S. E. Storck, S. Meister, J. Nahrath, J. N. Meißner, N. Schubert, A. Di Spiezio, S. Baches, R. E. Vandenbroucke, Y. Bouter, I. Prikulis, C. Korth, S. Weggen, A. Heimann, M. Schwaninger, T. A. Bayer, C. U. Pietrzik, Endothelial LRP1 transports amyloid-β(1-42) across the blood-brain barrier. *J. Clin. Invest.* **126**, 123–36 (2016).

21. S. E. Storck, A. M. S. Hartz, J. Bernard, A. Wolf, A. Kachlmeier, A. Mahringer, S. Weggen, J. Pahnke, C. U. Pietrzik, The concerted amyloid-beta clearance of LRP1 and ABCB1/P-gp across the blood-brain barrier is linked by PICALM. *Brain. Behav. Immun.* **73**, 21–33 (2018).

22. T. Kuroiwa, P. Ting, H. Martinez, I. Klatzo, The biphasic opening of the blood-brain barrier to proteins following temporary middle cerebral artery occlusion. *Acta Neuropathol.* **68**, 122–129 (1985).

23. D. Knowland, A. Arac, K. J. Sekiguchi, M. Hsu, S. E. Lutz, J. Perrino, G. K. Steinberg, B. A. Barres, A. Nimmerjahn, D. Agalliu, Stepwise Recruitment of Transcellular and Paracellular Pathways Underlies Blood-Brain Barrier Breakdown in Stroke. *Neuron*. **82**, 603–617 (2014).

24. W. Cai, K. Zhang, P. Li, L. Zhu, J. Xu, B. Yang, X. Hu, Z. Lu, J. Chen, Dysfunction of the neurovascular unit in ischemic stroke and neurodegenerative diseases: An aging effect. *Ageing Res. Rev.* **34**, 77–87 (2017).

25. G. J. Del Zoppo, The neurovascular unit in the setting of stroke. *J. Intern. Med.* **267**, 156–

171 (2010).

26. M. Yemisci, Y. Gursoy-Ozdemir, A. Vural, A. Can, K. Topalkara, T. Dalkara, Pericyte contraction induced by oxidative-nitrative stress impairs capillary reflow despite successful opening of an occluded cerebral artery. *Nat. Med.* **15**, 1031–1037 (2009).

27. C. N. Hall, C. Reynell, B. Gesslein, N. B. Hamilton, A. Mishra, B. A. Sutherland, F. M. O'Farrell, A. M. Buchan, M. Lauritzen, D. Attwell, Capillary pericytes regulate cerebral blood flow in health and disease. *Nature*. **508**, 55–60 (2014).

28. J. Sun, Y. Huang, J. Gong, J. Wang, Y. Fan, J. Cai, Y. Wang, Y. Qiu, Y. Wei, C. Xiong, J. Chen, B. Wang, Y. Ma, L. Huang, X. Chen, S. Zheng, W. Huang, Q. Ke, T. Wang, X. Li, W. Zhang, A. P. Xiang, W. Li, Transplantation of hPSC-derived pericyte-like cells promotes functional recovery in ischemic stroke mice. *Nat. Commun.* **11** (2020), doi:10.1038/s41467-020-19042-y.

29. C.-C. Tsao, J. Baumann, S.-F. Huang, D. Kindler, A. Schroeter, N. Kachappilly, M. Gassmann, M. Rudin, O. O. Ogunshola, Pericyte hypoxia-inducible factor-1 (HIF-1) drives blood-brain barrier disruption and impacts acute ischemic stroke outcome. *Angiogenesis*. **1** (2021), doi:10.1007/s10456-021-09796-4.

30. R. Daneman, L. Zhou, A. A. Kebede, B. A. Barres, Pericytes are required for blood-brain barrier integrity during embryogenesis. *Nature*. **468**, 562–6 (2010).

31. M. Martin, S. Vermeiren, N. Bostaille, M. Eubelen, D. Spitzer, M. Vermeersch, C. P. Profaci, E. Pozuelo, X. Toussay, J. Raman-Nair, P. Tebabi, M. America, A. de Groote, L. E. Sanderson, P. Cabochette, R. F. V. Germano, D. Torres, S. Boutry, A. de Kerchove D'Exaerde, E. J. Bellefroid, T. N. Phoenix, K. Devraj, B. Lacoste, R. Daneman, S. Liebner, B. Vanhollebeke, Engineered Wnt ligands enable blood-brain barrier repair in neurological disorders. *Science (80-.).* **375** (2022), doi:10.1126/science.abm4459.

32. Z. M. Wang, Z. Ying, A. Bosy-Westphal, J. Zhang, B. Schautz, W. Later, S. B. Heymsfield, M. J. Müller, Specific metabolic rates of major organs and tissues across adulthood: Evaluation by mechanistic model of resting energy expenditure. *Am. J. Clin. Nutr.* **92**, 1369–1377 (2010).

33. L. C. Aiello, P. Wheeler, The Expensive-Tissue Hypothesis. *Curr. Anthropol.* **36**, 199–221 (1995).

34. H. Ridley, *The Anatomy of the Brain* (Sam. Smith and Benj. Walford, London, 1695).

35. S. A. Liddelow, Fluids and barriers of the CNS: A historical viewpoint. *Fluids Barriers CNS*. **8**, 2 (2011).

36. P. Ehrlich, *Das Sauerstoff-Bedürfniss des Organismus: Eine farbenanalytische Studie* (A. Hirschwald, Berlin, 1885).

37. E. Goldmann, *Die äussere und Sekretion des gesunden und kranken Organismus im Lichte der "vitalen Färbung"* (Tubingen, 1909).

38. M. Lewandowsky, Zur lehre der cerebrospinal flüssigkeit. *Z. Klin. Med.* **40**, 480–494 (1900).

39. T. S. Reese, M. J. Karnovsky, Fine structural localization of a blood-brain barrier to exogenous peroxidase. *J. Cell Biol.* **34**, 207–217 (1967).

40. G. E. Palade, Blood capillaries of the heart and other organs. *Circulation*. **24**, 368–88 (1961).

41. M. W. Brightman, T. S. Reese, Junctions between intimately apposed cell membranes in the vertebrate brain. *J. Cell Biol.* **40**, 648–77 (1969).

42. E. De Robertis, H. M. Gerschenfeld, in *International Review of Neurobiology* (1961; https://linkinghub.elsevier.com/retrieve/pii/S0074774208600057), vol. 3, pp. 1–65.

43. N. Kutuzov, H. Flyvbjerg, M. Lauritzen, Contributions of the glycocalyx, endothelium, and extravascular compartment to the blood–brain barrier. *Proc. Natl. Acad. Sci.* **115**, E9429–E9438 (2018).

44. Y. Ando, H. Okada, G. Takemura, K. Suzuki, C. Takada, H. Tomita, R. Zaikokuji, Y. Hotta, N. Miyazaki, H. Yano, I. Muraki, A. Kuroda, H. Fukuda, Y. Kawasaki, H. Okamoto, T. Kawaguchi, T. Watanabe, T. Doi, T. Yoshida, H. Ushikoshi, S. Yoshida, S. Ogura, Brain-Specific Ultrastructure of Capillary Endothelial Glycocalyx and Its Possible Contribution for Blood Brain Barrier. *Sci. Rep.* **8**, 1–9 (2018).

45. M. Bundgaard, N. J. Abbott, All vertebrates started out with a glial blood-brain barrier 4-500 million years ago. *Glia*. **56**, 699–708 (2008).

46. N. M. O'Brown, S. J. Pfau, C. Gu, Bridging barriers: A comparative look at the blood-brain barrier across organisms. *Genes Dev.* **32**, 466–478 (2018).

47. F. Mayer, N. Mayer, L. Chinn, R. L. Pinsonneault, D. Kroetz, R. J. Bainton, Evolutionary Conservation of Vertebrate Blood-Brain Barrier Chemoprotective Mechanisms in Drosophila. *J. Neurosci.* **29**, 3538–3550 (2009).

48. S. L. Zhang, Z. Yue, D. M. Arnold, G. Artiushin, A. Sehgal, A Circadian Clock in the Blood-Brain Barrier Regulates Xenobiotic Efflux. *Cell*. **173**, 1–10 (2018).

49. E. Palm, On the occurrence in the retina of conditions corresponding to the blood-brain barrier. *Acta Ophthalmol.* **25**, 29–35 (1947).

50. J. G. Cunha-Vaz, M. Shakib, N. Ashton, Studies on the permeability of the blood-retinal barrier, I. On the existence, development, and site of a blood-retinal barrier. *Br. J. Opthalmology*. **50**, 441–453 (1966).

51. T. Nitta, M. Hata, S. Gotoh, Y. Seo, H. Sasaki, N. Hashimoto, M. Furuse, S. Tsukita, Size-selective loosening of the blood-brain barrier in claudin-5–deficient mice. *J. Cell Biol.* **161**, 653–660 (2003).

52. S. Liebner, A. Fischmann, G. Rascher, F. Duffner, E.-H. Grote, H. Kalbacher, H.

Wolburg, Claudin-1 and claudin-5 expression and tight junction morphology are altered in blood vessels of human glioblastoma multiforme. *Acta Neuropathol.* **100**, 323–331 (2000).

53. T. Hirase, J. M. Staddon, M. Saitou, Y. Ando-Akatsuka, M. Itoh, M. Furuse, K. Fujimoto, S. Tsukita, L. L. Rubin, Occludin as a possible determinant of tight junction permeability in endothelial cells. *J. Cell Sci.* **110**, 1603–1613 (1997).

54. M. Castro Dias, C. Coisne, I. Lazarevic, P. Baden, M. Hata, N. Iwamoto, D. Miguel, F. Francisco, M. Vanlandewijck, L. He, F. A. Baier, D. Stroka, R. Bruggmann, R. Lyck, G. En, U. Deutsch, C. Betsholtz, M. Furuse, T. Shoichiro, B. Engelhardt, M. Castro Dias, C. Coisne, I. Lazarevic, P. Baden, M. Hata, N. Iwamoto, D. M. F. Francisco, M. Vanlandewijck, L. He, F. A. Baier, D. Stroka, R. Bruggmann, R. Lyck, G. Enzmann, U. Deutsch, C. Betsholtz, M. Furuse, S. Tsukita, B. Engelhardt, Claudin-3-deficient C57BL/6J mice display intact brain barriers. *Sci. Rep.* **9**, 1–16 (2019).

55. M. Castro Dias, C. Coisne, P. Baden, G. Enzmann, L. Garrett, L. Becker, S. M. Hölter, A. Aguilar-Pimentel, T. Adler, D. H. Busch, N. Spielmann, K. Moreth, W. Hans, O. Amarie, J. Graw, J. Rozman, I. Radc, F. Neff, J. Calzada-Wack, B. Rathkolb, E. Wolf, T. Klopstock, W. Wurst, J. Beckers, M. Östereicher, G. Miller, H. Maier, C. Stoeger, S. Leuchtenberger, V. Gailus-Durner, H. Fuchs, M. Hrabě De Angelis, U. Deutsch, B. Engelhardt, Claudin-12 is not required for blood-brain barrier tight junction function. *Fluids Barriers CNS*. **16**, 1–17 (2019).

56. M. Vanlandewijck, L. He, M. A. Mäe, J. Andrae, K. Ando, F. Del Gaudio, K. Nahar, T. Lebouvier, B. Laviña, L. Gouveia, Y. Sun, E. Raschperger, M. Räsänen, Y. Zarb, N. Mochizuki, A. Keller, U. Lendahl, C. Betsholtz, A molecular atlas of cell types and zonation in the brain vasculature. *Nature*. **554**, 475–480 (2018).

57. C. Schulze, J. A. Firth, Immunohistochemical localization of adherens junction components in blood-brain barrier microvessels of the rat. *J. Cell Sci.* **104**, 773–782 (1993).

58. A. W. Vorbrodt, D. H. Dobrogowska, Molecular anatomy of interendothelial junctions in human blood-brain barrier microvessels. *Folia Histochem. Cytobiol.* **42**, 67–75 (2004).

59. E. Dejana, Endothelial cell-cell junctions: Happy together. *Nat. Rev. Mol. Cell Biol.* **5**, 261–270 (2004).

60. J. Ikenouchi, M. Furuse, K. Furuse, H. Sasaki, S. Tsukita, S. Tsukita, Tricellulin constitutes a novel barrier at tricellular contacts of epithelial cells. *J. Cell Biol.* **171**, 939–945 (2005).

61. S. Masuda, Y. Oda, H. Sasaki, J. Ikenouchi, T. Higashi, M. Akashi, E. Nishi, M. Furuse, LSR defines cell corners for tricellular tight junction formation in epithelial cells. *J. Cell Sci.* **124**, 548–555 (2011).

62. F. Sohet, C. Lin, R. N. Munji, S. Y. Lee, N. Ruderisch, A. Soung, T. D. Arnold, N. Derugin, Z. S. Vexler, F. T. Yen, R. Daneman, LSR/angulin-1 is a tricellular tight junction

protein involved in blood–brain barrier formation. *J. Cell Biol.* **208**, 703–711 (2015).

63. L. Guo, H. Zhang, Y. Hou, T. Wei, J. Liu, Plasmalemma vesicle–associated protein: A crucial component of vascular homeostasis (Review). *Exp. Ther. Med.* **12**, 1639–1644 (2016).

64. P. A. Stewart, Endothelial vesicles in the blood-brain barrier: Are they related to permeability? *Cell. Mol. Neurobiol.* **20**, 149–163 (2000).

65. M. F. Sabbagh, J. S. Heng, C. Luo, R. G. Castanon, J. R. Nery, A. Rattner, L. A. Goff, J. R. Ecker, J. Nathans, Transcriptional and epigenomic landscapes of CNS and non-CNS vascular endothelial cells. *Elife*. **7**, 1–44 (2018).

66. L. Herrnberger, R. Seitz, S. Kuespert, M. R. Bösl, R. Fuchshofer, E. R. Tamm, Lack of endothelial diaphragms in fenestrae and caveolae of mutant Plvap-deficient mice. *Histochem. Cell Biol.* **138**, 709–724 (2012).

67. E. K. Bosma, C. J. F. Van Noorden, R. O. Schlingemann, I. Klaassen, The role of plasmalemma vesicle-associated protein in pathological breakdown of blood-brain and blood-retinal barriers: Potential novel therapeutic target for cerebral edema and diabetic macular edema. *Fluids Barriers CNS*. **15**, 1–17 (2018).

68. R. Hallmann, D. N. Mayer, E. L. Berg, R. Broermann, E. C. Butcher, Novel mouse endothelial cell surface marker is suppressed during differentiation of the blood brain barrier. *Dev. Dyn.* **202**, 325–332 (1995).

69. A. Weindl, in *Frontiers in Neuroendocrinology*, W. Ganong, L. Martini, Eds. (Oxford University Press, London, 1973), pp. 3–32.

70. P. M. Gross, A. Weindl, Peering through the windows of the brain. *J. Cereb. Blood Flow Metab.* **7**, 663–672 (1987).

71. Y. Wang, M. F. Sabbagh, X. Gu, A. Rattner, J. Williams, J. Nathans, Beta-catenin signaling regulates barrier- specific gene expression in circumventricular organ and ocular vasculatures. *Elife*. **8**, 1–36 (2019).

72. W. Löscher, H. Potschka, Blood-brain barrier active efflux transporters: ATP-binding cassette gene family. *NeuroRx*. **2**, 86–98 (2005).

73. S. Shen, W. Zhang, ABC Transporters and Drug Efflux at the Blood-Brain Barrier. *Rev. Neurosci.* **21**, 29–53 (2010).

74. F. C. Lam, R. Liu, P. Lu, A. B. Shapiro, J. M. Renoir, F. J. Sharom, P. B. Reiner, β-Amyloid efflux mediated by p-glycoprotein. *J. Neurochem.* **76**, 1121–1128 (2001).

75. R. L. Juliano, V. Ling, A surface glycoprotein modulating drug permeability in Chinese hamster ovary cell mutants. *BBA - Biomembr.* **455**, 152–162 (1976).

76. J. R. Riordan, V. Ling, Purification of P-glycoprotein from plasma membrane vesicles of Chinese hamster ovary cell mutants with reduced colchicine permeability. *J. Biol. Chem.*

254, 12701–12705 (1979).

77. S. P. Cole, G. Bhardwaj, J. H. Gerlach, J. E. Mackie, C. E. Grant, K. C. Almquist, A. J. Stewart, E. U. Kurz, A. M. Duncan, R. G. Deeley, Overexpression of a transporter gene in a multidrug-resistant human lung cancer cell line. *Science*. **258**, 1650–4 (1992).

78. L. A. Doyle, D. D. Ross, Multidrug resistance mediated by the breast cancer resistance protein BCRP (ABCG2). *Oncogene*. **22**, 7340–7358 (2003).

79. F. Thiebaut, T. Tsuruo, H. Hamada, M. M. Gottesman, I. Pastan, M. C. Willingham, Immunohistochemical localization in normal tissues of different epitopes in the multidrug transport protein P170: evidence for localization in brain capillaries and crossreactivity of one antibody with a muscle protein. *J. Histochem. Cytochem.* **37**, 159–164 (1989).

80. C. Cordon-Cardo, J. P. O'Brien, D. Casals, L. Rittman-Grauer, J. L. Biedler, M. R. Melamed, J. R. Bertino, Multidrug-resistance gene (P-glycoprotein) is expressed by endothelial cells at blood-brain barrier sites. *Proc. Natl. Acad. Sci. U. S. A.* **86**, 695–8 (1989).

81. A. H. Schinkel, J. J. M. Smit, O. van Tellingen, J. H. Beijnen, E. Wagenaar, L. van Deemter, C. A. A. M. Mol, M. A. van der Valk, E. C. Robanus-Maandag, H. P. J. te Riele, A. J. M. Berns, P. Borst, Disruption of the mouse mdr1a P-glycoprotein gene leads to a deficiency in the blood-brain barrier and to increased sensitivity to drugs. *Cell*. **77**, 491–502 (1994).

82. S. Cisternino, C. Mercier, F. Bourasset, F. Roux, J. M. Scherrmann, Expression, Up-Regulation, and Transport Activity of the Multidrug-Resistance Protein Abcg2 at the Mouse Blood-Brain Barrier. *Cancer Res.* **64**, 3296–3301 (2004).

83. L. He, M. Vanlandewijck, E. Raschperger, M. Andaloussi Mäe, B. Jung, T. Lebouvier, K. Ando, J. Hofmann, A. Keller, C. Betsholtz, Analysis of the brain mural cell transcriptome. *Sci. Rep.* **6**, 35108 (2016).

84. S. Ohtsuki, C. Ikeda, Y. Uchida, Y. Sakamoto, F. Miller, F. Glacial, X. Decleves, J. M. Scherrmann, P. O. Couraud, Y. Kubo, M. Tachikawa, T. Terasaki, Quantitative targeted absolute proteomic analysis of transporters, receptors and junction proteins for validation of human cerebral microvascular endothelial cell line hCMEC/D3 as a human blood-brain barrier model. *Mol. Pharm.* **10**, 289–296 (2013).

85. W. M. Pardridge, The blood-brain barrier: Bottleneck in brain drug development. *NeuroRX*. **2**, 3–14 (2005).

86. W. M. Pardridge, Blood-brain barrier delivery. *Drug Discov. Today*. **12**, 54–61 (2007).

87. N. J. Abbott, E. U. Khan, C. M. Rollinson, A. Reichel, D. Janigro, S. M. Dombrowski, M. S. Dobbie, D. J. Begley, in *Mechanisms of Drug Resistance in Epilepsy: Lessons from Oncology*, G. Bock, J. Goode, Eds. (John Wiley & Sons, Chichester, 2002), vol. 243, pp. 38–53.

88. S. Syvänen, Ö. Lindhe, M. Palner, B. R. Kornum, O. Rahman, B. Långström, G. M. Knudsen, M. Hammarlund-Udenaes, O. Lindhe, M. Palner, B. R. Kornum, O. Rahman, B. Långström, G. M. Knudsen, M. Hammarlund-Udenaes, U. Applied, G. P. E. T. Systems, G. E. Healthcare, Species Differences in Blood-Brain Barrier Transport of Three Positron Emission Tomography Radioligands with Emphasis on P-Glycoprotein Transport. *Drug Metab. Dispos.* **37**, 635–643 (2009).

89. M. S. Warren, N. Zerangue, K. Woodford, L. M. Roberts, E. H. Tate, B. Feng, C. Li, T. J. Feuerstein, J. Gibbs, B. Smith, S. M. de Morais, W. J. Dower, K. J. Koller, Comparative gene expression profiles of ABC transporters in brain microvessel endothelial cells and brain in five species including human. *Pharmacol. Res.* **59**, 404–413 (2009).

90. H. W. Song, K. L. Foreman, B. D. Gastfriend, J. S. Kuo, S. P. Palecek, E. V. Shusta, Transcriptomic comparison of human and mouse brain microvessels. *Sci. Rep.* **10**, 12358 (2020).

91. J. B. Murphy, *The Lymphocyte in Resistance to Tissue Grafting, Malignant Disease, and Tuberculous Infection* (Rockefeller Institute for Medical Research, New York, 1926).

92. Y. Shirai, On the transplantation of the rat sarcoma in adult heterogeneous animals. *Japan Med. World*. **1**, 14–15 (1921).

93. P. B. Andersson, V. H. Perry, S. Gordon, The acute inflammatory response to lipopolysaccharide in cns parenchyma differs from that in other body tissues. *Neuroscience*. **48**, 169–186 (1992).

94. P. G. Stevenson, S. Hawke, D. J. Sloan, C. R. Bangham, The immunogenicity of intracerebral virus infection depends on anatomical site. *J. Virol.* **71**, 145–151 (1997).

95. I. Galea, I. Bechmann, V. H. Perry, What is immune privilege (not)? *Trends Immunol.* **28**, 12–18 (2007).

96. B. Engelhardt, P. Vajkoczy, R. O. Weller, The movers and shapers in immune privilege of the CNS. *Nat. Immunol.* **18**, 123–131 (2017).

97. D. D. Henninger, J. Panés, M. Eppihimer, J. Russell, M. Gerritsen, D. C. Anderson, D. N. Granger, Cytokine-induced VCAM-1 and ICAM-1 expression in different organs of the mouse. *J. Immunol.* **158**, 1825–32 (1997).

98. N. J. Abbott, A. A. K. Patabendige, D. E. M. Dolman, S. R. Yusof, D. J. Begley, Structure and function of the blood-brain barrier. *Neurobiol. Dis.* **37**, 13–25 (2010).

99. P. C. Preusch, in *Principles of Clinical Pharmacology*, A. J. Atkinson, D. R. Abernethy, C. E. Daniels, R. Dedrick, S. P. Markey, Eds. (Academic Press, 2006; https://linkinghub.elsevier.com/retrieve/pii/B9780124158368000025), pp. 197–227.

100. W. M. Pardridge, R. J. Boado, C. R. Farrell, Brain-type glucose transporter (GLUT-1) is selectively localized to the blood-brain barrier: Studies with quantitative Western blotting and in situ hybridization. *J. Biol. Chem.* **265**, 18035–18040 (1990).

101. E. M. Cornford, S. Hyman, B. E. Swartz, The human brain GLUT1 glucose transporter: Ultrastructural localization to the blood-brain barrier endothelia. *J. Cereb. Blood Flow Metab.* **14**, 106–112 (1994).

102. R. Daneman, L. Zhou, D. Agalliu, J. D. Cahoy, A. Kaushal, B. A. Barres, The Mouse Blood-Brain Barrier Transcriptome: A New Resource for Understanding the Development and Function of Brain Endothelial Cells. *PLoS One*. **5**, e13741 (2010).

103. R. J. Boado, J. Y. Li, M. Nagaya, C. Zhang, W. M. Pardridge, Selective expression of the large neutral amino acid transporter at the blood-brain barrier. *Proc. Natl. Acad. Sci. U. S. A.* **96**, 12079–12084 (1999).

104. E. G. Geier, E. C. Chen, A. Webb, A. C. Papp, S. W. Yee, W. Sadee, K. M. Giacomini, Profiling Solute Carrier Transporters in the Human Blood – Brain Barrier. *Clin Pharmacol Ther*. **94**, 636–639 (2013).

105. A. M. Suhy, A. Webb, A. C. Papp, E. G. Geier, W. Sadee, Expression and splicing of ABC and SLC transporters in the human blood-brain barrier measured with RNAseq. *Eur. J. Pharm. Sci.* **103**, 47–51 (2017).

106. P. Bouillet, V. Sapin, C. Chazaud, N. Messaddeq, D. Décimo, P. Dollé, P. Chambon, Developmental expression pattern of Stra6, a retinoic acid-responsive gene encoding a new type of membrane protein. *Mech. Dev.* **63**, 173–186 (1997).

107. R. Kawaguchi, J. Yu, J. Honda, J. Hu, J. Whitelegge, P. Ping, P. Wiita, D. Bok, H. Sun, A Membrane Receptor for Retinol Binding Protein Mediates Cellular Uptake of Vitamin A. *Science (80-.).* **315**, 820–825 (2007).

108. P. L. Tuma, A. L. Hubbard, Transcytosis: Crossing cellular barriers. *Physiol. Rev.* **83**, 871–932 (2003).

109. F. Hervé, N. Ghinea, J. M. Scherrmann, CNS delivery via adsorptive transcytosis. *AAPS J.* **10**, 455–472 (2008).

110. W. A. Jefferies, M. R. Brandon, S. V. Hunt, A. F. Williams, K. C. Gatter, D. Y. Mason, Transferrin receptor on endothelium of brain capillaries. *Nature*. **312**, 162–163 (1984).

111. W. M. Pardridge, J. Eisenberg, J. Yang, Human blood-brain barrier transferrin receptor. *Metabolism*. **36**, 892–895 (1987).

112. L. Descamps, M. P. Dehouck, G. Torpier, R. Cecchelli, Receptor-mediated transcytosis of transferrin through blood-brain barrier endothelial cells. *Am. J. Physiol. - Hear. Circ. Physiol.* **270** (1996), doi:10.1152/ajpheart.1996.270.4.h1149.

113. C. C. Visser, L. H. Voorwinden, D. J. A. Crommelin, M. Danhof, A. G. De Boer, Characterization and modulation of the transferrin receptor on brain capillary endothelial cells. *Pharm. Res.* **21**, 761–769 (2004).

114. W. M. Pardridge, J. Eisenberg, J. Yang, Human Blood-Brain Barrier Insulin Receptor. *J. Neurochem.* **44**, 1771–1778 (1985).

115. K. R. Duffy, W. M. Pardridge, Blood-brain barrier transcytosis of insulin in developing rabbits. *Brain Res.* **420**, 32–38 (1987).

116. B. V. Zlokovic, D. S. Skundric, M. B. Segal, M. N. Lipovac, J. B. Mackic, H. Davson, A saturable mechanism for transport of immunoglobulin G across the blood-brain barrier of the guinea pig. *Exp. Neurol.* **107**, 263–270 (1990).

117. B. Dehouck, L. Fenart, M. P. Dehouck, A. Pierce, G. Torpier, R. Cecchelli, A new function for the LDL receptor: Transcytosis of LDL across the blood-brain barrier. *J. Cell Biol.* **138**, 877–889 (1997).

118. P. Candela, F. Gosselet, F. Miller, V. Buee-Scherrer, G. Torpier, R. Cecchelli, L. Fenart, Physiological pathway for low-density lipoproteins across the blood-brain barrier: Transcytosis through brain capillary endothelial cells in vitro. *Endothel. J. Endothel. Cell Res.* **15**, 254–264 (2008).

119. P. L. Golden, T. J. Maccagnan, W. M. Pardridge, Human blood-brain barrier leptin receptor. Binding and endocytosis in isolated human brain microvessels. *J. Clin. Invest.* **99**, 14–18 (1997).

120. J. E. Preston, N. Joan Abbott, D. J. Begley, Transcytosis of macromolecules at the blood-brain barrier. *Adv. Pharmacol.* **71**, 147–63 (2014).

121. A. K. Kumagai, J. B. Eisenberg, W. M. Pardridge, Absorptive-mediated endocytosis of cationized albumin and a β-endorphin-cationized albumin chimeric peptide by isolated brain capillaries. Model system of blood-brain barrier transport. *J. Biol. Chem.* **262**, 15214–15219 (1987).

122. C. P. Profaci, R. N. Munji, R. S. Pulido, R. Daneman, The blood-brain barrier in health and disease: Important unanswered questions. *J. Exp. Med.* **217**, 1–16 (2020).

123. S. L. Zhang, N. F. Lahens, Z. Yue, D. M. Arnold, P. P. Pakstis, J. E. Schwarz, A. Sehgal, A circadian clock regulates efflux by the blood-brain barrier in mice and human cells. *Nat. Commun.* **12**, 1–12 (2021).

124. R. S. Pulido, R. N. Munji, T. C. Chan, C. R. Quirk, G. A. Weiner, B. D. Weger, M. J. Rossi, S. Elmsaouri, M. Malfavon, A. Deng, C. P. Profaci, M. Blanchette, T. Qian, K. L. Foreman, E. V. Shusta, M. R. Gorman, F. Gachon, S. Leutgeb, R. Daneman, Neuronal Activity Regulates Blood-Brain Barrier Efflux Transport through Endothelial Circadian Genes. *Neuron*. **108**, 937-952.e7 (2020).

125. N. Hudson, L. Celkova, A. Hopkins, C. Greene, F. Storti, E. Ozaki, E. Fahey, S. Theodoropoulou, P. F. Kenna, M. M. Humphries, A. M. Curtis, E. Demmons, A. Browne, S. Liddie, M. S. Lawrence, C. Grimm, M. T. Cahill, P. Humphries, S. L. Doyle, M. Campbell, Dysregulated claudin-5 cycling in the inner retina causes retinal pigment epithelial cell atrophy. *JCI Insight*. **4** (2019), doi:10.1172/jci.insight.130273.

126. G. Artiushin, S. L. Zhang, H. Tricoire, A. Sehgal, Endocytosis at the Drosophila blood–brain barrier as a function for sleep. *Elife*. **7**, 1–18 (2018).

127. V. A. Cuddapah, S. L. Zhang, A. Sehgal, Regulation of the Blood – Brain Barrier by Circadian Rhythms and Sleep. *Trends Neurosci.* **42**, 500–510 (2019).

128. A. C. Yang, M. Y. Stevens, M. B. Chen, D. P. Lee, D. Stähli, D. Gate, K. Contrepois, W. Chen, T. Iram, L. Zhang, R. T. Vest, A. Chaney, B. Lehallier, N. Olsson, H. du Bois, R. Hsieh, H. C. Cropper, D. Berdnik, L. Li, E. Y. Wang, G. M. Traber, C. R. Bertozzi, J. Luo, M. P. Snyder, J. E. Elias, S. R. Quake, M. L. James, T. Wyss-Coray, Physiological blood–brain transport is impaired with age by a shift in transcytosis. *Nature*. **583**, 425–430 (2020).

129. D. Attwell, A. M. Buchan, S. Charpak, M. Lauritzen, B. A. MacVicar, E. A. Newman, Glial and neuronal control of brain blood flow. *Nature*. **468**, 232–243 (2010).

130. L. Kaplan, B. W. Chow, C. Gu, Neuronal regulation of the blood–brain barrier and neurovascular coupling. *Nat. Rev. Neurosci.* **21**, 416–432 (2020).

131. C. F. Schmidt, J. P. Hendrix, The action of chemical substances on cerebral blood-vessels. *Res. Publ. Assoc. Res. Nerv. Ment. Dis.* **18**, 229–276 (1938).

132. W. Freygang, L. Sokoloff, Quantitative measurement of regional circulation in the central nervous system by the use of radioactive inert gas. *Adv. Biol. Med. Phys.* **6**, 263–79 (1958).

133. P. T. Fox, M. E. Raichle, M. A. Mintun, C. Dence, Nonoxidative glucose consumption during focal physiologic neural activity. *Science*. **241**, 462–4 (1988).

134. A. L. Lin, P. T. Fox, J. Hardies, T. Q. Duong, J. H. Gao, Nonlinear coupling between cerebral blood flow, oxygen consumption, and ATP production in human visual cortex. *Proc. Natl. Acad. Sci. U. S. A.* **107**, 8446–8451 (2010).

135. S. Ogawa, T. M. Lee, A. R. Kay, D. W. Tank, Brain magnetic resonance imaging with contrast dependent on blood oxygenation. *Proc. Natl. Acad. Sci. U. S. A.* **87**, 9868–72 (1990).

136. S. Ogawa, T. -M Lee, A. S. Nayak, P. Glynn, Oxygenation-sensitive contrast in magnetic resonance image of rodent brain at high magnetic fields. *Magn. Reson. Med.* **14**, 68–78 (1990).

137. K. K. Kwong, J. W. Belliveau, D. A. Chesler, I. E. Goldberg, R. M. Weisskoff, B. P. Poncelet, D. N. Kennedy, B. E. Hoppel, M. S. Cohen, R. Turner, H. M. Cheng -, T. J. Brady, B. R. Rosen, Dynamic magnetic resonance imaging of human brain activity during primary sensory stimulation. *Proc. Natl. Acad. Sci. U. S. A.* **89**, 5675–9 (1992).

138. U. Lindauer, C. Leithner, H. Kaasch, B. Rohrer, M. Foddis, M. Füchtemeier, N. Offenhauser, J. Steinbrink, G. Royl, M. Kohl-Bareis, U. Dirnagl, Neurovascular coupling in rat brain operates independent of hemoglobin deoxygenation. *J. Cereb. Blood Flow Metab.* **30**, 757–768 (2010).

139. G. Yang, Y. Zhang, M. E. Ross, C. Iadecola, Attenuation of activity-induced increases in

cerebellar blood flow in mice lacking neuronal nitric oxide synthase. *Am. J. Physiol. - Hear. Circ. Physiol.* **285**, 298–304 (2003).

140. M. R. Metea, E. A. Newman, Glial cells dilate and constrict blood vessels: A mechanism of neurovascular coupling. *J. Neurosci.* **26**, 2862–2870 (2006).

141. T. Takano, G. F. Tian, W. Peng, N. Lou, W. Libionka, X. Han, M. Nedergaard, Astrocyte-mediated control of cerebral blood flow. *Nat. Neurosci.* **9**, 260–267 (2006).

142. R. Nortley, D. Attwell, Control of brain energy supply by astrocytes. *Curr. Opin. Neurobiol.* **47**, 80–85 (2017).

143. M. Zonta, M. C. Angulo, S. Gobbo, B. Rosengarten, K. A. Hossmann, T. Pozzan, G. Carmignoto, Neuron-to-astrocyte signaling is central to the dynamic control of brain microcirculation. *Nat. Neurosci.* **6**, 43–50 (2003).

144. R. J. Davis, C. E. Murdoch, M. Ali, S. Purbrick, R. Ravid, G. S. Baxter, N. Tilford, R. L. G. Sheldrick, K. L. Clark, R. A. Coleman, EP4 prostanoid receptor-mediated vasodilatation of human middle cerebral arteries. *Br. J. Pharmacol.* **141**, 580–585 (2004).

145. M. Negishi, Y. Sugimoto, A. Ichikawa, Molecular mechanisms of diverse actions of prostanoid receptors. *Biochim. Biophys. Acta (BBA)/Lipids Lipid Metab.* **1259**, 109–119 (1995).

146. V. Serebryakov, S. Zakharenko, V. Snetkov, K. Takeda, Effects of prostaglandins E1 and E2 on cultured smooth muscle cells and strips of rat aorta. *Prostaglandins*. **47**, 353–365 (1994).

147. K. Niwa, E. Araki, S. G. Morham, M. E. Ross, C. Iadecola, Cyclooxygenase-2 contributes to functional hyperemia in whisker-barrel cortex. *J. Neurosci.* **20**, 763–770 (2000).

148. S. J. Mulligan, B. A. MacVicar, Calcium transients in astrocyte endfeet cause cerebrovascular constrictions. *Nature*. **431**, 195–199 (2004).

149. R. J. Roman, P-450 metabolites of arachidonic acid in the control of cardiovascular function. *Physiol. Rev.* **82**, 131–185 (2002).

150. G. R. J. Gordon, H. B. Choi, R. L. Rungta, G. C. R. Ellis-Davies, B. A. MacVicar, Brain metabolism dictates the polarity of astrocyte control over arterioles. *Nature*. **456**, 745–750 (2008).

151. P. Thakore, M. G. Alvarado, S. Ali, A. Mughal, P. W. Pires, E. Yamasaki, H. A. T. T. Pritchard, B. E. Isakson, C. H. T. Tran, S. Earley, C. Ha, T. Tran, S. Earley, Brain endothelial cell trpa1 channels initiate neurovascular coupling. *Elife*. **10**, 1–84 (2021).

152. C. Eberth, in *Handbuch der Lehre von der Gewegen des Menschen und der Tiere*, S. Stricker, Ed. (Englemann, Leipzig, 1871), pp. 191–213.

153. P. Dore-Duffy, K. Cleary, in *Methods in molecular biology (Clifton, N.J.)* (2011; http://link.springer.com/10.1007/978-1-60761-938-3), vol. 686, pp. 49–68.

154. D. Shepro, N. M. Morel, Pericyte physiology. *FASEB J.* **7**, 1031–8 (1993).

155. C. Rouget, Note sur le développement de la tunique contractile des vaisseaux. *C. R. Hebd. Seances Acad. Sci.* **79**, 559–562 (1874).

156. C. M. Peppiatt, C. Howarth, P. Mobbs, D. Attwell, Bidirectional control of CNS capillary diameter by pericytes. *Nature*. **443**, 700–704 (2006).

157. J. Grutzendler, M. Nedergaard, Cellular Control of Brain Capillary Blood Flow : In Vivo Imaging Veritas. *Trends Neurosci.*, 1–9 (2019).

158. F. Fernández-Klett, N. Offenhauser, U. Dirnagl, J. Priller, U. Lindauer, F. Fernandez-Klett, N. Offenhauser, U. Dirnagl, J. Priller, U. Lindauer, F. Fernández-Klett, N. Offenhauser, U. Dirnagl, J. Priller, U. Lindauer, Pericytes in capillaries are contractile in vivo, but arterioles mediate functional hyperemia in the mouse brain. *Proc. Natl. Acad. Sci. U. S. A.* **107**, 22290–22295 (2010).

159. R. A. Hill, L. Tong, P. Yuan, S. Murikinati, S. Gupta, J. Grutzendler, Regional Blood Flow in the Normal and Ischemic Brain Is Controlled by Arteriolar Smooth Muscle Cell Contractility and Not by Capillary Pericytes. *Neuron*. **87**, 95–110 (2015).

160. D. Attwell, A. Mishra, C. N. Hall, F. M. O'Farrell, T. Dalkara, What is a pericyte? *J. Cereb. Blood Flow Metab.* **36**, 451–455 (2016).

161. R. I. Grant, D. A. Hartmann, R. G. Underly, A. A. Berthiaume, N. R. Bhat, A. Y. Shih, Organizational hierarchy and structural diversity of microvascular pericytes in adult mouse cortex. *J. Cereb. Blood Flow Metab.* **39**, 411–425 (2019).

162. D. A. Hartmann, V. Coelho-Santos, A. Y. Shih, Pericyte Control of Blood Flow Across Microvascular Zones in the Central Nervous System. *Annu. Rev. Physiol.* **84**, 1–24 (2022).

163. R. L. Rungta, E. Chaigneau, B.-F. F. Osmanski, S. Charpak, Vascular Compartmentalization of Functional Hyperemia from the Synapse to the Pia. *Neuron*. **99**, 362-375.e4 (2018).

164. D. A. Hartmann, A. Berthiaume, R. I. Grant, S. A. Harrill, T. Koski, T. Tieu, K. P. Mcdowell, A. V Faino, A. L. Kelly, A. Y. Shih, Brain capillary pericytes exert a substantial but slow influence on blood flow. *Nat. Neurosci.* **24**, 633–645 (2021).

165. L. Alarcon-Martinez, S. Yilmaz-Ozcan, M. Yemisci, J. Schallek, K. Kılıç, A. Can, A. Di Polo, T. Dalkara, Capillary pericytes express α-smooth muscle actin, which requires prevention of filamentous-actin depolymerization for detection. *Elife*. **7**, 1–17 (2018).

166. K. Kisler, A. R. Nelson, S. V Rege, A. Ramanathan, Y. Wang, A. Ahuja, D. Lazic, P. S. Tsai, Z. Zhao, Y. Zhou, D. A. Boas, S. Sakadžić, B. V Zlokovic, Pericyte degeneration leads to neurovascular uncoupling and limits oxygen supply to brain. *Nat. Neurosci.* **20**, 406–416 (2017).

167. A. M. Nikolakopoulou, A. Montagne, K. Kisler, Z. Dai, Y. Wang, M. T. Huuskonen, A. P. Sagare, D. Lazic, M. D. Sweeney, P. Kong, M. Wang, N. C. Owens, E. J. Lawson, X. Xie,

Z. Zhao, B. V. Zlokovic, Pericyte loss leads to circulatory failure and pleiotrophin depletion causing neuron loss. *Nat. Neurosci.* **22**, 1089–1098 (2019).

168. A. N. Watson, A. A. Berthiaume, A. V. Faino, K. P. McDowell, N. R. Bhat, D. A. Hartmann, A. Y. Shih, Mild pericyte deficiency is associated with aberrant brain microvascular flow in aged PDGFRβ+/− mice. *J. Cereb. Blood Flow Metab.* **40**, 2387–2400 (2020).

169. A. A. Berthiaume, R. I. Grant, K. P. McDowell, R. G. Underly, D. A. Hartmann, M. Levy, N. R. Bhat, A. Y. Shih, Dynamic Remodeling of Pericytes In Vivo Maintains Capillary Coverage in the Adult Mouse Brain. *Cell Rep.* **22**, 8–16 (2018).

170. P. S. Hosford, I. N. Christie, A. Niranjan, Q. Aziz, N. Anderson, R. Ang, M. F. Lythgoe, J. A. Wells, A. Tinker, A. V. Gourine, A critical role for the ATP-sensitive potassium channel subunit KIR6.1 in the control of cerebral blood flow. *J. Cereb. Blood Flow Metab.* **39**, 2089–2095 (2019).

171. A. R. Nelson, M. A. Sagare, Y. Wang, K. Kisler, Z. Zhao, B. V. Zlokovic, Channelrhodopsin Excitation Contracts Brain Pericytes and Reduces Blood Flow in the Aging Mouse Brain in vivo. *Front. Aging Neurosci.* **12**, 1–11 (2020).

172. C. Glück, K. D. Ferrari, N. Binini, A. Keller, A. S. Saab, J. L. Stobart, B. Weber, Distinct signatures of calcium activity in brain mural cells. *Elife*. **10**, 1–27 (2021).

173. B. R. Chen, M. G. Kozberg, M. B. Bouchard, M. A. Shaik, E. M. C. Hillman, A critical role for the vascular endothelium in functional neurovascular coupling in the brain. *J. Am. Heart Assoc.* **3**, 1–14 (2014).

174. T. A. Longden, F. Dabertrand, M. Koide, A. L. Gonzales, N. R. Tykocki, J. E. Brayden, D. Hill-Eubanks, M. T. Nelson, Capillary K+-sensing initiates retrograde hyperpolarization to increase local cerebral blood flow. *Nat. Neurosci.* **20**, 717–726 (2017).

175. B. W. Chow, V. Nuñez, L. Kaplan, A. J. Granger, K. Bistrong, H. L. Zucker, P. Kumar, B. L. Sabatini, C. Gu, Caveolae in CNS arterioles mediate neurovascular coupling. *Nature*. **579**, 106–110 (2020).

176. A. Hariharan, N. Weir, C. Robertson, L. He, C. Betsholtz, T. A. Longden, The Ion Channel and GPCR Toolkit of Brain Capillary Pericytes. *Front. Cell. Neurosci.* **14**, 1–45 (2020).

177. S. A. Zambach, C. Cai, H. C. C. Helms, B. O. Hald, Y. Dong, J. C. Fordsmann, R. M. Nielsen, J. Hu, M. Lønstrup, B. Brodin, M. J. Lauritzen, Precapillary sphincters and pericytes at first-order capillaries as key regulators for brain capillary perfusion. *Proc. Natl. Acad. Sci.* **118** (2021), doi:10.1073/pnas.2023749118.

178. L. Alarcon-Martinez, D. Villafranca-Baughman, H. Quintero, J. B. Kacerovsky, F. Dotigny, K. K. Murai, A. Prat, P. Drapeau, A. Di Polo, Interpericyte tunnelling nanotubes regulate neurovascular coupling. *Nature*. **585**, 91–95 (2020).

179. C. S. Von Bartheld, J. Bahney, S. Herculano-Houzel, C. S. von Bartheld, J. Bahney, S. Herculano-Houzel, C. S. Von Bartheld, J. Bahney, S. Herculano-Houzel, C. S. von Bartheld, J. Bahney, S. Herculano-Houzel, C. S. Von Bartheld, J. Bahney, S. Herculano-Houzel, C. S. von Bartheld, J. Bahney, S. Herculano-Houzel, The search for true numbers of neurons and glial cells in the human brain: A review of 150 years of cell counting. *J. Comp. Neurol.* **524**, 3865–3895 (2016).

180. D. Attwell, S. B. Laughlin, An energy budget for signaling in the grey matter of the brain. *J. Cereb. Blood Flow Metab.* **21**, 1133–1145 (2001).

181. J. J. Harris, R. Jolivet, D. Attwell, Synaptic energy use and supply. *Neuron*. **75**, 762–77 (2012).

182. N. J. Allen, D. A. Lyons, Glia as architects of central nervous system formation and function. *Science (80-.).* **362**, 181–185 (2018).

183. L. Pellerin, P. J. Magistretti, Glutamate uptake into astrocytes stimulates aerobic glycolysis: A mechanism coupling neuronal activity to glucose utilization. *Proc. Natl. Acad. Sci. U. S. A.* **91**, 10625–10629 (1994).

184. P. J. Magistretti, I. Allaman, Lactate in the brain: From metabolic end-product to signalling molecule. *Nat. Rev. Neurosci.* **19**, 235–249 (2018).

185. L. K. Bak, A. B. Walls, CrossTalk opposing view: lack of evidence supporting an astrocyte-to-neuron lactate shuttle coupling neuronal activity to glucose utilisation in the brain. *J. Physiol.* **596**, 351–353 (2018).

186. A. L. F. van Deijk, N. Camargo, J. Timmerman, T. Heistek, J. F. Brouwers, F. Mogavero, H. D. Mansvelder, A. B. Smit, M. H. G. Verheijen, Astrocyte lipid metabolism is critical for synapse development and function in vivo. *Glia*. **65**, 670–682 (2017).

187. A. C. Yang, R. T. Vest, F. Kern, D. P. Lee, M. Agam, C. A. Maat, P. M. Losada, M. B. Chen, N. Schaum, N. Khoury, A. Toland, K. Calcuttawala, H. Shin, R. Pálovics, A. Shin, E. Y. Wang, J. Luo, D. Gate, W. J. Schulz-Schaeffer, P. Chu, J. A. Siegenthaler, M. W. McNerney, A. Keller, T. Wyss-Coray, A human brain vascular atlas reveals diverse mediators of Alzheimer's risk. *Nature*. **603**, 885–892 (2022).

188. Q. Ma, Z. Zhao, A. P. Sagare, Y. Wu, M. Wang, N. C. Owens, P. B. Verghese, J. Herz, D. M. Holtzman, B. V. Zlokovic, Blood-brain barrier-associated pericytes internalize and clear aggregated amyloid-β42 by LRP1-dependent apolipoprotein e isoform-specific mechanism. *Mol. Neurodegener.* **13**, 1–13 (2018).

189. J. Derk, H. E. Jones, C. Como, B. Pawlikowski, J. A. Siegenthaler, Living on the Edge of the CNS: Meninges Cell Diversity in Health and Disease. *Front. Cell. Neurosci.* **15**, 1–17 (2021).

190. L. H. Weed, The absorption of cerebrospinal fluid into the venous system. *Am. J. Anat.* **31**, 191–221 (1923).

191. K. G. Go, H. J. Houthoff, J. Hartsuiker, E. H. Blaauw, P. Havinga, Fluid secretion in arachnoid cysts as a clue to cerebrospinal fluid absorption at the arachnoid granulation. *J. Neurosurg.* **65**, 642–648 (1986).

192. A. Aspelund, S. Antila, S. T. Proulx, T. V. Karlsen, S. Karaman, M. Detmar, H. Wiig, K. Alitalo, A dural lymphatic vascular system that drains brain interstitial fluid and macromolecules. *J. Exp. Med.* **212**, 991–999 (2015).

193. A. Louveau, I. Smirnov, T. J. Keyes, J. D. Eccles, S. J. Rouhani, J. D. Peske, N. C. Derecki, D. Castle, J. W. Mandell, K. S. Lee, T. H. Harris, J. Kipnis, Structural and functional features of central nervous system lymphatic vessels. *Nature*. **523**, 337–341 (2015).

194. Q. Ma, B. V. Ineichen, M. Detmar, S. T. Proulx, Outflow of cerebrospinal fluid is predominantly through lymphatic vessels and is reduced in aged mice. *Nat. Commun.* **8** (2017), doi:10.1038/s41467-017-01484-6.

195. N. T. Zervas, T. M. Liszczak, M. R. Mayberg, P. Black McL., Cerebrospinal fluid may nourish cerebral vessels through pathways in the adventitia that may be analogous to systemic vasa vasorum. *J. Neurosurg.* **56**, 475–481 (1982).

196. J. J. Iliff, M. Wang, Y. Liao, B. A. Plogg, W. Peng, G. A. Gundersen, H. Benveniste, G. E. Vates, R. Deane, S. A. Goldman, E. A. Nagelhus, M. Nedergaard, A Paravascular Pathway Facilitates CSF Flow Through the Brain Parenchyma and the Clearance of Interstitial Solutes, Including Amyloid β. *Sci. Transl. Med.* **4** (2012), doi:10.1126/scitranslmed.3003748.

197. N. J. Abbott, M. E. Pizzo, J. E. Preston, D. Janigro, R. G. Thorne, The role of brain barriers in fluid movement in the CNS: is there a 'glymphatic' system? *Acta Neuropathol.* **135**, 387–407 (2018).

198. J. M. Wardlaw, H. Benveniste, M. Nedergaard, B. V. Zlokovic, H. Mestre, H. Lee, F. N. Doubal, R. Brown, J. Ramirez, B. J. MacIntosh, A. Tannenbaum, L. Ballerini, R. L. Rungta, D. Boido, M. Sweeney, A. Montagne, S. Charpak, A. Joutel, K. J. Smith, S. E. Black, Perivascular spaces in the brain: anatomy, physiology and pathology. *Nat. Rev. Neurol.* **16**, 137–153 (2020).

199. M. E. Pizzo, D. J. Wolak, N. N. Kumar, E. Brunette, C. L. Brunnquell, M. J. Hannocks, N. J. Abbott, M. E. Meyerand, L. Sorokin, D. B. Stanimirovic, R. G. Thorne, Intrathecal antibody distribution in the rat brain: surface diffusion, perivascular transport and osmotic enhancement of delivery. *J. Physiol.* **596**, 445–475 (2018).

200. A. J. Smith, X. Yao, J. A. Dix, B. J. Jin, A. S. Verkman, Test of the 'glymphatic' hypothesis demonstrates diffusive and aquaporin-4-independent solute transport in rodent brain parenchyma. *Elife*. **6**, 1–16 (2017).

201. H. Mestre, L. M. Hablitz, A. L. R. Xavier, W. Feng, W. Zou, T. Pu, H. Monai, G. Murlidharan, R. M. C. Rivera, M. J. Simon, M. M. Pike, V. Plá, T. Du, B. T. Kress, X. Wang, B. A. Plog, A. S. Thrane, I. Lundgaard, Y. Abe, M. Yasui, J. H. Thomas, M. Xiao,

H. Hirase, A. Asokan, J. J. Iliff, M. Nedergaard, Aquaporin-4-dependent glymphatic solute transport in the rodent brain. *Elife*. **7**, 1–31 (2018).

202. L. M. Hablitz, H. S. Vinitsky, Q. Sun, F. F. Stæger, B. Sigurdsson, K. N. Mortensen, T. O. Lilius, M. Nedergaard, Increased glymphatic influx is correlated with high EEG delta power and low heart rate in mice under anesthesia (2019).

203. A. Raghunandan, A. Ladron-De-guevara, J. Tithof, H. Mestre, T. Du, M. Nedergaard, J. H. Thomas, D. H. Kelley, Bulk flow of cerebrospinal fluid observed in periarterial spaces is not an artifact of injection. *Elife*. **10**, 1–15 (2021).

204. E. E. Ubogu, The molecular and biophysical characterization of the human blood-nerve barrier: Current concepts. *J. Vasc. Res.* **50**, 289–303 (2013).

205. A. P. Mizisin, A. Weerasuriya, Homeostatic regulation of the endoneurial microenvironment during development, aging and in response to trauma, disease and toxic insult. *Acta Neuropathol.* **121**, 291–312 (2011).

206. Y. Olsson, Topographical differences in the vascular permeability of the peripheral nervous system. *Acta Neuropathol.* **10**, 26–33 (1968).

207. Y. Olsson, Microenvironment of the peripheral nervous system under normal and pathological conditions. *Crit. Rev. Neurobiol.* **5** (1990), pp. 265–311.

208. J. F. Poduslo, G. L. Curran, C. T. Berg, Macromolecular permeability across the blood-nerve and blood-brain barriers. *Proc. Natl. Acad. Sci. U. S. A.* **91**, 5705–9 (1994).

209. E. Rechthand, S. Rapoport, Regulation of the microenvironment of peripheral nerve: Role of the blood-nerve barrier. *Prog. Neurobiol.* **28**, 303–343 (1987).

210. M. S. Bush, G. Allt, Blood-nerve barrier: distribution of anionic sites on the endothelial plasma membrane and basal lamina. *Brain Res.* **535**, 181–188 (1990).

211. C. Orte, J. G. Lawrenson, T. M. Finn, A. R. Reid, G. Allt, A comparison of blood-brain barrier and blood-nerve barrier endothelial cell markers. *Anat. Embryol. (Berl).* **199**, 509–517 (1999).

212. G. Allt, J. G. Lawrenson, The blood-nerve barrier: Enzymes, transporters and receptors - A comparison with the blood-brain barrier. *Brain Res. Bull.* **52**, 1–12 (2000).

213. Y. Sano, F. Shimizu, H. Nakayama, M. Abe, T. Maeda, S. Ohtsuki, T. Terasaki, M. Obinata, M. Ueda, R. Takahashi, T. Kanda, Endothelial cells constituting blood-nerve barrier have highly specialized characteristics as barrier-forming cells. *Cell Struct. Funct.* **32**, 139–147 (2007).

214. E. Parmantier, B. Lynn, D. Lawson, M. Turmaine, S. S. Namini, L. Chakrabarti, A. P. McMahon, K. R. Jessen, R. Mirsky, Schwann Cell–Derived Desert Hedgehog Controls the Development of Peripheral Nerve Sheaths. *Neuron*. **23**, 713–724 (1999).

215. S. P. Palladino, E. S. Helton, P. Jain, C. Dong, M. R. Crowley, D. K. Crossman, E. E.

Ubogu, The Human Blood-Nerve Barrier Transcriptome. *Sci. Rep.* **7**, 17477 (2017).

216. X. Ouyang, C. Dong, E. E. Ubogu, In situ molecular characterization of endoneurial microvessels that form the blood-nerve barrier in normal human adult peripheral nerves. *J. Peripher. Nerv. Syst.* **24**, 195–206 (2019).

217. J. F. Feeney, R. L. Watterson, The development of the vascular pattern within the walls of the central nervous system of the chick embryo. *J. Morphol.* **78**, 231–303 (1946).

218. P. A. Stewart, M. J. Wiley, Developing nervous tissue induces formation of blood-brain barrier characteristics in invading endothelial cells: A study using quail-chick transplantation chimeras. *Dev. Biol.* **84**, 183–192 (1981).

219. K. A. Hogan, C. A. Ambler, D. L. Chapman, V. L. Bautch, The neural tube patterns vessels developmentally using the VEGF signaling pathway. *Development*. **131**, 1503–1513 (2004).

220. Y. Komiya, R. Habas, Wnt signal transduction pathways. *Organogenesis*. **4**, 68–75 (2008).

221. H. Clevers, K. M. Loh, R. Nusse, Stem cell signaling. An integral program for tissue renewal and regeneration: Wnt signaling and stem cell control. *Science*. **346**, 1248012 (2014).

222. J. Mao, J. Wang, B. Liu, W. Pan, G. H. Farr, C. Flynn, H. Yuan, S. Takada, D. Kimelman, L. Li, D. Wu, Low-density lipoprotein receptor-related protein-5 binds to Axin and regulates the canonical Wnt signaling pathway. *Mol. Cell*. **7**, 801–809 (2001).

223. J. L. Stamos, M. L. H. Chu, M. D. Enos, N. Shah, W. I. Weis, Structural basis of GSK-3 inhibition by N-terminal phosphorylation and by the Wnt receptor LRP6. *Elife*. **2014**, 1–22 (2014).

224. J. Schuijers, M. Mokry, P. Hatzis, E. Cuppen, H. Clevers, Wnt-induced transcriptional activation is exclusively mediated by TCF/LEF. *EMBO J.* **33**, 146–156 (2014).

225. R. Daneman, D. Agalliu, L. Zhou, F. Kuhnert, C. J. Kuo, B. A. Barres, Wnt/beta-catenin signaling is required for CNS, but not non-CNS, angiogenesis. *Proc. Natl. Acad. Sci. U. S. A.* **106**, 641–6 (2009).

226. M. F. Sabbagh, J. Nathans, A genome-wide view of the de-differentiation of central nervous system endothelial cells in culture. *Elife*. **9**, 1–19 (2020).

227. J. M. Stenman, J. Rajagopal, T. J. Carroll, M. Ishibashi, J. McMahon, A. P. McMahon, Canonical Wnt Signaling Regulates Organ-Specific Assembly and Differentiation of CNS Vasculature. *Science (80-.).* **322**, 1247–1250 (2008).

228. S. Liebner, M. Corada, T. Bangsow, J. Babbage, A. Taddei, C. J. Czupalla, M. Reis, A. Felici, H. Wolburg, M. Fruttiger, M. M. Taketo, H. Von Melchner, K. H. Plate, H. Gerhardt, E. Dejana, Wnt/β-catenin signaling controls development of the blood - brain barrier. *J. Cell Biol.* **183**, 409–417 (2008).

229. S. Ma, H. J. Kwon, H. Johng, K. Zang, Z. Huang, Radial Glial Neural Progenitors Regulate Nascent Brain Vascular Network Stabilization Via Inhibition of Wnt Signaling. *PLoS Biol.* **11** (2013), doi:10.1371/journal.pbio.1001469.

230. Q. Xu, Y. Wang, A. Dabdoub, P. M. Smallwood, J. Williams, C. Woods, M. W. Kelley, L. Jiang, W. Tasman, K. Zhang, J. Nathans, Vascular development in the retina and inner ear: Control by Norrin and Frizzled-4, a high-affinity ligand-receptor pair. *Cell*. **116**, 883–895 (2004).

231. M. Warburg, Norrie's Disease, A New Hereditary Bilateral Pseudotumor of the Retina. *Acta Ophthalmol.* **39**, 757–772 (1961).

232. H. L. Rehm, D. S. Zhang, M. C. Brown, B. Burgess, C. Halpin, W. Berger, C. C. Morton, D. P. Corey, Z. Y. Chen, Vascular Defects and Sensorineural Deafness in a Mouse Model of Norrie Disease. *J. Neurosci.* **22**, 4286–4292 (2002).

233. M. Richter, J. Gottanka, C. A. May, U. Welge-Lüßen, W. Berger, E. Lütjen-Drecoll, Retinal vasculature changes in Norrie disease mice. *Investig. Ophthalmol. Vis. Sci.* **39**, 2450–2457 (1998).

234. P. M. Smallwood, J. Williams, Q. Xu, D. J. Leahy, J. Nathans, Mutational analysis of Norrin-Frizzled4 recognition. *J. Biol. Chem.* **282**, 4057–4068 (2007).

235. X. Ye, Y. Wang, H. Cahill, M. Yu, T. C. Badea, P. M. Smallwood, N. S. Peachey, J. Nathans, Norrin, Frizzled-4, and Lrp5 Signaling in Endothelial Cells Controls a Genetic Program for Retinal Vascularization. *Cell*. **139**, 285–298 (2009).

236. U. F. O. Luhmann, J. Neidhardt, B. Kloeckener-Gruissem, N. F. Schäfer, E. Glaus, S. Feil, W. Berger, Vascular changes in the cerebellum of Norrin/Ndph knockout mice correlate with high expression of Norrin and Frizzled-4. *Eur. J. Neurosci.* **27**, 2619–2628 (2008).

237. B. Vanhollebeke, O. A. Stone, N. Bostaille, C. Cho, Y. Zhou, E. Maquet, A. Gauquier, P. Cabochette, S. Fukuhara, N. Mochizuki, J. Nathans, D. Y. R. Stainier, Tip cell-specific requirement for an atypical Gpr124- and Reck-dependent Wnt/β-catenin pathway during brain angiogenesis. *Elife*. **4**, 1–25 (2015).

238. Y. Wang, A. Rattner, Y. Zhou, J. Williams, P. M. Smallwood, J. Nathans, Norrin/Frizzled4 signaling in retinal vascular development and blood brain barrier plasticity. *Cell*. **151**, 1332–1344 (2012).

239. Y. Zhou, Y. Wang, M. Tischfield, J. Williams, P. M. Smallwood, A. Rattner, M. M. Taketo, J. Nathans, Canonical WNT signaling components in vascular development and barrier formation. *J. Clin. Invest.* **124**, 3825–3846 (2014).

240. A. Kikuchi, H. Yamamoto, S. Kishida, Multiplicity of the interactions of Wnt proteins and their receptors. *Cell. Signal.* **19**, 659–671 (2007).

241. F. Kuhnert, M. R. Mancuso, A. Shamloo, H.-T. H. T. Wang, V. Choksi, M. Florek, H. Su, M. Fruttiger, W. L. Young, S. C. Heilshorn, C. J. Kuo, Essential regulation of CNS

angiogenesis by the orphan G protein-coupled receptor GPR124. *Science (80-.).* **330**, 985–989 (2010).

242. M. Cullen, M. K. Elzarrad, S. Seaman, E. Zudaire, J. Stevens, M. Y. Yang, X. Li, A. Chaudhary, L. Xu, M. B. Hilton, D. Logsdon, E. Hsiao, E. V. Stein, F. Cuttitta, D. C. Haines, K. Nagashima, L. Tessarollo, B. St. Croix, GPR124, an orphan G protein-coupled receptor, is required for CNS-specific vascularization and establishment of the blood-brain barrier. *Proc. Natl. Acad. Sci.* **108**, 5759–5764 (2011).

243. K. D. Anderson, L. Pan, X. M. Yang, V. C. Hughes, J. R. Walls, M. G. Dominguez, M. V. Simmons, P. Burfeind, Y. Xue, Y. Wei, L. E. Macdonald, G. Thurston, C. Daly, H. C. Lin, A. N. Economides, D. M. Valenzuela, A. J. Murphy, G. D. Yancopoulos, N. W. Gale, Angiogenic sprouting into neural tissue requires Gpr124, an orphan G protein-coupled receptor. *Proc. Natl. Acad. Sci. U. S. A.* **108**, 2807–2812 (2011).

244. Y. Zhou, J. Nathans, Gpr124 controls CNS angiogenesis and blood-brain barrier integrity by promoting ligand-specific canonical Wnt signaling. *Dev. Cell*. **31**, 248–256 (2014).

245. E. Posokhova, A. Shukla, S. Seaman, S. Volate, M. B. Hilton, B. Wu, H. Morris, D. A. Swing, M. Zhou, E. Zudaire, J. S. Rubin, B. St.Croix, GPR124 functions as a WNT7-specific coactivator of canonical β-catenin signaling. *Cell Rep.* **10**, 123–130 (2015).

246. J. Oh, R. Takahashi, S. Kondo, A. Mizoguchi, E. Adachi, R. M. Sasahara, S. Nishimura, Y. Imamura, H. Kitayama, D. B. Alexander, C. Ide, T. P. Horan, T. Arakawa, H. Yoshida, S. I. Nishikawa, Y. Itoh, M. Seiki, S. Itohara, C. Takahashi, M. M. Noda, The membrane-anchored MMP inhibitor RECK is a key regulator of extracellular matrix integrity and angiogenesis. *Cell*. **107**, 789–800 (2001).

247. C. Cho, P. M. Smallwood, J. Nathans, Reck and Gpr124 Are Essential Receptor Cofactors for Wnt7a/Wnt7b-Specific Signaling in Mammalian CNS Angiogenesis and Blood-Brain Barrier Regulation. *Neuron*. **95**, 1056-1073.e5 (2017).

248. M. Vallon, K. Yuki, T. D. Nguyen, J. Chang, J. Yuan, D. Siepe, Y. Miao, M. Essler, M. Noda, K. C. Garcia, C. J. Kuo, A RECK-WNT7 Receptor-Ligand Interaction Enables Isoform-Specific Regulation of Wnt Bioavailability. *Cell Rep.* **25**, 339-349.e9 (2018).

249. M. Eubelen, N. Bostaille, P. Cabochette, A. Gauquier, P. Tebabi, A. C. Dumitru, M. Koehler, P. Gut, D. Alsteens, D. Y. R. Stainier, A. Garcia-Pino, B. Vanhollebeke, A molecular mechanism for Wnt ligand-specific signaling. *Science (80-.).* **361** (2018), doi:10.1126/science.aat1178.

250. H. J. Junge, S. Yang, J. B. Burton, K. Paes, X. Shu, D. M. French, M. Costa, D. S. Rice, W. Ye, TSPAN12 Regulates Retinal Vascular Development by Promoting Norrin- but Not Wnt-Induced FZD4/β-Catenin Signaling. *Cell*. **139**, 299–311 (2009).

251. R. C. Janzer, M. C. Raff, Astrocytes induce blood–brain barrier properties in endothelial cells. *Nature*. **325** (1987), pp. 253–257.

252. A. Ben-Zvi, B. Lacoste, E. Kur, B. J. Andreone, Y. Mayshar, H. Yan, C. Gu, Mfsd2a is

critical for the formation and function of the blood-brain barrier. *Nature*. **509**, 507–11 (2014).

253. P. Lindahl, B. R. Johansson, P. Levéen, C. Betsholtz, Pericyte loss and microaneurysm formation in PDGF-B-deficient mice. *Science (80-.).* **277**, 242–245 (1997).

254. M. Hellström, M. Kalén, P. Lindahl, A. Abramsson, C. Betsholtz, Role of PDGF-B and PDGFR-beta in recruitment of vascular smooth muscle cells and pericytes during embryonic blood vessel formation in the mouse. *Development*. **126**, 3047–3055 (1999).

255. M. D. Tallquist, W. J. French, P. Soriano, Additive effects of PDGF receptor β signaling pathways in vascular smooth muscle cell development. *PLoS Biol.* **1**, 288–299 (2003).

256. A. Armulik, G. Genové, M. Mäe, M. H. Nisancioglu, E. Wallgard, C. Niaudet, L. He, J. Norlin, P. Lindblom, K. Strittmatter, B. R. Johansson, C. Betsholtz, Pericytes regulate the blood–brain barrier. *Nature*. **468**, 557–561 (2010).

257. R. D. Bell, E. A. Winkler, A. P. Sagare, I. Singh, B. LaRue, R. Deane, B. V. Zlokovic, Pericytes Control Key Neurovascular Functions and Neuronal Phenotype in the Adult Brain and during Brain Aging. *Neuron*. **68**, 409–427 (2010).

258. O. Török, B. Schreiner, J. Schaffenrath, H.-C. Tsai, U. Maheshwari, S. A. Stifter, C. Welsh, A. Amorim, S. Sridhar, S. G. Utz, W. Mildenberger, S. Nassiri, M. Delorenzi, A. Aguzzi, M. H. Han, M. Greter, B. Becher, A. Keller, Pericytes regulate vascular immune homeostasis in the CNS. *Proc. Natl. Acad. Sci. U. S. A.* **118**, e2016587118 (2021).

259. M. A. Mäe, L. He, S. Nordling, E. Vazquez-Liebanas, K. Nahar, B. Jung, X. Li, B. C. Tan, J. Chin Foo, A. Cazenave-Gassiot, M. R. Wenk, Y. Zarb, B. Lavina, S. E. Quaggin, M. Jeansson, C. Gu, D. L. Silver, M. Vanlandewijck, E. C. Butcher, A. Keller, C. Betsholtz, Single-Cell Analysis of Blood-Brain Barrier Response to Pericyte Loss. *Circ. Res.* **128**, e46–e62 (2021).

260. L. N. Nguyen, D. Ma, G. Shui, P. Wong, A. Cazenave-Gassiot, X. Zhang, M. R. Wenk, E. L. K. Goh, D. L. Silver, Mfsd2a is a transporter for the essential omega-3 fatty acid docosahexaenoic acid. *Nature*. **509**, 503–506 (2014).

261. B. W. Chow, C. Gu, Gradual Suppression of Transcytosis Governs Functional Blood-Retinal Barrier Formation. *Neuron*. **93**, 1325-1333.e3 (2017).

262. N. M. O'Brown, S. G. Megason, C. Gu, Suppression of transcytosis regulates zebrafish blood-brain barrier function. *Elife*. **8**, 1–21 (2019).

263. B. J. Andreone, B. W. Chow, A. Tata, B. Lacoste, A. Ben-Zvi, K. Bullock, A. A. Deik, D. D. Ginty, C. B. Clish, C. Gu, Blood-Brain Barrier Permeability Is Regulated by Lipid Transport-Dependent Suppression of Caveolae-Mediated Transcytosis. *Neuron*. **94**, 581-594.e5 (2017).

264. Z. Wang, C. H. Liu, S. Huang, Z. Fu, Y. Tomita, W. R. Britton, S. S. Cho, C. T. Chen, Y. Sun, J. X. Ma, X. He, J. Chen, Wnt signaling activates MFSD2A to suppress vascular

endothelial transcytosis and maintain blood-retinal barrier. *Sci. Adv.* **6** (2020), doi:10.1126/sciadv.aba7457.

265. A. J. Durston, J. P. M. Timmermans, W. J. Hage, H. F. J. Hendriks, N. J. De Vries, M. Heideveld, P. D. Nieuwkoop, Retinoic acid causes an anteroposterior transformation in the developing central nervous system. *Nature*. **340**, 140–144 (1989).

266. H. Toresson, A. M. De Urquiza, C. Fagerström, T. Perlmann, K. Campbell, Retinoids are produced by glia in the lateral ganglionic eminence and regulate striatal neuron differentiation. *Development*. **126**, 1317–1326 (1999).

267. J. A. Siegenthaler, A. M. Ashique, K. Zarbalis, K. P. Patterson, J. H. Hecht, M. A. Kane, A. E. Folias, Y. Choe, S. R. May, T. Kume, J. L. Napoli, A. S. Peterson, S. J. Pleasure, Retinoic Acid from the Meninges Regulates Cortical Neuron Generation. *Cell*. **139**, 597–609 (2009).

268. M. R. Mizee, D. Wooldrik, K. A. M. Lakeman, B. van het Hof, J. A. R. Drexhage, D. Geerts, M. Bugiani, E. Aronica, R. E. Mebius, A. Prat, H. E. de Vries, A. Reijerkerk, Retinoic Acid Induces Blood-Brain Barrier Development. *J. Neurosci.* **33**, 1660–1671 (2013).

269. S. Bonney, S. Harrison-Uy, S. Mishra, A. M. MacPherson, Y. Choe, D. Li, S.-C. Jaminet, M. Fruttiger, S. J. Pleasure, J. A. Siegenthaler, Diverse Functions of Retinoic Acid in Brain Vascular Development. *J. Neurosci.* **36**, 7786–7801 (2016).

270. S. Bonney, J. A. Siegenthaler, Differential effects of retinoic acid concentrations in regulating blood–brain barrier properties. *eNeuro*. **4**, 1–14 (2017).

271. S. Bonney, B. J. C. Dennison, M. Wendlandt, J. A. Siegenthaler, Retinoic Acid Regulates Endothelial β-catenin Expression and Pericyte Numbers in the Developing Brain Vasculature. *Front. Cell. Neurosci.* **12**, 1–16 (2018).

272. F. E. Arthur, R. R. Shivers, P. D. Bowman, Astrocyte-mediated induction of tight junctions in brain capillary endothelium: an efficient in vitro model. *Dev. Brain Res.* **36**, 155–159 (1987).

273. M. -P Dehouck, S. Méresse, P. Delorme, J. -C Fruchart, R. Cecchelli, An Easier, Reproducible, and Mass-Production Method to Study the Blood–Brain Barrier In Vitro. *J. Neurochem.* **54**, 1798–1801 (1990).

274. L. L. Rubin, D. E. Hall, S. Porter, K. Barbu, C. Cannon, H. C. Horner, M. Janatpour, C. W. Liaw, K. Manning, J. Morales, L. I. Tanner, K. J. Tomaselli, F. Bard, A cell culture model of the blood-brain barrier. *J. Cell Biol.* **115**, 1725–1735 (1991).

275. R. F. Haseloff, I. E. Blasig, H. C. Bauer, H. Bauer, In search of the astrocytic factor(s) modulating blood-brain barrier functions in brain capillary endothelial cells in vitro. *Cell. Mol. Neurobiol.* **25**, 25–39 (2005).

276. J. I. Alvarez, A. Dodelet-Devillers, H. Kebir, I. Ifergan, P. J. Fabre, S. Terouz, M.

Sabbagh, K. Wosik, L. Bourbonniere, M. Bernard, J. van Horssen, H. E. de Vries, F. Charron, A. Prat, The Hedgehog Pathway Promotes Blood-Brain Barrier Integrity and CNS Immune Quiescence. *Science (80-.).* **334**, 1727–1731 (2011).

277. S. Sharghi-Namini, M. Turmaine, C. Meier, V. Sahni, F. Umehara, K. R. Jessen, R. Mirsky, The Structural and Functional Integrity of Peripheral Nerves Depends on the Glial-Derived Signal Desert Hedgehog. *J. Neurosci.* **26**, 6364–6376 (2006).

278. C. Bänziger, D. Soldini, C. Schütt, P. Zipperlen, G. Hausmann, K. Basler, Wntless, a Conserved Membrane Protein Dedicated to the Secretion of Wnt Proteins from Signaling Cells. *Cell*. **125**, 509–522 (2006).

279. S. Guérit, E. Fidan, J. Macas, C. J. Czupalla, R. Figueiredo, A. Vijikumar, B. H. Yalcin, S. Thom, P. Winter, H. Gerhardt, K. Devraj, S. Liebner, Astrocyte-derived Wnt growth factors are required for endothelial blood-brain barrier maintenance. *Prog. Neurobiol.* **199** (2021), doi:10.1016/j.pneurobio.2020.101937.

280. M. I. Dorrell, E. Aguilar, M. Friedlander, Retinal vascular development is mediated by endothelial filopodia, a preexisting astrocytic template and specific R-cadherin adhesion. *Investig. Ophthalmol. Vis. Sci.* **43**, 3500–3510 (2002).

281. S. Ma, H. J. Kwon, Z. Huang, A Functional Requirement for Astroglia in Promoting Blood Vessel Development in the Early Postnatal Brain. *PLoS One*. **7** (2012), doi:10.1371/journal.pone.0048001.

282. K. Ando, S. Fukuhara, N. Izumi, H. Nakajima, H. Fukui, R. N. Kelsh, N. Mochizuki, Clarification of mural cell coverage of vascular endothelial cells by live imaging of zebrafish. *Dev.* **143**, 1328–1339 (2016).

283. M. W. Majesky, Developmental basis of vascular smooth muscle diversity. *Arterioscler. Thromb. Vasc. Biol.* **27**, 1248–1258 (2007).

284. C. S. Le Lièvre, N. M. Le Douarin, Mesenchymal derivatives of the neural crest: analysis of chimaeric quail and chick embryos. *J. Embryol. Exp. Morphol.* **34**, 125–154 (1975).

285. X. Jiang, S. Iseki, R. E. Maxson, H. M. Sucov, G. M. Morriss-Kay, Tissue Origins and Interactions in the Mammalian Skull Vault. *Dev. Biol.* **241**, 106–116 (2002).

286. A. Armulik, G. Genové, C. Betsholtz, Pericytes: Developmental, Physiological, and Pathological Perspectives, Problems, and Promises. *Dev. Cell*. **21**, 193–215 (2011).

287. M. Heglind, A. Cederberg, J. Aquino, G. Lucas, P. Ernfors, S. Enerbäck, Lack of the Central Nervous System- and Neural Crest-Expressed Forkhead Gene Foxs1 Affects Motor Function and Body Weight . *Mol. Cell. Biol.* **25**, 5616–5625 (2005).

288. D. E. Russ, R. B. P. Cross, L. Li, S. C. Koch, K. J. E. Matson, A. Yadav, M. R. Alkaslasi, D. I. Lee, C. E. Le Pichon, V. Menon, A. J. Levine, A harmonized atlas of mouse spinal cord cell types and their spatial organization. *Nat. Commun.* **12**, 1–20 (2021).

289. T. Rayon, R. J. Maizels, C. Barrington, J. Briscoe, Single-cell transcriptome profiling of

the human developing spinal cord reveals a conserved genetic programme with human-specific features. *Dev.* **148** (2021), doi:10.1242/DEV.199711.

290. M. Selleck, M. Bronner-Fraser, Origins of the avian neural crest: the role of neural plate-epidermal interactions. *Development*. **121**, 525–38 (1995).

291. M. L. Basch, M. Bronner-Fraser, M. I. García-Castro, Specification of the neural crest occurs during gastrulation and requires Pax7. *Nature*. **441**, 218–222 (2006).

292. L. A. Taneyhill, E. G. Coles, M. Bronner-Fraser, Snail2 directly represses cadherin6B during epithelial-to-mesenchymal transitions of the neural crest. *Development*. **134**, 1481–1490 (2007).

293. M. L. Martik, M. E. Bronner, Regulatory logic underlying diversification of the neural crest. *Trends Genet.* **33**, 715–727 (2017).

294. M. Rickmann, J. W. Fawcett, R. J. Keynes, The migration of neural crest cells and the growth of motor axons through the rostral half of the chick somite. *J. Embryol. Exp. Morphol.* **90**, 437–55 (1985).

295. L. S. Gammill, Guidance of trunk neural crest migration requires neuropilin 2/semaphorin 3F signaling. *Development*. **133**, 99–106 (2006).

296. N. M. Le Douarin, Cell line segregation during peripheral nervous system ontogeny. *Science*. **231**, 1515–22 (1986).

297. N. M. Le Douarin, J. Smith, Development of the peripheral nervous system from the neural crest. *Annu. Rev. Cell Biol.* **4**, 375–404 (1988).

298. N. M. Le Douarin, M. a Teillet, The migration of neural crest cells to the wall of the digestive tract in avian embryo. *J. Embryol. Exp. Morphol.* **30**, 31–48 (1973).

299. M. A. Teillet, C. Kalcheim, N. M. Le Douarin, Formation of the Dorsal Root Ganglia in the Avian Embryo: Segmental Origin and Migratory Behavior of Neural Crest Progenitor Cells. *Dev. Biol.* **120**, 329–347 (1987).

300. A. G. E. Pearse, J. M. Polak, F. W. D. Rost, J. Fontaine, C. Le Lièvre, N. Le Douarin, Demonstration of the neural crest origin of type I (APUD) cells in the avian carotid body, using a cytochemical marker system. *Histochemie.* **34**, 191–203 (1973).

301. G. P. Dushane, The origin of pigment cells in amphibia. *Science (80-.).* **80**, 620–621 (1934).

302. M. C. Johnston, D. M. Noden, R. D. Hazelton, J. L. Coulombre, A. J. Coulombre, Origins of avian ocular and periocular tissues. *Exp. Eye Res.* **29**, 27–43 (1979).

303. X. Jiang, D. H. Rowitch, P. Soriano, A. P. McMahon, H. M. Sucov, Fate of the mammalian cardiac neural crest. *Development*. **127**, 1607–1616 (2000).

304. S. N. Perera, L. Kerosuo, On the road again: Establishment and maintenance of stemness

in the neural crest from embryo to adulthood. *Stem Cells*. **39**, 7–25 (2021).

305. M. S. Simões-Costa, M. E. Bronner, Reprogramming of avian neural crest axial identity and cell fate. *Science*. **352**, 1570–3 (2016).

306. P. Betancur, M. Bronner-Fraser, T. Sauka-Spengler, Genomic code for Sox10 activation reveals a key regulatory enhancer for cranial neural crest. *Proc. Natl. Acad. Sci.* **107**, 3570–3575 (2010).

307. M. Barembaum, M. E. Bronner, Identification and dissection of a key enhancer mediating cranial neural crest specific expression of transcription factor, Ets-1. *Dev. Biol.* **382**, 567–575 (2013).

308. M. Sieber-Blum, A. M. Cohen, Clonal analysis of quail neural crest cells. *Dev. Biol.* **80**, 96–106 (1980).

309. M. Bronner-Fraser, S. E. Fraser, Cell lineage analysis reveals multipotency of some avian neural crest cells. *Nature*. **335**, 161–4 (1988).

310. S. E. Fraser, M. Bronner-Fraser, Migrating neural crest cells in the trunk of the avian embryo are multipotent. *Development*. **112**, 913–20 (1991).

311. A. Baggiolini, S. Varum, J. M. Mateos, D. Bettosini, N. John, M. Bonalli, U. Ziegler, L. Dimou, H. Clevers, R. Furrer, L. Sommer, Premigratory and migratory neural crest cells are multipotent in vivo. *Cell Stem Cell*. **16**, 314–322 (2015).

312. M. Bronner, Confetti clarifies controversy: Neural crest stem cells are multipotent. *Cell Stem Cell*. **16**, 217–218 (2015).

313. C. S. Le Lievre, G. G. Schweizer, C. M. Ziller, N. M. Le Douarin, Restrictions of developmental capabilities in neural crest cell derivatives as tested by in vivo transplantation experiments. *Dev. Biol.* **77**, 362–378 (1980).

314. D. W. Raible, J. S. Eisen, Restriction of neural crest cell fate in the trunk of the embryonic zebrafish. *Development*. **120**, 495–503 (1994).

315. T. F. Schilling, C. B. Kimmel, Segment and cell type lineage restrictions during pharyngeal arch development in the zebrafish embryo. *Development*. **120**, 483–94 (1994).

316. S. Krispin, E. Nitzan, Y. Kassem, C. Kalcheim, Evidence for a dynamic spatiotemporal fate map and early fate restrictions of premigratory avian neural crest. *Development*. **137**, 585–595 (2010).

317. L. George, M. Chaverra, V. Todd, R. Lansford, F. Lefcort, Nociceptive sensory neurons derive from contralaterally migrating, fate-restricted neural crest cells. *Nat. Neurosci.* **10**, 1287–1293 (2007).

318. L. Lo, E. L. Dormand, D. J. Anderson, Late-emigrating neural crest cells in the roof plate are restricted to a sensory fate by GDF7. *Proc. Natl. Acad. Sci. U. S. A.* **102**, 7192–7 (2005).

319. S. Bhatt, R. Diaz, P. A. Trainor, Signals and switches in Mammalian neural crest cell differentiation. *Cold Spring Harb. Perspect. Biol.* **5**, 1–20 (2013).

320. J. Chen, Y. Luo, H. Hui, T. Cai, H. Huang, F. Yang, J. Feng, J. Zhang, X. Yan, CD146 coordinates brain endothelial cell–pericyte communication for blood–brain barrier development. *Proc. Natl. Acad. Sci.* **114**, E7622–E7631 (2017).

321. A. Kumar, S. S. D'Souza, O. V. Moskvin, H. Toh, B. Wang, J. Zhang, S. Swanson, L. W. Guo, J. A. Thomson, I. I. Slukvin, Specification and Diversification of Pericytes and Smooth Muscle Cells from Mesenchymoangioblasts. *Cell Rep.* **19**, 1902–1916 (2017).

322. K. K. Hirschi, S. A. Rohovsky, P. A. D'Amore, PDGF, TGF-beta, and heterotypic cell-cell interactions mediate endothelial cell-induced recruitment of 10T1/2 cells and their differentiation to a smooth muscle fate. *J. Cell Biol.* **141**, 805–814 (1998).

323. C. Patsch, L. Challet-Meylan, E. C. Thoma, E. Urich, T. Heckel, J. F. O'Sullivan, S. J. Grainger, F. G. Kapp, L. Sun, K. Christensen, Y. Xia, M. H. C. Florido, W. He, W. Pan, M. Prummer, C. R. Warren, R. Jakob-Roetne, U. Certa, R. Jagasia, P. O. Freskgard, I. Adatto, D. Kling, P. Huang, L. I. Zon, E. L. Chaikof, R. E. Gerszten, M. Graf, R. Iacone, C. A. Cowan, Generation of vascular endothelial and smooth muscle cells from human pluripotent stem cells. *Nat. Cell Biol.* **17**, 994–1003 (2015).

324. C. Griffin, R. Bajpai, Neural Crest-Derived Human Cranial Pericytes Model Primary Forebrain Pericytes and Predict Disease-Specific Cranial Vasculature Defects. *SSRN Electron. J.* (2018), doi:10.2139/ssrn.3189103.

325. G. La Manno, K. Siletti, A. Furlan, D. Gyllborg, E. Vinsland, A. Mossi Albiach, C. Mattsson Langseth, I. Khven, A. R. Lederer, L. M. Dratva, A. Johnsson, M. Nilsson, P. Lönnerberg, S. Linnarsson, Molecular architecture of the developing mouse brain. *Nature*. **596**, 92–96 (2021).

326. K. Ando, W. Wang, D. Peng, A. Chiba, A. K. Lagendijk, L. Barske, J. G. Crump, D. Y. R. R. Stainier, U. Lendahl, K. Koltowska, B. M. Hogan, S. Fukuhara, N. Mochizuki, C. Betsholtz, Peri-arterial specification of vascular mural cells from naïve mesenchyme requires notch signaling. *Dev.* **146** (2019), doi:10.1242/dev.165589.

327. J. DeSisto, R. O'Rourke, H. E. Jones, B. Pawlikowski, A. D. Malek, S. Bonney, F. Guimiot, K. L. Jones, J. A. Siegenthaler, Single-Cell Transcriptomic Analyses of the Developing Meninges Reveal Meningeal Fibroblast Diversity and Function. *Dev. Cell*. **54**, 43-59.e4 (2020).

328. C. E. Dorrier, H. E. Jones, L. Pintarić, J. A. Siegenthaler, R. Daneman, Emerging roles for CNS fibroblasts in health, injury and disease. *Nat. Rev. Neurosci.* **23**, 23–34 (2021).

329. F. Li, Y. Lan, Y. Wang, J. Wang, G. Yang, F. Meng, H. Han, A. Meng, Y. Wang, X. Yang, Endothelial Smad4 Maintains Cerebrovascular Integrity by Activating N-Cadherin through Cooperation with Notch. *Dev. Cell*. **20**, 291–302 (2011).

330. E. A. Winkler, R. D. Bell, B. V. Zlokovic, Lack of Smad or Notch Leads to a Fatal Game

of Brain Pericyte Hopscotch. *Dev. Cell*. **20**, 279–280 (2011).

331. P. D. Langridge, G. Struhl, Epsin-Dependent Ligand Endocytosis Activates Notch by Force. *Cell*. **171**, 1383-1396.e12 (2017).

332. K. Hori, A. Sen, S. Artavanis-Tsakonas, Notch signaling at a glance. *J. Cell Sci.* **126**, 2135–2140 (2013).

333. S. J. Bray, M. Gomez-Lamarca, Notch after cleavage. *Curr. Opin. Cell Biol.* **51**, 103–109 (2018).

334. J. Kelleher, A. Dickinson, S. Cain, Y. Hu, N. Bates, A. Harvey, J. Ren, W. Zhang, F. C. Moreton, K. W. Muir, C. Ward, R. M. Touyz, P. Sharma, Q. Xu, S. J. Kimber, T. Wang, Patient-Specific iPSC Model of a Genetic Vascular Dementia Syndrome Reveals Failure of Mural Cells to Stabilize Capillary Structures. *Stem Cell Reports*. **13**, 817–831 (2019).

335. N. Nandagopal, L. A. Santat, L. LeBon, D. Sprinzak, M. E. Bronner, M. B. Elowitz, Dynamic Ligand Discrimination in the Notch Signaling Pathway. *Cell*. **172**, 869-880.e19 (2018).

336. B. D. Gastfriend, K. L. Foreman, M. E. Katt, S. P. Palecek, E. V. Shusta, Integrative analysis of the human brain mural cell transcriptome. *J. Cereb. Blood Flow Metab.* **41**, 3052–3068 (2021).

337. E. Tournier-Lasserve, A. Joutel, J. Melki, J. Weissenbach, G. M. Lathrop, H. Chabriat, J.-L. Mas, E.-A. Cabanis, M. Baudrimont, J. Maciazek, M.-A. Bach, M.-G. Bousser, Cerebral autosomal dominant arteriopathy with subcortical infarcts and leukoencephalopathy maps to chromosome 19q12. *Nat. Genet.* **3**, 256–259 (1993).

338. A. Joutel, C. Corpechot, A. Ducros, K. Vahedi, H. Chabriat, P. Mouton, S. Alamowitch, V. Domenga, M. Cécillion, E. Marechal, J. Maciazek, C. Vayssiere, C. Cruaud, E. A. Cabanis, M. M. Ruchoux, J. Weissenbach, J. F. Bach, M. G. Bousser, E. Tournier-Lasserve, Notch3 mutations in CADASIL, a hereditary adult-onset condition causing stroke and dementia. *Nature*. **383**, 707–10 (1996).

339. A. Joutel, F. Andreux, S. Gaulis, V. Domenga, M. Cecillon, N. Battail, N. Piga, F. Chapon, C. Godfrain, E. Tournier-Lasserve, The ectodomain of the Notch3 receptor accumulates within the cerebrovasculature of CADASIL patients. *J. Clin. Invest.* **105**, 597–605 (2000).

340. M. Ghosh, M. Balbi, F. Hellal, M. Dichgans, U. Lindauer, N. Plesnila, Pericytes are involved in the pathogenesis of cerebral autosomal dominant arteriopathy with subcortical infarcts and leukoencephalopathy. *Ann. Neurol.* **78**, 887–900 (2015).

341. Y. Wang, L. Pan, C. B. Moens, B. Appel, Notch3 establishes brain vascular integrity by regulating pericyte number. *Development*. **141**, 307–317 (2014).

342. C. Bondjers, L. He, M. Takemoto, J. Norlin, N. Asker, M. Hellström, P. Lindahl, C. Betsholtz, C. Bondjers, L. He, M. Takemoto, J. Norlin, N. Asker, M. Hellström, P.

Lindahl, C. Betsholtz, Microarray analysis of blood microvessels from PDGF-B and PDGF-Rβ mutant mice identifies novel markers for brain pericytes. *FASEB J.* **20**, 1703–1705 (2006).

343. J. A. Siegenthaler, Y. Choe, K. P. Patterson, I. Hsieh, D. Li, S.-C. S. C. Jaminet, R. Daneman, T. Kume, E. J. Huang, S. J. Pleasure, Foxc1 is required by pericytes during fetal brain angiogenesis. *Biol. Open*. **2**, 647–659 (2013).

344. A. Reyahi, A. M. Nik, M. Ghiami, A. Gritli-Linde, F. Pontén, B. R. Johansson, P. Carlsson, Foxf2 Is Required for Brain Pericyte Differentiation and Development and Maintenance of the Blood-Brain Barrier. *Dev. Cell*. **34**, 19–32 (2015).

345. Y. Zhang, K. Chen, S. A. Sloan, M. L. Bennett, A. R. Scholze, S. O'Keeffe, H. P. Phatnani, P. Guarnieri, C. Caneda, N. Ruderisch, S. Deng, S. A. Liddelow, C. Zhang, R. Daneman, T. Maniatis, B. A. Barres, J. Q. Wu, An RNA-Sequencing Transcriptome and Splicing Database of Glia, Neurons, and Vascular Cells of the Cerebral Cortex. *J. Neurosci.* **34**, 11929–11947 (2014).

346. T. D. Palmer, A. R. Willhoite, F. H. Gage, Vascular niche for adult hippocampal neurogenesis. *J. Comp. Neurol.* **425**, 479–494 (2000).

347. Q. Shen, S. K. Goderie, L. Jin, N. Karanth, Y. Sun, N. Abramova, P. Vincent, K. Pumiglia, S. Temple, Endothelial cells stimulate self-renewal and expand neurogenesis of neural stem cells. *Science (80-.).* **304**, 1338–1340 (2004).

348. A. Louissaint, S. Rao, C. Leventhal, S. A. Goldman, Coordinated interaction of neurogenesis and angiogenesis in the adult songbird brain. *Neuron*. **34**, 945–960 (2002).

349. M. Snapyan, M. Lemasson, M. S. Brill, M. Blais, M. Massouh, J. Ninkovic, C. Gravel, F. Berthod, M. Götz, P. A. Barker, A. Parent, A. Saghatelyan, Vasculature guides migrating neuronal precursors in the adult mammalian forebrain via brain-derived neurotrophic factor signaling. *J. Neurosci.* **29**, 4172–4188 (2009).

350. S. A. Goldman, Z. Chen, Perivascular instruction of cell genesis and fate in the adult brain. *Nat. Neurosci.* **14**, 1382–1389 (2011).

351. G. Kempermann, F. H. Gage, L. Aigner, H. Song, M. A. Curtis, S. Thuret, H. G. Kuhn, S. Jessberger, P. W. Frankland, H. A. Cameron, E. Gould, R. Hen, D. N. Abrous, N. Toni, A. F. Schinder, X. Zhao, P. J. Lucassen, J. Frisén, Human Adult Neurogenesis: Evidence and Remaining Questions. *Cell Stem Cell*. **23**, 25–30 (2018).

352. H. H. Tsai, J. Niu, R. Munji, D. Davalos, J. Chang, H. Zhang, A. C. Tien, C. J. Kuo, J. R. Chan, R. Daneman, S. P. J. Fancy, Oligodendrocyte precursors migrate along vasculature in the developing nervous system. *Science (80-.).* **351**, 379–384 (2016).

353. I. Paredes, J. R. Vieira, B. Shah, C. F. Ramunno, J. Dyckow, H. Adler, M. Richter, G. Schermann, E. Giannakouri, L. Schirmer, H. G. Augustin, C. Ruiz de Almodóvar, Oligodendrocyte precursor cell specification is regulated by bidirectional neural progenitor–endothelial cell crosstalk. *Nat. Neurosci.* **24**, 478–488 (2021).

354. M. Hamburgh, Analysis of the postnatal developmental effects of “reeler,” a neurological mutation in mice. A study in developmental genetics. *Dev. Biol.* **8**, 165–185 (1963).

355. V. Caviness Jr, Patterns of cell and fiber distribution in the neocortex of the reeler mutant mouse. *J. Comp. Neurol.* **170**, 435–447 (1976).

356. G. D’Arcangelo, G. G. Miao, S.-C. Chen, H. D. Scares, J. I. Morgan, T. Curran, A protein related to extracellular matrix proteins deleted in the mouse mutant reeler. *Nature*. **374**, 719–723 (1995).

357. Y. Jossin, Reelin functions, mechanisms of action and signaling pathways during brain development and maturation. *Biomolecules*. **10**, 1–31 (2020).

358. M. Segarra, M. R. Aburto, F. Cop, C. Llaó-Cid, R. Härtl, M. Damm, I. Bethani, M. Parrilla, D. Husainie, A. Schänzer, H. Schlierbach, T. Acker, L. Mohr, L. Torres-Masjoan, M. Ritter, A. Acker-Palmer, Endothelial Dab1 signaling orchestrates neuro-glia-vessel communication in the central nervous system. *Science (80-.).* **361**, eaao2861 (2018).

359. D. A. Nation, M. D. Sweeney, A. Montagne, A. P. Sagare, L. M. D’Orazio, M. Pachicano, F. Sepehrband, A. R. Nelson, D. P. Buennagel, M. G. Harrington, T. L. S. Benzinger, A. M. Fagan, J. M. Ringman, L. S. Schneider, J. C. Morris, H. C. Chui, M. Law, A. W. Toga, B. V. Zlokovic, Blood–brain barrier breakdown is an early biomarker of human cognitive dysfunction. *Nat. Med.* **25**, 270–276 (2019).

360. C. R. French, S. Seshadri, A. L. Destefano, M. Fornage, C. R. Arnold, P. J. Gage, J. M. Skarie, W. B. Dobyns, K. J. Millen, T. Liu, W. Dietz, T. Kume, M. Hofker, D. J. Emery, S. J. Childs, A. J. Waskiewicz, O. J. Lehmann, Mutation of FOXC1 and PITX2 induces cerebral small-vessel disease. *J. Clin. Invest.* **124**, 4877–81 (2014).

361. L. Ray, J. J. Iliff, J. J. Heys, Analysis of convective and diffusive transport in the brain interstitium. *Fluids Barriers CNS*. **16**, 1–18 (2019).

362. G. Hartung, S. Badr, S. Mihelic, A. Dunn, X. Cheng, S. Kura, D. A. Boas, D. Kleinfeld, A. Alaraj, A. A. Linninger, Mathematical synthesis of the cortical circulation for the whole mouse brain—part II: Microcirculatory closure. *Microcirculation*. **28**, 1–26 (2021).

363. B. Shaker, M. S. Yu, J. S. Song, S. Ahn, J. Y. Ryu, K. S. Oh, D. Na, LightBBB: Computational prediction model of blood-brain-barrier penetration based on LightGBM. *Bioinformatics*. **37**, 1135–1139 (2021).

364. B. Alberts, A. Johnson, J. Lewis, M. Raff, K. Roberts, P. Walter, *Molecular Biology of the Cell* (Garland Science, New York, 4th Ed., 2002).

365. H. Kim, M. Kim, S.-K. Im, S. Fang, Mouse Cre-LoxP system: general principles to determine tissue-specific roles of target genes. *Lab. Anim. Res.* **34**, 147 (2018).

366. M. Hupe, M. X. Li, S. Kneitz, D. Davydova, C. Yokota, J. Kele-Olovsson, B. Hot, J. M. Stenman, M. Gessler, Gene expression profiles of brain endothelial cells during embryonic development at bulk and single-cell levels. *Sci. Signal.* **10**, 1–13 (2017).

367. R. N. Munji, A. L. Soung, G. A. Weiner, F. Sohet, B. D. Semple, A. Trivedi, K. Gimlin, M. Kotoda, M. Korai, S. Aydin, A. Batugal, A. C. Cabangcala, P. G. Schupp, M. C. Oldham, T. Hashimoto, L. J. Noble-Haeusslein, R. Daneman, Profiling the mouse brain endothelial transcriptome in health and disease models reveals a core blood–brain barrier dysfunction module. *Nat. Neurosci.* **22**, 1892–1902 (2019).

368. M. H. Park, J. Y. Lee, K. H. Park, I. K. Jung, K.-T. T. Kim, Y.-S. S. Lee, H.-H. H. Ryu, Y. Jeong, M. Kang, M. Schwaninger, E. Gulbins, M. Reichel, J. Kornhuber, T. Yamaguchi, H.-J. J. Kim, S. H. Kim, E. H. Schuchman, H. K. Jin, J. sung Bae, Vascular and Neurogenic Rejuvenation in Aging Mice by Modulation of ASM. *Neuron*. **100**, 167-182.e9 (2018).

369. C. E. Dorrier, D. Aran, E. A. Haenelt, R. N. Sheehy, K. K. Hoi, L. Pintarić, Y. Chen, C. O. Lizama, K. M. Cautivo, G. A. Weiner, B. Popko, S. P. J. Fancy, T. D. Arnold, R. Daneman, CNS fibroblasts form a fibrotic scar in response to immune cell infiltration. *Nat. Neurosci.* **24**, 234–244 (2021).

370. L. Duan, X.-D. Di Zhang, W.-Y. Y. Miao, Y.-J. J. Sun, G. Xiong, Q. Wu, G. Li, P. Yang, H. Yu, H. Li, Y. Wang, M. Zhang, L.-Y. Y. Hu, X. Tong, W.-H. H. Zhou, X. Yu, PDGFRβ Cells Rapidly Relay Inflammatory Signal from the Circulatory System to Neurons via Chemokine CCL2. *Neuron*. **100**, 183-200.e8 (2018).

371. J. M. Dave, T. Mirabella, S. D. Weatherbee, D. M. Greif, Pericyte ALK5/TIMP3 Axis Contributes to Endothelial Morphogenesis in the Developing Brain. *Dev. Cell*. **5**, 1–14 (2018).

372. A. Zeisel, H. Hochgerner, P. Lönnerberg, A. Johnsson, F. Memic, J. van der Zwan, M. Häring, E. Braun, L. E. Borm, G. La Manno, S. Codeluppi, A. Furlan, K. Lee, N. Skene, K. D. Harris, J. Hjerling-Leffler, E. Arenas, P. Ernfors, U. Marklund, S. Linnarsson, Molecular Architecture of the Mouse Nervous System. *Cell*. **174**, 999-1014.e22 (2018).

373. X. Guo, T. Ge, S. Xia, H. Wu, M. Colt, X. Xie, B. Zhang, J. Zeng, J.-F. Chen, D. Zhu, A. Montagne, F. Gao, Z. Zhao, Atp13a5 Marker Reveals Pericytes of The Central Nervous System in Mice. *bioRxiv* (2021), doi:10.1101/2021.07.09.451694.

374. B. Jung, T. D. Arnold, E. Raschperger, K. Gaengel, C. Betsholtz, Visualization of vascular mural cells in developing brain using genetically labeled transgenic reporter mice. *J. Cereb. Blood Flow Metab.* **38**, 456–468 (2018).

375. R. A. Umans, H. E. Henson, F. Mu, C. Parupalli, B. Ju, J. L. Peters, K. A. Lanham, J. S. Plavicki, M. R. Taylor, CNS angiogenesis and barriergenesis occur simultaneously. *Dev. Biol.* **425**, 101–108 (2017).

376. A. Guemez-Gamboa, L. N. Nguyen, H. Yang, M. S. Zaki, M. Kara, T. Ben-Omran, N. Akizu, R. O. Rosti, B. Rosti, E. Scott, J. Schroth, B. Copeland, K. K. Vaux, A. Cazenave-Gassiot, D. Q. Y. Quek, B. H. Wong, B. C. Tan, M. R. Wenk, M. Gunel, S. Gabriel, N. C. Chi, D. L. Silver, J. G. Gleeson, Inactivating mutations in MFSD2A, required for omega-3 fatty acid transport in brain, cause a lethal microcephaly syndrome. *Nat. Genet.* **47**, 809–813 (2015).

377. H. C. Etchevers, C. Vincent, N. M. Le Douarin, G. F. Couly, The cephalic neural crest provides pericytes and smooth muscle cells to all blood vessels of the face and forebrain. *Development*. **128**, 1059–1068 (2001).

378. H. C. Etchevers, Pericyte Ontogeny: The Use of Chimeras to Track a Cell Lineage of Diverse Germ Line Origins. *Methods Mol. Biol.* **2235**, 61–87 (2021).

379. F. Benz, V. Wichitnaowarat, M. Lehmann, R. F. Germano, D. Mihova, J. Macas, R. H. Adams, M. M. Taketo, K.-H. Plate, S. Guérit, B. Vanhollebeke, S. Liebner, Low wnt/β-catenin signaling determines leaky vessels in the subfornical organ and affects water homeostasis in mice. *Elife*. **8**, 1–29 (2019).

380. W. M. Pardridge, Blood-Brain Barrier and Delivery of Protein and Gene Therapeutics to Brain. *Front. Aging Neurosci.* **11**, 1–27 (2020).

381. R. D. Bell, E. A. Winkler, I. Singh, A. P. Sagare, R. Deane, Z. Wu, D. M. Holtzman, C. Betsholtz, A. Armulik, J. Sallstrom, B. C. Berk, B. V. Zlokovic, Apolipoprotein e controls cerebrovascular integrity via cyclophilin A. *Nature*. **485**, 512–516 (2012).

382. B. Engelhardt, M. Laschinger, M. Schulz, U. Samulowitz, D. Vestweber, G. Hoch, The development of experimental autoimmune encephalomyelitis in the mouse requires α4-integrin but not α4β7-integrin. *J. Clin. Invest.* **102**, 2096–2105 (1998).

383. L. Piccio, B. Rossi, E. Scarpini, C. Laudanna, C. Giagulli, A. C. Issekutz, D. Vestweber, E. C. Butcher, G. Constantin, Molecular mechanisms involved in lymphocyte recruitment in inflamed brain microvessels: critical roles for P-selectin glycoprotein ligand-1 and heterotrimeric G(i)-linked receptors. *J. Immunol.* **168**, 1940–9 (2002).

384. M. S. Kariolis, R. C. Wells, J. A. Getz, W. Kwan, C. S. Mahon, R. Tong, D. J. Kim, A. Srivastava, C. Bedard, K. R. Henne, T. Giese, V. A. Assimon, X. Chen, Y. Zhang, H. Solanoy, K. Jenkins, P. E. Sanchez, L. Kane, T. Miyamoto, K. S. Chew, M. E. Pizzo, N. Liang, M. E. K. Calvert, S. L. DeVos, S. Baskaran, S. Hall, Z. K. Sweeney, R. G. Thorne, R. J. Watts, M. S. Dennis, A. P. Silverman, Y. J. Y. Zuchero, Brain delivery of therapeutic proteins using an Fc fragment blood-brain barrier transport vehicle in mice and monkeys. *Sci. Transl. Med.* **12**, 1–14 (2020).

385. J. V Georgieva, L. I. Goulatis, C. C. Stutz, S. G. Canfield, H. W. Song, B. D. Gastfriend, E. V Shusta, Antibody screening using a human iPSC-based blood-brain barrier model identifies antibodies that accumulate in the CNS. *FASEB J.* **34**, 12549–12564 (2020).

386. C. C. Stutz, J. V. Georgieva, E. V. Shusta, Coupling brain perfusion screens and next generation sequencing to identify blood–brain barrier binding antibodies. *AIChE J.* **64**, 4229–4236 (2018).

387. K. Kucharz, K. Kristensen, K. B. Johnsen, M. A. Lund, M. Lønstrup, T. Moos, T. L. Andresen, M. J. Lauritzen, Post-capillary venules are the key locus for transcytosis-mediated brain delivery of therapeutic nanoparticles. *Nat. Commun.* **12**, 4121 (2021).

388. H. Sasaguri, P. Nilsson, S. Hashimoto, K. Nagata, T. Saito, B. De Strooper, J. Hardy, R.

Vassar, B. Winblad, T. C. Saido, APP mouse models for Alzheimer's disease preclinical studies . *EMBO J.* **36**, 2473–2487 (2017).

389. C. Van Cauwenberghe, C. Van Broeckhoven, K. Sleegers, The genetic landscape of Alzheimer disease: clinical implications and perspectives. *Genet. Med.* **18**, 421–430 (2016).

390. C. S. Constantinescu, N. Farooqi, K. O'Brien, B. Gran, Experimental autoimmune encephalomyelitis (EAE) as a model for multiple sclerosis (MS). *Br. J. Pharmacol.* **164**, 1079–1106 (2011).

391. G. La Manno, D. Gyllborg, S. Codeluppi, K. Nishimura, C. Salto, A. Zeisel, L. E. Borm, S. R. W. Stott, E. M. Toledo, J. C. Villaescusa, P. Lönnerberg, J. Ryge, R. A. Barker, E. Arenas, S. Linnarsson, Molecular Diversity of Midbrain Development in Mouse, Human, and Stem Cells. *Cell*. **167**, 566-580.e19 (2016).

392. D. Polioudakis, L. de la Torre-Ubieta, J. Langerman, A. G. Elkins, X. Shi, J. L. Stein, C. K. Vuong, S. Nichterwitz, M. Gevorgian, C. K. Opland, D. Lu, W. Connell, E. K. Ruzzo, J. K. Lowe, T. Hadzic, F. I. Hinz, S. Sabri, W. E. Lowry, M. B. Gerstein, K. Plath, D. H. Geschwind, A Single-Cell Transcriptomic Atlas of Human Neocortical Development during Mid-gestation. *Neuron*. **103**, 785-801.e8 (2019).

393. W. Zhang, Q. Y. Liu, A. S. Haqqani, S. Leclerc, Z. Liu, F. Fauteux, E. Baumann, C. E. Delaney, D. Ly, A. T. Star, E. Brunette, C. Sodja, M. Hewitt, J. K. Sandhu, D. B. Stanimirovic, Differential expression of receptors mediating receptor-mediated transcytosis (RMT) in brain microvessels, brain parenchyma and peripheral tissues of the mouse and the human. *Fluids Barriers CNS*. **17**, 1–17 (2020).

394. S. Aday, R. Cecchelli, D. Hallier-Vanuxeem, M. P. Dehouck, L. Ferreira, Stem Cell-Based Human Blood-Brain Barrier Models for Drug Discovery and Delivery. *Trends Biotechnol.* **34**, 382–393 (2016).

395. K. D. Foust, E. Nurre, C. L. Montgomery, A. Hernandez, C. M. Chan, B. K. Kaspar, Intravascular AAV9 preferentially targets neonatal neurons and adult astrocytes. *Nat. Biotechnol.* **27**, 59–65 (2009).

396. B. E. Deverman, P. L. Pravdo, B. P. Simpson, S. R. Kumar, K. Y. Chan, A. Banerjee, W. L. Wu, B. Yang, N. Huber, S. P. Pasca, V. Gradinaru, Cre-dependent selection yields AAV variants for widespread gene transfer to the adult brain. *Nat. Biotechnol.* **34**, 204–209 (2016).

397. K. Y. Chan, M. J. Jang, B. B. Yoo, A. Greenbaum, N. Ravi, W. L. Wu, L. Sánchez-Guardado, C. Lois, S. K. Mazmanian, B. E. Deverman, V. Gradinaru, Engineered AAVs for efficient noninvasive gene delivery to the central and peripheral nervous systems. *Nat. Neurosci.* **20**, 1172–1179 (2017).

398. J. Hordeaux, Y. Yuan, P. M. Clark, Q. Wang, R. A. Martino, J. J. Sims, P. Bell, A. Raymond, W. L. Stanford, J. M. Wilson, The GPI-Linked Protein LY6A Drives AAV-PHP.B Transport across the Blood-Brain Barrier. *Mol. Ther.* **27**, 912–921 (2019).

399. Q. Huang, K. Y. Chan, I. G. Tobey, Y. A. Chan, T. Poterba, C. L. Boutros, A. B. Balazs, R. Daneman, J. M. Bloom, C. Seed, B. E. Deverman, Delivering genes across the blood-brain barrier: LY6A, a novel cellular receptor for AAV-PHP.B capsids. *PLoS One*. **14**, 1–17 (2019).

400. A. R. Batista, O. D. King, C. P. Reardon, C. Davis, Shankaracharya, V. Philip, H. Gray-Edwards, N. Aronin, C. Lutz, J. Landers, M. Sena-Esteves, Ly6a Differential Expression in Blood-Brain Barrier Is Responsible for Strain Specific Central Nervous System Transduction Profile of AAV-PHP.B. *Hum. Gene Ther.* **31**, 90–102 (2020).

401. J. Hordeaux, Q. Wang, N. Katz, E. L. Buza, P. Bell, J. M. Wilson, The Neurotropic Properties of AAV-PHP.B Are Limited to C57BL/6J Mice. *Mol. Ther.* **26**, 664–668 (2018).

402. P. D. Bowman, A. L. Betz, D. aR, J. S. Wolinsky, J. B. Penney, R. R. Shivers, G. W. Goldstein, Primary culture of capillary endothelium from rat brain. *In Vitro*. **17**, 353–362 (1981).

403. P. D. Bowman, S. R. Ennis, K. E. Rarey, A. Lorris Betz, G. W. Goldstein, Brain microvessel endothelial cells in tissue culture: A model for study of blood-brain barrier permeability. *Ann. Neurol.* **14**, 396–402 (1983).

404. G. Fricker, S. Nobmann, D. S. Miller, Permeability of porcine blood brain barrier to somatostatin analogues. *Br. J. Pharmacol.* **135**, 1308–1314 (2002).

405. S. Nakagawa, M. A. Deli, H. Kawaguchi, T. Shimizudani, T. Shimono, Á. Kittel, K. Tanaka, M. Niwa, A. Kittel, K. Tanaka, M. Niwa, Á. Kittel, K. Tanaka, M. Niwa, A new blood-brain barrier model using primary rat brain endothelial cells, pericytes and astrocytes. *Neurochem. Int.* **54**, 253–263 (2009).

406. A. R. Calabria, C. Weidenfeller, A. R. Jones, H. E. De Vries, E. V Shusta, Puromycin-purified rat brain microvascular endothelial cell cultures exhibit improved barrier properties in response to glucocorticoid induction, 922–933 (2006).

407. L. B. Thomsen, A. Burkhart, T. Moos, A triple culture model of the blood-brain barrier using porcine brain endothelial cells, astrocytes and pericytes. *PLoS One*. **10**, 1–16 (2015).

408. T. Fujimoto, Y. Morofuji, S. Nakagawa, A. Kovac, N. Horie, T. Izumo, M. Niwa, T. Matsuo, W. A. Banks, Comparison of the rate of dedifferentiation with increasing passages among cell sources for an in vitro model of the blood–brain barrier. *J. Neural Transm.* **127**, 1117–1124 (2020).

409. B. B. Weksler, Blood-brain barrier-specific properties of a human adult brain endothelial cell line. *FASEB J.* **26**, 1–27 (2005).

410. R. J. Rist, I. A. Romero, M. W. K. Chan, P. O. Couraud, F. Roux, N. J. Abbott, F-actin cytoskeleton and sucrose permeability of immortalised rat brain microvascular endothelial cell monolayers: Effects of cyclic AMP and astrocytic factors. *Brain Res.* **768**, 10–18 (1997).

411. Y. Omidi, L. Campbell, J. Barar, D. Connell, S. Akhtar, M. Gumbleton, Evaluation of the immortalised mouse brain capillary endothelial cell line, b.End3, as an in vitro blood-brain barrier model for drug uptake and transport studies. *Brain Res.* **990**, 95–112 (2003).

412. H. C. Helms, N. J. Abbott, M. Burek, R. Cecchelli, P.-O. Couraud, M. A. Deli, C. Förster, H. J. Galla, I. A. Romero, E. V Shusta, M. J. Stebbins, E. Vandenhaute, B. Weksler, B. Brodin, C. Forster, H. J. Galla, I. A. Romero, E. V Shusta, M. J. Stebbins, E. Vandenhaute, B. Weksler, B. Brodin, C. Förster, H. J. Galla, I. A. Romero, E. V Shusta, M. J. Stebbins, E. Vandenhaute, B. Weksler, B. Brodin, C. Forster, H. J. Galla, I. A. Romero, E. V Shusta, M. J. Stebbins, E. Vandenhaute, B. Weksler, B. Brodin, In vitro models of the blood–brain barrier: An overview of commonly used brain endothelial cell culture models and guidelines for their use. *J. Cereb. Blood Flow Metab.* **36**, 862–890 (2016).

413. C. Crone, S. P. Olesen, Electrical resistance of brain microvascular endothelium. *Brain Res.* **241**, 49–55 (1982).

414. Q. R. Smith, S. I. Rapoport, Cerebrovascular permeability coefficients to sodium, potassium, and chloride. *J. Neurochem.* **46**, 1732–42 (1986).

415. A. M. Butt, H. C. Jones, N. J. Abbott, Electrical resistance across the blood-brain barrier in anaesthetized rats: a developmental study. *J. Physiol.* **429**, 47–62 (1990).

416. A. R. Calabria, E. V. Shusta, A genomic comparison of in vivo and in vitro brain microvascular endothelial cells. *J. Cereb. Blood Flow Metab.* **28**, 135–148 (2008).

417. R. J. Boado, W. M. Pardridge, Differential expression of alpha-actin mRNA and immunoreactive protein in brain microvascular pericytes and smooth muscle cells. *J. Neurosci. Res.* **39**, 430–5 (1994).

418. A. R. Riveiro, J. M. Brickman, From pluripotency to totipotency: an experimentalist's guide to cellular potency. *Development*. **147** (2020), doi:10.1242/dev.189845.

419. M. H. Kaufman, M. J. Evans, Establishment in culture of pluripotential cells from mouse embryos. *Nature*. **292**, 154–156 (1981).

420. G. R. Martin, Isolation of a pluripotent cell line from early mouse embryos cultured in medium conditioned by teratocarcinoma stem cells. *Proc. Natl. Acad. Sci. U. S. A.* **78**, 7634–7638 (1981).

421. J. A. Thomson, J. Kalishman, T. G. Golos, M. Durning, C. P. Harris, R. A. Becker, J. P. Hearn, Isolation of a primate embryonic stem cell line. *Proc. Natl. Acad. Sci. U. S. A.* **92**, 7844–7848 (1995).

422. J. A. Thomson, Embryonic stem cell lines derived from human blastocysts. *Science (80-.).* **282**, 1145–1147 (1998).

423. K. Takahashi, S. Yamanaka, Induction of Pluripotent Stem Cells from Mouse Embryonic and Adult Fibroblast Cultures by Defined Factors. *Cell*. **126**, 663–676 (2006).

424. K. Takahashi, K. Tanabe, M. Ohnuki, M. Narita, T. Ichisaka, K. Tomoda, S. Yamanaka, Induction of Pluripotent Stem Cells from Adult Human Fibroblasts by Defined Factors. *Cell*. **131**, 861–872 (2007).

425. J. Yu, M. A. Vodyanik, K. Smuga-Otto, J. Antosiewicz-Bourget, J. L. Frane, S. Tian, J. Nie, G. A. Jonsdottir, V. Ruotti, R. Stewart, I. I. Slukvin, J. A. Thomson, Induced pluripotent stem cell lines derived from human somatic cells. *Science*. **318**, 1917–20 (2007).

426. Y. Shi, H. Inoue, J. C. Wu, S. Yamanaka, Induced pluripotent stem cell technology: A decade of progress. *Nat. Rev. Drug Discov.* **16**, 115–130 (2017).

427. R. Cecchelli, S. Aday, E. Sevin, C. Almeida, M. Culot, L. Dehouck, C. Coisne, B. Engelhardt, M. P. Dehouck, L. Ferreira, A stable and reproducible human blood-brain barrier model derived from hematopoietic stem cells. *PLoS One*. **9** (2014), doi:10.1371/journal.pone.0099733.

428. J. Boyer-Di Ponio, F. El-Ayoubi, F. Glacial, K. Ganeshamoorthy, O. Guillevic, P. O. Couraud, C. Driancourt, M. Godet, N. Perrie, G. Uzan, J. Boyer-Di Ponio, F. El-Ayoubi, F. Glacial, K. Ganeshamoorthy, C. Driancourt, M. Godet, N. Perrière, O. Guillevic, P. Olivier Couraud, G. Uzan, J. B. Ponio, F. El-Ayoubi, F. Glacial, K. Ganeshamoorthy, O. Guillevic, P. O. Couraud, C. Driancourt, M. Godet, N. Perrie, G. Uzan, Instruction of circulating endothelial progenitors in vitro towards specialized blood-brain barrier and arterial phenotypes. *PLoS One*. **9** (2014), doi:10.1371/journal.pone.0084179.

429. E. S. Lippmann, S. M. Azarin, J. E. Kay, R. A. Nessler, H. K. Wilson, A. Al-Ahmad, S. P. Palecek, E. V. Shusta, Derivation of blood-brain barrier endothelial cells from human pluripotent stem cells. *Nat. Biotechnol.* **30**, 783–791 (2012).

430. E. S. Lippmann, A. Al-Ahmad, S. M. Azarin, S. P. Palecek, E. V Shusta, A retinoic acid-enhanced, multicellular human blood-brain barrier model derived from stem cell sources. *Sci. Rep.* **4**, 4160 (2014).

431. M. J. Stebbins, H. K. Wilson, S. G. Canfield, T. Qian, S. P. Palecek, E. V. Shusta, Differentiation and characterization of human pluripotent stem cell-derived brain microvascular endothelial cells. *Methods*. **101**, 93–102 (2016).

432. H. K. Wilson, M. G. Faubion, M. K. Hjortness, S. P. Palecek, E. V. Shusta, Cryopreservation of Brain Endothelial Cells Derived from Human Induced Pluripotent Stem Cells Is Enhanced by Rho-Associated Coiled Coil-Containing Kinase Inhibition. *Tissue Eng. Part C Methods*. **22**, 1085–1094 (2016).

433. M. Ribecco-Lutkiewicz, C. Sodja, J. Haukenfrers, A. S. Haqqani, D. Ly, P. Zachar, E. Baumann, M. Ball, J. Huang, M. Rukhlova, M. Martina, Q. Liu, D. Stanimirovic, A. Jezierski, M. Bani-Yaghoub, A novel human induced pluripotent stem cell blood-brain barrier model: Applicability to study antibody-triggered receptor-mediated transcytosis. *Sci. Rep.* **8**, 1–17 (2018).

434. E. H. Neal, N. A. Marinelli, Y. Shi, P. M. McClatchey, K. M. Balotin, D. R. Gullett, K. A.

Hagerla, A. B. Bowman, K. C. Ess, J. P. Wikswo, E. S. Lippmann, A Simplified, Fully Defined Differentiation Scheme for Producing Blood-Brain Barrier Endothelial Cells from Human iPSCs. *Stem Cell Reports*. **12**, 1380–1388 (2019).

435. E. K. Hollmann, A. K. Bailey, A. V. Potharazu, M. D. Neely, A. B. Bowman, E. S. Lippmann, Accelerated differentiation of human induced pluripotent stem cells to blood–brain barrier endothelial cells. *Fluids Barriers CNS.* **14**, 9 (2017).

436. M. E. Katt, Z. S. Xu, S. Gerecht, P. C. Searson, Human Brain Microvascular Endothelial Cells Derived from the BC1 iPS Cell Line Exhibit a Blood-Brain Barrier Phenotype. *PLoS One*. **11**, e0152105 (2016).

437. M. E. Katt, R. M. Linville, L. N. Mayo, Z. S. Xu, P. C. Searson, Functional brain-specific microvessels from iPSC-derived human brain microvascular endothelial cells: the role of matrix composition on monolayer formation. *Fluids Barriers CNS.* **15**, 7 (2018).

438. R. M. Linville, J. G. DeStefano, M. B. Sklar, Z. Xu, A. M. Farrell, M. I. Bogorad, C. Chu, P. Walczak, L. Cheng, V. Mahairaki, K. A. Whartenby, P. A. Calabresi, P. C. Searson, Human iPSC-derived blood-brain barrier microvessels: validation of barrier function and endothelial cell behavior. *Biomaterials*. **190**–**191**, 24–37 (2019).

439. G. N. Grifno, A. M. Farrell, R. M. Linville, D. Arevalo, J. H. Kim, L. Gu, P. C. Searson, Tissue-engineered blood-brain barrier models via directed differentiation of human induced pluripotent stem cells. *Sci. Rep.* **9**, 1–13 (2019).

440. P. A. Clark, A. J. Al-Ahmad, T. Qian, R. R. Zhang, H. K. Wilson, J. P. Weichert, S. P. Palecek, J. S. Kuo, E. V. Shusta, Analysis of cancer-targeting alkylphosphocholine analogue permeability characteristics using a human induced pluripotent stem cell blood-brain barrier model. *Mol. Pharm.* **13**, 3341–3349 (2016).

441. Z. Ye, B. D. Gastfriend, B. J. Umlauf, D. M. Lynn, E. V. Shusta, Antibody-Targeted Liposomes for Enhanced Targeting of the Blood-Brain Barrier. *Pharm. Res.* (2022), doi:10.1007/s11095-022-03186-1.

442. G. D. Vatine, A. Al-Ahmad, B. K. Barriga, S. Svendsen, A. Salim, L. Garcia, V. J. Garcia, R. Ho, N. Yucer, T. Qian, R. G. Lim, J. Wu, L. M. Thompson, W. R. Spivia, Z. Chen, J. Van Eyk, S. P. Palecek, S. Refetoff, E. V Shusta, C. N. Svendsen, Modeling Psychomotor Retardation using iPSCs from MCT8-Deficient Patients Indicates a Prominent Role for the Blood-Brain Barrier. *Cell Stem Cell*, 1–13 (2016).

443. R. G. Lim, C. Quan, A. M. Reyes-Ortiz, S. E. Lutz, A. J. Kedaigle, T. A. Gipson, J. Wu, G. D. Vatine, J. Stocksdale, M. S. Casale, C. N. Svendsen, E. Fraenkel, D. E. Housman, D. Agalliu, L. M. Thompson, Huntington's Disease iPSC-Derived Brain Microvascular Endothelial Cells Reveal WNT-Mediated Angiogenic and Blood-Brain Barrier Deficits. *Cell Rep.* **19**, 1365–1377 (2017).

444. C. A. A. Lee, H. S. Seo, A. G. Armien, F. S. Bates, J. Tolar, S. M. Azarin, Modeling and rescue of defective blood–brain barrier function of induced brain microvascular endothelial cells from childhood cerebral adrenoleukodystrophy patients. *Fluids Barriers*

CNS. **15**, 9 (2018).

445. S. G. Canfield, M. J. Stebbins, B. S. Morales, S. W. Asai, G. D. Vatine, C. N. Svendsen, S. P. Palecek, E. V. Shusta, An isogenic blood–brain barrier model comprising brain endothelial cells, astrocytes, and neurons derived from human induced pluripotent stem cells. *J. Neurochem.* **140**, 874–888 (2017).

446. S. G. Canfield, M. J. Stebbins, M. G. Faubion, B. D. Gastfriend, S. P. Palecek, E. V. Shusta, An isogenic neurovascular unit model comprised of human induced pluripotent stem cell-derived brain microvascular endothelial cells, pericytes, astrocytes, and neurons. *Fluids Barriers CNS*. **16**, 1–12 (2019).

447. M. J. Stebbins, B. D. Gastfriend, S. G. Canfield, M.-S. S. Lee, D. Richards, M. G. Faubion, W.-J. J. Li, R. Daneman, S. P. Palecek, E. V. Shusta, Human pluripotent stem cell–derived brain pericyte–like cells induce blood-brain barrier properties. *Sci. Adv.* **5**, eaau7375 (2019).

448. A. J. Al-Ahmad, R. Patel, S. P. Palecek, E. V Shusta, Hyaluronan impairs the barrier integrity of brain microvascular endothelial cells through a CD44-dependent pathway. *J. Cereb. Blood Flow Metab.* **39**, 1759–1775 (2019).

449. J. J. Jamieson, R. M. Linville, Y. Y. Ding, S. Gerecht, P. C. Searson, Role of iPSC - derived pericytes on barrier function of iPSC - derived brain microvascular endothelial cells in 2D and 3D. *Fluids Barriers CNS*, 1–16 (2019).

450. J. G. DeStefano, Z. S. Xu, A. J. Williams, N. Yimam, P. C. Searson, Effect of shear stress on iPSC-derived human brain microvascular endothelial cells (dhBMECs). *Fluids Barriers CNS*. **14**, 20 (2017).

451. L. Delsing, P. Dönnes, J. Sánchez, M. Clausen, D. Voulgaris, A. Falk, A. Herland, G. Brolén, H. Zetterberg, R. Hicks, J. Synnergren, Barrier Properties and Transcriptome Expression in Human iPSC-Derived Models of the Blood–Brain Barrier. *Stem Cells*. **36**, 1816–1827 (2018).

452. T. M. Lu, S. Houghton, T. Magdeldin, J. G. Barcia Durán, A. P. Minotti, A. Snead, A. Sproul, D. H. T. Nguyen, J. Xiang, H. A. Fine, Z. Rosenwaks, L. Studer, S. Rafii, D. Agalliu, D. Redmond, R. Lis, Pluripotent stem cell-derived epithelium misidentified as brain microvascular endothelium requires ETS factors to acquire vascular fate. *Proc. Natl. Acad. Sci. U. S. A.* **118** (2021), doi:10.1073/pnas.2016950118.

453. E. S. Lippmann, S. M. Azarin, S. P. Palecek, E. V. Shusta, Commentary on human pluripotent stem cell-based blood–brain barrier models. *Fluids Barriers CNS*. **17**, 4–9 (2020).

454. T. M. Lu, J. G. Barcia Durán, S. Houghton, S. Rafii, D. Redmond, R. Lis, Human Induced Pluripotent Stem Cell-Derived Brain Endothelial Cells: Current Controversies. *Front. Physiol.* **12** (2021), doi:10.3389/fphys.2021.642812.

455. G. D. Vatine, R. Barrile, M. J. Workman, Z. Chen, J. Van Eyk, C. N. Svendsen, G. D.

Vatine, R. Barrile, M. J. Workman, S. Sances, B. K. Barriga, W. R. Spivia, Z. Chen, J. Van Eyk, C. N. Svendsen, Human iPSC-Derived Blood-Brain Barrier Chips Resource Chips Enable Disease Modeling and Personalized Medicine Applications. *Stem Cell*. **24**, 995-1005.e6 (2019).

456. M. J. Workman, C. N. Svendsen, Recent advances in human iPSC-derived models of the blood-brain barrier. *Fluids Barriers CNS*. **17**, 1–10 (2020).

457. S. Kusuma, Y.-I. Shen, D. Hanjaya-Putra, P. Mali, L. Cheng, S. Gerecht, Self-organized vascular networks from human pluripotent stem cells in a synthetic matrix. *Proc. Natl. Acad. Sci. U. S. A.* **110**, 12601–6 (2013).

458. X. Lian, X. Bao, A. Al-Ahmad, J. Liu, Y. Wu, W. Dong, K. K. Dunn, E. V. Shusta, S. P. Palecek, Efficient differentiation of human pluripotent stem cells to endothelial progenitors via small-molecule activation of WNT signaling. *Stem Cell Reports*. **3**, 804–816 (2014).

459. X. Bao, X. Lian, S. P. Palecek, Directed Endothelial Progenitor Differentiation from Human Pluripotent Stem Cells Via Wnt Activation Under Defined Conditions. *Methods Mol. Biol.* **1481**, 183–96 (2016).

460. I. Elcheva, V. Brok-Volchanskaya, A. Kumar, P. Liu, J. Lee, L. Tong, M. Vodyanik, S. Swanson, R. Stewart, M. Kyba, E. Yakubov, J. Cooke, J. A. Thomson, I. Slukvin, Direct induction of haematoendothelial programs in human pluripotent stem cells by transcriptional regulators. *Nat. Commun.* **5**, 4372 (2014).

461. K. Suknuntha, L. Tao, V. Brok-Volchanskaya, S. S. D'Souza, A. Kumar, I. Slukvin, Optimization of Synthetic mRNA for Highly Efficient Translation and its Application in the Generation of Endothelial and Hematopoietic Cells from Human and Primate Pluripotent Stem Cells. *Stem Cell Rev. Reports*. **14**, 525–534 (2018).

462. K. Wang, R. Z. Lin, X. Hong, A. H. Ng, C. N. Lee, J. Neumeyer, G. Wang, X. Wang, M. Ma, W. T. Pu, G. M. Church, J. M. Melero-Martin, Robust differentiation of human pluripotent stem cells into endothelial cells via temporal modulation of ETV2 with modified mRNA. *Sci. Adv.* **6**, 1–16 (2020).

463. A. H. M. Ng, P. Khoshakhlagh, J. E. Rojo Arias, G. Pasquini, K. Wang, A. Swiersy, S. L. Shipman, E. Appleton, K. Kiaee, R. E. Kohman, A. Vernet, M. Dysart, K. Leeper, W. Saylor, J. Y. Huang, A. Graveline, J. Taipale, D. E. Hill, M. Vidal, J. M. Melero-Martin, V. Busskamp, G. M. Church, A comprehensive library of human transcription factors for cell fate engineering. *Nat. Biotechnol.* **39**, 510–519 (2021).

464. C. Praça, S. C. Rosa, E. Sevin, R. Cecchelli, M.-P. P. Dehouck, L. S. Ferreira, Derivation of Brain Capillary-like Endothelial Cells from Human Pluripotent Stem Cell-Derived Endothelial Progenitor Cells. *Stem Cell Reports*. **13**, 599–611 (2019).

465. F. Roudnicky, B. K. Kim, Y. Lan, R. Schmucki, V. Küppers, K. Christensen, M. Graf, C. Patsch, M. Burcin, C. A. Meyer, P. D. Westenskow, C. A. Cowan, Identification of a combination of transcription factors that synergistically increases endothelial cell barrier

resistance. *Sci. Rep.* **10**, 1–9 (2020).

466. F. Roudnicky, J. D. Zhang, B. K. Kim, N. J. Pandya, Y. Lan, L. Sach-Peltason, H. Ragelle, P. Strassburger, S. Gruener, M. Lazendic, S. Uhles, F. Revelant, O. Eidam, G. Sturm, V. Kueppers, K. Christensen, L. D. Goldstein, M. Tzouros, B. Banfai, Z. Modrusan, M. Graf, C. Patsch, M. Burcin, C. A. Meyer, P. D. Westenskow, C. A. Cowan, Inducers of the endothelial cell barrier identified through chemogenomic screening in genome-edited hPSC-endothelial cells. *Proc. Natl. Acad. Sci. U. S. A.* **117**, 19854–19865 (2020).

467. L. Marchetti, B. Engelhardt, Immune cell trafficking across the blood-brain barrier in the absence and presence of neuroinflammation. *Vasc. Biol.* **2**, H1–H18 (2020).

468. H. Nishihara, B. D. Gastfriend, S. Soldati, S. Perriot, A. Mathias, Y. Sano, F. Shimizu, F. Gosselet, T. Kanda, S. P. Palecek, R. Du Pasquier, E. V. Shusta, B. Engelhardt, Advancing human induced pluripotent stem cell-derived blood-brain barrier models for studying immune cell interactions. *FASEB J.* **34**, 16693–16715 (2020).

469. H. Nishihara, S. Perriot, B. D. Gastfriend, M. Steinfort, C. Cibien, S. Soldati, K. Matsuo, S. Guimbal, A. Mathias, S. P. Palecek, E. V Shusta, R. Du Pasquier, B. Engelhardt, Intrinsic blood-brain barrier dysfunction contributes to multiple sclerosis pathogenesis. *Brain* (2022), doi:10.1093/brain/awac019.

470. S. Logan, T. Arzua, S. G. Canfield, E. R. Seminary, S. L. Sison, A. D. Ebert, X. Bai, Studying Human Neurological Disorders Using Induced Pluripotent Stem Cells: From 2D Monolayer to 3D Organoid and Blood Brain Barrier Models. *Compr. Physiol.* **9**, 565–611 (2019).

471. H. Okano, S. Morimoto, iPSC-based disease modeling and drug discovery in cardinal neurodegenerative disorders. *Cell Stem Cell*. **29**, 189–208 (2022).

472. R. A. Barker, M. Parmar, L. Studer, J. Takahashi, Human Trials of Stem Cell-Derived Dopamine Neurons for Parkinson's Disease: Dawn of a New Era. *Cell Stem Cell*. **21**, 569–573 (2017).

473. M. Wanjare, S. Kusuma, S. Gerecht, Stem Cell Reports. *Stem Cell Reports*. **2**, 561–575 (2014).

474. J. W. Blanchard, M. Bula, J. Davila-Velderrain, L. A. Akay, L. Zhu, A. Frank, M. B. Victor, J. M. Bonner, H. Mathys, Y. T. Lin, T. Ko, D. A. Bennett, H. P. Cam, M. Kellis, L. H. Tsai, Reconstruction of the human blood–brain barrier in vitro reveals a pathogenic mechanism of APOE4 in pericytes. *Nat. Med.* **26**, 952–963 (2020).

475. C. Cheung, A. S. Bernardo, M. W. B. Trotter, R. A. Pedersen, S. Sinha, Generation of human vascular smooth muscle subtypes provides insight into embryological origin–dependent disease susceptibility. *Nat. Biotechnol.* **30**, 165–173 (2012).

476. C. Cheung, Y. T. Y. Y. T. Y. Y. T. Goh, J. Zhang, C. Wu, E. Guccione, Modeling cerebrovascular pathophysiology in amyloid-β metabolism using neural-crest-derived

smooth muscle cells. *Cell Rep.* **9**, 391–401 (2014).

477. C. Cheung, A. S. Bernardo, R. A. Pedersen, S. Sinha, Directed differentiation of embryonic origin-specific vascular smooth muscle subtypes from human pluripotent stem cells. *Nat. Protoc.* **9**, 929–38 (2014).

478. G. Chen, D. R. Gulbranson, Z. Hou, J. M. Bolin, M. D. Probasco, K. Smuga-Otto, S. E. Howden, R. Nicole, N. E. Propson, R. Wagner, G. O. Lee, J. M. C. Teng, J. A. Thomson, V. Ruotti, M. D. Probasco, K. Smuga-Otto, S. E. Howden, N. R. Diol, N. E. Propson, R. Wagner, G. O. Lee, J. Antosiewicz-Bourget, J. M. C. Teng, J. A. Thomson, Chemically defined conditions for human iPS cell derivation and culture. *Nat. Methods*. **8**, 424–429 (2011).

479. B. D. Gastfriend, M. J. Stebbins, F. Du, E. V. Shusta, S. P. Palecek, Differentiation of Brain Pericyte-Like Cells from Human Pluripotent Stem Cell−Derived Neural Crest. *Curr. Protoc.* **1**, 1–32 (2021).

480. T. Faal, D. T. T. T. Phan, H. Davtyan, V. M. Scarfone, E. Varady, C. C. W. W. Hughes, M. A. Inlay, M. Blurton-Jones, C. C. W. W. Hughes, M. A. Inlay, Induction of Mesoderm and Neural Crest-Derived Pericytes from Human Pluripotent Stem Cells to Study Blood-Brain Barrier Interactions. *Stem Cell Reports*. **12**, 451–460 (2019).

481. I. Pediaditakis, K. R. Kodella, D. V. Manatakis, C. Y. Le, C. D. Hinojosa, W. Tien-Street, E. S. Manolakos, K. Vekrellis, G. A. Hamilton, L. Ewart, L. L. Rubin, K. Karalis, Modeling alpha-synuclein pathology in a human brain-chip to assess blood-brain barrier disruption. *Nat. Commun.* **12**, 1–17 (2021).

482. G. Nzou, R. T. Wicks, E. E. Wicks, S. A. Seale, C. H. Sane, A. Chen, S. V Murphy, J. D. Jackson, A. J. Atala, Human Cortex Spheroid with a Functional Blood Brain Barrier for High-Throughput Neurotoxicity Screening and Disease Modeling. *Sci. Rep.* **8**, 7413 (2018).

483. S. Seo, C. H. Choi, K. S. Yi, S. U. Kim, K. Lee, N. Choi, H. J. Lee, S. H. Cha, H. N. Kim, An engineered neurovascular unit for modeling neuroinflammation. *Biofabrication*. **13** (2021), doi:10.1088/1758-5090/abf741.

484. M. Eiraku, K. Watanabe, M. Matsuo-takasaki, M. Kawada, S. Yonemura, M. Matsumura, T. Wataya, A. Nishiyama, K. Muguruma, Y. Sasai, Article Self-Organized Formation of Polarized Cortical Tissues from ESCs and Its Active Manipulation by Extrinsic Signals. *Stem Cell*. **3**, 519–532 (2008).

485. T. Sato, R. G. Vries, H. J. Snippert, M. Van De Wetering, N. Barker, D. E. Stange, J. H. Van Es, A. Abo, P. Kujala, P. J. Peters, H. Clevers, Single Lgr5 stem cells build crypt-villus structures in vitro without a mesenchymal niche. *Nature*. **459**, 262–265 (2009).

486. T. Sato, H. Clevers, Growing self-organizing mini-guts from a single intestinal stem cell: Mechanism and applications. *Science (80-.).* **340**, 1190–1194 (2013).

487. M. A. Lancaster, J. A. Knoblich, Organogenesis in a dish: modeling development and

disease using organoid technologies. *Science*. **345**, 1247125 (2014).

488. M. A. Lancaster, M. Renner, C. Martin, D. Wenzel, L. S. Bicknell, M. E. Hurles, T. Homfray, J. M. Penninger, A. P. Jackson, J. A. Knoblich, Cerebral organoids model human brain development and microcephaly. *Nature*. **501**, 373–379 (2013).

489. M. A. Lancaster, J. A. Knoblich, Generation of cerebral organoids from human pluripotent stem cells. *Nat. Protoc.* **9**, 2329–2340 (2014).

490. J. G. Camp, F. Badsha, M. Florio, S. Kanton, T. Gerber, M. Wilsch-Bräuninger, E. Lewitus, A. Sykes, W. Hevers, M. Lancaster, J. A. Knoblich, R. Lachmann, S. Pääbo, W. B. Huttner, B. Treutlein, Human cerebral organoids recapitulate gene expression programs of fetal neocortex development. *Proc. Natl. Acad. Sci. U. S. A.* **112**, 15672–15677 (2015).

491. X. Qian, H. N. Nguyen, M. M. Song, C. Hadiono, S. C. Ogden, C. Hammack, B. Yao, G. R. Hamersky, F. Jacob, C. Zhong, K. J. Yoon, W. Jeang, L. Lin, Y. Li, J. Thakor, D. A. Berg, C. Zhang, E. Kang, M. Chickering, D. Nauen, C. Y. Ho, Z. Wen, K. M. Christian, P. Y. Shi, B. J. Maher, H. Wu, P. Jin, H. Tang, H. Song, G. L. Ming, Brain-Region-Specific Organoids Using Mini-bioreactors for Modeling ZIKV Exposure. *Cell*. **165**, 1238–1254 (2016).

492. F. Birey, J. Andersen, C. D. Makinson, S. Islam, W. Wei, N. Huber, H. C. Fan, K. R. C. Metzler, G. Panagiotakos, N. Thom, N. A. O'Rourke, L. M. Steinmetz, J. A. Bernstein, J. Hallmayer, J. R. Huguenard, S. P. Pasca, Assembly of functionally integrated human forebrain spheroids. *Nature*. **545**, 54–59 (2017).

493. L. Pellegrini, C. Bonfio, J. Chadwick, F. Begum, M. Skehel, M. A. Lancaster, Human CNS barrier-forming organoids with cerebrospinal fluid production. *Science (80-.).* **369**, 0–13 (2020).

494. P. R. Ormel, R. Vieira de Sá, E. J. van Bodegraven, H. Karst, O. Harschnitz, M. A. M. Sneeboer, L. E. Johansen, R. E. van Dijk, N. Scheefhals, A. Berdenis van Berlekom, E. Ribes Martínez, S. Kling, H. D. MacGillavry, L. H. van den Berg, R. S. Kahn, E. M. Hol, L. D. de Witte, R. J. Pasterkamp, Microglia innately develop within cerebral organoids. *Nat. Commun.* **9** (2018), doi:10.1038/s41467-018-06684-2.

495. M. T. Pham, K. M. Pollock, M. D. Rose, W. A. Cary, H. R. Stewart, P. Zhou, J. A. Nolta, B. Waldau, Generation of human vascularized brain organoids. *Neuroreport*. **29**, 588–593 (2018).

496. P. Wörsdörfer, N. Dalda, A. Kern, S. Krüger, N. Wagner, C. K. Kwok, E. Henke, S. Ergün, Generation of complex human organoid models including vascular networks by incorporation of mesodermal progenitor cells. *Sci. Rep.* **9**, 1–13 (2019).

497. Y. Shi, L. Sun, M. Wang, J. Liu, S. Zhong, R. Li, P. Li, L. Guo, A. Fang, R. Chen, W. P. Ge, Q. Wu, X. Wang, Vascularized human cortical organoids (vOrganoids) model cortical development in vivo. *PLoS Biol.* **18**, 1–29 (2020).

498. B. Cakir, Y. Xiang, Y. Tanaka, M. H. Kural, M. Parent, Y.-J. Kang, K. Chapeton, B.

Patterson, Y. Yuan, C.-S. He, M. S. B. Raredon, J. Dengelegi, K.-Y. Kim, P. Sun, M. Zhong, S. Lee, P. Patra, F. Hyder, L. E. Niklason, S.-H. Lee, Y.-S. Yoon, I.-H. Park, Engineering of human brain organoids with a functional vascular-like system. *Nat. Methods* (2019), doi:10.1038/s41592-019-0586-5.

499. A. A. Mansour, J. T. Gonçalves, C. W. Bloyd, H. Li, S. Fernandes, S. Johnston, S. L. Parylak, X. Jin, F. H. Gage, D. Quang, S. Johnston, S. L. Parylak, X. Jin, F. H. Gage, An in vivo model of functional and vascularized human brain organoids. *Nat. Biotechnol.* **36**, 432–441 (2018).

500. N. Daviaud, R. H. Friedel, H. Zou, Vascularization and engraftment of transplanted human cerebral organoids in mouse cortex. *eNeuro*. **5**, 1–18 (2018).

501. S. Darmanis, S. A. Sloan, Y. Zhang, M. Enge, C. Caneda, L. M. Shuer, M. G. Hayden Gephart, B. A. Barres, S. R. Quake, A survey of human brain transcriptome diversity at the single cell level. *Proc. Natl. Acad. Sci. U. S. A.* **112**, 7285–90 (2015).

502. R. D. Hodge, T. E. Bakken, J. A. Miller, K. A. Smith, E. R. Barkan, L. T. Graybuck, J. L. Close, B. Long, N. Johansen, O. Penn, Z. Yao, J. Eggermont, T. Höllt, B. P. Levi, S. I. Shehata, B. Aevermann, A. Beller, D. Bertagnolli, K. Brouner, T. Casper, C. Cobbs, R. Dalley, N. Dee, S. L. Ding, R. G. Ellenbogen, O. Fong, E. Garren, J. Goldy, R. P. Gwinn, D. Hirschstein, C. D. Keene, M. Keshk, A. L. Ko, K. Lathia, A. Mahfouz, Z. Maltzer, M. McGraw, T. N. Nguyen, J. Nyhus, J. G. Ojemann, A. Oldre, S. Parry, S. Reynolds, C. Rimorin, N. V. Shapovalova, S. Somasundaram, A. Szafer, E. R. Thomsen, M. Tieu, G. Quon, R. H. Scheuermann, R. Yuste, S. M. Sunkin, B. Lelieveldt, D. Feng, L. Ng, A. Bernard, M. Hawrylycz, J. W. Phillips, B. Tasic, H. Zeng, A. R. Jones, C. Koch, E. S. Lein, Conserved cell types with divergent features in human versus mouse cortex. *Nature*. **573**, 61–68 (2019).

503. X. Han, Z. Zhou, L. Fei, H. Sun, R. Wang, Y. Chen, H. Chen, J. Wang, H. Tang, W. Ge, Y. Zhou, F. Ye, M. Jiang, J. Wu, Y. Xiao, X. Jia, T. Zhang, X. Ma, Q. Zhang, X. Bai, S. Lai, C. Yu, L. Zhu, R. Lin, Y. Gao, M. Wang, Y. Wu, J. Zhang, R. Zhan, S. Zhu, H. Hu, C. Wang, M. Chen, H. Huang, T. Liang, J. Chen, W. Wang, D. Zhang, G. Guo, Construction of a human cell landscape at single-cell level. *Nature*. **581**, 303–309 (2020).

504. S. Zhong, W. Ding, L. Sun, Y. Lu, H. Dong, X. Fan, Z. Liu, R. Chen, S. Zhang, Q. Ma, F. Tang, Q. Wu, X. Wang, Decoding the development of the human hippocampus. *Nature*. **577**, 531–536 (2020).

505. F. J. Garcia, N. Sun, H. Lee, B. Godlewski, H. Mathys, K. Galani, B. Zhou, X. Jiang, A. P. Ng, J. Mantero, L.-H. Tsai, D. A. Bennett, M. Sahin, M. Kellis, M. Heiman, Single-cell dissection of the human brain vasculature. *Nature*. **603**, 893–899 (2022).

506. E. A. Winkler, C. N. Kim, J. M. Ross, J. H. Garcia, E. Gil, I. Oh, L. Q. Chen, D. Wu, J. S. Catapano, K. Raygor, K. Narsinh, H. Kim, S. Weinsheimer, D. L. Cooke, B. P. Walcott, M. T. Lawton, N. Gupta, B. V. Zlokovic, E. F. Chang, A. A. Abla, D. A. Lim, T. J. Nowakowski, A single-cell atlas of the normal and malformed human brain vasculature. *Science (80-.).* **7377**, 1–23 (2022).

507. M. Uhlén, L. Fagerberg, B. M. Hallström, C. Lindskog, P. Oksvold, A. Mardinoglu, Å. Sivertsson, C. Kampf, E. Sjöstedt, A. Asplund, I. M. Olsson, K. Edlund, E. Lundberg, S. Navani, C. A.-K. K. Szigyarto, J. Odeberg, D. Djureinovic, J. O. Takanen, S. Hober, T. Alm, P.-H. H. Edqvist, H. Berling, H. Tegel, J. Mulder, J. Rockberg, P. Nilsson, J. M. Schwenk, M. Hamsten, K. von Feilitzen, M. Forsberg, L. Persson, F. Johansson, M. Zwahlen, G. von Heijne, J. Nielsen, F. Pontén, Proteomics. Tissue-based map of the human proteome. *Science (80-.).* **347**, 1260419 (2015).

508. Roadmap Epigenomics Consortium, A. Kundaje, W. Meuleman, J. Ernst, M. Bilenky, A. Yen, A. Heravi-Moussavi, P. Kheradpour, Z. Zhang, J. Wang, M. J. Ziller, V. Amin, J. W. Whitaker, M. D. Schultz, L. D. Ward, A. Sarkar, G. Quon, R. S. Sandstrom, M. L. Eaton, Y. C. Wu, A. R. Pfenning, X. Wang, M. Claussnitzer, Y. Liu, C. Coarfa, R. A. Harris, N. Shoresh, C. B. Epstein, E. Gjoneska, D. Leung, W. Xie, R. D. Hawkins, R. Lister, C. Hong, P. Gascard, A. J. Mungall, R. Moore, E. Chuah, A. Tam, T. K. Canfield, R. S. Hansen, R. Kaul, P. J. Sabo, M. S. Bansal, A. Carles, J. R. Dixon, K. H. Farh, S. Feizi, R. Karlic, A. R. Kim, A. Kulkarni, D. Li, R. Lowdon, G. Elliott, T. R. Mercer, S. J. Neph, V. Onuchic, P. Polak, N. Rajagopal, P. Ray, R. C. Sallari, K. T. Siebenthall, N. A. Sinnott-Armstrong, M. Stevens, R. E. Thurman, J. Wu, B. Zhang, X. Zhou, A. E. Beaudet, L. A. Boyer, P. L. De Jager, P. J. Farnham, S. J. Fisher, D. Haussler, S. J. M. Jones, W. Li, M. A. Marra, M. T. McManus, S. Sunyaev, J. A. Thomson, T. D. Tlsty, L. H. Tsai, W. Wang, R. A. Waterland, M. Q. Zhang, L. H. Chadwick, B. E. Bernstein, J. F. Costello, J. R. Ecker, M. Hirst, A. Meissner, A. Milosavljevic, B. Ren, J. A. Stamatoyannopoulos, T. Wang, M. Kellis, Integrative analysis of 111 reference human epigenomes. *Nature*. **518**, 317–329 (2015).

509. S. C. Van Den Brink, F. Sage, Á. Vértesy, B. Spanjaard, J. Peterson-Maduro, C. S. Baron, C. Robin, A. van Oudenaarden, Single-cell sequencing reveals dissociation-induced gene expression in tissue subpopulations. *Nat. Methods*. **14**, 935–936 (2017).

510. C. Jia, M. P. Keasey, H. M. Malone, C. Lovins, R. R. Sante, V. Razskazovskiy, T. Hagg, Vitronectin from brain pericytes promotes adult forebrain neurogenesis by stimulating CNTF. *Exp. Neurol.* **312**, 20–32 (2019).

511. S. Ayloo, C. G. Lazo, S. Sun, W. Zhang, B. Cui, C. Gu, Pericyte-to-endothelial cell signaling via vitronectin-integrin regulates blood-CNS barrier. *Neuron*, 1–15 (2022).

512. B. J. Umlauf, P. A. Clark, J. M. Lajoie, J. V Georgieva, S. Bremner, B. R. Herrin, J. S. Kuo, E. V Shusta, Identification of variable lymphocyte receptors that can target therapeutics to pathologically exposed brain extracellular matrix. *Sci. Adv.* **5**, eaau4245 (2019).

513. B. T. Hawkins, T. P. Davis, The Blood-Brain Barrier / Neurovascular Unit in Health and Disease. *Pharmacol. Rev.* **57**, 173–185 (2005).

514. H. K. Wilson, E. V Shusta, in *Blood–Brain Barrier in Drug Discovery: Optimizing Brain Exposure of CNS Drugs and Minimizing Brain Side Effects for Peripheral Drugs*, L. Di, E. H. Kerns, Eds. (John Wiley & Sons, Hoboken, NJ, First Ed., 2015), pp. 238–73.

515. D. B. Stanimirovic, A. Friedman, Pathophysiology of the Neurovascular Unit: Disease

Cause or Consequence? *J. Cereb. Blood Flow Metab.* **32**, 1207–1221 (2012).

516. U. Tontsch, H. C. Bauer, Glial cells and neurons induce blood-brain barrier related enzymes in cultured cerebral endothelial cells. *Brain Res.* **539**, 247–253 (1991).

517. G. Savettieri, I. Di Liegro, C. Catania, L. Licata, G. L. Pitarresi, S. D'Agostino, G. Schiera, V. De Caro, G. Giandalia, L. I. Giannola, A. Cestelli, Neurons and ECM regulate occludin localization in brain endothelial cells. *Neuroreport*. **11**, 1081–4 (2000).

518. C. Weidenfeller, C. N. Svendsen, E. V Shusta, Differentiating embryonic neural progenitor cells induce blood-brain barrier properties. *J. Neurochem.* **101**, 555–565 (2007).

519. J. A. Brown, V. Pensabene, D. A. Markov, V. Allwardt, M. Diana Neely, M. Shi, C. M. Britt, O. S. Hoilett, Q. Yang, B. M. Brewer, P. C. Samson, L. J. McCawley, J. M. May, D. J. Webb, D. Li, A. B. Bowman, R. S. Reiserer, J. P. Wikswo, Recreating blood-brain barrier physiology and structure on chip: A novel neurovascular microfluidic bioreactor. *Biomicrofluidics*. **9**, 1–15 (2015).

520. J. A. Brown, S. G. Codreanu, M. Shi, S. D. Sherrod, D. A. Markov, M. D. Neely, C. M. Britt, O. S. Hoilett, R. S. Reiserer, P. C. Samson, L. J. McCawley, D. J. Webb, A. B. Bowman, J. A. McLean, J. P. Wikswo, Metabolic consequences of inflammatory disruption of the blood-brain barrier in an organ-on-chip model of the human neurovascular unit. *J. Neuroinflammation*. **13**, 306 (2016).

521. C.-F. Cho, J. M. Wolfe, C. M. Fadzen, D. Calligaris, K. Hornburg, E. A. Chiocca, N. Y. R. Agar, B. L. Pentelute, S. E. Lawler, Blood-brain-barrier spheroids as an in vitro screening platform for brain-penetrating agents. *Nat. Commun.* **8**, 15623 (2017).

522. L. Cucullo, M. Hossain, V. Puvenna, N. Marchi, D. Janigro, The role of shear stress in Blood-Brain Barrier endothelial physiology. *BMC Neurosci.* **12**, 40 (2011).

523. A. Herland, A. D. Van Der Meer, E. A. FitzGerald, T. E. Park, J. J. F. Sleeboom, D. E. Ingber, Distinct contributions of astrocytes and pericytes to neuroinflammation identified in a 3D human blood-brain barrier on a chip. *PLoS One*. **11**, 1–21 (2016).

524. E. Urich, C. Patsch, S. Aigner, M. Graf, R. Iacone, P.-O. Freskgård, Multicellular Self-Assembled Spheroidal Model of the Blood Brain Barrier. *Sci. Rep.* **3**, 1500 (2013).

525. G. Adriani, D. Ma, A. Pavesi, R. D. Kamm, E. L. K. Goh, A 3D neurovascular microfluidic model consisting of neurons, astrocytes and cerebral endothelial cells as a blood–brain barrier. *Lab Chip*. **17**, 448–459 (2017).

526. C.-H. Chou, J. D. Sinden, P.-O. Couraud, M. Modo, In Vitro Modeling of the Neurovascular Environment by Coculturing Adult Human Brain Endothelial Cells with Human Neural Stem Cells. *PLoS One*. **9**, e106346 (2014).

527. S. F. Spampinato, B. Obermeier, A. Cotleur, A. Love, Y. Takeshita, Y. Sano, T. Kanda, R. M. Ransohoff, Sphingosine 1 phosphate at the blood brain barrier: Can the modulation of

S1P receptor 1 influence the response of endothelial cells and astrocytes to inflammatory stimuli? *PLoS One*. **10**, 1–18 (2015).

528. F. R. Walter, S. Valkai, A. Kincses, A. Petneházi, T. Czeller, S. Veszelka, P. Ormos, M. A. Deli, A. Dér, A versatile lab-on-a-chip tool for modeling biological barriers. *Sensors Actuators, B Chem.* **222**, 1209–1219 (2016).

529. A. Appelt-Menzel, A. Cubukova, K. Günther, F. Edenhofer, J. Piontek, G. Krause, T. Stüber, H. Walles, W. Neuhaus, M. Metzger, Establishment of a Human Blood-Brain Barrier Co-culture Model Mimicking the Neurovascular Unit Using Induced Pluri- and Multipotent Stem Cells. *Stem Cell Reports*. **8**, 894–906 (2017).

530. H. Qosa, J. Lichter, M. Sarlo, S. S. Markandaiah, K. McAvoy, J. P. Richard, M. R. Jablonski, N. J. Maragakis, P. Pasinelli, D. Trotti, Astrocytes drive upregulation of the multidrug resistance transporter ABCB1 (P-Glycoprotein) in endothelial cells of the blood–brain barrier in mutant superoxide dismutase 1-linked amyotrophic lateral sclerosis. *Glia*. **64**, 1298–1313 (2016).

531. Y. I. Wang, H. E. Abaci, M. L. Shuler, Microfluidic blood–brain barrier model provides in vivo-like barrier properties for drug permeability screening. *Biotechnol. Bioeng.* **114**, 184–194 (2017).

532. K. Yamamizu, M. Iwasaki, H. Takakubo, T. Sakamoto, T. Ikuno, M. Miyoshi, T. Kondo, Y. Nakao, M. Nakagawa, H. Inoue, J. K. Yamashita, In Vitro Modeling of Blood-Brain Barrier with Human iPSC-Derived Endothelial Cells, Pericytes, Neurons, and Astrocytes via Notch Signaling. *Stem Cell Reports*. **8**, 634–647 (2017).

533. K. Zobel, U. Hansen, H. J. Galla, Blood-brain barrier properties in vitro depend on composition and assembly of endogenous extracellular matrices. *Cell Tissue Res.* **365**, 233–245 (2016).

534. E. S. Lippmann, C. Weidenfeller, C. N. Svendsen, E. V. Shusta, Blood-brain barrier modeling with co-cultured neural progenitor cell-derived astrocytes and neurons. *J. Neurochem.* **119**, 507–520 (2011).

535. B. T. Hawkins, S. Grego, K. L. Sellgren, Three-dimensional culture conditions differentially affect astrocyte modulation of brain endothelial barrier function in response to transforming growth factor β1. *Brain Res.* **1608**, 167–176 (2015).

536. J. D. Wang, E. S. Khafagy, K. Khanafer, S. Takayama, M. E. H. Elsayed, Organization of Endothelial Cells, Pericytes, and Astrocytes into a 3D Microfluidic in Vitro Model of the Blood-Brain Barrier. *Mol. Pharm.* **13**, 895–906 (2016).

537. A. C. C. da Fonseca, D. Matias, C. Garcia, R. Amaral, L. H. Geraldo, C. Freitas, F. R. S. Lima, The impact of microglial activation on blood-brain barrier in brain diseases. *Front. Cell. Neurosci.* **8**, 1–13 (2014).

538. B. Obermeier, R. Daneman, R. M. Ransohoff, Development, maintenance and disruption of the blood-brain barrier. *Nat. Med.* **19**, 1584–96 (2013).

539. R. Daneman, B. Engelhardt, Brain barriers in health and disease. *Neurobiol. Dis.* **107**, 1–3 (2017).

540. B. Engelhardt, S. Liebner, Novel insights into the development and maintenance of the blood-brain barrier. *Cell Tissue Res.* (2014), doi:10.1007/s00441-014-1811-2.

541. K. A. Tran, X. Zhang, D. Predescu, X. Huang, R. F. MacHado, J. R. Göthert, A. B. Malik, T. Valyi-Nagy, Y.-Y. Y. Zhao, Endothelial β-Catenin Signaling Is Required for Maintaining Adult Blood-Brain Barrier Integrity and Central Nervous System Homeostasis. *Circulation*. **133**, 177–86 (2016).

542. L. He, M. Vanlandewijck, M. A. Mäe, J. Andrae, K. Ando, F. Del Gaudio, K. Nahar, T. Lebouvier, B. Laviña, L. Gouveia, Y. Sun, E. Raschperger, Å. Segerstolpe, J. Liu, S. Gustafsson, M. Räsänen, Y. Zarb, N. Mochizuki, A. Keller, U. Lendahl, C. Betsholtz, Single-cell RNA sequencing of mouse brain and lung vascular and vessel-associated cell types. *Sci. data*. **5**, 180160 (2018).

543. T. N. Phoenix, D. M. Patmore, S. Boop, N. Boulos, M. O. Jacus, Y. T. Patel, M. F. Roussel, D. Finkelstein, L. Goumnerova, S. Perreault, E. Wadhwa, Y. J. Cho, C. F. Stewart, R. J. Gilbertson, Medulloblastoma Genotype Dictates Blood Brain Barrier Phenotype. *Cancer Cell*. **29**, 508–522 (2016).

544. Y. Uchida, S. Ohtsuki, Y. Katsukura, C. Ikeda, T. Suzuki, J. Kamiie, T. Terasaki, Quantitative targeted absolute proteomics of human blood-brain barrier transporters and receptors. *J. Neurochem.* **117**, 333–345 (2011).

545. R. Paolinelli, M. Corada, L. Ferrarini, K. Devraj, C. Artus, C. J. Czupalla, N. Rudini, L. Maddaluno, E. Papa, B. Engelhardt, P. O. Couraud, S. Liebner, E. Dejana, Wnt Activation of Immortalized Brain Endothelial Cells as a Tool for Generating a Standardized Model of the Blood Brain Barrier In Vitro. *PLoS One*. **8** (2013), doi:10.1371/journal.pone.0070233.

546. M. D. Laksitorini, V. Yathindranath, W. Xiong, S. Hombach-Klonisch, D. W. Miller, Modulation of Wnt/β-catenin signaling promotes blood-brain barrier phenotype in cultured brain endothelial cells. *Sci. Rep.* **9**, 1–13 (2019).

547. F. R. Kreitzer, N. Salomonis, A. Sheehan, M. Huang, J. S. Park, M. J. Spindler, P. Lizarraga, W. A. Weiss, P. So, B. R. Conklin, A robust method to derive functional neural crest cells from human pluripotent stem cells. *Am. J. Stem Cells*. **2**, 119–31 (2013).

548. X. Lian, J. Zhang, K. Zhu, T. J. Kamp, S. P. Palecek, Insulin inhibits cardiac mesoderm, not mesendoderm, formation during cardiac differentiation of human pluripotent stem cells and modulation of canonical wnt signaling can rescue this inhibition. *Stem Cells*. **31**, 447–457 (2013).

549. X. Bao, V. J. Bhute, T. Han, T. Qian, X. Lian, S. P. Palecek, Human pluripotent stem cell-derived epicardial progenitors can differentiate to endocardial-like endothelial cells. *Bioeng. Transl. Med.* **2**, 191–201 (2017).

550. B. Li, C. N. Dewey, RSEM: accurate transcript quantification from RNA-Seq data with or

without a reference genome. *BMC Bioinformatics*. **12**, 323 (2011).

551. B. Langmead, S. L. Salzberg, Fast gapped-read alignment with Bowtie 2. *Nat. Methods*. **9**, 357–359 (2012).

552. M. I. Love, W. Huber, S. Anders, Moderated estimation of fold change and dispersion for RNA-seq data with DESeq2. *Genome Biol.* **15**, 550 (2014).

553. S. Durinck, P. T. Spellman, E. Birney, W. Huber, Mapping identifiers for the integration of genomic datasets with the R/ Bioconductor package biomaRt. *Nat. Protoc.* **4**, 1184–1191 (2009).

554. P. Langfelder, S. Horvath, WGCNA: an R package for weighted correlation network analysis. *BMC Bioinformatics*. **9**, 559 (2008).

555. P. Shannon, A. Markiel, O. Ozier, N. S. Baliga, J. T. Wang, D. Ramage, N. Amin, B. Schwikowski, T. Ideker, Cytoscape: A Software Environment for Integrated Models of Biomolecular Interaction Networks. *Genome Res.* **13**, 2498–2504 (2003).

556. J. Schindelin, I. Arganda-Carreras, E. Frise, V. Kaynig, M. Longair, T. Pietzsch, S. Preibisch, C. Rueden, S. Saalfeld, B. Schmid, J. Tinevez, D. J. White, V. Hartenstein, K. Eliceiri, P. Tomancak, A. Cardona, Fiji: an open-source platform for biological-image analysis. *Nat. Methods*. **9**, 676–682 (2012).

557. S. A. Lambert, A. Jolma, L. F. Campitelli, P. K. Das, Y. Yin, M. Albu, X. Chen, J. Taipale, T. R. Hughes, M. T. Weirauch, Review The Human Transcription Factors. *Cell*. **172**, 650–665 (2018).

558. UniProt Consortium, UniProt: the universal protein knowledgebase in 2021. *Nucleic Acids Res.* **49**, D480–D489 (2021).

559. B. Zhang, S. Horvath, A General Framework for Weighted Gene Co-Expression Network Analysis. *Stat. Appl. Genet. Mol. Biol.* **4**, Article17 (2005).

560. A. D. Yates, P. Achuthan, W. Akanni, J. J. J. Allen, J. J. J. Allen, J. Alvarez-Jarreta, M. R. Amode, I. M. Armean, A. G. Azov, R. Bennett, J. Bhai, K. Billis, S. Boddu, J. C. Marugán, C. Cummins, C. Davidson, K. Dodiya, R. Fatima, A. Gall, C. G. Giron, L. Gil, T. Grego, L. Haggerty, E. Haskell, T. Hourlier, O. G. Izuogu, S. H. Janacek, T. Juettemann, M. Kay, I. Lavidas, T. Le, D. Lemos, J. G. Martinez, T. Maurel, M. McDowall, A. McMahon, S. Mohanan, B. Moore, M. Nuhn, D. N. Oheh, A. Parker, A. Parton, M. Patricio, M. P. Sakthivel, A. I. Abdul Salam, B. M. Schmitt, H. Schuilenburg, D. Sheppard, M. Sycheva, M. Szuba, K. Taylor, A. Thormann, G. Threadgold, A. Vullo, B. Walts, A. Winterbottom, A. Zadissa, M. Chakiachvili, B. Flint, A. Frankish, S. E. Hunt, G. IIsley, M. Kostadima, N. Langridge, J. E. Loveland, F. J. Martin, J. Morales, J. M. Mudge, M. Muffato, E. Perry, M. Ruffier, S. J. Trevanion, F. Cunningham, K. L. Howe, D. R. Zerbino, P. Flicek, Ensembl 2020. *Nucleic Acids Res.* **48**, D682–D688 (2019).

561. A. Liberzon, C. Birger, H. Thorvaldsdóttir, M. Ghandi, J. P. Mesirov, P. Tamayo, The Molecular Signatures Database Hallmark Gene Set Collection. *Cell Syst.* **1**, 417–425

(2015).

562. K.-A. Kim, M. Kakitani, J. Zhao, T. Oshima, T. Tang, M. Binnerts, Y. Liu, B. Boyle, E. Park, P. Emtage, W. D. Funk, K. Tomizuka, Mitogenic influence of human R-spondin1 on the intestinal epithelium. *Science*. **309**, 1256–9 (2005).

563. K.-A. Kim, M. Wagle, K. Tran, X. Zhan, M. A. Dixon, S. Liu, D. Gros, W. Korver, S. Yonkovich, N. Tomasevic, M. Binnerts, A. Abo, R-Spondin Family Members Regulate the Wnt Pathway by a Common Mechanism. *Mol. Biol. Cell*. **19**, 2588–2596 (2008).

564. J. Mazzoni, J. R. Smith, S. Shahriar, T. Cutforth, B. Ceja, D. Agalliu, The Wnt Inhibitor Apcdd1 Coordinates Vascular Remodeling and Barrier Maturation of Retinal Blood Vessels. *Neuron*. **96**, 1055-1069.e6 (2017).

565. Y. Zhou, J. Williams, P. M. Smallwood, J. Nathans, Sox7, Sox17, and Sox18 cooperatively regulate vascular development in the mouse retina. *PLoS One*. **10**, 1–22 (2015).

566. N. Santander, C. O. Lizama, E. Meky, G. L. McKinsey, B. Jung, D. Sheppard, C. Betsholtz, T. D. Arnold, Lack of Flvcr2 impairs brain angiogenesis without affecting the blood-brain barrier. *J. Clin. Invest.* **140**, 4050–4068 (2020).

567. K. P. Mouillesseaux, D. S. Wiley, L. M. Saunders, L. A. Wylie, E. J. Kushner, D. C. Chong, K. M. Citrin, A. T. Barber, Y. Park, J. D. J. J. D. Kim, L. A. Samsa, J. D. J. J. D. Kim, J. Liu, S. W. Jin, V. L. Bautch, Notch regulates BMP responsiveness and lateral branching in vessel networks via SMAD6. *Nat. Commun.* **7**, 1–12 (2016).

568. S. Tietz, B. Engelhardt, Brain barriers: Crosstalk between complex tight junctions and adherens junctions. *J. Cell Biol.* **209**, 493–506 (2015).

569. M. Aurrand-Lions, L. Duncan, C. Ballestrem, B. A. Imhof, JAM-2, a Novel Immunoglobulin Superfamily Molecule, Expressed by Endothelial and Lymphatic Cells. *J. Biol. Chem.* **276**, 2733–2741 (2001).

570. N. Harada, Y. Tamai, T. O. Ishikawa, B. Sauer, K. Takaku, M. Oshima, M. M. Taketo, Intestinal polyposis in mice with a dominant stable mutation of the β-catenin gene. *EMBO J.* **18**, 5931–5942 (1999).

571. M. Eto, A. Kouroedov, F. Cosentino, T. F. Lüscher, Glycogen synthase kinase-3 mediates endothelial cell activation by tumor necrosis factor-α. *Circulation*. **112**, 1316–1322 (2005).

572. M. A. Hermida, J. Dinesh Kumar, N. R. Leslie, GSK3 and its interactions with the PI3K/AKT/mTOR signalling network. *Adv. Biol. Regul.* **65**, 5–15 (2017).

573. E. Beurel, S. F. Grieco, R. S. Jope, Glycogen synthase kinase-3 (GSK3): Regulation, actions, and diseases. *Pharmacol. Ther.* **148**, 114–131 (2015).

574. A. Ben-Zvi, B. Lacoste, E. Kur, B. J. Andreone, Y. Mayshar, H. Yan, C. Gu, Mfsd2a is critical for the formation and function of the blood–brain barrier. *Nature*. **509**, 507–11

(2014).

575. B. Bauer, A. M. S. Hartz, G. Fricker, D. S. Miller, Pregnane X receptor up-regulation of P-glycoprotein expression and transport function at the blood-brain barrier. *Mol. Pharmacol.* **66**, 413–419 (2004).

576. V. Berezowski, C. Landry, M. P. Dehouck, R. Cecchelli, L. Fenart, Contribution of glial cells and pericytes to the mRNA profiles of P-glycoprotein and multidrug resistance-associated proteins in an in vitro model of the blood-brain barrier. *Brain Res.* **1018**, 1–9 (2004).

577. X. Lian, C. Hsiao, G. Wilson, K. Zhu, L. B. Hazeltine, S. M. Azarin, K. K. Raval, J. Zhang, T. J. Kamp, S. P. Palecek, Robust cardiomyocyte differentiation from human pluripotent stem cells via temporal modulation of canonical Wnt signaling. *Proc. Natl. Acad. Sci.* **109**, E1848–E1857 (2012).

578. G. A. Gomez, M. S. Prasad, M. Wong, R. M. Charney, P. B. Shelar, N. Sandhu, J. O. S. S. Hackland, J. C. Hernandez, A. W. Leung, M. I. Garcıá-Castro, M. I. García-Castro, M. I. Garcıá-Castro, M. I. García-Castro, WNT/β-catenin modulates the axial identity of embryonic stem cell-derived human neural crest. *Dev.* **146**, dev175604 (2019).

579. H. Sakaguchi, T. Kadoshima, M. Soen, N. Narii, Y. Ishida, M. Ohgushi, J. Takahashi, M. Eiraku, Y. Sasai, Generation of functional hippocampal neurons from self-organizing human embryonic stem cell-derived dorsomedial telencephalic tissue. *Nat. Commun.* **6** (2015), doi:10.1038/ncomms9896.

580. Q. Guo, A. Kim, B. Li, A. Ransick, H. Bugacov, X. Chen, N. Lindström, A. Brown, L. Oxburgh, B. Ren, A. P. McMahon, A β-catenin-driven switch in TCF/LEF transcription factor binding to DNA target sites promotes commitment of mammalian nephron progenitor cells. *Elife*. **10**, 1–47 (2021).

581. C. Y. Janda, D. Waghray, A. M. Levin, C. Thomas, K. C. Garcia, Structural basis of Wnt recognition by frizzled. *Science (80-.).* **336**, 59–64 (2012).

582. M. Corada, F. Orsenigo, G. P. Bhat, L. L. Conze, F. Breviario, S. I. Cunha, L. Claesson-Welsh, G. V Beznoussenko, A. A. Mironov, M. Bacigaluppi, G. Martino, M. E. Pitulescu, R. H. Adams, P. Magnusson, E. Dejana, Fine-Tuning of Sox17 and Canonical Wnt Coordinates the Permeability Properties of the Blood-Brain Barrier. *Circ. Res.* **124**, 511–525 (2019).

583. K. Hübner, P. Cabochette, R. Diéguez-Hurtado, C. Wiesner, Y. Wakayama, K. S. Grassme, M. Hubert, S. Guenther, H. G. Belting, M. Affolter, R. H. Adams, B. Vanhollebeke, W. Herzog, Wnt/β-catenin signaling regulates VE-cadherin-mediated anastomosis of brain capillaries by counteracting S1pr1 signaling. *Nat. Commun.* **9** (2018), doi:10.1038/s41467-018-07302-x.

584. T. Qian, S. E. Maguire, S. G. Canfield, X. Bao, W. R. Olson, E. V Shusta, S. P. Palecek, Directed differentiation of human pluripotent stem cells to blood-brain barrier endothelial cells. *Sci. Adv.* **3**, e1701679 (2017).

585. A. S. Munk, W. Wang, N. B. Bèchet, A. M. Eltanahy, A. X. Cheng, B. Sigurdsson, A. Benraiss, M. A. Mäe, B. T. Kress, D. H. Kelley, C. Betsholtz, K. Møllgård, A. Meissner, M. Nedergaard, I. Lundgaard, PDGF-B Is Required for Development of the Glymphatic System. *Cell Rep.* **26**, 2955-2969.e3 (2019).

586. U. Lendahl, P. Nilsson, C. Betsholtz, Emerging links between cerebrovascular and neurodegenerative diseases—a special role for pericytes. *EMBO Rep.* **20**, 1–18 (2019).

587. R. Nortley, N. Korte, P. Izquierdo, C. Hirunpattarasilp, A. Mishra, Z. Jaunmuktane, V. Kyrargyri, T. Pfeiffer, L. Khennouf, C. Madry, H. Gong, A. Richard-Loendt, W. Huang, T. Saito, T. C. Saido, S. Brandner, H. Sethi, D. Attwell, Amyloid β oligomers constrict human capillaries in Alzheimer's disease via signaling to pericytes. *Science (80-.).* **365**, eaav9518 (2019).

588. A. P. Sagare, R. D. Bell, Z. Zhao, Q. Ma, E. A. Winkler, A. Ramanathan, B. V. Zlokovic, Pericyte loss influences Alzheimer-like neurodegeneration in mice. *Nat. Commun.* **4**, 1–14 (2013).

589. A. Montagne, A. M. Nikolakopoulou, Z. Zhao, A. P. Sagare, G. Si, D. Lazic, S. R. Barnes, M. Daianu, A. Ramanathan, A. Go, E. J. Lawson, Y. Wang, W. J. Mack, P. M. Thompson, J. A. Schneider, J. Varkey, R. Langen, E. Mullins, R. E. Jacobs, B. V. Zlokovic, Pericyte degeneration causes white matter dysfunction in the mouse central nervous system. *Nat. Med.* **24**, 326–337 (2018).

590. Y. Zhang, S. A. Sloan, L. E. Clarke, C. Caneda, C. A. Plaza, P. D. Blumenthal, H. Vogel, G. K. Steinberg, M. S. B. Edwards, G. Li, J. A. Duncan, S. H. Cheshier, L. M. Shuer, E. F. Chang, G. A. Grant, M. G. H. H. Gephart, B. A. Barres, Purification and Characterization of Progenitor and Mature Human Astrocytes Reveals Transcriptional and Functional Differences with Mouse. *Neuron*. **89**, 37–53 (2016).

591. F. Tang, C. Barbacioru, Y. Wang, E. Nordman, C. Lee, N. Xu, X. Wang, J. Bodeau, B. B. Tuch, A. Siddiqui, K. Lao, M. A. Surani, mRNA-Seq whole-transcriptome analysis of a single cell. *Nat. Methods*. **6**, 377–382 (2009).

592. S. Islam, U. Kja, A. Moliner, P. Zajac, J. J.-B. Fan, S. Linnarsson, U. Kjallquist, A. Moliner, P. Zajac, J. J.-B. Fan, P. Lonnerberg, S. Linnarsson, Characterization of the single-cell transcriptional landscape by highly multiplex RNA-seq. *Genome Res.* **21**, 1160–1167 (2011).

593. B. Tasic, Z. Yao, L. T. Graybuck, K. A. Smith, T. N. Nguyen, D. Bertagnolli, J. Goldy, E. Garren, M. N. Economo, S. Viswanathan, O. Penn, T. Bakken, V. Menon, J. Miller, O. Fong, K. E. Hirokawa, K. Lathia, C. Rimorin, M. Tieu, R. Larsen, T. Casper, E. Barkan, M. Kroll, S. Parry, N. V. Shapovalova, D. Hirschstein, J. Pendergraft, H. A. Sullivan, T. K. Kim, A. Szafer, N. Dee, P. Groblewski, I. Wickersham, A. Cetin, J. A. Harris, B. P. Levi, S. M. Sunkin, L. Madisen, T. L. Daigle, L. Looger, A. Bernard, J. Phillips, E. Lein, M. Hawrylycz, K. Svoboda, A. R. Jones, C. Koch, H. Zeng, Shared and distinct transcriptomic cell types across neocortical areas. *Nature*. **563**, 72–78 (2018).

594. A. Butler, P. Hoffman, P. Smibert, E. Papalexi, R. Satija, Integrating single-cell

transcriptomic data across different conditions, technologies, and species. *Nat. Biotechnol.* **36**, 411–420 (2018).

595. T. Stuart, A. Butler, P. Hoffman, C. Hafemeister, E. Papalexi, W. M. Mauck, Y. Hao, M. Stoeckius, P. Smibert, R. Satija, Comprehensive Integration of Single-Cell Data. *Cell*. **177**, 1888-1902.e21 (2019).

596. C. Hafemeister, R. Satija, Normalization and variance stabilization of single-cell RNA-seq data using regularized negative binomial regression. *Genome Biol.* **20**, 296 (2019).

597. M. Karow, J. G. Camp, S. Falk, T. Gerber, A. Pataskar, M. Gac-Santel, J. Kageyama, A. Brazovskaja, A. Garding, W. Fan, T. Riedemann, A. Casamassa, A. Smiyakin, C. Schichor, M. Götz, V. K. Tiwari, B. Treutlein, B. Berninger, J. Gray Camp, S. Falk, T. Gerber, A. Pataskar, M. Gac-Santel, J. Kageyama, A. Brazovskaja, A. Garding, W. Fan, T. Riedemann, A. Casamassa, A. Smiyakin, C. Schichor, M. Götz, V. K. Tiwari, B. Treutlein, B. Berninger, Direct pericyte-to-neuron reprogramming via unfolding of a neural stem cell-like program. *Nat. Neurosci.* **21**, 932–940 (2018).

598. Y. Cui, Y. Zheng, X. Liu, L. Yan, X. Fan, J. Yong, Y. Hu, J. Dong, Q. Li, X. Wu, S. Gao, J. Li, L. Wen, J. Qiao, F. Tang, Single-Cell Transcriptome Analysis Maps the Developmental Track of the Human Heart. *Cell Rep.* **26**, 1934-1950.e5 (2019).

599. N. Aizarani, A. Saviano, Sagar, L. Mailly, S. Durand, J. S. Herman, P. Pessaux, T. F. Baumert, D. Grün, Sagar, L. Mailly, S. Durand, J. S. Herman, P. Pessaux, T. F. Baumert, D. Grün, A human liver cell atlas reveals heterogeneity and epithelial progenitors. *Nature*. **572**, 199–204 (2019).

600. K. J. Travaglini, A. N. Nabhan, L. Penland, R. Sinha, A. Gillich, R. V Sit, S. Chang, S. D. Conley, Y. Mori, J. Seita, G. J. Berry, J. B. Shrager, R. J. Metzger, C. S. Kuo, N. Neff, I. L. Weissman, S. R. Quake, M. A. Krasnow, A molecular cell atlas of the human lung from single-cell RNA sequencing. *Nature*. **587**, 619–625 (2020).

601. A. B. Rubenstein, G. R. Smith, U. Raue, G. Begue, K. Minchev, F. Ruf-Zamojski, V. D. Nair, X. Wang, L. Zhou, E. Zaslavsky, T. A. Trappe, S. Trappe, S. C. Sealfon, Single-cell transcriptional profiles in human skeletal muscle. *Sci. Rep.* **10**, 229 (2020).

602. V. K. Mootha, C. M. Lindgren, K.-F. Eriksson, A. Subramanian, S. Sihag, J. Lehar, P. Puigserver, E. Carlsson, M. Ridderstråle, E. Laurila, N. Houstis, M. J. Daly, N. Patterson, J. P. Mesirov, T. R. Golub, P. Tamayo, B. Spiegelman, E. S. Lander, J. N. Hirschhorn, D. Altshuler, L. C. Groop, PGC-1α-responsive genes involved in oxidative phosphorylation are coordinately downregulated in human diabetes. *Nat. Genet.* **34**, 267–273 (2003).

603. A. Subramanian, P. Tamayo, V. K. Mootha, S. Mukherjee, B. L. Ebert, M. A. Gillette, A. Paulovich, S. L. Pomeroy, T. R. Golub, E. S. Lander, J. P. Mesirov, Gene set enrichment analysis: A knowledge-based approach for interpreting genome-wide expression profiles. *Proc. Natl. Acad. Sci.* **102**, 15545–15550 (2005).

604. C. J. Bult, J. A. Blake, C. L. Smith, J. A. Kadin, J. E. Richardson, A. Anagnostopoulos, R. Asabor, R. M. Baldarelli, J. S. Beal, S. M. Bello, O. Blodgett, N. E. Butler, K. R. Christie,

L. E. Corbani, J. Creelman, M. E. Dolan, H. J. Drabkin, S. L. Giannatto, P. Hale, D. P. Hill, M. Law, A. Mendoza, M. McAndrews, D. Miers, H. Motenko, L. Ni, H. Onda, M. Perry, J. M. Recla, B. Richards-Smith, D. Sitnikov, M. Tomczuk, G. Tonorio, L. Wilming, Y. Zhu, Mouse Genome Database (MGD) 2019. *Nucleic Acids Res.* **47**, D801–D806 (2019).

605. L. McInnes, J. Healy, J. Melville, UMAP: Uniform manifold approximation and projection for dimension reduction. *arXiv* (2018) (available at http://arxiv.org/abs/1802.03426).

606. C. Bondjers, M. Kalén, M. Hellström, S. J. Scheidl, A. Abramsson, O. Renner, P. Lindahl, H. Cho, J. Kehrl, C. Betsholtz, Transcription profiling of platelet-derived growth factor-B-deficient mouse embryos identifies RGS5 as a novel marker for pericytes and vascular smooth muscle cells. *Am. J. Pathol.* **162**, 721–729 (2003).

607. S. M. Gritz, R. A. Radcliffe, Genetic effects of ATP1A2 in familial hemiplegic migraine type II and animal models. *Hum. Genomics*. **7**, 8 (2013).

608. C. A. Rich, S. N. Perera, J. Andratschke, C. C. Stolt, D. P. Buehler, E. M. Southard-Smith, M. Wegner, S. Britsch, C. V. H. Baker, Olfactory ensheathing cells abutting the embryonic olfactory bulb express Frzb, whose deletion disrupts olfactory axon targeting. *Glia*. **66**, 2617–2631 (2018).

609. B. Tepe, M. C. Hill, B. T. Pekarek, P. J. Hunt, T. J. Martin, J. F. Martin, B. R. Arenkiel, Single-Cell RNA-Seq of Mouse Olfactory Bulb Reveals Cellular Heterogeneity and Activity-Dependent Molecular Census of Adult-Born Neurons. *Cell Rep.* **25**, 2689-2703.e3 (2018).

610. K. R. Parker, D. Migliorini, E. Perkey, K. E. Yost, A. Bhaduri, P. Bagga, M. Haris, N. E. Wilson, F. Liu, K. Gabunia, J. Scholler, T. J. Montine, V. G. Bhoj, R. Reddy, S. Mohan, I. Maillard, A. R. Kriegstein, C. H. June, H. Y. Chang, A. D. Posey, A. T. Satpathy, Single-Cell Analyses Identify Brain Mural Cells Expressing CD19 as Potential Off-Tumor Targets for CAR-T Immunotherapies. *Cell*. **183**, 126-142.e17 (2020).

611. L. Muhl, L. He, Y. Sun, M. Andaloussi Mäe, R. Pietilä, J. Liu, G. Genové, L. Zhang, Y. Xie, S. Leptidis, G. Mocci, S. Stritt, A. Osman, A. Anisimov, K. A. Hemanthakumar, M. Räsänen, E. M. Hansson, J. Björkegren, M. Vanlandewijck, K. Blomgren, T. Mäkinen, X.-R. Peng, Y. Hu, P. Ernfors, T. D. Arnold, K. Alitalo, U. Lendahl, C. Betsholtz, *Stem cell reports*, in press, doi:10.1016/j.stemcr.2022.03.016.

612. Y. Zhu, G. Clair, W. B. Chrisler, Y. Shen, R. Zhao, A. K. Shukla, R. J. Moore, R. S. Misra, G. S. Pryhuber, R. D. Smith, C. Ansong, R. T. Kelly, S. Proteomics, Y. Zhu, G. Clair, W. B. Chrisler, Y. Shen, R. Zhao, A. K. Shukla, R. J. Moore, R. S. Misra, G. S. Pryhuber, R. D. Smith, C. Ansong, R. T. Kelly, Proteomic Analysis of Single Mammalian Cells Enabled by Microfluidic Nanodroplet Sample Preparation and Ultrasensitive NanoLC-MS. *Angew. Chemie Int. Ed.* **57**, 12370–12374 (2018).

613. M. Asp, S. Giacomello, L. Larsson, C. Wu, D. Fürth, X. Qian, E. Wärdell, J. Custodio, J. Reimegård, F. Salmén, C. Österholm, P. L. Ståhl, E. Sundström, E. Åkesson, O.

Bergmann, M. Bienko, A. Månsson-Broberg, M. Nilsson, C. Sylvén, J. Lundeberg, A Spatiotemporal Organ-Wide Gene Expression and Cell Atlas of the Developing Human Heart. *Cell*. **179**, 1647-1660.e19 (2019).

614. S. G. Rodriques, R. R. Stickels, A. Goeva, C. A. Martin, E. Murray, C. R. Vanderburg, J. Welch, L. M. Chen, F. Chen, E. Z. Macosko, Slide-seq: A scalable technology for measuring genome-wide expression at high spatial resolution. *Science (80-.).* **363**, 1463–1467 (2019).

615. C. Ortiz, J. F. Navarro, A. Jurek, A. Märtin, J. Lundeberg, K. Meletis, Molecular atlas of the adult mouse brain. *Sci. Adv.* **6**, eabb3446 (2020).

616. J. Korn, B. Christ, R. Kurz, H. Kurz, R. Kurz, H. Kurz, Neuroectodermal origin of brain pericytes and vascular smooth muscle cells. *J. Comp. Neurol.* **442**, 78–88 (2002).

617. C. Soderblom, X. Luo, E. Blumenthal, E. Bray, K. Lyapichev, J. Ramos, V. Krishnan, C. Lai-Hsu, K. K. Park, P. Tsoulfas, J. K. Lee, Perivascular Fibroblasts Form the Fibrotic Scar after Contusive Spinal Cord Injury. *J. Neurosci.* **33**, 13882–13887 (2013).

618. A. R. Calabria, E. V Shusta, A Genomic Comparison of *in vivo* and *in vitro* Brain Microvascular Endothelial Cells. *J. Cereb. Blood Flow Metab.* **28**, 135–148 (2008).

619. T. Sato, Neural crest determination by co-activation of Pax3 and Zic1 genes in Xenopus ectoderm. *Development*. **132**, 2355–2363 (2005).

620. J. Shen, G. Xu, R. Zhu, J. Yuan, Y. Ishii, T. Hamashima, T. Matsushima, S. Yamamoto, Y. Takatsuru, J. Nabekura, M. Sasahara, PDGFR-β restores blood-brain barrier functions in a mouse model of focal cerebral ischemia. *J. Cereb. Blood Flow Metab.* **39**, 1501–1515 (2019).

621. Q. Liu, R. Radwanski, R. Babadjouni, A. Patel, D. M. Hodis, P. Baumbacher, Z. Zhao, B. Zlokovic, W. J. Mack, Experimental chronic cerebral hypoperfusion results in decreased pericyte coverage and increased blood–brain barrier permeability in the corpus callosum. *J. Cereb. Blood Flow Metab.* **39**, 240–250 (2019).

622. W. A. Banks, A. Kovac, Y. Morofuji, Neurovascular unit crosstalk: Pericytes and astrocytes modify cytokine secretion patterns of brain endothelial cells. *J. Cereb. Blood Flow Metab.* **38**, 1104–1118 (2018).

623. P. T. Ronaldson, T. P. Davis, Regulation of blood–brain barrier integrity by microglia in health and disease: A therapeutic opportunity. *J. Cereb. Blood Flow Metab.* **40**, S6–S24 (2020).

624. Z. Zheng, M. Chopp, J. Chen, Multifaceted roles of pericytes in central nervous system homeostasis and disease. *J. Cereb. Blood Flow Metab.* **40**, 1381–1401 (2020).

625. K. Kisler, A. M. Nikolakopoulou, M. D. Sweeney, D. Lazic, Z. Zhao, B. V. Zlokovic, Acute Ablation of Cortical Pericytes Leads to Rapid Neurovascular Uncoupling. *Front. Cell. Neurosci.* **14**, 1–8 (2020).

626. S. Grubb, C. Cai, B. O. Hald, L. Khennouf, R. P. Murmu, A. G. K. Jensen, J. Fordsmann, S. Zambach, M. Lauritzen, Precapillary sphincters maintain perfusion in the cerebral cortex. *Nat. Commun.* **11**, 395 (2020).

627. A. Armulik, A. Abramsson, C. Betsholtz, Endothelial/pericyte interactions. *Circ. Res.* **97**, 512–523 (2005).

628. E. Yamanishi, M. Takahashi, Y. Saga, N. Osumi, Penetration and differentiation of cephalic neural crest-derived cells in the developing mouse telencephalon. *Dev. Growth Differ.* **54**, 785–800 (2012).

629. H. C. Etchevers, G. Couly, C. Vincent, N. M. Le Douarin, Anterior cephalic neural crest is required for forebrain viability. *Development*. **126**, 3533–43 (1999).

630. H. Wurdak, Inactivation of TGFβ signaling in neural crest stem cells leads to multiple defects reminiscent of DiGeorge syndrome. *Genes Dev.* **19**, 530–535 (2005).

631. N. M. Shah, a K. Groves, D. J. Anderson, Alternative neural crest cell fates are instructively promoted by TGFbeta superfamily members. *Cell*. **85**, 331–43 (1996).

632. L. Menendez, T. a. Yatskievych, P. B. Antin, S. Dalton, L. Menendez, T. a. Yatskievych, P. B. Antin, S. Dalton, Wnt signaling and a Smad pathway blockade direct the differentiation of human pluripotent stem cells to multipotent neural crest cells. *Proc. Natl. Acad. Sci.* **109**, 9220–9220 (2012).

633. G. Lee, H. Kim, Y. Elkabetz, G. Al Shamy, G. Panagiotakos, T. Barberi, V. Tabar, L. Studer, Isolation and directed differentiation of neural crest stem cells derived from human embryonic stem cells. *Nat. Biotechnol.* **25** (2007), doi:10.1038/nbt1365.

634. B. D. Gastfriend, S. P. Palecek, E. V Shusta, Modeling the blood–brain barrier: Beyond the endothelial cells. *Curr. Opin. Biomed. Eng.* **5**, 6–12 (2018).

635. J. Yu, K. Hu, K. Smuga-Otto, S. Tian, R. Stewart, I. I. Slukvin, J. A. Thomson, Human Induced Pluripotent Stem Cells Free of Vector and Transgene Sequences. *Science (80-.).* **324**, 797–801 (2009).

636. G. Chen, D. R. Gulbranson, Z. Hou, J. M. Bolin, V. Ruotti, M. D. Probasco, K. Smuga-Otto, S. E. Howden, N. R. Diol, N. E. Propson, R. Wagner, G. O. Lee, J. Antosiewicz-Bourget, J. M. C. Teng, J. A. Thomson, Chemically defined conditions for human iPSC derivation and culture. *Nat. Methods*. **8**, 424–9 (2011).

637. J. L. Everson, D. M. Fink, J. W. Yoon, E. J. Leslie, H. W. Kietzman, L. J. Ansen-Wilson, H. M. Chung, D. O. Walterhouse, M. L. Marazita, R. J. Lipinski, Sonic hedgehog regulation of *Foxf2* promotes cranial neural crest mesenchyme proliferation and is disrupted in cleft lip morphogenesis. *Development*. **144**, 2082–2091 (2017).

638. A. Dobin, C. A. Davis, F. Schlesinger, J. Drenkow, C. Zaleski, S. Jha, P. Batut, M. Chaisson, T. R. Gingeras, STAR: Ultrafast universal RNA-seq aligner. *Bioinformatics*. **29**, 15–21 (2013).

639. Y. Liao, G. K. Smyth, W. Shi, FeatureCounts: An efficient general purpose program for assigning sequence reads to genomic features. *Bioinformatics*. **30**, 923–930 (2014).

640. M. Kanehisa, S. Goto, KEGG: kyoto encyclopedia of genes and genomes. *Nucleic Acids Res.* **28**, 27–30 (2000).

641. M. Ashburner, C. A. Ball, J. A. Blake, D. Botstein, H. Butler, J. M. Cherry, A. P. Davis, K. Dolinski, S. S. Dwight, J. T. Eppig, M. A. Harris, D. P. Hill, L. Issel-Tarver, A. Kasarskis, S. Lewis, J. C. Matese, J. E. Richardson, M. Ringwald, G. M. Rubin, G. Sherlock, Gene ontology: tool for the unification of biology. The Gene Ontology Consortium. *Nat. Genet.* **25**, 25–9 (2000).

642. F. A. Wolf, P. Angerer, F. J. Theis, SCANPY: large-scale single-cell gene expression data analysis. *Genome Biol.* **19**, 15 (2018).

643. M. E. Floy, S. E. Givens, O. B. Matthys, T. D. Mateyka, C. M. Kerr, A. B. Steinberg, A. C. Silva, J. Zhang, Y. Mei, B. M. Ogle, T. C. McDevitt, T. J. Kamp, S. P. Palecek, Developmental lineage of human pluripotent stem cell-derived cardiac fibroblasts affects their functional phenotype. *FASEB J.* **35**, 1–23 (2021).

644. R. Lehal, J. Zaric, M. Vigolo, C. Urech, V. Frismantas, N. Zangger, L. Cao, A. Berger, I. Chicote, S. Loubéry, S. H. Choi, U. Koch, S. C. Blacklow, H. G. Palmer, B. Bornhauser, M. González-Gaitán, Y. Arsenijevic, V. Zoete, J. C. Aster, J. P. Bourquin, F. Radtke, Pharmacological disruption of the Notch transcription factor complex. *Proc. Natl. Acad. Sci. U. S. A.* **117**, 16292–16301 (2020).

645. R. Soldatov, M. Kaucka, M. E. Kastriti, J. Petersen, T. Chontorotzea, L. Englmaier, N. Akkuratova, Y. Yang, M. Häring, V. Dyachuk, C. Bock, M. Farlik, M. L. Piacentino, F. Boismoreau, M. M. Hilscher, C. Yokota, X. Qian, M. Nilsson, M. E. Bronner, L. Croci, W.-Y. Hsiao, D. A. Guertin, J.-F. Brunet, G. G. Consalez, P. Ernfors, K. Fried, P. V. Kharchenko, I. Adameyko, Spatiotemporal structure of cell fate decisions in murine neural crest. *Science (80-.).* **364**, eaas9536 (2019).

646. D. Bhattacharya, M. Rothstein, A. P. Azambuja, M. Simoes-Costa, Control of neural crest multipotency by Wnt signaling and the Lin28/let-7 axis. *Elife*. **7**, 1–24 (2018).

647. Y. Kubota, H. K. Kleinman, G. R. Martin, T. J. Lawley, Role of laminin and basement membrane in the morphological differentiation of human endothelial cells into capillary-like structures. *J. Cell Biol.* **107**, 1589–1598 (1988).

648. B. Lilly, S. Kennard, Differential gene expression in a coculture model of angiogenesis reveals modulation of select pathways and a role for Notch signaling. *Physiol. Genomics*. **36**, 69–78 (2009).

649. A. L. Gonzales, N. R. Klug, A. Moshkforoush, J. C. Lee, F. K. Lee, B. Shui, N. M. Tsoukias, M. I. Kotlikoff, D. Hill-Eubanks, M. T. Nelson, Contractile pericytes determine the direction of blood flow at capillary junctions. *Proc. Natl. Acad. Sci. U. S. A.* **117**, 27022–27033 (2020).

650. S. Chen, R. J. Lechleider, Transforming growth factor-beta-induced differentiation of smooth muscle from a neural crest stem cell line. *Circ. Res.* **94**, 1195–202 (2004).

651. L. A. Brown, P. Sava, C. Garcia, A. L. Gonzalez, Proteomic Analysis of the Pericyte Derived Extracellular Matrix. *Cell. Mol. Bioeng.* **8**, 349–363 (2015).

652. B. D. Gastfriend, H. Nishihara, S. G. Canfield, K. L. Foreman, B. Engelhardt, S. P. Palecek, E. V Shusta, Wnt signaling mediates acquisition of blood–brain barrier properties in naïve endothelium derived from human pluripotent stem cells. *Elife*. **10** (2021), doi:10.7554/eLife.70992.

653. B. K. Koo, M. Spit, I. Jordens, T. Y. Low, D. E. Stange, M. Van De Wetering, J. H. Van Es, S. Mohammed, A. J. R. Heck, M. M. Maurice, H. Clevers, Tumour suppressor RNF43 is a stem-cell E3 ligase that induces endocytosis of Wnt receptors. *Nature*. **488**, 665–669 (2012).

654. E. Stanganello, S. Scholpp, Role of cytonemes in Wnt transport. *J. Cell Sci.* **129**, 665–672 (2016).

655. Y. Miao, A. Ha, W. de Lau, K. Yuki, A. J. M. Santos, C. You, M. H. Geurts, J. Puschhof, C. Pleguezuelos-Manzano, W. C. Peng, R. Senlice, C. Piani, J. W. Buikema, O. M. Gbenedio, M. Vallon, J. Yuan, S. de Haan, W. Hemrika, K. Rösch, L. T. Dang, D. Baker, M. Ott, P. Depeille, S. M. Wu, J. Drost, R. Nusse, J. P. Roose, J. Piehler, S. F. Boj, C. Y. Janda, H. Clevers, C. J. Kuo, K. C. Garcia, Next-Generation Surrogate Wnts Support Organoid Growth and Deconvolute Frizzled Pleiotropy In Vivo. *Cell Stem Cell*. **27**, 840-851.e6 (2020).

656. H. Nishihara, B. D. Gastfriend, P. Kasap, S. P. Palecek, E. V. Shusta, B. Engelhardt, Differentiation of human pluripotent stem cells to brain microvascular endothelial cell-like cells suitable to study immune cell interactions. *STAR Protoc.* **2**, 100563 (2021).

657. X. Lian, J. Zhang, S. M. Azarin, K. Zhu, L. B. Hazeltine, X. Bao, C. Hsiao, T. J. Kamp, S. P. Palecek, Directed cardiomyocyte differentiation from human pluripotent stem cells by modulating Wnt/β-catenin signaling under fully defined conditions. *Nat. Protoc.* **8**, 162–75 (2013).

658. S. D. Lundy, W. Z. Zhu, M. Regnier, M. A. Laflamme, Structural and functional maturation of cardiomyocytes derived from human pluripotent stem cells. *Stem Cells Dev.* **22**, 1991–2002 (2013).

659. M. E. Floy, F. Shabnam, A. D. Simmons, V. J. Bhute, G. Jin, W. A. Friedrich, A. B. Steinberg, S. P. Palecek, Advances in Manufacturing Cardiomyocytes from Human Pluripotent Stem Cells. *Annu. Rev. Chem. Biomol. Eng.* **13** (2022), doi:10.1146/annurev-chembioeng-092120-033922.

660. C. R. Nicholas, J. Chen, Y. Tang, D. G. Southwell, N. Chalmers, D. Vogt, C. M. Arnold, Y. J. J. Chen, E. G. Stanley, A. G. Elefanty, Y. Sasai, A. Alvarez-Buylla, J. L. R. Rubenstein, A. R. Kriegstein, Functional maturation of hPSC-derived forebrain interneurons requires an extended timeline and mimics human neural development. *Cell*

Stem Cell. **12**, 573–586 (2013).

661. C. T. Fakhry, P. Choudhary, A. Gutteridge, B. Sidders, P. Chen, D. Ziemek, K. Zarringhalam, Interpreting transcriptional changes using causal graphs: New methods and their practical utility on public networks. *BMC Bioinformatics*. **17**, 1–15 (2016).

662. M. P. Kumar, J. Du, G. Lagoudas, Y. Jiao, A. Sawyer, D. C. Drummond, D. A. Lauffenburger, A. Raue, Analysis of Single-Cell RNA-Seq Identifies Cell-Cell Communication Associated with Tumor Characteristics. *Cell Rep.* **25**, 1458-1468.e4 (2018).

663. S. Jin, C. F. Guerrero-Juarez, L. Zhang, I. Chang, R. Ramos, C. H. Kuan, P. Myung, M. V. Plikus, Q. Nie, Inference and analysis of cell-cell communication using CellChat. *Nat. Commun.* **12**, 1–20 (2021).

664. D. Dimitrov, D. Türei, C. Boys, J. S. Nagai, R. O. Ramirez Flores, H. Kim, B. Szalai, I. G. Costa, A. Dugourd, A. Valdeolivas, J. Saez-Rodriguez, *bioRxiv*, in press (available at https://doi.org/10.1101/2021.05.21.445160).

665. C. P. Fulco, M. Munschauer, R. Anyoha, G. Munson, S. R. Grossman, E. M. Perez, M. Kane, B. Cleary, E. S. Lander, J. M. Engreitz, Systematic mapping of functional enhancer-promoter connections with CRISPR interference. *Science (80-.).* **354**, 769–773 (2016).

666. A. Claringbould, J. B. Zaugg, Enhancers in disease: molecular basis and emerging treatment strategies. *Trends Mol. Med.* **27**, 1060–1073 (2021).

667. K. F. Cho, T. C. Branon, S. Rajeev, T. Svinkina, N. D. Udeshi, T. Thoudam, C. Kwak, H. W. Rhee, I. K. Lee, S. A. Carr, A. Y. Ting, Split-TurboID enables contact-dependent proximity labeling in cells. *Proc. Natl. Acad. Sci. U. S. A.* **117** (2020), doi:10.1073/pnas.1919528117.

668. T. Takano, J. T. Wallace, K. T. Baldwin, A. M. Purkey, A. Uezu, J. L. Courtland, E. J. Soderblom, T. Shimogori, P. F. Maness, C. Eroglu, S. H. Soderling, Chemico-genetic discovery of astrocytic control of inhibition in vivo. *Nature*. **588**, 296–302 (2020).

669. L. Cong, F. A. Ran, D. Cox, S. Lin, R. Barretto, N. Habib, P. D. Hsu, X. Wu, W. Jiang, L. A. Marraffini, F. Zhang, Multiplex genome engineering using CRISPR/Cas systems. *Science (80-.).* **339**, 819–823 (2013).

670. L. A. Gilbert, M. A. Horlbeck, B. Adamson, J. E. Villalta, Y. Chen, E. H. Whitehead, C. Guimaraes, B. Panning, H. L. Ploegh, M. C. Bassik, L. S. Qi, M. Kampmann, J. S. Weissman, Genome-Scale CRISPR-Mediated Control of Gene Repression and Activation. *Cell*. **159**, 647–661 (2014).

671. J. D. Buenrostro, B. Wu, H. Y. Chang, W. J. Greenleaf, in *Current Protocols in Molecular Biology* (2015; http://www.ncbi.nlm.nih.gov/pubmed/25559105), vol. 109, pp. 21.29.1-21.29.9.